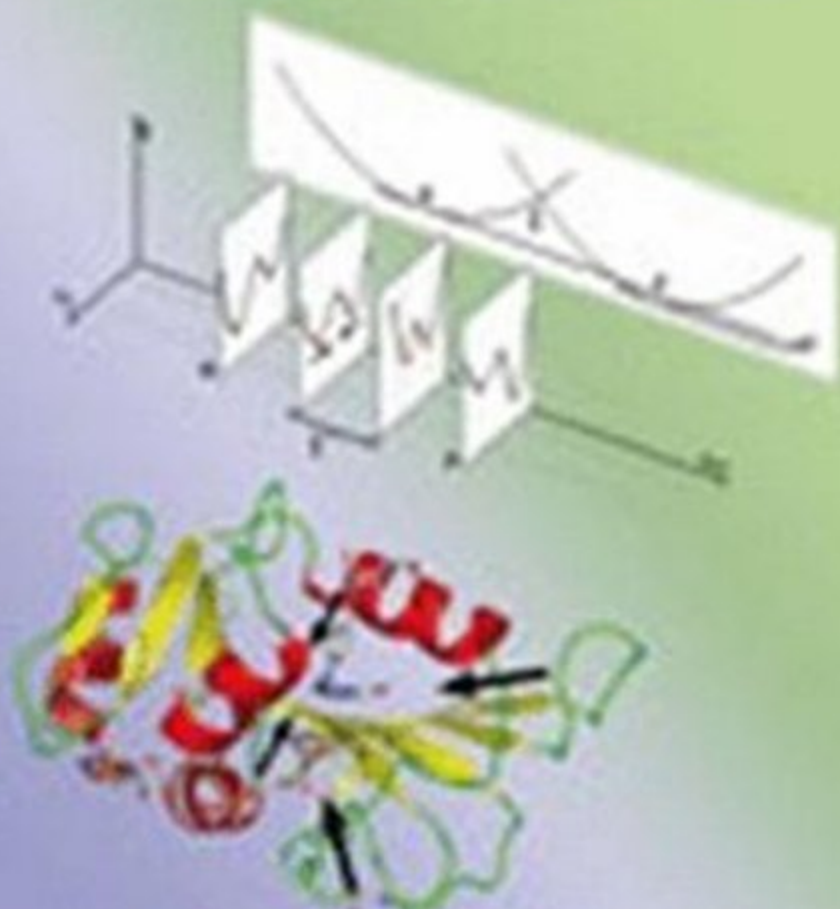


Edited by Rudolf K. Allemann and Nigel S. Scrutton

Quantum Tunnelling in Enzyme-Catalysed Reactions



Quantum Tunnelling in Enzyme-Catalysed Reactions

RSC Biomolecular Sciences

Editorial Board:

Professor Stephen Neidle (Chairman), *The School of Pharmacy, University of London, UK*

Dr Simon F Campbell CBE, FRS

Dr Marius Clore, *National Institutes of Health, USA*

Professor David M J Lilley FRS, *University of Dundee, UK*

This Series is devoted to coverage of the interface between the chemical and biological sciences, especially structural biology, chemical biology, bio and chemo informatics, drug discovery and development, chemical enzymology and biophysical chemistry. Ideal as reference and state of the art guides at the graduate and post graduate level.

Titles in the Series:

Biophysical and Structural Aspects of Bioenergetics

Edited by Märten Wikstrom, *University of Helsinki, Finland*

Computational and Structural Approaches to Drug Discovery: Ligand Protein Interactions

Edited by Robert M Stroud and Janet Finer Moore, *University of California in San Francisco, USA*

Exploiting Chemical Diversity for Drug Discovery

Edited by Paul A. Bartlett, *University of California, USA* and Michael Entzeroth, *S*Bio Pte Ltd, Singapore*

Metabolomics, Metabonomics and Metabolite Profiling

Edited by William J. Griffiths, *University of London, UK*

Nucleic Acid Metal Ion Interactions

Edited by Nicholas V. Hud, *Georgia Institute of Technology, USA*

Oxidative Folding of Peptides and Proteins

Edited by Johannes Buchner, *Technical University of Munich, Germany* and

Luis Moroder, *Max Planck Institute, Germany*

Protein Carbohydrate Interactions in Infectious Disease

Edited by Carole A. Bewley, *National Institutes of Health, USA*

Protein Folding, Misfolding and Aggregation: Classical Themes and Novel Approaches

Edited by Victor Muñoz, *University of Maryland, USA*

Protein Nucleic Acid Interactions: Structural Biology

Edited by Phoebe A. Rice, *The University of Chicago, USA* and Carl C. Correll, *Rosalind Franklin University, USA*

Quadruplex Nucleic Acids

Edited by Stephen Neidle, *University of London, UK* and Shankar Balasubramanian, *University of Cambridge, UK*

Quantum Tunnelling in Enzyme Catalysed Reactions

Edited by Nigel S. Scrutton, *University of Manchester, UK* and Rudolf K. Allemand, *Cardiff University, UK*

Ribozymes and RNA Catalysis

Edited by David MJ Lilley FRS, *University of Dundee, UK* and Fritz Eckstein, *Max Planck Institut for Experimental Medicine, Germany*

Sequence specific DNA Binding Agents

Edited by Michael Waring, *University of Cambridge, UK*

Structural Biology of Membrane Proteins

Edited by Reinhard Grisshammer and Susan K. Buchanan, *National Institutes of Health, USA*

Structure based Drug Discovery: An Overview

Edited by Roderick E. Hubbard, *University of York, UK* and Vernalis (R&D) Ltd, *UK*

Therapeutic Oligonucleotides

Edited by Jens Kurreck, *Free University, Germany*

Visit our website at www.rsc.org/biomolecularsciences

For further information please contact:

Sales and Customer Care, Royal Society of Chemistry, Thomas Graham House,

Science Park, Milton Road, Cambridge, CB4 0WF, UK

Telephone: +44 (0)1223 432360, Fax: +44 (0)1223 426017, Email: sales@rsc.org

Quantum Tunnelling in Enzyme-Catalysed Reactions

Edited by

Rudolf K. Allemann

School of Chemistry, Cardiff University, Cardiff, UK

Nigel S. Scrutton

*Manchester Interdisciplinary Biocentre, University of Manchester, Manchester,
UK*

RSC Publishing

ISBN: 978 0 85404 122 0

A catalogue record for this book is available from the British Library

© Royal Society of Chemistry 2009

All rights reserved

Apart from fair dealing for the purposes of research for non commercial purposes or for private study, criticism or review, as permitted under the Copyright, Designs and Patents Act 1988 and the Copyright and Related Rights Regulations 2003, this publication may not be reproduced, stored or transmitted, in any form or by any means, without the prior permission in writing of The Royal Society of Chemistry or the copyright owner, or in the case of reproduction in accordance with the terms of licences issued by the Copyright Licensing Agency in the UK, or in accordance with the terms of the licences issued by the appropriate Reproduction Rights Organization outside the UK. Enquiries concerning reproduction outside the terms stated here should be sent to The Royal Society of Chemistry at the address printed on this page.

Published by The Royal Society of Chemistry,
Thomas Graham House, Science Park, Milton Road,
Cambridge CB4 0WF, UK

Registered Charity Number 207890

For further information see our website at www.rsc.org

FOREWORD

Beyond the Historical Perspective on Hydrogen and Electron Transfers

RUDOLPH A. MARCUS

Noyes Laboratory of Chemical Physics, California Institute of Technology,
Pasadena, CA, USA

Abstract

A brief overview of proton and electron transfer history is given, and various features influencing enzymatic catalysis are discussed. Examples of generic behavior are considered, together with questions that can be addressed for both experimental and computational results. Examples of high and low pre-exponential factors A of the intrinsic rate constant k_H ranging from $\sim 10^{17} \text{ s}^{-1}$ to $\sim 10^4 \text{ s}^{-1}$ and normal ($\sim 10^{13}$) are noted with significant error bars and discussed.

This series of chapters covers almost every aspect of reactions in enzyme catalysis from many leading participants in the field. They range from pedagogic descriptions of the relevant quantum theory and quantum/classical theoretical methodology to the description of experimental results. The theoretical interpretation of these large systems includes both quantum-mechanical and statistical-mechanical computations, as well as simple more approximate models.

Most of the chapters focus on enzymatic catalysis of hydride, proton and $\text{H}\cdot$ transfer, an example of the latter being proton-coupled electron transfer. There is also a chapter on electron transfer in proteins, timely since the theoretical framework evolved some fifty years ago for treating electron transfers has been adapted to H -transfers and electron transfers in proteins. It is perhaps therefore of some interest to recall briefly some of the early history in the proton- and electron-transfer fields, briefly since the history covers some 85 or so years.

Brönsted's treatment of acid–base catalysis originated in the 1920s and involved in part the transfer of a proton from one reactant to another. It focused on linear kinetic-thermodynamic plots such as the logarithm of the reaction rate *vs.* some thermodynamic measure of the effect of the driving force of the reaction, for example, the logarithm of an acid or base strength (dissociation constant). These linear free-energy plots were subsequently applied to many other types of reaction rates in solution. A deviation from linearity was found by Eigen in the 1950s in his studies of very fast proton-transfer reactions. The deviation occurred at a high driving force. Ultimately, the reaction rate was limited by the rate of diffusion of the reactants toward each other. Many conferences were held on the theme of linear free-energy relations in chemical reaction rates.

In the late 1940s and in the 1950s, experiments on electron-transfer reactions between ions in solution differing only in their valence state were initiated using isotopes as radioactive tracers. These reactions form the simplest class of reactions in all of chemistry, no chemical bonds being broken or formed in some cases and there being zero chemical “driving force” – zero standard free energy of reaction. Such experimental studies provided information thereby on other factors that influence the reaction rate. Based on the results of such studies, Bill Libby in 1952, citing a suggestion of James Franck, introduced the notion of the Franck–Condon (FC) principle controlling the rate of electron transfer. Stimulated by Libby's work, I formulated in 1956 an electron-transfer theory. The task was to satisfy the FC principle without violating (as had previously been done) the law of conservation of energy during the electron transfer. A “reorganisation” of the system had to occur prior to and following the electron transfer in order to satisfy both criteria.

For simplicity, the solvent was treated as a dielectric continuum and a nonequilibrium dielectric polarisation of the solvent at every point was determined by converting the problem to one of thermodynamics of a system with a nonequilibrium dielectric polarisation in the transition state. One distinguished here between the fast (electronic) and slow (nuclear) polarisation of the solvent. In 1960 this work was extended using statistical mechanics instead of the dielectric continuum theory, and now included changes in nuclear configurations of the reactants (*e.g.*, bond lengths and angles). To this end a global reaction coordinate was needed and was introduced to treat the system of some 10^{23} coordinates. The coordinate used was the energy of the products/solvent in their nuclear environment minus that of the reactants/solvent with the same values of the nuclear solvent/vibrational coordinates (the vertical energy difference of the two 10^{23} or so dimensional potential-energy surfaces). It was possible in this way to reduce the description to that of a one-coordinate plot of the free energy of the reactants/solvent (a parabola) and that of the products/solvent along the reaction coordinate (a parabola) and calculate the free energy of activation, the transition state occurring at the intersection of the two parabolas.

The outcome of the theory were many predictions of relations between various types of rate constants, including the effect of driving force, and a hitherto unsuspected effect termed in this 1960 paper the “inverted effect.” It

was verified indirectly some years later, but required some 25 years before a direct verification was made. Much of the brief electron-transfer history mentioned here and the vitally important underlying experimental work has been described in more detail in my Nobel Lecture, as well as in many articles and books by other contributors.

In the case of the transfer of H^+ , H or $\text{H}\cdot$, we again have a transfer of a light particle. The Franck–Condon principle applies, though more weakly, when the mechanism is that of “jumping” of the H from one reactant to the other, a so-called nonadiabatic H transfer. For purposes of understanding some computations and formulating an approximate theory a “protein reorganisation” prior to the H-transfer is treated in this approach, the system proceeding from configurations of the atomic nuclei in the system favourable to the reactants to those favourable to the products *via* those favourable to the transition state (TS). The concepts and the mathematical formalism have been adapted to H-transfers in several ways and are described in a number of chapters in this book.

When the H transfer is not as sudden, for example, in an “adiabatic H transfer”, the reaction $\text{AH} + \text{B} \rightarrow \text{A} + \text{HB}$ (charges not shown) has strong electronic coupling between A and H and between H and B in the transition state. Some deviation from the simple nonadiabatic picture is expected and has been treated in several ways and in some analytic approximations given in the present volume. To treat this case, a different reaction coordinate has also been introduced into many of the computations, such as the length of the incipient newly forming bond minus that of the rupturing bond, for each nuclear configuration of the entire system. (In the enzyme the new coordinate goes from some small negative value of the order of one Å to a positive value of the same order.) We discussed (2007) the challenges of combining in approximate models the “nonadiabatic” nonequilibrium polarisation of the reorganisation of the protein with the adiabatically behaving AHB. The use of computational methods is permitting the detailed investigation of various aspects of adiabatic/nonadiabatic H transfer.

One principal focus in this book, and indeed in its title, is H-tunnelling, introduced into the chemical reaction rate literature in the 1930s by R. P. Bell. He assumed fixed positions of the heavy nuclei. Now, some seventy years later, more advanced treatments are used, as seen in the present volume. For enzymes the effect of tunnelling on the kinetic isotope effect (KIE, $k_{\text{H}}/k_{\text{D}}$) is as large as a factor of the order of 100 or as small as a factor of the order of unity, depending on the system and the experimental conditions. Tunnelling can also occur for reactions in solution of course. In either case tunnelling can be a large effect, though usually smaller than a factor of the order of 100. (The KIE itself is usually smaller than a factor of 100, and part of that is often due to zero-point energy differences for the H and D systems.) It is small compared with a catalytic effect of many orders of magnitude for reactions in enzymes relative to the rates of the corresponding reactions in solution. Nevertheless, the KIE and its temperature dependence are highly instructive.

Two types of $\text{H}\cdot$ transfer have been described in the literature and are found in this volume, a hydrogen-atom transfer (HAT) in which the proton and

electron are transferred from the same atom and another class of proton-coupled electron transfers (PCET) in which they are transferred from different atoms. Examples of both types are considered in this volume.

To understand better the enzymatic results it has been necessary to disentangle the overall reaction rate from the contributions due to the binding of the substrate reactant and of the substrate product to the enzyme – the “commitments”. The rate constant corrected for these commitments, *i.e.* the rate corrected to 100% binding of the substrate reactant and the product (the “intrinsic rate”), is of particular interest in theoretical analyses of the actual H-transfer step. In the study of the intrinsic rate, both the pre-exponential factor A and the activation energy provide added insight. We cite later some examples of A .

In the precomputer age of chemistry the emphasis in theory was on equations, Brönsted, Debye–Hückel, Onsager, Kramers, transition-state theory, RRKM, and many others, and particularly on the functional form of the equations and their applications to interpret and predict experimental data. In fortunate cases, as in electron-transfer reactions, one can relate different properties using the equations without adjustable parameters. Now, with the advent of modern computers, there is an emphasis on the final results of the theoretical computations for individual systems. Indeed, one can now get detailed answers to questions for individual systems that one couldn’t obtain in earlier days, the accuracy of the answers depending on the validity of the approximations made in the model. This volume contains examples of these valuable analyses. One of the few aspects not covered, the use of nuclear magnetic resonance techniques to study couplings and motions in proteins, has been the subject of several recent reviews in the literature.

One might ask what relationships or generalities are there in these enzyme systems, with qualitative or approximately quantitative answers. As we noted in an article in 2007 some of the relationships between experimental data that were predicted for electron transfers are addressable for H-transfers in solution but not for H-transfers in enzymes. For example, one does not have the crossrelations in enzymes relating the rate constants of crossreactions to those of the component self-exchange reactions, nor does one have the wide range of driving force available to proton and electron transfer in solution. In addition in the field of electron transfers one has the relation of the kinetic properties to charge-transfer spectra* and to the rates of ET reactions at electrodes. These predicted relationships and comparisons with experimental data enriched and enlarged the field. The electron-transfer formalism that has frequently been adapted to H-transfers in solution and in proteins includes several features:

(1) There is a work term w_r , a preorganisation of the reactants prior to any chemical change in the bonding and similarly a work term w_p for the reverse reaction, a preorganisation of the products. (The standard free energy of the H transfer step ΔG° was partitioned thereby into a sum $\Delta G_R^\circ + w_r - w_p$). For the

* A rare example of a charge transfer absorption for a group transfer was described for the I •CH₃I system by D.M. Cyr, C.G. Bailey, D. Serxner, M.G. Scarton, M.A. Johnson, *J. Chem. Phys.* 1994, **101**, 10507.

electron transfers for two approaching ions in solution w_r consisted of the electrostatic repulsion of the ions (and any other free-energy barrier that could not be reduced by favourable chemical alteration of the ΔG° for the actual transfer step). Extended to enzymes, w_r now includes both the free energy “barrier” due to a prior selection of substrate/cofactor separation distances, orientations and protein conformations before any protein and bond length/angle “reorganisation”. One cannot obtain w_r experimentally simply by finding the free-energy barrier that exists that cannot be overcome by a sufficiently favourable ΔG_R° , since a large variation of the latter is not practical for enzymes, in contrast to transfers in solution. So there will remain a judgment call on what part of the overall ΔG° to include in w_r . The w_r can be entropic or energetic in nature. For a wild-type enzyme operating at its natural temperature and with its natural substrate and coenzyme this w_r is expected to be smaller than its value for other experimental conditions and than for some mutants. The distance sampling in w_r is sometimes called gating, but the latter can also include additional contributions, such as reorientation of a blocking group.

(2) There is a “reorganisation” of the protein, as well as a change of distances within the reactants (more generally of their geometry) so as to facilitate the H-transfer. The protein reorganisation is approximately a harmonic function of the relevant coordinate, a parabola. The role of bond breaking-bond forming in AHB has been taken into account in several alternate ways. In one approach (empirical valence bond) it is treated *via* a pair of free-energy profiles that are approximately a pair of parabolas for the free energy of reactants and of products, and the resulting energy barrier is corrected by lowering it by a term that contains the element H_{AB} coupling the two valence states, (AH,B) (A,HB). In another approach (2007), the protein reorganisation is again treated using a pair of parabolas for the formation of the TS but a bond-breaking/bond-forming formalism is used for the AHB subsystem. A challenge in the 2007 paper was to combine these quite different approaches for the protein and AHB and calculate the free energy of formation of the TS. The result deviates somewhat from harmonic behaviour in its dependence on ΔG° .

(3) Introduction of tunnelling and the over the barrier crossing contributions of the H-transfer step completes the expression for the rate. The tunnelling depends on the separation distance R as do w_r and the protein reorganisation. The tunnelling contribution in this approximate analysis is calculated at each R and involves an average over R using this R -dependent expression as a weighting factor. The equation for the rate constant of the reverse reaction k_H^{rev} is obtained similarly, and the theoretical expression can be tested to see if the resulting equilibrium constant k_H/k_H^{rev} is independent of w_r and w_p , as it should be.

While detailed computations have been and continue to be highly instructive, it is also useful to consider, as in any field, whether any generalisations, actual or potential, have emerged for enzyme catalysis from the experiments or from the computations or both. Several possibilities are noted below, phrased in part as questions. Their validity and that of others can be explored in further experiments.

(1) Is the intrinsic KIE, namely the ratio of the intrinsic rate constants for H-transfer and D-transfer, k_H/k_D , largely temperature independent for wild-type

enzymes operating with their natural substrates in their natural temperature range of operation, *e.g.*, as in some recent results.^{1–9} One might have argued that such a temperature independence is the result of two opposing tendencies, and that they tend to cancel for these systems. The case of a lipoxygenase,⁹ which shows a weak temperature dependence discussed in this volume, may differ from some other enzymes^{1–8} whose KIE shows essentially no temperature dependence (above any “breakpoint” discussed in (2) below). If this temperature independent behaviour for the intrinsic KIE proves to be widespread, then a delicate balance between two opposing trends appears unlikely. A necessary condition can be imagined for k_H/k_D to be temperature-independent, namely that there be little or no w_r arising from the stretching of the rupturing H-bond (hence, no isotopically sensitive contribution). A protein reorganisation barrier exists but cancels in the ratio k_H/k_D , and both H and D are transferring from their lowest vibrational state.

(2) Is there some generic explanation as to why a “breakpoint” occurs for some enzymes? At temperatures above a breakpoint the KIE is temperature independent and at temperatures below the breakpoint the KIE is temperature dependent.^{1,5,8} In the case of a particular dihydrofolate reductase⁵ the k_D showed a breakpoint but not k_H , while for a thermophilic alcohol dehydrogenase¹ both plots showed a breakpoint. In each case, the KIE, k_H/k_D , showed a breakpoint. Essentially it is like a phase transition, with a sharp change of the properties of k_H/k_D . Both the activation energy and the entropy of activation for k_H/k_D changed. I don’t recall that this rather abrupt change has been captured as yet in computations. Models can be suggested and explored to understand these results. There can be artifacts if the rate constant is not corrected for the commitments. For example, the observed KIE for a dihydrofolate reductase showed a breakpoint but the intrinsic KIE did not.⁷ At lower temperatures, the commitments presumably became more important and, being isotopically insensitive, reduced the KIE towards unity.

(3) Is the pre-exponential factor A in the intrinsic rate constant, $k = A \exp(-E_a/kT)$, smaller than the typical value 10^{13} s^{-1} for a certain class of reactions? For example, data for soybean lipoxygenase, believed to be a proton-coupled electron-transfer reaction, show that at 30°C $k_H \sim 300 \text{ s}^{-1}$ and $E_a \sim 2 \text{ kcal mol}^{-1}$.⁹ Thereby, $A \sim 10^4 \text{ s}^{-1}$ and so is far smaller rather than 10^{13} s^{-1} . The small A is attributed to poor overlap of the relevant vibrational and electronic wavefunctions. Again, can A be much larger than 10^{13} s^{-1} at temperatures below a breakpoint for some protein? A thermophilic alcohol dehydrogenase has a breakpoint around 30°C .^{1,10,11} The rate constant k_H there is 25 s^{-1} . For $T < 30^\circ\text{C}$ we have $E_a \sim 21 \text{ kcal mol}^{-1}$ and so $A \sim 10^{17} \text{ s}^{-1}$, while just above 30°C we have $E_a \sim 14.5 \text{ kcal mol}$ and a normal value of A , $A \sim 10^{12} \text{ s}^{-1}$.^{10,11} The high A for $T < 30^\circ\text{C}$ cannot be explained by sampling a small subset of reactive conformations. The sampling would create an A much less than 10^{13} s^{-1} rather than much greater. We note that apart from tunnelling we have $A \sim 10^{13} \exp(\Delta S^\ddagger/k) \text{ s}^{-1}$, where ΔS^\ddagger is the entropy of activation of the H-transfer step. The difference in protein flexibility in the initial state above and below the breakpoint has been discussed,^{10,11} using results on the rate of hydrogen-deuterium exchange. A breakpoint has been observed in two thermophilic

enzymes^{1,5} and in a mutant thereof. We return later in some concluding remarks to an analogous behaviour on a very high A that we have noticed for viscous systems and so to a possible explanation of a very high A below the breakpoint.

There is another factor that influences A , and can be expected to arise in some cases (it has not been tested for enzymes, though it is known for reactions in solution). If the standard entropy of reaction ΔS° for that step is different from zero, then when $|\Delta G^\circ|$ is small ΔS^\ddagger contains a term $\sim \Delta S^\circ/2$ arising from this contribution, using the two-parabola formalism for the protein reorganisation. When the reaction is a charge-shift reaction, such as $\text{AH} + \text{B} \rightarrow \text{A} + \text{HB}$, then ΔS° may be close to zero. However, in the case of a charge separation ΔS° can be quite negative, while for charge recombinations it can be quite positive, due to the effect of the charges on the polarisation of the dipolar groups in the protein surrounding AHB. In a model reaction for lipoxygenase ΔS° has been measured for a hydrogen-atom transfer (HAT) where a dicatonic Fe (III) complex is formed from a Fe (II) complex,¹² as well as for other central metal atoms.¹³ The ΔS° was very negative, ~ -30 e.u., reflecting the extra stiffness (more polarised) state of the more highly charge-separated product, contributing *via* $\sim \Delta S^\circ/2$ a factor of $\sim 10^{-3}$ to the pre-exponential factor A .

(4) In some cases mutations some 20 Å from the active site can have a dramatic effect on the catalytic rate.¹⁴ How general is this phenomenon and does its origin lie in an effect on the reorganisation term λ *via* some hydrogenic bonded network, or some effect *via* the network on the local steric properties of the substrate-coenzyme pair and hence on w_r ? The possible effect of mutants on the network is discussed in this volume.

(5) In a comparison of two intrinsic KIEs, $k_{\text{H}}/k_{\text{D}}$, and the carbon isotope effect, ${}^{12}\text{k}/{}^{13}\text{k}$, do they show the same trend as a function of pressure, at least at higher pressures, as in a unique study in the literature¹⁵ (in particular they have a similar value of the intrinsic volume of activation) perhaps reflecting that the C atom is a component of the reaction coordinate in the TS. (Only in a special case is the H-tunnelling a purely H motion.) The effect of pressure on the H/D KIE, $k_{\text{H}}/k_{\text{D}}$, and on k_{H} and k_{D} was studied recently using a single-turnover stopped-flow apparatus.¹⁶ Since the reacting substrate-cofactor complex was fully bound, no correction for commitments was needed. The ratio $k_{\text{H}}/k_{\text{D}}$ increased with increasing pressure, as did k_{H} and k_{D} . Previously steady-state experiments had been made for different enzymes, and the current situation on steady-state and stopped-flow measurements is described in a chapter in the present volume.

The above discussion on the theoretical aspects focused on TS theory, a statistical reaction-rate theory, and one might ask what dynamical aspects can one consider to interpret the behaviour of the protein below the breakpoint. For example, if the protein at temperatures below the breakpoint is sufficiently rigid that the “internal viscosity” of the motion along the reaction coordinate becomes rate controlling, this motion would be diffusive in nature, leading to many (diffusive) recrossings of the transition state region and so, using the arguments introduced by Wigner¹⁷ in his seminal 1938 paper, lead to a rate lower than that given by transition-state theory. Recrossings of the region of

the TS for enzymatic reactions are frequently calculated in current computations, as in this volume. Usually the factor is close to unity, but the value for a “viscous phase” of the protein may not have been studied. To consider the behaviour below the breakpoint it is useful to summarise some earlier studies on recrossings.

We first recall that the role of recrossings in reducing the reaction rate below the TS value can been seen both in Wigner’s important explanation¹⁷ (recrossings cause some of the phase space of the TS to be “wasted”) and explicitly in the equations of Kramers¹⁸ in his celebrated 1940 theory on an internal frictional effect on reaction rate. This characterisation as celebrated is perhaps not inappropriate since his article has received more than 4000 citations.

The classical results in Kramers’ article are for a simple one-coordinate model, but they can be extended approximately to a multidimensional system by introducing a free-energy curve instead of the original one-dimensional potential-energy curve. His TS expression for the rate constant is then $k = v \exp(-\Delta G^*/kT)$, where ΔG^* is the free-energy barrier to reaching the TS (in the present case the sum of w_r plus the contributions due to the protein reorganisation and due to the bond breaking-bond forming terms). The v is the frequency for motion along the reaction coordinate at the bottom of the reactants’ free energy well. At the other limit, the limit of high internal friction coefficient ζ along the reaction coordinate, we have the Kramers’ equation for the “overdamped” limit, $k = (2\pi vv'/\zeta) \exp(-\Delta G^*/kT')$, when $\zeta/2 \gg 2\pi v'$. Here, v' is the frequency of the inverted parabola at the top of the TS barrier. With v and $v' \sim 10^{13} \text{ s}^{-1}$ and $\zeta/2 \gg 2\pi v'$ in the overdamped regime, this $2\pi vv'/\zeta$ factor in the rate constant k is less than 10^{13} s^{-1} , in agreement with an interpretation in terms of recrossings of the TS in this regime.

Some insight into the very high pre-exponential factor of the rate constant at temperatures below the breakpoint can be obtained by comparing the pre-exponential factors in viscous *vs.* nonviscous media obtained from the Kramers’ expressions for the rate constant k . A value of ζ can be estimated from a diffusion constant D and the Einstein equation, $\zeta = kT/mD$, or from the viscosity η and the Stokes equation, $\zeta = 6\pi\eta r/m$, where m and r denote the molecular mass and radius in the liquid (or $\zeta = 4\pi\eta r/m$ for a “stick” boundary condition). For a nonviscous liquid like acetonitrile ζ is about 10^{12} s^{-1} , and so the reacting system is not “overdamped”. For a viscous liquid like glycerol at 30 °C ζ is about 10^{15} s^{-1} , so $2\pi vv'/\zeta$ is significantly less than v and the system is overdamped. The pre-exponential factor in $2\pi vv'/\zeta$ for glycerol is about 10^{20} to 10^{23} s^{-1} depending on the temperature regime. Similarly, for a system such as silica above and below a transition temperature T_g one can calculate from the data¹⁹ that the pre-exponential factor for the viscosity is $\sim 10^6$ times smaller at temperatures below T_g . When introduced into the Kramers’ expression for the (overdamped) rate constant this factor yields a pre-exponential factor greater by a factor of $\sim 10^6$ than that at $T > T_g$. The motion for $T < T_g$ has been treated in the literature as hopping between structures, and as more fluid like for $T > T_g$.

Kramers’ work has been extended to include a frequency-dependent friction $\zeta(v')$ (Grote-Hynes) and to treat reactions where the reaction coordinate has a

fast component plus Kramers' slow diffusive component (Agmon and Hopfield; Sumi, Nadler and the author; Hynes). In both modifications the rate constant will depend less on the low-frequency ζ used above, but nevertheless the high A value found below the breakpoint may have the same origin as its counterpart in other viscous systems.

Current computations do not treat as yet the dynamics of the slow timescales of milliseconds for the overall H-transfer. Nevertheless, they may eventually be able to treat the dynamics of the short individual diffusive steps below the breakpoint at various points along a reaction coordinate and so provide further insight into the properties of the protein below the breakpoint.

The field of enzyme catalysis and H-tunnelling has seen an explosion of studies and understanding. This book provides a volume rich in its breadth and depth for experienced researchers in the field and for those new to it. It is a field where questions and challenges abound.

Bibliography and Acknowledgements

Many authors have made major contributions to the electron-transfer and H-transfer fields, as seen in the copious citations in the present volume. I am indebted to Judith Klinman, Amnon Kohen, Sharon Hammes-Schiffer and Maria-Elisabeth Michel-Beyerle for their helpful comments. The research described in this preface was supported by the National Science Foundation and the Office of Naval Research. Recent reviews and other articles are cited in the author's *J. Phys. Chem. B*, 2007, **111**, 6643 and *J. Chem. Phys.*, 2006, **25**, Art. No. 194504, which also elaborate on several of the topics mentioned here.

References

1. A. Kohen, R. Cannio, S. Bartolucci and J.P. Klinman, *Nature*, 1999, **399**, 496.
2. R.J. Harris, R. Meskys, M.J. Sutcliffe and N.S. Scrutton, *Biochemistry*, 2000, **39**, 1189.
3. J. Basran, M.J. Sutcliffe and N.S. Scrutton, *J. Biol. Chem.*, 2001, **276**, 24581.
4. J.L. Abad, F. Camps and G. Fabrias, *Angew. Chem. Int. Ed.*, 2000, **39**, 3279.
5. G. Maglia and R.K. Allemand, *J. Am. Chem. Soc.*, 2003, **125**, 13372.
6. N. Agarwal, B. Hong, C. Mihai and A. Kohen, *Biochemistry*, 2004, **43**, 1998.
7. R.S. Sikorski, L. Wang, K.A. Markham, P.T.R. Rajagopalan, S.J. Benkovic and A. Kohen, *J. Am. Chem. Soc.*, 2004, **126**, 4778.
8. B. Hong, F. Maley and A. Kohen, *Biochemistry*, 2007, **46**, 14188.
9. M.J. Knapp, K. Rickert and J.P. Klinman, *J. Am. Chem. Soc.*, 2002, **124**, 3865.

10. Z.X. Liang and J.P. Klinman, *Curr. Opin. Struct. Biol.*, 2004, **14**, 648.
11. Z.X. Liang, I. Tsigos, V. Bouriotis and J.P. Klinman, *J. Am. Chem. Soc.*, 2004, **126**, 9500.
12. E.A. Mader, E.R. Davidson and J.M. Mayer, *J. Am. Chem. Soc.*, 2007, **129**, 5153.
13. J.M. Mayer, private communication.
14. P.K. Agarwal, S.R. Billeter, P.T.R. Rajagopalan, S.J. Benkovic and S. Hammes-Schiffer, *Proc. Natl. Acad. Sci. USA*, 2002, **99**, 2794.
15. D.B. Northrop, *Philos. Trans. R. Soc. B.*, 2006, **361**, 1341.
16. S. Hay, M.J. Sutcliffe and N. Scrutton, *Proc. Natl. Acad. Sci. USA*, 2007, **104**, 507.
17. E. Wigner, *Trans. Faraday Soc.*, 1938, **34**, 29.
18. H.J. Kramers, *Physica*, 1940, **7**, 284.
19. R.H. Doremus, *J. Appl. Phys.*, 2002, **90**, 7619.

Preface

Chemical reactions in biological systems rarely occur in the absence of a catalyst. Enzymes are catalysts that often achieve exquisite reaction specificities and substrate selectivities coupled to remarkable rate accelerations relative to the uncatalysed reaction. While selectivity and specificity can often be explained by shape complementarity between enzyme and substrate, an understanding of the physical basis of the rate accelerations has been more difficult to achieve. Transition-state theory has been used as the basis of explanations of enzyme catalysis, but recent theoretical and experimental developments have highlighted potential roles for quantum-mechanical tunnelling in enzyme-catalysed hydrogen transfer. Over the last decade, it has become clear that a simple Bell tunnel correction of transition-state theory is not sufficient to adequately describe such reactions and theories have been developed that have evolved from the Marcus formalism for electron transfer to depict hydrogen transfer within a quantum-mechanical formalism.

Enzyme catalysis is a fascinating research area, which due to its interdisciplinarity is an ideal training ground for those who desire to obtain a broad education in biochemistry and biophysics including structural and molecular biology. We firmly believe that together with a solid training in the core disciplines, this interdisciplinarity will remain the strongest asset that students can acquire during their training in the molecular biosciences. Hence, the purpose of this book is to introduce modern theories of enzyme catalysis to a wide audience with particular emphasis on advanced level undergraduate and PhD students as well as early postdoctoral fellows who are new to the field. The focus is therefore different from recent publications that were geared towards established researchers in the field. In producing an 'early entry' volume our aim is to introduce important and emerging aspects of catalysis in biology to inexperienced workers and to fill the need for an educational resource that is currently unavailable.

RSC Biomolecular Sciences

Quantum Tunnelling in Enzyme Catalysed Reactions

Edited by Rudolf K. Allemann and Nigel S. Scrutton

© Royal Society of Chemistry 2009

Published by the Royal Society of Chemistry, www.rsc.org

While this book on ‘Quantum Tunnelling in Enzyme Catalysed Reactions’ is by no means a complete account of the field, it brings together contributions from many of the leading scientists in the field. Extensive literature citations at the end of each chapter will allow the reader to get a much more detailed insight into the intricacies of enzyme catalysis.

As with any research field, controversies and questions remain. The contributions illustrate the interdisciplinary nature of the field, but also reflect the different views held by practitioners in the field. That quantum tunnelling is a feature of enzyme reactions is now widely accepted, but whether this reflects a ‘catalytic’ contribution is currently vigorously debated. The link (if any) between tunnelling and ‘dynamics’ is a major problem and it remains the source of much discussion. Controversies of this type reflect an active and buoyant field; there is much to learn, challenges to be met and insight to be gained. This is an exciting period for studying enzyme systems, as is evident from the various contributions to this book. We hope the reader gains a sense of this excitement – as we have done in contributing and editing the work.

We are very grateful to all the contributors to this book who very willingly gave up significant amounts of time to contribute to our project and who by and large delivered their chapters promptly. We are also indebted to Dr E. Joel Loveridge for providing the cover picture, and to Drs Mahmoud Akhtar and E. Joel Loveridge for help with the editorial work.

Rudolf K. Allemand (Cardiff, UK)
Nigel S. Scrutton (Manchester, UK)

Contents

Chapter 1 The Transition-State Theory Description of Enzyme Catalysis for Classically Activated Reactions

Barry K. Carpenter

1.1	Introduction	1
1.2	Quantifying the Catalytic Activity of Enzymes	2
1.3	Free-Energy Analysis of Enzyme Catalysis	4
1.4	Transition-State Stabilisation or Ground-State Destabilisation?	8
1.5	Selective Stabilisation of Transition Structures by Enzymes	11
1.6	Enzyme Flexibility and Dynamics	14
	References	16

Chapter 2 Introduction to Quantum Behaviour – A Primer

Sam P. de Visser

2.1	Introduction	18
2.1.1	Classical Mechanics	19
2.2	Quantum Mechanics	19
2.2.1	Heisenberg Uncertainty Principle	19
2.2.2	The Schrödinger Equation	20
2.3	Electronic-Structure Calculations	22
2.3.1	Born–Oppenheimer Approximation	22
2.3.2	Hartree–Fock Theory	22
2.3.3	Basis Sets	25
2.3.4	Zero-Point Energy	26
2.4	Density Functional Theory	28

RSC Biomolecular Sciences

Quantum Tunnelling in Enzyme Catalysed Reactions

Edited by Rudolf K. Allemann and Nigel S. Scrutton

© Royal Society of Chemistry 2009

Published by the Royal Society of Chemistry, www.rsc.org

2.4.1	DFT Calculations of Free Energies of Activation of Enzyme Models	30
2.4.2	DFT Calculations of Kinetic Isotope Effects	31
2.5	Quantum-Mechanics/Molecular-Mechanics Methods	32
2.6	Summary and Outlook	34
	References	34

Chapter 3 Quantum Catalysis in Enzymes

Agnieszka Dybala-Defratyka, Piotr Paneth and Donald G. Truhlar

3.1	Introduction	36
3.2	Theory	39
3.2.1	Gas-Phase Variational Transition-State Theory	39
3.2.2	The Transmission Coefficient	42
3.2.3	Ensemble Averaging	51
3.3	Examples	55
3.3.1	Liver Alcohol Dehydrogenase – A Workhorse for Studying Hydride Transfer	55
3.3.2	Dihydrofolate Reductase – A Paradigmatic System	56
3.3.3	Soybean-Lipoxygenase-1 and Methylmalonyl-CoA Mutase – Enzymes Catalysing Hydrogen Atom Transfer Reactions that Exhibit the Largest KIEs Reported for any Biological System	60
3.3.4	Other Systems and Perspectives	62
3.4	Concluding Remarks	66
	Appendix – Quantum-Mechanical Rate Theory	67
	Acknowledgments	67
	References	67

Chapter 4 Selected Theoretical Models and Computational Methods for Enzymatic Tunnelling

Sharon Hammes-Schiffer

4.1	Introduction	79
4.2	Vibronically Nonadiabatic Reactions: Proton-Coupled Electron Transfer	80
4.2.1	Theory	81
4.2.2	Application to Lipoxygenase	85
4.3	Predominantly Adiabatic Reactions: Proton and Hydride Transfer	89
4.3.1	Theory	90
4.3.2	Application to Dihydrofolate Reductase	94

4.4 Emerging Concepts about Enzyme Catalysis	97
Acknowledgments	100
References	101

Chapter 5 Kinetic Isotope Effects from Hybrid Classical and Quantum Path Integral Computations

Jiali Gao, Kin-Yiu Wong, Dan T. Major, Alessandro Cembran, Lingchun Song, Yen-lin Lin, Yao Fan and Shuhua Ma

5.1 Introduction	105
5.2 Theoretical Background	107
5.2.1 Path Integral Quantum Transition-State Theory	107
5.2.2 Centroid Path Integral Simulations	110
5.2.3 Kinetic Isotope Effects	111
5.3 Potential-Energy Surface	116
5.3.1 Combined QM/MM Potentials	116
5.3.2 The MOVB Potential	118
5.4 Computational Details	119
5.5 Illustrative Examples	120
5.5.1 Proton Transfer between Nitroethane and Acetate Ion	120
5.5.2 The Decarboxylation of N-Methyl Picolinate	123
5.5.3 Proton Transfer between Chloroacetic Acid and Substituted α -Methoxystyrenes	126
5.6 Concluding Remarks	126
Acknowledgments	127
References	127

Chapter 6 Beyond Tunnelling Corrections: Full Tunnelling Models for Enzymatic C–H Activation Reactions

Judith P. Klinman

6.1 Introduction to Enzymatic C–H Activation Reactions	132
6.1.1 Methods of Study	132
6.1.2 The Semiclassical Origin of the Kinetic Isotope Effect	135
6.2 Detection of Hydrogen Tunnelling in the Context of a “Tunnelling Correction”	136
6.2.1 The Bell Correction	136
6.2.2 Implications for Swain–Schaad Relationships	137
6.2.3 Implication for Arrhenius Behaviour	139
6.3 Nonclassical Behaviour that Fails to Conform to the Tunnelling Correction	142

6.3.1	Swain–Schaad Relationships	142
6.3.2	Arrhenius-Behaviour Deviations	143
6.4	Full Tunnelling Behaviour under Physiological Conditions	145
6.4.1	Formalising H-transfer in the Context of Electron Tunnelling	145
6.4.2	A Simple Physical Model for H-tunnelling	145
6.5	Soybean Lipoxygenase-1 (SLO-1) as a Prototype of Full Tunnelling in an Enzyme	149
6.5.1	Overview of the Isotopic Properties of SLO-1 Catalysis	149
6.5.2	The Temperature Dependence of KIEs in the SLO-1 Reaction	150
6.6	Conclusions and Implications for Our Understanding of Enzyme Catalysis	155
	References	157

Chapter 7 Quantum Effects in Enzyme Kinetics

Arundhuti Sen and Amnon Kohen

7.1	Introduction	161
7.2	Kinetic Isotope Effects: Basic Terms and Concepts	163
7.2.1	Defining KIEs	163
7.2.2	Swain–Schaad Relationships for 1° and 2° KIEs	164
7.2.3	Kinetic Complexity	165
7.2.4	Coupling and Coupled Motion	168
7.2.5	Experimental Methods and Design	168
7.3	KIEs as Probes for Tunnelling	170
7.3.1	The Size of the KIE	170
7.3.2	Comparison of 2° KIEs and 2° EIEs	171
7.3.3	Deviations from Semiclassical 2° Swain–Schaad Relationships	171
7.3.4	Temperature Dependence of the KIEs	172
7.4	Test Cases: Alcohol Dehydrogenase, Dihydrofolate Reductase and Thymidylate Synthase	174
7.4.1	Alcohol Dehydrogenase	174
7.4.2	Dihydrofolate Reductase	175
7.4.3	Thymidylate Synthase	176
7.5	Conclusions	176
	References	176

Chapter 8 Direct Methods for the Analysis of Quantum-Mechanical Tunnelling: Dihydrofolate Reductase
E. Joel Loveridge and Rudolf K. Allemann

8.1	Introduction	179
8.1.1	The Kinetic Isotope Effect	180
8.1.2	The Significance of Tunnelling in Enzymatic Reactions	182
8.1.3	Experimental Methods of Observing the Chemical Step of the Reaction	184
8.2	Dihydrofolate Reductase: A Case Study	186
8.2.1	DHFR from <i>Escherichia coli</i>	188
8.2.2	DHFR from the Thermophile <i>Bacillus stearothermophilus</i>	192
8.2.3	DHFR from the Hyperthermophile <i>Thermotoga maritima</i>	192
8.3	Temperature Dependence of the KIEs for other Homologous Enzymes	193
8.4	Conclusions	194
	References	195

Chapter 9 Probing Coupled Motions in Enzymatic Hydrogen Tunnelling Reactions: Beyond Temperature-Dependence Studies of Kinetic Isotope Effects

Sam Hay, Michael J. Sutcliffe and Nigel S. Scrutton

9.1	Dynamics and Full Tunnelling Models for Enzymatic H-transfer	199
9.1.1	Towards a More Detailed Understanding of the Temperature Dependence of KIEs	201
9.1.2	Identifying a Promoting Motion in AADH and Rationalising the Apparent Temperature Independence of the KIE For Substrate C–H/D Bond Breakage	201
9.2	Pressure as a Probe of Hydrogen Tunnelling	203
9.2.1	Steady-State Analysis of the Pressure Dependence of H-transfer: A Case Study with Alcohol Dehydrogenase	203
9.2.2	Pressure Variation and Direct Analysis of the Chemical Step: A Case Study with Morphinone Reductase	205

9.2.3 Modelling the Pressure Dependence of an Environmentally Coupled H-tunnelling Reaction	208
9.3. Other Probes of Tunnelling: Future Prospects for Experimental Studies	209
9.3.1 Secondary KIEs	209
9.3.2 Driving Force	211
9.3.3 Viscosity	211
9.3.4 Multiple Reactive Configurations and a Place for Single-Molecule Measurements	213
9.4 Conclusions	215
References	216

Chapter 10 Computational Simulations of Tunnelling Reactions in Enzymes

Jiayun Pang, Nigel S. Scrutton and Michael J. Sutcliffe

10.1 Introduction	219
10.2 Molecular Mechanical Methods	220
10.3 Quantum Mechanical Methods	222
10.4 Combined Quantum Mechanical/Molecular Mechanical Methods	222
10.5 Improving Semiempirical QM Calculations	223
10.6 Calculation of Potential Energy Surfaces and Free Energy Surfaces	224
10.7 Simulation of the H-tunnelling Event	224
10.8 Calculation of H-tunnelling Rates and Kinetic Isotope Effects	225
10.9 Analysing Molecular Dynamics Trajectories	225
10.10 A Case Study: Aromatic Amine Dehydrogenase (AADH)	226
10.10.1 Preparation of the System	226
10.10.2 Analysis of the H-tunnelling Step in AADH	229
10.10.3 Analysis of the Role of Promoting Motions in Driving Tunnelling	232
10.10.4 Comparison of Short-Range Motions in AADH with Long-Range Motions in Dihydrofolate Reductase	235
10.11 Summary	238
References	238

Chapter 11 Tunnelling does not Contribute Significantly to Enzyme Catalysis, but Studying Temperature Dependence of Isotope Effects is Useful*Hanbin Liu and Arieh Warshel*

11.1	Introduction	242
11.2	Methods	244
11.3	Simulating Temperature Dependence of KIEs in Enzymes	248
11.4	Concluding Remarks	256
	Acknowledgement	264
	References	264

Chapter 12 The Use of X-ray Crystallography to Study Enzymic H-tunnelling*David Leys*

12.1	Introduction	268
12.2	X-ray Crystallography: A Brief Overview	269
12.2.1	Accuracy of X-ray Diffraction Structures	270
12.2.2	Dynamic Information from X-ray Crystallography	275
12.3	Examples of H-tunnelling Systems Studied by Crystallography	278
12.3.1	Crystallographic Studies of AADH Catalytic Mechanism	278
12.3.2	Crystallographic Studies of MR	284
12.4	Conclusions	286
	References	287

Chapter 13 The Strengths and Weaknesses of Model Reactions for the Assessment of Tunnelling in Enzymic Reactions*Richard L. Schowen*

13.1	Model Reactions for Biochemical Processes	292
13.2	Model Reactions Relevant to Enzymic Tunnelling	294
13.3	Isotope Effect Temperature Dependences and the Configurational-Search Framework (CSF) for their Interpretation	294
13.3.1	The Traditionally Dependent Category	296
13.3.2	The Underdependent Tunnelling Category	296
13.3.3	The Overdependent Tunnelling Category	297
13.4	Example 1. Hydride Transfer in a Thermophilic Alcohol Dehydrogenase	298

13.4.1	The Kirby–Walwyn Intramolecular Model Reaction	298
13.4.2	The Powell–Bruice Tunnelling Model Reaction	300
13.4.3	Enzymic Tunnelling in Alcohol Dehydrogenases	301
13.4.4	Model Reactions and the Catalytic Power of Alcohol Dehydrogenase	303
13.5	Example 2. Hydrogen-Atom Transfer in Methylmalonyl Coenzyme A Mutase (MCM)	304
13.5.1	Nonenzymic Tunnelling in the Finke Model Reactions for MCM	305
13.5.2	Enzymic Tunnelling in MCM	308
13.5.3	Model Reactions and MCM Catalytic Power	309
13.6	The Roles of Theory in the Comparison of Model and Enzymic Reactions	310
13.7	Model Reactions, Enzymic Accelerations, and Quantum Tunnelling	310
	References	311

Chapter 14 Long-Distance Electron Tunnelling in Proteins

Alexei A. Stuchebrukhov

14.1	Introduction	314
14.2	Electronic Coupling and Tunnelling Pathways	315
14.2.1	Direct Method	317
14.2.2	Avoided Crossing	317
14.2.3	Application of Koopmans' Theorem	318
14.2.4	Generalised Mulliken–Hush Method	319
14.2.5	The Propagator Method	320
14.2.6	Protein Pruning	322
14.2.7	Tunnelling Pathways	323
14.3	The Method of Tunnelling Currents	324
14.3.1	General Relations	324
14.3.2	Many-Electron Picture	328
14.4	Many-Electron Aspects	331
14.4.1	One Tunnelling Orbital (OTO) Approximation and Polarisation Effects	333
14.4.2	The Limitation of the SCF Description of Many-Electron Tunnelling	334
14.4.3	Correlation Effects. Polarisation Cloud Dynamics. Beyond Hartree–Fock Methods	335

14.4.4	Quantum Interference Effects. Quantised Vertices	336
14.4.5	Electron Transfer or Hole Transfer? Exchange Effects	338
14.5	Dynamical Aspects	339
	Acknowledgments	341
	References	342

Chapter 15 Proton-Coupled Electron Transfer: The Engine that Drives Radical Transport and Catalysis in Biology

Steven Y. Reece and Daniel G. Nocera

15.1	Introduction	345
15.2	PCET Model Systems	351
15.2.1	Unidirectional PCET Networks	351
15.2.2	Bidirectional PCET Networks	357
15.2.3	PCET Biocatalysis	357
15.3	PCET in Enzymes: A Study of Ribonucleotide Reductase	360
15.3.1	The PCET Pathway in RNR	361
15.3.2	PCET in the $\beta 2$ Subunit of RNR	361
15.3.3	PCET in $\alpha 2$ Subunit of RNR: PhotoRNRs	364
15.3.4	A Model for PCET in RNR	368
15.4	Concluding Remarks	370
	Acknowledgements	370
	References	370
	Subject Index	378

CHAPTER 1

The Transition-State Theory Description of Enzyme Catalysis for Classically Activated Reactions

BARRY K. CARPENTER

School of Chemistry, Main Building, Cardiff University, CF10 3AT, Cardiff,
UK

1.1 Introduction

Two facts about enzymes have probably been primarily responsible for the many thousands of person-years of research devoted to understanding their mechanisms of action: enzymes are ubiquitous catalysts for biochemical transformations, and they are able to achieve rate enhancements and/or substrate selectivities that have rarely been matched by designed catalysts.

Perhaps it is the combination of these two phenomena that has led some researchers to look for a “vital force” that might give enzymes catalytic powers outside of those explicable by the normal models of condensed-phase kinetics.¹ One does not need to be particularly mystically inclined to subscribe to this view, because enzymes could have evolved, at least in principle, to optimise effects that would otherwise play negligible roles in reaction kinetics. Ideally, the existence or otherwise of such special effects could be probed by comparing observed catalytic capabilities of enzymes with those derived from computer simulations based on standard kinetic models. If the observed effect were significantly different

from the calculated one, the discrepancy might indeed be a sign that some important phenomenon had been omitted from the simulation. Unfortunately, with rare exceptions, our theoretical models are not yet sufficiently reliable to permit such quantitative comparisons. Consequently, the question of the *deus ex machina* in enzyme catalysis must, for now, be classified as unresolved.

For the purposes of this chapter the issue will be set aside. We will assume that, although enzymes are remarkably good catalysts, the mechanisms by which they operate can be fully described by the standard model of condensed-phase kinetics: transition-state theory (TST).² Furthermore, since the focus of most of the rest of this book is on quantum tunnelling, we will begin by factoring that term out of the TST expression. To do so, it is convenient to employ the generalised TST expression (eqn (1.1)) for a rate constant, presented by Truhlar and coworkers.³

$$k(T) = \gamma(T)(C^0)^{1-n} \frac{k_B T}{h} e^{-\frac{\Delta^\ddagger G^0}{RT}} \quad (1.1)$$

Here $k(T)$ is the temperature-dependent rate constant, $\gamma(T)$ is a generalised transmission coefficient, C^0 is the standard-state concentration (or, sometimes, pressure in a gas-phase reaction), n is the molecularity of the reaction, k_B and h are, respectively, the Boltzmann and Planck constants, R is the gas constant, and $\Delta^\ddagger G^0$ is the standard-state free energy of activation. It is the $\gamma(T)$ term that contains any quantum-tunnelling effects,³ but here will be explicitly set equal to unity. Thus, this chapter will seek to lay a foundation for the later discussion of quantum tunnelling by describing the part of enzyme catalysis that can be ascribed to effects of the protein on the magnitude of the free-energy barrier for a classically activated reaction.

1.2 Quantifying the Catalytic Activity of Enzymes

To begin the discussion, it is necessary to define as clearly as possible the phenomenon that we wish to explain. The following analysis is based on the 1996 article of Cannon *et al.*⁴

One starts by considering an irreversible, unimolecular conversion of a substrate, **S**, into a product, **P**. (Special issues associated with enzyme catalysis of bimolecular reactions have been reviewed by Jencks,⁵ but will not be considered explicitly here.) The rate law for such a reaction is, of course, eqn (1.2). The rate constant k_{uncat} is seen to be the proportionality constant



between the rate of product formation and the *substrate* concentration.

The enzyme-catalysed reaction can be represented by the usual Michaelis–Menten formulation,



where \mathbf{E} is the enzyme and \mathbf{ES} is an enzyme–substrate complex. Application of the steady-state approximation to the concentration of \mathbf{ES} yields

$$\frac{d[\mathbf{P}]}{dt} = \frac{k_{\text{cat}}[\mathbf{E}]_{\text{tot}}[\mathbf{S}]}{[\mathbf{S}] + K_M} \quad (1.4)$$

where K_M , the Michaelis constant, has units of concentration and is equal to $(k_{\text{off}} + k_{\text{cat}})/k_{\text{on}}$, and $[\mathbf{E}]_{\text{tot}} = [\mathbf{E}] + [\mathbf{ES}]$. The maximum rate of product formation occurs when $[\mathbf{S}] \gg K_M$ – so-called saturation conditions – under which circumstances:

$$\frac{d[\mathbf{P}]}{dt} = k_{\text{cat}}[\mathbf{E}]_{\text{tot}} \quad (1.5)$$

At first sight, everything looks set for a definition of the rate enhancement brought about by the enzyme. In eqns (1.2) and (1.5) we have unimolecular rate constants for both the catalysed and uncatalysed reaction, and so the dimensionless quantity $k_{\text{cat}}/k_{\text{uncat}}$ looks like the obvious way to determine the quantitative effect of the catalyst. Indeed, many papers and books on enzyme catalysis do use $k_{\text{cat}}/k_{\text{uncat}}$ for that purpose. However, closer inspection of eqn (1.5) reveals a potential problem: k_{cat} is the proportionality constant between the rate of product formation and the *enzyme* concentration. It is consequently not measuring the same thing that k_{uncat} did. The proper comparison requires that we rewrite eqn (1.4) as

$$\frac{d[\mathbf{P}]}{dt} = k_{\text{eff}}[\mathbf{S}] \quad (1.6)$$

where

$$k_{\text{eff}} = k_{\text{cat}} \frac{[\mathbf{E}]_{\text{tot}}}{[\mathbf{S}] + K_M} \quad (1.7)$$

The effective “rate constant” k_{eff} is seen not to be a constant at all, since its value depends on the substrate concentration (eqn (1.7)). Furthermore, the quantity $[\mathbf{E}]_{\text{tot}}/([\mathbf{S}] + K_M)$ will generally be $\ll 1$, especially under the saturation conditions that lead to the maximum rate of product formation. Hence, one sees that the ratio $k_{\text{cat}}/k_{\text{uncat}}$ will almost always overestimate the catalytic power

of an enzyme. However, the more defensible $k_{\text{eff}}/k_{\text{uncat}}$ varies with substrate concentration and, somewhat confusingly, actually approaches its maximum value of $k_{\text{cat}}[\mathbf{E}]_{\text{tot}}/(k_{\text{uncat}}K_M)$ as $[\mathbf{S}] \rightarrow 0$.

For a series of enzymes used at identical concentrations, the quantity $k_{\text{cat}}/(k_{\text{uncat}}K_M)$ – Wolfenden’s “catalytic proficiency”⁶ – will provide a reliable estimate of *relative* activities, which are found to cover a range spanning many orders of magnitude, from carbonic anhydrase at $10^8 M^{-1}$ to arginine decarboxylase at $10^{23} M^{-1}$.⁶ At a typical enzyme concentration of $10^{-5} M$, the corresponding maximum rate enhancements, $\{k_{\text{eff}}/k_{\text{uncat}}\}_{\text{max}}$ thus vary from 10^3 – 10^{18} , and at real (*i.e.* nonzero) substrate concentrations, the true rate enhancements drop further. Nevertheless, there clearly remains something worthy of explanation, particularly at the high end of the range.

1.3 Free-Energy Analysis of Enzyme Catalysis

Most effects in mechanistic organic chemistry are described in structural and/or energetic terms. It is therefore tempting to take the rate enhancements described in the previous section and, through our reduced TST expression (*i.e.* with the generalised transmission coefficient set to unity, eqn (1.8)) to express them as differences in standard-state activation free energies for the catalysed and uncatalysed reactions.

$$k(T) = (C^0)^1 \cdot n \frac{k_B T}{h} e^{-\frac{\Delta_f G^0}{RT}} \quad (1.8)$$

There are a number of potential pitfalls with this approach. The first is one of interpretation. Comparison of activation free energies for two reactions presumably implies that one believes the reactions in question to be similar enough for the energy difference to be physically meaningful. Few people would expect a comparison of activation barriers for a Diels–Alder reaction and an aldol reaction to yield useful insight. In the case of enzyme catalysis, one needs to enquire whether the mechanisms of the catalysed and uncatalysed reactions are the same. Actually, this question easily leads to a philosophical quagmire. Strictly speaking, the mechanisms of the catalysed and uncatalysed reactions can never be the same – after all one involves a catalyst and one does not! In some cases, the mechanism of the enzyme-catalysed reaction is so obviously different from the uncatalysed one that the energetic comparison is clearly meaningless (*e.g.* when the enzymatic reaction involves covalent bond formation to cofactor that is not available to the uncatalysed reaction). However, even when that is not the case, the interpretation of energy differences requires careful thought and clear definition of terms.

One conceptual (and possibly computational) way of tackling the problem is summarised in Figure 1.1. In this figure, and elsewhere in this chapter, the convention employed is that a subscript or superscript following the Δ defines the type of free-energy difference being described. A double dagger following

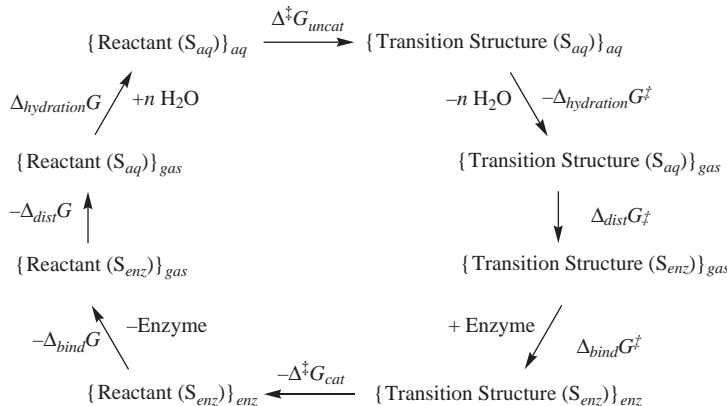


Figure 1.1 A thermodynamic cycle for defining the contributing components to the catalytic effect of an enzyme. The subscript on the S (for structure) defines the medium in which the geometry of the substrate or transition structure is a stationary point, while the subscript on the braces, {}, defines the medium in which the substrate or transition structure finds itself.

the G means that the two free energies being compared are both for the transition structure. Thus, Δ^{\ddagger} means a difference in free energy between transition state and ground state, whereas, for example, $\Delta_{\text{dist}}G^{\ddagger}$ means a difference in free energy between two transition structures of different geometry.

The quantity $\Delta^{\ddagger}G_{\text{uncat}} - \Delta^{\ddagger}G_{\text{cat}}$ can, in principle, be determined experimentally. It is related, *via* eqn (1.9), to the rate constants k_{uncat} and k_{cat} , discussed above.

$$\Delta^{\ddagger}G_{\text{uncat}} - \Delta^{\ddagger}G_{\text{cat}} = RT \ln\left(\frac{k_{\text{cat}}}{k_{\text{uncat}}}\right) \quad (1.9)$$

From the thermodynamic cycle in Figure 1.1, $\Delta^{\ddagger}G_{\text{uncat}} - \Delta^{\ddagger}G_{\text{cat}}$ can be decomposed into conceptual components that might provide insight into the origins of enzymic catalysis (although it is perhaps prudent to re-emphasise here that $\Delta^{\ddagger}G_{\text{uncat}} - \Delta^{\ddagger}G_{\text{cat}}$ will overestimate the magnitude of the real catalytic effect, for the reasons discussed in the previous section).

$$\begin{aligned} \Delta^{\ddagger}G_{\text{uncat}} - \Delta^{\ddagger}G_{\text{cat}} &= \Delta_{hydration}G^{\ddagger} - \Delta_{hydration}G \\ &\quad + \Delta_{dist}G - \Delta_{dist}G^{\ddagger} + \Delta_{bind}G - \Delta_{bind}G^{\ddagger} \end{aligned} \quad (1.10)$$

The first two terms on the right-hand side of eqn (1.10) evaluate the hydration free energies of the transition structure and reactant, respectively, for the uncatalysed reaction. The third and fourth terms recognise that the minimum-energy

geometries of reactant and transition structure might not be the same for the uncatalysed and enzyme-catalysed reactions, and evaluates the free-energy changes for distortion of one to the other. The final two terms evaluate the binding free energies of, respectively, the transition structure and reactant (at the geometries of each appropriate for the catalysed reaction) to the enzyme-active site. These binding terms might involve important contributions from water molecules that are displaced from the active site by the substrate or the transition structure.⁷

Although the left-hand side of eqn (1.10) can sometimes be determined experimentally, the terms on the right-hand side usually cannot. However, they might be susceptible to calculation. If they were, the magnitudes of the various terms would provide insight into the physical origins of catalysis. Unfortunately, as discussed later, the reduction of this ideal to practice is far from straightforward.

The analysis of eqn (1.10) is further compromised for the many enzyme-catalysed reactions that involve formation of charged intermediates, because then the gas-phase mechanism may not exist at all, or may be so high in energy above alternative charge-neutral pathways that it cannot be reliably calculated. To emphasise this point, it is perhaps worth recalling that the solvolysis of *tert*-butyl bromide, which occurs readily at room temperature in aqueous media, would have a 298 K half-life of $\sim 10^{87}$ years in the gas phase! In fact, without the beneficial effects of solvation on the polar pathway, C-Br *homolysis* is more facile than heterolysis by 340 kJ mol. When an enzyme-catalysed reaction has no gas-phase counterpart, the thermodynamic cycle in Figure 1.1 must be telescoped, so that free-energy changes are calculated directly between aqueous and enzyme-bound structures. However, such a calculation inevitably confounds intrinsic properties of the substrate (*i.e.* the relative free energies of various structures) with solvation and/or binding energies. This blending of effects hampers efforts to decompose the catalytic phenomenon into clearly comprehensible physical components.

A second potential pitfall with free-energy analyses of enzyme catalysis concerns the standard-state concentration term, $(C^0)^{1/n}$, in eqn (1.8).⁸ For a unimolecular reaction, such as that in eqn (1.2), $n = 1$, and so the term becomes unity. Hence, the activation free energy (difference in free energy between the transition state and reactant) is independent of the chosen standard state. However, for the enzyme-catalysed reaction $n = 2$. Consequently the overall free energy of the enzyme-bound transition structure with respect to free substrate and enzyme has a value that does depend on the selected standard state. For solution-phase reactions, the most common standard state is 1 M. However, it is important to recognise that the actual concentrations at which enzymes and substrates exist in biological systems are typically many orders of magnitude lower than that. Figure 1.2 illustrates what happens to the relative standard-state free energies for an uncatalysed unimolecular reaction and its enzyme-catalysed counterpart as the concentration changes.⁸

The left-hand panel of Figure 1.2 illustrates a situation where the enzyme-catalysed reaction is faster than the uncatalysed one. This arises because the

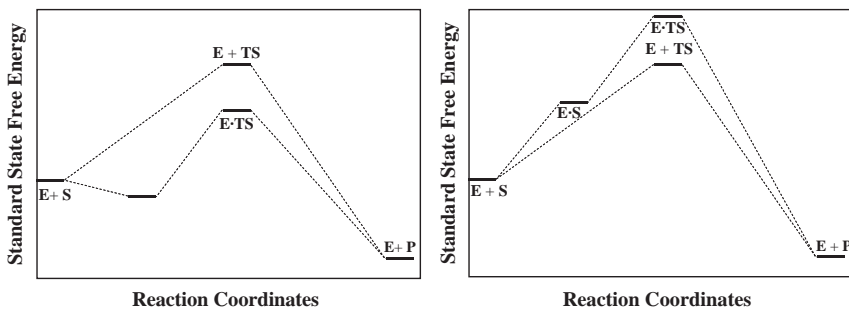


Figure 1.2 Schematic standard state free energy profiles for an enzyme catalysed reaction and its uncatalysed counterpart. The left hand panel depicts the situation where the components are present in high enough concentration for the enzyme catalysed process to be preferred. As the concentration is reduced the enzyme catalysed reaction becomes disfavoured until, in the right hand panel, the uncatalysed reaction is actually faster ($E + TS$ is below $E \bullet TS$).

standard-state free energies of binding for both the substrate and the transition structure are negative, but the latter is more negative. By reducing the concentrations of *all* of the components in solution, one raises the standard-state free energy of the Michaelis complex $E \bullet S$ with respect to the separate components $E + S$, and of the enzyme-bound transition structure, $E \bullet TS$ with respect to $E + TS$. However, the standard-state free-energy differences between $E + TS$ and $E + S$, and between $E \bullet TS$ and $E \bullet S$ are independent of concentration because each step is unimolecular (the enzyme is included in the uncatalysed reaction simply to keep the stoichiometry consistent; it doesn't actually participate in the reaction). If the reduction in concentration is sufficient, the enzyme-catalysed reaction can cease to be the favoured pathway, as illustrated in the right-hand panel of Figure 1.2. Of course, enzymes have evolved to operate under conditions like those in the left-hand diagram, but nonetheless it is important to recognise that the relative favourabilities of enzyme-catalysed and uncatalysed reactions are concentration dependent.

One last point: there may appear to be a contradiction between Figure 1.2, which seems to show that the catalysed reaction becomes less favourable as the concentration decreases, and the earlier analysis (eqn (1.7)) in which we had concluded that the rate enhancement caused by an enzyme reaches a maximum as $[S]$ approached zero. This is actually not a contradiction because the concentration change between the two panels of Figure 1.2 applies to *all* components, whereas the analysis of eqn (1.7) involved reducing *only* the substrate concentration. One can see in eqn (1.7) that reducing the enzyme concentration reduces k_{eff} , whereas reducing the substrate concentration increases it. However, the former effect is more important because of the constant K_M in the denominator. Hence reducing *both* $[E]_{\text{tot}}$ and $[S]$ at the same time will reduce k_{eff} .

1.4 Transition-State Stabilisation or Ground-State Destabilisation?

The recognition that, to be effective catalysts, enzymes must bind the transition structure for a chemical reaction more tightly than they bind the substrate is usually attributed to Linus Pauling.⁹ However, as Wolfenden has pointed out,⁶ essentially the same conclusion, about catalysts in general, had been published by Polanyi over 20 years earlier.¹⁰

This necessary property of catalysts leaves open the question of whether the principal effect arises from the distortion terms^{11–13} or the binding terms^{14,15} in eqn (1.10). Both points of view have been passionately advanced and defended. At one extreme, it could be that the reactant and transition structure in the enzyme-active site have geometries, and therefore free energies, that are very similar to those in aqueous solution. Under such circumstances, the quantity $\Delta_{\text{dist}}G - \Delta_{\text{dist}}G^\ddagger$ would be negligible, and catalysis would have to arise from the sum of the remaining four terms in eqn (1.10) being positive. This would be the case if the difference between transition-structure and reactant binding free energies greatly exceeded the difference in their hydration free energies. In other words, one could view the enzyme to be a protein that had evolved to have a particularly good binding affinity for the reaction transition structure, and a much poorer affinity for the substrate.

At the other extreme, it might be that the difference in binding free energies of the transition structure and reactant to the enzyme is about equal to the difference in their hydration energies. Under such circumstances catalysis could still be expressed, provided that the quantity $\Delta_{\text{dist}}G - \Delta_{\text{dist}}G^\ddagger$ were positive. One way (but not the only way, since, in general, we don't know the signs of the distortion free energy terms) would be to make $\Delta_{\text{dist}}G$ a large positive quantity (or, in any event, more positive than $\Delta_{\text{dist}}G^\ddagger$). In other words, one could view the enzyme to be a protein that had evolved to put the substrate on a rack, and to mechanically force it into a high-energy, and presumably transition-structure-like geometry.¹³

In the judgement of the present author, the dispute between proponents of these extreme points of view has added relatively little to our understanding of enzyme catalysis. In fact, a number of researchers are beginning to conclude that the separation of the catalytic phenomenon into ground-state and transition-state effects is not really meaningful.^{4,16,17} For example, if the enzyme's active site had evolved to be complementary to the reaction transition structure, one consequence should be that the conformations of the reactant bearing the closest resemblance to the transition structure ought to be the most tightly bound to the protein. Under such circumstances, the tight binding of the transition structure and the distortion of the reactant upon binding could simply be viewed as two expressions of the same underlying physical phenomenon.

A case in point is provided by the much-studied group of chorismate mutase enzymes. These enzymes catalyse the conversion of chorismate to prephenate (Figure 1.3) – a step in the shikimate biosynthetic pathway for plants and bacteria.¹⁸ The transformation is apparently a concerted aliphatic Claisen

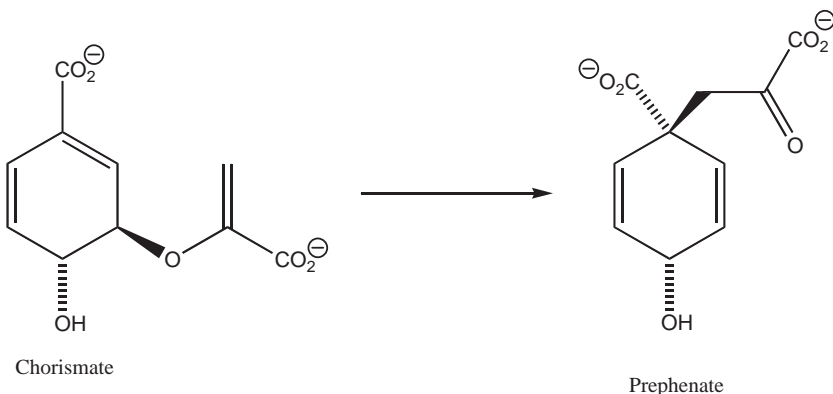


Figure 1.3 The reactant and product in the chorismate rearrangement.

rearrangement, both in the uncatalysed and enzyme-catalysed versions of the reaction.¹⁹ The aqueous-solution reaction occurs with activation parameters²⁰ $\Delta^\ddagger H = 85.8 \pm 1.7 \text{ kJ/mol}$, $\Delta^\ddagger S = -54.0 \pm 1.7 \text{ J/(mol K)}$. In the chorismate mutases from *B. subtilis*, *E. coli*, *K. pneumoniae*, and *S. aureofaciens*, respectively, these parameters are modified to $\Delta^\ddagger H = 53.1 \pm 1.7 \text{ kJ/mol}$, $\Delta^\ddagger S = -38.1 \pm 5.0 \text{ J/(mol K)}$; $\Delta^\ddagger H = 68.2 \pm 2.1 \text{ kJ/mol}$, $\Delta^\ddagger S = -12.6 \pm 6.7 \text{ J/(mol K)}$; $\Delta^\ddagger H = 66.5 \pm 1.7 \text{ kJ/mol}$, $\Delta^\ddagger S = -4.6 \pm 5.0 \text{ J/(mol K)}$; $\Delta^\ddagger H = 60.7 \pm 1.7 \text{ kJ/mol}$, $\Delta^\ddagger S = -6.7 \pm 4.6 \text{ J/(mol K)}$.²⁰ Hence, the enzymes achieve their roughly 10^6 values for $k_{\text{cat}}/k_{\text{uncat}}$ by reducing $\Delta^\ddagger H$ and increasing (making less negative) $\Delta^\ddagger S$. In general, the former effect is larger, although the apportioning of the catalysis between enthalpic and entropic effects seems to be organism specific.

In aqueous solution, NMR studies suggest that chorismate exists in pseudo-diequatorial and pseudododiaxial conformers, with the latter being higher in free energy by only about 5 kJ/mol at 25 °C.²¹ The calculations of Martí *et al.* suggest that there is a substantial solvent contribution to this value.²² They estimate that in the gas phase the pseudododiaxial conformers are significantly less favoured. While it is true that one of the pseudododiaxial conformers is geometrically closer than the other conformers to the transition structure for the Claisen rearrangement, selective binding of this conformer to the enzyme-active site could not, by itself, explain the observed catalysis, since a difference of roughly 35 kJ/mol in $\Delta^\ddagger G^0$ is observed between aqueous and enzyme-catalysed reactions.

A number of hybrid quantum-mechanical and molecular-mechanical (QM/MM) simulations have been conducted on the aqueous and enzyme-catalysed reactions, in an effort to elucidate the principal origins of the catalytic effect.^{17,20,23-33} Although the authors of the calculations agree on some important issues, they differ somewhat on the details, and differ considerably in their descriptions of what is occurring. The principal point of agreement is that a pseudododiaxial conformer of chorismate is favoured upon binding to the active site, and that this conformer is substantially different in geometry from any found as local minima in aqueous solution. In particular, the bound conformer of the substrate seems to have a much

shorter distance between the carbons that are destined to form a bond in the ensuing Claisen rearrangement ($\sim 2.9\text{ \AA}$ in the enzyme *vs.* $\sim 3.5\text{ \AA}$ as the closest approach in any of the aqueous-phase local minima). There is clearly an energetic cost to the substrate from this distortion. Furthermore, since the distortion moves the substrate along the reaction coordinate for the Claisen rearrangement, the reactant destabilisation serves to reduce the barrier for the reaction.

The principal points of disagreement among the researchers who have investigated the chorismate mutases are, first, the teleological question of how to characterise what the enzymes are doing, and, second, whether there is any significant component of catalysis arising from factors beyond this substrate distortion. On the matter of teleology, one could argue that the enzymes have evolved to select from solution the rare high-energy conformations (not necessarily local minima) that are closest in structure to the transition state for the Claisen rearrangement, and have provided stabilisation through binding to these privileged “near-attack conformations” (NACs).^{27,33} Alternatively, one could argue that the enzymes have evolved to provide a mechanical stress on the substrate, forcing together the carbons that will become bonded during the Claisen rearrangement,³⁰ and thereby reducing the barrier for the reaction through a “spatiotemporal” effect.^{34,35} Or, seemingly different again, one could argue that the enzymes have evolved to bind the transition structure for the Claisen rearrangement as tightly as possible, and that, as a direct consequence of this strong binding, the substrate will experience a distorting force that alters its geometry in the direction of the transition structure.²⁹ However, it is the present author’s opinion that these questions fall more in the realm of semantics than science, and that they simply represent alternative verbal characterisations of the same underlying physics. If one tried to bind chorismate in its predominant (pseudodiequatorial) aqueous conformation to the active site of a chorismate mutase, there is no doubt that the standard-state binding free energy would be much less negative than that for the reaction transition structure. *That has to be true for catalysis to occur.* However, since the preferred conformation of the substrate bound to the active site is *not* the same as that in solution, one has to decide where to claim that the substrate has paid the energy penalty for this structural change, and how it has been compensated by the enzyme. The various descriptions of the catalytic phenomenon merely choose different accounting schemes to balance these free-energy books.

Where there is truly scientific disagreement among the researchers into chorismate mutases is on the matter of whether there are additional catalytic factors that go beyond the substrate distortion. Evidence has been provided from both experimental^{36–38} and computational²⁶ studies to suggest that the transition structure for the chorismate Claisen rearrangement is more polar than the reactant, and that additional catalytic effect arises from electrostatic²⁹ (including hydrogen bonds^{20,24,31,39}) stabilisation of the transition structure in the active site. However, there is not yet agreement about whether this polar stabilisation is a significant factor.³³ In other enzyme-catalysed reactions, for which charged intermediates are formed, there is no doubt that polar stabilisation plays an important role. It, and other means of stabilising transition structures, are described in the next section.

1.5 Selective Stabilisation of Transition Structures by Enzymes

The point of view of the present author – that the various free-energy analyses of enzyme catalysis differ only in semantics – permits any one of the common descriptions to be selected as the basis for further discussion. In the remainder of this chapter, the language used will be the original Polanyi–Pauling description of selective transition-structure binding.

One of the possible mechanisms for stabilising transition structures selectively is through electrostatic interactions. Warshel has proposed that this effect is the most important in enzyme catalysis (see Chapter 10).⁴⁰ However, he argues that recognition of that fact requires a careful analysis of the *uncatalysed* (*i.e.* aqueous) reaction. As discussed earlier, direct comparison of enzyme-catalysed reactions with their aqueous counterparts corresponds to a telescoping of the thermodynamic cycle in Figure 1.1, with a consequent blending of intrinsic substrate energetics and solvation (hydration) effects. This is important for the following reason. Pairwise interactions of polar functionalities in the reaction transition structure with polar groups in an enzyme-active site are typically not very different in magnitude from interactions of the transition structure with individual water molecules. This fact would, at first sight, seem to argue against selective electrostatic stabilisation of the transition state by the enzyme. However, the water interactions with the transition structure come at a cost of solvent reorganisation energy – *i.e.* partial disruption of the hydrogen bonding structure of pure liquid water. By contrast, the enzyme-active site has preorganised polar groups that have evolved to be complementary to the transition structure, and have paid their organisation energy penalty at the time of folding of the protein. This, Warshel argues, is the principal factor that gives an enzyme its advantage over water.⁴⁰

An obvious factor that enzymes can and do provide for stabilisation of transition structures is a preorganised hydrogen-bond network. Although the proper description of hydrogen bonds is still a matter of debate,^{41,42} it seems clear that a large component of the attractive interaction can be described in electrostatic (*i.e.* ion–dipole or dipole–dipole) terms. Consequently, hydrogen-bond stabilisation could, in general, be viewed as a special case of electrostatic stabilisation. An exception to that conclusion might occur with the so-called low-barrier hydrogen bonds (LBHBs), in which a hydrogen is symmetrically bonded to two heteroatoms (oxygen or nitrogen) that are held at a distance within the sum of their van der Waals radii, and that constitute functional groups of very similar pK_a .^{43,44} It has been suggested that LBHBs are unusually strong, and that they play important roles in enzyme catalysis.⁴³

An example is provided by the classic serine proteases,⁴⁴ which catalyse the hydrolytic cleavage of peptide bonds. They do so by making an acyl–enzyme intermediate, using the hydroxyl group of an active-site serine. This normally poor nucleophile is apparently activated by general-base catalysis, involving a histidine and an aspartate. The three amino acids constitute the so-called catalytic triad (Figure 1.4). Early proposals for the mechanism of the acyl–enzyme

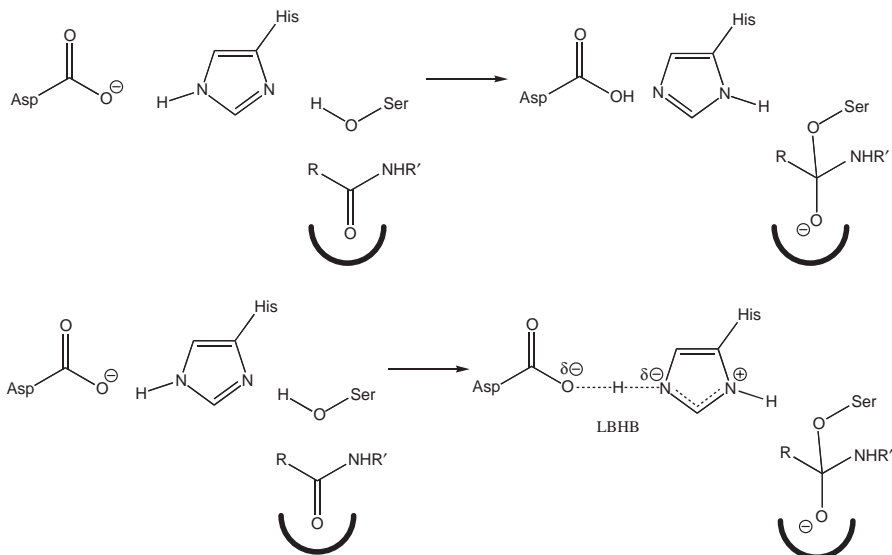


Figure 1.4 Two mechanistic proposals by which the “catalytic triad” of aspartate, histidine, and serine in the active site of the serine protease enzymes could catalyse hydrolysis of a peptide bond. In the upper scheme the “charge relay” mechanism two proton transfers take place. In the lower “LBHB” mechanism, the catalysis benefits from the formation of a stable low barrier hydrogen bond between the aspartate and protonated histidine. The bold curve in each mechanism represents the part of the protein known as the oxyanion hole, in which backbone N H bonds are oriented correctly to provide H bond stabilisation of the alkoxide in the tetrahedral intermediate.

formation (generally believed to be the rate-determining step of the overall reaction) involved a so-called charge-relay mechanism,⁴⁵ consisting of two proton transfers. However, subsequent experiments have suggested that only a single proton transfer occurs.⁴⁶ That fact could be accommodated within the LBHB proposal, which posits that the formation of a LBHB between the aspartate and histidine leads to stabilisation of the transition state, and consequent catalysis for the reaction.⁴⁴ Similar effects have been proposed for a variety of other enzyme-catalysed reactions.⁴³

Experimental support for the LBHB proposal was adduced from the ¹H NMR chemical shift of the proton shared between the aspartate and histidine in the protonated state of chymotrypsin, and in its complexes with various analogues of the tetrahedral intermediate. All occurred at ~18 ppm in the spectrum – substantially downfield from hydrogens involved in “normal” hydrogen bonds between oxygen and nitrogen.⁴⁴ This downfield shift has been identified as a characteristic of LBHBs. However, in a recent QM/MM simulation,⁴⁷ Ishida has found that the hydrogen between the aspartate and histidine remains localised on the histidine ring throughout the reaction. Despite

that, the calculated ^1H chemical shift reaches $\delta 20.5$, because of large electrostatic effects. Thus, Ishida's analysis suggests that NMR chemical shift may not be a reliable criterion for the formation of LBHBs. The proposals of important catalytic consequences from LBHB formation in other enzyme-catalysed reactions are awaiting similarly detailed analyses.

Since, in transition-state theory, reaction rates depend on activation free energies, and since free energies, in turn, have enthalpic and entropic components, it is reasonable to enquire whether the selective stabilisation of a transition structure by an enzyme is primarily an effect on $\Delta^\ddagger H$ or $\Delta^\ddagger S$. The idea that an increase in activation entropy (with respect to that for the aqueous reaction), particularly for bimolecular reactions, could be a significant contributor to enzyme catalysis was advanced persuasively by Page and Jencks in 1971.⁴⁸ Although their analysis was probably as careful and detailed as it could be, given the information and capabilities of the time, it may not have been quantitatively correct. In a 2000 paper in which the question was revisited, Villà *et al.* have concluded that some of the approximations used by Page and Jencks were flawed, and that the entropic contribution to enzyme catalysis is, in most cases, quite small.⁴⁹ In any event, direct experimental measurements of activation entropies for enzyme-catalysed reactions are difficult to obtain, and even more difficult to interpret. Although our interest may be in entropy changes associated with the substrate(s) during reaction, experiments determine entropy changes for the whole system (substrate, solvent, and enzyme), and deconvolution into individual contributions from these components can be difficult or impossible.

More recently, Zhang and Houk have paid close attention to the most proficient enzymes, and have concluded that their catalytic effects can only reasonably be explained by (at least partial) covalent bond formation between the enzyme and the reaction transition structure.⁵⁰ The principal basis for this proposal is the calculation of association constants for truly noncovalent complexes of small molecules to biological macromolecules, and comparison with the deduced "association constants" (not directly observable, of course) for enzymes with the transition structures of the reactions that they catalyse. The reference association constants are of antibodies with antigens, averaging $\sim 10^6 \text{ M}^{-1}$, and of enzymes with transition-structure analogues (*i.e.* inhibitors), averaging $\sim 10^9 \text{ M}^{-1}$. The kinetically deduced association constants for enzymes with the actual transition structures were found to be much higher, averaging $\sim 10^{16} \text{ M}^{-1}$, and rising in a few cases to almost 10^{30} M^{-1} .⁵⁰ In several of the cases included in the Zhang–Houk analysis, there is no doubt that there are covalent bonds formed with enzyme active-site residues, or with cofactors. The problem is that the aqueous-phase, uncatalysed reaction, lacks the capability to follow the same path, and so the mechanisms of catalysed and uncatalysed reactions are really incomparably different. As pointed out in the introductory section of this chapter, the interpretation of a difference in activation free energy for two reactions of unrelated mechanism is problematic. However, some of the enzyme-catalysed reactions included in the Zhang–Houk review do follow mechanisms that are sufficiently similar to those for the

uncatalysed analogues that a free-energy analysis of the kind illustrated in Figure 1.1 is meaningful. The question is then whether these reactions, too, must benefit from covalent bond formation during the enzyme catalysis, if the full magnitude of the catalytic effect is to be explained. At least two commentators^{40,51} think that the “covalent catalysis” proposal is unnecessary, and that the higher association constants of enzymes for the true transition structures than for their inhibitory analogues arises simply from the fact that perfect transition structure analogues are hard to prepare. However, given its relatively recent vintage, the last words of this debate may not have been heard.

Finally, for this section, it is useful to pay attention to the cautionary words of Kraut *et al.* on the difficulty of interpreting data from site-directed mutagenesis in the analysis of enzyme catalysis.⁵² Superficially, the ability to introduce at will new amino acids, even non-natural ones, into selected sites of a protein would seem to give biochemists the freedom to conduct the structure–reactivity analyses that have for so long provided the foundation of mechanistic understanding in physical organic chemistry. Indeed such experiments can and have been done for enzymes.⁵³ The problem, as always, lies in the interpretation of the results. When one makes a change in the chemical constitution of a compound, as usually occurs in a structure–reactivity study, it ceases to be possible to make direct energy comparisons between the original and the modified molecule. Changes in the rates of related chemical reactions of the two molecules, arising from the structural modification, consequently cannot be ascribed unambiguously to ground-state or transition-state effects. If one chooses to set the reactants at the same free energy for the purposes of the rate comparison, then the effect will seem to have occurred in the transition state. However, it would be equally valid to choose the transition states to be at the same free energy, with the resulting appearance of a ground-state effect. This ambiguity has repeatedly led to controversy in physical organic chemistry, for example concerning the origin of substituent effects on bond dissociation enthalpies.^{54,55} Similarly, in site-directed mutagenesis studies of enzymes, one cannot separate catalytic effects from binding effects brought about by the change of an amino acid.⁵² The implication is not that mutation studies are worthless – far from it – but merely that the quantitative effects of an amino-acid substitution on the catalytic activity of an enzyme need to be interpreted with due caution.

1.6 Enzyme Flexibility and Dynamics

The thermodynamic cycle in Figure 1.1 carries a hidden asymmetry. It depicts explicitly the desolvation and distortion of the substrate and reaction transition structure, but does not do the same for the enzyme. However, the vast amounts of structural and dynamic information that have become available in recent years as a result of X-ray diffraction and magnetic resonance studies, and from computer simulations, reveal that changes in hydration state and structure of the enzyme during its catalytic cycle really cannot be ignored.⁵⁶

The rather static, almost architectural picture of organic molecules that was encouraged by the mechanical molecular models in common use in the mid- to late-twentieth century is quickly dispelled as soon as one looks at a movie from a molecular-dynamics simulation. Even relatively small organic molecules are undergoing quite large-scale and complex gyrations at all times. A simple calculation reveals that in a mole of some 10-atom compound at room temperature there is almost no chance that any two molecules would instantaneously have the same structure, if one defines that to be all bond lengths equal to within $\pm 0.001 \text{ \AA}$ and all bond angles and dihedrals equal to within 0.1° . There are 24 degrees of freedom in our molecule, each one of which will have > 100 possible structural values, given a typical room-temperature excursion, and the precision with which we have defined the measurement. This translates to a probability of < 1 in 10^{114} of finding two molecules with the same geometry in a mole. Our bulk measurements and the molecular properties that we derive from them are consequently revealing only average behaviour to which no single molecule is likely to conform!

The possibility of structural heterogeneity obviously becomes vastly greater when one starts to consider molecules as large as enzymes. Now there is not only an incomprehensibly large number of actual geometries within the sample, but there is also a huge range of timescales for interconversions between geometries. Large-scale conformational changes of the protein may take place in milliseconds, whereas the vibrational changes in C–H bond lengths are occurring in femtoseconds.

The first correction to our earlier discussion of enzyme catalysis that should occur as a result of this recognition is a modification of the static and detailed description of binding of substrate and transition structure to the enzyme. Instead, we must recognise that there is a distribution of continuously changing enzyme–substrate complexes each of which will react *via* a different enzyme–transition–structure complex.

An interesting question, and a topic of much current research, is how the dynamical changes in structure of the enzyme are coupled to the changes in the substrate that accompany its passage through the transition state and on to the product. The slow conformational changes of the protein cannot couple directly to the reaction coordinate, but they often do have important roles to play nonetheless, because they can make a deeply buried active site temporarily accessible for binding of the substrate and release of the product.

The more controversial question is whether higher-frequency, more localised motions of the protein could couple to the reaction coordinate in a way that would provide the enzyme with catalytic advantage.^{15,57,58} In the most general terms, the answer to that question is “yes,” because it is guaranteed that there will be protein vibrational motions of the right frequency, and of sufficient proximity to the substrate for coupled motion to occur. The matter of contemporary debate is whether evolution could have selected *particular* dynamical motions of the protein to assist in the catalysis. Discussions of that question in the context of hydrogen tunnelling will appear in several of the later chapters of this book.

References

1. T. D. H. Bugg, *Nat. Prod. Rep.*, 2001, **18**, 465.
2. H. Eyring and A. E. Stearn, *Chem. Rev.*, 1939, **24**, 253.
3. M. Garcia-Viloca, J. Gao, M. Karplus and D. G. Truhlar, *Science*, 2004, **303**, 186.
4. W. R. Cannon, S. F. Singleton and S. J. Benkovic, *Nat. Struct. Biol.*, 1996, **3**, 821.
5. W. P. Jencks, *Adv. Enzymol. Relat. Areas Mol. Biol.*, 1975, **43**, 219.
6. R. Wolfenden and M. J. Snider, *Acc. Chem. Res.*, 2001, **34**, 938.
7. J. D. Dunitz, *Science*, 1994, **264**, 670.
8. M. I. Page, *Int. J. Biochem.*, 1980, **11**, 331.
9. L. Pauling, *Chem. Eng. News*, 1946, **24**, 1375.
10. M. Polanyi, *Z. Elektrochem.*, 1921, **27**, 142.
11. F. M. Menger, *Biochemistry*, 1992, **31**, 5368.
12. J. R. Burke and P. A. Frey, *Biochemistry*, 1993, **32**, 13220.
13. W. P. Jencks, *Philos. T. Roy. Soc. A*, 1993, **345**, 3.
14. A. Warshel, *Proc. Natl. Acad. Sci. USA*, 1978, **75**, 5250.
15. R. L. Schowen, *Proc. Natl. Acad. Sci. USA*, 2003, **100**, 11931.
16. S. Marti, M. Roca, J. Andres, V. Moliner, E. Silla, I. Tunon and J. Bertran, *Chem. Soc. Rev.*, 2004, **33**, 98.
17. J. Giraldo, D. Roche, X. Rovira and J. Serra, *FEBS Lett.*, 2006, **580**, 2170.
18. U. Pindur and G. H. Schneider, *Chem. Soc. Rev.*, 1994, **23**, 409.
19. B. Ganem, *Angew. Chem. Int. Edit.*, 1996, **35**, 937.
20. C. C. Galopin, S. Zhang, D. B. Wilson and B. Ganem, *Tetrahedron Lett.*, 1996, **37**, 8675.
21. S. D. Copley and J. R. Knowles, *J. Am. Chem. Soc.*, 1987, **109**, 5008.
22. S. Marti, J. Andres, V. Moliner, E. Silla, I. Tunon and J. Bertran, *Theochem.*, 2003, **632**, 197.
23. P. D. Lyne, A. J. Mulholland and W. G. Richards, *J. Am. Chem. Soc.*, 1995, **117**, 11345.
24. M. M. Davidson, I. R. Gould and I. H. Hillier, *J. Chem. Soc. Perkin Trans. 2*, 1996, 525.
25. H. Guo, Q. Cui, W. N. Lipscomb and M. Karplus, *Proc. Natl. Acad. Sci. USA*, 2001, **98**, 9032.
26. S. E. Worthington, A. E. Roitberg and M. Krauss, *J. Phys. Chem. B*, 2001, **105**, 7087.
27. S. Hur and T. C. Bruice, *Proc. Natl. Acad. Sci. USA*, 2002, **99**, 1176.
28. Y. S. Lee, S. E. Worthington, M. Krauss and B. R. Brooks, *J. Phys. Chem. B*, 2002, **106**, 12059.
29. A. Shurki, M. Strajbl, J. Villa and A. Warshel, *J. Am. Chem. Soc.*, 2002, **124**, 4097.
30. C. R. W. Guimaraes, M. P. Repasky, J. Chandrasekhar, J. Tirado-Rives and W. L. Jorgensen, *J. Am. Chem. Soc.*, 2003, **125**, 6892.
31. S. Marti, J. Andres, V. Moliner, E. Silla, I. Tunon and J. Bertran, *J. Am. Chem. Soc.*, 2004, **126**, 311.

32. K. E. Ranaghan and A. J. Mulholland, *Chem. Commun.*, 2004, 1238.
33. X. D. Zhang, X. H. Zhang and T. C. Bruice, *Biochemistry*, 2005, **44**, 10443.
34. F. M. Menger, *Pure Appl. Chem.*, 2005, **77**, 1873.
35. N. A. Khanjin, J. P. Snyder and F. M. Menger, *J. Am. Chem. Soc.*, 1999, **121**, 11831.
36. P. Kast, J. D. Hartgerink, M. AsifUllah and D. Hilvert, *J. Am. Chem. Soc.*, 1996, **118**, 3069.
37. D. Hilvert, *Abstr. Pap. Am. Chem. Soc.*, 1997, **214**, 167.
38. D. J. Gustin, P. Mattei, P. Kast, O. Wiest, L. Lee, W. W. Cleland and D. Hilvert, *J. Am. Chem. Soc.*, 1999, **121**, 1756.
39. A. Kienhofer, P. Kast and D. Hilvert, *J. Am. Chem. Soc.*, 2003, **125**, 3206.
40. A. Warshel, P. K. Sharma, M. Kato, Y. Xiang, H. B. Liu and M. H. M. Olsson, *Chem. Rev.*, 2006, **106**, 3210.
41. I. Rozas, *Phys. Chem. Chem. Phys.*, 2007, **9**, 2782.
42. A. M. Pendas, M. A. Blanco and E. Francisco, *J. Chem. Phys.*, 2006, **125**, #184112.
43. W. W. Cleland and M. M. Kreevoy, *Science*, 1994, **264**, 1887.
44. P. A. Frey, S. A. Whitt and J. B. Tobin, *Science*, 1994, **264**, 1927.
45. W. S. Brinigar and T. L. Chao, *Biochem. Biophys. Res. Commun.*, 1975, **63**, 78.
46. N. Wellner and G. Zundel, *J. Mol. Struct.*, 1994, **317**, 249.
47. T. Ishida, *Biochemistry*, 2006, **45**, 5413.
48. M. I. Page and W. P. Jencks, *Proc. Natl. Acad. Sci. USA*, 1971, **68**, 1678.
49. J. Villa, M. Strajbl, T. M. Glennon, Y. Y. Sham, Z. T. Chu and A. Warshel, *Proc. Natl. Acad. Sci. USA*, 2000, **97**, 11899.
50. X. Y. Zhang and K. N. Houk, *Acc. Chem. Res.*, 2005, **38**, 379.
51. T. C. Bruice and P. Y. Bruice, *J. Am. Chem. Soc.*, 2005, **127**, 12478.
52. D. A. Kraut, K. S. Carroll and D. Herschlag, *Annu. Rev. Biochem.*, 2003, **72**, 517.
53. G. Winter, A. R. Fersht, A. J. Wilkinson, M. Zoller and M. Smith, *Nature*, 1982, **299**, 756.
54. S. Gronert, *J. Org. Chem.*, 2006, **71**, 1209.
55. K. U. Ingold and G. A. Dilabio, *Org. Lett.*, 2006, **8**, 5923.
56. H. G. Nagendra, N. Sukumar and M. Vijayan, *Proteins*, 1998, **32**, 229.
57. D. Antoniou and S. D. Schwartz, *J. Phys. Chem. B*, 2001, **105**, 5553.
58. V. L. Schramm, *Arch. Biochem. Biophys.*, 2005, **433**, 13.

CHAPTER 2

Introduction to Quantum Behaviour – A Primer

SAM P. DE VISSER

The Manchester Interdisciplinary Biocentre and the School for Chemical Engineering and Analytical Science, The University of Manchester, 131 Princess Street, Manchester M1 7DN, UK

2.1 Introduction

There are many computational procedures available to calculate atomistic systems ranging from *ab initio* methods, whereby a system is calculated from scratch, *i.e.* without prior knowledge of the chemical system, to (semi)empirical methods that include experimentally derived parameters (*e.g.* bond stretching and bending parameters). Generally, quantum-mechanical (QM) methods fall into the first category and are based on solving the Schrödinger equation (see below). Although, with QM methods one can calculate systems with reasonable accuracy, they do scale with the number of atoms/electrons in the system. Therefore, these methods are not suitable for studies on enzymatic systems. However, alternative methods, such as molecular mechanics (MM) that can treat systems with tens of thousands of atoms, cannot model bond-breaking/formation processes. Therefore, new methods have been developed that combine the speed of MM with the accuracy of QM. Thus, computational procedures nowadays are able to describe enzymatic systems of which many examples will be given in this and other chapters here.

Recent advances in density functional theory (DFT) in combination with increased computational power have resulted in increased interest in theoretical

RSC Biomolecular Sciences

Quantum Tunnelling in Enzyme Catalysed Reactions

Edited by Rudolf K. Allemann and Nigel S. Scrutton

© Royal Society of Chemistry 2009

Published by the Royal Society of Chemistry, www.rsc.org

chemistry procedures. In particular, DFT calculations nowadays can predict free energies of activation with reasonable accuracy (\pm a few kcal mol⁻¹) with respect to experiment at low computational cost: studying chemical systems of up to 200 atoms is routinely done these days. As a result of that DFT calculations are being performed more often to support experimental, such as biochemical and inorganic, studies to assist with the interpretation of data and to guide novel experiments. To introduce the nonexpert into the basic principles underlying DFT and theoretical chemistry procedures in general, this chapter summarises the basic theories of quantum mechanics and DFT and explains how these methods can be applied to calculate accurate reaction mechanisms including ones leading to tunnelling.

2.1.1 Classical Mechanics

Generally, movements of macroscopic objects are accurately described by classical mechanics (Newtonian mechanics) equations, whereby the energy is split into kinetic energy (based on the movement, *i.e.* momentum, of a particle) and potential energy, which is determined by the position of the particle and is influenced by the forces acting on it.^{1 3} The classical mechanics equations were found to be useful for descriptions of everyday objects, but failed to explain systems of atomic size or with small momentum or energy. Therefore, a new theory was developed (quantum mechanics) that describes atomistic systems appropriately. There are many good and detailed books available that describe the theories of quantum mechanics; for space economy we will give a brief summary here for the nonexpert.^{3 5}

2.2 Quantum Mechanics

2.2.1 Heisenberg Uncertainty Principle

In the first half of the 20th century the theory of quantum mechanics was developed that went one step further from classical mechanics in the sense that it takes the Heisenberg uncertainty principle into consideration. Thus, the Heisenberg uncertainty principle rules that it is impossible to know the values accurately of conjugate properties.⁶ For instance, for a particle on a line the momentum (p), *i.e.* the velocity of the particle, and the position (x) are conjugate properties for which Heisenberg derived:

$$\Delta p \Delta x = h \quad (2.1)$$

In other words, the uncertainty in the momentum (Δp) multiplied with the uncertainty in the position (Δx) is equal to Planck's constant (h). That means that for atomic systems one cannot accurately determine the particle speed (momentum) and position at the same time and therefore they are conjugated

parameters. Many quantum-mechanical variables are conjugate parameters such as energy (E) and time (t) and as a result their uncertainty is also connected to Planck's constant via $\Delta E \Delta t = h$. These uncertainty principles basically prevent the use of the classical mechanics equations for atomistic systems. Therefore, more appropriate equations have been developed that take the Heisenberg principles into account and enables one to describe atomic and molecular systems.

2.2.2 The Schrödinger Equation

In the beginning of the 20th century it was shown by Schrödinger, de Broglie and others that atomic particles (nuclei, electrons) behave as waves (with a wavelength) and as particles (with momentum), which was termed the duality of matter. Thus, in quantum mechanics the particles in a system are described by a wavefunction (Ψ) and all perturbations that influence this wavefunction determine the actual shape and size of the wavefunction. Thus, in the electronic ground state the kinetic and potential energy contributions give the system its minimum energy E as described by the Schrödinger equation shown below in eqn (2.2).⁷ The perturbations that determine the wavefunction and the energy of the system are assembled in a mathematical function called the Hamilton operator (\hat{H}), named after the physicist W. R. Hamilton, and contain potential as well as kinetic perturbations.

$$\hat{H}\Psi = E\Psi \quad (2.2)$$

The Hamilton operator (or Hamiltonian for short) of a molecular system describes the interactions of the electrons and protons within the molecule. For instance, the Hamiltonian for the interactions of an electron and a proton in the hydrogen atom is described as:

$$\hat{H} = -\frac{\hbar^2}{2m_e} \nabla^2 + \frac{e^2}{4\pi\epsilon_0 R} \quad (2.3)$$

The first term represents the kinetic energy of the electron with mass m_e , whereas the second term is the Coulombic attraction at distance R between the proton and electron each with charge e . In this equation \hbar is Planck's constant divided by 2π and ϵ_0 is the permittivity in vacuum. The symbol ∇ , called the Laplacian, represents the sum of all partial derivatives to each individual coordinate, *i.e.* $\nabla^2 = \frac{\partial^2}{\partial x^2} + \frac{\partial^2}{\partial y^2} + \frac{\partial^2}{\partial z^2}$. The system can be described in Cartesian coordinates using a defined x -, y -, and z -axis, but alternatively can be written in internal coordinates where the particles are connected *via* a distance (r), an angle (ϕ) and dihedral angle (θ). The latter is usually preferable since in some cases the angular and radial components can be separated, so that the wavefunction can be split

into a radial (R) and angular (Θ) part and solved independently, *i.e.* $\Psi=R\Theta$. In this way, for the radial contribution of the wavefunction for the hydrogen atom mathematical solutions of the Schrödinger equation are obtained from associated Laguerre functions:

$$R_{nl}(r) = - \left\{ \left(\frac{2Z}{na} \right)^3 \frac{(n-l-1)!}{2n[(n+l)!]^3} \right\} \rho^l L_{n+l}^{2l+1}(\rho) e^{-\rho/2} \quad (2.4)$$

In equation 2.4, $R_{nl}(r)$ is the radial wavefunction as a function of the distance r between the electron and the proton, while n is the principal quantum number and l the orbital angular momentum. The atomic number is Z , while a is a constant ($a = 4\pi\epsilon_0 h^2/\mu e^2$) dependent on the charge e and reduced mass μ of the system. Finally, ρ is a function of the atomic number and the distance *via* $\rho=(2Z/na)r$. This wavefunction gives rise to one-electron wavefunctions called atomic orbitals, which are labelled according to principal quantum number (n) and orbital angular momentum (l): nl , whereby the orbital angular momentum has the label $s, p, d, f, g \dots$ rather than $0, 1, 2, 3, 4 \dots$ Figure 2.1 shows examples of typical atomic orbitals with $n=2$ and $l=1$ ($2p$ orbitals) and with $n=3$ and $l=2$ ($3d$ orbitals) as generated from a DFT calculation on the fluoride atom. To distinguish the three individual $2p$ or five individual $3d$ orbitals a sublabel is added identifying the coordinate system, *i.e.* the subscript xy in $3d_{xy}$ for instance. Officially, there is a third quantum number (the magnetic quantum number m_l) that has an integer value between $+l$ and $-l$ that distinguishes each individual orbital angular momentum orbital but this quantum number is less commonly used in theoretical chemistry procedures to identify orbitals.

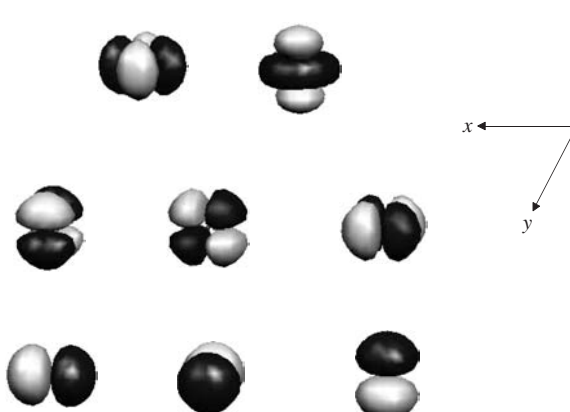


Figure 2.1 Drawings of the three $2p$ (bottom) and five $3d$ (top) atomic orbitals as obtained from UB3LYP/6 31G* calculations on a fluoride atom.

2.3 Electronic-Structure Calculations

2.3.1 Born Oppenheimer Approximation

Basically, electronic-structure calculations use the Schrödinger equation to calculate molecular geometries and energies. These equations become increasingly complex with the size of the system and only exact solutions for the hydrogen atom and the hydrogen molecule cation are known. Therefore, assumptions are made to be able to solve the Schrödinger equation numerically for molecular systems. The first approximation is the Born–Oppenheimer approximation that assumes that movements of the electrons can be separated from the movements of the nuclei.⁸ The mass of the electron is 1822 times smaller than the mass of a proton, so that the velocity (and hence momentum) of the electron will be much larger than the one for a nucleus. As such, the nuclei can be seen as rigid in the plane of the fast-moving electrons. The Born–Oppenheimer approximation, therefore, assumes that the coordinates of the nuclei are constant including the distances between the nuclei and that only the electrons move. This then gives rise to an electronic wavefunction that describes the electrons in the field of the nuclei. The Hamiltonian describing this electronic system with N_e electrons and N_p protons can be written as follows:

$$\hat{H} = -\frac{\hbar^2}{2m_e} \sum_i^{N_e} \nabla_i^2 - \sum_i^{N_e} \sum_I^{N_p} \frac{Z_I e^2}{4\pi\epsilon_0 r_{Ii}} + \frac{1}{2} \sum_{i,j}^{N_e} \frac{e^2}{4\pi\epsilon_0 r_{ij}} \quad (2.5)$$

The first term is the kinetic-energy contribution of the electrons and is similar to the first term in eqn (2.3) earlier. The second term is the electron–nucleus attraction and the last term the electron–electron repulsion. These two terms are the sum of all the interactions of N_e electrons with N_p protons and of N_e electrons with $N_e - 1$ other electrons. As such, the larger the molecular system, the more complex the expression in eqn (2.5) becomes. Generally, eqn (2.5) is the basis of the electronic Schrödinger equation and is being solved in quantum-chemical calculations.

The wavefunction is split into n one-electron wavefunctions (orbitals, ϕ) that contain an orbital wavefunction and a spin function,

$$\Psi = \frac{1}{\sqrt{n!}} \det |\phi_a(1)\phi_b(2)\dots\phi_z(n)| \quad (2.6)$$

2.3.2 Hartree Fock Theory

In this section we will describe how the Schrödinger equation is solved for a system with Hamiltonian (eqn (2.5)) and wavefunction (eqn (2.6)). In Hartree–Fock theory (HF) equations are set up to solve all individual one-electron

wavefunctions, *e.g.* for electron 1 in orbital ϕ_a :

$$f_1 \phi_a(1) = \epsilon_a \phi_a(1) \quad (2.7)$$

eqn (2.7) uses the Fock operator f_1 to calculate the orbital energy (ϵ_a) of an electron in orbital ϕ_a . The Fock operator is split into three parts: a core Hamiltonian (h_1) that describes the kinetic energy and one-electron integrals and expressions for the two-electron integrals: the Coulomb operator (J_u) and the exchange operator (K_u), eqns (2.8)–(2.10).

$$f_1 = h_1 + \sum_u \{J_u(1) - K_u(1)\} \quad (2.8)$$

$$J_u(1)\phi_a(1) = \left\{ \int \phi_u^*(2) \frac{e^2}{4\pi\epsilon_0 r_{12}} \phi_u(2) d\mathbf{x}_2 \right\} \phi_a(1) \quad (2.9)$$

$$K_u(1)\phi_a(1) = \left\{ \int \phi_u^*(2) \frac{e^2}{4\pi\epsilon_0 r_{12}} \phi_u(2) d\mathbf{x}_2 \right\} \phi_u(1) \quad (2.10)$$

In order to describe the wavefunction it was suggested to introduce basis functions (θ_j) and express the wavefunction as a linear combination (with coefficients c_{ji}) of the M basis functions:^{9,10}

$$\phi_i = \sum_{j=1}^M c_{ji} \theta_j \quad (2.11)$$

Using these basis functions the overlap matrix (\mathbf{S}_{ij}) and Fock matrix (\mathbf{F}_{ij}) are calculated:

$$\mathbf{S}_{ij} = \int \theta_i^*(1) \theta_j(1) d\mathbf{r}_1 \quad (2.12)$$

$$\mathbf{F}_{ij} = \int \theta_i^*(1) f_1 \theta_j(1) d\mathbf{r}_1 \quad (2.13)$$

Essentially, eqns (2.8)–(2.13) give rise to the Roothaan equations, and the algorithm used by electronic-structure packages to solve the equations is shown in Figure 2.2. Thus, one gives the program a starting structure, *i.e.* a molecular geometry of the positions of the nuclei and chooses a set of basis functions θ_j , *i.e.* a basis set. Using these basis functions, a set of trial coefficients (c_{ja}) are created to calculate the overlap matrix (eqn (2.12)) and the

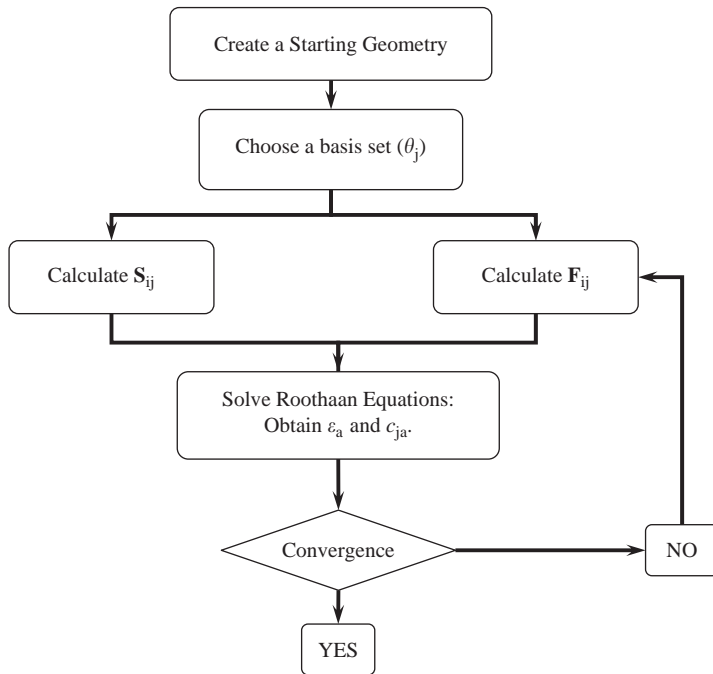


Figure 2.2 Flow chart for a typical quantum chemical calculation.

Fock matrix (eqn (2.13)). These are embedded into the secular determinant:

$$\det|F - \epsilon_a S| = 0 \quad (2.14)$$

Solving this determinant gives energies (ϵ_a) and coefficients (c_{ja}). The new coefficients are compared with the previous coefficients and when they are considered identical the calculation is said to be converged (finished). However, when the new coefficients are significantly different from the old coefficients the process is repeated until the coefficients do converge. The converged wavefunction is, therefore, the ‘best’ computational energy for this particular structure. However, this energy is still connected to the input geometry. In a subsequent calculation the geometry is optimised to its lowest energy point on the potential-energy surface. Basically, this is done iteratively by repeating the flow-chart of Figure 2.2 for different geometries. Thus, after convergence of the wavefunction for geometry 1 the program changes the coordinates of the starting structure slightly to create geometry 2 and repeats the flow-chart in Figure 2.2 to converge the wavefunction again. Thereafter, the first derivative of the energy to the molecular coordinates is taken to create a new geometry 3. The system keeps on repeating this process until the absolute energy, the first derivative of the energy to the

nuclear coordinates and the change of coordinates no change within certain cutoff points. In other words the geometry optimisation has converged and an optimised geometry has been found with corresponding minimal electronic energy.

Generally, however, Hartree–Fock theory does not give accurate energies since it does not account for electron–electron interactions properly especially for electron interactions with electrons of opposite spin. In order to solve these problems and obtain more accurate energies methods have been introduced that supply this electron correlation, such as configuration interaction (CI) and Møller–Plesset perturbation theory (*e.g.* MP2). These methods work by taking excitations of electrons from occupied to virtual orbitals into account and entering those perturbations into the wavefunction. Although, these methods give considerable improvement in the energetics, they are not always practical because due to their increased computational costs can only be applied to small systems (these days up to 30 atoms with MP2 is possible). Since, the focus of this book is on biosystems these methods are generally not applicable to the systems under study here and we will not describe these methods in detail and the interested reader is referred to the many quantum-chemical books available, see, *e.g.*, refs. 3–5.

2.3.3 Basis Sets

The orbital wavefunctions of the hydrogen atom are shown to be a function proportional to $\exp(-\zeta r)$, called Slater-type orbitals, and conform to eqn (2.4) above. However, these functions are difficult to integrate computationally, therefore, an alternative procedure has been developed whereby the orbitals are described as a sum of several Gaussian-type functions proportional to $\exp(-\zeta r^2)$. Equations (2.15)–(2.17) show mathematical functions of the three primitive Gaussian functions for an s , p_y and d_{xy} orbital, respectively, with α being a constant describing the radical extent of the basis function.⁴ The molecular orbitals are then a linear combination of these basis functions.

$$g_s = \left(\frac{2\alpha}{\pi}\right)^{\frac{3}{4}} e^{-\alpha r^2} \quad (2.15)$$

$$g_y = \left(\frac{128\alpha^5}{\pi^3}\right)^{\frac{1}{4}} ye^{-\alpha r^2} \quad (2.16)$$

$$g_{xy} = \left(\frac{2048\alpha^7}{\pi^3}\right)^{\frac{1}{4}} xye^{-\alpha r^2} \quad (2.17)$$

Thus, during the SCF convergence of a molecule the atomic orbitals mix to form molecular orbitals. An example of this is shown in Figure 2.3 that shows the formation of the orbitals of H_2 from atomic contributions, *i.e.* as a linear combination of atomic orbitals (LCAO). This results in a series of bonding (σ)

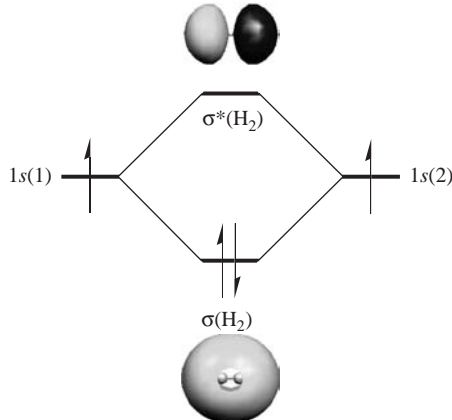


Figure 2.3 The mixing of two atomic 1s orbitals to form molecular orbitals in the H_2 molecule.

and antibonding (σ^*) orbitals and the sum of the energies of these orbitals is equal to the sum of the energies of isolated reactants. Since in H_2 both electrons reside in the low-lying $\sigma(\text{H}_2)$ orbital, the energy of the hydrogen molecule is lower than that of isolated atoms, hence forming a molecule is energetically favoured over isolated atoms.

In order to mathematically describe the shape and size of a molecular orbital, such as the σ and σ^* orbitals in Figure 2.3, a linear combination of atomic orbitals is used. The 1s and 2s orbitals of the hydrogen atom, however, are spherical symmetric around the individual atoms so that it is impossible to describe the σ and σ^* orbitals as a linear combination of *s*-type orbitals. To overcome this problem, polarisation functions are added that supply a set of *p*-orbitals to the wavefunction of hydrogen atoms and a set of *d*-functions to heavier elements.

Furthermore, when the molecule has lone-pair orbitals or is overall anionic it is generally required to add diffuse basis functions for a correct description of the chemical system. Thus, lone-pair or anionic orbitals are usually larger in shape, *i.e.* more diffuse, than normal bonding orbitals and are much better described with an extra set of valence orbitals, *i.e.* a set of 3s orbitals on hydrogen and a set of 3*p* orbitals on heavier (first-row) elements. These basis functions are labelled diffuse basis functions and identified with a '+' symbol in the basis set, whereas polarisation functions with a '*' symbol in the basis set. Thus, a 6-31+G* basis set refers to a Gaussian-type basis set with a set of diffuse and polarisation functions on all heavy (nonhydrogen) atoms.

2.3.4 Zero-Point Energy

Solving the secular determinant in eqn (2.14) gives orbital energies that sum up to a total electronic energy (E_e), which represents the ground-state energy of the

system in the gas phase at 0 K temperature. However, this is not the correct absolute energy of the system since electrons occupy vibrational levels. To correct this, a geometry optimisation is followed by a frequency calculation that determines these vibrational energy levels. The energy at a temperature of 0 K is then corrected with a zero-point energy (ZPE) that represents the lowest vibrational level of the system. Essentially, the actual energy in the lowest rovibronic state (E_0) equals $E_e + \text{ZPE}$, whereby E_0 is the actual energy of the system at 0 K, and can be correlated to differences in enthalpies of formation of a system at 0 K.

A frequency calculation has several important features in addition to the calculation of the ZPE. First, a molecular system of N atoms in a local minimum should have $3N - 6$ real vibrational frequencies ($3N - 5$ for linear molecules). On the other hand, the calculation of a first-order saddle point (transition state, TS) of a nonlinear molecule should produce $3N - 5$ real frequencies and one imaginary frequency. This is because along one degree of freedom the energy of the TS is on a maximum rather than an energetic minimum of the curve as shown in Figure 2.4. Thus, the number of imaginary frequencies in the calculation tells us what order of saddle point has been calculated. This is in contrast to the reactant and product species that are minimum-energy structures with real frequencies only.

Pople and coworkers^{11,12} developed an empirical model to estimate accurate enthalpies of formation of molecules based on the fact that computational methods tend to give a systematic difference (either overestimating or underestimating energies) with experimental data. The earliest of those procedures were the G2 and G3 methods, which were shown to reproduce experimental enthalpies of formation within chemical accuracy, *i.e.* within 1 kcal mol⁻¹. However, these methods are computationally demanding and can only be applied to systems of up to 20 atoms or so.

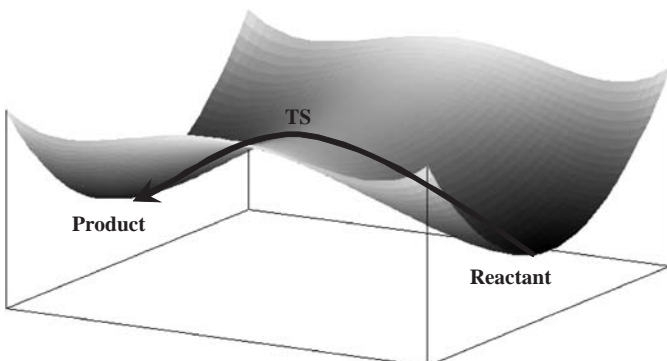


Figure 2.4 Potential energy surface of the reaction of reactant leading to product via a transition state. Energetically, the reactant and product are located in a local minimum, whereas the transition state (TS) is a first order saddle point.

2.4 Density Functional Theory

Density functional theory (DFT), in contrast to wavefunction quantum mechanics, describes the energy as a functional of the electron density: $\rho(\mathbf{r})$.¹³ Kohn *et al.* derived a set of one-electron equations that enables one to calculate the electron density and consequently the total energy of the system.^{14,15} This methodology has been proven to be very successful recently as calculations using this method have been shown to be much less computationally expensive, while at the same time reasonable agreement with experiment for relatively large chemical systems is observed.¹⁶

Thus, similarly to a Hartree–Fock calculation as shown above, also the total energy (E_{el}) of a DFT calculation (eqn (2.18)) is split into a kinetic energy term, a term representing the electron–nucleus attractions, a term for the Coulomb interactions between the electrons and an exchange-correlation term (E_{xc}), respectively.¹³ The first three terms resemble the Hartree–Fock Hamiltonian shown in eqn (2.5) above as a function of the nuclear coordinates (\mathbf{R}), and the coordinates of the electrons (\mathbf{r}).

$$\begin{aligned} E_{\text{el}} = & -\frac{1}{2} \sum_i \int \phi_i(\mathbf{r}_1) \nabla^2 \phi_i(\mathbf{r}_1) d\mathbf{r}_1 \\ & + \sum_A \int \frac{Z_A}{|\mathbf{R}_A - \mathbf{r}_1|} \rho(\mathbf{r}_1) d\mathbf{r}_1 \\ & + \frac{1}{2} \int \frac{\rho(\mathbf{r}_1)\rho(\mathbf{r}_2)}{|\mathbf{r}_1 - \mathbf{r}_2|} d\mathbf{r}_1 d\mathbf{r}_2 + E_{\text{xc}} \end{aligned} \quad (2.18)$$

The exchange-correlation functional is unknown and therefore approximate equations have been set up to estimate its contribution. Generally, E_{xc} is split into an exchange functional (E_X) and a correlation functional (E_C). The exchange functional essentially represents the interactions of two ferromagnetic spins in different orbitals, whereas the correlation is the pairing energy of electrons in the same orbital.

Often, the exchange energy is estimated from the Slater exchange function:

$$E_X^{\text{Slater}} = -\frac{9}{4\alpha_{\text{ex}}} \left(\frac{3}{4\pi} \right)^{1/3} \sum_{\gamma} \int [\rho_1^{\gamma}(\mathbf{r}_1)]^{4/3} d\mathbf{r}_1 \quad (2.19)$$

In this equation α_{ex} is an exchange scale factor that has the value 2/3 for an electron gas.

A commonly used correlation energy functional (E_C^{VWN}) is due to Vosko, Wilk and Nusair¹⁷ and represents the correlation energy per electron in a

gas $\varepsilon_c[\rho_1^\alpha, \rho_1^\beta]$ with spin densities ρ_1^α and ρ_1^β :

$$E_C^{\text{VWN}} = \int \rho_1(\mathbf{r}_1) \varepsilon_c \left[\rho_1^\alpha(\mathbf{r}_1), \rho_1^\beta(\mathbf{r}_1) \right] d\mathbf{r}_1 \quad (2.20)$$

Combination of Slater exchange and Vosko–Wilk–Nusair correlation, which are both directly derived from the homogenous electron-gas equations, gives the local density approximation. However, to correct for nonlocal terms other (better) exchange and correlation functionals have been developed. Two popular approaches are due to Lee, Yang and Parr (LYP correlation functional)¹⁸ and Perdew and Wang (PW91 correlation functional),¹⁹ but there are many more available functionals all with their own qualities and/or drawbacks.

A breakthrough in DFT and computational chemistry in general appeared when Becke developed the hybrid density functional procedures.²⁰ Thus, Becke benchmarked DFT methods against a test set of experimentally known ionisation energies, electron affinities and proton affinities with high accuracy. He came up with a three-parameter (hybrid) density functional method to estimate the contributions of the exchange and correlation functions and optimised the values of these three fit parameters (A , B , and C) against the experimental data in the test set. There are many possibilities of combining the various exchange and correlation functionals, but throughout the years the most popular one has become the B3LYP method, although it should be realised that it is not necessarily the most accurate one. Becke used B3PW91 rather than B3LYP in his original paper, but we will use B3LYP here as an example since it is the most popular DFT method.²⁰ Essentially the hybrid density functional method B3LYP has the following form:

$$E_{\text{xc}}^{\text{B3LYP}} = AE_{\text{X}}^{\text{Slater}} + (1 - A)E_{\text{X}}^{\text{HF}} + B\Delta E_{\text{X}}^{\text{Becke}} + E_C^{\text{VWN}} + C\Delta E_C^{\text{LYP}} \quad (2.21)$$

Thus, it takes the local density approximation functions of Slater and Vosko–Wilk–Nusair (eqns (2.19) and (2.20)), the Hartree–Fock exchange, a correction term for the exchange due to Becke and the Lee–Yang–Parr correction for nonlocal correlation factors. The coefficients A , B , and C are essentially fit parameters obtained through fitting the energies of B3LYP/6–31G* calculations against experimentally obtained ionisation energies and electron affinities. Consequently, the B3LYP method in essence is not an *ab initio* method any longer as the term *ab initio* means starting from scratch without prior knowledge of experiment. Nevertheless, these fit parameters have created an accurate and low-cost computational method and as a result B3LYP has become one of the widest used techniques in science over the past decade. The B3LYP method, as well as other hybrid and nonhybrid DFT methods, has been shown to be extremely accurate and versatile for computational chemists. Although in general the accuracy of DFT is not as good as high-level *ab initio* methods, such

as coupled cluster methods, their speed in combination with reasonable accuracy makes them a very popular and useful methodology.

In his original paper Becke already published calculated energies within 2 kcal mol⁻¹ of experiment, which is not too far from the ultimate accuracy goal of computational chemistry of 1 kcal mol⁻¹ (chemical accuracy) defined by Pople *et al.* Over the years, improvement of the fitting parameters has been obtained by enlarging the test set. Thanks to this achievement, DFT has become one of the most extensively used methods in chemistry that combines reasonable accuracy with speed. Recent comparative calculations on the complete test-set molecules using three different techniques, *i.e.* Hartree–Fock theory, MP2 theory and DFT methods (using B3LYP) showed that the B3LYP methodology gives a considerable improvement over Hartree–Fock as well as over MP2 calculations.¹⁶ In some cases, DFT reproduces results obtained with the much more computationally demanding G2 methodology of Pople *et al.* Therefore, DFT is a low-cost alternative to quantum-chemical procedures and as such highly suitable to calculate biochemical systems.

2.4.1 DFT Calculations of Free Energies of Activation of Enzyme Models

Apart from reproducing enthalpies of formation of atoms and molecules, it has also been tested whether DFT can reproduce rate constants and free energies of activation of reaction processes. In our group, we recently reported DFT calculations on styrene epoxidation by a cytochrome P450 mimic, and the reaction mechanism is shown in Figure 2.5.²¹ The P450s are a large group of heme enzymes involved in many monooxygenation processes in biosystems involving, *e.g.*, the detoxification of organic compounds from the liver, the biosynthesis of hormones and drug metabolism. The active species of this enzyme is believed to be an oxoiron species inside a heme group, but due to its short lifetime this species has never been trapped and characterised experimentally. DFT studies are therefore useful to complement experimental data and make predictions regarding reaction processes and mechanisms especially when short-lived species are involved. This oxoiron active species (Compound I, CpdI) has close-lying quartet and doublet spin states both with three unpaired electrons: two located on the oxoiron group and a third on the heme.²² As a result of that, the reaction with substrates takes place on competing quartet and doublet spin state surfaces *via* multistate reactivity patterns.²³ We set up a model of the active species of P450 that includes the oxoiron group, heme without side chains and thiolate for the axial bound cysteinate group. Subsequently, we calculated the reaction mechanism of styrene epoxidation by this catalyst and the B3LYP result is shown in Figure 2.5. Thus, the reaction is stepwise *via* an initial C–O bond formation transition state (TS1) leading to a radical intermediate (Int) with a radical on the substrate. The radical centre than attacks the oxo group *via* a ring-closure transition state (TS2) to form epoxide products (Prod). On the doublet spin surface the intermediate collapses to products

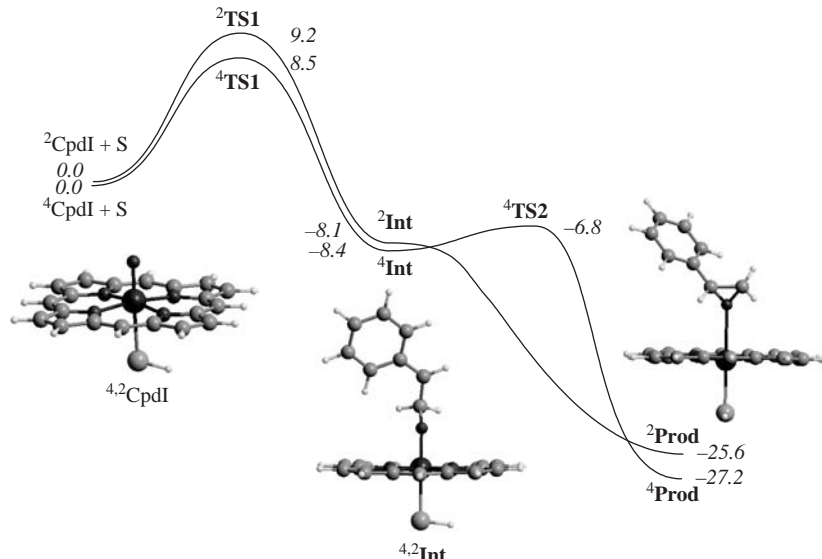


Figure 2.5 Potential energy profile for the epoxidation of styrene by a Cpdl model of P450 in the quartet and doublet spin states, as adapted from ref. 21. The superscript identifies the spin state of the system. All energies are in kcal mol^{-1} relative to isolated reactants in the quartet spin state and contain ZPE corrections.

without significant ring-closure barrier, so that the lifetime of this intermediate will be short. The initial reaction barrier, *i.e.* via TS1, is rate determining and has barriers of $\Delta E + ZPE = 8.5$ and $9.2 \text{ kcal mol}^{-1}$ in the quartet and doublet spin states, respectively. Adding entropic and thermal corrections to the $\Delta E + ZPE$ values gives the free energy of activation $\Delta G^\ddagger = 20.9 \text{ kcal mol}^{-1}$ for TS1, which compares well with the experimentally determined value of 24–25 kcal mol^{-1} as predicted for the reaction of styrene with P450_{cam}.

2.4.2 DFT Calculations of Kinetic Isotope Effects

Recent DFT studies on an oxoiron nonheme biomimetic with an N4Py [*N,N*-bis(2-pyridylmethyl)-*N*-bis(2-pyridyl)methylamine] pentadentate ligand were performed and the reactivity patterns with respect to arenes calculated and compared with experiment.²⁴ Thus, theory (B3LYP) predicts FeON4Py to be an efficient catalyst that is able to hydroxylate arenes with low barriers. In the case of benzene hydroxylation a free energy of activation $\Delta G^\ddagger = 16.1 \text{ kcal mol}^{-1}$ was calculated, while an experimentally determined value for anthracene hydroxylation by the same catalyst was measured as $19.6 \text{ kcal mol}^{-1}$. This is very good agreement of experimentally and theoretically obtained free energies of activation and rate constants and implies that DFT barriers are reliable and accurate and should be able to predict kinetic isotope effects. We then

calculated the free energy of activation (ΔG_D^\ddagger) of the fully deuterated substrate (C_6D_6) by recalculating the frequencies using the heavier isotopes. The classical (Eyring) isotope effect (KIE_{Eyring}) is then calculated from the ratio of the rate constants (k_H and k_D) of C_6H_6 versus C_6D_6 :

$$KIE_{\text{Eyring}} = \frac{k_H}{k_D} = \exp\left(\frac{\Delta G_D^\ddagger - \Delta G_H^\ddagger}{RT}\right) \quad (2.22)$$

Further corrections by multiplying KIE_{Eyring} with the tunnelling ratio (Q_{tH}/Q_{tD}) of the hydrogen versus deuterium substituted systems gives the Wigner kinetic isotope effect (KIE_{Wigner}).

$$Q_{tH} = 1 + \frac{1}{24} \left(\frac{hv}{k_B T} \right)^2 \quad (2.23)$$

In eqns (2.22) and (2.23), R is the gas constant, T the estimated temperature (298 K), h is Planck's constant, k_B is Boltzmann's constant and v the value of the imaginary frequency in the transition state. The estimated rate constants for the substrate and the deuterium-substituted substrate indicate that there is an inverse isotope effect of $KIE_{\text{Wigner}} = 0.9$ for the reaction, which is in perfect agreement with experimentally determined kinetic isotope effects.

2.5 Quantum-Mechanics/Molecular-Mechanics Methods

Although DFT methods are relatively fast and cheap computational methods, they are still only applicable to systems of up to 200 atoms or so. Therefore, methodologies have been developed that can treat biological systems, such as enzymes but that retain the accuracy of either DFT or *ab initio* methods. The quantum-mechanics/molecular-mechanics (QM/MM) methodology splits a chemical system, such as an enzyme into two regions: an inner core that describes the essential features of the catalytic centre and an outer range of the full protein surrounding and solvent.²⁵ The inner core is then calculated with accurate computational methods, such as DFT or *ab initio*, whereas the outer range is calculated using cheap molecular mechanics (MM) based on classical empirical potentials. A very detailed review on QM/MM can be found in ref. ²⁵, we will here give one example of the method only.

Recently, we applied the QM/MM methodology to study the active species of enzyme taurine/ α -ketoglutarate dioxygenase (TauD).²⁶ This is a nonheme enzyme in *E. coli* that hydroxylates taurine, which acts a sulfur source for the bacterium.²⁷ α -Ketoglutarate dioxygenase enzymes are a large class of enzymes involved in the biosynthesis of antibiotics (in bacteria), the biosynthesis of collagen in mammals as well as DNA base repair. The active species that

performs the hydroxylation reaction is an oxoiron species that is linked to the protein backbone *via* linkages with two histidine and one aspartic acid residue. In the catalytic cycle, α -ketoglutarate and dioxygen bind to the iron centre and are converted into succinate and an oxoiron species. The latter abstracts a hydrogen atom from the substrate (taurine) and rebinds the hydroxyl group to form hydroxylated taurine products. Thus, to find out how taurine is hydroxylated, we ran QM/MM as well as DFT calculations on models of the oxoiron species of TauD, see Figure 2.6. The DFT model contains histidine groups replaced by imidazole and succinate and aspartate by acetate and counts 46 atoms.²⁸ By contrast in the QM/MM model a sphere of 15 Å around the iron atom is considered for the MM space, while the QM region contains all direct ligands of iron, *i.e.* the imidazole chains of histidine, the acetic acid groups of succinate and aspartate as well as taurine and part of an arginine side chain with a total of 671 atoms in the model of which 57 in the QM region. Optimised geometries using B3LYP/LANL2DZ are shown in Figure 2.6 for the lowest-lying quintet, triplet and septet spin states. As can be seen the protein environment in QM/MM calculations has a small effect on the Fe–O bond distances and also affects the energy separation between the three low-lying spin states. Therefore, QM/MM calculations describe a chemical system in its native environment and the local perturbations, such as electrostatic and solvent interactions of the surrounding are taken into account in the calculations. As a

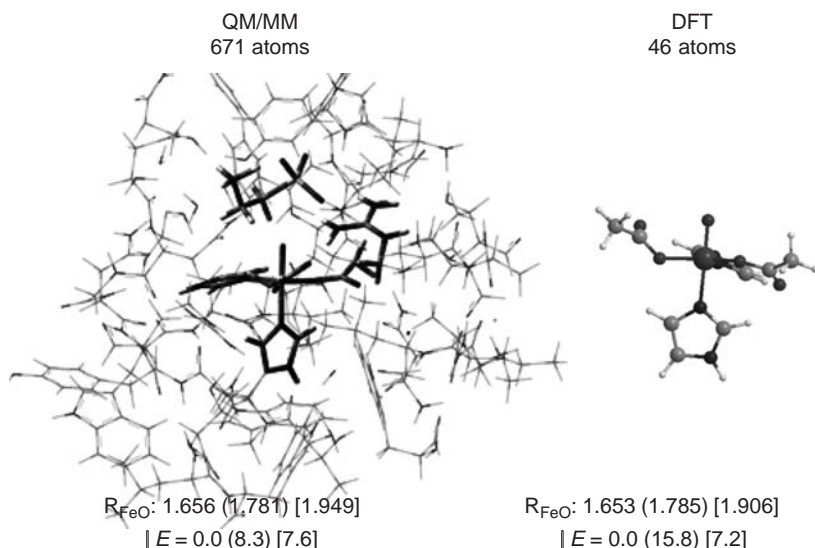


Figure 2.6 Optimized geometries of the oxoiron species of TauD as calculated with QM/MM (left) and DFT (right). The QM region is shown in bold sticks, while the shaded sticks represent the MM region. Highlighted data are the oxoiron distance (R_{FeO} in Å) and the energy difference (ΔE in kcal mol^{-1}) between the quintet, triplet (in parenthesis) and septet (in square brackets) spin states.

result, these calculations are expected to give a more reliable reproduction of a natural system.

2.6 Summary and Outlook

In this chapter the basic background has been given of the theories behind computational chemistry procedures. There are many different computational chemistry procedures all with advantages and disadvantages. It is up to the user to find the most appropriate methods to address the scientific questions, but generally the methods have become more accurate in recent years. This should enable users to apply computational methods to enzyme-catalysed reactions and predict tunnelling effects with reasonable accuracy. Indeed such approaches are becoming more and more routine and many examples of those will be given in later chapters in this book.

References

1. P. W. Atkins, *Physical Chemistry*, 4th edn, Oxford University Press, Oxford, 1990.
2. G. M. Barrow, *Physical Chemistry*, 6th edn, McGraw-Hill Companies, Inc., New York, 1996.
3. F. Jensen, *Introduction to Computational Chemistry*, 2nd edn, John Wiley & Sons, Ltd., Chichester, 2007.
4. J. B. Foresman and A. Frisch, *Exploring Chemistry with Electronic-structure methods*, 1st edn, Gaussian Inc., 1993.
5. P. W. Atkins and R. S. Friedman, *Molecular Quantum Mechanics*, 3rd edn, Oxford University Press, 1997.
6. W. Heisenberg, *Z. Phys.*, 1927, **43**, 172.
7. E. Schrödinger, *Phys. Rev.*, 1926, **28**, 1049.
8. M. Born and J. R. Oppenheimer, *Ann. Phys.*, 1927, **84**, 457.
9. C. C. J. Roothaan, *Rev. Mod. Phys.*, 1951, **23**, 69.
10. G. G. Hall, *Proc. Roy. Soc. (London) A*, 1951, **205**, 541.
11. J. A. Pople, M. Head-Gordon, D. J. Fox, K. Raghavachari and L. A. Curtiss, *J. Chem. Phys.*, 1989, **90**, 5622.
12. L. A. Curtiss, C. Jones, G. W. Trucks, K. Raghavachari and J. A. Pople, *J. Chem. Phys.*, 1990, **93**, 2537.
13. T. Ziegler, *Chem. Rev.*, 1991, **91**, 651.
14. P. Hohenberg and W. Kohn, *Phys. Rev. B*, 1964, **136**, 864.
15. W. Kohn and L. J. Sham, *Phys. Rev. A*, 1965, **140**, 1133.
16. P. E. M. Siegbahn, *Quart. Rev. Biophys.*, 2003, **36**, 91.
17. S. H. Vosko, L. Wilk and M. Nusair, *Can. J. Phys.*, 1980, **58**, 1200.
18. C. Lee, W. Yang and R. G. Parr, *Phys. Rev. B*, 1988, **37**, 785.
19. J. P. Perdew and Y. Wang, *Phys. Rev. B*, 1992, **45**, 13244.
20. A. D. Becke, *J. Chem. Phys.*, 1993, **98**, 5648.
21. D. Kumar, S. P. de Visser and S. Shaik, *Chem. Eur. J.*, 2005, **11**, 2825.

22. S. P. de Visser, S. Shaik, P. K. Sharma, D. Kumar and W. Thiel, *J. Am. Chem. Soc.*, 2003, **125**, 15779.
23. S. P. de Visser, F. Ogliaro, N. Harris and S. Shaik, *J. Am. Chem. Soc.*, 2001, **123**, 3037.
24. S. P. de Visser, K. Oh, A.-R. Han and W. Nam, *Inorg. Chem.*, 2007, **46**, 4632.
25. H. M. Senn and W. Thiel, *Top. Curr. Chem.*, 2007, **268**, 173.
26. E. Godfrey, C. S. Porro, S. P. de Visser, *J. Phys. Chem. A*, 2008, **112**, 2464.
27. J. M. Bollinger Jr., J. C. Price, L. M. Hoffart, E. W. Barr and C. Krebs, *Eur. J. Inorg. Chem.*, 2005, 4245.
28. S. P. de Visser, *J. Am. Chem. Soc.*, 2006, **128**, 9813.

CHAPTER 3

Quantum Catalysis in Enzymes

AGNIESZKA DYBALA-DEFRATYKA,^a PIOTR PANETH^a
AND DONALD G. TRUHLAR^b

^a Institute of Applied Radiation Chemistry, Technical University of Lodz,
Zeromskiego 116, 90-924 Lodz, Poland; ^b Department of Chemistry and
Supercomputing Institute, University of Minnesota, 207 Pleasant Street S.E.,
Minneapolis, MN 55455-0431, USA

3.1 Introduction

Enzyme-catalysed reactions span a wide range of reaction types and mechanisms. In many cases the rate-determining step is the transfer of a proton, hydride ion, or hydrogen atom; such reactions are almost always dominated by quantum-mechanical tunnelling. The effective barrier for tunnelling is highly dependent on the evolution of zero-point energy along the reaction path, and zero-point energy is one of the multidimensional effects that one must include in a reliable treatment of quantum-mechanical tunnelling. Even when tunnelling is negligible, changes in the zero-point energy of participating vibrational modes when the system passes from the reactant state to the transition state can have accelerating, or, less often, decelerating effects on reaction rates, and these kinds of vibrational effects, as well as the change in thermal vibrational energy of low-frequency quantised vibrational modes, are very important for studying kinetic isotope effects, which are one of the chief experimental tools for elucidating reaction mechanisms and probing the nature of transition states. Theoretical methods for systematically including the quantum effects of multidimensional tunnelling and quantised vibrations in the description of enzyme-catalysed reactions have been

developed and applied^{1–5} and are reviewed from a pedagogical perspective in this chapter.

Aside from quantum-mechanical scattering theory (see Appendix), which is only applicable to very small gas-phase systems, the best available theory of chemical reaction rates is transition-state theory, which has a long history of productive use for chemical reactions in the gas phase, in condensed phases, and in enzymes.^{1–14} Transition-state theory in its most basic form is a classical mechanical theory that corresponds to calculating the one-way flux through a coordinate-space hypersurface (usually one just says “surface”) that separates reactants from products.^{7,15–17} (More generally, the hypersurface could be defined in phase space, but for enzymatic reactions coordinate space will suffice.) The dividing surface is called the transition state^{7,9} (in some of the older literature it was often called the activated complex⁸). The vibrational mode normal to this surface is called the reaction coordinate, although this term is also used to refer to a global progress variable measuring the advance from reactants to the transition state to products. Sometimes, but not always, these two reaction coordinates coincide in the vicinity of the transition state. Note that the transition state is not a single geometric point but rather is the ensemble of all the points in the dividing surface. Transition-state theory employs statistical mechanics to sum the fluxes through all these points (“transition points”), properly weighted for a canonical ensemble.

In a classical-mechanical world, transition-state theory would be exact if the states of the reactant are populated according to a Boltzmann distribution, that is, a canonical ensemble (transition-state theory can also be extended to microcanonical ensembles, but that is more useful for gas-phase reactions than for enzymatic reactions, and it will not be considered further in this chapter), and if no classical trajectories recross the transition state without first being thermalised in the product region of coordinate space (or – for reverse trajectories – in the reactant region of coordinate space). The no-recrossing criterion will be satisfied exactly if the reaction coordinate is separable (that is, if the Hamiltonian may be written as a sum of a term depending only on the reaction coordinate and its conjugate momentum and other terms depending only on the other coordinates and their conjugate momenta, with no cross terms), and it will be approximately valid if the Hamiltonian is approximately separable. (Note that this separability is required not only in the nearby vicinity of the saddle point but also far enough along the reaction coordinate toward reactants and products that trajectories leaving the saddle point in either direction do not reflect back through the dividing surface.)

Quantum-mechanical effects can be incorporated into transition-state theory by two main routes.

In the first route, which has been used since the early days of transition-state theory, quantum effects are incorporated in two steps.^{6,8,11,17,19,20} First, all classical-mechanical vibrational partition functions are replaced by partition functions for quantised vibrations^{6,8,19} and electronic partition functions are added to account for multiple potential-energy surfaces.²¹ The calculated rate constant at this stage is sometimes called hybrid²⁰ and sometimes called quasiclassical;¹⁴ these labels denote that quantum effects are still not included on the reaction coordinate

at the transition state because that mode of motion is not represented by a partition function. In the second step, one introduces quantum-mechanical effects on the reaction–coordinate motion by multiplying the transition-state theory rate constant by a transmission coefficient. (The multiplicative transmission coefficient is sometimes also used to correct for recrossing.) In the early history of transition-state theory, the tunnelling was usually calculated by a one-dimensional model,^{22,23} but it has been known for a long time²⁴ that (except in special cases where the tunnelling effect is small) one-dimensional treatments are inadequate, and multi-dimensional tunnelling models^{20,25–28} must be used. Therefore the transmission coefficient also accounts for some of the effects of the nonseparability of the reaction coordinate. Furthermore, special care must be employed so that the transmission coefficient is normalised consistently with the underlying transition-state calculation.^{20,29,30}

In traditional treatments of chemical-reaction dynamics, it is usually assumed that the reaction occurs along a single valley from reactants to products, with this valley centred on a saddle point in the region of the transition state, and this valley is well described in terms of the coordinates of the reagents (that is, the coordinates of solvents and catalysts, if any, are not needed to describe the dividing surface). There are three ways in which this simple form of transition-state theory must be generalised, one of which (A) is important even for simple gas-phase reactions, and the other two of which (B and C) are especially important for enzymes and some other condensed-phase reactions.

(A) When the no-recrossing criterion is satisfied, the transition state may be considered to be a dynamical bottleneck.¹⁷ Sometimes a dynamical bottleneck does exist, but the transition state dividing surface corresponding to this dynamical bottleneck does not pass through the saddle point. In such a case one should not use the conventional definition of a transition state (by which it passes through the saddle point), but rather one should locate the transition state variationally to minimise recrossing.^{15,17,18,26,31–34} This is called variational transition-state theory (VTST). In the original formulation of variational transition-state theory, the reaction valley is still centred on, or at least defined by, a single reaction coordinate. Usually this passes through a saddle point, which is called the conventional transition state; however, trial dividing surfaces may be defined at other points along the reaction path, and these are called generalised transition states.

(B) For reactions occurring in the presence of a solvent or catalyst, or in general for condensed-phase reactions, it is convenient to divide the coordinates into two groups, those of the reagents and those of their surroundings. The former may be called solute, substrate, or reagent coordinates (where “reagents” denotes reactants and products), and the latter may be called solvent, bath, or environmental coordinates, with the understanding that the latter include solvent, enzyme, and coenzyme coordinates. We will use the reagent/environment language. It may happen that the description of the best (*i.e.* least recrossed) dividing surface cannot be accomplished entirely in terms of reagent coordinates; that is, one must also include environmental coordinates. Note that describing the dividing surface is equivalent to specifying the reaction coordinate since the latter is normal to the

former. Thus, this effect may be called participation of environmental coordinates in the reaction coordinate. Historically, it has been identified by the confusing label of nonequilibrium solvation. Although this label can be justified, the effect does not involve a breakdown of the Boltzmann distribution, but rather an inability to define a no-recrossed dividing surface unless environmental coordinates are included in the definition of the dividing surface.³⁵

(C) Even when the environment is allowed to participate in the reaction coordinate, a liquid-phase or enzymatic reaction may proceed through several different valleys, each going through its own saddle point (multiple passes across a mountain range, arranged as in parallel electric circuits, not in series). In such a case we must consider not just an ensemble of transition points at the mountain pass of one reaction valley (centred on a particular drainage line or valley floor, which may be called a reaction path), but also an ensemble of reaction valleys,^{36,37} which may be called an ensemble of reaction paths.

The method of ensemble-averaged variational transition-state theory^{2,3,38,40} has been developed to account for features B and C, which can both be very important in enzymatic reactions. At the same time, ensemble-averaged variational transition-state theory is formulated in such a way as to allow the incorporation of quantised vibrations and multidimensional tunnelling contributions. The present chapter surveys this theory with a special emphasis on the quantum effects. A broader review of the incorporation of quantum mechanics into enzyme kinetics modelling is presented elsewhere.¹

3.2 Theory

3.2.1 Gas-Phase Variational Transition-State Theory

In conventional transition-state theory (TST) the expression for the thermal rate constant of a bimolecular reaction is given by:

$$k^\ddagger = \frac{k_B T}{h} \frac{Q^\ddagger(T)}{\Phi^R(T)} \exp(-V^\ddagger/k_B T) \quad (3.1)$$

where k_B is the Boltzmann constant, T is the temperature, Q^\ddagger is the vibrationally quantised partition functions of the transition state (\ddagger) that, being a surface, is missing one degree of freedom (the reaction coordinate), Φ^R is the vibrationally quantised partition function per unit volume of the pair of reactants (R), and V is the potential energy difference between reactants and the transition state (which is called the classical barrier height). If we set $V=0$ at the equilibrium state of reactants, then

$$V^\ddagger = V_{\text{MEP}}(s=0) - V_{\text{MEP}}(s=s_R) \quad (3.2)$$

where s is the reaction coordinate, $V_{\text{MEP}}(s)$ is the potential energy along the minimum-energy path (MEP) from reactants to products, $s=0$ denotes the

location of the saddle point (where V_{MEP} takes its highest value), and s_R denotes the reactant value of s (for a gas-phase bimolecular reaction, $s_R = -\infty$). In formulating eqn (3.1), we removed the coordinates and momenta of the overall centre of mass, which is irrelevant. Thus, $Q^\ddagger(T)$ has no translational partition function, but Φ^R has a relative translational partition function, which is why it is included on a per volume basis. Note that for a liquid-phase reaction the relative translational degree of freedom is better considered to be a relative liberation⁴¹ coordinate. The transition-state-theory approximation can be improved by introducing a transmission coefficient that can be further divided into three contributions:

$$k = \Gamma(T)g(T)\kappa(T)k^\ddagger(T) \quad (3.3)$$

In this equation Γ describes deviation from the no-recrossing assumption; it can often be neglected if there is a single reaction path and the location of the dynamical bottleneck is variationally optimised along this path. The factor g is a measure of the deviation from the assumption⁴² that reactant molecules are locally equilibrated, and κ introduces the contribution from the nonclassical transmission through the barrier and is usually dominated by tunnelling but also includes nonclassical reflections. By the very nature of recrossing, Γ accounts for nonseparability of the reaction coordinate, but, as mentioned above, multi-dimensional tunnelling models, used for κ , also account for reaction-coordinate nonseparability.

For reactions in which energy transfer is fast enough to keep the relative population of the reactant states at equilibrium, g is approximately equal to unity,^{4,43–46} and only the remaining two factors of the transmission coefficient need to be considered. Instead of including $\Gamma(T)$ to correct eqn (3.1), we can employ VTST, where $k^\ddagger(T)$ is replaced by a variational transition-state theory rate constant so that $\Gamma(T)$ is usually small enough to be neglected. Thus, one replaces eqn (3.3) by a combination of a transmission coefficient κ and VTST, where κ accounts for quantum effects on the reaction coordinate. We shall, however, reintroduce Γ when we consider ensemble-averaged VTST.

We will discuss the inclusion of quantum effects in canonical VTST, that is, VTST for a canonical ensemble; this is usually called canonical variational theory (CVT). In CVT^{33,34} the transition state is optimised with respect to s , a distance, along a given reaction path, most frequently the minimum-energy path (MEP), from the saddle point, which location by convention is at $s=0$. The optimisation consists of varying the location of the dividing surface (generalised transition state) by placing it so that the forward flux through it is minimised.^{15,31 34,47 49}

The expression for the rate constant analogous to that given by eqn (3.1) is:

$$k^{\text{CVT}} = \kappa(T) \frac{k_B T}{h} \frac{Q^{\text{GT}}(T, s_*^{\text{CVT}}(T))}{\Phi^R(T)} \exp(-V_{\text{MEP}}(s_*^{\text{CVT}}(T))/k_B T) \quad (3.4)$$

where Φ^R is the quantised partition function per unit volume of the reactant, Q^{GT} is the quantised partition function of the generalised transition state at location s along the reaction path, and s^* is the location of the CVT dividing surface. The variational dividing surface is labelled with “*” to clearly distinguish it from the conventional TST one at $s=0$ that is labelled with “‡”. The quasithermodynamic equivalent to eqn (3.4) is:

$$k^{CVT} = \kappa(T) \frac{k_B T}{h} K^{\ddagger,o} \exp\left(-\Delta G_T^{CVT,o} / RT\right) \quad (3.5)$$

where $K^{\ddagger,o}$ is the reciprocal of concentration in the standard state for bimolecular reactions, R is the universal gas constant, and

$$\Delta G_T^{CVT,o} = \max_s \Delta G_T^{GT,o}(s) \quad (3.6)$$

where $\Delta G_T^{GT,o}$ is the generalised⁵⁰ standard-state free energy of activation^{8, 9, 51–53} for the trial dividing surface at s at temperature T . Equation (3.5) is called quasithermodynamic because the generalised transition states are missing one degree of freedom (and thus are not true thermodynamic species), and $\Delta G_T^{GT,o}$ is called generalised because we do not restrict the transition state to pass through the saddle point as in conventional TST.

When there are two or more local maxima in $\Delta G_T^{GT,o}$ in series as a function of s , one may account for them by the canonical unified statistical (CUS) model,^{54,55} which is an extension of the microcanonical unified statistical (US) model.^{56,57} In these models, one recognises that a system can be thermalised or randomised as an intermediate between dynamical bottlenecks. In the limit when the intermediate corresponds to a deep well, the system may exit with equal likelihood in either direction. This can introduce a transmission coefficient between 0.5 and 1.

Equations (3.1)–(3.6) can also be extended to unimolecular reactions in solution, which is a good starting point for treating the catalytic step in most enzyme reaction since this step is usually the reaction of a Michaelis complex. To do this generalisation, one replaces Φ^R , which is a partition function per unit volume, by $Q^R(T)$, which is a unitless partition function, since there is no translation (and hence no volume factor to remove), one sets s^R to a finite negative value, and one includes solvent effects on V_{MEP} , on the partition coefficients, and on the transmission coefficient κ .

When the solvent does not participate in the reaction coordinate and when the temperature dependence of the free energy of solvation may be neglected in calculating the effective potential for tunnelling, solvent effects may be included in κ by replacing the potential energy of the solute by its potential of mean force as a function of all solute coordinates.^{30,58}

If desired, one can optimise the shape and orientation of the dividing surface as well as the location at which it intersects the MEP.^{59–61} In fact it is strongly recommended to define the reaction coordinate (and hence the dividing surface, which is the hypersurface corresponding to some constant value of the reaction

coordinate) in curvilinear coordinates;⁶⁰ this corresponds to a curved dividing surface (as opposed to the hyperplane defined by a Cartesian treatment).

CVT accounts for the recrossing of the conventional transition state by choosing a better location for the transition state. CVT includes quantum effects on degrees of freedom orthogonal to the reaction by quantising partition functions, just as in conventional TST. Even more important in many cases, though, is that VTST allows a consistent treatment of the nonclassical penetration of the reaction barrier, *i.e.* quantum effects on the reaction coordinate. The most important part of the theoretical evaluation of the rate constants for many reactions is estimation of the tunnelling contributions. There are two aspects to this inclusion. One is the tunnelling dimensionality and the other its directionality. Before going into the details of tunnelling we will briefly discuss these two issues and categorise basic “types” of tunnelling.

3.2.2 The Transmission Coefficient

Inclusion of tunnelling requires substantially more information about the energetic landscape of the reaction than is necessary to describe the same reaction without including κ . In consequence, the calculations are more time consuming.

The quantum-mechanical probability of tunnelling depends on the energy of the reactants, the masses of the atoms that move during the process (actually, they all move, but light atoms participating strongly in the reaction coordinate or strongly coupled to it move in the most significant ways, and it is their masses that matter the most), the width and shape of the effective barrier, and the nature of the tunnelling paths. The dependence of the tunnelling probability on the barrier shape and tunnelling paths is the main reason for the already mentioned extra cost of the quantum-mechanical calculations of rate constants because the shape of the potential energy or potential of mean force landscape cannot be restricted to the vicinity of stationary points when calculating the tunnelling probability.

As stated in Section 3.1, early models treated the tunnelling problem as a one-dimensional problem, in particular, they modelled tunnelling based only on the probability of transmitting a mass point through a one-dimensional analytic^{23,62} barrier. Technically, these calculations were quite simple, and they required a minimum of information about the potential-energy surface. This approximation not only neglects contributions from other coordinates but also from cross terms and couplings. Sometimes these methods strongly underestimate the tunnelling contribution to the total reaction flux, but they can also provide overestimates.

Calculations of tunnelling contributions based on considering more than one coordinate are called multidimensional models. The simplest one is called zero-curvature tunnelling (ZCT), and it differs from the one-dimensional models in that quantisation of all vibrational modes along the MEP is included. Since the vibrational frequencies change along the reaction paths, so do the quantised energy requirements. If vibrations orthogonal to the reaction coordinate retain their state (*i.e.* retain their quantum numbers, *i.e.* evolve vibrationally adiabatically), their energy must be added to the potential energy. Whereas V_{MEP}

ultimately (by the Born–Oppenheimer approximation^{63–66}) represents the energy tied up in electronic energy and nuclear repulsion because the electronic state evolves adiabatically (*i.e.* does not change) in a thermal reaction, the difference between the vibrationally adiabatic ground-state potential-energy curve and V_{MEP} represents the quantised vibrational energy of modes transverse to the reaction coordinate that is also tied up and is unavailable for reaction–coordinate motion if the system is locally vibrationally adiabatic^{29,67–77} all along the reaction path. When all vibrations are in their ground (G) state they produce the following effective potential:^{29,69,70,77}

$$V_a^G = V_{\text{MEP}}(s) + \varepsilon_{\text{vib}}^G(s) \quad (3.7)$$

where “a” stands for adiabatic, and $\varepsilon_{\text{vib}}^G$ is the local zero point vibrational energy; V_a^G is called the vibrationally adiabatic ground-state potential curve. Often it is more convenient to work with the relative vibrationally adiabatic ground-state potential-energy curve defined by

$$\Delta V_a^G = V_a^G(s) - V_a^G(s = s^R) \quad (3.8)$$

The justification for considering that V_a^G or ΔV_a^G provides an effective barrier for tunnelling is presented elsewhere.^{18,20,25,29,67–77} ZCT can be considered an intermediate approximation between one-dimensional models and the full multidimensional models described below.

The models described above differ in dimensionality but as a common feature have tunnelling paths being identical with the MEP. Although the wavefunctions decay most slowly when the system tunnels under the lowest-energy part of the lowest barrier, the distance over which this decay operates depends on the tunnelling path. Thus, the optimum path is a compromise between the path length and the effective potential along the path. As a result, the optimum tunnelling path does not coincide with the MEP but occurs on its concave site. Effectively, the tunnelling path is thus shorter than MEP.^{17,19,25,74,78–88} This is called the “corner-cutting” effect, and it will be discussed more fully in Section 3.2.2.2.

In order to calculate the multiplicative transmission coefficient κ one should optimise the tunnelling path, *e.g.*, find a path that minimises semiclassical imaginary action integrals, which in turn maximise the tunnelling probability.^{84,89–91} This path is called the least-action path (LAP). The costly effort of searching for the LAP is not usually required. Instead, it is usually sufficient to employ an approximate variational procedure called optimised multidimensional tunnelling^{27,28,92,93} (OMT). This method is based on two approximations, one called small-curvature tunnelling^{94,95} (SCT) and the other called large-curvature tunnelling^{82,92–94,96,97} (LCT), which assume that the curvature of the reaction path is small and large, respectively. The SCT is accurate for small-to-intermediate curvature, while LCT is accurate for intermediate-to-large curvature. The SCT approximation extends the physical model that underlies the Marcus and Coltrin

approximation for the collinear H + H₂ identity reaction²⁵ to general three-dimensional polyatomic reactions; the effective potential is vibrationally adiabatic. The LCT approximation involves tunnelling with a partly vibrationally adiabatic and partly vibrational nonadiabatic potential along a weighted set of straight-line paths. Both approximations will be discussed in Section 3.2.2.2. The SCT and LCT tunnelling probabilities (P) are evaluated for each tunnelling energy E , and the larger tunnelling probability is selected, yielding the so-called microcanonically optimised multidimensional tunnelling (μ OMT) approximation, also called OMT for short:

$$P^{\mu\text{OMT}} = \max \begin{cases} P^{\text{SCT}}(E) \\ P^{\text{LCT}}(E) \end{cases} \quad (3.9)$$

Making the assumption^{18,29} that the vibrationally adiabatic potentials of all excited vibrational states that contribute appreciably to the thermally averaged rate have the same shape as the ground-state one, the transmission coefficient is given by:

$$\kappa = \frac{1}{k_B T} \frac{\int_0^\infty dE \exp(-E/k_B T) P^G(E)}{\exp[-V_a^G(s=s_*^{\text{CVT}}(T))/k_B T]} \quad (3.10)$$

where V_a^G is the ground-state vibrationally adiabatic potential curve described by eqn (3.7), and $P^G(E)$ is the ground-state quantum-mechanical transmission probability at energy E . The numerator of eqn (3.10) is proportional to the thermal average of the μ OMT ground-state transmission probability, and the denominator is proportional to the thermal average of the ground-state transmission probability implied by CVT when used without a transmission coefficient. The latter probability corresponds to classical motion along the reaction coordinate and equals a step function at E equal to $V_a^G(s=s_*^{\text{CVT}})$, where s_*^{CVT} is defined below eqn (3.4). By detailed balance, the exact transmission coefficient is the same for the forward and reverse reactions, so one needs to calculate only one of them; for non-thermoneutral reactions, the convention used in the LCT approximation is to always calculate P^G in the exoergic direction. The G in P^G refers to the ground state of reactants. Since the SCT approximation is vibrationally adiabatic, tunnelling proceeds only into the ground vibrational state of products. However, although the theory is vibrationally adiabatic in the tunnelling region, it does not require the system to be vibrationally adiabatic either before or after that region, and most reactants are *not* vibrationally adiabatic for low-frequency vibrations or rotations in the reactant and product regions. The LCT approximation is not vibrationally adiabatic even in the tunnelling region, and the tunnelling probability is summed over final states.

The generalisation of these procedures to reactions governed by liquid-phase potentials of mean force (PMFs, which are free energies) rather than gas-phase potential energies is given elsewhere.^{30,58,98,99}

“Tunnelling” is actually a correct description of the quantum-mechanical reaction–coordinate motion only for energies below the vibrationally adiabatic barrier height. Above that, the classical transmission probability would be equal to unity, but the quantal one only gradually approaches unity as the energy is increased still further (this will be illustrated in Section 3.3.4). The deviation from unity is called nonclassical reflection; it may be envisioned as diffraction of the deBroglie wave by the barrier top. Although nonclassical reflection for an energy ΔE above the effective barrier top is comparable in magnitude to tunnelling for an energy ΔE below the effective barrier top,^{68,100 102} the energies at which nonclassical reflection occurs are weighted by smaller Boltzmann factors than those for energies below the barrier tops, where tunnelling occurs; thus nonclassical reflection has only a small effect on most rate constants. In the OMT approximation it is treated by a parabolic uniformisation procedure.^{100 102}

We have described how the various elements of a multidimensional tunnelling calculation are put together, and what remains is to describe how the tunnelling probability itself, P^G , is calculated. We present that next in two stages: first (Section 3.2.2.1) a pedagogical introduction to quantum-mechanical tunnelling theory, and second (Section 3.2.2.2) a brief overview of how this is extended to multidimensional tunnelling.

3.2.2.1 One-Dimensional Tunnelling

We begin with a quantum-mechanical description of the one-dimensional motion of a particle of mass m governed by a potential-energy function V . The local kinetic energy is

$$T = E - V(x) \quad (3.11)$$

where E is the total energy. The local momentum is

$$p = \sqrt{2m[E - V(x)]} \quad (3.12)$$

If V were constant, p would also be constant, and the wavefunction would be

$$\psi = e^{ipx/\hbar} \quad (3.13)$$

Next we introduce the Wentzel–Kramers–Brillouin (WKB) approximation,^{100 103} a “semiclassical” approximation in which the wavefunction is approximated, to lowest order in \hbar , by

$$\psi \sim e^{i \int^x p(x') dx' / \hbar} \quad (3.14)$$

Since the word “semiclassical” is used with a myriad of meanings (*e.g.*, some workers use it to denote what we here call “quasiclassical,” other workers use it

for treatments of a multidimensional system in which some coordinates are classical and others are quantal, *etc.*), we emphasise that the word “semi-classical” refers here to expanding of the phase of the wavefunction in powers of \hbar and truncating the expansion to yield an approximate wavefunction part way between quantum mechanics and classical mechanics.¹⁰³

There are two noteworthy aspects of eqn (3.14). First, it replaces the solution of a differential equation by a quadrature. Second, as emphasised by Smith,¹⁰⁴ this expression involves computing an approximate wavefunction by integrating over the coordinate and momentum variables of an actual classical motion, and the resulting integral in eqn (3.14) is the classical action of the one-dimensional classical trajectory.

When, at some location x , $V > E$, the kinetic energy is negative at that x , and the classical momentum is imaginary; the approximation to the wavefunction becomes

$$\psi \sim e^{-\int^x |p(x')| dx' / \hbar} \quad (3.15)$$

The primitive approximation to the tunnelling amplitude becomes¹⁰³

$$T_{\text{tun}} = e^{-\theta(E)/\hbar} \quad (3.16)$$

$$\theta = \int_{\xi_R}^{\xi_P} |p(\xi)| d\xi \quad (3.17)$$

where θ is the magnitude of the imaginary part of the action integral over the tunnelling region of x , ξ_R is the beginning of the tunnelling region (where $E = V(x_R)$) on the reactant side, and ξ_P is where the particle emerges from under the barrier on the product side (where $E = V(x_P)$). Note that ξ is a progress variable along the tunnelling path; it is a dummy variable, and it could equally well be called x or x' . The tunnelling probability is the absolute square of the tunnelling amplitude:

$$P = e^{-2\theta/\hbar} \quad (3.18)$$

When x_R is close to x_P , this approximation breaks down. When E equals the maximum value of V , x_R becomes the same as x_P , and the primitive approximation to P in eqn (3.18) tends to unity. The correct result is of the order of one half, and for a parabolic barrier it is exactly one half.^{100,103} This is corrected by the parabolic uniformisation^{100 102} mentioned above, which yields

$$P = \frac{1}{1 + e^{2\theta/\hbar}} \quad (3.19)$$

When P is small (“deep tunnelling”), eqns (3.18) and (3.19) agree well. We always use the latter.

3.2.2.2 Multidimensional Tunnelling

For a one-dimensional problem there is only one path through the barrier, namely along x from x_R to x_P . For a multidimensional problem there is a choice of paths. To extend eqn (3.19) to a multidimensional case we must specify the tunnelling path or paths, prescribe how to average over the paths if there is more than one path to be considered at a given E , and provide a prescription for ξ , ξ_R , ξ_P , and $p(\xi)$ in eqn (3.17). In general we write

$$p = \sqrt{2\mu_{\text{eff}}(\xi)[E - V_{\text{eff}}(\xi)]} \quad (3.20)$$

where μ_{eff} and V_{eff} are, respectively, the effective reduced mass and the effective potential along a given tunnelling path.

In a general coordinate system, the reduced mass depends on the direction of motion. Consider, for example, the collision of an atom A with a diatomic molecule BC. There are nine coordinates, which may be written as the components of a 9-vector

$$\mathbf{q} = \begin{pmatrix} R_{BC,x} \\ R_{BC,y} \\ R_{BC,z} \\ R_{A,BC,x} \\ R_{A,BC,y} \\ R_{A,BC,z} \\ R_{ABC,x} \\ R_{ABC,y} \\ R_{ABC,z} \end{pmatrix} \quad (3.21)$$

where \mathbf{R}_{BC} is a 3-vector from B to C, $\mathbf{R}_{A,BC}$ is a 3-vector from A to the centre of mass of BC, and \mathbf{R}_{ABC} is a 3-vector from the origin to the centre of mass of ABC. Motion in the direction of any of the components of \mathbf{R}_{BC} has a reduced mass equal to $m_B m_C / (m_B + m_C)$, motion in the direction of the components of $\mathbf{R}_{A,BC}$ has the reduced mass of $(m_A m_{BC} / m_A + m_{BC})$, and motion along any of the three component directions of \mathbf{R}_{ABC} has the reduced mass m_{ABC} , which is the total mass of the system. The coordinate system of eqn (3.21) is usually called the Jacobi coordinate system because of its historical use by Carl Jacobi to treat 3-body problems in planetary mechanics. We could equally well have used the atomic Cartesians, \mathbf{R}_A , \mathbf{R}_B , and \mathbf{R}_C , with reduced mass m_A , m_B , and m_C , respectively. Notice that the Jacobi coordinates are linear combinations of atomic Cartesians, e.g.

$$R_{A,BC,y} = R_{A,y} - \frac{m_B R_{B,y} + m_C R_{C,y}}{m_B + m_C} \quad (3.22)$$

Any coordinates that are linear combinations of atomic Cartesian coordinates are called rectilinear coordinates because a straight line in atomic

Cartesians transforms into a straight line in any such coordinate system. It is straightforward to find the reduced mass for any straight motion in a rectilinear coordinate system, and such a reduced mass is a constant, as in the examples above.

As mentioned above, between eqns (3.8) and (3.9), the optimum tunnelling path is the least-action path that, for tunnelling, is a shorthand way of referring to the path with least imaginary action. This is a generalisation of a least-action principle of classical mechanics,^{105 108} but now it is applied to a trajectory with complex momenta (for the one-dimensional problem above, the momentum was purely imaginary, but for multidimensional problems it could be real or almost real in some directions, for example, those corresponding to spectator coordinates, and imaginary or complex in other directions). In order to find the least-action tunnelling path one needs to know μ_{eff} and V_{eff} for motions along arbitrary paths.

One way to simplify this problem is to transform to isoinertial coordinates. Isoinertial coordinates are rectilinear coordinates in which the reduced mass is the same for straight-line motion in all directions. Vibrational spectroscopists usually use mass-weighted Cartesian coordinates^{109,110} in which each atomic Cartesian $R_{A,\alpha}$ (with $\alpha = x, y$, or z) is transformed to

$$q_{A,\alpha} \equiv \sqrt{m_A} R_{A,\alpha} \quad (3.23)$$

where $q_{A,\alpha}$ is a generalised coordinate. This transforms the kinetic energy from

$$T = \frac{1}{2} \sum_A \sum_\alpha m_A \dot{R}_{A,\alpha}^2 \quad (3.24)$$

where an overdot denotes a time derivative, to

$$T = \frac{1}{2} \sum_A \sum_\alpha \dot{q}_{A,\alpha}^2 \quad (3.25)$$

Equation (3.25) shows that mass-weighted coordinates are isoinertial with a unitless mass of unity and with coordinates that have units of (mass)^{1/2} (distance). Such units are inconvenient, confusing, or both, so we prefer mass-scaled generalised coordinates defined by

$$Q_{A,\alpha} = \sqrt{\frac{m_A}{\mu}} R_{A,\alpha} \quad (3.26)$$

which convert the kinetic energy to

$$T = \frac{1}{2}\mu \sum_A \sum_\alpha \dot{Q}_{A,\alpha}^2 \quad (3.27)$$

where μ is an arbitrary mass, which is usually taken as 1 amu (in older papers on gas-phase bimolecular reactions we typically took it as the reduced mass of relative translation of reactants, for example, $\mu_{A,BC}$ for an atom–diatom collision of A with BC). Note that one can also obtain an isoinertial coordinate system with reduced mass μ by starting with Jacobi coordinates and scaling them by $(\mu_{AB}/\mu)^{1/2}$, $(\mu_{A,BC}/\mu)^{1/2}$, and $(\mu_{ABC}/\mu)^{1/2}$, respectively. In fact there are an infinite number of isoinertial coordinate systems, but they are all related by orthogonal transformations; thus, *e.g.*, the MEP is the same in all of them.¹⁹ In isoinertial coordinates, the motion of N particles in 3 dimensions becomes equivalent to the motion of a single particle in $3N$ dimensions.^{105a} Furthermore, straight-line paths in atomic Cartesian coordinates transform into straight-line paths in isoinertial coordinates; thus isoinertial cases are a special case of “rectilinear”^{110a} coordinates.

Minimisation of the tunnelling action integral of eqns (3.17) and (3.20) can be accomplished by choosing the path with the optimum combination of small effective reduced mass (because the square root of the effective mass appears in the integrand; see eqns (3.17) and (3.20)), short length (because the action integral is an integral over the length of the path), and low barrier (because $[V_{\text{eff}}(x) - E]^{1/2}$ appears in the integrand). This is simpler in isoinertial coordinates because all directions have the same reduced mass, so the compromise of three factors reduces to a compromise of two, namely path length and barrier. In general, the tunnelling path is shortened by corner cutting, that is, the tunnelling path is on the concave side of the MEP; this increases the barrier as compared to tunnelling along the MEP, and the best compromise is determined by eqns (3.17), (3.19), and (3.20).

Although it has been known for a long time that it is inaccurate to take the tunnelling path as the MEP,^{24,111} tunnelling along the MEP provides a good starting point for discussion and a good reference for measuring the extent of corner cutting. Taking the tunnelling path as the MEP is called the zero-curvature tunnelling approximation because if the MEP were straight (had zero curvature) in isoinertial coordinates, the MEP would indeed be the most favourable tunnelling path. In the ZCT approximation, ξ is simply the distance s along the MEP, μ_{eff} is μ (the scaling mass of the isoinertial coordinate system being used), and V_{eff} is as defined in eqn (3.7). There are three reasons for using the V_a^G of eqn (3.7) rather than V_{MEP} as the effective potential for tunnelling. First, it is the only choice consistent^{29,69} with transition-state theory, which assumes⁶ quantised vibrational modes at the transition state. Second, extensive empirical evidence has accumulated that energy requirements of quantised vibrations are consistent with experimental data on kinetic isotope effects.¹¹² Third, accurate quantum-mechanical scattering calculations show that quantised vibrational energy requirement quantitatively predict threshold energies for overbarrier reaction.^{68,72,75,76,111,113}

When reaction-path curvature is small, one may make the following argument. In the limit of small curvature, the only corner cutting that is advantageous is that which has no energetic penalty. Since the system has zero-point energy in modes transverse to the reaction path, any path between the zero-point

vibrational turning points of the transverse modes should incur no additional energy requirement. A path satisfying this criterion that is dynamically favourable when internal centrifugal effects are dominant is a smooth path that rides close to the envelope of vibrational turning points on the concave side of the MEP in the direction of the reaction-path curvature. The distance along this path must be modelled in a way that does not fail when the distance from the MEP to the turning point exceeds the radius of curvature. Putting these elements together yields the small-curvature tunnelling (SCT) approximation.

A key element in the SCT approximation is that the tunnelling is calculated for a single dominant tunnelling path at each tunnelling energy. In the small-curvature regime, this is a much better model of the tunnelling process than averaging over tunnelling paths.⁷⁴

In the limit where reaction-path curvature is large, straight-line tunnelling paths provide the best approximation because the amount of path shortening that can be accomplished in isoinertial coordinates by corner cutting becomes very large.^{82,85} In this limit it is sometimes competitive to tunnel even before reaching the point where $V_a^G(s)=E$. Thus, several tunnelling paths contribute even at a given tunnelling energy and even for tunnelling into a given final state. Furthermore, in the LCT approximation one must consider tunnelling directly into excited vibrational states (sometimes this even dominates the rate).^{85,114} Figure 3.1 illustrates the general characters of typical tunnelling paths in the LCT approximation. Although the reaction is not dominated by as narrow a distribution of tunnelling paths as those that dominate in the small-curvature

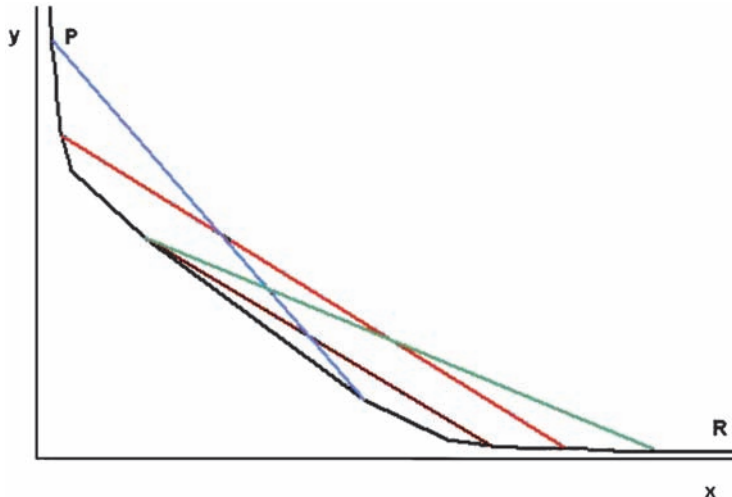


Figure 3.1 Schematic illustration of LCT tunnelling paths; R and P denote reactant and product regions, the black curve from R to P is an MEP, and the abscissa and ordinate are the bond lengths of the forming and breaking bonds. The blue, green, and red curves are schematic representations of possible LCT tunnelling paths for various systems.

case, one can still identify representative tunnelling paths and draw certain generalisations, for example, that deuterium typically tunnels at a smaller donor–acceptor distance than protium.⁸⁵ One can also make analogies to electron-transfer theory, *e.g.*, the straight line paths may be visualised as analogues of a sudden or Franck–Condon transition.⁵¹

Full details of the procedures for carrying out CVT overbarrier calculations and ZCT, SCT, LCT, and OMT tunnelling calculations are given elsewhere.^{28,55,94,97} These tunnelling approximations are collectively referred to as examples of multidimensional tunnelling (MT), and the use of CVT with any of them is called VTST/MT or CVT/MT.

3.2.3 Ensemble Averaging

As mentioned above, VTST can be extended to reactions in condensed phases. When a liquid-phase reaction is not in the diffusion-controlled limit, the bimolecular rate constant can be written as:

$$k^{\text{CVT}} = \kappa(T) \frac{k_B T}{hC^\circ} \exp\left\{-[G_T^\circ(\text{CVT}) - G_T^\circ(\text{R})]/RT\right\} \quad (3.28)$$

where C° is the concentration corresponding to the standard state, $G_T^\circ(\text{R})$ is the condensed-phase standard-state free energy of reactants at temperature T , and $G_T^\circ(\text{CVT}) - G_T^\circ(\text{R})$ is the condensed-phase standard-state free energy of activation^{8,9,50–53} at temperature T . Analogously to the gas-phase case, the variational free energy of activation is given by:

$$\Delta G_T^\circ = \max_s \Delta G_T^\circ(\text{GT}, s) \quad (3.29)$$

where $\Delta G_T^\circ(\text{GT}, s)$ is the standard-state free energy of activation for a generalised transition state at a location s along the reaction path.

In condensed-phase reactions the generalised-transition-state dividing surface may depend on more than just the solute coordinates. It can, for example, depend on the protein coordinates for an enzyme-catalysed reaction. While for a simple reaction in the gas phase almost all of the reaction flux passes through a single TS on a single reaction path, an enzyme-catalysed reaction may proceed through a large number of reaction paths, each passing through a different saddle point. In fact, the number of saddle points may be so numerous that they must be treated by statistical-mechanical theories. One way to account for this situation is to sample the space of saddle points and average the results – this can be accomplished by ensemble-averaged^{2,3,38–40} VTST (EA-VTST). It can be augmented by the inclusion of the tunnelling contributions in the same way as discussed for the gas-phase reactions; this results in the EA-VTST/OMT^{2,3,38–40} method. Sometimes it is not necessary to optimise the tunnelling paths. EA-VTST with any of the multidimensional tunnelling approximations (ZCT, SCT, LCT, or OMT) is called simply EA-VTST/MT.

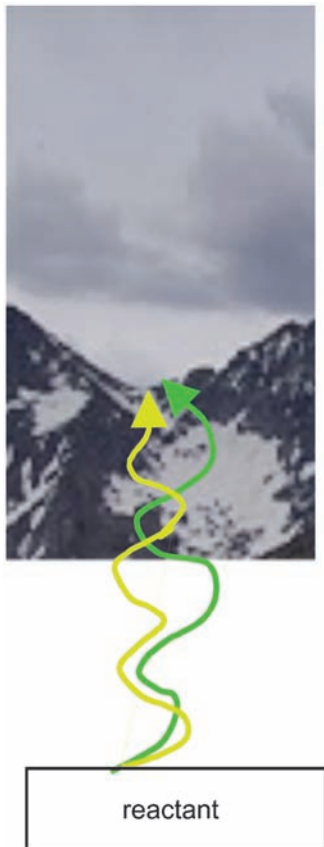


Figure 3.2 In the gas phase or a crystal, transition state theory accounts for all trajectories in a valley through a dividing surface at or near the saddle point.

Figure 3.2 illustrates that a VTST calculation based on a single reaction path samples an ensemble of trajectories or wave packets associated with that path. Figure 3.3 illustrates that EA-VTST samples several parallel reaction paths. Each reaction path is the MEP for a primary reaction zone (*e.g.*, the substrate and key parts of the enzyme, coenzyme, or solvent) with the rest of the system (called the secondary reaction zone) temporarily approximated as frozen. Since the reaction paths are different for different secondary reaction zone configurations, this allows the secondary reaction zone to participate in the reaction coordinate, in the language introduced in Section 3.1 (*see items B and C in that section*). Because the transmission coefficient for individual reaction paths does not include the motion of the secondary reaction zone as a function of progress along the reaction coordinate, this is called the static secondary zone (SSZ) approximation, which is somewhat of a misnomer because averaging over an ensemble of secondary reaction zones does include the motion of the secondary reaction zone effectively.

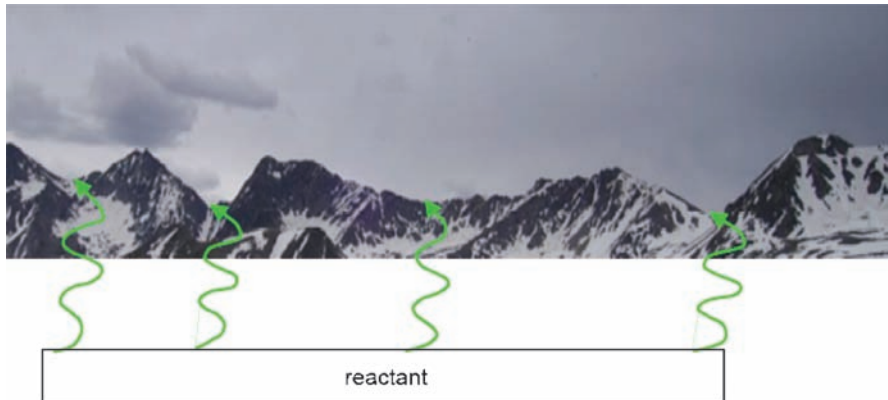


Figure 3.3 In liquids, amorphous materials, or enzymes there is an ensemble of reaction valleys and saddle points. We average over an ensemble of these valleys; each has its own reaction coordinate.

An EA-VTST/MT calculation with the SSZ approximation is carried out in two stages. Full details of these calculations are provided in refs 38–40, and they are reviewed in refs 2–4. Here, we provide an overview.

In the first stage (which is quasiclassical, by which we mean that the reaction coordinate at the transition state is treated classically but bound vibrations are treated quantum mechanically), one selects a nonoptimised reaction coordinate, called the distinguished reaction coordinate z , and carries out a VTST calculation (in particular a CVT calculation) with this reaction coordinate, with primary reaction zone quantised (by using quantised vibrational partition functions), and with all atoms of both the primary and secondary reaction zones unfrozen. A classical-mechanical simulation is carried out to obtain a one-dimensional classical-mechanical PMF (a one-dimensional PMF is the free energy with one coordinate, the control variable or reaction coordinate z , fixed, with the PMF being a function of that variable). Using the relation⁹⁸ between the PMF and the free energy of activation, one may then compute a stage-1 classical mechanical free energy of activation profile. In step 2 of stage 1, one adds the difference¹¹⁵ between the quantised vibrational free energy and the classical vibrational free energy to obtain a stage-1 quasiclassical free energy of activation profile. This is called quasiclassical because the reaction coordinate is still classical at the transition state, although the quantised vibrational step converts the treatment of all other vibrational coordinates at the transition state and all vibrational coordinates at the reactant to a quantised form. This leads to a stage-1 rate constant that may also be called a single-reaction-coordinate rate constant, that is given by

$$k^{(1)} = \frac{k_B T}{h} \exp\left(-\Delta G_T^{(1)} / RT\right) \quad (3.30)$$

where $\Delta G_T^{(1)}$ is the stage-1 approximation to the quasiclassical free energy of activation; $k^{(1)}$ may also be called the single-reaction-coordinate approximation

to the quasiclassical rate constant. Note that $\Delta G_T^{(1)}$ is a quasithermodynamic quantity in that it includes no contributions from a transmission coefficient.

By sampling the variationally optimised transition-state ensemble of stage 1, one finds an ensemble of I optimised saddle points and reaction paths, which are calculated with a static secondary reaction zone. The SSZ quasiclassical rate constant is then given by

$$k^{\text{QC}} = \Gamma(T) k^{(1)} \quad (3.31)$$

and

$$\Gamma = \frac{\sum_{i=1}^I \Gamma_i(T)}{I} \quad (3.32)$$

where each Γ_i corrects the stage-1 rate constant for the recrossing that is eliminated by using optimised reaction coordinate i . Since reaction–coordinate motion is still classical, k^{QC} is still quasiclassical, and in fact if one stops at stage 2, it is the final estimate of the EA-VTST quasiclassical rate constant. In practice, each $\Gamma_i(T)$ is computed from a new variational transition-state calculation with its own reaction path. Thus, one is now averaging not just over the valley associated with a single reaction path but over an ensemble of reaction paths. Thus fluctuations of the primary reaction zone are included directly in the reaction-path dynamics, and fluctuations of the secondary reaction zone are contained in the ensemble average over reaction paths.

In the second (final) step of stage 2 one includes tunnelling and nonclassical reflection for each reaction path, leading to a tunnelling transmission coefficient Γ_i . The rate constant is now calculated as

$$k^{\text{EA-VTST/MT}} = \gamma(T) k^{(1)}(T) \quad (3.33)$$

where

$$\gamma = \frac{\sum_{i=1}^I \kappa_i(T) \Gamma_i(T)}{I} \quad (3.34)$$

Full computational details of SSZ calculations are given elsewhere.^{38,39}

One can also add an additional stage (stage 3) of calculation where the free-energy change due to motion of the secondary reaction zone is added as a function of progress along each reaction coordinate. This is called the equilibrium secondary zone (ESZ) approximation. Full computational details are given elsewhere.^{38,40}

An important difference between gas-phase and condensed-phase or enzyme-catalysed reactions is the size of the system. Inclusion of solvent, an enzyme, or both results in systems of thousands of atoms. Furthermore, ensemble

averaging over configurations sampled from a canonical ensemble is essential for reliable results.¹ Quantum-mechanical electronic-structure calculations with appropriate averaging on systems of such size are only feasible with highly simplified methods such as those employing neglect of diatomic differential overlap.^{116,117} The currently state-of-the-art way around this problem is to use the combined QM/MM approach,^{1,118–129} in which a quantum-mechanical (QM) level is used to describe a small fragment of the system vital to reactivity, and a molecular-mechanics (MM) level of description is used for the remaining, bulk part (solvent, bath, or enzyme). This division into parts treated by different theory levels need not be the same as the division into primary and secondary reaction zones for dynamics.

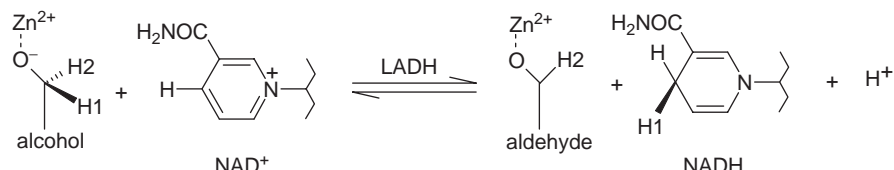
The EA-VTST/OMT method can provide detailed insight into mechanisms of enzyme-catalysed reactions. In the remaining part of this chapter, examples of applications of the EA-VTST/OMT to enzymatic systems will be presented. Four such systems were chosen to be presented with regard to their nonclassical behaviour.

3.3 Examples

3.3.1 Liver Alcohol Dehydrogenase A Workhorse for Studying Hydride Transfer

One of the most extensively studied groups of enzymes are those from the alcohol dehydrogenases family. One of these enzymes that has been examined thoroughly both experimentally^{130–143} and theoretically^{38,144–163} is liver alcohol dehydrogenase (LADH). It catalyses the reversible conversion of an alcohol to an aldehyde by transferring hydride from the substrate to the cofactor (nicotinamide adenine dinucleotide, abbreviated NAD⁺) as shown in Scheme 3.1. LADH is a metalloenzyme containing two Zn ions. One of them plays a structural role and the other is catalytically important because it interacts with the initial alcohol and the final aldehyde oxygen atoms, respectively.

Although the rate of ethanol dehydrogenation in wild-type LADH is limited by release of the product^{130–132} the chemical step may be ‘unmasked’ in the kinetics by changing the substrate to benzyl alcohol or *para*-substituted benzyl



Scheme 3.1 The postulated mechanism for LADH catalysed reaction. H1 and H2 denote primary and secondary hydrogen, respectively. (Do not confuse the secondary hydrogen H2 with the C(O)NH₂ amide group.)

alcohols and by mutagenesis at hydrophobic residues surrounding the active-site binding pocket.¹³⁵ The general conclusion drawn from a series of studies by Klinman and coworkers is that the chemical step in alcohol dehydrogenation catalysed by the wild-type LADH, mutant LADH, and yeast alcohol dehydrogenase involves a significant amount of tunnelling¹⁶⁴ but it is sometimes masked by kinetic complexity. Observed primary kinetic isotope effects (KIEs) for the hydride-transfer step in various alcohol dehydrogenase transformations of benzyl alcohol and *para*-substituted benzyl alcohols are $k_H/k_D = 3.7\text{--}4.7$ and $k_H/k_T = 7.0\text{--}7.8$. In the case of secondary KIEs these values are 1.2–1.3 and 1.3–1.4, respectively.^{133,135,136,165} Klinman and coworkers inferred significant tunnelling contributions to the process primarily from two observations. Firstly, the exponent, α defined as $\alpha = \ln(k_H/k_T)/\ln(k_D/k_T)$ from the Swain–Schaad relationship¹⁶⁶ was found to be in the range 4–10,^{125,129,145} whereas values around 3.34 are usually assumed to be the upper limit in the absence of tunnelling.¹⁶⁷ Secondly, the ratio of Arrhenius pre-exponential factors A_H/A_T for the primary KIE was observed¹³³ to have a value as low as 0.5, whereas a value below 0.6 is again considered the lower limit in the absence of tunnelling.¹⁶⁸

EA-VTST/MT was tested against the reaction dynamics taking place in the LADH active site.^{38,145} Both the SSZ and ESZ approximations were used. These studies showed that the elevated Swain–Schaad exponents for the secondary KIEs can be obtained when quantum-tunnelling effects are included in the computation of the rate constants, but not otherwise, confirming that the large Swain–Schaad exponent for the secondary KIEs is experimental evidence for hydrogen tunnelling in LADH catalysis. It was also found that coupled motion of the secondary hydrogen in the reaction coordinate is critical for interpreting the observed secondary KIEs. The results obtained are compared to experimental data in Table 3.1. It is particularly striking that the calculations can reproduce both the primary and secondary kinetic isotope effects quite well because earlier tunnelling models¹⁶⁹ were unable to do that with realistic potential-energy surfaces. Analysis¹⁴⁵ of the multidimensional tunnelling calculations showed significant contribution to the kinetic isotope effects from isotope-dependent effective barrier widths and an isotope-dependent extent of corner cutting, neither of which is present in one-dimensional tunnelling models. (See Figure 4 in ref. 145 and associated discussion.)

3.3.2 Dihydrofolate Reductase A Paradigmatic System

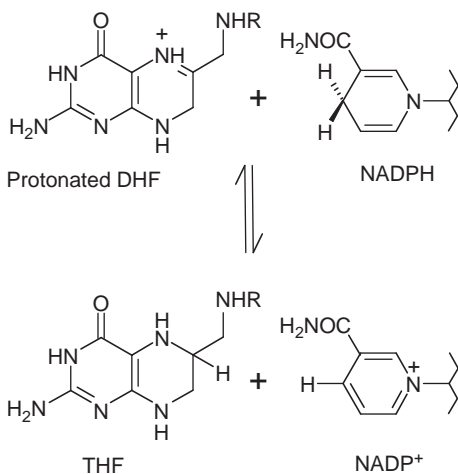
Dihydrofolate reductase (DHFR) catalyses the conversion of 7,8-dihydrofolate (DHF) to 5,6,7,8-tetrahydrofolate (THF) using reduced nicotinamide adenine dinucleotide phosphate (NADPH) as a cofactor (Scheme 3.2). To an extent that is better documented than for any other enzyme, this small protein adopts different conformations during the catalytic cycle,^{170–187} and the impact of these conformations on the hydride-transfer step has become a platform for numerous theoretical studies.^{99,188–216}

Table 3.1 Primary and secondary KIEs and Swain–Schaad exponents for the reaction of benzyl alcoholate with NAD^+ , catalysed by LADH, to form benzaldehyde and reduced nicotinamide adenine dinucleotide (abbreviated NADH) at 298 K.

	$k_{\text{H}}/k_{\text{D}}$	$EA \text{ CVT}/\mu\text{OMT}^a$		Experiment^b
		SSZ	ESZ	
Primary	$k_{\text{H}}/k_{\text{D}}$	4.6	5.6	3.8 ± 0.7
	$k_{\text{H}}/k_{\text{T}}$	6.9	7.5	7.1
	$k_{\text{D}}/k_{\text{T}}$	1.8	1.7	1.9 ± 0.01
Secondary	$k_{\text{H}}/k_{\text{T}}$	1.26	1.36	1.33
	$k_{\text{D}}/k_{\text{T}}$	1.05	1.08	1.07
Exponent	α_{prim}	3.3	3.6	3.1
	α_{sec}	5.0	4.2	4.1

^aAlhambra *et al.* 2001 (ref. 38)

^bBahnsen *et al.* 1993, Bahnsen and Klinman 1995 (refs 133,135)



Scheme 3.2 The hydride transfer reaction catalysed by DHFR.

At high pH rate-determining step is the transfer of a hydride ion from a carbon atom of NADPH to a carbon atom of protonated DHF; see Scheme 3.2. *E. coli* DHFR originally provided an opportunity to compare theory¹⁹⁷ and experiment²¹⁷ for the primary H/D KIE, and good agreement was obtained (theory: 2.8; experiment: 3.0). At the same time, a large quantum effect was predicted for the as-yet-unmeasured secondary H/D KIE. In particular, a nontunnelling calculation yielded a 3% effect, whereas including multidimensional tunnelling raised this to 13%. After this result was published,¹⁹⁷ the value was independently inferred from new experiments to be 13%.¹⁷⁹ This is a rare case where theory made a prediction prior to the experiments, and the success of theory for this case is very encouraging.

Table 3.2 Primary and secondary deuterium KIEs (k_H/k_D) for the hydride-transfer reaction catalysed by *E. coli* DHFR at 278, 298 and 318 K.

Temperature (K)	Calculated ^a		Experimental ^b	
	Primary	Secondary	Primary	Secondary
278	3.22		3.54 ± 0.16	
298	2.83 ^c	1.13 ^c	3.50 ± 0.20	1.13
318	3.01		3.58 ± 0.15	

^aresults from ref. 207 at 278 and 318 K^bresults from ref. 179^cresults from the earlier report¹⁹⁷

Both primary and secondary H/D KIEs and their temperature dependence have been measured¹⁷⁹ for the *E. coli* DHFR. The results were interpreted in terms of environmentally coupled tunnelling and vibrationally enhanced ground-state tunnelling, where the modulation of the tunnelling amplitude by a gated motion varies with temperature. No coupling between primary and secondary hydrogen positions was observed, contrary to what had been observed for alcohol dehydrogenase.^{164,218} Calculations using EA-VTST/MT with a combined QM/MM potential reproduced the observed weak temperature dependence of the KIEs as well as agreeing with their magnitude.²⁰⁷ The results are compared to the original experimental data¹⁷⁹ in Table 3.2; later experiments¹⁸¹ showed somewhat smaller pH-dependent KIEs.

Two interesting features have been identified from the theoretical temperature-dependent studies. First, there is a transition-state shift along the reaction coordinate when the temperature is changed; this shift partly cancels the temperature dependence that would be expected for the KIE in calculations with a temperature-independent effective barrier. The second interesting feature is an unusual temperature dependence of the width of the effective potential barrier for tunnelling. The EA-VTST/MT calculations including these effects predict a KIE that changes only by 6.5% over the temperature range from 278 K to 318 K, which is only slightly larger than the experimental uncertainty of the KIE. Without these two mechanisms, the KIE would have decreased by 16%. The experimentally found kinetic isotope effect for the Arrhenius pre-exponential factors of 4.0 ± 1.5 ¹⁷⁹ was reproduced qualitatively using the above calculation framework (1.9). The authors of the later experiments¹⁸¹ that showed a dependence on pH concluded that their results suggested that “the mechanism by which H transfer in DHFR is coupled to protein fluctuations depends on the pH of the environment”. They also concluded, in light of the two competing temperature effects uncovered in the theoretical¹⁹⁷ studies that “it is perhaps not surprising that in such a system the temperature dependence varies with reaction conditions”.

Primary H/D KIEs have also been measured for the hydride-transfer step catalysed by the hyperthermophilic *Thermotoga maritima* DHFR (TmDHFR) within the 279–338 K temperature range; biphasic behaviour has been observed with the breakpoint at approximately 298 K.¹⁷⁴ The temperature-independent

KIEs observed in this study for higher temperatures were interpreted as indicating that tunnelling is not modulated by the environment or that such a contribution is very small. Below 298 K the observed H/D kinetic isotope effect becomes inverse, and the difference between the activation energies for protonated and deuterated substrates increases. This may suggest an increased role of active-site dynamics that alters the distance at which hydrogen is transferred. TmDHFR is therefore a good system for testing the environmentally coupled tunnelling hypothesis, and EA-VTST/MT studies were carried out²¹⁰ based on the same combined QM/MM potential energy parameters as employed earlier¹⁹⁷ for *E. coli* DHFR. The PMF profiles were computed at 278, 298, and 338 K for the wild-type homodimer enzyme. In addition, in order to shed light on the effect of the dimerisation on the enzyme activity, a simulation was carried out at 298 K where only the protein monomer was included. The calculated H/D primary KIEs from these simulations are compared to the experimental data in Table 3.3.

Since TmDHFR exists as a homodimer, which is believed to be mainly responsible for its thermal stability being higher than that of other DHFRs, which are monomeric, the catalytic reaction was simulated at 298 K for both the dimer and for the experimentally inaccessible monomer.²¹⁰ The free energy of activation was found to be 3.4 kcal/mol lower for the dimer, indicating that dimerisation is important not only for stability but for catalysis. Of the 3.4 kcal/mol enhancement, 2.6 kcal/mol can be accounted for classically so the enhancement is mainly classical with a 0.8 kcal/mol quantum contribution, primarily from quantised vibrations. In light of this finding at 298 K, all temperature-dependent studies were carried out on the dimer.²¹⁰

Significant changes in the PMF barrier shape and shift of the locations of variational transition states were observed (see Figure 3.4) at different temperatures, similar to the shifts that partly explained the weakly temperature-dependent KIE in *E. coli* DHFR. The standard deviations of the tunnelling, recrossing and overall transmission coefficients turned out to be smaller at high temperature than at low temperature. A similar temperature-dependent behaviour of the transmission coefficients has also been observed in the *E. coli* DHFR system.²⁰⁷ Viewing these deviations as a reflection of fluctuations of the dynamical barrier, the obtained results might suggest that at high temperature the system tunnels through more rigid barriers, which fluctuate less significantly than those at low temperatures.

Table 3.3 Primary KIEs for the hydride-transfer reaction catalysed by TmDHFR at 278, 298 and 338 K.

Temperature (K)	k_H/k_D calculated	k_H/k_D experimental
278	3.0	6.7
298	2.9 (2.5) ^a	4.0
338	2.2	3.4

^aValue in parentheses for monomer; other calculated values and experiment are for the dimer.

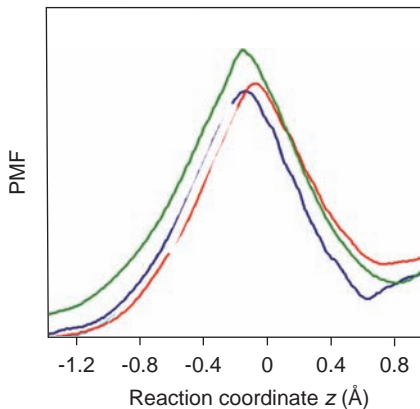
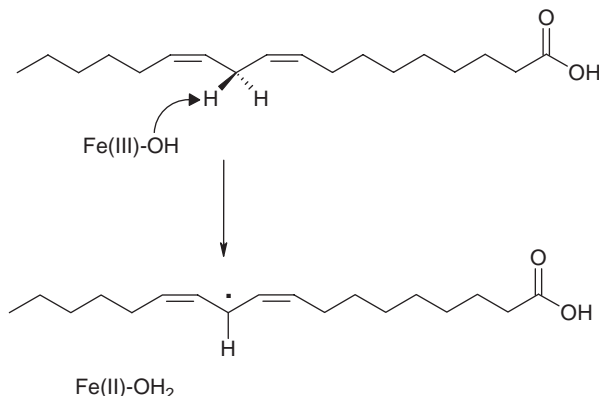


Figure 3.4 The computed classical mechanical PMF (in kcal/mol) vs., the reaction coordinate for dimeric TmDHFR at 278 K (blue line), 298 K (orange line), and 338 K (light blue line).

3.3.3 Soybean-Lipoxygenase-1 and Methylmalonyl-CoA Mutase Enzymes Catalysing Hydrogen Atom Transfer Reactions that Exhibit the Largest KIEs Reported for any Biological System

Soybean lipoxygenase-1 (SLO1) is a nonheme iron enzyme that catalyses the oxidation of linoleic acid. The chemical step is a net hydrogen-atom transfer (Scheme 3.3). This enzymatic reaction has been of great interest to both experimentalists and theoreticians for the last 15 years.^{156,164,209,219–243} One reason for the intense study of this enzymatic reaction is the large value of the experimental deuterium KIE, in particular k_H/k_D is found to be greater than 80 at 303 K. This large kinetic isotope effect is accompanied by a weak temperature dependence for both k_{cat} and its KIE over the 278–323 K temperature range.^{228,229,233,240} This large KIE is clear evidence for extensive hydrogen tunnelling in this system, and it is very interesting to understand both the magnitude of the KIE and how such a large KIE can have such a small temperature dependence.

Several approaches^{156,224,227,234–243} have been used to describe atomistic aspects of the SLO1 reaction. Some of the methods do not include the protein environment explicitly and others are based on combined QM/MM schemes.^{156,237,242,243} Two groups have studied the SLO1-catalysed reaction by employing VTST/MT. Hillier and coworkers¹⁵⁶ obtained an activation energy of 6.9 kcal/mol and a KIE of 18.9 at 300 K by using the SCT approximation. However, their results are based on only one reactive configuration (which is thought to be representative of the overall average, or most common pathway, in view of the generally good agreement of the calculated properties with experiment), and that is too small a sample for reliable rate calculations. Very recently, Tejero *et al.*²⁴² have reported QM/MM-based EA-VTST/MT results for hydrogen abstraction from linoleic acid by the Fe(III)-OH cofactor in soybean

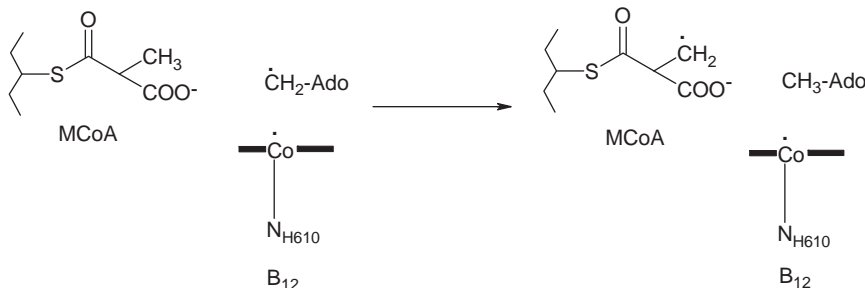


Scheme 3.3 Hydrogen abstraction step in the reaction catalysed by SLO1 with the Fe(III) OH cofactor.

lipoxygenase-1. Although a correction had to be applied to the potential-energy barrier in order to reproduce the enormous experimental KIE, the huge contribution of tunnelling was confirmed and correlated with the width of the effective potential-energy barrier for tunnelling. This barrier is particularly narrow because of the compression of the substrate binding pocket by bulky leucine and isoleucine side chains. By comparing the results obtained for the wild-type enzyme with those for the Ile553Ala mutant, it was shown that, in the case of the mutant, the substrate-binding pocket is more expanded. The replacement of the bulky isoleucine residue with a small alanine removes the compression and rigidity observed in the wild-type enzyme. Different binding pocket flexibility leads to different barrier widths and therefore different values for KIEs.

Another example of a catalysed reaction exhibiting large involvement of tunnelling in the catalytic step is B₁₂-dependent methylmalonyl-CoA mutase (MMCM). MMCM catalyses the rearrangement of methylmalonyl-CoA (MCoA) to succinyl-CoA. An anomalously large KIE, in particular 50 at 278 K, has been observed for the hydrogen-atom transfer from the substrate to the 5'-deoxyadenosyl radical (dAdo) in the step that initiates the isomerisation reaction in the enzyme.²⁴⁴ The key reaction is a hydrogen radical transfer as illustrated in Scheme 3.4.

Several attempts have been made in order to elucidate the mechanism of the initial events in the MMCM-catalysed cycle. TST calculations including multidimensional tunnelling contributions performed on model systems^{245,246} yielded primary KIEs at 293 K of 32–94, depending on the PES and model system. Although these results seem to be in reasonable agreement with the experimental primary KIE of 36 at this temperature, they do not allow for a detailed picture of the tunnelling dynamics taking place in the active site of the enzyme. Since the experience on this system indicates that only inclusion of a substantial part of the enzyme environment yields results that are pertinent to the enzyme-catalysed reaction,²⁴⁷ EA-VTST/MT calculations were carried



Scheme 3.4 Hydrogen atom transfer from substrate to cofactor in the mutase catalysed reaction. Ado[·]CH₂ denotes the 5' deoxyadenosyl radical, and AdoCH₃ denotes 5' deoxyadenosine. The corrin ring of vitamin B₁₂ is shown as a thick horizontal line, and the side chain of the ring is not shown, to avoid crowding in the illustration. Histidine 610 is the most important amino acid because it serves as the lower axial ligand of cobalt.

out²⁴⁸ employing a combined quantum-mechanical and molecular-mechanical (QM/MM) potential-energy surface with unrestricted²⁴⁹ AM1.¹¹⁶ The calculations show that in the absence of tunnelling, the kinetic isotope effect at 278 K would only be 14. When tunnelling is included the calculated kinetic isotope effect is increased to 51 at 278 K, in excellent agreement with experiment. This provides confidence in the detailed dynamic picture of the reactive events that is afforded by the computer simulation.

Because the final results of the quantum-mechanical atomistic simulation agree with experiment so well, it is possible to analyse the nature of the tunnelling events. It was found that the tunnelling of H or D is strongly coupled to motions of the other atoms in the active site of the enzyme, and the geometrical configuration at the critical configuration of the tunnelling process was identified.

It is interesting to compare the transmission coefficients for the various members of the transition state ensemble, and this is done in Table 3.4, which contains previously unpublished details of calculations reported elsewhere.²⁴⁸ The standard deviations of the transmission coefficients given in Table 3.4 are small compared to the effect of reaction-path curvature, indicating that the participation of fluctuating coordinates in the tunnelling path is dominated by the coordinates in the primary reaction zone, not the fluctuations of the rest of the substrate, coenzyme and protein. A special treatment near the saddle point was used that resulted in the recrossing transmission factors Γ being equal to unity; thus the only contribution to γ in this case is due to κ .

3.3.4 Other Systems and Perspectives

We will not consider other systems in detail, but rather just give a brief set of pointers to some particularly relevant literature. A more comprehensive survey of transmission coefficients with a considerable emphasis on tunnelling and coverage of a greater number of systems is given in another review²⁵⁰ that also includes data similar to that in Table 3.4 for several other reactions. An earlier

Table 3.4 Individual κ factors, for the MMCM-catalysed reaction at 278 K.

	<i>CH</i> ₃				<i>CD</i> ₃			
	ZCT	SCT	LCT	μ OMT	ZCT	SCT	LCT	μ OMT
1	12.1	81.1	54.4	83.2	7.7	21.7	16.2	22.8
2	12.9	80.2	76.2	91.4	7.7	22.6	23.9	25.7
3	11.5	71.8	65.2	86.2	8.0	24.7	16.4	23.6
4	8.8	43.0	90.3	94.4	5.8	23.6	20.0	21.9
5	13.5	82.4	57.7	83.6	9.1	30.4	17.5	30.4
6	14.0	88.4	68.4	95.3	9.0	26.0	19.2	27.6
7	14.9	93.4	54.1	93.5	9.9	29.6	18.2	30.0
8	13.2	92.3	89.9	118.0	8.3	25.2	21.8	28.5
Average	12.6	79.1	69.5	93.2	8.2	25.5	19.2	26.3
SD ^a	1.9	16.2	14.7	11.0	1.2	3.1	2.7	3.3

^aStandard deviation

review¹ on the incorporation of quantum mechanics in the theoretical treatment of enzyme kinetics covers both the use of QM/MM potential-energy surfaces and also the inclusion of quantum-mechanical effects in the simulation of the dynamics; again the coverage of other systems is broad.

Three reviews of transition-state theory in general that include sections covering EA-VTST/MT are available,^{4,37,77} and two reviews specifically devoted to EA-VTST/MT are also available.^{2,3} The latter³ of these includes a table summarising quantum effects on the phenomenological free energy of activation for several enzyme-catalysed reactions;^{38–40,145,197,251–253} Table 3.5 extends this table to also include the methylmalonyl-CoA mutase reaction²⁴⁸ discussed in Section 3.3.3. The reactions in Table 3.5 are all hydrogen-transfer reactions, that is, reactions in which a proton, hydride ion, or hydrogen radical is transferred. The basis for Table 3.5 is explained next.

In general we may write the rate constants, *i.e.* the experimental rate constant or the final result of a calculation, as

$$k = \frac{k_B T}{h} \exp[-\Delta G_{\text{act}}(T)/RT] \quad (3.35)$$

where ΔG_{act} is called the phenomenological free energy of activation. Experimental results for k_{cat} are often reported as ΔG_{act} rather than (or in addition to) reporting k itself. Equation (3.35) may also be applied to theoretical data. For example, applying it to eqns (3.31) and (3.33) and using eqn (3.30) yields

$$\Delta G_{\text{act}}^{\text{QC}} = \Delta G_T^{(1)} - RT \ln \Gamma(T) \quad (3.36)$$

and

$$\Delta G_{\text{act}}^{\text{EA-VTST/MT}} = \Delta G_T^{(1)} - RT \ln \gamma(T) \quad (3.37)$$

The difference between these two phenomenological free energies of activation is given in the “Tunnelling” column of Table 3.5. The “Quantised

Table 3.5 Magnitudes of nuclear-motion quantum effects on phenomenological free energies of activation for enzyme-catalysed reactions.

	Contribution to free energy of activation		
	Ref.	Quantised vibrations	(kcal/mol)
			Factor in rate
Enolase	251	2.1	0.3
Alcohol dehydrogenase	38,145	1.8	0.8
Methylamine dehydrogenase	252	3.2	2.5
Xylose isomerase	39,253	1.3	1.1
Dihydrofolate reductase	197	1.6	0.6
Acyl CoA dehydrogenase	40	3.1	0.8
Methylmalonyl CoA mutase ^a	248	2.2	2.5
Average		2.2	1.2
			320 ^b

^aThis row is for 278 K; all other rows are for 298 K.

^bThis is computed from the sum of the averages in the two previous columns.

vibrations” column of Table 3.5 is similarly obtained by comparing $\Delta G_{\text{act}}^{\text{QC}}$ to the free energy of activation calculated by a stage-1 procedure where vibrations are not quantised. Both columns contain negative numbers because those quantum effects speed up the reactions in all these cases. The total speed up factor is given in the last column.

Table 3.5 shows the importance of including the quantum effects on nuclear motion in modelling enzyme-catalysed hydrogen-transfer reactions. The rate enhancements range from 41 to 15 000 and those values correspond to the free energy of activation contributions of -2.2 to -5.7 kcal/mol. The effect of quantising vibrations is especially important for hydrogen-transfer reactions because the frequency of the stretching vibration corresponding to the bond to the hydrogen that is about to be transferred usually decreases significantly (of the order of a factor of two) as one proceeds to the midpoint of the transfer process. Since hydrogen stretching vibrations are usually high-frequency modes ($\sim 2500\text{--}4000\text{ cm}^{-1}$),²⁵⁴ this releases a considerable amount of energy into the reaction–coordinate motion, and it can contribute significantly to lowering the effective barrier to the reaction. This effect often dominates the “Quantised vibrations” effect in Table 3.5; the “Quantised vibrations” column of Table 3.5 includes the effect of quantising all the vibrational modes, including the reaction coordinate, of the reactants but not including the reaction coordinate at the variational transition state since that is excluded from the partition functions in eqn (3.4). The effect of quantisation of the reaction coordinate of the transition state is included in the “Tunnelling” column of Table 3.5, which is labelled that way because tunnelling effects dominate κ_i .

The average value by which tunnelling lowers the free energy of activation is -1.2 kcal/mol. Two systems presented in Table 3.5 exhibit twice as high a contribution of tunnelling: methylamine dehydrogenase and methylmalonyl-CoA

mutase. As discussed in the original references^{38, 40, 145, 197, 248, 251–253} and a review,³ VTST/MT yielded good agreement with experiment for kinetic isotope effects in all of these enzyme-catalysed reactions, showing it is capable of treating reactions even with large tunnelling and quantised-vibration effects. Recent concerns²⁵⁵ that transition-state theory is inadequate for enzyme-catalysed hydrogen transfer and that a new conceptual framework is required seem to be based mainly on a lack of appreciation of the broad applicability of transition-state concepts and the consistent way (see below) that multidimensional tunnelling has been integrated into the theory.

In addition to the study in Table 3.5,²⁵² the methylamine dehydrogenase reaction and reactions catalysed by other amine dehydrogenases have also been simulated by other groups,^{156, 239, 256–265} and the reader is referred to these papers for many interesting insights into the tunnelling dynamics.

One additional study that we would like to single out for special attention is the careful VTST/MT modelling of the proton transfer in the reaction catalysed by triosephosphate isomerase by Cui and Karplus.²⁶⁶

Another perspective on the quantum effects on reaction-coordinate motion is to not separately calculate the result with classical reaction-coordinate motion. Then, the tunnelling contribution is included in the phenomenological free energy of activation from the very beginning, and it may be interpreted as a Heisenberg broadening of the transition-state energy levels. This interpretation is discussed in another review.¹¹³ It is worth mentioning that the final result is independent of whether or not it is factored into a quasiclassical part and a tunnelling transmission coefficient. This factorisation is useful though for interpretative purposes. (For example, the ability to factor the rate constant in VTST/MT calculations allows one to analyse tunnelling contributions in a way that is not possible otherwise.²⁶⁷)

We conclude this section with a brief discussion of the way that transition-state quantisation affects the microcanonical rate constants in small gas-phase systems because this perspective is helpful for understanding how these effects are fully included in a consistent way in the quantised transition-state theory reviewed here. The rate constant $k(T)$ for a canonical ensemble at temperature T may be written in terms of the rate constants $k(E)$ for microcanonical ensemble of reactants at total energy E by the formula^{19, 34, 113}

$$k(T) = \frac{\int dE \rho^R(E) \exp[-(E - V^\ddagger)/k_B T] k(E)}{\Phi^R(T)} \exp(-V^\ddagger/k_B T) \quad (3.38)$$

where $k_B T$, $\Phi^R(T)$, and V^\ddagger have the same meaning as in eqn (3.1), $\rho^R(E)$ is the reactants' density of states per unit energy and per unit volume, and the rate constant at energy E may be written as^{268, 269}

$$k(E) = \frac{\sum_n \sum_{n'} P_{nn'}(E)}{h \rho^R(E)} \quad (3.39)$$

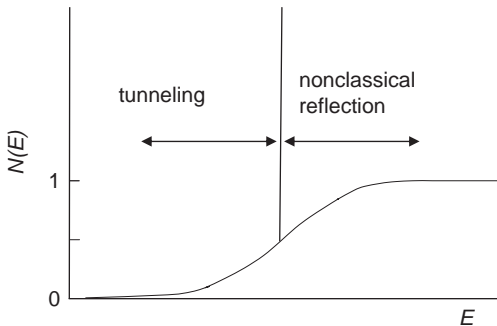


Figure 3.5 A typical step in the cumulative reaction probability as a function of energy.

The quantity in the numerator of eqn (3.39) is called the cumulative reaction probability $N(E)$, and eqn (3.39) may be written as²⁷⁰

$$k(E) = \frac{N(E)}{h\rho^R(E)} \quad (3.40)$$

If transition-state theory were valid but the reaction–coordinate motion was classical, $N(E)$ would be a series of unit steps at the quantised transition states. Accurate quantum-mechanical dynamics calculations show that these steps are present, are typically centred close to the energies of the maxima of the vibrationally adiabatic potential curves, and typically have close-to-unit height, but are rounded,^{75,76,113,269,271,272} as shown for a typical step in Figure 3.5. The rounded portion on the low-energy side of the step corresponds to tunnelling, and the rounded portion on the high-energy side corresponds to nonclassical reflection. If all of these rounded steps had the same shape, the assumption introduced before eqn (3.10) would be exact. Although there are important quantitative differences in the step shapes that can be understood in terms of the effective barrier shapes presented by the excited-state vibrationally adiabatic potential curves, it turns out that many of the low-energy steps have very similar peak shapes.^{75,76,113,269,271,272} Thus, the transmission coefficient is a very reasonable way to correct for the quantum-mechanical nature of the reaction–coordinate motion.

3.4 Concluding Remarks

EA-VTST/MT builds on the success of VTST/MT methods that are well validated for gas-phase reactions.^{4,27,37,77,273,274} The theoretical studies summarised above are fully consistent with the conclusion that quantum-mechanical effects in enzyme-catalysed reactions can be understood in terms of the same principles that govern reactions in liquid-phase solution and in the gas

phase, namely quantised vibrations (including zero-point energy) and thermally activated multidimensional tunnelling.

For enzyme-catalysed reactions, quantum effects are particularly important for hydrogen transfer, that is for transfers of protons, hydride ions, and hydrogen radicals. It has been shown that quantised vibrations and quantum-mechanical tunnelling can both be included based on a reaction coordinate that is dominated by the coordinates of the breaking and forming bonds, and quantum-mechanical effects are included in transition-state theory for enzyme-catalysed reactions in the same way as for simple gas-phase reactions, by quantising vibrational motions in phase space and by a transmission coefficient that includes quantal transmission through the same barriers that control overbarrier thresholds. Enzyme-catalysed hydrogen-transfer reactions are usually electronically adiabatic. The extra complexity of enzymes and coenzymes contributes in three ways: (i) an ensemble of reaction paths corresponding to a distribution of protein conformational states must be considered; (ii) there are many degrees of freedom coupled to the substrate component of the reaction coordinate, and a great variety of coupling mechanisms are possible; (iii) the importance of biological reactions and their consequent study as catalysed by a myriad of wild-type and mutated enzymes has uncovered a cornucopia of fascinating variations on the central paradigm, each with its own nuances.

Appendix – Quantum-Mechanical Rate Theory

This appendix contains a few comments about how one would treat reactive rate constants by exact quantum mechanics. Although converged quantum-mechanical calculations are impractical for enzyme reactions, consideration of the formalisms for converged calculations adds perspective. To calculate an accurate rate constant in the gas phase one first calculates reaction cross sections²⁷⁵ by quantum-mechanical scattering theory.^{275–279} By averaging these over a Maxwell–Boltzmann distribution of collision energies and a Boltzmann distribution of internal states, one then obtains reaction rate constants.^{280,281} Accurate rates may also be calculated directly from flux correlation functions.^{282–286} In a liquid, only the flux correlation function method remains applicable, and a variety of formulations is possible.^{287–292} The relationship of transition-state theory to the accurate flux correlation function approach is discussed elsewhere.^{12,283,288,290}

Acknowledgments

This work was supported in part by the National Science Foundation under grant no. CHE07-04974.

References

1. J. Gao and D. G. Truhlar, *Annu. Rev. Phys. Chem.*, 2002, **53**, 467.

2. D. G. Truhlar, J. Gao, C. Alhambra, M. Garcia-Viloca, J. Corchado, M. L. Sánchez and J. Villà, *Acc. Chem. Res.*, 2002, **35**, 341.
3. D. G. Truhlar, J. Gao, M. Garcia-Viloca, C. Alhambra, J. Corchado, M. L. Sanchez and T. D. Poulsen, *Int. J. Quantum Chem.*, 2004, **100**, 1136.
4. D. G. Truhlar, in *Isotope Effects in Chemistry and Biology*, ed. A. Kohen and H.-H. Limbach, Taylor & Francis, Boca Raton, FL, 2006, pp. 579–619.
5. A. Dybala-Defratyka, P. Paneth, R. Banerjee and D. G. Truhlar, *Proc. Natl. Acad. Sci. USA*, 2007, **104**, 10774.
6. H. Eyring, *J. Chem. Phys.*, 1935, **3**, 107.
7. E. Wigner, *Trans. Faraday Soc.*, 1938, **34**, 29.
8. H. Eyring, *Trans. Faraday Soc.*, 1938, **34**, 41.
9. M. G. Evans, *Trans. Faraday Soc.*, 1938, **34**, 51.
10. S. Glasstone, K. J. Laidler and E. Eyring, *The Theory of Rates Processes*, McGraw-Hill, New York, 1941.
11. H. S. Johnston, *Gas-Phase Reaction-Rate Theory*, Ronald Press, New York, 1966.
12. D. G. Truhlar, W. L. Hase and J. T. Hynes, *J. Phys. Chem.*, 1983, **87**, 2664.
13. D. G. Truhlar, B. C. Garrett and S. J. Klippenstein, *J. Phys. Chem.*, 1996, **100**, 12771.
14. M. Garcia-Viloca, J. Gao, M. Karplus and D. G. Truhlar, *Science*, 2004, **303**, 186.
15. J. C. Keck, *Adv. Chem. Phys.*, 1967, **13**, 85.
16. B. H. Mahan, *J. Chem. Educ.*, 1974, **52**, 709.
17. S. C. Tucker and D. G. Truhlar, in *New Theoretical Concepts for Understanding Organic Reactions*, ed. J. Bertrán and I. G. Csizmadia, Kluwer, Dordrecht, 1989, pp. 291–346.
18. D. G. Truhlar and B. C. Garrett, *Acc. Chem. Res.*, 1980, **13**, 440.
19. B. C. Garrett and D. G. Truhlar, *J. Phys. Chem.*, 1979, **83**, 1079. Erratum: 1983, **87**, 4553.
20. D. G. Truhlar, A. D. Isaacson, R. T. Skodje and D. G. Truhlar, *J. Phys. Chem.*, 1982, **86**, 2252.
21. D. G. Truhlar, *J. Chem. Phys.*, 1972, **56**, 3189. Erratum: 1974, **61**, 440.
22. E. Wigner, *Z. Physik. Chem.*, 1932, **B19**, 203.
23. R. P. Bell, *Trans. Faraday Soc.*, 1959, **55**, 1.
24. D. G. Truhlar and A. Kuppermann, *Chem. Phys. Lett.*, 1971, **9**, 269.
25. R. A. Marcus and M. E. Coltrin, *J. Chem. Phys.*, 1977, **67**, 2609.
26. D. G. Truhlar and B. C. Garrett, *Annu. Rev. Phys. Chem.*, 1984, **35**, 159.
27. T. C. Allison and D. G. Truhlar, in *Modern Methods for Multidimensional Dynamics Calculations in Chemistry*, ed. D. L. Thompson, World Scientific, Singapore, 1998, pp. 618–712.
28. A. Fernandez-Ramos, B. A. Ellingson, B. C. Garrett and D. G. Truhlar, in *Reviews in Computational Chemistry*, ed. K. B. Lipkowitz and T. R. Cundari, Wiley-VCH, Hoboken, NJ, 2007, pp. 125–232.
29. B. C. Garrett, D. G. Truhlar, R. S. Grev and A. W. Magnuson, *J. Phys. Chem.*, 1980, **84**, 1730. Erratum: 1983, **87**, 4554.

30. D. G. Truhlar, Y.-P. Liu, G. K. Schenter and B. C. Garrett, *J. Phys. Chem.*, 1994, **98**, 8396.
31. E. Wigner, *J. Chem. Phys.*, 1937, **5**, 720.
32. J. Horiuti, *Bull. Chem. Soc. Japan*, 1938, **13**, 210.
33. B. C. Garrett and D. G. Truhlar, *J. Chem. Phys.*, 1979, **70**, 1593.
34. B. C. Garrett and D. G. Truhlar, *J. Phys. Chem.*, 1979, **83**, 1052. Erratum: 1983, **87**, 4553.
35. G. K. Schenter, B. C. Garrett and D. G. Truhlar, *J. Phys. Chem. B*, 2001, **105**, 9672.
36. P. G. Bolhuis, C. Dellago and D. Chandler, *Faraday Discuss.*, 1998, **110**, 421–482.
37. B. C. Garrett and D. G. Truhlar, in *Theory and Applications of Computational Chemistry: The First Forty Years*. ed. C. E. Dykstra, ed. C. E. Dykstra, G. Frenking, K. S. Kim and G. E. Scuseria, Elsevier, Amsterdam, 2005, pp. 67–87.
38. C. Alhambra, J. Corchado, M. L. Sánchez, M. García-Viloca, J. Gao and D. G. Truhlar, *J. Phys. Chem. B*, 2001, **105**, 11326.
39. M. García-Viloca, C. Alhambra, D. G. Truhlar and J. Gao, *J. Comput. Chem.*, 2003, **24**, 177.
40. T. D. Poulsen, M. García-Viloca, J. Gao and D. G. Truhlar, *J. Phys. Chem. B*, 2003, **107**, 9567.
41. A. Ben-Naim, *Statistical Thermodynamics for Chemists and Biochemists*, Plenum, New York, 1992, p. 38.
42. R. K. Boyd, *Chem. Rev.*, 1977, **77**, 93.
43. C. Lim and D. G. Truhlar, *J. Phys. Chem.*, 1985, **89**, 5.
44. C. Lim and D. G. Truhlar, *J. Phys. Chem.*, 1986, **90**, 2616.
45. H. Teitelbaum, *Chem. Phys.*, 1993, **173**, 91.
46. H. Teitelbaum, *Chem. Phys. Lett.*, 1993, **202**, 242.
47. J. C. Keck, *J. Chem. Phys.*, 1960, **32**, 1035.
48. R. L. Jaffe, J. M. Henry and J. B. Anderson, *J. Chem. Phys.*, 1973, **59**, 1128.
49. W. H. Miller, *J. Chem. Phys.*, 1974, **61**, 1823.
50. B. C. Garrett and D. G. Truhlar, *J. Am. Chem. Soc.*, 1979, **101**, 4534.
51. M. M. Kreevoy and D. G. Truhlar, in *Investigation of Rates and Mechanisms of Reactions*, ed. C. F. Bernasconi, John Wiley and Sons, New York, 1986, part 1, pp. 13–95.
52. K. A. Connors, in *Chemical Kinetics: The Study of Reaction Rates in Solution*, VCH Publishers, New York, 1990, p. 207.
53. M. J. Pilling and P. W. Seakins, *Reaction Kinetics*, Oxford University Press, Oxford, United Kingdom, 1995, p. 155.
54. B. C. Garrett and D. G. Truhlar, *J. Chem. Phys.*, 1982, **76**, 1853.
55. D. G. Truhlar, A. D. Isaacson and B. C. Garrett, in *Theory of Chemical Reaction Dynamics*, ed. M. Baer, CRC Press, Boca Raton, FL, 1985, pp. 65–137.
56. J. O. Hirschfelder and E. Wigner, *J. Chem. Phys.*, 1939, **7**, 616.
57. W. H. Miller, *J. Chem. Phys.*, 1976, **65**, 2216.

58. Y.-Y. Chuang, C. J. Cramer and D. G. Truhlar, *Int. J. Quantum Chem.*, 1998, **70**, 887.
59. J. Villà and D. G. Truhlar, *Theor. Chem. Acc.*, 1997, **97**, 317.
60. C. F. Jackels, Z. Gu and D. G. Truhlar, *J. Chem. Phys.*, 1995, **102**, 3188.
61. P. L. Fast and D. G. Truhlar, *J. Chem. Phys.*, 1998, **109**, 3721.
62. C. Eckart, *Phys. Rev.*, 1930, **35**, 1303.
63. C. A. Mead, in *Mathematical Frontiers in Computational Chemical Physics*, ed. D. G. Truhlar, Springer-Verlag, New York, 1988, pp. 1–17.
64. J. Simons and J. Nichols, *Quantum Mechanics in Chemistry*, Oxford University Press, New York, 1997, p. 43.
65. D. G. Truhlar, in *The Encyclopedia of Physical Science and Technology*, ed. R. A. Meyers, 3rd edn, Academic Press, New York, 2001, **Vol. 13**, pp. 9–13.
66. P. Atkins and R. Friedman, *Molecular Quantum Mechanics*, 4th edn, Oxford University Press, Oxford, 2005, p. 249.
67. R. A. Marcus, *J. Chem. Phys.*, 1966, **45**, 4500.
68. D. G. Truhlar and A. Kuppermann, *J. Chem. Phys.*, 1970, **52**, 3841.
69. D. G. Truhlar and A. Kuppermann, *J. Am. Chem. Soc.*, 1971, **93**, 1840.
70. D. G. Truhlar, *J. Chem. Phys.*, 1970, **53**, 2041.
71. J. M. Bowman, A. Kuppermann, J. T. Adams and D. G. Truhlar, *Chem. Phys. Lett.*, 1973, **20**, 229.
72. J. W. Duff and D. G. Truhlar, *Chem. Phys. Lett.*, 1973, **23**, 327.
73. D. G. Truhlar and R. E. Wyatt, *Annu. Rev. Phys. Chem.*, 1976, **27**, 1.
74. R. T. Skodje, D. G. Truhlar and B. C. Garrett, *J. Chem. Phys.*, 1982, **77**, 5955.
75. D. C. Chatfield, R. S. Friedman, D. G. Truhlar, B. C. Garrett and D. W. Schwenke, *J. Am. Chem. Soc.*, 1991, **113**, 486.
76. D. C. Chatfield, R. S. Friedman, D. G. Truhlar and D. W. Schwenke, *Faraday Discuss. Chem. Soc.*, 1991, **91**, 289.
77. D. G. Truhlar and B. C. Garrett, in *Hydrogen Transfer Reactions*, ed. J. T. Hynes, J. P. Klinman, H. H. Limbach and R. L. Schowen, Wiley-VCH, Weinheim, Germany, 2007, **Vol. 2**, pp. 833–874.
78. R. A. Marcus, *J. Chem. Phys.*, 1966, **45**, 4493.
79. R. A. Marcus, *J. Chem. Phys.*, 1968, **49**, 2617.
80. A. Kuppermann, J. T. Adams and D. G. Truhlar, in Abstracts Papers, *Int. Conf. Phys. Electron. At. Coll. Beograd*, ed. B. C. Cubic and M. V. Kurepa, Belgrade, Serbia, 1973, **8**, 149.
81. R. T. Skodje and D. G. Truhlar, *J. Phys. Chem.*, 1981, **85**, 624.
82. B. C. Garrett, D. G. Truhlar, A. F. Wagner and T. H. Dunning Jr., *J. Chem. Phys.*, 1983, **78**, 4400.
83. D. K. Bondi, J. N. L. Connor, B. C. Garrett and D. G. Truhlar, *J. Chem. Phys.*, 1983, **78**, 5981.
84. B. C. Garrett and D. G. Truhlar, *J. Chem. Phys.*, 1983, **79**, 4931.
85. M. M. Kreevoy, D. Ostovic, D. G. Truhlar and B. C. Garrett, *J. Phys. Chem.*, 1986, **90**, 3766.
86. D. G. Truhlar and B. C. Garrett, *J. Chim. Phys.*, 1987, **84**, 365.

87. D. G. Truhlar and M. S. Gordon, *Science*, 1990, **249**, 491.
88. Y. Kim, D. G. Truhlar and M. M. Kreevoy, *J. Am. Chem. Soc.*, 1991, **113**, 7837.
89. T. Taketsugu and K. Hirao, *J. Chem. Phys.*, 1997, **107**, 10506.
90. C. S. Tautermann, A. F. Voegel, T. Loerting and K. R. Leidl, *J. Chem. Phys.*, 2002, **117**, 1962.
91. B. K. Dey and P. W. Ayers, *Mol. Phys.*, 2007, **105**, 71.
92. Y. P. Liu, D.-h. Lu, A. Gonzalez-Lafont, D. G. Truhlar and B. C. Garrett, *J. Am. Chem. Soc.*, 1993, **115**, 7806.
93. A. Fernandez-Ramos and D. G. Truhlar, *J. Chem. Phys.*, 2001, **114**, 1491.
94. D.-h. Lu, T. N. Truong, V. S. Melissas, G. C. Lynch, Y.-P. Liu, B. C. Garrett, R. Stechkler, A. D. Isaacson, S. N. Rai, G. C. Hancock, J. G. Lauderdale, T. Joseph and D. G. Truhlar, *Comput. Phys. Commun.*, 1992, **71**, 235.
95. Y.-P. Liu, G. C. Lynch, T. N. Truong, D.-h. Lu, D. G. Truhlar and B. C. Garrett, *J. Am. Chem. Soc.*, 1993, **115**, 2408.
96. B. C. Garrett, T. Joseph, T. N. Truong and D. G. Truhlar, *Chem. Phys.*, 1989, **136**, 271.
97. T. N. Truong, D.-h. Lu, G. C. Lynch, Y.-P. Liu, V. S. Melissas, J. J. P. Stewart, R. Steckler, B. C. Garrett, A. D. Isaacson, A. Gonzalez-Lafont, S. N. Rai, G. C. Hancock, T. Joseph and D. G. Truhlar, *Comput. Phys. Commun.*, 1993, **75**, 143.
98. G. K. Schenter, B. C. Garrett and D. G. Truhlar, *J. Chem. Phys.*, 2003, **119**, 5828.
99. J. B. Watney, A. V. Soudackov, K. F. Wong and S. Hammes-Schiffer, *Chem. Phys. Lett.*, 2006, **418**, 268.
100. E. C. Kemble, *Fundamental Principles of Quantum Mechanics with Elementary Applications*, Dover, New York, 1937.
101. J. Heading, *An Introduction to Phase Integral Methods*, Methuen, London, 1961.
102. B. C. Garrett and D. G. Truhlar, *J. Phys. Chem.*, 1979, **83**, 2921.
103. K. Gottfried and T.-M. Yan, *Quantum Mechanics: Fundamentals*, 2nd edn, Springer, New York, 2003, pp. 103, 217–228.
104. F. T. Smith, *J. Chem. Phys.*, 1965, **42**, 2419.
105. H. C. Corben and P. Stehle, *Classical Mechanics*, 2nd edn, Robert E. Krieger Publishing Co., Huntington, NY, 1960, p. 170, (a) p. 32.
106. I. M. Gelfand and S. V. Fomin, *Calculus of Variations*, Prentice-Hall, Englewood Cliffs, NJ, 1963, p. 84.
107. H. Goldstein, C. Poole and J. Safko, *Classical Mechanics*, Addison Wesley, San Francisco, 2002, pp. 353–362.
108. E. C. G. Sudarshan and N. Mukunda, *Classical Dynamics: A Modern Perspective*, John Wiley & Sons, New York, 1974, pp. 12–29.
109. E. B. Wilson Jr., J. C. Decius and P. C. Cross, *Molecular Vibrations*, Dover Publications, New York, 1955, p. 14.
110. S. Califano, *Vibrational States*, John Wiley & Sons, London, 1976, p. 21, (a) p. 256.

111. D. G. Truhlar and A. Kuppermann, *J. Chem. Phys.*, 1972, **56**, 2232.
112. L. Melander and W. H. Saunders Jr., *Reaction Rates of Isotopic Molecules*, John Wiley & Sons, New York, 1980.
113. D. C. Chatfield, R. S. Friedman, S. L. Mielke, G. C. Lynch, T. C. Allison, D. G. Truhlar and D. W. Schwenke, in *Dynamics of Molecules and Chemical Reactions*, ed. R. E. Wyatt and J. Z. H. Zhang, Marcel Dekker, New York, 1996, pp. 323–386.
114. B. C. Garrett, H. Abusalbi, D. J. Kouri and D. G. Truhlar, *J. Chem. Phys.*, 1985, **83**, 2252.
115. M. Garcia-Viloca, C. Alhambra, D. G. Truhlar and J. Gao, *J. Chem. Phys.*, 2001, **114**, 9953.
116. (a) M. J. S. Dewar, E. Zoebisch, E. F. Healy and J. J. P. Stewart, *J. Am. Chem. Soc.*, 1985, **107**, 3902; (b) J. J. P. Stewart, *J. Comp. Chem.*, 1989, **10**, 209.
117. N. G. J. Richards, in *Molecular Orbital Calculations for Biological Systems*, ed. A.-M. Sapse, Oxford University Press, New York, 1998, p. 11.
118. P. Amara, M. J. Field, C. Alhambra and J. Gao, *Theor. Chem. Acc.*, 2000, **104**, 336.
119. A. Shurki and A. Warshel, *Adv. Protein Chem.*, 2003, **66**, 249.
120. U. Ryde, *Curr. Opinion Struct. Biol.*, 2003, **3**, 136.
121. G. Tresadern, S. Nunez, P. F. Faulder, H. Wang, I. H. Hillier and N. A. Burton, *Faraday Discuss.*, 2003, **122**, 223.
122. P. Amara and M. J. Field, *Theor. Chem. Acc.*, 2003, **109**, 43.
123. J. Pu, J. Gao and D. G. Truhlar, *J. Phys. Chem. A*, 2004, **108**, 632.
124. (a) F. Claeysens, K. E. Ranaghan, F. R. Manby, J. N. Harvey and A. J. Mulholland, *Chem. Comm.*, 2005, **2005**, 5068; (b) A. J. Mulholland, *Chem. Central J.*, 2007, **1**, 19.
125. W. L. Jorgensen and J. Tirado-Rives, *J. Comp. Chem.*, 2005, **26**, 1689.
126. T. Vreven, K. S. Byun, I. Komaromi, S. Dapprich, J. A. Montgomery, K. Morokuma Jr. and M. J. Frisch, *J. Chem. Theory Comput.*, 2006, **2**, 815.
127. J. J. Ruiz-Pernia, E. Silla, I. Tuñon and S. Martí, *J. Phys. Chem. B*, 2006, **110**, 17663.
128. H. Lin and D. G. Truhlar, *Theor. Chem. Acc.*, 2007, **117**, 185.
129. H. M. Senn and W. Thiel, *Curr. Opin. Struct. Biol.*, 2007, **11**, 182.
130. P. F. Cook, J. S. Blanchard and W. Cleland, *Biochemistry*, 1980, **19**, 4853.
131. V. C. Sekhar and B. V. Plapp, *Biochemistry*, 1990, **29**, 4289.
132. G. L. Shearer, K. Kim, K. M. Lee, C. K. Wang and B. V. Plapp, *Biochemistry*, 1993, **32**, 11186.
133. B. J. Bahnsen and J. P. Klinman, *Methods Enzymol.*, 1995, **249**, 373.
134. C. L. Stone, W. F. Bosron and M. F. Dunn, *J. Biol. Chem.*, 1993, **268**, 892.
135. B. J. Bahnsen, D.-H. Park, K. Kim, B. V. Plapp and J. P. Klinman, *Biochemistry*, 1993, **32**, 5503.
136. B. J. Bahnsen, T. D. Colby, J. K. Chin, B. M. Goldstein and J. P. Klinman, *Proc. Natl. Acad. Sci. USA*, 1997, **94**, 12797.

137. H. Deng, J. F. Schneider, K. B. Berst, B. V. Plapp and R. Callender, *Biochemistry*, 1998, **37**, 14267.
138. S. Ramaswamy, D.-H. Park and B. V. Plapp, *Biochemistry*, 1999, **38**, 13951.
139. J. K. Rubach, S. Ramaswamy and B. V. Plapp, *Biochemistry*, 2001, **40**, 12686.
140. J. K. Rubach and B. V. Plapp, *Biochemistry*, 2002, **41**, 15770.
141. B. V. Plapp, in *Isotope Effects in Chemistry and Biology*, ed. A. Kohen and H.-H. Limbach, CRC/Taylor & Francis, Boca Raton, FL, 2006, pp. 811–835.
142. Z. D. Nagel and J. P. Klinman, *Chem. Rev.*, 2006, **106**, 3095.
143. R. Meijers, H.-W. Adolph, Z. Dauter, K. S. Wilson, V. S. Lamzin and E. S. Cedergren-Zappezauer, *Biochemistry*, 2007, **46**, 5446.
144. P. K. Agarwal, S. P. Webb and S. Hammes-Schiffer, *J. Am. Chem. Soc.*, 2000, **122**, 4803.
145. C. Alhambra, J. Gao, J. C. Corchado, M. L. Sanchez and D. G. Truhlar, *J. Am. Chem. Soc.*, 2000, **122**, 8197.
146. S. Hammes-Schiffer and S. R. Billeter, *Int. Rev. Phys. Chem.*, 2001, **20**, 591.
147. S. R. Billeter, S. P. Webb, P. K. Agarwal, T. Iordanov and S. Hammes-Schiffer, *J. Am. Chem. Soc.*, 2001, **123**, 11262.
148. J. Luo and T. C. Bruice, *J. Am. Chem. Soc.*, 2001, **123**, 11952.
149. S. R. Billeter, S. P. Webb, T. Iordanov, P. K. Agarwal and S. J. Hammes-Schiffer, *J. Chem. Phys.*, 2001, **114**, 6925.
150. J. Villa and A. Warshel, *J. Phys. Chem. B*, 2001, **105**, 7887.
151. S. P. Webb, P. K. Agarwal and S. Hammes-Schiffer, *J. Phys. Chem. B*, 2001, **104**, 8894.
152. Q. Cui, M. Elstner and M. Karplus, *J. Phys. Chem. B*, 2002, **106**, 2721.
153. S. Cartzoulas, J. S. Mincer and S. D. Schwartz, *J. Am. Chem. Soc.*, 2002, **124**, 3270.
154. A. Kohen and J. H. Jensen, *J. Am. Chem. Soc.*, 2002, **124**, 3858.
155. J. Luo and T. C. Bruice, *Proc. Natl. Acad. Sci. USA*, 2002, **99**, 16597.
156. G. Tresadern, J. P. McNamara, M. Mohr, H. Wang, N. A. Burton and I. H. Hillier, *Chem. Phys. Lett.*, 2002, **358**, 489.
157. C. Kalyanaraman and S. D. Schwartz, *J. Phys. Chem. B*, 2002, **106**, 13111.
158. J. S. Mincer and S. D. Schwartz, *J. Phys. Chem. B*, 2003, **107**, 366.
159. A. Warshel and J. Villà-Friexa, *J. Phys. Chem. B*, 2003, **107**, 12370.
160. S. D. Schwartz, *J. Phys. Chem. B*, 2003, **107**, 12372.
161. G. Tresadern, P. F. Faulder, M. P. Gleeson, Z. Tai, G. MacKenzie, N. A. Burton and I. H. Hillier, *Theor. Chem. Acc.*, 2003, **109**, 108.
162. J. Luo and T. C. Bruice, *Proc. Natl. Acad. Sci. USA*, 2004, **101**, 13152.
163. J. Luo and T. C. Bruice, *Biophys. Chem.*, 2007, **126**, 80.
164. A. Kohen and J. P. Klinman, *Acc. Chem. Res.*, 1998, **31**, 397.
165. Y. Cha, C. J. Murray and J. P. Klinman, *Science*, 1989, **243**, 1325.

166. C. G. Swain, E. C. Stivers, J. E. Reuwer and L. J. Schaad, *J. Am. Chem. Soc.*, 1958, **80**, 5885.
167. W. H. Saunders, *J. Am. Chem. Soc.*, 1985, **107**, 164.
168. M. E. Schneider and M. J. Stern, *J. Am. Chem. Soc.*, 1972, **94**, 1517.
169. J. Rucker and J. P. Klinman, *J. Am. Chem. Soc.*, 1999, **121**, 1997.
170. M. R. Sawaya and J. Kraut, *Biochemistry*, 1997, **36**, 586.
171. C. J. Falzone, P. E. Wright and S. E. Benkovic, *Biochemistry*, 1994, **33**, 439.
172. M. J. Osborne, J. Schnell, S. J. Benkovic, H. J. Dyson and P. E. Wright, *Biochemistry*, 2001, **40**, 9846.
173. P. T. R. Rajagopalan, S. Lutz and B. J. Benkovic, *Biochemistry*, 2002, **41**, 12618.
174. G. Maglia and R. K. Allemand, *J. Am. Chem. Soc.*, 2003, **125**, 13372.
175. P. Shrimpton, A. Mullaney and R. L. Allemand, *Proteins: Struct. Funct. Genet.*, 2003, **51**, 216.
176. J. R. Schnell, H. J. Dyson and P. E. Wright, *Annu. Rev. Biophys. Biomol. Struct.*, 2004, **33**, 119.
177. R. S. Swanwick, P. J. Shrimpton and R. K. Allemand, *Biochemistry*, 2004, **43**, 4119.
178. R. P. Venkitakrishnan, E. Zaborowski, D. McElheny, S. J. Benkovic, H. J. Dyson and P. E. Wright, *Biochemistry*, 2004, **43**, 16046.
179. R. S. Sikorski, L. Wang, K. A. Markham, P. T. R. Rajagopalan, S. Benkovic and A. Kohen, *J. Am. Chem. Soc.*, 2004, **126**, 4778.
180. D. McElheny, J. R. Schnell, J. C. Lansing, H. J. Dyson and P. E. Wright, *Proc. Natl. Acad. Sci. USA*, 2005, **102**, 5032.
181. R. S. Swanwick, G. Maglia, L.-H. Tey and R. K. Allemand, *Biochem. J.*, 2006, **394**, 259.
182. L. Wang, S. Tharp, T. Selzer, S. J. Benkovic and A. Kohen, *Biochemistry*, 2006, **45**, 1383.
183. D. D. Boehr, H. J. Dyson and P. E. Wright, *Chem. Rev.*, 2006, **106**, 3055.
184. L. Wang, N. Goodey, S. J. Benkovic and A. Kohen, *Philos. Trans. Roy. Soc. B*, 2006, **361**, 1307.
185. R. K. Allemand, R. M. Evans, L.-H. Tey, G. Maglia, J. Pang, R. Rodriguez, P. J. Shrimpton and R. S. Swanwick, *Philos. Trans. Roy. Soc. B*, 2006, **361**, 1317.
186. L. Wang, N. M. Goodey, S. J. Benkovic and A. Kohen, *Proc. Natl. Acad. Sci. USA*, 2006, **103**, 15753.
187. D. D. Boehr, D. McElhenny, H. J. Dyson and P. E. Wright, *Science*, 2006, **313**, 1638.
188. P. L. Cummins, K. Ramnaryan, U. C. Singh and J. E. Gready, *J. Am. Chem. Soc.*, 1991, **113**, 8247.
189. P. L. Cummins and J. E. Gready, *J. Comp. Chem.*, 1998, **19**, 977.
190. R. Castillo, J. Andres and V. Moliner, *J. Am. Chem. Soc.*, 1999, **121**, 12140.
191. S. Hammes-Schiffer, *Biochemistry*, 2002, **41**, 13335.
192. P. K. Agarwal, S. R. Billeter and S. Hammes-Schiffer, *J. Phys. Chem. B*, 2002, **106**, 3283.

193. P. L. Cummins, S. P. Greatbanks, A. P. Rendall and J. E. Gready, *J. Phys. Chem. B*, 2002, **106**, 9934.
194. P. K. Agarwal, S. R. Billeter, P. T. R. Rajagopalan, S. J. Benkovic and S. Hammes-Schiffer, *Proc. Natl. Acad. Sci. USA*, 2002, **99**, 2794.
195. P. Shrimpton and R. K. Allemann, *Prot. Sci.*, 2002, **11**, 1442.
196. Y. Y. Sham, B. Ma, C.-J. Tsai and R. Nussinov, *Proteins: Struct. Funct. Genet.*, 2002, **46**, 308.
197. M. Garcia-Viloca, D. G. Truhlar and J. Gao, *Biochemistry*, 2003, **42**, 13558.
198. J. B. Watney, P. K. Agarwal and S. Hammes-Schiffer, *J. Am. Chem. Soc.*, 2003, **125**, 3745.
199. S. Ferrer, E. Silla, I. Tuñón, S. Martí and V. Moliner, *J. Phys. Chem. B*, 2003, **107**, 14036.
200. I. F. Thorpe and C. L. Brooks III, *J. Phys. Chem. B*, 2003, **107**, 14042.
201. S. Hammes-Schiffer, *Curr. Opinion Struct. Biol.*, 2004, **14**, 192.
202. K. F. Wong, J. B. Watney and S. Hammes-Schiffer, *J. Phys. Chem. B*, 2004, **108**, 12231.
203. I. F. Thorpe and C. L. Brooks III, *Proteins: Struct. Function Bioinf.*, 2004, **57**, 444.
204. I. F. Thorpe and C. L. Brooks III, *J. Am. Chem. Soc.*, 2005, **127**, 12997.
205. J. Pu, M. Garcia-Viloca, J. Gao, D. G. Truhlar and A. Kohen, *J. Am. Chem. Soc.*, 2005, **127**, 14879.
206. H. Alonso, M. B. Gilles, P. L. Cummins, A. A. Bliznyuk and J. E. Gready, *J. Comp.-Aided Molec. Des.*, 2005, **19**, 6807.
207. J. Pu, S. Ma, J. Gao and D. G. Truhlar, *J. Phys. Chem. B.*, 2005, **109**, 8551.
208. K. F. Wong, T. Selzer, S. J. Benkovic and S. Hammes-Schiffer, *Proc. Natl. Acad. Sci. USA*, 2005, **102**, 6807.
209. S. Hammes-Schiffer, *Acc. Chem. Res.*, 2006, **39**, 93.
210. J. Pang, J. Pu, J. Gao, D. G. Truhlar and R. K. Allemann, *J. Am. Chem. Soc.*, 2006, **128**, 8015.
211. A. Sergi, J. B. Watney, K. F. Wong and S. Hammes-Schiffer, *J. Phys. Chem. B*, 2006, **110**, 2435.
212. J. B. Watney and S. Hammes-Schiffer, *J. Phys. Chem. B*, 2006, **110**, 10130.
213. J. Pang and R. K. Allemann, *Phys. Chem. Chem. Phys.*, 2007, **9**, 711.
214. S. Hammes-Schiffer and J. B. Watney, *Philos. Trans. Roy. Soc. B*, 2006, **361**, 1365.
215. I. V. Khavrutskii, D. J. Price, J. Lee and C. L. Brooks III, *Prot. Sci.*, 2007, **16**, 1087.
216. P. L. Cummins, I. V. Rostov and J. E. Gready, *J. Chem. Theory and Comput.*, 2007, **3**, 1203.
217. C. A. Fierke, K. A. Johnson and S. J. Benkovic, *Biochemistry*, 1987, **26**, 4085.
218. A. Kohen and J. P. Klinman, *Chem. Biol.*, 1999, **6**, R191.
219. G. A. Veldink, *Biochemistry*, 1994, **33**, 3974.
220. M. H. Glickman, J. S. Wiseman and J. P. Klinman, *J. Am. Chem. Soc.*, 1994, **116**, 793.

221. M. H. Glickman and J. P. Klinman, *Biochemistry*, 1995, **34**, 14077.
222. N. Moiseyev, J. Rucker and M. H. Glickman, *J. Am. Chem. Soc.*, 1997, **119**, 3853.
223. K. W. Rickert and J. P. Klinman, *Biochemistry*, 1999, **38**, 12218.
224. A. M. Kuznetsov and J. Ulstrup, *Can. J. Chem.*, 1999, **77**, 1085.
225. V. B. O'Donnell, K. B. Taylor, S. Parthasarathy, H. Kühn, D. Koesling, A. Friebe, A. Bloodsworth, V. M. Darley-Usmar and B. A. Freeman, *J. Biol. Chem.*, 1999, **274**, 20083.
226. E. I. Solomon, T. C. Brunold, M. I. Davis, J. N. Kemsley, S. K. Lee, N. Lehnert, F. Neese, A. J. Skulan, Y. S. Yang and J. Zhou, *Chem. Rev.*, 2000, **100**, 235.
227. M. J. Knapp and J. P. Klinman, *Eur. J. Biochem.*, 2002, **269**, 3113.
228. M. J. Knapp, K. Rickert and J. P. Klinman, *J. Am. Chem. Soc.*, 2002, **124**, 3865.
229. A. Kohen, *Prog. React. Kinet. Mech.*, 2003, **28**, 119.
230. V. C. Ruddat, S. Whitman, T.-R. Holman and C. F. Bernsconi, *Biochemistry*, 2003, **42**, 4172.
231. E. N. Segraves and T. R. Holman, *Biochemistry*, 2003, **42**, 5236.
232. M. J. Knapp and J. P. Klinman, *Biochemistry*, 2003, **42**, 11466.
233. Z. X. Liang and J. P. Klinman, *Curr. Opin. Struct. Biol.*, 2004, **14**, 648.
234. M. H. M. Olsson, P. E. M. Siegbahn and A. Warshel, *J. Am. Chem. Soc.*, 2004, **126**, 2820.
235. E. Hatcher, A. V. Soudackov and S. Hammes-Schiffer, *J. Am. Chem. Soc.*, 2004, **126**, 5763.
236. N. Lehnert and E. I. Solomon, *J. Biol. Inorg. Chem.*, 2003, **8**, 294.
237. M. H. M. Olsson, P. E. M. Siegbahn and A. Warshel, *J. Biol. Inorg. Chem.*, 2004, **9**, 96.
238. T. Borowski and E. Broclawik, *J. Phys. Chem. B*, 2003, **107**, 4639.
239. W. Siebrand and Z. Smedarchina, *J. Phys. Chem. B*, 2004, **108**, 4185.
240. I. Tejero, L. A. Eriksson, Á. González-Lafont, J. Marquet and J. M. Lluch, *J. Phys. Chem. B*, 2004, **108**, 13831.
241. M. P. Meyer and J. P. Klinman, *Chem. Phys.*, 2005, **319**, 283.
242. I. Tejero, M. Garcia-Viloca, A. Gonzalez-Lafont, J. M. Lluch and D. M. York, *J. Phys. Chem. B*, 2006, **110**, 24708.
243. E. Hatcher, A. V. Soudackov and S. Hammes-Schiffer, *J. Am. Chem. Soc.*, 2007, **129**, 187.
244. S. Chowdhury and R. Banerjee, *J. Am. Chem. Soc.*, 2000, **122**, 5417.
245. A. Dybala-Defratyka and P. Paneth, *J. Inorg. Biochem.*, 2001, **86**, 681.
246. R. Banerjee, D. G. Truhlar, A. Dybala-Defratyka and P. Paneth, in *Hydrogen Transfer Reactions*, ed. J. T. Hynes, J. P. Klinman, H.-H. Limbach and R. L. Schowen, Wiley, Weinheim, Germany, 2007, **Vol. 4**, pp. 1473–1495.
247. R. Banerjee, A. Dybala-Defratyka and P. Paneth, *Philos. Trans. R Soc. London B Biol. Sci.*, 2006, **361**, 1341.
248. A. Dybala-Defratyka, P. Paneth, R. Banerjee and D. G. Truhlar, *Proc. Natl. Acad. Sci. USA*, 2007, **104**, 10774.
249. J. A. Pople and R. K. Nesbet, *J. Chem. Phys.*, 1954, **22**, 571.

250. J. Pu, J. Gao and D. G. Truhlar, *Chem. Rev.*, 2006, **106**, 3140.
251. C. Alhambra, J. Gao, J. C. Corchado, J. Villà and D. G. Truhlar, *J. Am. Chem. Soc.*, 1999, **121**, 2253.
252. C. Alhambra, M. L. Sánchez, J. C. Corchado, J. Gao and D. G. Truhlar, *Chem. Phys. Lett.*, 2001, **347**, 512. Corrected version: 2002, **355**, 388.
253. M. Garcia-Viloca, C. Alhambra, D. G. Truhlar and J. Gao, *J. Am. Chem. Soc.*, 2002, **124**, 7268.
254. N. B. Colthup, L. H. Daly and S. E. Wiberley, *Introduction to Infrared and Raman Spectroscopy*, Academic Press, Boston, 1990, p. 177.
255. See, e.g., (a) ref. 228, (b) J. P. Klinman, *Pure Appl. Chem.*, 2003, **75**, 601 and (c) J. P. Klinman, *Philos. Trans. Roy. Soc. B*, 2006, **361**, 1323.
256. J. Basran, S. Patel, M. J. Sutcliffe and N. S. Scrutton, *J. Biol. Chem.*, 2001, **276**, 6234.
257. P. F. Faulder, G. Tresadern, K. K. Chohan, N. S. Scrutton, M. J. Sutcliffe, I. H. Hillier and N. A. Burton, *J. Am. Chem. Soc.*, 2001, **123**, 8604.
258. M. J. Sutcliffe and N. S. Scrutton, *Eur. J. Biochem.*, 2002, **269**, 3096.
259. G. Tresadern, H. Wang, P. F. Faulder, N. A. Burton and I. H. Hillier, *Mol. Phys.*, 2003, **101**, 2775.
260. L. Masgrau, J. Basran, P. Hothi, M. J. Sutcliffe and N. S. Scrutton, *Arch. Biochem. Biophys.*, 2004, **428**, 41.
261. L. Masgrau, A. Roujeinikova, L. O. Johannissen, P. Hothi, J. Basran, K. E. Ranaghan, A. J. Mulholland, M. J. Sutcliffe, N. S. Scrutton and D. Leys, *Science*, 2006, **312**, 237.
262. M. J. Sutcliffe, L. Masgrau, A. Roujeinikova, L. O. Johannissen, P. Hothi, J. Basran, K. E. Ranaghan, A. J. Mulholland, D. Leys and N. S. Scrutton, *Philos. Trans. Roy. Soc. B*, 2006, **361**, 1375.
263. S. Nuñez, G. Tresadern, I. H. Hillier and N. A. Burton, *Philos. Trans. Roy. Soc. B*, 2006, **361**, 1387.
264. L. O. Johannissen, S. Hay, N. S. Scrutton and M. J. Sutcliffe, *J. Phys. Chem. B*, 2007, **111**, 2631.
265. K. E. Ranaghan, L. Masgrau, N. S. Scrutton, M. J. Sutcliffe and A. J. Mulholland, *ChemPhysChem*, 2007, **8**, 1816.
266. (a) Q. Cui and M. Karplus, *J. Am. Chem. Soc.*, 2002, **124**, 3093; (b) Q. Cui and M. Karplus, *J. Phys. Chem. B*, 2002, **106**, 7927; (c) Q. Cui and M. Karplus, *Adv. Protein Chem.*, 2003, **66**, 315.
267. B. C. Garrett, D. G. Truhlar, J. M. Bowman, A. F. Wagner, D. Robie, S. Arepalli, N. Presser and R. J. Gordon, *J. Am. Chem. Soc.*, 1986, **108**, 3515.
268. R. A. Marcus, *J. Chem. Phys.*, 1966, **45**, 2138.
269. D. C. Chatfield, R. S. Friedman, D. G. Truhlar, B. C. Garrett and D. W. Schwenke, *J. Am. Chem. Soc.*, 1991, **113**, 486.
270. W. H. Miller, *J. Chem. Phys.*, 1975, **62**, 1899.
271. D. C. Chatfield, R. S. Friedman, D. W. Schwenke and D. G. Truhlar, *J. Phys. Chem.*, 1992, **96**, 2414.
272. D. C. Chatfield, R. S. Friedman, G. C. Lynch, D. G. Truhlar and D. W. Schwenke, *J. Chem. Phys.*, 1993, **98**, 342.

273. J. Pu, J. C. Corchado and D. G. Truhlar, *J. Chem. Phys.*, 2001, **115**, 6266.
274. J. Pu and D. G. Truhlar, *J. Chem. Phys.*, 2002, **117**, 1479.
275. R. B. Bernstein, ed. *Atom-Molecule Collision Theory: A Guide for the Experimentalist*, Plenum, New York, 1979.
276. G. C. Schatz and A. Kuppermann, *J. Chem. Phys.*, 1976, **65**, 4642.
277. D. W. Schwenke, K. Haug, M. Zhao, D. G. Truhlar, Y. Sun, J. Z.-H. Zhang and D. J. Kouri, *J. Phys. Chem.*, 1988, **92**, 3202.
278. D. G. Truhlar, D. W. Schwenke and D. J. Kouri, *J. Phys. Chem.*, 1996, **94**, 7346.
279. R. E. Wyatt and J. Z. H. Zhang, ed. *Dynamics of Molecules and Chemical Reactions*, Marcel Dekker, New York, 1996.
280. A. Kuppermann and E. F. Greene, *J. Chem. Educ.*, 1968, **45**, 2361.
281. S. L. Mielke, K. A. Peterson, D. W. Schwenke, B. C. Garrett, D. G. Truhlar, J. V. Michael, M.-C. Su and J. W. Sutherland, *Phys. Rev. Lett.*, 2003, **91**, 63201.
282. T. Yamamoto, *J. Chem. Phys.*, 1960, **33**, 281.
283. W. H. Miller, S. D. Schwartz and J. W. Tromp, *J. Chem. Phys.*, 1983, **79**, 4889.
284. T. J. Park and J. C. Light, *J. Chem. Phys.*, 1989, **91**, 974.
285. P. N. Day and Donald G. Truhlar, *J. Chem. Phys.*, 1991, **94**, 2045.
286. F. Huarte-Larrañaga and U. Manthe, *J. Chem. Phys.*, 2001, **114**, 9683.
287. R. Zwanzig, *Annu. Rev. Phys. Chem.*, 1965, **16**, 67.
288. D. Chandler, *J. Chem. Phys.*, 1978, **68**, 2959.
289. J. T. Hynes, in *Theory of Chemical Reaction Rates*, ed. M. Baer, CRC Press, Boca Raton, FL, 1985, Vol. 4, pp. 171–234.
290. K. Haug, G. Wahnström and H. Metiu, *J. Chem. Phys.*, 1990, **92**, 2083.
291. E. Sim, G. Krilov and B. J. Berne, *J. Phys. Chem. A*, 2001, **105**, 2824.
292. I. R. Craig and D. E. Manolopoulos, *J. Chem. Phys.*, 2005, **123**, 34102.

CHAPTER 4

Selected Theoretical Models and Computational Methods for Enzymatic Tunnelling

SHARON HAMMES-SCHIFFER

Department of Chemistry, 104 Chemistry Building, Pennsylvania State University, University Park, PA 16802, USA

4.1 Introduction

Enzymes catalyse a broad spectrum of hydrogen-tunnelling reactions. In such reactions, the quantum-mechanical nature of the hydrogen nucleus enables sampling of classically forbidden regions and hence tunnelling through potential-energy barriers. In one type of model that describes hydrogen tunnelling in enzymes, the transferring hydrogen nucleus is represented by a quantum-mechanical wavefunction that depends on the solvated enzyme environment. The quantum-mechanical effects of the electrons must also be included in these models to allow the breaking and forming of chemical bonds. In general, these models require reorganisation of the enzyme/solvent environment to provide configurations that are conducive to hydrogen tunnelling. Such reorganisation is necessary to bring the proton donor and acceptor atoms closer together, orient the ligands properly, and provide an appropriate electrostatic environment. In this framework, fast thermal fluctuations of the enzyme and solvent lead to conformational sampling that in turn results in configurations that enable hydrogen tunnelling. The rates of these reactions are

determined mainly by the efficiency of this conformational sampling and the probability of hydrogen tunnelling in the favourable configurations.

This chapter will describe tunnelling models for two different types of enzymatic reactions: vibronically nonadiabatic proton-coupled electron-transfer (PCET) reactions and predominantly adiabatic proton- or hydride-transfer reactions. In general, chemical reactions are electronically (or vibrationally) adiabatic when the system remains in the electronic (or vibrational) ground state and are electronically (or vibrationally) nonadiabatic when excited electronic (or vibrational) states are involved. PCET reactions entail the simultaneous transfer of an electron and a proton and typically involve two distinct electronic states, corresponding to the reactant and product electron-transfer states. These reactions can be described in terms of nonadiabatic transitions between reactant and product vibronic states, which are mixtures of electronic and proton vibrational states. In contrast, proton- and hydride-transfer reactions are usually electronically adiabatic and hence remain in the electronic ground state. These reactions can be described in terms of the evolution of the proton vibrational wavefunction on the electronic ground state in the field of the moving enzyme and solvent. Both types of reactions require a quantum-mechanical description of the electrons and the transferring proton, as well as the conformational sampling of the enzyme and solvent environment to provide configurations conducive to hydrogen tunnelling.

An outline of this chapter is as follows. Section 4.2 will focus on vibronically nonadiabatic proton-coupled electron-transfer reactions. A general theoretical formulation, as well as an application to PCET in soybean lipoxygenase (SLO), will be presented. Section 4.3 will centre on predominantly adiabatic proton- and hydride-transfer reactions. This section will present a general theoretical model and a hybrid quantum/classical molecular dynamics approach, followed by an application to hydride transfer in dihydrofolate reductase (DHFR). Emerging concepts on the role of enzyme motion and conformational sampling will be discussed in Section 4.4.

4.2 Vibronically Nonadiabatic Reactions: Proton-Coupled Electron Transfer

PCET reactions involve the simultaneous transfer of an electron and a proton. These reactions are typically vibronically nonadiabatic with respect to the solvent and protein environment because the coupling between the reactant and product electron–proton vibronic states is much less than the thermal energy $k_B T$. For these reactions, the vibronic states correspond to mixed electronic/proton vibrational states, and, in some cases, the vibronic coupling can be expressed as the product of an electronic coupling and a hydrogen vibrational overlap. For vibronically nonadiabatic reactions, perturbative approaches such as those based on the golden rule can be used to derive rate expressions in various limits. This section will describe a theoretical formulation for vibronically nonadiabatic PCET reactions in solution and enzymes and will illustrate this theory by an application to the PCET reaction catalysed by SLO.

4.2.1 Theory

A general theoretical formulation for nonadiabatic PCET reactions in solution and enzymes has been developed.^{1–4} In this theory, the active electrons and transferring proton(s) are treated quantum mechanically, and the PCET reaction is described in terms of nonadiabatic transitions between pairs of reactant and product mixed electron–proton vibronic states. The reactant states correspond to the localisation of the transferring electron on its donor, and the product states correspond to the localisation of the transferring electron on its acceptor. The hydrogen nucleus is represented by a quantum-mechanical wavefunction, and the solvent or protein environment can be described with a dielectric continuum model or with explicit molecules. The nonadiabatic PCET rate-constant expressions have been derived in various limits using the golden-rule formalism in conjunction with linear response theory.

The fundamental mechanism of PCET reactions is illustrated in Figure 4.1. The reaction is described in terms of two diabatic electronic states. In the reactant state, the electron is localised on the donor, and in the product state, the electron is localised on the acceptor. For illustrative purposes, the proton is depicted as moving in a one-dimensional double-well potential, and the adiabatic hydrogen vibrational states are calculated for each potential. When the electron is localised on the donor, the donor well of the proton potential is lower in energy due to attractive electrostatic interactions. Similarly, the acceptor well is lower in energy when the electron is localised on the acceptor. In the simplest picture, initially the system is in the reactant state, where the electron and proton are localised on their donors. Reorganisation of the protein/solvent environment leads to the degeneracy of the reactant and product vibronic states, and a nonadiabatic transition from the reactant to the product state can occur with a probability proportional to the square of the vibronic coupling. Further reorganisation of the protein/solvent environment stabilises the system in the product state, where the electron and proton are localised on their acceptors. In this framework, the electron and proton tunnel simultaneously between two degenerate vibronic states. The nonadiabatic PCET rate constant is the Boltzmann-weighted sum of the rate constants for nonadiabatic transitions between all pairs of reactant and product vibronic states.

Within this framework, the PCET rate constant for fixed proton donor–acceptor distance has been expressed as:²

$$k = \sum_{\mu} P_{\mu}^I \sum_{\nu} \frac{|V_{\mu\nu}|^2}{h} \sqrt{\frac{\pi}{\lambda_{\mu\nu} k_B T}} \exp \left[-\frac{(\Delta G_{\mu\nu}^0 + \lambda_{\mu\nu})^2}{4\lambda_{\mu\nu} k_B T} \right] \quad (4.1)$$

where the summations are over the reactant and product vibronic states, P_{μ}^I is the Boltzmann probability for the reactant state, $V_{\mu\nu}$ is the coupling between the reactant and product vibronic states, $\Delta G_{\mu\nu}^0$ is the reaction free energy, and $\lambda_{\mu\nu}$ is the reorganisation energy. The latter two quantities are depicted in Figure 4.2 for

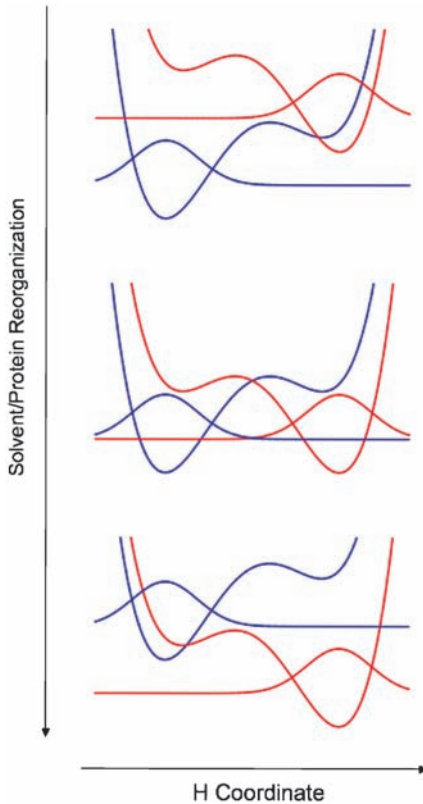


Figure 4.1 Schematic illustration of the proton potential energy curves and corresponding ground state proton vibrational wavefunctions as functions of the proton coordinate for the reactant (blue) and product (red) PCET states. The electron is localised on the donor for the reactant and on the acceptor for the product. The reorganisation of the solvent and protein changes the relative energies of the reactant and product vibronic states. The nonadiabatic transition, which involves hydrogen tunnelling, can occur when the two states are degenerate, as in the middle picture.

two-dimensional electron–proton vibronic free-energy surfaces. The equilibrium effects of the proton donor–acceptor distance R variation can be included by thermally averaging the rate constant in eqn (4.1) over a Boltzmann distribution for R . Related expressions were derived previously for electron-transfer reactions in the context of Marcus theory.^{5–10}

The initial formulation of this PCET theory was based on a multistate continuum theory, where the solvent/protein environment was represented as a dielectric continuum.^{1,2} For this case, analytical expressions were derived for the reactant and product electronic free-energy surfaces as functions of two collective solvent coordinates corresponding to proton and electron transfer. The implementation of the multistate continuum theory requires two types of

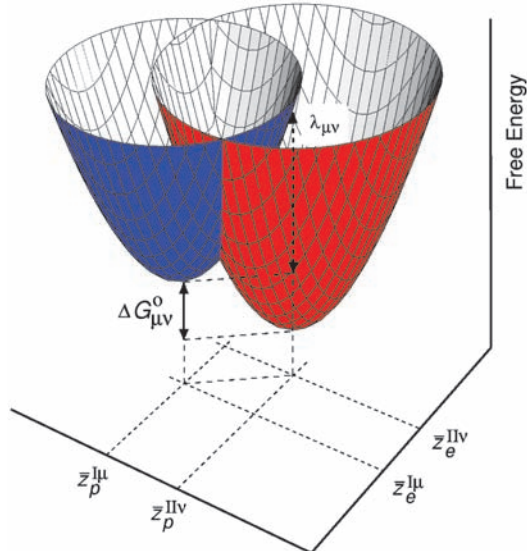


Figure 4.2 Two dimensional electron proton vibronic free energy surfaces as functions of two collective solvent coordinates for a PCET reaction. The lowest energy reactant and product free energy surfaces are shown. The free energy difference $\Delta G_{\mu\nu}^0$ and outer sphere reorganisation energy $\lambda_{\mu\nu}$ are indicated. Reproduced from [ref. 3].

input quantities. The gas-phase empirical valence bond (EVB) matrix elements for the solute are represented by standard molecular-mechanical terms that are parameterised to fit electronic-structure calculations and experimental data.¹¹ The solvent/protein reorganisation energy matrix elements are calculated with electrostatic dielectric continuum models. These quantities are used as input for the analytical expressions describing the reactant and product electronic free-energy surfaces. Subsequently, the hydrogen vibrational wavefunctions are calculated for the reactant and product electronic surfaces, leading to two sets of two-dimensional electron–proton vibronic surfaces, as depicted in Figure 4.2. These surfaces provide the reorganisation energies, free energies of reaction, and couplings, which are utilised in eqn (4.1) to calculate the PCET rate constant. This formulation has been applied to a variety of PCET reactions in solution and has reproduced trends in rates and kinetic isotope effects, as well as the temperature and pH dependences in some cases.¹² As discussed below, it has also been successfully applied to PCET catalysed by the enzyme lipoxygenase.¹³

This theory has been extended to include explicit solvent and protein, the proton donor–acceptor motion, and the corresponding dynamical effects.⁴ In this formulation, the nonadiabatic PCET rate constant is expressed as the time integral of a probability flux correlation function that depends on the vibronic coupling and on time–correlation functions of the energy gap \mathcal{E} (*i.e.* the

difference between the energies of the product and reactant vibronic states) and the proton donor–acceptor distance R . The vibronic coupling between the reactant and product mixed electron–proton vibronic states is assumed to decrease exponentially with R and to be of the form:^{14–17}

$$V_{\mu\nu}(R) \approx V_{\mu\nu}^{(0)} \exp[-\alpha_{\mu\nu}(R - R_\mu)] \quad (4.2)$$

where R_μ is the equilibrium value of the R coordinate on the reactant surface μ , $V_{\mu\nu}^{(0)}$ is the vibronic coupling between states μ and ν at distance R_μ , and $\alpha_{\mu\nu}$ is a parameter that reflects the distance dependence of the vibronic coupling. For applications of this general dynamical rate-constant expression to PCET reactions in solution^{17,18} and enzymes,¹⁹ the time–correlation functions are calculated with classical molecular-dynamics simulations for the reactant state, and the vibronic coupling is calculated with quantum-mechanical methods.

Based on this dynamical formulation, a series of analytical rate expressions have been derived.^{4,18,19} A useful analytical form of the rate expression is:¹⁹

$$k = \sum_{\mu} P_{\mu}^l \sum_{\nu} \frac{\left| V_{\mu\nu}^{(0)} \right|^2}{h} \exp \left[\frac{2k_B T \alpha_{\mu\nu}^2}{M \Omega^2} \right] \sqrt{\frac{\pi}{\lambda_{\mu\nu} k_B T}} \exp \left[-\frac{(\Delta G_{\mu\nu}^0 + \lambda_{\mu\nu})^2}{4\lambda_{\mu\nu} k_B T} \right] \quad (4.3)$$

where M and Ω are the effective mass and frequency corresponding to the R mode, and the other quantities are defined above. In comparison to eqn (4.1), which was derived for fixed R , eqn (4.3) includes the exponential term $\exp[2k_B T \alpha_{\mu\nu}^2 / M \Omega^2]$ arising from the dependence of the vibronic coupling on the proton donor–acceptor vibrational motion. Related expressions have been derived for vibrationally nonadiabatic proton-transfer reactions.^{14–16,20–22} For simplification, the reorganisation energy $\lambda_{\mu\nu}$ and coupling parameter $\alpha_{\mu\nu}$ can be assumed to be the same for all pairs of reactant and product states. In addition, the reaction free energy can be expressed as $\Delta G_{\mu\nu}^0 = \Delta G_{00}^0 + \Delta \epsilon_{\mu\nu}$, where $\Delta \epsilon_{\mu\nu}$ is the difference between the product and reactant vibronic energy levels relative to the ground states. Analogues of these rate-constant expressions that include the quantum-mechanical effects of the R coordinate motion have also been derived.¹⁹

The rate-constant expression in eqn (4.3) is related to other rate-constant expressions used for various purposes. This expression becomes equivalent to eqn (4.1), the rate constant expression for fixed R , when $\alpha_{\mu\nu} = 0$. Further approximation that $V_{\mu\nu}^{(0)} \approx V^{\text{el}} S_{\mu\nu}^{(0)}$, the product of an effective electronic coupling V^{el} and the overlap $S_{\mu\nu}^{(0)}$ between the reactant and product hydrogen vibrational wavefunctions, leads to the Marcus theory rate expression for nonadiabatic electron transfer modified by the inclusion of Franck–Condon overlap terms for the transferring hydrogen.^{23,24} Moreover, a direct connection can also be made to the rate-constant expression of Kuznetsov and Ulstrup²⁵ as implemented by Klinman and coworkers,^{26,27} where the Marcus theory rate expression for nonadiabatic electron transfer is modified by the inclusion of R -dependent

Franck–Condon overlap terms for the transferring hydrogen, thermally averaged over a Boltzmann distribution for R . This alternative rate expression leads to eqn (4.3) if the overlap between the reactant and product hydrogen vibrational wavefunctions is assumed to depend exponentially on R , as in eqn (4.2), with $V_{\mu\nu}^{(0)} = V^{\text{el}} S_{\mu\nu}^{(0)}$.²⁸

All of the quantities in the rate expression given in eqn (4.3) can be calculated from classical molecular-dynamics simulations on the reactant surface and quantum-mechanical calculations of the vibronic couplings.¹⁸ In linear response theory,⁵ the reorganisation energy $\lambda_{\mu\nu}$ can be expressed in terms of the energy gap variance as $\lambda_{\mu\nu} = \langle \delta \mathcal{E}_{\mu\nu}^2 \rangle / 2k_B T$, and the reaction free energy can be calculated as $\Delta G_{\mu\nu}^0 = -\langle \mathcal{E}_{\mu\nu} \rangle - \lambda_{\mu\nu}$.^{29,30} The average R coordinate R and the quantity $k_B T / M\Omega^2 = \langle \delta R^2 \rangle$ can also be calculated directly from the molecular-dynamics simulations. The effective mass M and frequency Ω corresponding to the R mode can be determined independently by fitting the R -coordinate time-correlation function from the classical molecular dynamics to the corresponding analytical expression for an undamped classical harmonic oscillator for the relevant timescale. The magnitude and distance dependence of the vibronic coupling (*i.e.* $V_{\mu\nu}^{(0)}$ and $\alpha_{\mu\nu}$ in eqn (4.2)) can be determined from quantum-mechanical methods.

The rate-constant expression in eqn (4.3) leads to a simple expression for the KIE if the relatively weak isotopic dependences of the free energy of reaction and reorganisation energy are neglected. If only the nonadiabatic transition between the two ground states is considered, the KIE can be approximated as¹⁹

$$\text{KIE} \approx \frac{|S_H|^2}{|S_D|^2} \exp \left\{ \frac{2k_B T}{M\Omega^2} (\alpha_H^2 - \alpha_D^2) \right\} \quad (4.4)$$

where S_H and S_D are the overlaps of the hydrogen and deuterium wavefunctions, respectively, at R , and α_H and α_D represent the exponential dependence of this overlap on R for hydrogen and deuterium, respectively. Here, we have assumed that $V_{\mu\nu}^{(0)} = V^{\text{el}} S_{\mu\nu}^{(0)}$, where the effective electronic coupling V^{el} is independent of isotope. The simplified expression for the KIE given in eqn (4.4) provides insight into the magnitude and temperature dependence of the KIE for PCET systems. The effects of excited vibronic states can be included by summing over these states in eqn (4.3). Alternative theories for describing the temperature dependence of kinetic isotope effects have been developed by other groups.^{31–33}

4.2.2 Application to Lipoxygenase

Lipoxygenases catalyse the oxidation of unsaturated fatty acids and have a wide range of biomedical applications.³⁴ Kinetic studies have shown that the hydrogen-abstraction step in SLO is rate limiting above 32 °C.³⁵ In this step, the pro-*S* hydrogen atom from carbon atom C11 of the linoleic acid substrate is transferred to the Fe(III)–OH cofactor, forming a radical intermediate substrate and Fe(II)–OH₂, as shown in Figure 4.3.³⁶ This hydrogen-abstraction step occurs by a

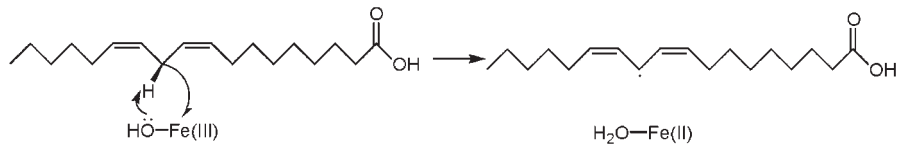


Figure 4.3 The hydrogen abstraction step of the reaction catalysed by soybean lipoxygenase with its natural substrate linoleic acid. In this step, a hydrogen is abstracted from the linoleic acid to the iron cofactor. Reproduced from [ref. 19].

PCET mechanism, in which the electron transfers from the π -system of the substrate to the iron of the cofactor, while the proton transfers from the C11 carbon of the substrate to the hydroxyl ligand of the cofactor. The PCET mechanism is supported by both computational and experimental results. Electronic-structure calculations indicate that the electron transfers from an orbital on the substrate backbone to an orbital on the iron.³⁷ Moreover, a thermodynamic analysis based on electrochemical data indicates that the single-proton and electron-transfer reactions are highly endothermic by 30–40 kcal/mol, whereas the PCET reaction is slightly exothermic by ~5 kcal/mol.^{13,27} The PCET mechanism avoids these high-energy intermediates. This reaction is vibronically nonadiabatic due to relatively small couplings between the reactant and product vibronic states. The SLO reaction has been studied with a variety of theoretical approaches.^{13,19,26,27,31,36,44}

The multistate continuum theory for PCET reactions has been applied to PCET in lipoxygenase.¹³ The inner-sphere reorganisation energy of the iron cofactor was determined to be ~19 kcal/mol from density functional theory calculations on a model system. The outer-sphere reorganisation energy of the protein was calculated to be ~2.5 kcal/mol with an electrostatic dielectric continuum model for conformations obtained from docking simulations. The total reorganisation energy was estimated to be the sum of these inner-sphere and outer-sphere components. The gas-phase EVB matrix elements were represented by standard molecular-mechanical terms. The relative energies of the diabatic states were fit to electrochemical data, and the electronic couplings corresponding to electron transfer and proton transfer were fit to the experimental rate and KIE at 303 K.

As shown in Figure 4.4, the calculations reproduce the experimentally determined temperature dependence of the rates and KIEs.²⁷ The weak temperature dependence is due to the small free-energy barrier, which arises from a balance between the total reorganisation energy and the driving force. The unusually large KIE of 81 at room temperature results from the relatively small overlap between the reactant and product proton vibrational wavefunctions and the dominance of the lowest-energy reactant and product vibronic states for the tunnelling process. Based on the nonadiabatic PCET rate expression in eqn (4.1), the ratio of the rate for hydrogen to that for deuterium is approximately proportional to the ratio of the squares of the vibronic couplings, which in turn is approximately proportional to the ratio of the squares of the overlaps

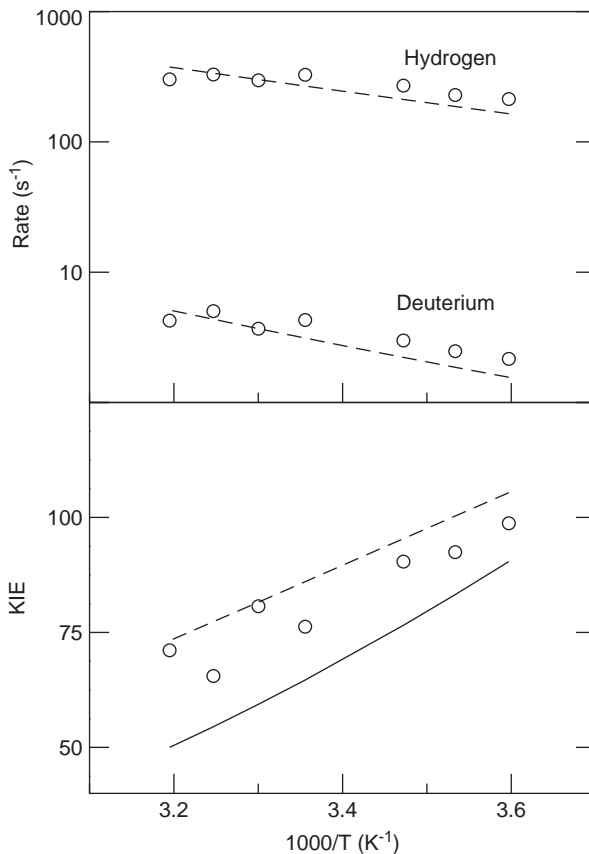


Figure 4.4 Temperature dependence of the rates and KIEs for the PCET reaction catalysed by soybean lipoxygenase. The experimental data²⁷ are denoted with open circles, the results from the multistate continuum theory calculations¹³ are denoted with dashed lines, and the KIEs calculated from molecular dynamics simulations¹⁹ are denoted by a solid line. Note that the solid line was obtained without fitting any parameters directly to kinetic data, and the input to the rate expression was obtained from molecular dynamics simulations of the entire solvated enzyme and vibronic coupling calculations on a model system. An experimental data point at high T is omitted for clarity.

depicted in Figure 4.1. The overlaps decay exponentially as the proton donor–acceptor distance increases, but the overlap for deuterium decays faster than that for hydrogen. As a result, the ratio of the overlaps for hydrogen and deuterium increases, and hence the KIE increases, as the overlap decreases (*i.e.* as the proton donor–acceptor distance increases).

The dependence of the rate on the proton donor–acceptor distance was also investigated with the multistate continuum theory. As shown in Figure 4.5(a), the maximum contribution to the rate occurs at a C–O distance of $\sim 2.7\text{ \AA}$.

Figure 4.5(b) indicates that the equilibrium C–O distance is significantly larger than this dominant distance and that the Boltzmann probability at 2.7 Å is extremely small. On the other hand, the coupling between the vibronic states increases dramatically as the C–O distance decreases. The dominant distance is determined by a balance between the larger coupling and the smaller Boltzmann probability as the C–O distance decreases. The rate is dominated by a relatively low-probability C–O distance because of the larger coupling. If the system were frozen, the C–O distance would not be able to decrease enough to allow efficient catalysis. Motion of the enzyme is critical to ensure sampling of these smaller C–O distances. These calculations illustrate that the proton donor–acceptor motion plays a vital role in decreasing the dominant donor–acceptor distance relative to its equilibrium value. The quantum-mechanical effects of the donor–acceptor motion were found to impact the magnitude of the rate slightly but to have negligible impact on the temperature dependence. Within the framework of the multistate continuum theory, the magnitude and temperature dependence of the KIE are determined mainly by the dominant donor–acceptor distance.

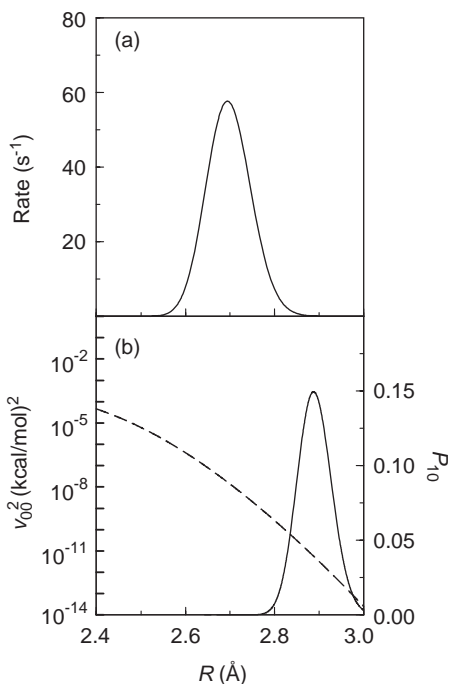


Figure 4.5 Analysis of the dependence of the rate of the PCET reaction catalysed by SLO on the proton donor acceptor distance R . (a) Contribution to the overall rate as a function of R . The overall rate is obtained by integration of this function. (b) The square of the coupling V_{00}^2 (dashed) and the Boltzmann probability P_{10} (solid) for the lowest energy reactant and product states as functions of R . Reproduced from [ref. 13].

The dynamical theoretical formulation for PCET reactions with explicit solvent and protein was also applied to SLO.¹⁹ The time-correlation functions of the energy gap and R coordinate, as well as their average values, were calculated from classical molecular-dynamics simulations of the entire solvated lipoxygenase system, in which all atoms were allowed to move. These simulations provided an estimate of 39 kcal/mol for the total reorganisation energy. The vibronic couplings were estimated to within a constant factor by calculating the overlaps between reactant and product hydrogen vibrational wavefunctions for model systems. The dynamical behaviour (*i.e.* the time dependence) of the probability flux correlation function was found to be dominated by the equilibrium protein and solvent motions and was not significantly influenced by the proton donor–acceptor motion. The magnitude of the overall rate, however, was strongly influenced by the frequency of the proton donor–acceptor motion, the magnitude and distance dependence of the vibronic coupling, and the protein/solvent reorganisation energy.

As shown in Figure 4.4, these calculations reproduced the experimentally observed²⁷ magnitude and temperature dependence of the KIE for the SLO enzyme reaction without fitting any parameters directly to the experimental kinetic data. Note that the previous multistate continuum theory calculations required fitting of the couplings to the experimental kinetic data at a single temperature. Within the framework of the dynamical PCET theory, the temperature dependence of the KIE is determined mainly by the effective proton donor–acceptor frequency, which can be calculated from the R coordinate variance in the molecular-dynamics simulations, and the distance dependence of the vibronic couplings for hydrogen and deuterium, which can be calculated from the vibrational wavefunctions for model systems. The ratio of the overlaps of the hydrogen and deuterium vibrational wavefunctions strongly impacts the magnitude of the KIE but does not significantly influence the temperature dependence. These trends are summarised in the relatively simple, approximate expression for the KIE given in eqn (4.4). Similar to the results from the multistate continuum theory, the PCET molecular-dynamics simulations imply that the large magnitude of the KIE arises mainly from the dominance of tunnelling between the ground vibronic states and the relatively large ratio of the overlaps between the corresponding hydrogen and deuterium vibrational wavefunctions. In addition, the PCET molecular-dynamics simulations indicate that the weak temperature dependence of the KIE is due in part to the dominance of the local component of the proton donor–acceptor motion.

4.3 Predominantly Adiabatic Reactions: Proton and Hydride Transfer

Proton- and hydride-transfer reactions in solution and enzymes are typically electronically adiabatic (*i.e.* occur on the electronic ground state), but, in some cases, these reactions are vibrationally nonadiabatic (*i.e.* involve excited vibrational states). In contrast to PCET reactions, these types of reactions can

be described in terms of a single electronic state. Moreover, often the vibrational coupling is not less than the thermal energy $k_B T$, so a perturbative approach based on the golden rule is not appropriate. The rate constants for these types of reactions can be derived in the framework of the reactive flux formulation of transition-state theory. This section will describe a theoretical formulation for electronically adiabatic proton- and hydride-transfer reactions in solution and enzymes and will illustrate this theory by an application to the hydride-transfer reaction catalysed by DHFR.

4.3.1 Theory

Numerous mixed quantum/classical molecular dynamics methods have been developed to include nuclear quantum effects in proton- and hydride-transfer reactions in enzymes.^{45–58} This chapter focuses on a hybrid quantum-classical approach that includes electronic and nuclear quantum effects, as well as the motion of the complete solvated enzyme.^{57,58} The electronic quantum effects are included with an empirical valence bond (EVB) potential,¹¹ where the EVB matrix elements are represented by molecular-mechanical terms fit to electronic-structure calculations and/or experimental data. The nuclear quantum effects are included by representing the transferring hydrogen nucleus as a three-dimensional vibrational wavefunction calculated with Fourier grid methods.⁵⁹ Alternative quantum-mechanical/molecular-mechanical (QM/MM) potentials for including the electronic quantum effects and path integral formulations for including the nuclear quantum effects⁶⁰ can also be used in this framework.

The fundamental mechanism of an electronically adiabatic proton-transfer reaction in solution or an enzyme is depicted in Figure 4.6. For illustrative purposes, the proton is depicted as moving in a one-dimensional double-well potential, and the adiabatic hydrogen vibrational states are calculated for each potential by solving a one-dimensional Schrödinger equation. In the simplest picture, initially the donor well is lower in energy, and the proton is localised on the donor. Reorganisation of the protein/solvent environment leads to a symmetric double-well potential, and the hydrogen vibrational wavefunction becomes delocalised between the donor and acceptor. Further reorganisation of the protein/solvent environment causes the acceptor well to become lower in energy, and the proton becomes localised on the acceptor. For a vibrationally adiabatic reaction, the proton remains in the vibrational ground state during this entire process. vibrationally nonadiabatic effects can lead to transitions to excited vibrational states, typically when the hydrogen is moving in a virtually symmetric environment. When the two lowest delocalised vibrational states are lower than the barrier for the symmetric double-well potential, the hydrogen can tunnel through the barrier. As the splitting between the two delocalised states decreases, the probability of tunnelling decreases, and the probability of a nonadiabatic transition increases. In general, higher excited vibrational states can also be involved in the hydrogen-tunnelling process, so a symmetric hydrogen potential is not necessary.

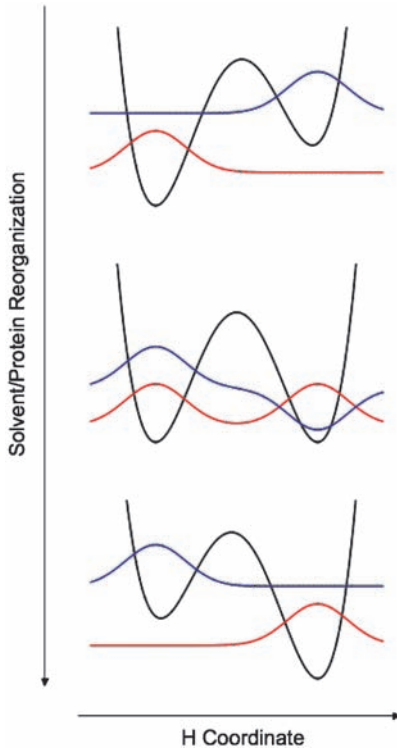


Figure 4.6 Schematic illustration of the proton potential energy curves and corresponding ground (red) and excited (blue) state proton vibrational wavefunctions as functions of the proton coordinate for the electronically adiabatic ground state of a proton or hydride transfer reaction. The reorganisation of the solvent and protein changes the shape of the proton potential energy curve. Hydrogen tunnelling can occur when the proton potential is virtually symmetric and the two proton vibrational wavefunctions are delocalised over both wells, as in the middle picture.

In the framework of transition-state theory,^{61,62} the proton- or hydride-transfer rate constant can be expressed as:

$$k = \kappa k_{\text{TST}} \quad (4.5)$$

where k_{TST} is the equilibrium transition-state theory rate constant and κ is the transmission coefficient accounting for dynamical recrossings of the barrier. Using the reactive flux formulation of transition-state theory,^{63–66} k_{TST} for a general reaction coordinate can be expressed as:⁶⁷

$$k_{\text{TST}} = \left\{ \left(\frac{k_{\text{B}} T Z_{\xi}}{2\pi\beta} \right)^{1/2} \right\}_{\xi^{\ddagger}}^{\text{cond}} \frac{e^{-\beta W(\xi^{\ddagger})}}{\int_{-\infty}^{\xi^{\ddagger}} d\xi e^{-\beta W(\xi)}} \quad (4.6)$$

where

$$Z_\xi \equiv \sum_{i=1}^{3N} \frac{1}{M_i} \left(\frac{\partial \xi}{\partial R_i} \right)^2 \quad (4.7)$$

Here, $W(\xi)$ is the potential of mean force along the reaction coordinate ξ , $\xi = \xi^\dagger$ at the dividing surface, N is the number of classical nuclei, M_i is the mass associated with degree of freedom i , and the brackets indicate a conditional configuration average evaluated at the dividing surface. Analogous expressions have been derived in different forms.^{68,69} This form of the rate constant enables the straightforward calculation of rates for infrequent events with conventional umbrella sampling and free-energy perturbation methods. In some cases, the simpler, approximate form $k_{\text{TST}} = (k_B T/h) \exp(-\Delta G^\ddagger/k_B T)$, where ΔG^\ddagger is the activation free-energy barrier determined from the potential of mean force, has been utilised.

In the implementation of this approach for single proton- or hydride-transfer reactions, typically the system is represented by a two-state EVB potential, where the two states correspond to the hydrogen being bonded to the donor or acceptor. In this case, the collective reaction coordinate is defined as the difference between the energies of the two VB states averaged over the lowest-energy hydrogen vibrational wavefunction:

$$\Lambda(\mathbf{R}) = \langle \Phi_0(\mathbf{r}; \mathbf{R}) | V_{11}(\mathbf{r}, \mathbf{R}) - V_{22}(\mathbf{r}, \mathbf{R}) | \Phi_0(\mathbf{r}; \mathbf{R}) \rangle \quad (4.8)$$

where \mathbf{r} represents the coordinate of the transferring hydrogen nucleus and \mathbf{R} represents the coordinates of the remaining nuclei. $V_{11}(\mathbf{r}, \mathbf{R})$ and $V_{22}(\mathbf{r}, \mathbf{R})$ are the energies of VB states 1 and 2, respectively, and $\Phi_0(\mathbf{r}; \mathbf{R})$ represents the ground-state hydrogen vibrational wavefunction. The physical meaning of this energy gap reaction coordinate is illustrated in Figure 4.6, where the reaction coordinate is negative when the donor well is lower, zero for the symmetric double-well potential, and positive when the acceptor well is lower. Typically, the dividing surface (*i.e.* the transition state) is defined as $\Lambda=0$. In this framework, the transition states are not saddle points on the potential-energy surface, but rather the transition states correspond to configurations in which the hydrogen moves in a virtually symmetric environment. This reaction coordinate has been shown to be physically meaningful for two-state charge-transfer processes.^{5,29,70} Moreover, for enzymatic reactions described within the framework of transition-state theory, this reaction coordinate leads to estimates of the transmission coefficient (*i.e.* recrossing factor) that are close to unity.^{57,71} Note that this collective reaction coordinate includes motions of the enzyme, substrate, and cofactor.

The calculation of the transition-state theory rate constant requires the calculation of the potential of mean force (*i.e.* the free-energy profile) along a collective reaction coordinate and the calculation of the gradient of this

reaction coordinate at the dividing surface. A series of mapping potentials can be used to sample the relevant range of the collective reaction coordinate. These mapping potentials are defined to be linear combinations of the energies of the two VB states:¹¹

$$V_{\text{map}}(\mathbf{r}, \mathbf{R}; \lambda) = (1 - \lambda)V_{11}(\mathbf{r}, \mathbf{R}) + \lambda V_{22}(\mathbf{r}, \mathbf{R}) \quad (4.9)$$

As the mapping parameter λ is varied from zero to unity, the reaction progresses from the reactant state to the product state. For each window specified by λ , molecular dynamics trajectories governed by the mapping potential are propagated. In this umbrella sampling approach, a segment of the total free-energy profile is generated for each window using standard binning techniques. The individual segments are connected using thermodynamic integration or the weighted histogram analysis method (WHAM)⁷² to form the free-energy profile corresponding to the unbiased Hamiltonian. A free-energy perturbation formula has been derived to incorporate the vibrationally adiabatic nuclear quantum effects for the transferring hydrogen nucleus into the free-energy profile.⁵⁸ This procedure enables the generation of the entire adiabatic quantum free-energy profile along the reaction coordinate. Assuming adequate sampling, the use of this perturbation formula is rigorously identical to adiabatic mixed quantum/classical molecular-dynamics simulations that include feedback between the quantum and classical subsystems.^{48,53}

The transmission coefficient can be calculated with a reactive flux approach,^{73–77} in which a large number of trajectories are initiated at the top of the barrier and are propagated backward and forward in time.⁵⁸ This reactive flux approach for infrequent events can be combined with the molecular dynamics with the quantum transitions (MDQT) surface hopping method^{78,79} to include vibrationally nonadiabatic effects (*i.e.* the effects of excited vibrational states). The fundamental principle of MDQT for proton-transfer reactions is that an ensemble of trajectories is propagated, and each trajectory moves classically on a single adiabatic surface except for instantaneous transitions among the adiabatic hydrogen vibrational states. The adiabatic hydrogen vibrational states $\Phi_n(r, R)$ can be calculated at each classical molecular dynamics time step with Fourier grid methods.⁵⁹ The classical nuclei evolve according to classical equations of motion on the occupied adiabatic vibrational state. The time-dependent Schrödinger equation is integrated simultaneously with the classical equations of motion to determine the quantum probabilities for all of the adiabatic states. The surface-hopping algorithm correctly apportions trajectories among the adiabatic states according to the quantum probabilities with the minimum required number of quantum transitions (neglecting difficulties with classically forbidden transitions). Extensions of this approach for simulating infrequent events^{75–77} have been developed.⁸⁰ This MDQT reactive flux approach has been applied to a model proton-transfer reaction coupled to a dissipative bath.⁸¹ The MDQT results agree well with the numerically exact quantum-dynamical calculations

performed by Topaler and Makri⁸² for moderate to high friction. These calculations provide validation for the application of this general approach to proton and hydride transfer in enzymes.

4.3.2 Application to Dihydrofolate Reductase

DHFR catalyses the conversion of dihydrofolate (DHF) to tetrahydrofolate (THF).⁸³ This enzyme maintains the levels of THF required for the biosynthesis of purines, pyrimidines, and amino acids and is associated with a variety of pharmacological applications. Although the mechanism of DHFR involves both proton and hydride transfer, as depicted in Figure 4.7, most simulation studies have focused on the hydride transfer from the NADPH cofactor to the protonated DHF. This hydride-transfer reaction is electronically adiabatic (*i.e.* occurs on the electronic ground state) due to a large splitting between the ground and excited electronic states. A number of theoretical approaches have been used to study this hydride-transfer reaction.^{71,84,93}

The hybrid quantum/classical molecular dynamics approach described above was applied to the DHFR-catalysed hydride-transfer reaction.^{71,84,85} Inclusion of the nuclear quantum effects of the transferring hydrogen decreases the free-energy barrier by 2.4 kcal/mol.⁷¹ Analysis of the nuclear wavefunctions and the splittings between the ground and excited vibrational states for the transition-state configurations indicates that hydrogen tunnelling plays a significant role in this reaction. The calculated KIE was consistent with the experimental value of 3.^{71,94} The transmission coefficient was calculated to be $\kappa = 0.88$, indicating that dynamical barrier recrossings occur but do not significantly impact the overall rate.⁷¹ Qualitatively similar results were obtained by Gao, Truhlar, and coworkers using different methodology that includes the nuclear quantum effects of more atoms but makes additional assumptions about other aspects of the calculations.⁸⁹

Analysis of the simulation data resulted in the identification and characterisation of a network of coupled motions in DHFR.^{71,84} As illustrated in Figure 4.8,

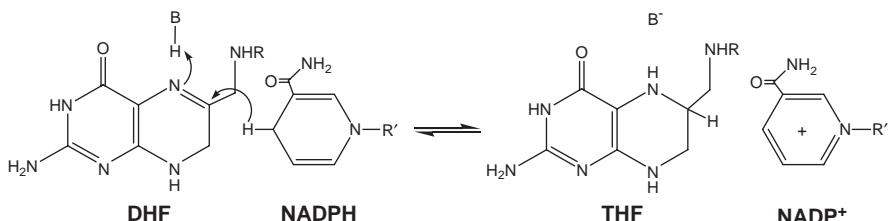


Figure 4.7 The reaction catalysed by DHFR. The reactant substrate is DHF (dihydrofolate), the product substrate is THF (tetrahydrofolate), and the cofactor is NADPH/NADP⁺ (nicotinamide adenine dinucleotide phosphate). The calculations focus on the hydride transfer reaction from NADPH to the protonated DHF. Reproduced from [ref. 3].

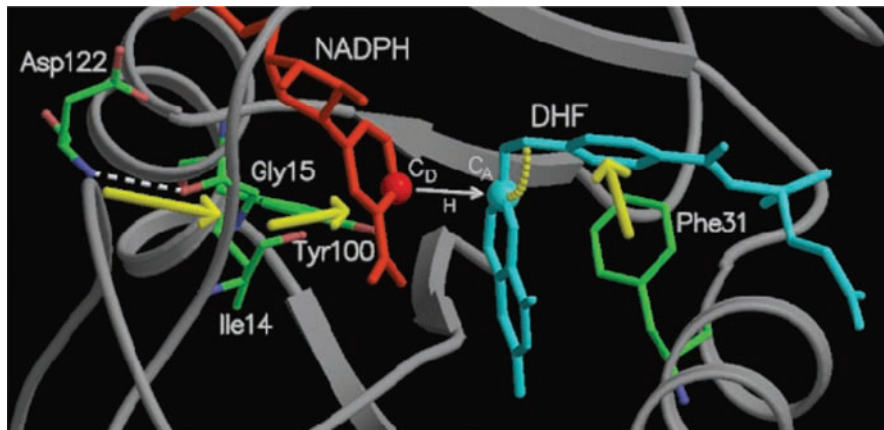


Figure 4.8 Schematic diagram of a portion of a network of coupled motions in DHFR. The yellow arrows and arc indicate the coupled motions. This picture does not represent a complete or unique network but rather illustrates the general concept of reorganisation of the enzymatic environment to provide configurations conducive to the hydride transfer reaction. Reproduced from [ref. 84].

these equilibrium, thermally averaged motions are located throughout the enzyme, spanning the active site and the exterior. These motions represent conformational changes along the collective reaction coordinate corresponding to reorganisation of the environment to facilitate hydride transfer by bringing the donor and acceptor closer, orienting the substrate and cofactor properly, and providing a favourable electrostatic environment. These motions are not *dynamically* coupled to the chemical reaction, but rather represent equilibrium conformational changes that enable hydride transfer. Fluorescence resonance energy transfer (FRET) experiments, in which pairs of residues are labelled with fluorescent probes, indicate that at least some of these motions occur on the millisecond timescale attributed to the hydride-transfer step in the catalytic cycle.⁹⁵

These coupled motions were elucidated by analysing changes in the structure, hydrogen bonding, and electrostatics along the collective reaction coordinate.⁸⁵ The three-dimensional structure of wild-type DHFR is depicted in Figure 4.9. Analysis of the thermally averaged reactant, transition state, and product structures indicates that the key features of the enzyme structure are retained throughout the reaction, but significant structural differences are apparent in the loop regions. Moreover, a number of hydrogen bonds are broken and formed throughout the enzyme during the reaction. Analysis of the electrostatic potential for the thermally averaged reactant, transition state, and product structures implies that the electrostatic potential changes dramatically during the reaction, even in regions far from the active site. The electrostatic contributions from a number of residues distal to the active site were found to change significantly during the reaction. This detailed analysis illustrates that

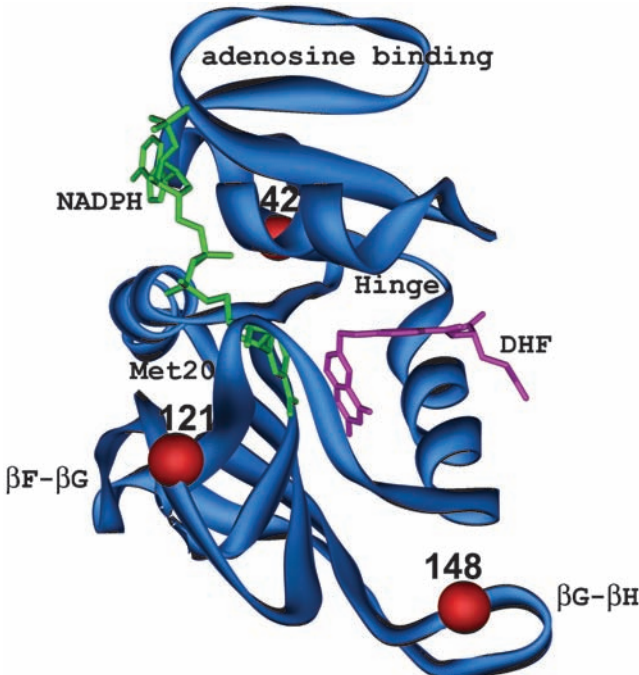


Figure 4.9 Three dimensional structure of wild type DHFR, with the NADPH cofactor shown in green and the DHF substrate shown in magenta. The important loop regions are identified, and the residues involved in the mutant DHFR enzymes studied are labelled with red spheres.⁸⁷ Reproduced from [ref. 102].

the rather subtle conformational changes occurring during the hydride-transfer reaction substantially alter the hydrogen bonding and electrostatics throughout the entire enzyme.

The hybrid quantum/classical molecular dynamics approach was also applied to the G121V mutant DHFR enzyme.⁸⁶ As illustrated in Figure 4.9, this residue is located more than 12 Å from the active site and is on the exterior of the enzyme. Nevertheless, kinetic experiments showed that mutation of residue 121 from glycine to valine decreased the rate of hydride transfer by a factor of 163.^{96,97} The calculated free-energy barrier was 3.4 kcal/mol greater for the mutant than for the wild-type enzyme. This increase in the barrier is consistent with the experimental observation of a decrease in the rate by a factor of 163, which corresponds to a ~3.0 kcal/mol increase in the free-energy barrier when the effects of the transmission coefficient are neglected. The transmission coefficient is not significantly altered by the mutation. Analysis of the thermally averaged structural properties along the collective reaction coordinate indicates that some of the motions correlated to hydride transfer in the wild-type enzyme are attenuated or absent in the mutant. These results suggest that this distal mutation interrupts the network of coupled motions,

thereby decreasing the probability of sampling configurations conducive to hydride transfer and increasing the free-energy barrier.

The hybrid quantum/classical molecular dynamics approach was also applied to the triple mutant M42F-G121S-S148A and the corresponding single and double mutants.⁸⁷ The locations of these distal residues are depicted in Figure 4.9. Kinetic experiments indicate that these distal mutations significantly decrease the rate of hydride transfer and that some of these mutations are nonadditive (*i.e.* the change in the free-energy barrier for the multiple mutation is not equal to the sum of the changes for the single mutations). The simulations illustrate that residues throughout the enzyme participate in the network of coupled motions correlated to hydride transfer and that each mutant samples a unique distribution of motions. The observation of nonadditive changes to the network of coupled motions provides an explanation for the experimentally observed nonadditivity of the rates. This study implies that distal mutations can lead to nonlocal structural changes⁹⁸ and significantly impact the probability of sampling conformations conducive to hydride transfer.^{90,91}

The hybrid quantum/classical molecular dynamics method was also used to study hydride transfer in *Bacillus subtilis* dihydrofolate reductase (DHFR).⁹⁹ *E. coli* and *B. subtilis* DHFR have 44% sequence identity, and the experimentally determined structures and hydride-transfer rates are similar.¹⁰⁰ The simulations indicate that the tertiary structures of both enzymes evolve in a similar manner during the hydride-transfer reaction. In both enzymes, the donor–acceptor distance decreases to $\sim 2.7\text{ \AA}$ at the transition-state configurations to enable hydride transfer. Zero point energy and hydrogen-tunnelling effects are found to be significant for both enzymes. Covariance and rank correlation analyses of motions throughout the protein and ligands illustrate that *E. coli* and *B. subtilis* DHFR exhibit both similarities and differences in the equilibrium fluctuations and the conformational changes correlated to hydride transfer, suggesting a balance of conservation and flexibility across species. The simulations were used to identify a common set of residues that play a significant role in the network of coupled motions leading to configurations conducive to hydride transfer for both *E. coli* and *B. subtilis* DHFR.

4.4 Emerging Concepts about Enzyme Catalysis

A general physical picture of enzyme catalysis is emerging from both theoretical and experimental studies. According to the perspective presented in this chapter, the catalysed reaction can be described as occurring along a collective reaction coordinate that represents conformational changes in the enzyme and ligands. In general, the free energy along this collective reaction coordinate corresponds to the relative probabilities of sampling configurations with a specified reaction coordinate, where higher free energies correspond to lower probabilities. Thus, the free-energy barrier is a measure of the probability of sampling transition-state configurations relative to reactant configurations. Thermal motions in the enzyme and ligands lead to conformational sampling of configurations that facilitate the chemical reaction by bringing the ligands closer together, orienting them properly, and providing an appropriate electrostatic environment. These

thermal motions are Brownian in nature but occur within the confines of the protein structure. Since these fast thermal motions occur on the femtosecond to picosecond timescale, they are in equilibrium during the typically millisecond or longer timescale of the enzymatic reaction. In this model, the overall equilibrium conformational changes from the reactant to the transition-state configurations occur on this slower timescale, but the chemical reaction itself occurs virtually instantaneously relative to this timescale when the enzyme and ligands are in a favourable configuration.

This picture of conformation-coupled enzyme catalysis is particularly relevant to enzymes that catalyse hydrogen-tunnelling reactions. For vibronically non-adiabatic PCET reactions, reorganisation of the environment by conformational sampling of the enzyme and ligands leads to the degeneracy of the reactant and product vibronic states, as shown in Figure 4.1. The electron and proton can tunnel simultaneously with a probability that depends on the vibronic coupling between the reactant and product vibronic states, which in turn is strongly influenced by the proton donor–acceptor distance. For these types of reactions, the kinetic isotope effect arises mainly from the ratio of the vibronic couplings for hydrogen and deuterium and can become quite large, as shown by the value of ~ 80 for soybean lipoxygenase. For electronically adiabatic proton- and hydride-transfer reactions, conformational sampling of the enzyme and ligands can lead to a symmetric hydrogen potential on the electronic ground state, as shown in Figure 4.6. For predominantly adiabatic reactions of this type, the kinetic isotope effect arises mainly from zero-point energy effects and tends to be moderate, as illustrated by the value of ~ 3 for DHFR.

Both types of reactions require conformational sampling of the enzyme and ligands to provide configurations conducive to hydrogen tunnelling. The experimentally measured rate constants are strongly impacted by the time required for the conformational changes leading to the active “transition state” configurations. Figure 4.10 illustrates the free-energy profile along the collective reaction coordinate for the predominantly adiabatic hydride-transfer reaction catalysed by DHFR, along with a series of thermally averaged equilibrium configurations of DHFR. The overall equilibrium conformational changes from the reactant to the transition-state configurations occur on the experimentally measured millisecond timescale, but the hydrogen tunnelling occurs virtually instantaneously relative to this timescale when the enzyme and ligands are in a favourable configuration (*i.e.* for the configurations corresponding to the top of the barrier). For vibronically nonadiabatic reactions, the experimentally measured rate constant is also impacted by the square of the vibronic coupling, which depends strongly on the proton donor–acceptor distance.

Within the context of this physical picture, the free-energy landscape for enzyme catalysis can be viewed as a multidimensional catalytic network, as illustrated in Figure 4.11.¹⁰¹ Here, the landscape is depicted as a function of the reaction coordinate and ensemble conformations. The reaction coordinate axis corresponds to the various mechanistic steps, such as substrate binding, the chemical reaction, and product release. As discussed above,

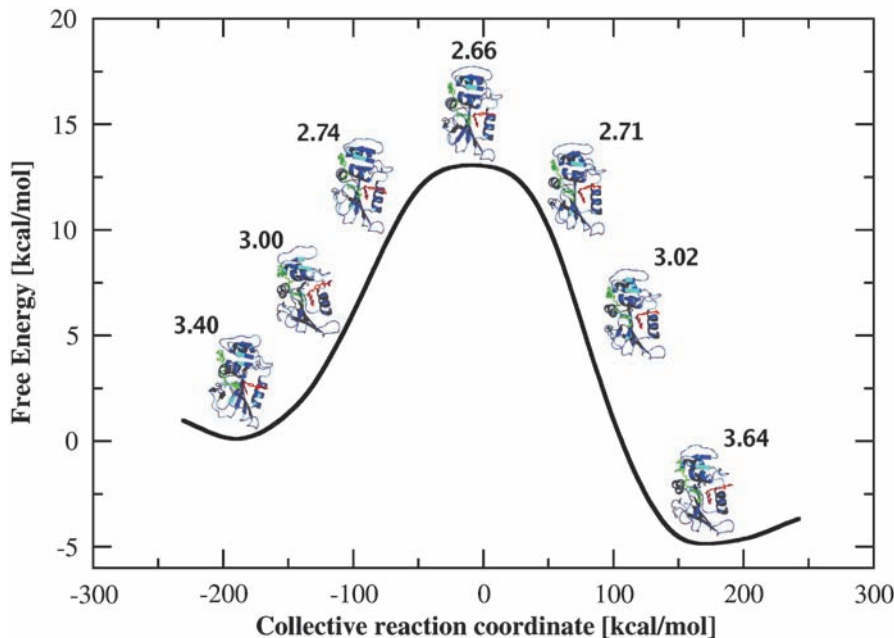


Figure 4.10 Free energy profile of the DHFR catalysed hydride transfer reaction as a function of a collective reaction coordinate that includes motions of the enzyme, substrate, and cofactor. The magnitude of the free energy barrier is determined by the relative probabilities of sampling the transition state and the reactant configurations. The thermally averaged equilibrium structures, as well as the average donor acceptor distances in Angstroms, are provided for selected values of the reaction coordinate. Note that the donor acceptor distance decreases as the reaction evolves from the reactant to the transition state. The conformational changes along the collective reaction coordinate are attained by equilibrium thermal motions occurring within the confines of the protein fold. These conformational changes facilitate the hydride transfer reaction by bringing the donor and acceptor closer together, orienting the substrate and cofactor properly, and providing a favourable electrostatic environment. Figure and caption reproduced from [ref. 88].

evolving along the reaction coordinate involves conformational changes to facilitate the chemical reaction. The ensemble conformations axis corresponds to the ensemble of configurations available for all values of the reaction coordinate. The stochastic thermal motions of the enzyme and ligands enable the system to sample the conformational space represented by this free-energy landscape. A plane bisecting the free-energy surface along the top ridge, parallel to the ensemble conformations axis, separates the system into the reactant (*i.e.* substrate) and product. The system can progress from the reactant to the product by multiple parallel pathways involving conformational changes during and in between all steps of the enzyme mechanism. The large number of

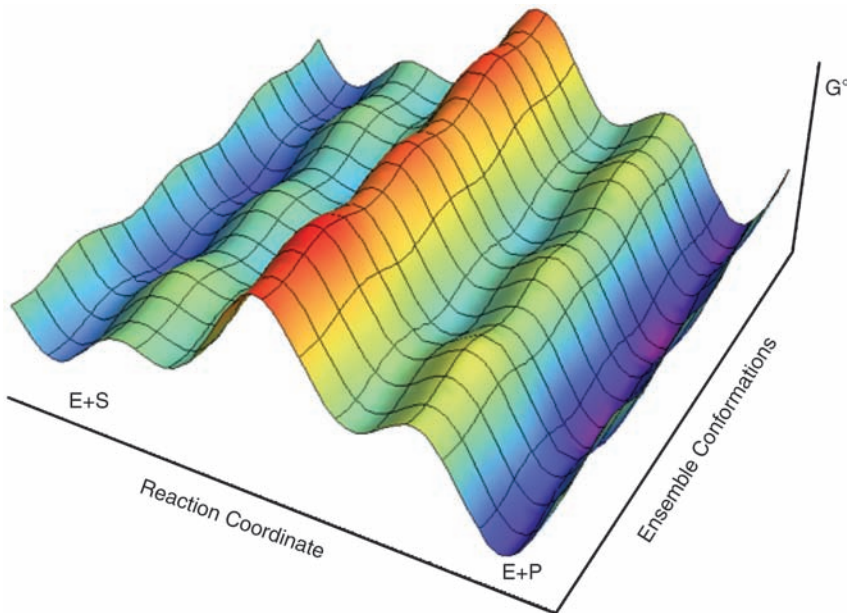


Figure 4.11 Schematic representation of the standard free energy landscape for the catalytic network of an enzyme reaction. Conformational changes occur along both axes. The conformational changes occurring along the reaction coordinate axis correspond to the environmental reorganisation that facilitates the chemical reaction. In contrast, the conformational changes occurring along the ensemble conformations axis represent the ensembles of configurations existing at all stages along the reaction coordinate, leading to a large number of parallel catalytic pathways. This figure illustrates the multiple populations of conformations, intermediates and transition states. Strong coupling can occur between the reaction coordinates and the conformation ensembles, *i.e.* the reaction paths can slide along and between both coordinates. For real enzymes the number of maxima and minima along the coordinates is expected to be greater than shown. The dominant catalytic pathways will be altered by external conditions and protein mutations. Figure by Sarah Jane Edwards. Figure and caption reproduced from [ref. 101].

minima and transition states shown in Figure 4.11 illustrates the complexity of enzymatic reactions.

Acknowledgments

The author gratefully acknowledges support from NSF grant CHE-05-01260 and NIH Grant GM56207. The author also thanks Sarah Jane Edwards for creating Figures 4.1, 4.6, and 4.10, Elizabeth Hatcher for creating Figures 4.3–4.5, and James Watney for creating Figures 4.7–4.9.

References

1. A. Soudackov and S. Hammes-Schiffer, *J. Chem. Phys.*, 1999, **111**, 4672–4687.
2. A. Soudackov and S. Hammes-Schiffer, *J. Chem. Phys.*, 2000, **113**, 2385–2396.
3. S. Hammes-Schiffer, *Acc. Chem. Res.*, 2001, **34**, 273–281.
4. A. Soudackov, E. Hatcher and S. Hammes-Schiffer, *J. Chem. Phys.*, 2005, **122**, 014505.
5. R. A. Marcus, *Annu. Rev. Phys. Chem.*, 1964, **15**, 155–196.
6. N. R. Kestner, J. Logan and J. Jortner, *J. Phys. Chem.*, 1974, **78**, 2148–2166.
7. M. Bixon and J. Jortner, *Adv. Chem. Phys.*, 1999, **106**, 35–202.
8. J. Ulstrup and J. Jortner, *J. Chem. Phys.*, 1975, **63**, 4358.
9. P. F. Barbara, T. J. Meyer and M. A. Ratner, *J. Phys. Chem.*, 1996, **100**, 13148–13168.
10. M. D. Newton and N. Sutin, *Annu. Rev. Phys. Chem.*, 1984, **35**, 437–480.
11. A. Warshel, *Computer Modeling of Chemical Reactions in Enzymes and Solutions*, John Wiley & Sons, Inc, New York, 1991.
12. S. Hammes-Schiffer and N. Iordanova, *Biochim. Biophys. Acta-Bioenergetics*, 2004, **1655**, 29–36.
13. E. Hatcher, A. V. Soudackov and S. Hammes-Schiffer, *J. Am. Chem. Soc.*, 2004, **126**, 5763–5775.
14. L. I. Trakhtenberg, V. L. Klochikhin and S. Y. Pshevzetsky, *Chem. Phys.*, 1982, **69**, 121–134.
15. D. Borgis, S. Lee and J. T. Hynes, *Chem. Phys. Lett.*, 1989, **162**, 19–26.
16. A. Suarez and R. Silbey, *J. Chem. Phys.*, 1991, **94**, 4809–4816.
17. E. Hatcher, A. Soudackov and S. Hammes-Schiffer, *Chem. Phys.*, 2005, **319**, 93–100.
18. E. Hatcher, A. Soudackov and S. Hammes-Schiffer, *J. Phys. Chem. B*, 2005, **109**, 18565–18574.
19. E. Hatcher, A. V. Soudackov and S. Hammes-Schiffer, *J. Am. Chem. Soc.*, 2007, **129**, 187–196.
20. D. Borgis and J. T. Hynes, *J. Chem. Phys.*, 1991, **94**, 3619–3628.
21. P. M. Kiefer and J. T. Hynes, *Solid State Ionics*, 2004, **168**, 219–224.
22. P. M. Kiefer and J. T. Hynes, *J. Phys. Chem. A*, 2004, **108**, 11793–11808.
23. R. I. Cukier, *J. Phys. Chem.*, 1996, **100**, 15428–15443.
24. R. I. Cukier and D. G. Nocera, *Annu. Rev. Phys. Chem.*, 1998, **49**, 337–369.
25. A. M. Kuznetsov and J. Ulstrup, *Can. J. Chem.*, 1999, **77**, 1085–1096.
26. M. J. Knapp and J. P. Klinman, *Eur. J. Biochem.*, 2002, **269**, 3113–3121.
27. M. J. Knapp, K. W. Rickert and J. P. Klinman, *J. Am. Chem. Soc.*, 2002, **124**, 3865–3874.
28. S. Hammes-Schiffer, E. Hatcher, H. Ishikita, J. H. Skone and A. V. Soudackov, *Coord. Chem. Rev.*, 2008, **252**, 384–394.
29. A. Warshel, *J. Phys. Chem.*, 1982, **86**, 2218–2224.

30. J.-K. Hwang and A. Warshel, *J. Am. Chem. Soc.*, 1987, **109**, 715–720.
31. W. Siebrand and Z. Smedarchina, *J. Phys. Chem. B*, 2004, **108**, 4185–4195.
32. J. Pu, S. Ma, J. Gao and D. G. Truhlar, *J. Phys. Chem. B*, 2005, **109**, 8551–8556.
33. J. S. Mincer and S. D. Schwartz, *J. Chem. Phys.*, 2004, **120**, 7755–7760.
34. B. Samuelsson, S.-E. Dahlen, J. A. Lindgren, C. A. Rouzer and C. N. Serhan, *Science*, 1987, **237**, 1171–1176.
35. M. H. Glickman and J. P. Klinman, *Biochemistry*, 1995, **34**, 14077–14092.
36. K. W. Rickert and J. P. Klinman, *Biochemistry*, 1999, **38**, 12218–12228.
37. N. Lehnert and E. I. Solomon, *J. Biol. Inorg. Chem.*, 2003, **8**, 294–305.
38. A. M. Kuznetsov and J. Ulstrup, *Can. J. Chem.*, 1999, **77**, 1085–1096.
39. G. Tresadern, J. P. McNamara, M. Mohr, H. Wang, N. A. Burton and I. H. Hillier, *Chem. Phys. Lett.*, 2002, **358**, 489–494.
40. M. H. M. Olsson, P. E. M. Siegbahn and A. Warshel, *J. Am. Chem. Soc.*, 2004, **126**, 2820–2828.
41. M. H. M. Olsson, P. E. M. Siegbahn and A. Warshel, *J. Biol. Inorg. Chem.*, 2004, **9**, 96–99.
42. T. Borowski, M. Krol, M. Chruscz and E. Broclawik, *J. Phys. Chem. B*, 2001, **105**, 12212–12220.
43. T. Borowski and E. Broclawik, *J. Phys. Chem. B*, 2003, **107**, 4639–4646.
44. I. Tejero, L. A. Eriksson, A. Gonzalez-Lafont, J. Marquet and J. M. LLuch, *J. Phys. Chem. B*, 2004, **108**, 13831–13838.
45. A. Warshel and Z. T. Chu, *J. Chem. Phys.*, 1990, **93**, 4003–4015.
46. J.-K. Hwang, Z. T. Chu, A. Yadav and A. Warshel, *J. Phys. Chem.*, 1991, **95**, 8445–8448.
47. D. Li and G. A. Voth, *J. Phys. Chem.*, 1991, **95**, 10425–10431.
48. H. Azzouz and D. Borgis, *J. Chem. Phys.*, 1993, **98**, 7361–7375.
49. R. Pomes and B. Roux, *Chem. Phys. Lett.*, 1995, **234**, 416–424.
50. M. E. Tuckerman, D. Marx, M. L. Klein and M. Parrinello, *Science*, 1997, **275**, 817–20.
51. D. Borgis, G. Tarjus and H. Azzouz, *J. Phys. Chem.*, 1992, **96**, 3188–3191.
52. D. Laria, G. Ciccotti, M. Ferrario and R. Kapral, *J. Chem. Phys.*, 1992, **97**, 378–388.
53. A. Staib, D. Borgis and J. T. Hynes, *J. Chem. Phys.*, 1995, **102**, 2487–2505.
54. P. Bala, P. Grochowski, B. Lesyng and J. A. McCammon, *J. Phys. Chem.*, 1996, **100**, 2535–2545.
55. C. Alhambra, J. Corchado, M. L. Sanchez, M. Garcia-Viloca, J. Gao and D. G. Truhlar, *J. Phys. Chem. B*, 2001, **105**, 11326–11340.
56. D. G. Truhlar, J. Gao, C. Alhambra, M. Garcia-Viloca, J. C. Corchado, M. L. Sanchez and J. Villa, *Acc. Chem. Res.*, 2002, **35**, 341–349.
57. S. R. Billeter, S. P. Webb, P. K. Agarwal, T. Iordanov and S. Hammes-Schiffer, *J. Am. Chem. Soc.*, 2001, **123**, 11262–11272.
58. S. R. Billeter, S. P. Webb, T. Iordanov, P. K. Agarwal and S. Hammes-Schiffer, *J. Chem. Phys.*, 2001, **114**, 6925–6936.

59. S. P. Webb and S. Hammes-Schiffer, *J. Chem. Phys.*, 2000, **113**, 5214–5227.
60. Q. Wang and S. Hammes-Schiffer, *J. Chem. Phys.*, 2006, **125**, 184102.
61. E. Wigner, *J. Chem. Phys.*, 1937, **5**, 720–725.
62. E. Wigner, *Trans. Faraday Soc.*, 1937, **34**, 29.
63. D. Chandler, *J. Chem. Phys.*, 1978, **68**, 2959–2970.
64. P. Hanggi, P. Talkner and M. Borkovec, *Rev. Mod. Phys.*, 1990, **62**, 251–341.
65. W. H. Miller, *J. Chem. Phys.*, 1974, **61**, 1823–1834.
66. J. T. Hynes, in *Theory of Chemical Reaction Dynamics*, ed. M. Baer, CRC, Boca Raton, 1985, Vol. 4, pp. 171–234.
67. J. B. Watney, A. V. Soudackov, K. F. Wong and S. Hammes-Schiffer, *Chem. Phys. Lett.*, 2006, **418**, 268–271.
68. E. A. Carter, G. Ciccotti, J. T. Hynes and R. Kapral, *Chem. Phys. Lett.*, 1989, **156**, 472–477.
69. G. K. Schenter, B. C. Garrett and D. G. Truhlar, *J. Chem. Phys.*, 2003, **119**, 5828–5833.
70. L. D. Zusman, *Chem. Phys.*, 1980, **49**, 295–304.
71. P. K. Agarwal, S. R. Billeter and S. Hammes-Schiffer, *J. Phys. Chem. B*, 2002, **106**, 3283–3293.
72. S. Kumar, J. M. Rosenberg, D. Bouzida, R. H. Swendsen and P. A. Kollman, *J. Comp. Chem.*, 1992, **13**, 1011–1021.
73. D. Chandler, in *Classical and Quantum Dynamics in Condensed Phase Simulations*, ed. B. J. Berne, G. Ciccotti, D. F. Coker, World Scientific, Singapore, 1998, pp. 3–23.
74. E. Neria and M. Karplus, *J. Chem. Phys.*, 1996, **105**, 10812–10818.
75. C. H. Bennett, *Algorithms for Chemical Computation*, American Chemical Society, Washington, DC, 1997.
76. J. C. Keck, *J. Chem. Phys.*, 1960, **32**, 1035–1050.
77. J. B. Anderson, *J. Chem. Phys.*, 1973, **58**, 4684–4692.
78. J. C. Tully, *J. Chem. Phys.*, 1990, **93**, 1061–1071.
79. S. Hammes-Schiffer and J. C. Tully, *J. Chem. Phys.*, 1994, **101**, 4657–67.
80. S. Hammes-Schiffer and J. C. Tully, *J. Chem. Phys.*, 1995, **103**, 8528–37.
81. S. Y. Kim and S. Hammes-Schiffer, *J. Chem. Phys.*, 2006, **124**, 244102.
82. M. Topaler and N. Makri, *J. Chem. Phys.*, 1994, **101**, 7500–7519.
83. G. P. Miller and S. J. Benkovic, *Chem. Biol.*, 1998, **5**, R105–R113.
84. P. K. Agarwal, S. R. Billeter, P. T. R. Rajagopalan, S. J. Benkovic and S. Hammes-Schiffer, *Proc. Natl. Acad. Sci. USA*, 2002, **99**, 2794–2799.
85. K. F. Wong, J. B. Watney and S. Hammes-Schiffer, *J. Phys. Chem. B*, 2004, **108**, 12231–12241.
86. J. B. Watney, P. K. Agarwal and S. Hammes-Schiffer, *J. Am. Chem. Soc.*, 2003, **125**, 3745–3750.
87. K. F. Wong, T. Selzer, S. J. Benkovic and S. Hammes-Schiffer, *Proc. Natl. Acad. Sci. USA*, 2005, **102**, 6807–6812.
88. A. Sergi, J. B. Watney, K. F. Wong and S. Hammes-Schiffer, *J. Phys. Chem. B*, 2006, **110**, 2435–2441.

89. M. Garcia-Viloca, D. G. Truhlar and J. Gao, *Biochemistry*, 2003, **42**, 13558–13575.
90. I. F. Thorpe and C. L. Brooks, III, *J. Phys. Chem. B*, 2003, **107**, 14042–14051.
91. I. F. Thorpe and C. L. Brooks III, *Proteins: Struct. Funct. Bioinf.*, 2004, **57**, 444–457.
92. R. Castillo, J. Andres and V. Moliner, *J. Am. Chem. Soc.*, 1999, **121**, 12140–12147.
93. P. L. Cummins, S. P. Greatbanks, A. P. Rendell and J. E. Gready, *J. Phys. Chem. B*, 2002, **106**, 9934–9944.
94. C. A. Fierke, K. A. Johnson and S. J. Benkovic, *Biochemistry*, 1987, **26**, 4085–92.
95. N. M. Antikainen, R. D. Smiley, S. J. Benkovic and G. G. Hammes, *Biochemistry*, 2005, **44**, 16835–16843.
96. C. E. Cameron and S. J. Benkovic, *Biochemistry*, 1997, **36**, 15792–15800.
97. P. T. R. Rajagopalan, S. Lutz and S. J. Benkovic, *Biochemistry*, 2002, **41**, 12618–12628.
98. R. S. Swanwick, P. J. Shrimpton and R. K. Allemann, *Biochemistry*, 2004, **43**, 4119–4127.
99. J. B. Watney and S. Hammes-Schiffer, *J. Phys. Chem. B*, 2006, **110**, 10130–10138.
100. M. A. Wilson, A. R. Horswill, G. Fan, S. J. Benkovic, D. Ring, G. A. Petsko, manuscript in preparation.
101. S. J. Benkovic, G. G. Hammes, S. Hammes-Schiffer, *Biochemistry* 2008, **47**, 3317–3321.
102. S. Hammes-Schiffer, *Acc. Chem. Res.*, 2006, **39**, 93–100.

CHAPTER 5

Kinetic Isotope Effects from Hybrid Classical and Quantum Path Integral Computations

JIALI GAO, KIN-YIU WONG, DAN T. MAJOR,
ALESSANDRO CEMBRAN, LINGCHUN SONG,
YEN-LIN LIN, YAO FAN AND SHUHUA MA

Department of Chemistry, Digital Technology Center and Supercomputer Institute, University of Minnesota, 207 Pleasant Street S.E., Minneapolis, MN 55455-0431, USA

5.1 Introduction

Proton, hydride and hydrogen-atom transfer reactions are ubiquitous in biological processes,¹ and because of their relatively small mass, zero-point energy and quantum tunnelling are significant in determining free-energy reaction barriers.^{2,3} The incorporation of nuclear quantum effects (NQE) is also important for reactions involving heavy atoms since one of the most direct experimental assessment of the transition state and the mechanism of a chemical reaction is by measurements of kinetic isotope effects (KIE),¹ which are of quantum-mechanical origin. This is illustrated by the work of Schramm and coworkers,⁴ who developed highly potent inhibitors to the enzyme purine nucleoside phosphorylase (PNP) based on the transition-state structure derived from measured KIEs. In principle, Schramm's approach can be applied to other enzymes, but in practice it is often limited by the lack of an adequate model to match computed and experimental KIEs. Therefore, it is of great

interest to develop practical computation methods to estimate KIEs for enzymatic reactions.

The challenge to theory is the difficulty to accurately determine the small difference in free energy of activation due to isotope replacements. This is further exacerbated by the complexity and size of an enzyme system that requires statistical averaging. The computational accuracy demands both an adequate treatment of the potential-energy surface that can properly describe the change of the bond orders of the primary and secondary sites and an efficient sampling procedure that can yield converged properties.⁵ In this chapter, we describe an integrated path integral free-energy perturbation and umbrella sampling (PI-FEP/UM) approach in molecular-dynamics simulations, and an analytic, integration-free approach based on Kleinert's variational perturbation theory⁶ that can systematically improve the accuracy and avoid numerical convergence problems,⁷ to compute KIEs for chemical reactions.^{8–10} In addition, we present a mixed molecular-orbital and valence-bond (MOVB) theory^{11–14} that combines quantum mechanics with molecular mechanics (QM/MM)^{15,16} to represent the potential surface of the reactive system. We show that this coupling of a combined QM-MOVB/MM potential-energy surface to describe the electronic structure with path integral-free energy simulation to model the nuclear quantum effects can yield remarkably accurate KIEs for reactions in solution and in enzymes.

Of course, a variety of methods have been developed to treat NQE for gas-phase reactions (see a recent review¹⁷). In principle, these techniques can be directly extended to condensed-phase systems; however, the size and complexity of these systems make it intractable computationally. Thus, a main goal is to develop new methods, or to extend gas-phase techniques to condensed phases or biomolecular systems. One method that has been successfully introduced to computational enzymology is the ensemble-averaged variational transition-state theory with QM/MM sampling (EA-VTST-QM/MM),^{18,19} which has been applied to a number of enzyme systems.^{2,20,21} Both primary and secondary KIEs can be computed using the EA-VTST-QM/MM method and the method includes contributions of multidimensional tunnelling. In another approach, Hammes-Schiffer and coworkers utilised a grid-based hybrid approach to model NQE in hydrogen-transfer reactions by numerically solving the vibrational wavefunction of the transferring hydrogen nucleus.²² So far, only primary KIEs have been computed by this approach.

The discrete Feynman path integral method^{23,24} has been used in a variety of applications since it offers an efficient and general approach for treating nuclear quantum effects in condensed-phase simulations.^{25–31} In principle, centroid path integral simulations can be directly used to determine KIEs by carrying out two separate calculations for the heavy and light isotope, respectively, and indeed, this has been the approach in most applications; however, the convergence of the computed free-energy barrier from dynamics simulations is typically not sufficient to ensure the desired accuracy for KIE, especially when heavy isotopes and secondary effects are involved. To this end, we have developed a free-energy perturbation technique¹⁰ by perturbing the atomic mass from light to heavy

isotopes in a bisection path integral sampling scheme,^{8,9} and this has tremendously reduced the statistical uncertainty in the computed KIEs.³²

The integrated path integral-free energy perturbation and umbrella sampling (PI-FEP/UM) method involves two computational steps.¹⁰ First, classical molecular-dynamics simulation is carried out to obtain the potential of mean force along the reaction coordinate for a given reaction. Then, centroid path integral simulations are performed to determine the nuclear quantum effects. The most significant feature of these studies is that classical and quantum simulations are fully separated, making it particularly attractive and efficient for enzymatic reactions. This computational approach has been explored previously in the work of Sprik *et al.*²⁵ and in the quantised classical path (QCP) method by Warshel and coworkers.^{33–35} The special feature in the PI-FEP/UM method is to use a free-energy perturbation scheme to obtain accurate KIEs for chemical reactions, by changing the atomic mass from one isotope into another in path integral sampling.¹⁰

Discretised path integral simulations often face numerical convergence difficulties, especially in view of the required accuracy is less than a fraction of a tenth of one kilocalorie per mole for computing KIEs. The analytic integration results based on Kleinert's variational perturbation theory does not have this problem, and the perturbation series has been shown to be convergent exponentially and uniformly,^{6,36,37} making the second-order perturbation (KP2) sufficiently accurate for chemical applications.⁷ We describe an automated, numerical integration-free centroid path integral method⁷ for estimating KIEs for proton-transfer reactions to illustrate the computational power for potential applications to enzymatic reactions.

In the following we first summarise the theoretical background, the representation of the potential-energy surface, and the PI-FEP/UM computational details. Then, results and discussion are presented. The paper is concluded with highlights of main findings.

5.2 Theoretical Background

5.2.1 Path Integral Quantum Transition-State Theory

The theoretical framework in the present discussion is path integral quantum transition-state theory (QTST), which yields an expression of the quantum-mechanical rate constant. In the discrete Feynman path integral method, each quantised nucleus is represented by a ring of P quasiparticles called beads, whose coordinates are denoted as $\mathbf{r} = \mathbf{r}_i; i = 1, \dots, P$.²³ The discrete paths are closed with $\mathbf{r}_{P+1} = \mathbf{r}_1$, in which each particle (bead) is connected harmonically with its neighbours, corresponding to the imaginary time slices $\tau_i = (i - 1)\hbar\beta/P$. A key concept in QTST is the centroid variable in path integration,^{27,38–42} defined as the geometrical centre of the quasiparticles:

$$\mathbf{r}^{(n)} = \frac{1}{P} \sum_{i=1}^P \mathbf{r}_i^{(n)} \quad (5.1)$$

where the superscript (n) specifies the n th quantised atom. The discretisation parameter P is chosen to be sufficiently large such that the numerical results converge to the quantum limit. In this approach, the quantum-mechanical equilibrium properties are obtained from the classical averages for a fictitious system governed by the effective potential²³

$$V_{\text{eff}}[\{\mathbf{r}_i^{(n)}\}, \mathbf{S}] = \sum_{n=1}^N \frac{\pi P}{\beta \lambda_n^2} \sum_i^P (\mathbf{r}_i^{(n)} - \mathbf{r}_{i+1}^{(n)})^2 + \frac{1}{P} \sum_i^P U(\mathbf{r}_i^{(1)}, \dots, \mathbf{r}_i^{(N)}, \mathbf{S}) \quad (5.2)$$

where N is the number of quantised atoms, \mathbf{S} represents the coordinates of all classical particles, $U(\mathbf{r}_i^{(1)}, \dots, \mathbf{r}_i^{(N)}, \mathbf{S})$ is the potential energy of the system, and $\beta = 1/k_B T$ with k_B being Boltzmann's constant and T the temperature. In eqn (5.2), the de Broglie thermal wavelength of atom n with a mass of M_n is given by $\lambda_n = (2\pi\beta\hbar^2/M_n)^{1/2}$. Note that the dynamics generated by the effective potential of eqn (5.2) has no physical significance; it is merely used as a procedure to obtain the correct ensemble of configurations.^{23,24}

QTST is derived by writing the rate expression analogous to classical TST, which includes a quantum activation term and a dynamical correction factor,^{39,42,43} and the QTST rate constant is given by

$$k_{\text{QTST}} = \frac{1}{2} \langle |\dot{z}| \rangle_{z'} e^{-\beta w(z')} \left/ \int_{-\infty}^{z'} dz e^{-\beta w(z)} \right. \quad (5.3)$$

where $w(z)$ is the potential of mean force (PMF) as a function of the centroid reaction coordinate $z[\mathbf{r}]$, z^* is the value of $z[\mathbf{r}]$ at the maximum of the PMF, and $\langle |\dot{z}| \rangle_{z'} = (2/\pi\beta M_{\text{eff}})^{1/2}$ is a dynamical frequency factor approximated by the velocity for a free particle of effective mass M_{eff} along the reaction coordinate $z[\mathbf{r}]$ direction. The exact rate constant is obtained by multiplying the QTST rate constant by a correction factor or transmission coefficient γ_q :⁴³

$$k = \gamma_q \cdot k_{\text{QTST}} \quad (5.4)$$

Equations (5.3) and (5.4) have identical forms to that of the classical rate constant, but unlike classical variational transition-state theory, there is no variational upper bound in the QTST rate constant because the quantum transmission coefficient γ_q may be greater than or less than unity. Equation (5.3) was initially derived with the assumption of a planar dividing surface along a rectilinear reaction coordinate. Messina *et al.* described a generalisation of the dividing surface that may depend both on the centroid coordinates and on its momenta.⁴²

There is no practical procedure to compute the quantum transmission coefficient γ_q in eqn (5.4). For a model reaction with a parabolic barrier along the reaction coordinate coupled to a bath of harmonic oscillators, the quantum

transmission coefficient is the Grote–Hynes (GH) classical transmission coefficient κ_{GH} .^{39,44} Often, the classical γ_q is used to approximate the quantum transmission coefficient; however, there is no correspondence between classical and quantum dynamic trajectories and the effects of tunnelling may greatly affect reaction dynamics near the barrier top.

As in classical TST, the PMF, $w(z)$, can be computed from the equilibrium average without any dynamical information, and it is defined by

$$e^{-\beta[w(z) - w(z_R)]} = e^{-\beta\Delta F(z)} = \frac{\langle \delta(z[\mathbf{r}] - z) \rangle}{\langle \delta(z[\mathbf{r}] - z_R) \rangle} \quad (5.5)$$

where z_R is the minimum point at the reactant state in the PMF and the ensemble average $\langle \dots \rangle$ is obtained by the effective potential of eqn (5.2). Equation (5.5) also serves as a definition of the path integral centroid free energy, $\Delta F(z)$, at z relative to that at the reactant state minimum. Note that the inherent nature of quantum mechanics is at odds with a potential of mean force as a function of a finite reaction coordinate. Nevertheless, the reaction coordinate function $z[\mathbf{r}]$ can be evaluated from the path centroids \mathbf{r} ,^{42–45} first recognised by Feynman and Hibbs as the most classical-like variable in quantum statistical mechanics.²³ Studies have shown that the activation free energy in the centroid path integral QTST “captures most of the tunnelling and quantisation effects”; which give rise to deviations from classical TST.^{46–49}

It is also useful to rewrite eqn (5.3) in combination with eqn (5.5) as follows

$$k_{\text{QTST}} = \frac{1}{\beta h} e^{-\beta\Delta F_{\text{CPI}}^{\neq}} \quad (5.6)$$

where the centroid path integral free energy of activation $\Delta F_{\text{CPI}}^{\neq}$ is defined by

$$\Delta F_{\text{CPI}}^{\neq} = \Delta F(z^{\neq}) - F_{\text{CPI}}^{\text{R}} \quad (5.7)$$

and

$$F_{\text{CPI}}^{\text{R}} = -\frac{1}{\beta} \ln \frac{1}{\lambda_{\text{eff}}} \int_{-\infty}^{z^{\neq}} dz e^{-\beta[\Delta F(z)]} \quad (5.8)$$

$F_{\text{CPI}}^{\text{R}}$ corresponds to the free energy of the system in the reactant (R) state region relative to the lowest point (z_R), which may be interpreted as the entropic contributions or motions correlating with the progress coordinate z . λ_{eff} is the de Broglie thermal wavelength of the centroid reaction coordinate with an effective mass M_{eff} at the dividing surface, which is determined in the centroid path transition state ensemble.

5.2.2 Centroid Path Integral Simulations

In centroid path integral, the centroid position, r , is used as the principle variable and the canonical QM partition function of a hybrid quantum and classical system, consisting of one quantised atom for convenience, can be written as follows:²³

$$Q_P^{\text{qm}} = \frac{1}{\Omega} \int dS \int ds \left(\frac{P}{\lambda_M^2} \right)^{3P/2} \int dR e^{-\beta V_{\text{eff}}(\{r\}, S)} \quad (5.9)$$

where Ω is the volume element of classical particles, P is the number of quasiparticles, $V_{\text{eff}}(\{r\}, S)$ is the effective potential (eqn (5.2)), $\int dR = \int d\mathbf{r}_1 \cdots \int d\mathbf{r}_P \delta(\mathbf{r} = \mathbf{s})$ in which the delta function $\delta(\mathbf{r} = \mathbf{s})$ is introduced for use in later discussion, and the centroid \mathbf{r} is defined in eqn (5.1). Importantly, eqn (5.9) can be rewritten exactly as a double average in eqn (5.10), which is the theoretical basis in the simulation approach of Sprik *et al.*, called the hybrid classical and path integral,²⁵ of Hwang and Warshel, called QCP,^{34,35} and later, of Major and Gao, called PI-FEP/UM.⁸⁻¹⁰

$$Q_{P \rightarrow \infty}^{\text{qm}} = Q_{\text{cm}} \langle \langle e^{-\beta \Delta U(\mathbf{r}, S)} \rangle_{\text{FP}, \mathbf{r}} \rangle_U \quad (5.10)$$

where the average $\langle \dots \rangle_U$ is a purely classical ensemble average obtained according the potential $U(\mathbf{r}, S)$ (the potential U in eqn (5.2) with a single centroid position for the quantised particle), the average differential potential is given by

$$\Delta U(\mathbf{r}, S) = \frac{1}{P} \sum_i^P \{ U(\mathbf{r}_i, S) - U(\mathbf{r}, S) \} \quad (5.11)$$

and the inner average $\langle \dots \rangle_{\text{FP}, \mathbf{r}}$ represents a path-integral free-particle sampling, carried out without the external potential $U(\mathbf{r}, S)$:^{10,34,35}

$$\langle \dots \rangle_{\text{FP}, \mathbf{r}} = \frac{\int dR \{ \dots \} e^{-(\pi P / \lambda_M^2) \sum_i^P (\Delta \mathbf{r}_i)^2}}{\int dR e^{-(\pi P / \lambda_M^2) \sum_i^P (\Delta \mathbf{r}_i)^2}} \quad (5.12)$$

where $\Delta \mathbf{r}_i = \mathbf{r}_i - \mathbf{r}_{i+1}$. In eqn (5.10), the factor Q_{cm} is the classical partition function defined in,²³

$$Q_P^{\text{cm}} = \frac{1}{\Omega} \int dS \int ds e^{-\beta U(s, S)} \left(\frac{P}{\lambda^2} \right)^{3P/2} \int dR e^{-(\pi P / \lambda_M^2) \sum_i^P (\Delta \mathbf{r}_i)^2} \quad (5.13)$$

where we have defined the position of the quantised particle centroid to coincide with the coordinates of the corresponding classical particle $s = r$.

We note that Warshel and coworkers have exploited this idea, which they called the quantised classical path (QCP) method, to estimate NQE for chemical reactions in solution and catalysed by enzymes.^{34,35} In QCP, the classical simulations and quantum corrections are fully separated.^{50,51} The expression of eqn (5.10) is particularly useful because the quantum free energy of the system can be obtained first by carrying out classical trajectories according to the classical distribution, $\exp[-\beta U(\mathbf{r}, \mathbf{S})]$, and then, by determining the quantum contributions through free particle sampling based on the distribution $\exp[-\beta(\pi P/\beta\lambda_M^2)\sum_i^P (\Delta\mathbf{r}_i)^2]$. This double averaging yields the exact path integral centroid density,^{10,25,34,35} which can be used to determine the centroid potential of mean force:

$$e^{-\beta w(z)} = e^{-\beta w_{cm}(z)} \langle \delta(z = z) \langle e^{-\beta \Delta U(z|\mathbf{r}, \mathbf{S})} \rangle_{FP,z} \rangle_U \quad (5.14)$$

where $w(z)$ and $w_{cm}(z)$ are the centroid quantum-mechanical and the classical-mechanical PMF, respectively, and the average difference potential energy $\Delta U(z|\mathbf{r}, \mathbf{S})$ is given in eqn (5.11).

5.2.3 Kinetic Isotope Effects

We first present two algorithms for estimating KIEs using centroid path integral simulations in the context of QCP³⁴ or hybrid quantum and classical sampling.²⁵ Then, we present a third algorithm, making use of Kleinert variational perturbation (KP) theory⁶ that determines the centroid potential of the mean force analytically without the need of performing discretised path integral sampling.⁷

5.2.3.1 Sequential Centroid Path Integral and Umbrella Sampling (PI/UM)

Using eqn (5.6), the kinetic isotope effects between a light isotope L and a heavy isotope H can be computed by

$$\text{KIE} = \frac{k^L}{k^H} = e^{-\beta[\Delta F^L(z_L^f) - \Delta F^H(z_H^f)]} e^{-\beta\{F_{CPI,L}^R(z_L^R) - F_{CPI,H}^R(z_H^R)\}} \quad (5.15)$$

where z_L^f , z_H^f , z_L^R , and z_H^R are, respectively, the values of the centroid reaction coordinate at the transition state and reactant state minimum for the light and heavy isotopes, and $F_{CPI,L}^R(z_L^R)$ and $F_{CPI,H}^R(z_H^R)$ are the free energies defined by eqn (5.8) for the two isotopes, respectively, which depend on the effective masses associated with the centroid reaction coordinate at the transition state. Equation (5.15) shows that KIEs may be determined by computing the potentials of mean force separately for the L and H isotopes,^{9,10,34,35,52} and this can be achieved by first performing umbrella sampling using classical molecular dynamics and then by performing centroid path integral free-particle sampling with the constraints that the centroids of the quantised particles coincide with

the corresponding positions sampled in the classical trajectory. This is, indeed, what is typically done.^{9,34,35,52} However, the statistical fluctuations in the actual simulation for computing the potential of mean force is typically as large as, or even greater than, the isotope effect itself, resulting in poor convergence.¹⁰ To alleviate this difficulty, in refs 9 and 10, we have introduced a procedure such that the discretised beads positions for the heavy and light atoms are obtained from exactly the same sampling sequence. Thus, the heavy and light path integral beads distributions differ only by their relative spread from the centroid position, which is determined by the corresponding de Broglie wavelength.

To enhance convergence in these centroid path integral simulations, we have developed a bisection sampling technique for a ring of beads, called BQCP, by extending the original approach of Ceperley for free particle sampling in which the initial and final beads are not connected.^{53,54} In our implementation, we first make the bisection sampling as originally proposed by Ceperley,^{53,54} enforcing the first and last beads to be identical to enclose the polymer ring.^{8,9} Then, we make rigid-body translation of the centroid position of the new beads configuration to coincide with the target (classical) coordinate. Since the free-particle distribution is known exactly at a given temperature, each ring-bead distribution is generated according to this distribution and thus 100% accepted.⁵⁴ Furthermore, in this construction, each new configuration is created independently, starting from a single initial bead position, allowing the new configuration to move into a completely different region of configurational space. This latter point is especially important in achieving convergence by avoiding being trapped in a local region of the classical potential in the path integral sampling. The BQCP method has been thoroughly tested^{8,9} and applied to several condensed-phase systems.^{9,10,55,56}

5.2.3.2 The PI-FEP/UM Method

The second algorithm is to obtain the ratio of the quantum partition functions (eqn (5.10)) for two different isotopes directly through free-energy perturbation (FEP) theory by perturbing the mass from the light isotope to the heavy isotope.¹⁰ In other words, only one simulation of a given isotopic reaction is performed, while the ratio of the partition function, *i.e.* the KIE, to a different isotopic reaction, is obtained by FEP within this simulation. This is in contrast to algorithem 1, in which two separate simulations are performed, and this difference results in a major improvement in computation accuracy for KIE calculations.^{10,32}

Specifically, eqn (5.15) for computing kinetic isotope effect is rewritten in terms of the ratio of the partial partition functions at the centroid reactant and transition state and is given by:

$$\text{KIE} = \frac{k^L}{k^H} = \left[\frac{Q_{\text{qm}}^L(z_L^{\neq})}{Q_{\text{qm}}^H(z_H^{\neq})} \right] \left[\frac{Q_{\text{qm}}^H(z_H^R)}{Q_{\text{qm}}^L(z_L^R)} \right] e^{-\beta \{ F_{\text{CPI},L}^R(z_L^R) - F_{\text{CPI},H}^R(z_H^R) \}} \quad (5.16)$$

where the ratio of the partition function can be written as follows:

$$\frac{Q_{\text{qm}}^H(z)}{Q_{\text{qm}}^L(z)} = \frac{\langle \delta(z-z) \langle e^{\frac{\beta}{\hbar} \sum_i \Delta U_i^{L \rightarrow H}} e^{-\beta \Delta U_L} \rangle_{\text{FP},L} \rangle_U}{\langle \delta(z-z) e^{-\beta [F_L(z,S) - F_{\text{FP}}^0]} \rangle_U} \quad (5.17)$$

where the subscripts L specifies that the ensemble averages are done using the light isotope, ΔU_L is defined by eqn (5.12), F_{FP}^0 is the free energy of the free particle reference state for the quantised particles,²³ and $\Delta U_i^{L \rightarrow H} = U(\mathbf{r}_{i,H}) - U(\mathbf{r}_{i,L})$ represents the difference in “classical” potential energy at the heavy and light bead positions $\mathbf{r}_{i,H}$ and $\mathbf{r}_{i,L}$. In the bisection sampling scheme, the perturbed heavy isotope positions are related to the lighter ones by

$$\frac{\mathbf{r}_{i,L}}{\mathbf{r}_{i,H}} = \frac{\lambda_{M_L} \theta_i}{\lambda_{M_H} \theta_i} = \sqrt{\frac{M_H}{M_L}}; \quad i = 1, 2, \dots, P \quad (5.18)$$

where $\mathbf{r}_{i,L}$ and $\mathbf{r}_{i,H}$ are the coordinates for bead i of the corresponding light and heavy isotopes, λ_{M_L} and λ_{M_H} are isotopic masses for the light and heavy nuclei, and θ_i is the position vector in the bisection sampling scheme that depends on the previous sequence of directions and has been fully described in ref. 8. Equation (5.18) indicates that the position vectors for the corresponding heavy and light isotope beads in the path integral simulation are identical, thereby, resulting in the relationship that bead positions are solely determined by the ratio of the square roots of masses.

In eqn (5.17), we obtain the free-energy (inner average) difference between the heavy and light isotopes by carrying out the bisection path integral sampling with the light atom and then perturbing the heavy isotope positions according to eqn (5.18). Then, the free-energy difference between the light and heavy isotope ensembles is weighted by a Boltzmann factor for each quantised configuration.

5.2.3.3 Kleinert’s Variational Perturbation (KP) Theory

The canonical partition function Q_{QM} for a quantised particle in the bath of classical solvent can be written in terms of the effective centroid potential w , as a classical configuration integral:

$$Q_{\text{P}}^{\text{qm}} = \sqrt{\frac{Mk_B T}{2\pi\hbar^2}} \int_{-\infty}^{\infty} e^{-\beta w(\mathbf{r})} d\mathbf{r} \quad (5.19)$$

where M is the mass of the quantised particle, \hbar is Planck’s constant divided by 2π . In the 1980s, three groups proposed a variational method,^{39,57,58} known as the Feynman and Kleinert (FK) variational method that yields an upper bound of $w(\mathbf{r})$ and has been successfully used in a variety of applications.^{59–62} Kleinert later showed that the FK approach in fact is just the first-order approximation to a general variation perturbation theory,^{6,36} and the new Kleinert perturbation theory (KP) has been shown in several model systems to have very attractive features, including exponentially and uniformly convergent. For

example, the electronic ground-state energy of a hydrogen atom converges at accuracies of 85%, 95% and 98% in the first three orders of KP expansion. The KP theory does not suffer from the numerical convergence issues in discretised path integral simulations; however, it has so far only been applied to a few limited model cases beyond the first-order approximation, *i.e.* the Feynman–Kleinert approach.

We have shown recently that the KP theory can be adopted in chemical applications to determine KIEs for chemical reactions, and because of its fast convergence the second-order perturbation, denoted by KP2, can yield excellent results for a series of proton-transfer reactions.⁷ We briefly summarise the key elements of our theoretical development based on the Kleinert variational perturbation theory.

The n th-order KP approximation $W_\Omega^n(\mathbf{r})$ to the centroid potential $w(\mathbf{r})$ is given by

$$\begin{aligned} -\beta W_\Omega^n(\mathbf{r}) = & \ln Q_\Omega(\mathbf{r}) - \frac{1}{h} \left\langle V_p^\mathbf{r}[\mathbf{r}(\tau_1)] \right\rangle_{\Omega,c}^\mathbf{r} + \frac{1}{2!h^2} \left\langle V_p^\mathbf{r}[\mathbf{r}(\tau_1)] V_p^\mathbf{r}[\mathbf{r}(\tau_2)] \right\rangle_{\Omega,c}^\mathbf{r} \\ & + \dots + \frac{(-1)^n}{n!h^n} \left\langle \prod_{k=1}^n V_p^\mathbf{r}[\mathbf{r}(\tau_k)] \right\rangle_{\Omega,c}^\mathbf{r} \end{aligned} \quad (5.20)$$

where the angular frequency Ω is a variational parameter, which is introduced to define the perturbation potential $V_p^\mathbf{r}[\mathbf{r}] = U(\mathbf{r}, S) - U_\Omega^\mathbf{r}(\mathbf{r})$ about the reference state at \mathbf{r} with the harmonic potential $U_\Omega^\mathbf{r}(\mathbf{r}) = (M/2)\Omega^2(\mathbf{r} - \mathbf{r})^2$. The local quantum partition function of the harmonic reference state $Q_\Omega(\mathbf{r})$ is given as follows:

$$Q_\Omega(\mathbf{r}) = \frac{\beta h \Omega(\mathbf{r}) / 2}{\sinh(\beta h \Omega(\mathbf{r}) / 2)} \quad (5.21)$$

The remaining terms in eqn (5.20) are the n th-order corrections to approximate the real system, in which the expectation value $\langle \dots \rangle_{\Omega,c}^\mathbf{r}$ is called the cumulant. The cumulants can be written in terms of the standard expectation value $\langle \dots \rangle_\Omega^\mathbf{r}$ by cumulant expansion. Kleinert and coworkers derived the expression for the expectation value of a function in terms of Gaussian smearing convolution integrals:⁶

$$\begin{aligned} \left\langle \prod_{k=1}^n F[\mathbf{r}_k(\tau_k)] \right\rangle_\Omega^\mathbf{r} = & \frac{\prod_{j=1}^n \int_0^{\beta h} d\tau_j \prod_{k=1}^n \int_{-\infty}^{\infty} d\mathbf{r}_k F(\mathbf{r}_k(\tau_k))}{\{(2\pi)^n \text{Det}[a_{\tau_k \tau_{k'}}^2(\Omega)]\}^{3/2}} \\ & \times \exp \left\{ -\frac{1}{2} \sum_{k'=1}^n \sum_{k=1}^n (\mathbf{r}_k - \mathbf{r}) \cdot a_{\tau_k \tau_{k'}}^{-2}(\Omega) (\mathbf{r}_{k'} - \mathbf{r}) \right\} \end{aligned} \quad (5.22)$$

where $\text{Det}[a_{\tau_k \tau_{k'}}^2(\Omega)]$ is the determinant of the $n \times n$ matrix consisting of the Gaussian width $a_{\tau_k \tau_{k'}}^2(\Omega)$, $a_{\tau_k \tau_{k'}}^{-2}(\Omega)$ is an element of the inverse matrix of the Gaussian width, which is given by

$$a_{\tau_k \tau_{k'}}^2(\Omega) = \frac{1}{\beta M \Omega^2} \left\{ \frac{\beta h \Omega \cosh[(|\tau_k - \tau_{k'}| - \beta h/2)\Omega]}{2 \sinh[\beta h \Omega/2]} - 1 \right\} \quad (5.23)$$

As n tends to infinity, $W_\Omega^n(\mathbf{r})$ becomes independent of the variational parameter Ω . At a given order of the KP theory, the optimal frequency is given by the least dependence of $W_\Omega^n(\mathbf{r})$ on Ω , which is the solution to the equation of the lowest-order derivative of $W_\Omega^n(\mathbf{r})$ setting to zero.⁶ Thus, a self-consistent iterative procedure is carried out. Given an initial trial of Ω , the corresponding Gaussian widths are determined using eqn (5.23), with which a new $W_\Omega^n(\mathbf{r})$ is obtained. This is then used to obtain a further value of Ω until it is converged.⁷

An especially attractive feature of eqn (5.20) is that if the real system potential U is expressed as a series of polynomials or Gaussian functions, analytic expressions of eqn (5.18) can be obtained,⁷ making the computation extremely efficient because there is no need to perform the time-consuming Monte Carlo or molecular dynamics sampling of the path integrals. If the real potential is expanded to the m th-order polynomial and the KP theory is terminated at the n th order (eqn (5.20)), we denote our results as KP_n/P_m .

If the number of quantised particles is N , the angular frequency variational variable is a $3N \times 3N$ matrix, and this coupled with the $2n$ -dimension integrals in eqn (5.22) makes the use of KP theory rather laborious and has been a major factor limiting its applications beyond the KP1 level, the original FK approach. To render the KP theory feasible for many-body systems with N nuclei for a given configuration $\{\mathbf{r}_i; i = 1, \dots, N\}$, we make use of instantaneous normal mode (INM) coordinates $\{q(\mathbf{r}_i; i = 1, \dots, N)\}^{3N}$ and assume their motions can be decoupled. Thus, system potential $U(\{\mathbf{r}\}, \mathbf{S})$ can be expanded in terms of the INM coordinates at $\{\mathbf{r}_i; i = 1, \dots, N\}$, and hence, the multidimensional potential is effectively reduced to $3N$ one-dimensional potentials along each normal coordinate. This approximation is particularly suited for the KP theory because of the exponentially decaying property of the Gaussian convolution integrations in eqn (5.22). With the INM approximation, the total effective centroid potential for N -quantised nuclei can be simplified as:

$$W_\Omega^n(\{\mathbf{r}_i\}^{3N}) \approx U(\{\mathbf{r}_i\}^{3N}, \mathbf{S}) + \sum_{i=1}^{3N} W_{\Omega_i}^n(\{q_i\}^{3N}, \mathbf{S}) \quad (5.24)$$

where $W_{\Omega_i}^n(\{q_i\}^{3N}, \mathbf{S})$ is the centroid potential for normal mode i of the quantised system in the classical bath coordinates of the remainder of the system. Although the INM approximation sacrifices some accuracy, in return, it allows analyses of quantum-mechanical vibration and tunnelling and their separate contributions to the total quantum effects. Note that positive and

negative values of $W_{\Omega_i}^n(\{q_i\}^{3N}, \mathbf{S})$ in eqn (5.24) raise (vibration) and lower (tunnelling) the classical potential $U(\{\mathbf{r}_i\}^{3N}, \mathbf{S})$, respectively.

5.3 Potential-Energy Surface

Almost all enzyme reactions can be well described by the Born–Oppenheimer approximation, in which the sum of the electronic energy and the nuclear repulsion provides a potential-energy function, or potential-energy surface (PES), governing the interatomic motions. Therefore, the molecular modelling problem breaks into two parts: the PES and the dynamics simulations.

The potential-energy function describes the energetic changes as a function of the variations in atomic coordinates, including thermal fluctuations and rearrangements of the chemical bonds. The accuracy of the potential-energy function used to carry out molecular-dynamics simulations directly affects the reliability of the computed $\Delta F_{\text{TST}}^\#$ and its nuclear quantum correction.^{5,20} The accuracy can be achieved by the use of analytical functions fitted to reproduce key energetic, structural, and force constant data, from either experiments or high-level *ab initio* calculations. Molecular-mechanical (MM) potentials or force fields,^{63,64} however, are not general for chemical reactions, and it requires reparameterisation of the empirical parameters for every new reaction, which severely limits its applicability. More importantly, often, little information is available in regions of the PES other than the stationary reactant and product states and the saddle point (transition state). On the other hand, combined quantum-mechanical and molecular-mechanical (QM/MM) potentials offer the advantages of both computational efficiency and accuracy for all regions of the PES.^{65,66}

5.3.1 Combined QM/MM Potentials

In combined QM/MM potentials, the system is divided into a QM region and an MM region.^{12,15,16,65,67–70} The QM region typically includes atoms that are directly involved in the chemical step and they are treated explicitly by a quantum-mechanical electronic-structure method, whereas the MM region consists of the rest of the system and is approximated by an MM force field. The method of combining QM with MM was first developed by Warshel and Karplus for the treatment of conjugated polyenes with QM and the framework with a force field,¹⁵ and it was subsequently applied to an enzyme by Warshel and Levitt in which electrostatic interactions between QM and MM were introduced.¹⁶ The remarkable applicability of this approach that it enjoys today was in fact not appreciated until more than a decade later when molecular dynamics and Monte Carlo simulations using combined QM/MM potentials began to emerge.^{65,68,71} The QM/MM potential is given by:^{66,67}

$$U_{\text{tot}} = \langle \Psi(S) | H_{\text{qm}}^{\text{o}}(S) + H_{\text{qm/mm}}(S) | \Psi(S) \rangle + U_{\text{mm}} \quad (5.25)$$

where $H_{\text{qm}}^{\text{o}}(S)$ is the Hamiltonian of the QM-subsystem (the substrate and key amino-acid residues) in the gas phase, U_{mm} is the classical (MM) potential

energy of the remainder of the system, $H_{\text{qm/mm}}(S)$ is the QM/MM interaction Hamiltonian between the two regions, and $\Psi(S)$ is the molecular wavefunction of the QM-subsystem optimised for $H_{\text{qm}}^{\circ}(S) + H_{\text{qm/mm}}(S)$.

We have found that it is most convenient to rewrite eqn (5.25) as follows:^{65,68}

$$U_{\text{tot}} = E_{\text{qm}}^{\circ}(S) + \Delta E_{\text{qm/mm}}(S) + U_{\text{mm}} \quad (5.26)$$

where $E_{\text{qm}}^{\circ}(S)$ is the energy of an isolated QM subsystem in the gas phase,

$$E_{\text{qm}}^{\circ}(S) = \langle \Psi^{\circ}(S) | H_{\text{qm}}^{\circ}(S) | \Psi^{\circ}(S) \rangle \quad (5.27)$$

In eqn (5.26), $\Delta E_{\text{qm/mm}}(S)$ is the interaction energy between the QM and MM regions, corresponding to the energy change of transferring the QM subsystem from the gas phase into the condensed phase, which is defined by:

$$\Delta E_{\text{qm/mm}}(S) = \langle \Psi(S) | H_{\text{qm}}^{\circ}(S) + H_{\text{qm/mm}}(S) | \Psi(S) \rangle - E_{\text{g}}^{\circ}(S) \quad (5.28)$$

In eqns (5.25)–(5.28), we have identified the energy terms involving electronic degrees of freedom by E and those purely empirical functions by U , the combination of which is also an empirical potential.

Equation (5.26) is especially useful in that the total energy of a hybrid QM and MM system is separated into two “*independent*” terms – the gas-phase energy and the interaction energy – which can now be evaluated using different QM methods. There is sometimes confusion about the accuracy of applications using semiempirical QM/MM potentials.⁷² Equation (5.26) illustrates that there are two issues. The first is the intrinsic performance of the model, *e.g.*, the $E_{\text{qm}}^{\circ}(S)$ term, which is indeed not adequate using semiempirical models and that would require *extremely* high-level QM methods to achieve the desired accuracy. This is only possible by using CCSD(T), CASPT2 or well-tested density functionals along with a large basis set, none of which methods are tractable for applications to enzymes. When semiempirical methods are used, the PES for the $E_{\text{qm}}^{\circ}(S)$ term, is either reparameterised to fit experimental data, or replaced by high-level results. Only in rare occasions when a semiempirical model yields good agreement with experiment, are these methods directly used without alteration.^{73,74}

The second issue on accuracy is in the calculation of the $\Delta E_{\text{qm/mm}}(S)$ term. It was recognised early on,^{65,69,75} when explicit QM/MM simulations were carried out, that combined QM/MM potential is an empirical model, which contains empirical parameters and should be optimised to describe QM/MM interactions. By systematically optimising the associated van der Waals parameters for the “QM-atoms”,^{65,69,75} both semiempirical and *ab initio* (Hartree–Fock) QM/MM potentials can yield excellent results for hydrogen-bonding and dispersion interactions in comparison with experimental data. The use of semiempirical methods such as the Austin model 1 (AM1)⁷⁶ or parameterised model 3

(PM3)⁷⁷ in QM/MM simulations has been validated through extensive studies of a variety of properties and molecular systems, including computations of free energies of solvation and polarisation energies of organic compounds,^{65,78} the free-energy profiles for organic reactions,^{55,73,79} and the effects of solvation on molecular structures and on electronic transitions.^{80,81}

The QM/MM PES combines the generality of quantum-mechanical methods for treating chemical processes with the computational efficiency of molecular mechanics for large molecular systems. The use of an explicit electronic-structure method to describe the enzyme-active site is important because understanding the changes in electronic structure along the reaction path can help to design inhibitors and novel catalysts. It is also important because the dynamic fluctuations of the enzyme and aqueous solvent system have a major impact on the polarisation of the species involved in the chemical reaction, which, in turn, affects the chemical reactivity.^{65,82} Combined QM/MM methods have been reviewed in several articles.^{66,67,83,85}

5.3.2 The MOVB Potential

A novel combined QM/MM approach has been developed that utilises a mixed molecular-orbital and valence-bond (MOVB) theory to represent the reactive potential-energy surface. In this MOVB approach, molecular orbital theory based on a block-localised orbital scheme is used to define the Lewis resonance structures.^{11,86} These Lewis resonance structures are called effective diabatic states, representing the reactant state, the product state or other states important for the transition state of the chemical reaction under investigation, which are coupled by configuration interaction (CI).^{12–14} A closely analogous model is the empirical valence bond (EVB) potential that has been used by Warshel and coworkers,⁸⁷ who approximate these effective diabatic states by an empirical force field, making the computation cheap for simulation studies. Although it is perfectly reasonable to use empirical force field to represent these diabatic states, provided that the force field is adequately parameterised to reflect the true electronic structure for the entire system, in practice, it is often assumed that the atomic partial charges are invariant by taking values at the reactant state and product state, respectively. This is a major shortcoming because intramolecular charge polarisation is ignored, which leads to inconsistent representation of the bond orders for the “primary” and “secondary” sites when KIEs are being computed. Note that although it is possible to parameterise the free-energy barrier and its change from water to the enzyme by reproducing experimental results, there is no rigorous justification for the accuracy of the 3N-degree of freedom PES, casting doubt on results that require a knowledge of the gradient and Hessian of the potential surface, a prerequisite for computing KIEs.

Truhlar and coworkers developed a multiconfiguration molecular-mechanics (MCMM) method that involves a systematic parameterisation for the off-diagonal element.^{88,89} The MCMM method is fitted to reproduce *ab initio*

energies and gradients. Thus, the MCMM potential as well as the MOVB theory are proper empirical and first-principle functions, respectively, for use in computing nuclear quantum effects and kinetic isotope effects.

5.4 Computational Details

In the path integral simulations using algorithms 1 and 2, we employ a combined QM/MM potential in molecular-dynamics simulations.^{65,66} In these studies, the solute is represented explicitly by an electronic-structure method and the solvent is approximated by the three-point charge TIP3P model for water.⁹⁰ In the deprotonation of nitroethane by acetate ion, the standard semiempirical AM1 model⁷⁶ failed to yield adequate energetic results. Consequently, a set of specific reaction parameters (SRP) has been developed within the AM1 formalism to fit results from high-level *ab initio* theory as well as from experiments.^{10,55} The performance of the SRP-AM1 model has been reported previously, and we focus here on the study of the kinetic isotope effects using the PI-FEP/UM method.

In the study of carbon acid deprotonation using the KP2 theory, the solute is treated by B3LYP/6-31 + G(d,p) density functional theory, whereas the solvent is represented by the polarisable continuum model with a dielectric constant of 78 for water. Note that the KP centroid path-integral method is numerical integration free; thus, high-level electronic-structure methods such as DFT with a relatively large basis set can be used. In these calculations, the potential along each normal mode direction for the reactant state, transition state and product state is determined at the B3LYP level by stepping in each direction at an interval of 0.1 Å, and the resulting potential is fitted to a 20th-order polynomial, whose Gaussian smearing integrals (eqn (5.22)) have been derived analytically at the KP2 level. Thus, our results are obtained at the KP2/P20 level for the proton-transfer reactions of a series of aryl-substituted α -methoxystyrene compounds to acetate ion.

For algorithms 1 and 2, the simulations were performed using periodic boundary conditions in the isothermal-isobaric (NPT) ensemble at 25 °C and 1 atm. A total of 898 water molecules were included in a cubic box of about $30 \times 30 \times 30$ Å³. Nonbonded electrostatic interactions are described by the particle-mesh Ewald summation method for QM/MM simulations,⁹¹ whereas van der Waals interactions are smoothed to zero at 9.5 Å based on group-group separations. The bond lengths and angles of solvent water molecules are constrained by the SHAKE algorithm, and an integration step of 1 fs was used for all calculations.⁹²

The potential of mean force (PMF) profile is obtained using the umbrella sampling technique.⁹³ For the proton-transfer reaction between nitroethane and acetate ion, the classical reaction coordinate is defined as the difference in distance for the proton between the donor (α carbon of nitroethane) and the acceptor (an oxygen of the acetate ion) atom: $Z_{\text{PT}} = r(\text{C}_\alpha - \text{H}) - r(\text{H} - \text{O})$. A total of *ca.* 4 ns of simulations were performed (with time step of 1 fs).

The BQCP simulations employed 29 168 classical configurations for each isotope (^1H , ^2H , and ^3H ; or H, D, and T), combined with 10 path-integral steps per classical step. For the deprotonation reaction the nitroethane C α -atom, the abstracting acetate oxygen, the transferring proton, as well as the secondary hydrogen atom, are quantised. Each quantised atom has spawned into 32 beads.

To estimate statistical uncertainties in the computed KIEs, the entire path integral simulations have been divided into ten segments, each of which is treated as independent simulations. Standard uncertainties ($\pm 1\sigma$) were determined from the total average and those from the ten separate blocks. All simulations employed the CHARMM program⁹⁴ and all path-integral simulations used a parallel version that efficiently distributes integral calculations for the quantised beads.^{8 10}

5.5 Illustrative Examples

5.5.1 Proton Transfer between Nitroethane and Acetate Ion

The proton-abstraction reaction of nitroalkane by acetate ion is a classical example, exhibiting an unusual Brønsted relationship in water, known as the nitroalkane anomaly.^{95 97} This process is also catalysed by the nitroalkane oxidase in the initial step of the oxidation of nitroalkanes.⁹⁸ Valley and Fitzpatrick reported a KIE of 9.2 ± 0.4 for the di-deuterated substrate ($1,1\text{-}^2\text{H}_2$) nitroethane in nitroalkane oxidase, and 7.8 ± 0.1 for uncatalysed reaction by an acetate ion in water.⁹⁹ We have previously studied the solvent effects and reported preliminary results of H/D kinetic isotope effects.⁵⁵ Then, the KIEs for all D and T primary and secondary isotope effects were determined.³²

The computed PMF, in which the “primary” and “secondary” hydrogen atoms as well as the donor carbon and acceptor oxygen atoms are quantised for the deprotonation of nitroethane by acetate, reveals a computed barrier of 24.4 kcal/mol,^{10,32,55} in reasonable accord with the experimental values of 24.8.⁹⁹ Without the quantum contribution the computed barrier would have been 27.4 kcal/mol, illustrating the importance of including nuclear quantum effects to accurately determine the free energy of activation for proton-transfer reactions.¹⁰⁰

The computed primary and secondary KIEs for D and T substitutions are listed in Table 5.1. Figure 5.1 depicts an illustrative example of the computed ratio of the partial quantum partition functions as a function of the centroid path integral reaction coordinate. The kinetic isotope effects have been computed without including the free-energy difference given in eqn (5.16), which may introduce some errors in the present calculations. The computed H/D primary and secondary intrinsic KIEs are $k_{\text{H}}^{\text{H}}/k_{\text{D}}^{\text{H}} = 6.63 \pm 0.31$ and $k_{\text{H}}^{\text{H}}/k_{\text{H}}^{\text{D}} = 1.34 \pm 0.13$, respectively, whereas the total effect where both primary and secondary hydrogen atoms are replaced by a deuterium isotope is $k_{\text{H}}^{\text{H}}/k_{\text{D}}^{\text{D}} = 8.31 \pm 0.13$ (Table 5.1), which may be compared with the

Table 5.1 Computed and experimental primary and secondary kinetic isotope effects for the proton-transfer reaction between nitroethane and acetate ion in water at 25 °C.^a

KIE	PI FEP/UM	Expt. ^b
Primary KIE		
k_H^H/k_D^H	6.63 ± 0.31	
k_H^H/k_T^H	12.96 ± 0.98	
K_D^D/k_T^D	2.17 ± 0.04	
Secondary KIE		
k_H^H/k_H^D	1.340 ± 0.132	
k_H^H/k_H^T	1.375 ± 0.183	
K_D^D/k_D^T	1.096 ± 0.039	
Total KIE		
k_H^H/k_D^D	8.31 ± 0.13	7.8

^aKinetic isotope effects are determined by using the average value of the top two bins in the potential of the mean force for the ratio of the partial quantum partition function for the transition state, and the average value of the middle fifteen bins for the reactant state. The bin size used for data collection is 0.05 Å in the reaction coordinate, half of which may be considered as the error in the reaction coordinate value.

^bRef. [99].

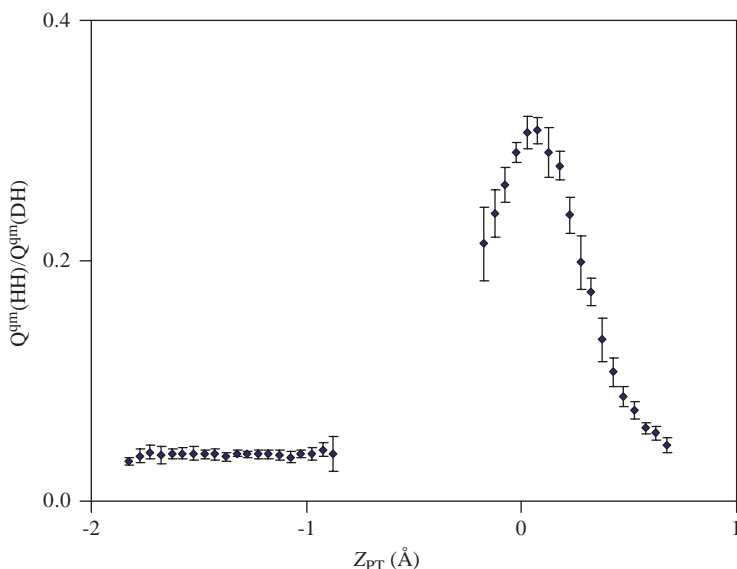


Figure 5.1 Computed ratio of the quantum mechanical partition functions for the primary H/D kinetic isotope effects in which the secondary site is occupied by a hydrogen along the proton transfer reaction coordinate. The PI FEP/UM method was used.

experimental value of 7.8.⁹⁹ There are no experimental data for comparison with the results of single-site substitutions.

The computational results allow us to examine the rule of the geometric mean (RGM),¹⁰¹ which is expressed as follows:

$$k_{\text{H}}^{\text{H}}/k_{\text{D}}^{\text{H}} = k_{\text{H}}^{\text{D}}/k_{\text{D}}^{\text{D}} = \frac{(k_{\text{H}}^{\text{H}}/k_{\text{D}}^{\text{D}})}{(k_{\text{H}}^{\text{H}}/k_{\text{H}}^{\text{D}})} \quad (5.29)$$

The RGM states that there is no isotope effect from a second site on the kinetic isotope effect of the first site.¹⁰² The rule was originally derived at the high-temperature limit with small quantum tunnelling corrections,¹⁰¹ and it has been shown to have negligible deviations on model systems using semiclassical transition-state theory.¹⁰³ However, deviations or the observations of RGM breakdown are often used as a measure of the extent of tunnelling in the system.¹⁰² Using the RGM of eqn (5.29), we obtain an estimated value of 8.88 (6.63×1.34) for the total deuterium KIE if the free energies of the primary and secondary KIE were additive. This gives a ratio of 1.07 over the actual computed value (8.31). Another way of interpreting the results is that there is a secondary kinetic isotope effect of 1.07 on the primary kinetic isotope effects:

$$g_{\text{HD}}^{\text{HD}} = \frac{(k_{\text{H}}^{\text{H}}/k_{\text{D}}^{\text{H}})}{(k_{\text{H}}^{\text{D}}/k_{\text{D}}^{\text{D}})} = \frac{6.630}{(8.308/1.340)} = 1.07 \quad (5.30)$$

This result indicates that there is some correction in the motions between the secondary hydrogen and the primary hydrogen in the proton-transfer reaction between nitroethane and acetate ion in water.

Primary and secondary tritium kinetic isotope effects are also given in Table 5.1, which have values of $k_{\text{H}}^{\text{H}}/k_{\text{T}}^{\text{H}} = 12.96 \pm 0.98$ and $k_{\text{H}}^{\text{H}}/k_{\text{T}}^{\text{D}} = 1.37 \pm 0.18$. These effects are greater than the deuterium KIEs because of its larger mass. Employing the rule of the geometric mean, an estimated total tritium KIE of $k_{\text{H}}^{\text{H}}/k_{\text{T}}^{\text{D}} = 17.8$ is obtained.

The single site Swain–Schaad exponents¹⁰⁴ is expressed below using the notation of Huskey,¹⁰²

$$n_{\text{HD}} = \frac{\ln(k_{\text{H}}^{\text{H}}/k_{\text{T}}^{\text{H}})}{\ln(k_{\text{H}}^{\text{H}}/k_{\text{D}}^{\text{H}})} \quad (5.31)$$

and

$$n_{\text{DT}} = \frac{\ln(k_{\text{H}}^{\text{H}}/k_{\text{T}}^{\text{H}})}{\ln(k_{\text{D}}^{\text{H}}/k_{\text{T}}^{\text{H}})} \quad (5.32)$$

These equations assume that the isotope effects are determined solely by the use of a one-frequency model with contributions only from the zero-point energy without tunnelling. Studies have shown that the value of n_{HD} for primary KIEs is typically in the range of 1.43–1.45.¹⁰² Deviations from these values are

thought to be indications of contributions from tunnelling.¹⁰⁵ Using the data in Table 5.1, we obtained a single-site Swain–Schaad exponent of $n_{\text{HD}}^{(1)} = 1.35$ for the primary KIE, and of $n_{\text{HD}}^{(2)} = 1.09$ for the secondary KIE. The exponents, $n_{\text{DT}}^{(1)}$ and $n_{\text{DT}}^{(2)}$, for D/T ratios are 3.82 and 12.3, respectively. These values show significant deviations from the semiclassical limits, particularly on secondary KIEs, which can have greater computational errors because of the small free-energy difference. The deviations may be attributed to too large a secondary H/D effect.

Mixed isotopic Swain–Schaad exponent is often used to assess tunnelling:¹⁰⁴

$$n_{\text{DT}}^{\text{DD}} = \frac{\ln(k_{\text{H}}^{\text{H}}/k_{\text{T}}^{\text{H}})}{\ln(k_{\text{D}}^{\text{D}}/k_{\text{T}}^{\text{D}})} \quad (5.33)$$

and

$$n_{\text{DD}}^{\text{DT}} = \frac{\ln(k_{\text{H}}^{\text{H}}/k_{\text{H}}^{\text{T}})}{\ln(k_{\text{D}}^{\text{D}}/k_{\text{D}}^{\text{T}})} \quad (5.34)$$

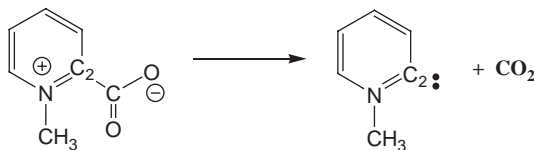
The first equation is the primary Swain–Schaad exponent, which describes the relationship between H/T primary KIE when the secondary position is occupied by a hydrogen atom with the D/T primary KIE when the secondary position is occupied by a deuterium isotope. The second equation describes a similar relationship for the secondary kinetic isotope effects. Values of the mixed Swain–Schaad exponents significantly greater than 3.3 are typically attributed to contributions from tunnelling,¹⁰⁵ and experimental studies showed that the secondary exponent is more sensitive than the primary exponent in this type of analysis.

For the proton-transfer reaction between nitroethane and acetate ion in water, we obtain a primary KIE Swain–Schaad exponent of $n_{\text{DT}}^{\text{DD}} = 3.31$ and a secondary exponent of $n_{\text{DT}}^{\text{DD}} = 3.47$. These results are close to the semiclassical limit, suggesting that tunnelling contributions are not significant for this reaction in aqueous solution. It will be interesting to examine the effects of the enzyme-active site on tunnelling and the Swain–Schaad exponents.^{98,99}

5.5.2 The Decarboxylation of N-Methyl Picolinate

The primary and secondary heavy atom kinetic isotope effects for the decarboxylation of N-methyl picolinate have been determined by Rishavy and Cleland.¹⁰⁶ QM/MM simulations were carried out for N-methyl picolinate, treated by the AM1 Hamiltonian, in a cubic box ($30 \times 30 \times 30 \text{ \AA}^3$) of 888 water molecules, described by the TIP3P potential.¹⁰ As usual, long-range electrostatic interactions were treated by the PME method for QM/MM potentials.⁹¹ 2 ns of classical dynamics simulations were performed followed by path integral PI-FEP/UM simulations, employing a total of 97 800 classical configurations

for each isotope (^{12}C , ^{13}C , ^{14}N , and ^{15}N), combined with 10 path-integral steps per classical configuration. Each quantised atom was described by 32 beads.



Solvent effects are significant, increasing the free-energy barrier by 15.2 kcal/mol to a value of 26.8 kcal/mol, which is accompanied by a net free energy of reaction of 24.7 kcal/mol. The large solvent effect is due to the presence of a positive charge on the pyridine nitrogen, which is annihilated in the decarboxylation reaction.

Both the $^{12}\text{C}/^{13}\text{C}$ primary KIE and the $^{14}\text{N}/^{15}\text{N}$ secondary KIE have been determined (Table 5.2), with the immediate adjacent atoms about the isotopic substitution site quantised as well. To our knowledge, we are not aware of any such simulations prior to our work for a condensed-phase reaction with converged secondary heavy isotope effects.¹⁰ This demonstrate the applicability and accuracy of the PI-FEP/UM method.¹⁰ Figures 5.2 and 5.3 depict the difference between the ^{12}C and ^{13}C quantum effects along the reaction path to illustrate the computational sensitivity using algorithem 1 (PI/UM) and algorithem 2 (PI-FEP/UM). First, the nuclear quantum effects are non-negligible even for bond cleavage involving two carbon atoms, which reduce the free-energy barrier by 0.45 kcal/mol (Figure 5.2). The computed intrinsic ^{13}C primary KIE, without including the reactant state quantum free energy term in eqn (5.16), is 1.0345 ± 0.0051 at 25 °C (Table 5.1). To emphasise the sensitivity of the computational result, the computed KIE is equivalent to a free-energy difference of merely 0.0187 kcal/mol, which is feasible by the use of free-energy perturbation/umbrella sampling techniques. For comparison, the experimental value is 1.0281 ± 0.0003 at 25 °C. For the secondary ^{15}N KIE, the PI-FEP/UM simulation yields an average value of 1.0083 ± 0.0026 , which may be compared with experiment (1.0070 ± 0.0003).¹⁰⁶ The agreement between theory and experiment is excellent, which provides support for a unimolecular decarboxylation mechanism in this model reaction.

Table 5.2 Computed and experimental primary $^{12}\text{C}/^{13}\text{C}$ and secondary $^{14}\text{N}/^{15}\text{N}$ kinetic isotope effects for the decarboxylation of N-methyl picolinate at 25 °C in water.

	$^{12}k/^{13}k$	$^{14}k/^{15}k$
Exp (120 °C)	1.0212 ± 0.0002	1.0053 ± 0.0002
Exp (25 °C)	1.0281 ± 0.0003	1.0070 ± 0.0003
PI/UM	1.035 ± 0.877	1.007 ± 0.886
PI FEP/UM	1.034 ± 0.005	1.008 ± 0.003

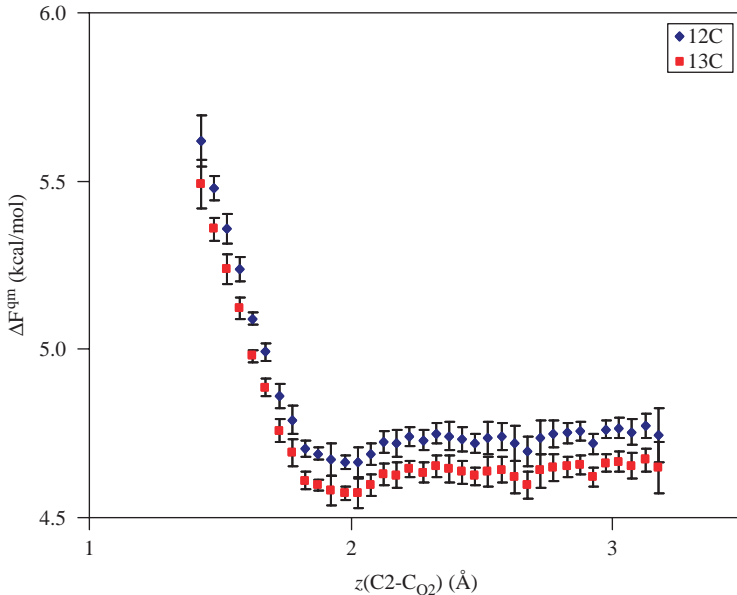


Figure 5.2 Nuclear quantum mechanical free energy corrections for the decarboxylation reaction of N methyl picolinate in aqueous solution from PI/UM calculations. Two separate path integral simulations are performed in this method.

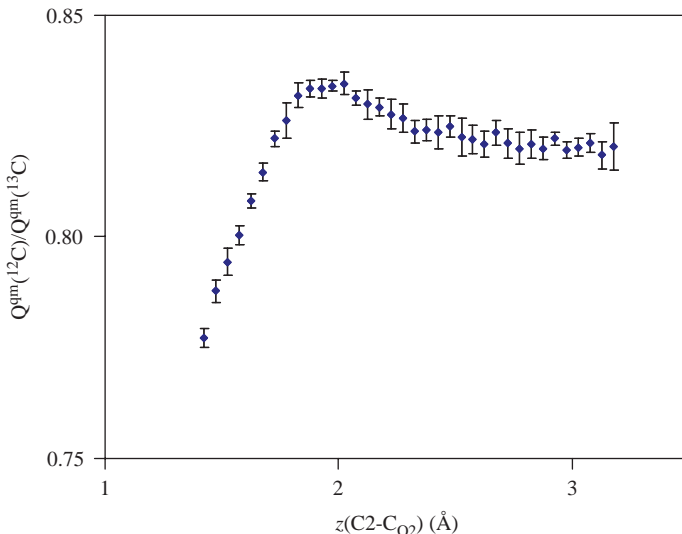


Figure 5.3 The ratio of the quantum mechanical partition functions between ^{12}C and ^{13}C isotopic substitutions at the carboxyl carbon position from the PI FEP/UM method. A single path integral simulation was performed.

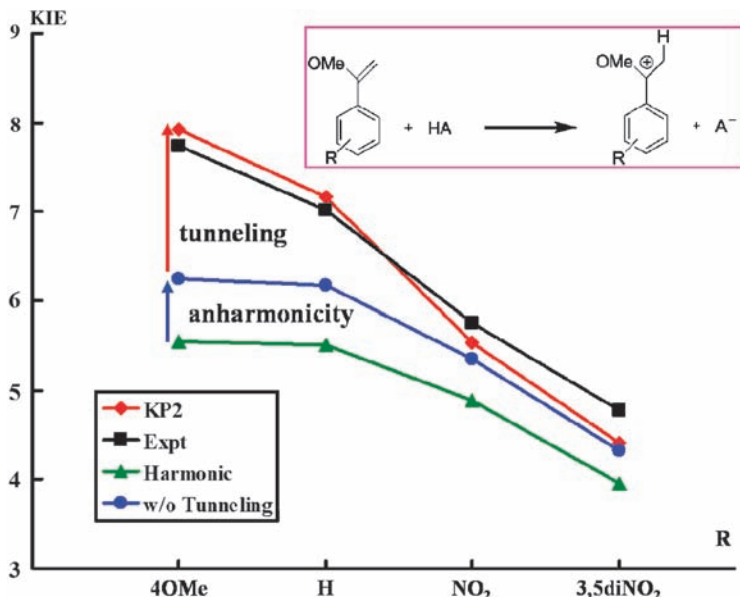


Figure 5.4 Computed primary (protium/deuterium) kinetic isotope effects for the proton transfer reaction from chloroacetic acid to substituted methoxy styrenes (colour lines) in water represented by a polarizable dielectric continuum model using the KP2/P20 theory (1 = 4 methoxy, 2 = H, 3 = 4 Nitro, and 4 = 3,5 dinitro groups).

5.5.3 Proton Transfer between Chloroacetic Acid and Substituted α -Methoxystyrenes

Richard and coworkers reported the product isotope effects of a series of interesting reactions involving the formation of carbocations from aryl-substituted (R) α -methoxystyrenes by proton transfer from chloroacetic acid.^{107,108} These product isotope effects have been converted into KIEs, and the effects of substituents on the observed KIEs have been determined by the KP2/P20 theory.⁷ Figure 5.4 shows the computed KIEs using only harmonic frequencies (zero-point energies) and the KP2/P20 values that include tunnelling and anharmonic corrections. Clearly, although the harmonic values correctly reproduced the experimental trend as a function of substituent electron-withdrawing power, the absolute values are significantly underestimated in comparison with experiment. Inclusion of anharmonicity for the description of the individual potential along each normal mode coordinate and tunnelling near the barrier top is critical to obtaining quantitative results for the computed KIEs.

5.6 Concluding Remarks

Centroid path integral methods have been presented for computing kinetic isotope effects for chemical reactions in aqueous solution. Three algorithms are

described: the first two algorithms involve discretised centroid path integral simulations to make quantum corrections to the classical free-energy path, and the third algorithm employs Kleinert variational perturbation theory at the second order in which the path integrals have been integrated analytically. In computing kinetic isotope effects, the first discretised simulation method is similar to the quantised classical path (QCP) approach developed by Hwang and Warshel, but we have developed a fast-converging sampling scheme, namely the bisection sampling method BQCP, by extending the method originally used by Ceperley and coworkers. In the second simulation algorithm, free-energy perturbation is employed by perturbing the light isotope mass into a heavier one in one single simulation, thereby avoiding the need of subtracting two quantum free energies with equally large fluctuations from two separate simulations. Thus, the accuracy in the computed KIEs is significantly improved. In Kleinert variational perturbation theory, analytical results are obtained when the potential surface is represented as a polynomial function, avoiding numerical convergence problems altogether. These methods are illustrated by computing the primary and secondary KIEs, analysing the results of the rule of geometric mean, and elucidating substituents effects. Three reactions have been considered: the proton abstraction of nitroethane by acetate ion, the proton-transfer reaction between substituted methoxystyrenes and chloracetic acid, and the decarboxylation of N-methyl picolinate, all of which are in water.

These examples illustrate the shortcomings of the two-separate simulation strategy of algorithem 1, typically used in the literature in path integral-based calculations of KIEs, and improved accuracy in the integrated centroid path integral-free energy perturbation and umbrella sampling scheme (algorithem 2) that uses a single simulation of a single isotope by perturbing its mass in the context of bisection sampling. Finally, the Kleinert variational perturbation theory gives an automated, numerical integration-free method for computing KIEs. The KP theory has the feature of exponentially and uniformly convergent such that the second-order perturbation (KP2) is sufficient to provide accurate results. An instantaneous normal mode approximation was made to extend the KP2 theory to multidimensional systems.

Acknowledgments

This work has been supported in part by the National Institutes of Health (grant number GM46736) and by a grant from the Office of Naval Research to develop integrated tools for computational chemical dynamics.

References

1. A. Kohen, H. H. Limbach (Eds.) *Isotope Effects in Chemistry and Biology*, Taylor & Francis Group, CRC Press, New York, 2005.
2. J. Pu, J. Gao and D. G. Truhlar, *Chem. Rev.*, 2006, **106**, 3140–3169.
3. J. Gao, S. Ma, D. T. Major, K. Nam, J. Pu and D. G. Truhlar, *Chem. Rev.*, 2006, **106**, 3188–3209.

4. V. L. Schramm, *Acc. Chem. Res.*, 2003, **36**, 588–596.
5. J. Gao and D. G. Truhlar, *Ann. Rev. Phys. Chem.*, 2002, **53**, 467–505.
6. H. Kleinert, *Path Integrals in Quantum Mechanics, Statistics, Polymer Physics, and Financial Markets*, 3rd edn ed. Singapore, World Scientific; 2004.
7. (a) K.-Y. Wong and J. Gao, *J. Chem. Phys.*, 2007, **127**, 211103. (b) K.-Y. Wong and J. Gao, *J. Chem. Theory Comput.*, 2008, **4**, 1409–1422.
8. D. T. Major and J. Gao, *J. Mol. Graph. Model.*, 2005, **24**, 121–127.
9. D. T. Major, M. Garcia-Viloca and J. Gao, *J. Chem. Theory Comput.*, 2006, **2**, 236–245.
10. D. T. Major and J. Gao, *J. Chem. Theory Comput.*, 2007, **3**, 949–960.
11. Y. Mo and J. Gao, *J. Comput. Chem.*, 2000, **21**, 1458–1469.
12. Y. Mo and J. Gao, *J. Phys. Chem. A*, 2000, **104**, 3012–3020.
13. J. Gao and Y. Mo, *Prog. Theor. Chem. Phys.*, 2000, **5**, 247–268.
14. J. Gao, M. Garcia-Viloca, T. D. Poulsen and Y. Mo, *Adv. Phys. Org. Chem.*, 2003, **38**, 161–181.
15. A. Warshel and M. Karplus, *J. Am. Chem. Soc.*, 1972, **94**, 5612–5625.
16. A. Warshel and M. Levitt, *J. Mol. Biol.*, 1976, **103**, 227–249.
17. A. Fernandez-Ramos, J. A. Miller, S. J. Klippenstein and D. G. Truhlar, *Chem. Rev.*, 2006, **106**, 4518–4584.
18. C. Alhambra, J. Gao, J. C. Corchado, J. Villa and D. G. Truhlar, *J. Am. Chem. Soc.*, 1999, **121**, 2253–2258.
19. C. Alhambra, J. Corchado, M. L. Sanchez, M. Garcia-Viloca, J. Gao and D. G. Truhlar, *J. Phys. Chem. B*, 2001, **105**, 11326–11340.
20. D. G. Truhlar, J. Gao, C. Alhambra, M. Garcia-Viloca, J. Corchado, M. L. Sanchez and J. Villa, *Acc. Chem. Res.*, 2002, **35**, 341–349.
21. M. Garcia-Viloca, J. Gao, M. Karplus and D. G. Truhlar, *Science*, 2004, **303**, 186–195.
22. S. Hammes-Schiffer, *Curr. Opin. Struct. Biol.*, 2004, **14**, 192–201.
23. R. P. Feynman and A. R. Hibbs, *Quantum Mechanics and Path Integrals*, McGraw-Hill, New York, 1965.
24. D. Chandler and P. G. Wolynes, *J. Chem. Phys.*, 1981, **74**, 4078–4095.
25. M. Sprik, M. L. Klein and D. Chandler, *Phys. Rev. B*, 1985, **31**, 4234–4244.
26. B. J. Berne and D. Thirumalai, *Ann. Rev. Phys. Chem.*, 1986, **37**, 401–424.
27. G. A. Voth, *Adv. Chem. Phys.*, 1996, **93**, 135–218.
28. N. Chakrabarti, T. Carrington Jr. and B. Roux, *Chem. Phys. Lett.*, 1998, **293**, 209–220.
29. D. Marx, M. E. Tuckerman and G. J. Martyna, *Comp. Phys. Commun.*, 1999, **118**, 166–184.
30. M. E. Tuckerman and D. Marx, *Phys. Rev. Lett.*, 2001, **86**, 4946–4949.
31. M. H. M. Olsson, P. E. M. Siegbahn and A. Warshel, *J. Biol. Inorg. Chem.*, 2004, **9**, 96–99.
32. J. Gao, K.-Y. Wong and D. T. Major, *J. Comput. Chem.*, 2008, **29**, 514–522.
33. J. K. Hwang, Z. T. Chu, A. Yadav and A. Warshel, *J. Phys. Chem.*, 1991, **95**, 8445–8448.

34. J. K. Hwang and A. Warshel, *J. Phys. Chem.*, 1993, **97**, 10053–10058.
35. J.-K. Hwang and A. Warshel, *J. Am. Chem. Soc.*, 1996, **118**, 11745–11751.
36. H. Kleinert, *Phys. Rev. D*, 1998, **57**, 2264.
37. W. Janke and H. Kleinert, *Phys. Rev. Lett.*, 1995, **75**, 2787.
38. M. J. Gillan, *Phys. Rev. Lett.*, 1987, **58**, 563–566.
39. G. A. Voth, D. Chandler and W. H. Miller, *J. Chem. Phys.*, 1989, **91**, 7749–7760.
40. J. Cao and G. A. Voth, *J. Chem. Phys.*, 1994, **101**, 6184–6192.
41. J. N. Gehlen, D. Chandler, H. J. Kim and J. T. Hynes, *J. Phys. Chem.*, 1992, **96**, 1748–1753.
42. M. Messina, G. K. Schenter and B. C. Garrett, *J. Chem. Phys.*, 1993, **98**, 8525–8536.
43. G. A. Voth, *J. Phys. Chem.*, 1993, **97**, 8365–8377.
44. R. F. Grote and J. T. Hynes, *J. Chem. Phys.*, 1981, **74**, 4465–4475.
45. M. J. Gillan, *Philos. Mag. A*, 1988, **58**, 257–283.
46. D. E. Makarov and M. Topaler, *Phys. Rev. E: Stat. Phys., Plasmas, Fluids, Relat. Interdiscip. Top.*, 1995, **52**, 178–188.
47. M. Messina, G. K. Schenter and B. C. Garrett, *J. Chem. Phys.*, 1995, **103**, 3430–3435.
48. G. Mills, G. K. Schenter, D. E. Makarov and H. Jonsson, *Chem. Phys. Lett.*, 1997, **278**, 91–96.
49. S. Jang, G. A. Voth, *J. Chem. Phys.* 2000, **112**, 8747–8757. Erratum: 2001. **8114**, 1944.
50. I. Feierberg, V. Luzhkov and J. Aqvist, *J. Biol. Chem.*, 2000, **275**, 22657–22662.
51. J. Villa and A. Warshel, *J. Phys. Chem. B*, 2001, **105**, 7887–7907.
52. M. H. M. Olsson, P. E. M. Siegbahn and A. Warshel, *J. Am. Chem. Soc.*, 2004, **126**, 2820–2828.
53. E. L. Pollock and D. M. Ceperley, *Phys. Rev. B*, 1984, **30**, 2555–2568.
54. D. M. Ceperley, *Rev. Mod. Phys.*, 1995, **67**, 279–355.
55. D. T. Major, D. M. York and J. Gao, *J. Am. Chem. Soc.*, 2005, **127**, 16374–16375.
56. D. T. Major and J. Gao, *J. Am. Chem. Soc.*, 2006, **128**, 16345–16357.
57. R. P. Feynman and H. Kleinert, *Phys. Rev. A*, 1986, **34**, 5080.
58. R. Giachetti and V. Tognetti, *Phys. Rev. Lett.*, 1985, **55**, 912.
59. T. D. Hone, J. A. Poulsen, P. J. Rossky and D. E. Manolopoulos, *J. Phys. Chem. B.*, 2008, **112**, 294–300.
60. J. A. Poulsen, G. Nyman and P. J. Rossky, *J. Chem. Theory Comput.*, 2006, **2**, 1482–1491.
61. B. Palmieri and D. Ronis, *Phys. Rev. E*, 2006, **74**, 061105.
62. D. F. Coker, S. Bonella, *Springer Series in Chemical Physics*, 2007, **83**, 321.
63. A. D. MacKerell Jr., D. Bashford, M. Bellott, R. L. Dunbrack, J. D. Evanseck, M. J. Field, S. Fischer, J. Gao, H. Guo, S. Ha, *et al.*: *J. Phys. Chem. B* 1998, **102**, 3586–3616.
64. J. W. Ponder and D. A. Case, *Adv. Protein Chem.*, 2003, **66**, 27–85.

65. J. Gao and X. Xia, *Science*, 1992, **258**, 631–635.
66. J. Gao, in *Rev. Comput. Chem.* ed. K. B. Lipkowitz, D. B. Boyd: VCH, 1995, 119–185. **vol 7**.
67. M. J. Field, P. Bash and A. M. Karplus, *J. Comput. Chem.*, 1990, **11**, 700–733.
68. J. Gao, *J. Phys. Chem.*, 1992, **96**, 537–540.
69. M. Freindorf and J. Gao, *J. Comput. Chem.*, 1996, **17**, 386–395.
70. I. H. Hillier, *Theochem.*, 1999, **463**, 45–52.
71. P. A. Bash, M. J. Field and M. Karplus, *J. Am. Chem. Soc.*, 1987, **109**, 8092–8094.
72. A. Warshel, *Ann. Rev. Biophys. Biomol. Struct.*, 2003, **32**, 425–443.
73. J. Gao, *J. Am. Chem. Soc.*, 1995, **117**, 8600–8607.
74. N. Wu, Y. Mo, J. Gao and E. F. Pai, *Proc. Natl. Acad. Sci. USA*, 2000, **97**, 2017–2022.
75. J. Gao, *ACS Symp. Ser.*, 1994, **569**, 8–21.
76. M. J. S. Dewar, E. G. Zoebisch, E. F. Healy and J. J. P. Stewart, *J. Am. Chem. Soc.*, 1985, **107**, 3902–3909.
77. J. J. P. Stewart, *J. Comp. Chem.*, 1989, **10**, 209–220.
78. M. Orozco, F. J. Luque, D. Habibollahzadeh and J. Gao, *J. Chem. Phys.*, 1995, **103**, 9112.
79. J. Gao, *Acc. Chem. Res.*, 1996, **29**, 298–305.
80. J. Gao, *J. Am. Chem. Soc.*, 1994, **116**, 9324–9328.
81. J. Gao and K. Byun, *Theor. Chem. Acc.*, 1997, **96**, 151–156.
82. M. Garcia-Viloca, D. G. Truhlar and J. Gao, *J. Mol. Biol.*, 2003, **327**, 549–560.
83. J. Aqvist, M. Fothergill and A. Warshel, *J. Am. Chem. Soc.*, 1993, **115**, 631–635.
84. J. Gao and M. A. Thompson, *Combined Quantum Mechanical and Molecular Mechanical Methods*, **vol 712**, American Chemical Society, Washington, DC, 1998.
85. A. J. Mulholland, *Theor. Comput. Chem.*, 2001, **9**, 597–653.
86. Y. Mo, Y. Zhang, J. Gao, *J. Am. Chem. Soc.* 1999, **121**, 5737–5742.
87. A. Warshel and R. M. Weiss, *Ann. N. Y. Acad. Sci.*, 1981, **367**, 370–382.
88. Y. Kim, J. C. Corchado, J. Villa, J. Xing and D. G. Truhlar, *J. Chem. Phys.*, 2000, **112**, 2718–2735.
89. T. V. Albu, J. C. Corchado and D. G. Truhlar, *J. Phys. Chem. A*, 2001, **105**, 8465–8487.
90. W. L. Jorgensen, J. Chandrasekhar, J. D. Madura, R. W. Impey and M. L. Klein, *J. Chem. Phys.*, 1983, **79**, 926–935.
91. K. Nam, J. Gao and D. M. York, *J. Chem. Theory Comput.*, 2005, **1**, 2–13.
92. M. P. Allen and D. J. Tildesley, *Computer Simulation of Liquids*, Oxford University Press, Oxford, 1987.
93. J. P. Valleau, G. M. Torrie, in *Modern Theoretical Chemistry*, vol 5, ed. B. J. Berne, Plenum, 1977, 169–194.

94. B. R. Brooks, R. E. Brucolieri, B. D. Olafson, D. J. States, S. Swaminathan and M. Karplus, *J. Comput. Chem.*, 1983, **4**, 187.
95. C. F. Baernasconi, *Acc. Chem. Res.*, 1992, **25**, 9.
96. F. G. Bordwell and W. J. Boyle Jr., *J. Am. Chem. Soc.*, 1972, **94**, 3907.
97. A. Kresge, *Can. J. Chem.*, 1974, **52**, 1897.
98. M. P. Valley and P. F. Fitzpatrick, *Biochemistry*, 2003, **42**, 5850–5856.
99. M. P. Valley and P. F. Fitzpatrick, *J. Am. Chem. Soc.*, 2004, **126**, 6244–6245.
100. M. Garcia-Viloca, C. Alhambra, D. G. Truhlar and J. Gao, *J. Chem. Phys.*, 2001, **114**, 9953–9958.
101. J. Bigeleisen, *J. Chem. Phys.*, 1955, **23**, 2264.
102. Huskey, in *Hydrogen-Transfer Reactions*, vol 4, ed. J. T. Hynes, J. P. Klinman, H. H. Limbach, R. L. Schowen, Wiley-VCH Verlag GmbH & Co. KgaA, 2006, 1285.
103. W. H. Saunders Jr, *J. Am. Chem. Soc.*, 1985, **107**, 164–169.
104. C. G. Swain, E. C. Stivers, J. F. Reuwer and L. J. Schaad, *J. Am. Chem. Soc.*, 1958, **80**, 558.
105. Y. Cha, C. J. Murray and J. P. Klinman, *Science*, 1989, **243**, 1325–1330.
106. M. A. Rishavy and W. W. Cleland, *Biochemistry*, 2000, **39**, 4569–4574.
107. W.-Y. Tsang and J. P. Richard, *J. Am. Chem. Soc.*, 2007, **129**, 10330–10331.
108. J. P. Richard and K. B. Williams, *J. Am. Chem. Soc.*, 2007, **129**, 6952–6961.

CHAPTER 6

Beyond Tunnelling Corrections: Full Tunnelling Models for Enzymatic C–H Activation Reactions

JUDITH P. KLINMAN

Departments of Chemistry and Molecular and Cell Biology, University of California, Berkeley, CA 94720, USA

6.1 Introduction to Enzymatic C–H Activation Reactions

The biological utilisation of energy from carbon-based metabolites is intimately linked to the enzymatic activation of C–H bonds, *via* proton, hydride and hydrogen-atom transfer mechanisms. An example of each type of reaction is shown in Scheme 6.1, with proton and hydride abstraction being found commonly in metabolic pathways (*e.g.*, glycolysis and fatty acid oxidation). Hydrogen-atom abstraction is generally a more specialised process, involving poorly activated substrates and enzymes that contain redox active metal or organic cofactors at their active sites.

6.1.1 Methods of Study

Early steady-state kinetic analyses of enzymes indicated the multistep nature of catalysis, as regards the involvement of both chemical intermediates and

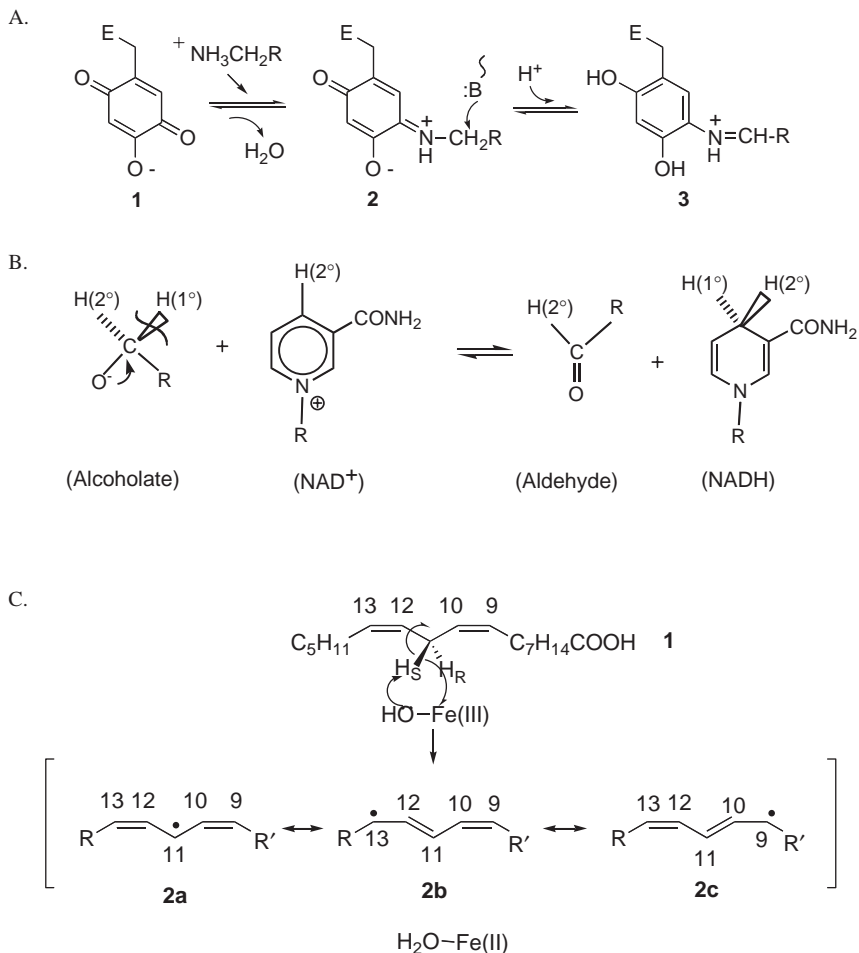
RSC Biomolecular Sciences

Quantum Tunnelling in Enzyme Catalysed Reactions

Edited by Rudolf K. Allemann and Nigel S. Scrutton

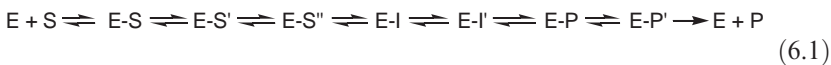
© Royal Society of Chemistry 2009

Published by the Royal Society of Chemistry, www.rsc.org



Scheme 6.1 Examples from this laboratory of enzymatic activation of C–H via proton, hydride, and hydrogen atom pathways. (A) The oxidation of amines by topa quinone in the copper amine oxidases. The proton abstraction step involves conversion of the substrate Schiff base to the product Schiff base *via* a proton abstraction catalysed by an active site aspartate (ref. 1). (B) The oxidation of a deprotonated alcohol (alcoholate) *via* hydride transfer to NAD^+ , catalysed by alcohol dehydrogenase (ref. 2). (C) The oxidation of the fatty acid, linoleic acid, by the enzyme soybean lipoxygenase (ref. 3).

protein conformational changes subsequent to formation of the enzyme substrate complex:⁴



where, E-S, E-I, and E-P represent multiple protein conformational states containing bound substrate, a chemical intermediate and product, respectively. The resulting complexity has necessitated the introduction of methods for characterising the fundamental properties of enzymatic hydrogen transfer independent of other rate-contributing steps. A major tool for the study of hydrogen transfer is the comparison of the reaction dynamics for each of its three isotopes: protium, deuterium and tritium. In fact, the kinetic isotope effect (KIE), which measures relative rates for H-abstraction, k_H/k_D , k_H/k_T , k_D/k_T , has been a mainstay of reaction mechanism studies in both chemistry and biochemistry.⁵

In early years, the experimental focus in enzyme mechanisms was on using the KIE to distinguish whether hydrogen transfer was contributing to the measured rate of a reaction. In general, the relationship of an observed to an intrinsic KIE on a single step is written in the form:⁶

$$\text{KIE}_{(\text{obs})} = \frac{(\text{KIE}_{(\text{int})} + C)}{(1 + C)} \quad (6.2)$$

where C measures the ratio of the rate constant for the C–H abstraction step to other rate constants and is referred to as the kinetic commitment. Tools for increasing the contribution of the H-transfer step to the measured rate have been frequently utilised, for example by studying the enzymatic reaction of interest at a nonoptimal pH, using an alternative substrate that makes the H-transfer step more rate determining or by applying site-specific mutagenesis (cf. ref. 7). Comparison of the magnitude of isotope effects on k_{cat}/K_m (which measures all steps from substrate binding up to and including the first irreversible step) to k_{cat} (which measures steps subsequent to formation of the E–S complex up through the regeneration of free enzyme) can be extremely useful: when both external and internal commitments have been eliminated, the expectation is that the observed KIEs on both k_{cat}/K_m and k_{cat} converge toward a common value (cf. ref. 8). Comparison of steady-state to presteady-state rates and KIEs has, in a similar vein, been used to infer the degree to which the H-transfer step is rate determining.⁹ Finally, it is possible to calculate the $\text{KIE}_{(\text{int})}$ from the $\text{KIE}_{(\text{obs})}$ when two pairs of KIEs can be measured, *i.e.* by contrasting k_H/k_D to k_H/k_T or k_D/k_T to k_H/k_T . As recognised by Northrop,¹⁰ subtracting unity from each measured KIE eliminates the commitment term and relates the measured KIEs to their intrinsic values, *e.g.*, for the k_H/k_D and k_H/k_T pair:

$$\frac{(k_H/k_{D(\text{obs})} - 1)}{(k_H/k_{T(\text{obs})} - 1)} = \frac{(k_H/k_{D(\text{int})} - 1)}{(k_H/k_{T(\text{int})} - 1)} \quad (6.3)$$

The Swain–Schaad expression relates the magnitude of the individual intrinsic KIEs to one another, *e.g.*, for the k_H/k_D and k_H/k_T pair:

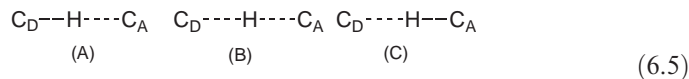
$$[k_H/k_{D(\text{int})}]^{1.44} = k_H/k_{T(\text{int})} \quad (6.4)$$

In this manner, eqn (6.3) has only a single unknown, allowing the magnitude of the intrinsic KIE to be calculated from experimentally accessible KIEs. As will be discussed below, the Swain–Schaad relationship can show deviations from semiclassical behaviour when tunnelling is present.¹¹ However, experimental observation of this behaviour has been limited to secondary KIEs, with little or no accompanying deviation in the primary KIEs (cf. ref. 12 and refs therein). The latter property makes it possible to utilise eqns (6.3) and (6.4) to calculate intrinsic primary isotope effects even in the event that tunnelling contributes to the reaction under study.^{12,13}

6.1.2 The Semiclassical Origin of the Kinetic Isotope Effect

Once the intrinsic hydrogen KIE has been isolated kinetically, the properties of this value become of considerable mechanistic significance. One of the main themes of this book concerns the fundamental properties of C–H activation in the condensed phase, in particular the movement away from a classical to a quantum-mechanical (QM) understanding of this hydrogen transfer. The first QM “correction” arises from the differences in vibrational frequencies for isotopically labelled bonds, illustrated in Figure 6.1(A). According to the resulting semiclassical theory for KIEs, ground-state vibrational differences among H, D and T establish the maximum kinetic difference in rate among the isotopic bonds, which in the case of k_H/k_D for C–H abstraction is *ca.* 7.

This KIE is formulated as arising from the conversion of a ground-state stretching vibration to a translation at the transition state, such that the TS has one less degree of vibrational freedom than the ground state.¹⁴ Very early theoretical analyses were primarily focused on how the observed KIE could fall *below* the maximum of 7. This led to a model put forth by Westheimer,¹⁵ in which he showed that residual vibrational modes at the position of the transition state could contribute to and cancel the loss of a ground-state stretching mode, leading first, to reduced values for the experimental KIE and second, the prediction that the magnitude of the measured KIE would reflect the position of the transition state. According to the Westheimer model, a maximum KIE was anticipated for a symmetrical TS in which the transferred hydrogen resides halfway from the H-donor to acceptor [(B) in eqn (6.5)], whereas asymmetric transition states in which the transferred hydrogen retains more bonding either to the donor or acceptor atoms [(A) and (C) in eqn (6.5)] are predicted to have KIEs below the maximum value:



This model, in which the magnitude of the measured KIE implies a TS structure, persisted for many years. It should be noted that there are experimental examples in which a plot of the magnitude of an observed KIE has been

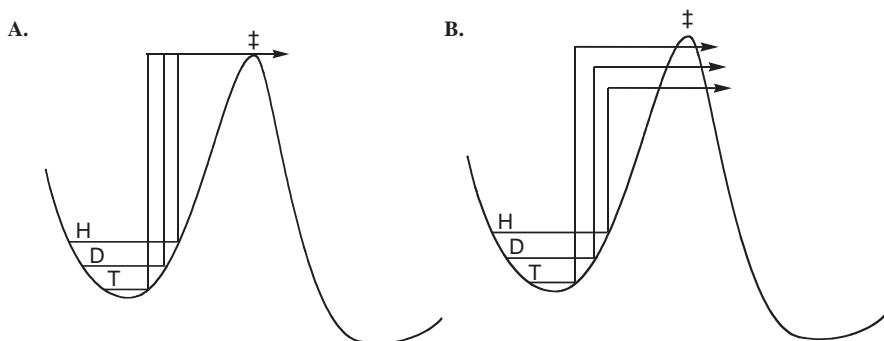


Figure 6.1 Reaction profiles for hydrogen transfer. **A.** The origin of the semiclassical hydrogen isotope effect, arising from differences in zero point energy for protium, deuterium, and tritium. **B.** Illustration of the crossing of the barrier below the transition state, where this occurs in an isotope dependent manner ($H > D > T$).

found to correlate with reaction driving force, in apparent accord with the general trend predicted by the Westheimer model.⁵ However, in the context of hydrogen tunnelling, such experimental trends cannot provide detailed information regarding “the position of the hydrogen within a semiclassical transition-state structure” and must be reconsidered in the context of quite different quantum-mechanical models.

6.2 Detection of Hydrogen Tunnelling in the Context of a “Tunnelling Correction”

6.2.1 The Bell Correction

There has been a long-standing recognition that quantum-mechanical tunnelling can contribute to chemical reactions at very low temperatures: in the absence of thermal activation at temperatures near absolute zero, the only recourse for reaction dynamics may involve tunnelling through the reaction barrier. Bell, in his classic text, “The Tunnel Effect in Chemistry”,¹⁶ emphasised the fact that tunnelling may also be expected to participate in a reaction near room temperature and that this behaviour would have important consequences for the relative rates at which protium, deuterium and tritium would react. According to the formalism introduced by Bell, the quantum correction is defined as Q_L , where Q is the ratio of the rate that occurs by tunnelling divided by the rate that occurs purely by thermal activation and the subscript L, pertains to protium, deuterium or tritium.

$$Q_L = h\nu^\ddagger / 2k_B T / \sin(h\nu^\ddagger / 2k_B T) \quad (6.6)$$

The key determinant of the magnitude of Q is v^\ddagger , the reaction coordinate frequency, which is dependent on mass; h is Planck's constant; k_B is the Boltzmann's constant and T is temperature. The expression in eqn (6.6) is referred to as the truncated Bell expression, with an expanded version available (refs. 16,17).

The observed rate constant, k_{obs} , is subsequently formulated as the product of the semiclassical rate, k_{sc} and the tunnelling correction:

$$k_{\text{obs}} = Q k_{\text{sc}} \quad (6.7)$$

The value of Q inflates quite rapidly with the value of v^\ddagger , such that when $v^\ddagger=1000\text{i}$, $Q > 2$ at room temperature. A physical picture that incorporates the tunnelling correction to the rate is given in Figure 6.1(B), where all three isotopes of hydrogen are shown to cross the reaction barrier at some point below the classical barrier. As the smallest isotope, with the attendant largest wavelength, protium can cross the barrier at a wider point than either deuterium or tritium, giving rise to a greater contribution of Q to the observed rate. The immediate impact of this property is that the presence of Q inflates the predicted value for the deuterium KIE above its semiclassical limit of 7 (with values in the range of 12 or possibly greater possible for C–H bond cleavage reactions).

The expression in eqn (6.7) can be expanded somewhat, to illustrate the respective origins of the rate effects:

$$k_{\text{obs}} = \gamma(T) e^{-\Delta G^\ddagger / RT} \quad (6.8)$$

where $\gamma(T)$ is comprised of $r(T)$, the dynamical recrossing of the barrier, and $\kappa(T)$, the actual tunnelling correction.¹⁸ Equation (6.8) illustrates the “pre-exponential” property of the tunnelling correction, with the expectation that most of the rate effects arise from the ΔG^\ddagger term. Equation (6.8) has formed the basis of innumerable treatments of hydrogen transfer in condensed phase and is the starting point for quite sophisticated methods such as the variational transition-state theory developed by Truhlar and his associates.^{19,20} One of the aspects of the formulation put forth by Bell is that it treats the reaction barrier as static. There has been increasing recognition that this is likely to be a very poor approximation in the case of enzyme-catalysed hydrogen-transfer reactions.

6.2.2 Implications for Swain–Schaad Relationships

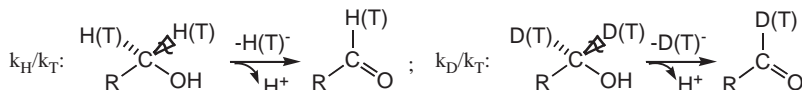
The Swain–Schaad relationship, as originally defined,²¹ is given in eqn (6.4). This relationship derives from the difference in masses among the three isotopes of hydrogen, making its origin analogous to the impact of isotopic substitution on the zero-point energy of the C–L bond (which is the source of the semi-classical kinetic isotope effect itself), Figure 6.1(A). The Swain–Schaad

relationship can be expressed in terms of any two pairs of isotopes and is commonly rewritten in a form in which tritium, rather than deuterium, is the isotope of reference:

$$[k_D/k_{T(\text{int})}]^{3.26} = [k_H/k_{T(\text{int})}] \quad (6.9)$$

The anticipated impact of a tunnelling correction on the Swain–Schaad relationship can be viewed in the context of Figure 6.1(B), where the relative ease with which the transferred particle crosses below the top of the barrier is shown as $H > D > T$. The eqn (6.9) offers a particularly straightforward way to understand this impact of tunnelling, since the common-isotope effect, tritium, is the one that tunnels the least and crosses the barrier closest to the top.¹¹ In this instance, deviations from semiclassical behaviour are seen to be reflected in a faster rate of tunnelling for protium than deuterium, with the prediction that the exponent of 3.26 will become inflated relative to the situation where tunnelling is absent.

One of the prime experimental systems for examining tunnelling deviations from the Swain–Schaad relationship has been the dehydrogenase reactions that utilise the nicotinamide cofactors, NADH or NADPH.^{11,22,23} Studies of these systems have focused on multiply labelled substrates from which both primary and secondary D/T and H/T isotope effects can be measured, illustrated below for the oxidation of an alcohol:



where the primary kinetic isotope effect reflects the bond undergoing cleavage and the secondary isotope effect refers to the hydrogen that remains affixed to the reacting carbon. Two key results that emerged from the measured isotope effects were (i) the presence of enormous inflations in the exponents relating the secondary k_H/k_T and k_D/k_T measurements (Table 6.1) and (ii) very small (if any) deviation within experimental error, for the primary kinetic isotope effects.^{7,11,22} One fortuitous feature regarding the interpretation of the secondary isotope effects is that the degree of breakdown for the Swain–Schaad relationship is predicted to go in opposite directions for the separate events of kinetic complexity *vs.* hydrogen tunnelling (Table 6.2).^{10,11}

The results in Table 6.1 constituted some of the earliest evidence for hydrogen tunnelling in enzyme-catalysed reactions. It should be emphasised that these data were initially taken as a confirmation of the presence of a “tunnelling correction” in enzyme-catalysed hydride-transfer reactions, with the deviant properties at the secondary hydrogen arising from a coupling of motion between the primary, tunnelling hydrogen and the secondary position. It was further postulated that the absence of a breakdown from the Swain–Schaad relationship for the transferred hydrogen was likely due to the much larger size of the primary isotope effect and a resulting reduced sensitivity to deviations from semiclassical

Table 6.1 Summary of exponents relating experimental secondary isotope effects in the alcohol dehydrogenase reaction.

Enzyme source	Exponent	Ref
Yeast alcohol dehydrogenase	10	[11]
Horse liver alcohol dehydrogenase, L57F mutant	8.5	[7]
<i>B. stearothermophilus</i> alcohol dehydrogenase	15	[22]

Table 6.2 Opposite expected trends in the magnitude of exponents relating secondary hydrogen isotope effects under conditions of hydrogen tunnelling *vs.* kinetic complexity.

Equation in text	Exponent		
	Semiclassical	Tunnelling	Kinetic complexity
(6.4)	1.44	< 1.44	> 1.44
(6.9)	3.26	> 3.26	< 3.26

behaviour. As will be discussed below (Section 6.3.1), both interpretations require re-examination in the context of the current availability of a larger body of experimental data that implicates full tunnelling behaviour in enzyme reactions.

6.2.3 Implication for Arrhenius Behaviour

It has been generally accepted that tunnelling will dominate a hydrogen-transfer reaction as the temperature is lowered toward absolute zero. Under this condition of vanishing thermal energy, the only option for the transferred particle is to move through rather than over the barrier. This process is illustrated *via* an Arrhenius plot, Figure 6.2, for the transfer of protium; note that the slope approaches zero at very low temperatures. In the context of Figure 6.2, a transition temperature (T_c) can be defined, above which the particle's behaviour is altered from moving through the barrier to proceeding over the top of the barrier (cf. ref. 23). It is illustrative to compare the properties of protium to deuterium and tritium at reduced temperatures. Given the strong dependence of tunnelling on the mass of the transferred particle, the temperature at which tunnelling begins to dominate the reaction path is lower for deuterium than protium and lower yet for tritium. This can be restated as $T_{c(H)} > T_{c(D)} > T_{c(T)}$.

Within the model represented in Figure 6.2, the actual behaviour that can be expected for each isotope will be a function of the temperature under consideration. At very low temperatures where there is little or no thermal activation available for any of the isotopes, all three particles will undergo activationless tunnelling [$E_{a(H)} = E_{a(D)} = E_{a(T)} = 0$]. Under these conditions the isotope effect on the intercept (*e.g.*, A_H/A_D) will be equal to the observed

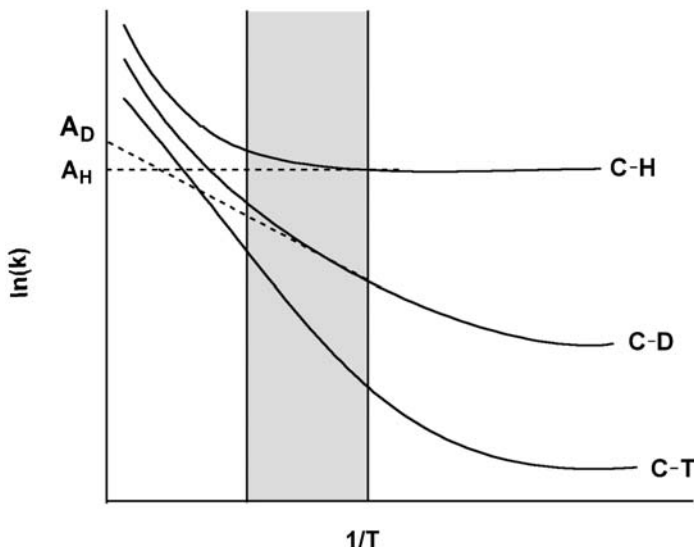


Figure 6.2 Arrhenius plots for the cleavage of a C–L bond over a very large temperature range. Three temperature limits are illustrated. In the high temperature limit (classical behaviour), all lines extrapolate to approximately the same point on the Y axis ($A_1/A_2 \approx 1$). In the low temperature limit (full tunnelling) all slopes go to zero, which, together with very large KIEs, produces $A_1/A_2 \gg 1$. The intermediate temperature (gray bar) represents the experimentally accessible range. Due to an isotope dependence of the curvature in the Arrhenius plots within this regime, tangents to the individual lines produce slopes in the order of $E_a(T) > E_a(D) > E_a(H)$, leading to $A_1/A_2 \ll 1$.

isotope effect k_H/k_D , which itself is expected to be huge. At the other extreme of very high temperatures, as the excited-state vibrational levels for the X–H bond become extensively populated, the differences among the isotopes begin to vanish leading to a ratio of $A_H/A_D \sim 1$.

The situation becomes particularly interesting near room temperature, conditions where biological catalysts are generally studied. The shaded bar in Figure 6.2 is meant to indicate an experimentally accessible range for the study of proteins, e.g. from 5 to 50 °C. The behaviour in Figure 6.2 predicts that the degree of curvature within the Arrhenius plot will be isotope dependent, with more tunnelling contributing to the reaction of protium in relation to deuterium and tritium. This can be seen mathematically by drawing a tangent to each curve within the experimentally accessible temperature range. This produces a trend in which $E_{a(H)} < E_{a(D)} < E_{a(T)}$. Extrapolating each line back to the intercept produces a phenomenological crossing of the line for the heavy isotope by the line for the light isotope, resulting in $A_H < A_D < A_T$. This produces the prediction of $A_1/A_2 \ll 1$ under the condition of an isotope-dependent tunnelling correction (where A_1 represents the light isotope and A_2 represents the heavy isotope).

Along with Swain-Schaad deviations, early evidence for tunnelling in enzyme-catalysed reactions also came from analyses of temperature-dependent isotope effects. The first such analysis, in which conditions were carefully established to isolate the C–H bond-cleavage step from other partially rate-determining steps, was for the proton-abstraction reaction catalysed by the copper and topa quinone containing enzyme bovine serum amine oxidase²⁴ (cf. the general mechanism in Scheme 6.1(A)). The fact that the magnitude of the observed KIEs was in excess of values predicted from a semiclassical model, Figure 6.1(A), provided an initial indication that hydrogen tunnelling was contributing to the reaction path. The subsequent analysis of the KIEs as a function of temperature indicated values for $A_1/A_2 \ll 1$, Table 6.3.

The most transparent interpretation for the source of $A_1/A_2 \ll 1$ in bovine serum amine oxidase, as well as many of the other enzyme reactions listed in Table 6.3, was that tunnelling was moderate, with its presence contributing a mass-dependent “correction” to the rate. This seemingly straightforward interpretation was later challenged by Bruno and Bialek,²³ who showed that it was possible to analyse the available data for bovine serum amine oxidase according to an alternative model in which H, D and T were all assumed to move through the barrier *via* quantum-mechanical tunnelling. According to the Bruno and Bialek model, the origin of the temperature dependence of the KIEs was the shorter wavelength for D (or T) in comparison to H. For all isotopes, it was proposed that the initial distance between the H-donor and acceptor was too long for effective wavefunction overlap, consistent with X-ray structural analyses of proteins in complexation with substrates or substrate analogues where distances of 3.2 to 3.5 Å are commonly observed between a carbon H-donor and the H-acceptor. By contrast, theoretical calculations indicate that protium tunnelling requires the distance between heavy atoms to be reduced to *ca.* 2.7 to 2.8 Å (cf. ref. 29). Within a protein-active site, the requisite reduction in interatomic distances can be achieved *via* the introduction of a “gating” or distance sampling mode. A key feature of the Bruno and Bialek model was the recognition that the distance reduction for effective wavefunction overlap is mass dependent, with the shorter wavelength isotopes, D and T, requiring a closer approach between the donor and acceptor atoms. This property can be restated in terms of the mass dependence for the energy barrier that controls gating, E_x , where $E_{x(T)} > E_{x(D)} > E_{x(H)}$. It is remarkable how well this early

Table 6.3 Examples of enzyme reactions in which the isotope effect on the Arrhenius prefactor, A_1/A_2 , is less than unity.

System	KIE ^a	A_1/A_2	Ref.
Bovine serum amine oxidase	(H/T) 35	(A_H/A_T) 0.12	[24]
Monoamine oxidase	(H/T) 20	(A_H/A_T) 0.13	[25]
Glucose oxidase	(D/T) 2.2	(A_D/A_T) 0.57	[26]
Galactose oxidase	(H/D) 16	(A_H/A_D) 0.25	[27]
Methylmalonyl CoA mutase	(H/D) 36	(A_H/A_D) 0.08	[28]

^aAt or near room temperature

reassessment of the properties for H-transfer in condensed phase has held up in the face of new data and theory for H-transfer in condensed phase (see Sections 6.3 and 6.4, below).

6.3 Nonclassical Behaviour that Fails to Conform to the Tunnelling Correction

6.3.1 Swain–Schaad Relationships

The hydride-transfer reaction, catalysed by the nicotinamide cofactor-dependent alcohol dehydrogenases, has provided some of the most compelling evidence for a breakdown from the predicted mass dependence among multiple isotope effects within a semiclassical Swain–Schaad framework. As introduced in Section 6.2 above and summarised in Table 6.2, the experimentally observed Swain–Schaad breakdowns have been restricted to secondary KIEs. A prominent feature of these measurements is that (due to the ease of synthesis) D/T secondary KIEs have been measured under conditions of deuterium transfer from donor to acceptor, with the corresponding secondary H/T KIE reflecting protium movement between the heavy atoms. Within a tunnelling correction model, where tunnelling is predicted to be more dominant for the lighter isotope, the degree of departure from semiclassical behaviour is expected to reside within the H/T measurement. In fact, in the original publications it was stated that the experimental D/T KIEs could be used to approximate the “position of the semiclassical transition state”, with deviations from this interpretation residing primarily within the H/T measurements.

Over a period of approximately a decade, a very large number of Swain–Schaad relationships were collected using three paradigmatic alcohol dehydrogenases, the original yeast alcohol dehydrogenase for which tunnelling was first detected (YADH),¹¹ horse liver alcohol dehydrogenase (HLADH),⁷ and a thermophilic alcohol dehydrogenase, (ht-ADH).²² In all three systems, the impact of perturbations in substrate and enzyme structure or reaction conditions was interrogated. In the case of YADH, the properties of a series of *para*-substituted benzyl alcohols were contrasted, in order to assess the impact of the reaction driving force on tunnelling behaviour. Using the cloned and expressed HLADH, a series of mutants was prepared, with a particular focus on the valine (203) that resides behind C-4 of the nicotinamide ring of bound cofactor. Finally, for ht-ADT, the effects of changing temperature were studied. The impact of perturbations on the magnitude of the secondary k_H/k_T and k_D/k_T and the exponent that relates these values have been summarised in Table 6.4 for YADH and HLADH.

One of the surprising features of the data in Table 6.4 is that, contrary to expectation, the magnitude of the secondary H/T is found to be independent of either the enzyme source or the nature of the imposed perturbation, yielding an average value of 1.34 ± 0.01 .³⁰ The trend in the value of the exponent from a high of 10.2 toward the semiclassical limit is seen to reside exclusively in the

Table 6.4 Magnitude of secondary H/T kinetic isotope effects (protium in the cleaved position) and D/T isotope effects (deuterium in the cleaved position) for yeast alcohol dehydrogenase (YADH) and horse liver alcohol dehydrogenase (HLADH).

Enzyme ^a	$\alpha 2^\circ k_H/k_T^a$	$\alpha 2^\circ k_D/k_T^a$	EXP ^b	Ref.
YADH, WT (p H) ^c	1.35 (0.015)	1.03 (0.006)	10.2 (2.4)	[11]
YADH, WT (p Cl) ^c	1.34 (0.01)	1.03 (0.010)	9.9 (4.2)	[30]
HLADH, L57F	1.318 (0.007)	1.033 (0.004)	8.5 (1)	[7]
HLADH, F93W	1.333 (0.004)	1.048 (0.004)	6.3 (0.5)	[7]
HLADH, V203A	1.316 (0.006)	1.058 (0.004)	4.9 (0.3)	[31]
HLADH, L57V	1.332 (0.003)	1.065 (0.011)	4.55 (0.75)	[7]
HLADH, V203L	1.38 (0.005)	1.074 (0.004)	4.5 (0.2)	[31]
HLADH, WT ^d	1.335 (0.003)	1.073 (0.008)	4.1 (0.44)	[7]
HLADH, ESE ^d	1.332 (0.004)	1.075 (0.003)	3.96 ((0.16))	[7]
HLADH, V203A:F93W	1.325 (0.004)	1.075 (0.004)	3.9 (0.2)	[31]
HLADH, V203G	1.358 ((0.007))	1.097 (0.007)	3.3 (0.2)	[31]
YADH WT (p MeO) ^c	1.34 (0.04)	1.12 (0.02)	2.78 (0.82)	[30]

^aReported values \pm the standard errors.

^bThe error was calculated as follows:

$$\text{error} = \exp\left[\{\delta \ln(k_H/k_T)\}/\ln(k_H/k_T)\}^2 + \{\delta \ln(k_D/k_T)\}/\ln(k_D/k_T)\}^2\right]^{1/2}$$

^cThese experiments used benzyl alcohols with either H, Cl, or MeO substituents in the *para* position of the ring.

^dH transfer may not be fully rate determining for these two enzyme forms, leading to a somewhat reduced value for EXP.

magnitude of the D/T measurements. When the exponent is greatly inflated away from its semiclassical value, the D/T measurement is anomalously small. As the size of the D/T KIE rises, the value of the exponent approaches its semiclassical limit. *What is remarkable about these data is that they cannot be explained by either a semiclassical model for C–H activation or by a Bell-type tunnel correction in which deviations from semiclassical behaviour are expected to be greatest under conditions of protium transfer* (cf. refs. 2,32).

6.3.2 Arrhenius-Behaviour Deviations

In recent years, an increasingly large number of enzyme reactions have revealed an isotope dependence for their Arrhenius behaviour that introduces the same conundrum as the aggregate data for secondary isotope effects in the alcohol dehydrogenase family of reactions, *i.e.* experimentally observed data that cannot be rationalised by either a semiclassical model for C–H activation or *via* the application of a tunnelling correction. The specific experimental observation is apparent energies of activation for cleavage of both the light and heavy isotopes of hydrogen that are either very similar or identical, *e.g.* $E_{a(D)} - E_{a(H)} \cong 0$ at or

near room temperature. These enthalpies of activation are generally obtained from tangents to individual Arrhenius lines in an experimentally accessible temperature regime and then extrapolated back to the y -axis to yield values for A_1/A_2 that are greater than unity. In some instances, competitive KIEs have been measured and the \ln KIE plotted directly as a function of reciprocal temperature to obtain ΔE_a and A_1/A_2 . The observation of temperature-independent KIEs has now been seen for enzymes that activate hydrogen *via* hydride ion, proton, or hydrogen-atom abstraction, producing a diagnostic for anomalous behaviour that goes beyond the Swain–Schaad deviations, which thus far have been restricted to the alcohol dehydrogenases. A partial summary of the enzyme systems that display temperature-independent KIEs at or near room temperature is given in Table 6.5.

It is always important to keep in mind the possible introduction of more than one rate-limiting step as an enzyme system is investigated at variable temperatures. For each of the studies listed in Table 6.5, considerable care was taken to establish that H-transfer was fully rate limiting under the experimental conditions. It is, additionally, reassuring that the data in Table 6.5 were collected under greatly varying experimental conditions that included steady-state and single-turnover kinetics, as well as *via* the calculation of intrinsic isotope effects from experimental pairs of kinetic isotope effects (cf. Section 6.1.1 above). The surprising and new property of temperature-independent isotope effects in enzyme-catalysed reactions has been dominantly observed using a native form of enzyme operating on its preferred substrate under optimal reaction conditions. By contrast, the vast majority of C–H abstraction reactions conducted in solution show temperature-dependent KIEs, often with the properties expected under conditions of moderate tunnelling. *This raises the highly provocative and important question: what properties of an enzyme-active site are capable of producing temperature-independent KIEs.* When coupled with the unexpected properties of the enzymatic secondary D/T and H/T KIEs (Table 6.4), the available data for enzyme-based reactions have necessitated the introduction of alternative physical models and mathematical treatments that are capable of accommodating the experimental observations.

Table 6.5 Illustrative examples of enzyme systems that display nearly temperature-independent primary kinetic isotope effects.

Enzyme	k_H/k_D , 25 °C	A_H/A_D	Ref.
Soybean lipoxygenase	81	18	[3]
High temperature alcohol dehydrogenase	3.2	2.2	[22]
Peptidylglycine α hydroxylating mono oxygenase	10	5.9	[12]
Methylamine dehydrogenase	17	13	[33]
Trimethylamine dehydrogenase	4.6	7.8	[34]
Sarcosine dehydrogenase	7.3	5.8	[35]
Acyl CoA desaturase	23	2.2	[36]
Dihydrofolate reductase	3.5	4.0	[37]
Choline oxidase	11	11	[38]

6.4 Full Tunnelling Behaviour under Physiological Conditions

6.4.1 Formalising H-transfer in the Context of Electron Tunnelling

The recognition of a similar physical underpinning for both hydrogen and electron transfer has been the single most important feature in advancing theories for C–H activation in enzyme-catalysed reactions. Although the mass for hydrogen is *ca.* 1800-fold larger than for the electron, the calculated de Broglie wavelengths for hydrogen and electron of *ca.* 0.5 and 20 Å, respectively, are similar to the distances these particles are expected to be transferred between their donor and acceptor atoms.¹¹ With a resulting focus on wavefunction overlap as the primary determinant of reactivity, the Marcus theory of electron transfer^{39,40} provides an excellent starting point for understanding the properties of the enzyme reactions summarised in Table 6.5.

6.4.2 A Simple Physical Model for H-tunnelling

The formalism put forth by Kuznetsov and Ullstrup in 1999⁴¹ and modified by Knapp and Klinman in 2002³ has been particularly useful in rationalising the properties of H-transfer. Focusing on nonadiabatic reactions, for which there is relatively small coupling between reactants,⁴² it is possible to put forth the following equation as a context to understand the rate of H-tunnelling:

$$k_{tun} = (\text{Const.}) \exp \left\{ \frac{-(\Delta G^\circ + \lambda)^2}{(4\lambda RT)} \right\} \exp^{-m_H \omega_H r_H^2 / 2\hbar} \quad (6.10)$$

As written, the reaction rate is proportional to two exponentials, with the first being the Marcus term advanced to describe the barriers to electron transfer, and the second the Franck–Condon expression for wavefunction overlap between H-donor and acceptor. The proportionality factor (Const. in eqn (6.10) is an electronic coupling that appears as a pre-exponential term. Note that the expression in eqn (6.10) represents reaction from the zero-point vibrational levels in the reactant and product wells; a treatment that involves excited-state vibrational levels can be found in ref. 3. The first exponential in eqn (6.10), the Marcus term, shows that both reaction driving force (ΔG° , a thermodynamic parameter) and environmental reorganisation (λ , a kinetic parameter) will influence barrier penetration by hydrogen. The dependence on the reaction driving force comes from the fact that tunnelling can only occur from matched, quantised states. If the reaction under study has an equilibrium constant that is either endergonic or exergonic, energy must be added to the system to achieve transient degeneracy between the ground-state vibrational levels of the reactant and product wells. Once degeneracy is achieved, the wavelength for hydrogen in the donor well can move to the acceptor well with

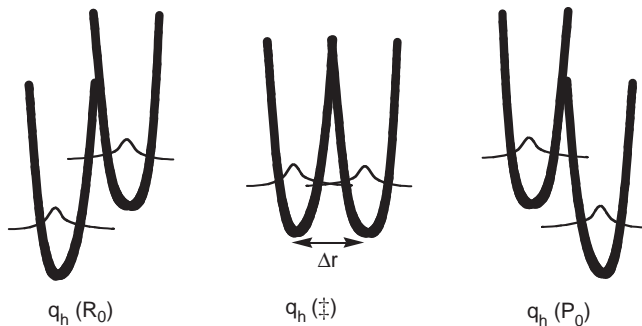


Figure 6.3 A free energy profile showing the transient degeneracy between the reactant and product wells, q_h (\ddagger) that permits wavefunction overlap from the reactant to product wells. At this configuration, there may also be a sampling of distances between the reactants, labelled Δr .

the resulting wavefunction overlap leading to a transient tunnelling resonance between the two wells. Net reaction occurs once this transient degeneracy has been broken or “relaxed” (cf. Figure 6.3). The parameter λ , reflects the extent to which the reactant state is altered, *via* thermal activation, prior to movement of the hydrogen from its donor to acceptor wells. This alteration will be a combination of changes in bond lengths/bond angles within the reactant (referred to as λ_{in}) as well as changes in the surrounding environment to accommodate accompanying changes in geometry and charge that are occurring within the reactant (referred to as λ_{out}).^{39,40} Note that the first exponential is temperature dependent, but largely mass independent. Some mass dependence will be introduced from the equilibrium isotope effect on ΔG° as well as a small impact of isotopic substitution on λ ; both of these effects are expected to be of little consequence for primary hydrogen isotope effects in relation to the isotope effect introduced *via* the Franck–Condon overlap term. A more significant mass effect can be introduced when tunnelling occurs from or to vibrationally excited states, but this effect is still relatively small in relation to the Franck–Condon term.

The second exponential in eqn (6.10) shows the dependence of the wavefunction overlap on the mass of the transferred nucleus, m_H , together with the frequency of the particle, ω_H and the distance that it travels, r_H (where \hbar is Planck’s constant divided by 2π). Note that though this second exponential, is greatly influenced by mass, it is independent of temperature. *It is the contrasting properties of the two exponentials in eqn (6.10) that predict a largely temperature-independent KIE.* This is a consequence of the fact that the temperature dependence (first exponential) and mass dependence (second exponential) of the reaction appear in noninteracting terms.

In the above manner it is possible to provide a theoretical context for the interpretation of the data in Table 6.5. There are several issues that arise however, that require further consideration prior to the availability of a general theory for C–H activation in enzyme catalysis. The first concerns the fact that

H-tunnelling from carbon is expected to occur at distances between the heavy atom donor and acceptor of *ca.* 2.7 to 2.8 Å, yet initial donor/acceptor van der Waals distances are in the range of 3.2 to 3.5 Å. The second feature is that numerous enzyme systems show temperature-dependent KIEs. Further, and perhaps more significantly, when a given enzyme is mutated or subjected to a nonoptimal substrate or reaction condition, the observed KIE is often observed to move from temperature independent to temperature dependent (cf. ref. 2). It seems highly unlikely that a new theory for H-transfer is necessary in these cases. A far more satisfactory solution would be to provide a mathematical treatment that allows for the full range of behaviour.

This can be accomplished by incorporating a third exponential into the rate expression given in eqn (6.10) to generate eqn (6.11):

$$k_{tun} = (\text{Const.}) \exp \left\{ \frac{-(\Delta G^\circ + \lambda)^2}{(4\lambda RT)} \right\} \int_{r_1}^{r_0} \exp^{-m_H \omega_H r_H^2 / 2\hbar} \exp^{-E_x / k_b T} dx \quad (6.11)$$

where $E_x = 1/2\hbar\omega_x X^2$, ω_x is the frequency for the distance sampling and X is the distance sampling (gating) coordinate. The expression for $X = r_x \sqrt{m_x \omega_x / \hbar}$ contains the mass of the gating coordinate (m_x) and the distance over which the gating unit moves (r_x). Note that the integration of the Franck–Condon over the different internuclear distances takes place from an initial distance, r_0 , to some distance of closest approach, r_1 . The third exponential in eqn (6.11) reflects the expected great sensitivity of H-tunnelling to the donor–acceptor distance. Integrating the Franck–Condon overlap term over varying distances between the H-donor and acceptor results in a family of configurations from which tunnelling can occur. It is useful to define a dominant distance between the donor and acceptor that results from a balancing of the extra energetic input needed to get the donor and acceptor closer than van der Waals distance and the enhancement of the wavefunction overlap that results from the closer distances. A key feature of the third exponential in eqn (6.11) is that this is both temperature and mass dependent. The latter results from the larger mass and shorter wavelength for D (or T) than H, meaning that the dominant distance for tunnelling must be shorter when deuterium (or tritium) is transferred.

Examination of eqn (6.11) indicates a model that is capable of rationalising the full range of observed behaviours in enzyme reactions. For enzymes that are fully optimised and can achieve the requisite very close approach between the H-donor and acceptor (2.7 to 2.8 Å), the degree of distance sampling will be small and the experimental KIE will approximate a temperature-independent behaviour. Alternatively, when an enzyme reaction is either incompletely evolved for optimal function or has been modified in some manner (*via* site-specific mutagenesis, acting on a nonoptimal substrate or under nonoptimal reaction conditions) the initial distance between the donor and acceptor is no longer close enough for effective wavefunction overlap. This leads to the requirement for enhanced donor/acceptor distance sampling with its accompanying temperature, and importantly, mass dependence. When the latter

condition prevails, the measured KIE is predicted to become temperature dependent.

One feature that needs further elaboration is how, in the optimal case, the H-donor and acceptor are able to achieve an initial distance of *ca.* 2.7 to 2.8 Å, at least 0.5 Å shorter than the van der Waals distance. While such short interatomic distances can be realised for H-bonding between heteroatoms such as oxygen and nitrogen, few if any of the reactions summarised in Table 6.5 are expected to be able to achieve this close approach in the initially formed enzyme–substrate complex. The observation of temperature independence for the experimental KIEs, thus requires another type of protein dynamical motion that permits the H-donor and acceptor to achieve a “compressed” geometry. This has led to our parsing of protein motions into two categories: the first is the reorganisation represented in the final eqn (6.11). The second type of motion is termed preorganisation, a terminology used by Brooks⁴³ and Hammes-Schiffer and Benkovic⁴⁴ in their discussion of the role of protein motions into enzyme catalysis.⁴⁵ According to our model of preorganisation, Figure 6.4, the protein undergoes numerous interconversions and sampling among a large number of protein conformations. Only a small subset of these conformations is able to achieve the requisite interactions between the H-donor and acceptor that can support productive tunnelling; these interactions allow the H-donor and acceptor to approach the 2.7 to 2.8 Å interatomic distance. *An important consequence of the detection of temperature-independent KIEs is that these data provide a key experimental link between the phenomenon of protein conformational sampling (preorganisation) and the nature of the enzyme-active site within its catalytic configuration(s).*

Although the contributions of protein reorganisation and preorganisation may not be strictly independent in all cases, their separation allows us to conceptualise the actual physical processes that contribute to the tunnelling process. For example, to the extent that preorganisation involves a sampling of protein states of similar energies (allowing rapid sampling among many protein

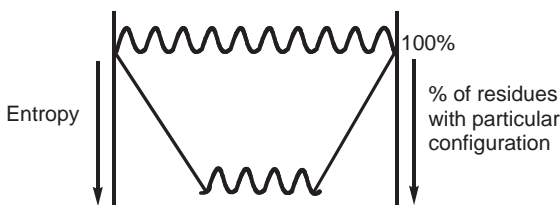


Figure 6.4 Illustration of the preorganisation process that a protein is proposed to undergo, prior to tunnelling of hydrogen from the donor to acceptor wells. Given the very large number of interactions that are anticipated for a productive active site configuration, the probability of reaching this family of protein substates is fairly low. As a frame of reference, the probability of the protein achieving a conformational substate characterised by a very small number of the requisite interactions between enzyme and substrate is set at 100%.

substrates), the barrier to preorganisation can be thought of as largely entropic in origin, reflecting the probability of achieving the catalytically viable family of protein conformations. By contrast, reorganisation is expected to be impacted by protein motions more proximal to the active site, and can thought of as the “fine tuning” of the active site. The reorganisation term is also expected to represent a significant portion of the enthalpic barrier to catalysis.

At this juncture, it is possible to address the origins of the unexpected trends in secondary KIEs summarised in Table 6.4 for alcohol dehydrogenases.^{2,32} Within the context of a full tunnelling model, the secondary KIEs will reflect the inner sphere reorganisation (λ_{in}) contribution to the first exponent in eqn (6.11). In the case of deuterium tunnelling, the shortened C–D---O distance at the reactive configuration (relative to C–H---O) may be expected to lead to extreme crowding within a conserved active-site geometry of the alcohol dehydrogenase family. Under these circumstances, inner-sphere reorganisation can proceed for protium transfer, but will be sterically impeded for deuterium transfer reducing the magnitude of the secondary deuterium KIE. The changes in active-site geometry that accompany alterations in the substrate or *via* site-specific mutagenesis relieve this crowding, leading to longer initial distances (r_0) between the hydrogen donor and acceptor and a rise in the magnitude of the secondary deuterium KIE. In this manner, the perturbations that bring about the trend from $A_1/A_2 > 1$ to $A_1/A_2 < 1$ also produce “more normal” values for λ_{in} for D-transfer and a corresponding increase in the secondary D/T KIEs.

In retrospect, it is quite ironic that the experimentally observed inflations of the exponent relating secondary D/T and H/T KIEs, which were originally predicted under conditions of a tunnelling correction, are a consequence of the excessive crowding that can take place within an enzyme-active site when deuterium is being transferred. The above explanation leads to the expectation that secondary KIEs in model reactions characterised by tunnelling may display quite different behaviour (cf. ref. 46) from that in Table 6.4 for YADH and HLADH.

6.5 Soybean Lipoxygenase-1 (SLO-1) as a Prototype of Full Tunnelling in an Enzyme

6.5.1 Overview of the Isotopic Properties of SLO-1 Catalysis

Soybean lipoxygenase has emerged as the most completely described example of hydrogen tunnelling in enzyme reactions, serving as a platform for the development of theories of tunnelling in enzymes, as well as a frame of reference for the interpretation of experimental studies in a myriad of other systems. The active site of SLO contains a ferric-hydroxide centre that is characterised by a high redox potential of ca. 0.6 V *vs.* NHE.⁴⁷ The preferred substrate, linoleic acid, undergoes reaction at an activated methylene (carbon-11), which is flanked by two double bonds. C–H activation from the pro-*S* position at carbon-11 produces a formal pentadienyl radical (Scheme 6.1(C)), though the degree of free-radical delocalisation across all five carbons within the

intermediate has been debated. The resulting delocalised radical is trapped by molecular oxygen in a regio- and stereospecific manner to produce the 13-(S)-hydroperoxy-9,11-(*Z,E*)-octadecadienoic acid product.

The reaction of SLO-1 with its substrates is characterised by a lag period, during which a ferrous-water form of SLO-1 is converted to the catalytically active ferric-hydroxide.³ Lag times increase when either deuterated substrate or mutated enzyme is employed, resulting from reduced rates for accumulation of sufficient product hydroperoxide to completely convert the inactive, ferrous-water form of enzyme to its catalytically relevant, ferric-hydroxide state. Reactions have been studied extensively in the steady state, by following either the absorbance of the conjugated hydroperoxide product by UV/Vis spectroscopy or by monitoring O₂ uptake on a Clark electrode. Single turnover studies have also allowed direct monitoring of the reduction of the active-site ferric-hydroxide centre by substrate.⁴⁸ Although the K_m for O₂ is well below the ambient dissolved O₂ concentration at 25 °C with wild-type enzyme, changes in temperature or the use of less active, mutant forms of enzyme can lead to some elevation of the K_m for O₂, requiring correction of the apparent k_{cat} to obtain values that represent saturating O₂ levels.³

An astonishing early observation for SLO-1 was a kinetic deuterium isotope effect in the range of 80.⁴⁹ This represented the first well-documented example of such huge KIEs in an enzyme reaction. Although many more examples now exist, the experimental observations for SLO-1 were subjected to numerous controls to establish that the observed deuterium isotope effect on k_{cat} represented a single step of C–H bond *via* tunnelling. Some of the alternate explanations, *e.g.*, that the enormous KIE was due to the magnetic influence of the neighbouring iron centre (a magnetic KIE)⁵⁰ or to a branching mechanism leading to multiple products,⁵¹ were disproved in turn. The size of the initially measured deuterium isotope effect was for a substrate that had been dideuterated at the C-11 position.⁵² In a separate experiment, using a stereospecifically labelled deuterated substrate, it could be shown that the secondary deuterium KIE was quite small and that the “anomaly” in the SLO-1 measurements was due almost entirely to the primary position,⁵² *i.e.* the bond undergoing cleavage. One very unusual observation during the investigations to separate the primary from the secondary KIE at the C-11 position of substrate was a loss of stereochemistry when the deuterium label was solely in the reactive (*S*)-position.⁵² As a result of the huge KIE in SLO, monodeuteration made it easier for the enzyme to remove protium from the 11-(*R*) position than deuterium from the normally stereospecific 11-(*S*) position.

6.5.2 The Temperature Dependence of KIEs in the SLO-1 Reaction

There is every indication that the C–H bond-cleavage step remains fully rate determining for k_{cat} between 5 and 55 °C in the SLO-1 reaction. While the deuterium KIE on k_{cat}/K_m is, under certain conditions, seen to fall below the

deuterium KIE on k_{cat} , reflecting partial rate limitation by substrate binding to enzyme, all deuterium KIEs on k_{cat} reported thus far remain huge. This property is also true for a series of active-site mutants, where deuterium KIEs equal to or greater than 80 are the norm (see below). SLO-1 was the first enzyme reaction to be shown to give rise to a value for $A_{\text{H}}/A_{\text{D}} \gg 1$. The enthalpy of activation for the wild-type SLO-1 is also quite small ($E_{\text{a}} = 2 \text{ kcal/mol}$), leading to an initial analysis of the SLO-1 data in the context of the low-temperature regime of a tunnelling correction model⁵⁰ (Figure 6.2). This was never a very satisfactory explanation since the E_{a} value is clearly elevated above zero and even further so for selected site-specific mutants of SLO-1. The emergence of full tunnelling models for H-transfer at or near room temperature, together with the growing observation of similar, temperature-independent KIEs for many enzyme classes (Table 6.5), represented a turning point for a full tunnelling analysis of SLO-1 and enzymes in general.

Site-specific mutagenesis has been pursued in SLO-1 in an effort to understand the tunnelling mechanism, with the focus on three hydrophobic residues that reside near the active-site ferric-hydroxide. Though an X-ray structure is not available for the complex of SLO-1 and its substrate, minimisation of the energy for the binding of linoleic acid to a high-resolution structure for the SLO-1 active site leads to an enzyme substrate complex in which the reactive, C-11 position of substrate is pointing toward the ferric hydroxide.³ Inspection of this complex indicates three protein side chains that are in close proximity to the substrate: Leu 546 and Leu 754, which sandwich the reactive C-11 position, and Ile 553 that is one helix turn away from Leu 546 and may be within van der Waals contact of the C-14 methylene carbon of bound substrate (Figure 6.5). Initial mutagenesis studies were focused on Ala replacements at each of these three positions.³ The L546A and L754A alterations produced a reduction in rate and elevation in E_{a} , together with similar values for the KIE at 30 °C relative to a wild-type enzyme. One very surprising result initially was the increase in the temperature dependence of the KIE, such that the values for $A_{\text{H}}/A_{\text{D}}$ are reduced relative to the value observed for a wild-type enzyme. Mutation at Ile553 to Ala was found to produce an even more dramatic impact on $A_{\text{H}}/A_{\text{D}}$, which falls below unity; in the case of I553A, the rate and E_{a} are similar to the wild-type enzyme.³

The ability to alter the value of $A_{\text{H}}/A_{\text{D}}$ via site-specific mutagenesis has profound ramifications for our understanding of H-transfer at enzyme-active sites. The model put forth by Knapp *et al.* in 2002 specifically addresses the observation of a range of values for $A_{\text{H}}/A_{\text{D}}$ (both $\ll 1$ and $\gg 1$) within a single enzyme-active site. It was argued that specific interactions between the hydrophobic side chains in SLO-1 and its bound substrate enable a close approach between the H-donor and acceptor, generating $A_{\text{H}}/A_{\text{D}} \gg 1$. Generation of active-site “packing defects” via mutagenesis impairs the ability for the H-donor and acceptor to get close enough to achieve functional wavefunction overlap, introducing the requirement for distance sampling. As elaborated upon in Section 6.4.1 above, when distance sampling becomes a significant part of the reaction trajectory, $E_{x_{(\text{D})}} > E_{x_{(\text{H})}}$, a direct result of the

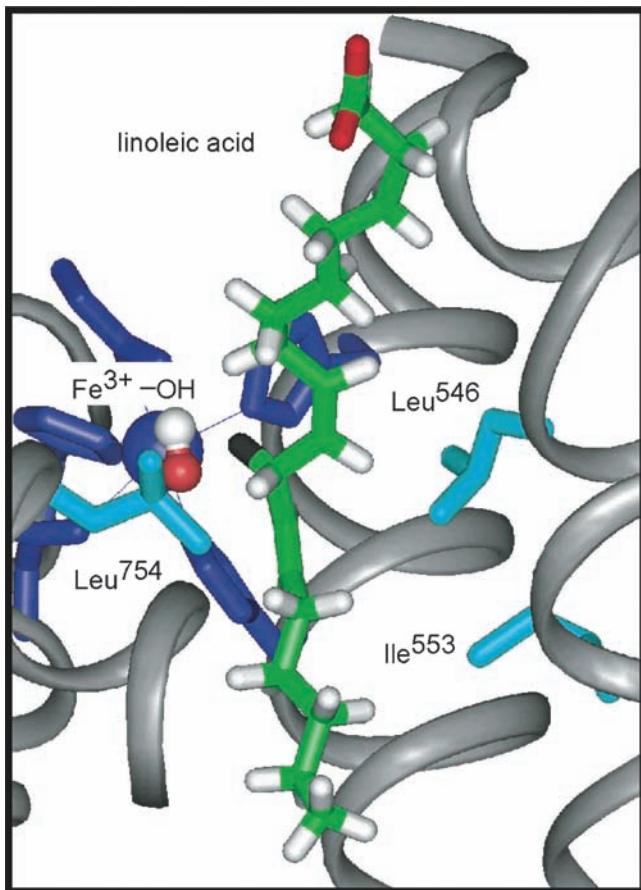
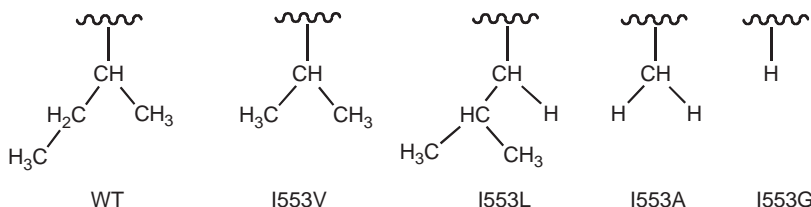


Figure 6.5 Active site of soybean lipoxygenase illustrating the placement of hydrophobic residues (Leu546, Leu754, and Ile553) in relation to the substrate linoleic acid, where the latter has been modelled into the active site.³

smaller wavelength for the heavier particle; it is this increase in $E_{x(D)}$ in relation to $E_{x(H)}$ that produces a reduction in the value for A_H/A_D .

The phenomenon in which the initial distance between the H-donor and acceptor is impacted by active-site packing, has been further interrogated by introducing a series of side chains of varying bulk into a single residue, Ile553. The fact that the backbone of Ile553 resides fairly distant from the active-site iron ($\sim 15\text{ \AA}$) removes the likelihood of a direct impact on the active-site chemistry, making it possible to examine the role of longer-range perturbations on active-site structure and dynamics. The actual series of mutations that has been studied involves a progressive decrease in size at the beta-carbon of the Ile side chain⁸ illustrated in Scheme 6.2.



Scheme 6.2 Series of mutations performed at position 553 of the enzyme soybean lipoxygenase.

The kinetic impact of the amino acid substitutions of Scheme 6.2 is summarised in Table 6.6.^{8,53} The trends in A_H/A_D are unmistakable: as the size of the substituent at the beta carbon of the 553 position decreases, the value of A_H/A_D gets progressively smaller. The most severe effect is for I553G⁸ where the rate for H-transfer is reduced five- to six-fold, the value of the KIE at 30 °C is almost double that of the wild-type enzyme and $A_H/A_D = 0.026$. Modeling of the data according to eqn (6.11) above allows a numerical evaluation of two key parameters as a function of mutation, the initial distance between the H-donor and acceptor (r_0) and the frequency of the oscillation that alters the donor–acceptor distance (ω_x). While the absolute values for these calculated parameters need to be viewed with caution, the trends in the values are quite compelling.

First, as the region that is normally occupied by Ile at position 553 becomes increasingly vacant, the computed r_0 is seen to undergo a regular increase in its value. This results in a progressive need for a gating motion to promote tunnelling, with the greatest impact being on $E_{a(D)}$. Note from Table 6.6 that the change in A_H/A_D (reflected in the experimental enthalpic difference, $E_{a(D)} - E_{a(H)}$) is significantly greater than the change in $E_{a(H)}$. The most straightforward interpretation for this behaviour is that the longer wavelength for protium permits reasonably good wavefunction overlap, even as the initial C–H---O distance lengthens. By contrast, deuterium, with its shorter wavelength finds itself unable to traverse the distance, requiring the introduction of a sizeable gating term for reaction to take place. The increased value of the KIE for I553G at 30 °C⁸ is significant in this context; this elevated value implies that gating within the I553G mutant is unable to overcome completely the initial misalignment of the H-donor and acceptor, so that when reaction does occur it does so at a longer distance than occurs for reaction of wild type or any of the other 553 mutants.

X-ray structures have been obtained for each of the position 553 mutants of SLO-1, as a frame of reference for interpretation of the kinetic data.⁸ Shown in Figure 6.6 are the comparative structures for the WT- and I553G proteins. These two proteins, together with all the Ile553 mutants, are identical outside of the active site, with some small differences seen within the active site. The latter involve first, a rotation of the side chain for Leu546 (located on the other side of

Table 6.6 Summary of empirical and computed Arrhenius parameters for the soybean lipoxygenase reaction.^{8,53}

Enzyme	Experimental Arrhenius parameters		Calculated Arrhenius parameters ^b		Input parameters ^a		
	$E_a(H)$, kcal/mol	$E_a(D)-E_a(H)$, kcal/mol	A_H/A_D	$E_a(D)-E_a(H)$, kcal/mol	A_H/A_D	r_0 , Å	ω_x , cm ⁻¹
WT	2.1 (0.2)	0.9 (0.2)	18 (5)	1.0	1.5	0.66	292
Ile ⁵⁵³ → Val	2.4 (0.5)	2.6 (0.5)	0.3 (0.2)	3.1	0.4	1.24	64
Ile ⁵⁵³ → Leu	0.4 (0.7)	3.4 (0.6)	0.3 (0.4)	3.4	0.2	1.43	56
Ile ⁵⁵³ → Ala	1.9 (0.2)	4.0 (0.3)	0.12 (0.06)	4.0	0.11	1.79	47
Ile ⁵⁵³ → Gly	0.03 (0.04)	5.3 (0.7)	0.027 (0.034)	5.2	0.027	2.55	38

^a r_0 is the initial distance that hydrogen would have to transfer between the donor and acceptor (prior to gating). ω_x is the frequency of the gating mode.

^bCalculated by treating the hydrogen wavefunctions as Morse oscillators. The listed input parameters differ slightly from values published in refs (8) and (53), due to an erroneous sign inversion in the code for calculating the Arrhenius parameters (we thank Sharon Hammes-Schiffer for pointing this out). The trends remain as they were in the original reports and do not alter the conclusions in any way. In any case, the significance of these calculations is the trends in parameters, not their absolute magnitude.

the helix turn from Ile553), which is seen in one of the two indicated positions for all the mutants with no obvious correlation between the position of this side chain and the experimental kinetic parameters. The second observed structural change involves a small difference in the positioning of a ligand (His499) to the iron, once again with no correlation between the observed position of His 499 among the mutants and the experimental parameters. Of greatest significance is the fact that compete deletion of the side at position 553 neither introduces a collapse of the active-site structure nor the filling of the cavity by ordered water molecules. The reduced value for the gating frequency among the Ile553 mutants can, then, be rationalised in the context of the I553G structure in Figure 6.6, bottom. The progressive loss of a side chain is expected to create less steric restriction and, hence, a reduced force constant (softer potential) for the distance-sampling mode, compatible with the calculated values for ω_x among the mutant proteins. An explanation for the small rate changes seen for protium transfer among the I553 X series may lie with the combined impact of an increase in the H-donor and acceptor distance, r_0 , and an increased probability of distance sampling due to the reduction in the frequency of the gating mode, ω_x .

At this juncture it appears that a satisfactory structural and kinetic picture has emerged that is compatible with the measured temperature dependence of the KIEs in both wild-type and mutant forms of SLO-1. Though the story is not yet complete, the experimental and theoretical work on SLO-1 provide a valuable platform for the study and evaluation of other enzyme systems.

6.6 Conclusions and Implications for Our Understanding of Enzyme Catalysis

In closing, it is of value to consider briefly the properties of a thermophilic alcohol dehydrogenase (ht-ADH), recently reviewed in Nagel and Klinman.² Though catalysing a very different reaction from that of SLO-1, the ht-ADH has also been shown to display a temperature-independent KIE at elevated temperatures (where the organism from which the enzyme has been isolated functions). As the experimental temperature is reduced to 30 °C and below, this property of temperature-independent KIEs ($A_H/A_D > 1$) is transformed to that of temperature-dependent KIEs ($A_H/A_D < 1$). Thus, ht-ADH offers another system in which a single enzyme-active site can support the behaviour of both temperature-independent and temperature-dependent KIEs. As an adjunct to kinetic analyses of the ht-ADH, it has been possible to examine the degree of protein flexibility using hydrogen/deuterium exchange methods both above and below the 30 °C transition point.⁵⁴ These studies show very clearly that the ht-ADH is more flexible at the elevated-temperature condition that produces the temperature-independent KIEs. This has raised the conundrum of how the increase in protein flexibility leads to increased immobilisation (less distance sampling) within the active site. The parsing of protein motions into two categories (as introduced in Section 6.4.1) provides a satisfactory reconciliation. The conformational sampling of protein substrates that has been termed

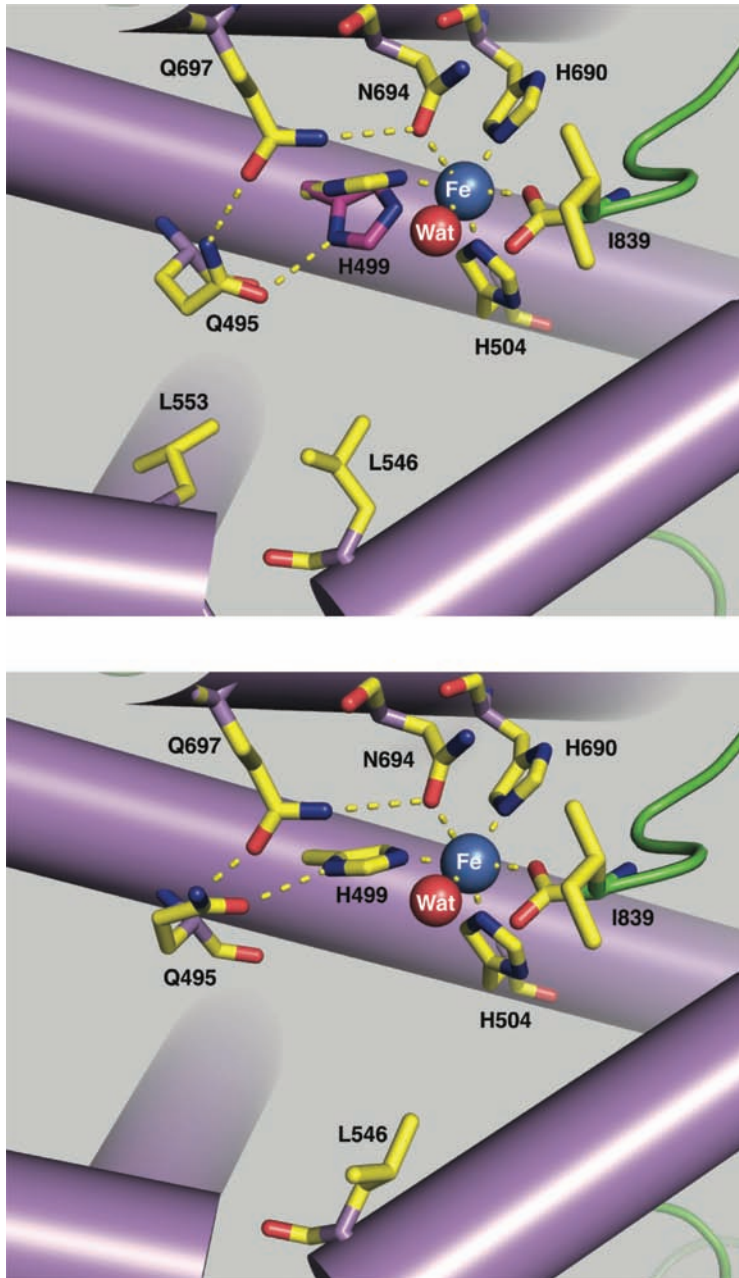


Figure 6.6 Comparative active site structures for the wild type soybean lipoxygenase (top) and I553G mutant (bottom).

preorganisation relies on the property of protein flexibility, more available to ht-ADH above 30 °C. Under this condition of elevated temperature, ht-ADH is able to sample substates that bring about a very close approach between donor and acceptor atoms, manifesting itself in $A_1/A_2 > 1$. The immobilisation of the thermophilic protein that occurs at reduced temperature puts a “clamp” on these protein motions, with the consequence that the optimal active-site configurations for tunnelling are more difficult to achieve. In this instance, the distance-sampling term of eqn (6.11)11 becomes a necessary component of the reorganisation barriers that lead to efficient wavefunction overlap.

A similar conceptualisation of the SLO-1 reaction in the context of both preorganisation and reorganisation can provide a satisfactory physical picture for the properties of the wild-type enzyme and its mutants. The implied ability of the wild-type form of SLO-1 to achieve initial distances for the reactive C–H---O interaction that are shorter than van der Waals radii can be attributed to the ability of the enzyme to sample the family of protein conformational substates that lead to shorter than equilibrium interatomic distances, with a resulting increased efficiency of tunnelling accompanied by a relatively small distance sampling term (*i.e.* the phenomenology of temperature-independent KIEs). As described for the low-temperature regime for the ht-ADH, site-specific mutagenesis of SLO-1 restricts the energy landscape available during the preorganisation process, leading to suboptimal active-site geometries and $A_1/A_2 < 1$. One final feature of interest is that the magnitude of E_a for I553 mutants in SLO-1 (Table 6.6) is either equal to or less than the E_a value observed for the wild-type enzyme, implying an increase in the entropic barrier. This is consistent with the expectation that remote mutations in proteins may dominantly affect the energetics of a protium-tunnelling reaction *via* an alteration of preorganisation which, as discussed in Section 6.4.1, may arise primarily from entropic factors.

It can be concluded that detailed studies of the properties of kinetic isotope effects in enzyme-catalysed H-transfer reactions have not only indicated the central role of tunnelling on these processes, but have also opened up a very special window into the detailed properties of enzyme-active sites that are modulated by protein motions both proximal and distal to reacting bonds. It is also important to bear in mind that the progression from a tunnelling correction view of catalysis to a model in which an H-transfer reaction is treated as a full tunnelling means that it is no longer appropriate to ask the question: how much more of a tunnelling correction need to be considered for an enzyme reaction in relation to a comparable reaction in solution? The appropriate question becomes: how does the enzyme preorganise itself and fine tune the active site to make tunnelling a highly efficient process?

References

1. M. Mure, S. A. Mills and J. P. Klinman, *Biochemistry*, 2002, **41**, 9269.
2. Z. D. Nagel and J. P. Klinman, *Chem. Rev.*, 2006, **106**, 3095.

3. M. J. Knapp, K. Rickert and J. P. Klinman, *J. Am. Chem. Soc.*, 2002, **124**, 3865.
4. W. W. Cleland, in: *Steady State Kinetics in the Enzymes*, 3rd edn, ed. P. Bayer Academic Press, New York, 1970, Vol. 2, p. 1.
5. R. P. Bell, *The Proton in Chemistry*, 2nd edn, Chapman and Hall, London, 1973.
6. D. B. Northrop , in *Isotope Effects in Enzyme-Catalysed Reactions*, ed. W. W. Cleland, M. H. O'Leary, D. B. Northrop, University Park Press, Baltimore, MD. 1977.
7. B. J. Bahnsen, D. H. Park, K. Kim, B. V. Plapp and J. P. Klinman, *Biochemistry*, 1993, **31**, 50503.
8. M. P. Meyer, D. Tomchick and J. P. Klinman, *Proc. Natl. Acad. Sci. USA*, 2008, **105**, 1146.
9. P. F. Cook and W. W. Cleland, *Enzyme Kinetics and Mechanism*, Garland Science, London and New York, 2007.
10. D. B. Northrop, *Biochemistry*, 1975, **14**, 2644.
11. Y. Cha, Y. C. J. Murray and J. P. Klinman, *Science*, 1989, **243**, 1325.
12. W. A. Francisco, M. J. Knapp, N. J. Blackburn and J. P. Klinman, *J. Am. Chem. Soc.*, 2002, **124**, 8194.
13. L. Wang, N. M. Goodey, S. J. Benkovic and A. Kohen, *Proc. Natl. Acad. Sci. USA*, 2006, **103**, 15733.
14. J. P. Klinman, *Adv. Enzymol. Relat. Areas Mol. Biol.*, 1978, **46**, 415.
15. F. H. Westheimer, *Chem. Rev.*, 1961, **61**, 265.
16. R. P. Bell, in *The Tunnel Effect in Chemistry*, Chapman and Hall, New York, 1980.
17. M. J. Knapp, M. Meyer, J. P. Klinman, in *Hydrogen Transfer Reactions*, ed. J. T. Hynes, J. P. Klinman, H. H. Limbach and R. L. Schowen, Wiley-VCH, Vol. 4, p. 1241.
18. M. Garcia-Viloca, J. Gao, M. Karplus and D. G. Truhlar, *Science*, 2004, **303**, 186.
19. B. C. Garrett, D. G. Truhlar, A. F. Wagner and T. H. Dunning Jr, *J. Chem. Phys.*, 1983, **78**, 4400.
20. D. G. Truhlar, A. D. Isaacson and B. C. Garrett, in *Theory of Chemical Reaction Dynamics*, ed. M. Baer, CRC Press, Boca Raton, FL, 1985, Vol 4, p. 65.
21. C. G. Swain, E. C. Stivers, J. F. Reuwer Jr, and L. J. Schaad, *J. Am. Chem. Soc.*, 1982, **104**, 3263.
22. A. Kohen, R. Cannio, S. Bartolucci and J. P. Klinman, *Nature*, 1999, **399**, 496.
23. W. J. Bruno and W. Bialek, *Biophys. J.*, 1992, **63**, 689.
24. K. L. Grant and J. P. Klinman, *Biochemistry*, 1989, **28**, 6597.
25. T. Jonsson, D. Edmondson and J. P. Klinman, *Biochemistry*, 1994, **33**, 14871.
26. S. L. Seymour and J. P. Klinman, *Biochemistry*, 2002, **41**, 8747.
27. M. M. Whittaker, D. P. Ballou and J. W. Whittaker, *Biochemistry*, 1998, **37**, 8426.

28. S. Chowdbury and R. Banerjee, *J. Am. Chem. Soc.*, 2000, **122**, 5417.
29. (a) E. Hatcher, A. V. Soudackov and S. Hammes-Schiffer, *J. Phys. Chem. B*, 2005, **109**, 18565; (b) E. Hatcher, A. V. Soudackov and S. Hammes-Schiffer, *J. Am. Chem. Soc.*, 2007, **129**, 187.
30. J. Rucker, Y. Cha, T. Jonsson, K. L. Grant and J. P. Klinman, *Biochemistry*, 1992, **31**, 11489.
31. B. J. Bahnsen, J. D. Colby, J. K. Chin, B. M. Goldstein and J. P. Klinman, *Proc. Natl. Acad. Sci. USA*, 1997, **94**, 12797.
32. J. P. Klinman, *Philos. Trans. R. Soc. B*, 2006, **361**, 1323.
33. J. Basran, M. J. Sutcliffe and N. S. Scrutton, *Biochemistry*, 1999, **38**, 3218.
34. J. Basran, S. Pabel, M. J. Sutcliffe and N. S. Scrutton, *J. Biol. Chem.*, 2001, **276**, 2438.
35. R. J. Harris, R. Meskys, M. J. Sutcliffe and N. S. Scrutton, *Biochemistry*, 2000, **39**, 1189.
36. J. L. Abad, F. Campo and G. Fabrias, *Angew. Chem. Int. Ed.*, 2000, **39**, 3279.
37. R. S. Sikorski, L. Wang, K. A. Markham, P. T. R. Rajagopalan, S. J. Benkovic and A. Kohen, *J. Am. Chem. Soc.*, 2004, **126**, 4778.
38. F. Fan and G. Gadda, *J. Am. Chem. Soc.*, 2005, **127**, 7954.
39. N. Sutin, in *Progress in Inorganic Chemistry*, ed. S. J. Lippard, John Wiley & Sons, Inc., Vol. **30**, 1983, p. 5441.
40. R. A. Marcus, *J. Chem. Phys.*, 1965, **43**, 679.
41. A. M. Kuznetsov and J. Ullstrup, *Can. J. Chem.*, 2002, **77**, 1085.
42. S. Hammes-Schiffer, E. Hatcher, H. Ishikita, J. H. Skone and A. V. Soudackov, *Coord. Chem. Rev.*, 2008, **252**, 384.
43. J. L. Radkiewicz and C. L. Brooks III, *J. Am. Chem. Soc.*, 2000, **122**, 225.
44. S. J. Benkovic and S. Hammes-Schiffer, *Science*, 2003, **30**, 1196.
45. The types of motions that contribute to H-transfer have been given different names by ourselves and others. The designations given here are aimed at encompassing many of the previous nomenclatures. For example, within eq (X.11), the Marcus term has been called a “passive” motion and the distance sampling term an “active” motion.³ Since the physical origins that give rise to both types of motions may be similar, we no longer make the distinction between “passive” and “active”. Further, the term gating was invoked earlier to describe the dynamical change in distance between the H-donor and acceptor atoms. This term is retained and may be used interchangeably with the designation of distance sampling mode.
46. Ralph Pollack at the University of Maryland (BC) has demonstrated a breakdown from the rule of the geometric mean for secondary isotope effects in ketosteroid isomerase that is different from the model reaction (T. C. Wilde, G. Blotny and R. M. Pollack, *J. Am. Chem. Soc.*, 2008, **130**, 6577.).
47. K. Rickert and J.P. Klinman, in *Biological Inorganic Chemistry: Structure and Reactivity*, ed. I. Bertini, H. Gray, E. I. Stiefel and J. S. Valentine, University Science Books, Inc., Mill Valley, California, 2006, p. 607.
48. T. Jonsson, M. H. Glickman, S. Sun and J. P. Klinman, *J. Am. Chem. Soc.*, 1996, **118**, 10319.

49. M. H. Glickman, J. S. Wiseman and J. P. Klinman, *J. Am. Chem. Soc.*, 1994, **116**, 793.
50. C.-C. Hwang and C. B. Grissom, *J. Am. Chem. Soc.*, 1994, **116**, 795.
51. M. H. Glickman and J. P. Klinman, *Biochemistry*, 1996, **35**, 12882.
52. K. Rickert and J. P. Klinman, *Biochemistry*, 1999, **38**, 12218.
53. M. P. Meyer and J. P. Klinman, *Chem. Phys.*, 2005, **319**, 283.
54. Z.-X. Liang, T. Lee, K. A. Resing, N. G. Ahn and J. P. Klinman, *Proc. Natl. Acad. Sci. USA*, 2004, **101**, 9556.

CHAPTER 7

Quantum Effects in Enzyme Kinetics

ARUNDHUTI SEN AND AMNON KOHEN

Department of Chemistry, University of Iowa, Iowa City, IA 52242, USA

7.1 Introduction

Historically, the study of enzymatic catalysis has been characterised by multidisciplinary approaches to the investigation of a range of issues: structural features relevant to catalysis, substrate binding and product-release patterns, the role of functional residues (*e.g.* general bases or acids) *etc.* One contemporary topic in enzymology is that of quantum-mechanical effects, including zero-point energies (ZPE) and quantum tunnelling, and the contribution these physical phenomena make to enzyme catalysis.ⁱ As mentioned in previous chapters, traditional theories of enzymatic catalysis focus on concepts such as transition-state stabilisation and ground-state destabilisation to account for the enormous rate enhancements seen in enzyme reactions.^{1,2} These concepts were grounded in classical transition-state theory, which did not consider quantum-mechanical effects. In the past two decades, however, experimental data demonstrating tunnelling and related quantum effects in enzymes has given rise to a number of theoretical models that attempt to rationalise the empirical findings. Some of these models (the Bell correction to transition-state theory, various ‘Marcus-like’ models) have been elaborated

ⁱ It should be noted that any attempt to separate catalysis into constituent additive contributions is a somewhat artificial process, since the quantitative degree of each contribution is inherently model dependent.

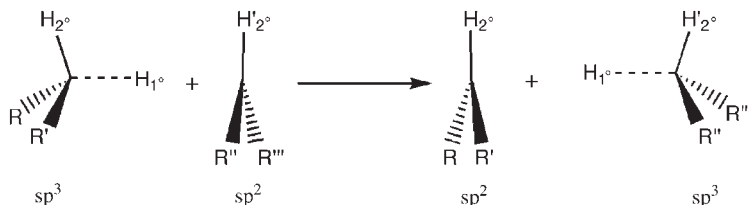


Figure 7.1 The general H transfer reaction used as a model reaction in the text.

upon in the previous chapters, and their individual importance can be gauged by their ability to interpret and explain experimental findings. The present chapter focuses on a significant experimental tool used to examine tunnelling and coupled motion in enzymatic systems, *viz.* kinetic isotope effects (KIEs).

The kinetic isotope effect is simply the ratio of rates between two molecules that differ only in their isotopic composition (isotopologues), and has traditionally been one of the most useful probes of the potential-energy surface for organic reactions. A well-designed KIEⁱⁱ experiment can, in essence, focus on the chemical step of an enzyme reaction within the intricate kinetic pathway associated with enzymatic catalysis, thus providing information only about the mechanistic step of interest. For example, when the reaction under consideration is a H-transfer reaction, as in Figure 7.1, then the KIEs for protium, deuterium, and tritium-labelled substrates may provide substantial information about the reaction coordinate and the nature of the transition state.³ H-transfer reactions are particularly interesting since (i) due to the large mass ratio of D/H (2) and T/H (3) the KIEs are large, and (ii) due to the small mass of hydrogen, quantum effects are more likely to be significant. The de Broglie wavelength of the hydrogen atom corresponds to the H-transfer distance in many biological systems, which in turn corresponds to the width of the barrier that must be traversed for tunnelling to occur.⁴ Enzymatic reactions that involve H-transfer are thus excellent cases with which to investigate the role of quantum-mechanical tunnelling in catalysis.

The following section (7.2) provides an introduction to the terminology and theory of kinetic isotope effects, as well as a discussion of two important mathematical formulations: the Swain–Schaad relationships for 1° and 2° KIEs, and the Northrop equations for the extraction of intrinsic KIEs from observed values. Section 7.3 describes the ways in which KIEs can be used to probe tunnelling and coupled motion in enzymatic systems, and Section 7.4 summarises recent examples from studies of three different systems: alcohol dehydrogenase, dihydrofolate reductase and thymidylate synthase.

ⁱⁱ A ‘well designed’ KIE experiment would ensure that only the kinetic step of interest is isotopically sensitive, and that the intrinsic KIE on this step is not masked by other kinetic steps.

7.2 Kinetic Isotope Effects: Basic Terms and Concepts

7.2.1 Defining KIEs

The Bigeleisen equation defines the kinetic isotope effect for two isotopically labelled systems in terms of their partition functions. Thus, for reactants labelled with light (L) and heavy (H) isotopes, with reaction rates k_L and k_H , respectively, the KIE would be expressed as follows:

$$\text{KIE} = \frac{k_L}{k_H} = (\kappa_L/\kappa_H)^* \text{ZPE}^* \text{MMI}^* \text{EXC} \quad (7.1)$$

where κ is the transmission coefficient and the other terms are the isotope effects on the zero-point energies (ZPE), on the rotational and translational energies (mass moments of inertia or MMI), and on populations of excited vibrational states (EXC)^{5,6}. Since the rate of a reaction is exponentially related to the activation barrier for that reaction, the ratio of rates (KIE) is proportional to the difference in activation free energies of the light and heavy isotopes:

$$\text{KIE} = \frac{k_L}{k_H} \approx e^{(\Delta G_H^\ddagger - \Delta G_L^\ddagger)/RT} \quad (7.2)$$

In most cases, the difference in activation energy between isotopologues, *i.e.* $\Delta G_H^\ddagger - \Delta G_L^\ddagger$, can largely be attributed to the change in zero-point energies between the ground state and transition state for each reactant (Figure 7.2).⁷

The very definition of the KIE allows for considerable variation in experimental design, particularly in the following respects: (i) the manner in which the KIE is measured and (ii) the selection of labelling patterns for the isotopologue reactants. Based on the position of the labelled atom relative to the atom being transferred, two kinds of KIE can be defined: primary (1°) KIEs, measured for a bond cleavage or formation wherein one of the bound atoms is isotopically labelled, and secondary (2°) KIEs, where the labelled atom is not one of the atoms participating in bond cleavage or formation. 2° KIEs result from changes in bonding force constants and vibrational frequencies during the reaction, and generally have smaller values than 1° KIEs. Additionally, KIE values can be broadly classified as normal or inverse, where normal values are those above 1 (*i.e.* the lighter isotope transferred faster than the heavier one) and inverse KIEs are smaller than 1 (the heavier isotope transferred faster than the lighter one). Another term relevant to the discussion of KIEs is the equilibrium isotope effect (EIE). Unlike KIEs, EIEs are not dependent on transition-state properties, but arise from the equilibrium distribution of isotopes between two stable states, such as the reactant and the product states in a given reaction. In other words, the EIE is affected by changes when going from reactants to products, while the KIE originates in differences between the ground state and the transition state.

At the simplest level, the value of the KIE can be used to assess the location of the transition state (late or early) and the nature of the change in bond order

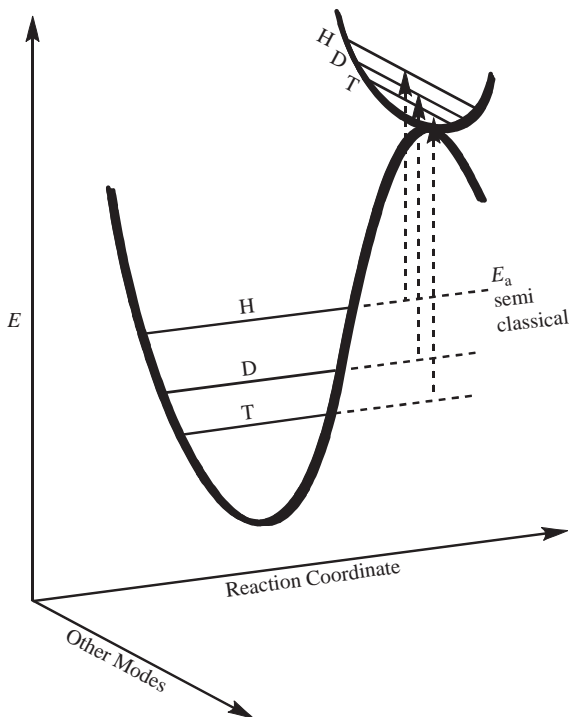


Figure 7.2 Different energies of activation (ΔE_a) for H, D, and T, resulting from their different zero point energies (ZPE) at the ground state (GS) and transition state (TS). The GS ZPE is constituted by all degrees of freedom but mostly by the C H stretching frequency, and the TS ZPE is constituted by all degrees of freedom orthogonal to the reaction coordinate. This type of consideration is depicted as “semiclassical”.

(sp^3 to sp^2 , etc.). For example, the magnitude of 2° KIEs have traditionally been compared to the reaction’s 2° EIE in order to determine whether the reaction had an early or late transition state.³ This simple analysis assumes that the bond order of the 2° labelled atom is changing in proportion to the reaction progress and that the maximum change is reached at the product state. According to this model, the 2° EIE will be the larger value and will express the full magnitude of the change, while the 2° KIE will be between unity (for an early transition state) and the EIE (for a late transition state). More recently, it has been suggested that simple comparisons between 2° EIE and KIE values are not good indicators of the position of the transition state, due to the number and complexity of factors influencing the 2° KIE.^{8 12}

7.2.2 Swain Schaad Relationships for 1° and 2° KIEs

Equation (7.1) is considered semiclassical since certain quantum-mechanical effects (such as ZPE) are included in the description and others, such as

tunnelling, are left out. Within this semiclassical description, the kinetic relationship among the three isotopes of hydrogen is determined, for the most part, by their relative ZPEs at the ground *vs.* transition states (Figure 7.2). The relationship among the three reaction rates can be developed quite simply from the reduced masses of the isotopes involved, to give the Swain–Schaad exponential relationship first defined by Swain *et al.* in 1958:¹³

$$\frac{k_H}{k_T} = \left(\frac{k_H}{k_D} \right)^{\text{EXP}} \quad \text{or} \quad \text{SSE} = \frac{\ln(k_H/k_T)}{\ln(k_H/k_D)} \quad (7.3)$$

where k_i is the reaction rate constant for isotope i , and SSE denotes the Swain–Schaad exponent. SSE is calculated from eqn (7.1) as follows:

$$\text{SSE} = \frac{\ln(k_H/k_T)}{\ln(k_H/k_D)} = \frac{1/\sqrt{\mu_H} - 1/\sqrt{\mu_T}}{1/\sqrt{\mu_H} - 1/\sqrt{\mu_D}} \quad (7.4)$$

where μ_i is the reduced mass of the isotope i . The exponent thus calculated for H/T *vs.* H/D KIEs has a value of 1.42 (a value of 1.44 is calculated using atomic masses). When the experiment calls for labelling patterns that use T as the reference isotope, to obtain H/T *vs.* D/T KIEs, the equation for SSE is modified accordingly:

$$\text{SSE} = \frac{\ln(k_H/k_T)}{\ln(k_D/k_T)} = \frac{1/\sqrt{\mu_H} - 1/\sqrt{\mu_T}}{1/\sqrt{\mu_D} - 1/\sqrt{\mu_T}} \quad (7.5)$$

The SSE calculated from eqn (7.5) has a value of 3.26 (for atomic masses, and 3.34 using reduced masses). The utility of the Swain–Schaad relationships lies in their simplicity, and apparent independence from many of the factors influencing the reaction potential surface. Due to this latter quality, the Swain–Schaad equations can be used to relate unknown intrinsic KIEs to observed values, as in the Northrop method (Section 7.2.3). Other applications include the use of the 2° Swain–Schaad exponents (2° SSEs) as a probe for tunnelling and as an indicator of coupled motion between primary and secondary hydrogens for hydride-transfer reactions (Section 7.3.2).

7.2.3 Kinetic Complexity

As mentioned previously, KIEs provide direct insights into the nature of H-transfer reactions and the associated potential-energy surfaces. However, one limitation of the KIE technique should be evident upon inspection of eqn (7.2): in order to use the KIE as a probe of the H-transfer step, the H-transfer step must indeed be the ‘rate limiting’ (slowest) step of the enzymatic reaction. Most enzyme reactions consist of a complex series of events (such as binding of substrate, conformational changes of reactive intermediates, product release,

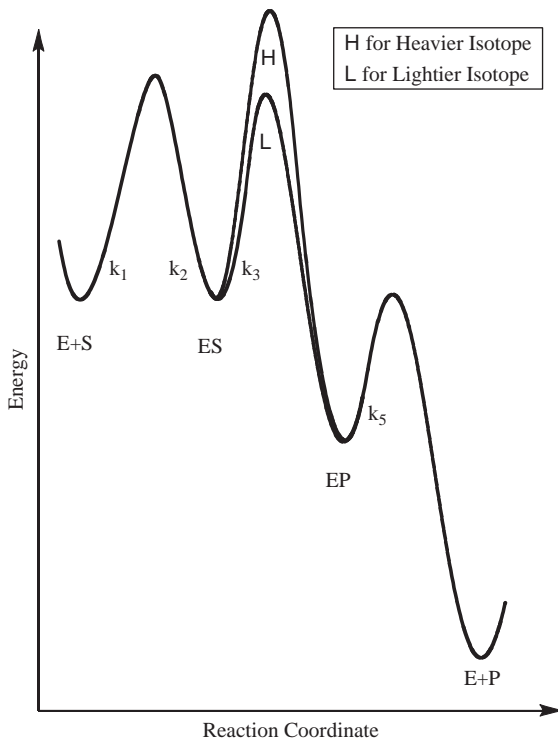


Figure 7.3 An illustration of a reaction coordinate for the mechanism shown in Eq. 7.6.

etc.), each of which can be rate-limiting under the appropriate conditions. In such cases, KIE measurements must be conducted with due consideration of the following questions:

1. Is the KIE measured truly an ‘intrinsic’ KIE (*i.e.* measured on a single kinetic step) or is it being measured on a kinetically complex rate constant (*e.g.* k_{cat}/K_M or k_{cat})?
2. Are steps other than the one under consideration isotopically sensitive?

These points can be illustrated using a relatively simple, single substrate reaction mechanism as follows (Figure 7.3):



If the KIE on the chemical step is to be measured, the rate constant k_3 alone must be isotopically sensitive, since the conversion from ES to EP involves the bond-breaking and formation steps. However, unless the bond-breaking step is the slowest step in the reaction ($k_3 \ll k_1, k_2, k_5$), the observed isotope effect on k_3

will be masked by the rates of the preceding and following isotopically insensitive steps. This phenomenon is called kinetic complexity. For 1° KIEs, such kinetic complexity and the resultant experimental artifacts cause the observed KIE (KIE_{obs}) to be smaller than the intrinsic KIE (KIE_{int}).

Mathematically, kinetic complexity can be expressed in terms of the commitment to catalysis, or the ratio between the isotopically sensitive steps and the isotopically nonsensitive steps that lead to the decomposition of the reactive complex. The relationship between KIE_{obs} , KIE_{int} and the forward and reverse commitments to catalysis (C_f and C_r , respectively) is given by the expression:^{14,15}

$$KIE_{obs} = \frac{KIE_{int} + C_f + C_r \cdot EIE}{1 + C_f + C_r} \quad (7.7)$$

Here, C_f is the ratio between the rate of the isotopically sensitive step forward and the rates of the preceding isotopically insensitive steps backward; C_r is the ratio between the rates of the isotopically sensitive step backward and the succeeding isotopically insensitive steps forward. For the reaction given by eqn (7.6), $C_f = k_3/k_2$ and $C_r = k_3/k_5$.¹⁶

With some algebraic modification, eqn (7.7) can be used in combination with the Swain–Schaad exponents to calculate the commitments to catalysis and, more importantly, to calculate the KIE_{int} from KIE_{obs} . This technique was developed by Dexter B. Northrop, and assumes close concurrence between the intrinsic 1° SSEs and their semiclassically predicted values. The details of this method have been described elsewhere^{17,18} and are not presented in this chapter; the final result allows calculation of an intrinsic KIE (e.g., $(k_H/k_T)_{int}$ in eqn (7.8) when two observed KIE values are available $((k_H/k_D)_{obs}$ and $(k_H/k_T)_{obs}$):

$$\frac{(k_H/k_T)_{obs} - 1}{(k_H/k_D)_{obs} - 1} = \frac{(k_H/k_T)_{int} - 1}{((k_H/k_T)_{int})^{1/1.44} - 1} \quad (7.8)$$

Equation (7.8) cannot be solved analytically (due to transcendental functions) and must be solved numerically once values are available for the observed KIEs.^{iii,iv} Intrinsic KIEs are directly relevant to the reaction potential surface of a specific barrier, and can thus be compared to theoretical calculations that commonly focus on a single step. Practically, the Northrop method

ⁱⁱⁱ References [17,18] include tables containing numerical solutions for a wider range of KIEs. Today, these can easily be calculated with a calculator or computer, see <http://crick.et.chem.uiowa.edu/~kohen/tools.html>

^{iv} In cases where the chemical step is reversible and a small 1° EIE cannot be assumed, a numerical solution requires the calculation of the reverse commitment (C_r). For such cases, Cleland has identified a range for the KIE_{int} values between the observed KIE and the product of the EIE and KIE_{obs} for the reverse reaction ($KIE_{obs\ rev} * EIE$).¹⁹

removes the kinetic complexity and unmasks the intrinsic KIE, which is the value of interest in mechanistic enzymology.

7.2.4 Coupling and Coupled Motion

In mechanistic enzymology, the term ‘coupling’ is applied to two distinct phenomena: (i) primary–secondary (1° – 2°) coupled motion and (ii) environmentally coupled tunnelling. The first refers to H-transfer reactions and defines the coupling between the transferred hydrogen and another hydrogen bound to the donor or acceptor heavy atom. The second term refers to the way the tunnelling of the transferred hydrogen is coupled to the enzymatic environment, and is synonymous with other terms such as ‘tunnelling-promoting vibrations’ and ‘vibrationally enhanced tunnelling’. More generally, when two coordinates interact in such a way that a change in one coordinate affects the potential energy of the other, they are said to be coupled.^v For example, when two hydrogens bound to the same carbon are coupled (as is the case for the alcohol dehydrogenase, Section 7.4.1), the cleavage of one C–H bond is not independent of the isotopic composition of the other hydrogen on the same carbon (or the acceptor carbon). In terms of bond vibrations, the stretching mode of one bond (that is converted into a translation at bond cleavage) is coupled to vibrational modes of the other. 1° – 2° coupled motion is a phenomenon associated with tunnelling of the transferred atom, and in the case of H-transfer reactions can be exposed using mixed-labelling experiments (Section 7.2.5.2).

7.2.5 Experimental Methods and Design

7.2.5.1 Competitive vs. Noncompetitive KIE Measurements

KIE measurements can be performed in two distinct ways, *via* competitive or noncompetitive experiments. The noncompetitive method measures the rates of reaction for individual isotopologue reactants in separate experiments. Then, the rates are divided to yield the KIE and the errors from each measurement are propagated to the KIE. Competitive measurements involve a mixture of isotopologue substrates in a single reaction vessel. During the reaction, either the depletion of the heavy isotope in the product or its enrichment in the reactant is followed, and used to calculate the KIE directly (without needing to measure reaction rates). Each method has its own advantages and disadvantages: noncompetitive experiments, for example, measure the isotope effect on k_{cat} as well as k_{cat}/K_m , whereas competitive experiments can be shown to measure the isotope effect only on k_{cat}/K_m .¹⁴ On the other hand, competitive measurements result in lower errors than the noncompetitive experiments, thus limiting the

^v From the mathematical point of view, coupling may be defined as the mixing between two states (motion along two coordinates). Coupling matrix elements will be proportional to the second derivative of the potential energy with respect to both coordinates.

noncompetitive method to the measurement of KIEs greater than 1.25.²⁰ Additionally, noncompetitive KIEs cannot examine radioactive isotopes (*e.g.*, T), due to the extreme levels of radioactivity needed while working with pure, 100% labelled, radioactive reactants, while in a competitive experiment the radioactive isotope is only present in a trace amount, enabling measurements of H/T and other KIEs. This makes competitive measurements more appealing, particularly when measuring small isotope effects involving radioactive materials such as 2° H/T, 1° D/T KIEs or heavy-atom KIEs.

7.2.5.2 Mixed-Labelling Experiments

An experimental method relevant to enzymatic tunnelling studies is mixed labelling of isotopologue reactants. These experiments are used when deviations in the 2° SSEs are sought as indicators of tunnelling (Section 7.3.3). Mixed-labelling experiments employ an isotopic labelling pattern than is more involved than that used in the original Swain–Schaad relationship, but are considered sensitive indicators of H-tunnelling.^{8,21,22}

A mixed-labelling experiment would measure the 2° H/T KIE with H in the 1° position, and the 2° D/T KIE with D in the 1° position (Figure 7.4). These KIEs would be denoted by $k_{\text{HH}}/k_{\text{HT}}$ and $k_{\text{DD}}/k_{\text{DT}}$, respectively, where k_{ij} is the rate constant for H-transfer with isotope *i* in the 1° position and isotope *j* in the 2° position. Thus, the 2° Swain–Schaad relationship can be expressed as:

$$2^{\circ}\text{M SSE} = \frac{\ln(k_{\text{HH}}/k_{\text{HT}})}{\ln(k_{\text{DD}}/k_{\text{DT}})} \quad (7.9)$$

This mixed-labelling relationship is distinguished from the usual SSE by the exponent ^MSSE. The 2° ^MSSE is particularly interesting, since it is used as a probe for both tunnelling and coupled motion between 1° and 2° hydrogens (as explained in Section 7.3.3).

A rigorous mathematical treatment explaining the high sensitivity of the mixed-labelling experiment to H-tunnelling can be found in refs. 23 and 22. Huskey and Saunders both independently showed that very large values of ^MEXP are only calculated for 2° KIEs that arise from coupled motion and tunnelling in the system of interest.^{23–25} Both concluded that the extra isotopic substitution at the geminal position is essential for the experimental design,

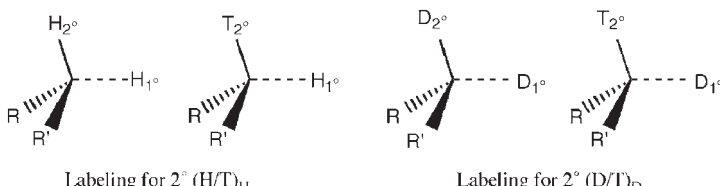


Figure 7.4 The isotopic labeling pattern for a mixed labeling experiment.

thus making a case for the mixed labelling method. More recent calculations have further emphasized the validity of this method, as well as limitations when applied in certain contexts.^{10,26}

7.3 KIEs as Probes for Tunnelling

Once a set of intrinsic KIEs have been obtained (as described in Section 7.2), the results can be interpreted to clarify a variety of issues, such as transition-state geometry, mechanistic details, and quantum-mechanical effects. When studying tunnelling in enzymatic systems, the following three methods are frequently employed to obtain signatures of tunnelling: (i) comparing the magnitude of the KIE to that expected from eqn (7.1) (nontunnelling model); (ii) identifying cases of deviation of 2°MSE from the semiclassically expected values; and (iii) measuring the temperature dependence of the intrinsic KIEs and using both the difference in activation energies between the isotopes and the isotope effects on the Arrhenius pre-exponential factors to diagnose the extent of tunnelling in the system. The last method has the added advantage of being able to distinguish between data that comply with a tunnelling correction to the transition-state theory, and data that must be fitted to a Marcus-like model of tunnelling (see Chapter 5).

7.3.1 The Size of the KIE

For hydrogen-transfer reactions, the simplest indication of tunnelling is an anomalously large primary KIE that significantly exceeds the semiclassical limit (for H/D KIEs, this value is ~ 7 at room temperature³). For instance, in the case of soybean lipoxygenase (SBL-1)²⁷ and galactose oxidase,²⁸ the sheer size of the 1° KIE was enough to suggest tunnelling. SBL-1 is an Fe(III)-dependent enzyme that catalyses the conversion of linoleic acid, an essential fatty acid, to 13(S)-hydroperoxy-9(Z),11(E)-octadecanoic acid, with H-transfer being the rate-limiting step above 32°C . The measured room-temperature H/D KIE for SBL-1 was ~ 81 , and both proton and deuterium transfer rates as well as the KIEs themselves were weakly temperature dependent (see Section 7.4.3 for the temperature dependence of KIEs).²⁷ These two observations together (the large KIE value and temperature-dependent KIEs) can be interpreted as indicative of environmentally coupled tunnelling, especially since other explanations (magnetic coupling, branching of isotopically sensitive steps²⁹) for the large KIE had already been discarded. Another system of interest in this context is galactose oxidase (GO), a radical-coupled copper oxidase catalysing the oxidation of a range of primary alcohols to produce aldehydes and hydrogen peroxide. At low substrate concentrations, substrate oxidation is the rate-determining step, and steady-state measurements under these conditions yielded large isotope effects (from 22.5 at 4°C to 13 at 45°C).²⁸ Once again, the large value of the KIE coupled with the strong temperature dependence of the KIEs was interpreted as indicative of tunnelling of the hydrogen atom at the rate-determining step.

7.3.2 Comparison of 2° KIEs and 2° EIEs

One of the first experimental indications of tunnelling in an enzymatic system came from kinetic studies of yeast formate dehydrogenase, an NAD⁺-dependent enzyme that catalyses the conversion of formate to CO₂.³⁰ Blanchard and Cleland measured noncompetitive 2° H/D KIEs for NAD⁺, using formate or deuterated formate as substrates (*i.e.* H or D in the 1° position). The measured intrinsic 2° H/D KIEs (1.23 ± 0.03 with H-transfer, 1.07 ± 0.02 with D-transfer) were both larger than the measured EIE of 0.89.³¹ From these results, they concluded that the reaction involved both coupling of the 1°–2° hydrogens as well as tunnelling from the 1° position. Tunnelling at the 1° position would explain the difference in the magnitude of the 2° KIE with replacement of the 1° H with D, as well as the larger size of the 2° KIE relative to the measured EIE.

7.3.3 Deviations from Semiclassical 2° Swain Schaad Relationships

When it comes to tunnelling, eqn (7.5) is expected to be a much more sensitive probe than eqn (7.4). For 1° KIEs, the highest SSE values found in literature do not exceed 3.7; in fact, even in cases where other signs of tunnelling were evident (from mixed-labelling experiments or temperature-dependence studies of KIEs), the 1° SSE did not differ greatly from the semiclassically predicted values of 3.3 for $\ln(k_H/k_T)/\ln(k_D/k_T)$ and 1.4 for $\ln(k_H/k_T)/\ln(k_H/k_D)$. Recent theoretical works have also provided support for the idea that tunnelling does not affect the value of the 1° SSE in a dramatic way.^{32,33} Hence the semiclassical Swain–Schaad relationships can be used to calculate intrinsic KIEs from a set of observed KIEs. The method employed for this calculation is simply the Northrop method mentioned in Section 7.2.3.

The 2° ^MSSE, on the other hand, is more sensitive to tunnelling effects than its primary counterpart. When 2° KIEs are measured using mixed-labelling experiments (Section 7.2.5.2), an observed breakdown in the 2° Swain–Schaad relationship suggests both tunnelling and coupled motion between primary and secondary hydrogens. The expression for ^MSSE combines the rule of the geometric mean (RGM) and regular expression for the SSE. The RGM states that if the two hydrogens (1° and 2°) are independent of each other, the isotopic label at one position should not affect the isotope effect at the other.³⁴ Thus:

$$r = \frac{\ln(k_{Hi}/k_{HT})}{\ln(k_{Di}/k_{DT})} = 1 \quad (7.10)$$

with $i = \text{H}$ or D . In the absence of coupling, the RGM predicts equivalence between the 2° SSE and the 2° ^MSSE:

$${}^{2\circ}\text{SSE} = \frac{\ln(k_{HH}/k_{HT})}{\ln(k_{HD}/k_{HT})} = \frac{\ln(k_{HH}/k_{HT})}{\ln(k_{DD}/k_{DT})} = {}^{2\circ\text{M}}\text{SSE} \quad (7.11)$$

However, if the motions of 1° and 2° hydrogens are coupled along the reaction coordinate, a breakdown of the RGM will result in an inflated 2° ^MSSE (*i.e.* 2° ^MSSE $>$ 2° SSE).

The following rationalisation has often been used to explain why the 2° ^MSSE is a more sensitive indicator of coupled motion than the 1° ^MSSE: if the 1° and 2° hydrogens are coupled, the 1° KIE will have a secondary component, and will be deflated, but because the 2° H/D KIE is generally small, the deflation expected in the 1° ^MSSE is also very small. Conversely, the 2° KIE will have a primary component, which is much larger than the original 2° KIE. Thus, because H-tunnelling is more significant than D-tunnelling, coupling between 1° and 2° hydrogens results in an inflated 2° ^MSSE.

However, the KIEs for alcohol dehydrogenases (from various sources) and their relevant mutants reveal an interesting trend in the size of the 2° ^MSSE. From a survey of the available data, Klinman³⁵ reported relatively constant 2° H/T KIE values for a range of experiments, but a good correlation between the size of the 2° D/T KIE and that of the 2° ^MSSEs: as the magnitude of the 2° D/T KIE decreases, the 2° ^MSSE increases. This is an unexpected result considering the conventional rationalisation of deviations from the 2° ^MSSE. A proposed explanation for this sensitivity of 2° KIEs to D-transfer (rather than H-transfer) is based on steric hindrance at the active site. If the donor–acceptor distance in the active site has evolved for H-tunnelling, then D-transfer must require an abnormal decrease in this distance. However, a change in the donor–acceptor distance may cause a steric change in the environment surrounding the donor and acceptor atoms, which in turn could lead to a deflation of the 2° KIE.^{vi}

7.3.4 Temperature Dependence of the KIEs

According to transition-state theory (TST), the reaction coordinate of an enzyme-catalysed reaction can be described in terms of a free-energy minimum and maximum, which correspond to the reactant well or ground state (GS) and the transition state (TS) respectively. Furthermore, GS and TS are assumed to be in pseudoequilibrium with each other, thus allowing their relative populations to be determined by the Boltzmann distribution. This simplifying assumption leads to the following exponential relationship between the reaction rate and the absolute temperature, generally known as the Arrhenius equation:

$$k = A \cdot e^{-(E_a/RT)} \quad (7.12)$$

where, A is the Arrhenius pre-exponential factor, E_a is the activation energy, T is the absolute temperature, and R is the gas constant. From eqn (7.12) and the

^{vi}This intuitive explanation is yet to be addressed in a more rigorous fashion.

definition of the KIE, we obtain the following expression for the temperature dependence of KIEs:

$$\text{KIE} = \frac{k_L}{k_H} = \frac{A_L}{A_H} e^{\Delta E_{a(H-L)}/RT} \quad (7.13)$$

As long as the reaction is thermally activated, eqn (7.13) can be used to obtain values for A_L/A_H and $\Delta E_{a(H-L)}$. Since tunnelling from the GS is temperature independent, if tunnelling is the dominant contributor to the rates of both isotopes, the KIEs will be temperature independent. Thus, $\Delta E_{a(H-L)}$ will be close to zero and A_L/A_H will be close to the KIEs at the experimental temperature. In the case of both thermal and tunnelling contributions, the extent of tunnelling can be assessed from the deviation of the Arrhenius parameters from these two extremes. At low temperatures, tunnelling contributions become significant enough that the Arrhenius plot begins to show nonlinear behaviour and we obtain curved plots (see Figure 7.5) whose significance has been discussed elsewhere.³⁶

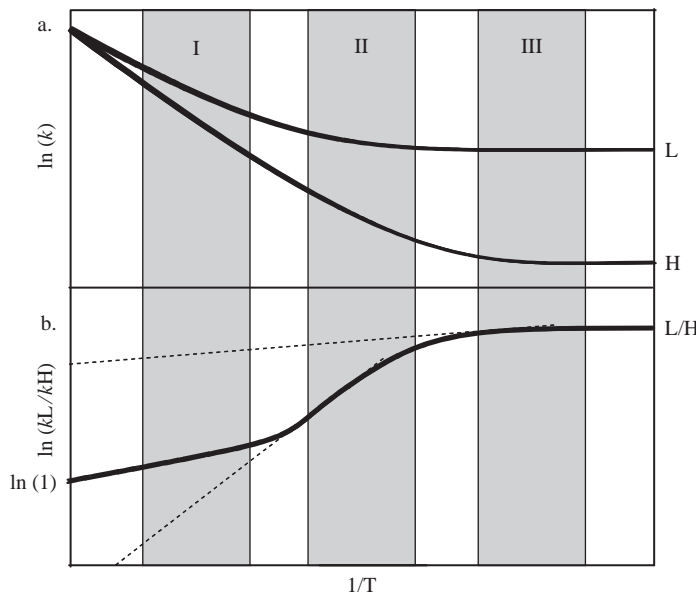


Figure 7.5 An Arrhenius plot of a hydrogen transfer that is consistent with a tunnelling correction to transition state theory. (a) Arrhenius plot of a light isotope (L) and heavy isotope (H). (b) Arrhenius plot of their KIE (L/H). Highlighted are experimental temperature ranges for three systems: I, a system with no tunneling contribution, II, a system with moderate tunnelling, and III, a system with extensive tunnelling contribution. The dashed lines are the tangents to the plot in each region.

The interpretation of KIE temperature dependence as a probe for tunnelling is a much discussed topic,^{4,37} particularly in cases where the experimental data does not fit any of the aforementioned tunnelling regimes. This can occur when $\Delta E_{a(H-L)}$ is close to zero but the ΔH^\ddagger is not zero (in contrast to the prediction illustrated in region III in Figure 7.5). In these cases, it is common to favour Marcus-like models of tunnelling over tunnelling corrections to TST, as discussed in previous chapters in the current work (see Chapters 4 and 5).

7.4 Test Cases: Alcohol Dehydrogenase, Dihydrofolate Reductase and Thymidylate Synthase

The three enzymatic systems described below have all been studied using techniques that are described in Sections 7.2 and 7.3 (e.g. temperature dependence of KIEs, competitive mixed labelling measurements, *etc.*). While tunnelling behaviour has been observed in all three enzymes, alcohol dehydrogenase (ADH) has, to date, been the only system studied that has shown 1°–2° coupled motion (*via* a breakdown of the 2° Swain–Schaad relationship and the rule of the geometric mean). In addition, the studies that suggest coupled motion in ADH all looked at the oxidation of the alternative substrate benzyl alcohol to aldehyde, rather than at the oxidation of the natural substrate. Experiments performed with dihydrofolate reductase (DHFR) revealed no such breakdown of the RGM, and hence suggest the absence of any coupled motions. Thus, until other systems are studied in a similar fashion and also show signs of coupled motion, 2° SSEs must be interpreted with caution.

7.4.1 Alcohol Dehydrogenase

Alcohol dehydrogenases (ADHs) catalyse the reversible conversion of alcohols to aldehydes, using NAD⁺ as the oxidising agent. Yeast and horse liver alcohol dehydrogenases, and a thermophilic ADH from *Bacillus stearothermophilus* (YADH, HLADH, and *bs*ADH, respectively) have been studied extensively in the context of tunnelling and coupled motion. For HLADH and selected mutants, 2° KIEs were measured using mixed-labelling experiments, and deviations from 2°^MSSE were observed. These studies yielded two particularly interesting results:^{38–40} (i) X-ray crystallography and KIE measurements suggested that 2°^MSSE increases with decreasing distance between donor and acceptor⁴⁰ and (ii) for an entire set of mutants, the catalytic efficiency (k_{cat}/K_m) and the 2°^MSSEs appear correlated.³⁹ The first result suggests that the donor–acceptor distance (*i.e.* the tunnelling barrier width) indeed plays a critical role in the 1°–2° coupled motion and tunnelling, while the second result indicates the importance of 1°–2° coupled motion to the catalysed reaction.

For the thermophilic *bs*ADH, small KIEs were reported (~3) along with large enthalpies of activation and the KIEs were temperature independent at temperatures close to the physiological temperature of this thermophile (75 °C).^{41,42} At temperatures much lower than the physiological temperature (30 °C), however,

the KIEs became temperature dependent. These data can be interpreted using a Marcus-like model of tunnelling as having perfect prearrangement (no gating required) at physiological temperature but poor prearrangement (significant gating) at low temperature. In addition, measured 2° M^{SS}E_s were inflated (much larger than 3.3 and up to 15!) at the physiological temperature and sharply decreased at temperatures below 30 °C toward semiclassical values. This decrease in 2° M^{SS}E_s was accompanied by an increase in the enthalpy of activation (14.6 to 23.6 kcal/mol for H-transfer; 15.1 to 31.4 kcal/mol for D-transfer). The mechanistic phase transition was accompanied by an increase in the rigidity of the protein.^{42–44} Together, these results indicate a decrease in tunnelling contributions, or a change in the tunnelling properties, at lower temperatures. This finding can be interpreted by considering the increased rigidity of the enzyme at low temperatures.

7.4.2 Dihydrofolate Reductase

Dihydrofolate reductase (DHFR) is an essential participant in folic acid metabolism, catalysing the conversion of 7,8-dihydrofolate (H₂F) to 5,6,7,8-tetrahydrofolate (H₄F), with nicotinamide adenine dinucleotide phosphate (NADPH) acting as the hydride donor. The reaction involves transfer of the pro-R hydride from C4 of NADPH to C6 of H₂F, with concurrent reduction at the N5 of the H₂F. The small-size and well-characterised kinetic and mechanistic pathways of DHFR, and its biological importance, make it an attractive subject of studies in protein dynamics.⁴⁵ The complex kinetic pathway of DHFR has been extensively studied.⁴⁶

Recently, 1° H/T and D/T KIEs were measured for DHFR across a temperature range of 5–45 °C and the temperature dependence of the intrinsic KIEs was calculated.⁴⁷ The intrinsic KIEs were found to be temperature independent. The intrinsic 1° H/D KIE was 3.5 ± 0.2 , a value that is nearly identical to the KIE of 3.4 calculated from mixed quantum/molecular-dynamics simulations.⁴⁸ The A_H/A_T was 7.2 ± 3.5 , much above the semiclassically expected value. This kind of temperature dependence is indicative of perfect prearrangement of the tunnelling conformations (see Chapter 5). Three distal mutants were also studied (G121V, M42W and G121V-M42W).^{49–51} The mutants were found to exhibit different tunnelling patterns from the wild type (WT) and from each other: while the WT enzyme required no modification of the donor–acceptor distance to facilitate tunnelling, the single mutants did require some rearrangement to arrive at the appropriate tunnelling distance. The double mutant, on the other hand, required significant rearrangement before tunnelling could occur, thus showing a stronger temperature dependence than either of the single mutants.

The finding that mutations at remote residues affected the tunnelling behaviour at the active site suggest the presence of a network of residues that are remote from the active site but are dynamically coupled to the reaction chemistry. The results of these studies are supported by hybrid quantum/classical-molecular-dynamics simulations.^{52–54}

7.4.3 Thymidylate Synthase

Thymidylate synthase catalyses the reductive methylation of 2'-deoxyuridine-5'-monophosphate (dUMP) to 2'-deoxythymidine-5'-monophosphate (dTDP). N⁵,N¹⁰-methylene-5,6,7,8-tetrahydrofolate acts as both a methylene and a hydride donor.⁵⁵ Recent studies on the hydride-transfer step using competitive H/T and D/T KIEs resulted in the calculation of temperature independent intrinsic KIEs, with H/T values close to 7 and $A_H/A_T = 6.8 \pm 2.8$. Interestingly, the reaction had a small enthalpy of activation ($E_a = 4.0 \pm 0.1$ kcal/mol).⁴⁸ As for the DHFR findings presented above, the results with thymidylate synthase could not be explained simply by the tunnelling regimes defined in Section 7.3.4. Models that separated the temperature dependence of the isotopically sensitive and insensitive steps, namely Marcus-like models, rationalised the findings. Thus, the temperature-dependent rates are explained as arising from the isotopically insensitive preorganisation of the system, while the temperature-independent KIEs arise due to the isotopically sensitive tunnelling step.

7.5 Conclusions

The measurement of kinetic isotope effects can play a dramatic role in clarifying the mechanistic and kinetic details of complex enzymatic reactions. In the context of tunnelling, the size and temperature dependence of the KIEs, as well as the Swain–Schaad relationships, can indicate tunnelling in a system. The advantage of KIE measurements lies in their ability to follow changes in the transition state of the reaction, while causing minor disruptions (at most) of the reaction potential surface (isotopes do not affect the electronic configuration of the molecules). As demonstrated in Section 7.2, obstacles such as kinetic complexity can be overcome by using judicious labelling patterns in the KIE experiment, and intrinsic KIEs can be calculated that provide insight into the potential surface of the reaction. Furthermore, experimental measurements of the temperature dependence of KIE have contributed to the development of Marcus-like models of tunnelling. These models are better able to explain different cases of temperature dependence of KIEs, and can shed light on the role of tunnelling and enzyme dynamics in catalysis.

References

1. A. Fersht, *Structure and Mechanism in Protein Sciences: A Guide to Enzyme Catalysis and Protein Folding*, W. H. Freeman, New York, 1998.
2. W. P. Jencks, *Catalysis in Chemistry and Enzymology*, McGraw-Hill, New York, 1987.
3. L. Melander and W. H. Saunders, *Reaction Rates of Isotopic Molecules*, R.E. Krieger, Malabar, FL, 1987.
4. A. Kohen and J. P. Klinman, *Acc. Chem. Res.*, 1998, **31**, 397.
5. J. Bigeleisen and M. G. Mayer, *J. Chem. Phys.*, 1947, **15**, 261.

6. J. Bigeleisen and M. Wolfsberg, *Adv. Chem. Phys.*, 1958, **1**, 15.
7. P. M. Kiefer and J. T. Hynes, *J. Phys. Chem. A*, 2003, **107**, 9022.
8. W. P. Huskey and R. L. Schowen, *J. Am. Chem. Soc.*, 1983, **105**, 5704.
9. D. Ostovic, R. M. G. Roberts and M. M. Kreevoy, *J. Am. Chem. Soc.*, 1983, **105**, 7629.
10. A. Kohen and J. Jensen, *J. Am. Chem. Soc.*, 2002, **124**, 3858.
11. J. Rucker and J. P. Klinman, *J. Am. Chem. Soc.*, 1999, **121**, 1997.
12. J. Pu, S. Ma, M. Garcia-Viloca, J. Gao, D. J. Truhlar and A. Kohen, *J. Am. Chem. Soc.*, 2005, **127**, 14879.
13. C. G. Swain, E. C. Stivers, J. F. Reuwer and L. J. Schaad, *J. Am. Chem. Soc.*, 1958, **80**, 5885.
14. W. W. Cleland, in *Isotope Effects in Chemistry and Biology*, ed. A. Kohen and H. H. Limbach, Taylor & Francis, CRC Press, Boca Raton, FL, 2006, p. 915.
15. D. B. Northrop, in *Isotope Effects in Chemistry and Biology*, ed. A. Kohen and H. H. Limbach, Taylor & Francis, CRC Press, Boca Raton, FL, 2006, p. 837.
16. W. E. Karsten and P. F. Cook, in *Isotope effects in Chemistry and Biology*, ed. A. Kohen and H. H. Limbach, Taylor & Francis, CRC Press, Boca Raton, FL, 2006, p. 794.
17. D. B. Northrop, in *Isotope Effects on Enzyme-catalysed Reactions*, ed. W. W. Cleland, M. H. O'Leary and D. B. Northrop, University Park Press, Baltimore, MD, 1977, p. 122.
18. D. B. Northrop, in *Enzyme Mechanism from Isotope Effects*, ed. P. F. Cook, CRC Press, Boca Raton, FL, 1991, p. 181.
19. W. W. Cleland, *Adv. Enzymol.*, 1977, **45**, 273.
20. D. W. Parkin, in *Enzyme Mechanism from Isotope Effects*, ed. P. F. Cook, CRC Press, Boca Raton, FL, 1991, p. 269.
21. W. H. Saunders, *J. Am. Chem. Soc.*, 1985, **107**, 164.
22. A. Kohen, in *Isotope Effects in Chemistry and Biology*, ed. A. Kohen and H. H. Limbach, Taylor & Francis CRC Press, Boca Raton, FL, 2006, p. 743.
23. W. P. Huskey, *J. Phys. Org. Chem.*, 1991, **4**, 361.
24. W. H. Saunders, *Croat. Chem. Acta*, 1992, **65**, 505.
25. S. Lin and W. H. Saunders, *J. Am. Chem. Soc.*, 1994, **116**, 6107.
26. J. Hirschi and D. A. Singleton, *J. Am. Chem. Soc.*, 2005, **127**, 3294.
27. T. Jonsson, M. H. Glickman, S. J. Sun and J. P. Klinman, *J. Am. Chem. Soc.*, 1996, **118**, 10319.
28. M. M. Whittaker, D. P. Ballou and J. W. Whittaker, *Biochemistry*, 1998, **37**, 8426.
29. M. H. Glickman and J. P. Klinman, *Biochemistry*, 1995, **34**, 14077.
30. W. W. Cleland and J. S. Blanchard, *Biochemistry*, 1980, **19**, 3543.
31. J. D. Hermes, S. W. Morrical, M. H. O'Leary and W. W. Cleland, *Biochemistry*, 1984, **23**, 5479.
32. Z. Smedarchina and W. Siebrand, *Chem. Phys. Lett.*, 2005, **410**, 370.

33. C. S. Tautermann, M. J. Loferer, A. F. Voegele and K. R. Liedla, *J. Chem. Phys.*, 2004, **120**, 11650.
34. J. Bigeleisen, *J. Chem. Phys.*, 1955, **23**, 2264.
35. J. P. Klinman, *Philos. Trans. Royal Soc. B*, 2006, **361**, 1323.
36. D. G. Truhlar and A. Kohen, *Proc. Natl. Acad. Sci. USA*, 2001, **98**, 848.
37. A. Kohen and J. P. Klinman, *Chem. Biol.*, 1999, **6**, 191.
38. B. J. Bahnsen, D. H. Park, K. Kim, B. V. Plapp and J. P. Klinman, *Biochemistry*, 1993, **32**, 5503.
39. B. J. Bahnsen, T. D. Colby, J. K. Chin, B. M. Goldstein and J. P. Klinman, *Proc. Natl. Acad. Sci. USA*, 1997, **94**, 12797.
40. T. D. Colby, B. J. Bahnsen, J. K. Chin, J. P. Klinman and B. M. Goldstein, *Biochemistry*, 1998, **37**, 9295.
41. A. Kohen, R. Cannio, S. Bartolucci and J. P. Klinman, *Nature*, 1999, **399**, 496.
42. A. Kohen and J. P. Klinman, *J. Am. Chem. Soc.*, 2000, **122**, 10738.
43. C. E. Atreya, E. F. Johnson, J. Williamson, S. Y. Chang, P. H. Liang and K. S. Anderson, *J. Biol. Chem.*, 2003, **278**, 28901.
44. Z. X. Liang, T. Lee, K. A. Resing, N. G. Ahn and J. P. Klinman, *Proc. Natl. Acad. Sci. USA*, 2004, **101**, 9556.
45. S. Hammes-Schiffer and S. J. Benkovic, *Annu. Rev. Biochem.*, 2006, **75**, 519.
46. C. A. Fierke, K. A. Johnson and S. J. Benkovic, *Biochemistry*, 1987, **26**, 4085.
47. R. S. Sikorski, L. Wang, K. A. Markham, P. T. R. Rajagopalan, S. J. Benkovic and A. Kohen, *J. Am. Chem. Soc.*, 2004, **126**, 4778.
48. N. Agrawal, B. Hong, C. Mihai and A. Kohen, *Biochemistry*, 2004, **43**, 1998.
49. L. Wang, S. Tharp, T. Selzer, S. J. Benkovic and A. Kohen, *Biochemistry*, 2006, **45**, 1383.
50. L. Wang, N. M. Goodey, S. J. Benkovic and A. Kohen, *Philos. Trans. Royal Soc. B*, 2006, **361**, 1307.
51. L. Wang, N. M. Goodey, S. J. Benkovic and A. Kohen, *Proc. Natl. Acad. Sci. USA*, 2006, **103**, 15753.
52. P. K. Agarwal, S. R. Billeter, P. T. R. Rajagopalan, S. J. Benkovic and S. Hammes-Schiffer, *Proc. Natl. Acad. Sci. USA*, 2002, **99**, 2794.
53. J. B. Watney, P. K. Agarwal and S. Hammes-Schiffer, *J. Am. Chem. Soc.*, 2003, **125**, 3745.
54. A. Warshel and H. Liu, *J. Phys. Chem. B*, 2007, **111**, 7852.
55. D. V. Santi and C. F. Brewer, *J. Am. Chem. Soc.*, 1968, **90**, 6236.

CHAPTER 8

Direct Methods for the Analysis of Quantum-Mechanical Tunnelling: Dihydrofolate Reductase

E. JOEL LOVERIDGE AND RUDOLF K. ALLEMANN

School of Chemistry, Cardiff University, Cardiff, CF10 3AT, UK

8.1 Introduction

The catalytic power of enzymes has fascinated scientists for many decades but has long remained mysterious. The exquisite specificity and selectivity of enzymes can be explained, at least to a first approximation, by the simple lock and key model proposed more than a century ago by Emil Fischer to generate a reactive conformation¹ and its adaptation to ground-state destabilisation by Haldane.² The enormous catalytic power of enzymes, which accelerate chemical reactions by up to 20 orders of magnitude, has been explained by a lowering of the transition-state energy and/or an increase of the ground-state energy in a static energy barrier. This view of biological catalysis, which has its roots in Eyring's transition-state theory (TST),^{3,4} was the driving force behind the design of transition-state analogues for the inhibition of pharmacologically important enzymes and for the creation of catalytic antibodies. However, over the last decade or so it has become increasingly clear that there is more to enzyme catalysis than a repositioning of the relative energies of ground and transition states

along a static energy barrier, and the role of quantum-mechanical tunnelling by protein dynamics has become established, at least for some enzymes that transfer particles of relatively low mass such as electrons or hydrogen atoms.

Previous chapters have focused on the quantum-tunnelling phenomenon itself and its relevance to enzymology, and have discussed extensively how quantum tunnelling in enzymatic reactions can be inferred from the kinetic isotope effects (KIE), the Swain–Schaad exponents, the ratios of the Arrhenius pre-exponential factors (*i.e.* the KIE at infinite temperature), and the difference between the activation energies of the reaction with heavy and light isotopes. Deviations of these parameters from their classical values are thereby considered indicative of tunnelling. Here, we will concentrate on experimental and computational methods mostly applied to the enzyme dihydrofolate reductase to determine the existence and extent of tunnelling in an enzymatic reaction and a comparison of the results obtained by different methods.

8.1.1 The Kinetic Isotope Effect

The measurement of kinetic isotope effects has been central to probing chemical mechanism since their values provide information on the reaction coordinate. Primary KIEs arise when hydrogen is transferred during the reaction. In a semiclassical treatment of transition-state theory, the kinetic isotope effect arises from differences in the zero-point energies of different isotopes of the same element. When comparing protium to deuterium transfer, the KIE is defined as

$$k_{\text{H}}/k_{\text{D}} = A_{\text{H}}/A_{\text{D}} \exp\{(1/2hv_{\text{H}} - 1/2hv_{\text{D}})/RT\}$$

where v_{H} and v_{D} are the vibrational frequencies of the transferring H or D (Figure 8.1(a)). This leads to a higher energy barrier for heavier isotopes and a correspondingly lower rate of reaction. In the case of the isotopes of hydrogen, the zero-point energy of a typical bond to carbon is highest for protium, lower for deuterium, and lower still for tritium. These differences in zero-point energy represent the maximum differences in activation energy for the isotopes, and lead to a maximum primary H/D KIE of ~ 7 , a maximum H/T KIE of ~ 18 , and a maximum D/T KIE of ~ 2 at 300 K, while at infinite temperature the ratio of the pre-exponential factors is approximately unity.⁵ The isotopes of hydrogen have large KIEs due to their large relative difference in mass. The isotopes of carbon, for example, which have much smaller relative differences in mass, display much smaller KIEs and rates for ^{12}C are typically only 1.04 times faster than those for ^{13}C .

The unusually high KIEs observed in some organic hydrogen-transfer reactions led to the development of the Bell model of tunnelling.⁶ In the case of hydrogen isotopes, the mass of the atom is sufficiently small, and therefore the de Broglie wavelength sufficiently large, for the uncertainty in its position to be large enough for quantum-mechanical tunnelling to contribute significantly to the reaction (Figure 8.1(b)). This arises from the overlap of the reactant and product

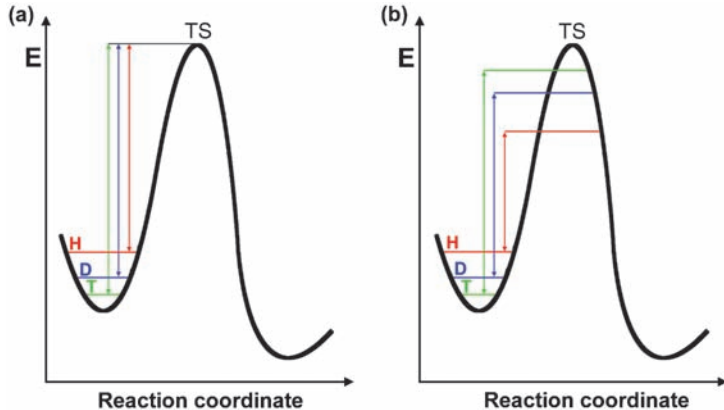


Figure 8.1 (a) Within the semiclassical model, KIEs arise from differences between the zero point energies of the three isotopes of hydrogen leading to activation energies $E_a^{\text{H}} < E_a^{\text{D}} < E_a^{\text{T}}$. The maximum KIE is fixed by this difference in zero point energy under the assumption of vanishing isotopic differences in the transition state (TS). (b) In the Bell correction to the semiclassical model tunnelling occurs from a thermally excited state near TS, and is characterised by greater tunnelling distances for lighter isotopes (allowing tunnelling to occur at lower energies for lighter isotopes), increasing the difference in activation energies and hence the KIEs. The maximum KIE is dependent on the barrier width.

wavefunctions in the classically forbidden region of the energy barrier. In this case, both the barrier height (determined by the energy difference between the ground state and transition state) and its width (which is determined by the donor–acceptor distance along the reaction coordinate) must be taken into account. This may provide a further increase in the KIE above that predicted semiclassically, as tunnelling may occur when the barrier width is equal to or less than the de Broglie wavelength. As the three isotopes of hydrogen have different masses, they also have different de Broglie wavelengths – that of protium will be higher than that of deuterium, which will be higher than that of tritium. Protium will therefore be able to tunnel at a lower energy than deuterium, which in turn will be able to tunnel at a lower energy than tritium. A wide, low barrier will therefore display only a very slightly elevated maximum KIE; whereas a narrow, high barrier will give KIEs far higher than those possible in the absence of tunnelling.

In some cases, measurement of the KIE alone is sufficient to show that tunnelling may be playing a role in the reaction. KIEs greatly in excess of the classical limits are strong indicators of tunnelling. In other cases, the KIE may not be large but tunnelling may still be playing a role, and it is the temperature dependence of the KIE that can be used to infer the presence of tunnelling. In the semiclassical picture (Figure 8.1(a)), the sole contributor to the KIE is the difference in activation energy between reactions involving the two isotopes.

In this case, the Arrhenius plots with the heavy and light isotopes will have different gradients (the gradient being equal to $-E_a/R$), and the difference in the activation energies should not be larger than the difference in zero-point energies (typically 5.4 kJ mol⁻¹ for H and D at 300 K). The KIE will therefore be temperature dependent, decreasing as the temperature increases. Furthermore, at infinite temperature, where there is always sufficient energy for the reaction to occur and therefore no isotope effect, the Arrhenius plots from the two isotopes will converge to a single value of $\ln A$ and so the ratio A_H/A_D will be approximately 1. Deviations from this semiclassical behaviour such as, for example, greatly inflated KIEs, a temperature-independent KIE and/or usually high or low A_H/A_D ratios are strong indicators that tunnelling is playing a role in the reaction. In some cases, as tunnelling causes an apparent decrease in the Arrhenius prefactor, A_H will be smaller than A_D (as H tunnels at lower energy) and so the ratio A_H/A_D will be less than 1. On the other hand, where tunnelling leads to a nearly temperature-independent KIE (see below) A_H/A_D will be approximately equal to the KIE itself, *i.e.* greater than 1. The gradients of the Arrhenius plots with the heavy and light isotopes will also show if the difference in the activation energies is larger than that expected for semiclassical behaviour. In addition, in the semiclassical model the Swain–Schaad exponent, which relates the H/T and D/T KIEs, has a characteristic value of 3.3 ($k_H/k_T = (k_D/k_T)^{3.3}$). Deviations from this value have been used as evidence of tunnelling.

8.1.2 The Significance of Tunnelling in Enzymatic Reactions

Tunnelling is significant as it provides an alternative route to classical over-the-barrier catalysis in reactions involving transfer of hydrogen or electrons. It therefore provides a reduction in the activation energy of the reaction over and above that offered by transition-state stabilisation or ground-state destabilisation. The discovery of tunnelling as a significant effect in enzymatic reactions provides a further extension to our knowledge of the workings of enzymes by revealing an additional method by which the activation energy of a reaction can be lowered and hence the rate increased. In some cases, tunnelling has a dramatic effect on the reaction rate. KIEs close to 100 have been observed for enzymes such as soybean lipoxygenase⁷ and methane mono-oxygenase,⁸ with soybean lipoxygenase also displaying a greatly inflated A_H/A_D ratio of 18, well above the semiclassical limit of 1.3 (the largest deviation that can be adequately explained by experimental error).

When considering tunnelling in the context of an enzymatic system, the dynamics of the protein must also be taken into account. Proteins are not static entities, but exist in a constant state of motion, which may have an effect on the degree of tunnelling observed in the enzyme-catalysed reaction. Most notably, the motion of the enzyme is temperature dependent, whereas tunnelling itself is not. Therefore, if the degree of tunnelling can be shown to be temperature dependent, then that suggests that tunnelling is coupled to the motion of the

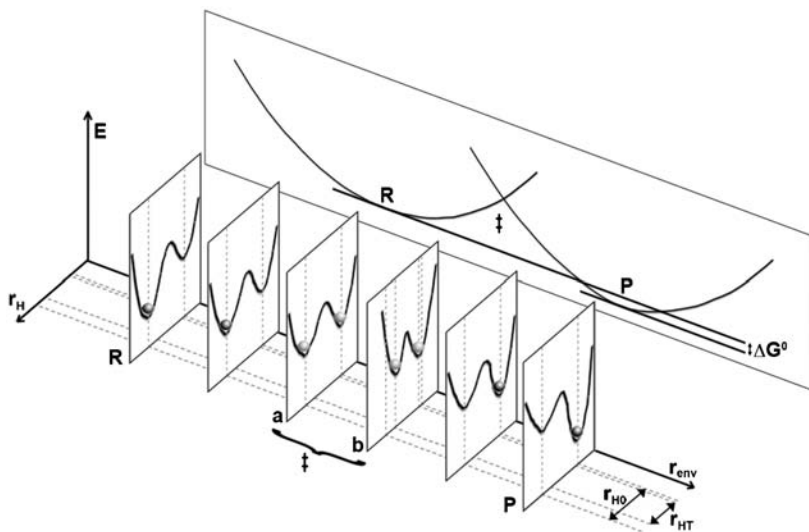


Figure 8.2 Coupling of enzyme motions to catalysis. The transferred hydrogen is shown as a gray sphere. The axes are E =energy, r_{env} =environmental reaction coordinate (controlled by passive dynamics) excluding the transferred hydrogen, and r_H =hydrogen reaction coordinate (controlled by active dynamics). The small vertical panels show the double well potential energy as the reaction progresses from the reactant state (R) to the product state (P). Panels a and b represent the pseudotransition state (double dagger), where in panel a the reactant and product states are almost equal in energy but r_{H0} is greater than the maximum tunnelling distance r_{HT} , and in panel b an active gating motion has compressed the hydrogen coordinate such that tunnelling may now occur. The rear vertical panel shows the free energy curves along the environmental coordinate, where ΔG is the free energy of the reaction.

enzyme. Breakpoints in the temperature dependence of the KIE provide a stronger indication of motion-coupled tunnelling (see Section 2.3), as these can be explained by tunnelling being affected by a motion that is only active above the breakpoint temperature. Protein motions affecting tunnelling have been divided into two categories, dubbed “active” and “passive” dynamics (Figure 8.2).⁹ Active dynamics, also referred to as “gating”, is a term that describes motions along the hydrogen reaction coordinate. These motions alter the donor–acceptor distance, and so allow increased tunnelling when the distance is shortened and the barrier to reaction therefore narrowed. Passive dynamics then describe more general motions, which are not along the hydrogen coordinate but that organise the enzyme into a configuration more conducive to the reaction and comprise all other dimensions of the reaction coordinate. This distinction is somewhat artificial, as active dynamics are really a subset of the passive dynamics of the enzyme, rather than a separate set of motions that can be isolated from the other coordinates. Nevertheless, it serves a useful purpose within the formalism of the coupling of protein motions and catalysis. More

recently, the terms “active” and “passive” dynamics have been replaced with alternative expressions, for example “reorganisation” and “preorganisation” respectively, in an attempt to clarify this.¹⁰ For the purposes of this chapter, the terms active (gating) and passive dynamics will be used.

The high stability of thermophilic enzymes allows the measurement of the KIEs over a relatively large temperature range. In several cases it has been observed that at high temperatures the reactions catalysed by thermophilic enzymes show semiclassical behaviour, while on reduction of the temperature tunnelling competes efficiently with over the barrier transfers.^{11,12} The same argument applies for mesophilic enzymes when the chemical step of the reaction is much faster than the rate-limiting step. There may not be a selective advantage of tunnelling when the reaction is limited by physical steps such as substrate binding or product release rather than by the chemical step. Furthermore, studies of a series of B₁₂-dependent mutases have revealed that the enzyme-catalysed reaction proceeds with the same degree of tunnelling as the uncatalysed reaction.^{13,14} Of course this does not diminish the importance of tunnelling to enzymatic reactions, and in any case by this argument tunnelling may be selected for in enzymes where the chemical step is rate limiting and temperatures are low.

8.1.3 Experimental Methods of Observing the Chemical Step of the Reaction

To determine KIEs of the chemical step of a reaction and to use the measured values to analyse tunnelling, it is essential that the relevant chemical step itself be observed. By relevant, we mean the step that is affected by the isotopic composition of the molecule. Enzymatic reactions are not single-step processes, but require substrate binding, chemical steps (of which there may be many), rearrangement of the substrate, intermediates and/or enzyme, and product release to be taken into account. The simplest conceivable enzymatic reaction would have to consist of at least three components (Figure 8.3), with the overall (steady-state) rate of the reaction being determined by the rate-limiting step. In some cases, where the chemical step of the reaction is also the rate-limiting step, it is possible to observe this chemical step directly using steady-state methods. Alternatively, if the rate of the chemical step is pH dependent (or, more importantly, more pH dependent than the other steps), it may be possible to observe the reaction using steady-state methods at a pH where the chemical step becomes rate limiting. In the majority of cases, the relevant chemical step is



Figure 8.3 Kinetic scheme for a simple three component enzymatic reaction. E = enzyme, S = substrate and P = product. The rate constant k_2 refers to the chemical step of the reaction.

not rate limiting under physiological conditions. In these cases, the steady-state rate will often display a KIE close to unity, and would therefore be unsuitable as an experimental method.

Where a step other than the chemical step is rate limiting, transient-state kinetics methods may be used to directly monitor its rate rather than to measure the overall turnover.¹⁵ Extensive use has been made of stopped-flow techniques to isolate the chemical step. The stopped-flow apparatus itself is quite simple in concept (Figure 8.4). The two (or more) reactants are stored in temperature-controlled syringes, which are operated by a single push-plate driven by a compressed gas cylinder to ensure an equal volume of each is used. On firing the syringes, the two reactants pass through a mixer and into the detector, forcing the solution previously in the detector out into a third syringe. The volume of sample used is determined by this third syringe, which may only move a certain distance before meeting a stop plate.

Due to the time required for efficient mixing, a stopped-flow apparatus has a dead time of a few milliseconds. This technique therefore cannot measure rate constants much above 10^3 s^{-1} . For such reactions, continuous-flow methods are required. Here, the two reactant streams are gently combined so no significant mixing occurs, then passed into a chamber that narrows to a mixing sphere at the tip. Flow over the sphere gives intense mixing and the mixed solution forms a continuous jet, which passes through the detector.

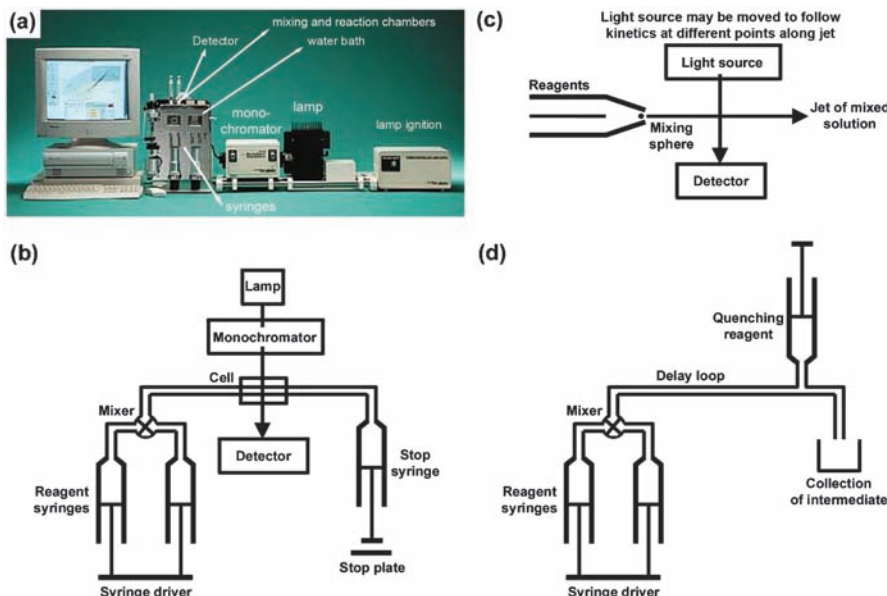


Figure 8.4 (a) A typical stopped flow apparatus indicating the major components, mixing and reaction chamber and detector. Reproduced with permission from *Applied Photophysics*. (b) Schematic diagrams of stopped flow, (c) continuous flow apparatus and (d) quench flow equipment.

Continuous-flow methods may give dead times of only a few microseconds allowing much faster reactions to be observed than with stopped-flow methods, although with a concurrent sharp increase in the amount of sample required.

In other cases, stopped-flow techniques may not be used as the kinetics cannot be followed by a suitable detection method. In such cases quench-flow techniques may be used. Here, the substrates are rapidly mixed in the same way as for stopped-flow, but the reaction is then terminated at various times by addition of a quenching reagent. The quenched reaction mixture is then analysed to determine the concentration and isotope incorporation of the product or trapped intermediate.

Steady-state kinetics at raised or lowered pH and transient-state kinetics each have their own advantages and disadvantages. A major advantage of transient-state measurements is that these can be made under conditions more closely resembling the physiological conditions of the enzyme. Steady-state methods at nonphysiological pH may lead to difficulties in interpreting the data, as the results are obtained under conditions in which the enzyme's behaviour may be different from that observed in its natural environment. Steady-state methods at nonphysiological pH, however, allow the use of competitive experiments, as discussed by Sen and Kohen in Chapter 7. Competitive experiments not only allow use of radioactive isotopes – thus allowing H/T KIEs to be measured, but are also more sensitive than noncompetitive measurements, leading to smaller experimental errors and so allowing the facile measurement of smaller KIEs (for example those observed in heavy atoms or secondary KIEs). Competitive experiments to determine H/T and D/T KIEs also allow the intrinsic KIE to be unmasked by the method of Northrop.^{16,17} This is important where some residual kinetic complexity partially masks the chemical step, as the observed primary KIE will be smaller than the intrinsic KIE of the chemical step. A disadvantage of competitive experiments is that these only allow the KIE on k_{cat}/K_m to be measured, whereas noncompetitive experiments also allow the KIE on k_{cat} to be measured. A drawback to transient-state kinetics, particularly using continuous-flow methods, is that these typically require rather high concentrations of enzyme, which can often prevent these methods from being practically useful.

Quantum tunnelling has also been studied extensively using computational methods.¹⁸ These have the advantage that reactions not amenable to experimental observation can be studied, and also that the different contributions to the overall reaction may be more readily separated from one another. To date, however, computational methods have been more successful in predicting trends rather than absolute values.

8.2 Dihydrofolate Reductase: A Case Study

Dihydrofolate reductase (DHFR) is a ubiquitous enzyme that plays a central role in the metabolism of one-carbon units by catalysing the conversion of 7,8-dihydrofolate (H_2F) to 5,6,7,8-tetrahydrofolate (H_4F). DHFR utilises reduced

nicotinamide adenine dinucleotide phosphate (NADPH) as the hydride donor, catalysing transfer of the C4 pro R hydride of NADPH to the Re face of C6 of H₂F with the concomitant protonation of N5 of H₂F (Figure 8.5). H₄F acts as a carrier of one-carbon units in various oxidation states, and is essential for the production of purine bases, deoxy-thymidine triphosphate, methionine and, in prokaryotes, pantothenic acid.

Due to its vital role in maintaining intracellular pools of tetrahydrofolate, DHFR has long been recognised as an important target for anticancer and antibacterial drugs. DHFRs from more than thirty organisms from the three domains of life have been characterised and the enzyme has been studied extensively by X-ray crystallography,^{19–22} NMR spectroscopy^{23–33} and computation.^{34–52} DHFR from *Escherichia coli* (EcDHFR) is a monomeric enzyme consisting of four α -helices, eight β -sheets, and four mobile loops (Figure 8.6). The enzyme is separated into two domains, the adenosine binding domain (ABD) and the loop domain (LD). All chromosomally encoded DHFRs share the same three-dimensional fold.

Despite the complex kinetic mechanism of EcDHFR (Figure 8.7),⁵³ the chemical step is simple and readily observable, as the reaction can be monitored spectrophotometrically from the loss of absorbance at 340 nm (or fluorescence emission at 450 nm) as NADPH is consumed. In addition, the presence of an active-site tryptophan residue allows the use of fluorescence resonance energy transfer (FRET) experiments, as tryptophan fluoresces at around 345 nm (thereby exciting NADPH) following excitation at 290 nm. Notably, the rate of the chemical step (hydride transfer) is strongly affected by pH due to protonation of the substrate. At low pH, the rate of hydride transfer is greatly accelerated (although the steady-state rate remains similar to that at pH 7, as it is limited by the pH-independent rate of product release), whereas at pH 9 and

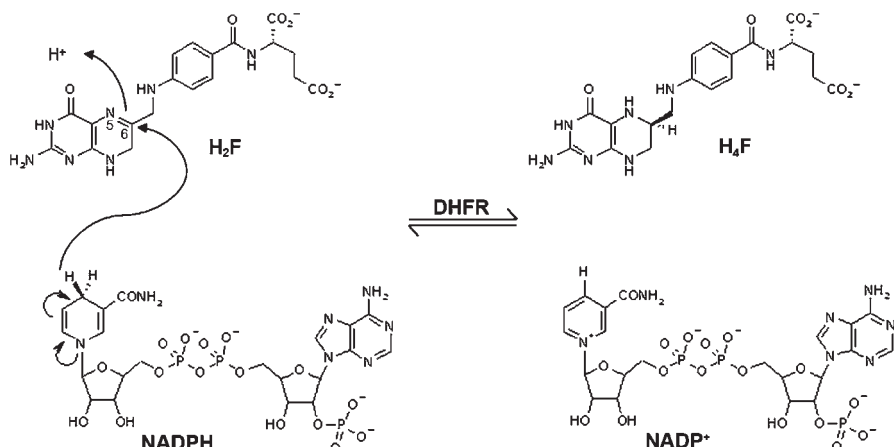


Figure 8.5 The reaction catalysed by DHFR in which H_{Re} is transferred from the reduced cofactor (NADPH) to the Re face on C6 of H₂F.

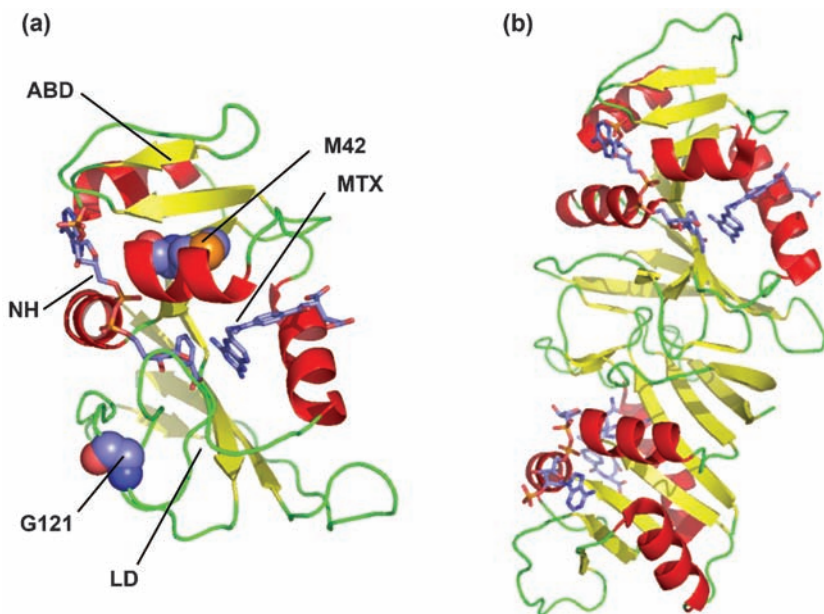


Figure 8.6 Structures of EcDHFR (a) and TmDHFR (b) complexed to NADPH (NH) and methotrexate (MTX). The adenosine binding (ABD) and loop (LD) domains and the residues M42 and G121 are highlighted in EcDHFR. This figure was created from 1DRE (a)²² and 1D1G (b).⁷⁸

above, hydride transfer becomes rate limiting (Figure 8.7) and so may be observed using steady-state methods.

Unlike other enzymes, where the inflated KIEs alone have indicated that tunnelling plays a major role in the reaction, in the case of DHFR the KIEs are rather small and fall within the semiclassical range.^{12,54–58} Tunnelling has instead been inferred from the temperature dependence of the KIE, the ratio of the Arrhenius prefactors, and the activation-energy differences on isotopic substitution. The temperature dependences of the KIEs of mesophilic DHFR from *Escherichia coli* (EcDHFR), thermophilic DHFR from *Bacillus stearothermophilus* (BsDHFR) and hyperthermophilic DHFR from *Thermotoga maritima* (TmDHFR) have been determined, allowing a comparison of the degree of tunnelling in these enzymes.

8.2.1 DHFR from *Escherichia coli*

The most extensively studied DHFR is that of the mesophile *E. coli*. The temperature dependence of the KIEs of the EcDHFR-catalysed reduction of H₂F has been observed by a number of methods, both in the wild-type enzyme and in a series of mutants.

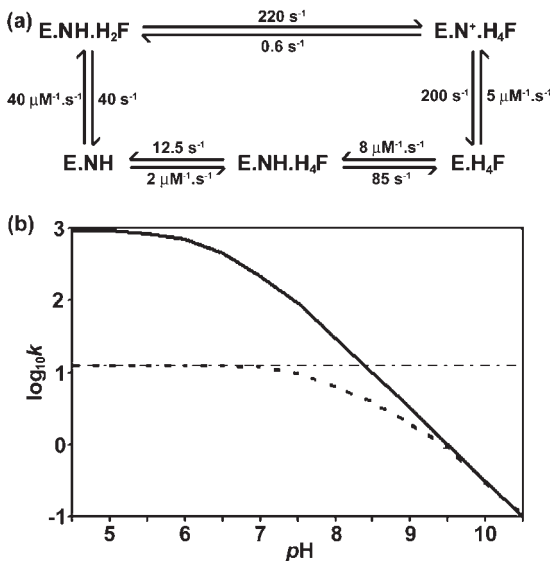


Figure 8.7 (a) Simplified kinetic scheme of EcDHFR at pH 7.0 showing the reaction cycle. E = EcDHFR; NH = NADPH; N⁺ = NADP⁺; H₂F = dihydro folate; H₄F = tetrahydrofolate. (b) Logarithmic plot of the hydride transfer rate (solid line) and k_{cat} (dotted line) against pH showing how hydride transfer becomes rate limiting at high pH and k_{cat} becomes limited by the rate of H₄F release (dashed dotted line) at low pH. Figures adapted from Fierke *et al.*⁵³

Work by Benkovic and coworkers has made use of noncompetitive stopped-flow techniques to study the presteady-state kinetics of EcDHFR and found a primary KIE of around 2.7 at pH 7.⁵³ A computational analysis of the EcDHFR-catalysed reaction revealed a primary KIE of 2.8, mainly as a consequence of the quantisation of the bound vibrations, while the secondary KIE was due to dynamical effects on the reaction coordinate, especially tunnelling.⁵⁹ Kohen and coworkers took advantage of the observation that the ratio of the hydride-transfer rate to the steady-state rate is strongly pH dependent⁵³ to obtain H/T, H/D and D/T KIEs in competitive experiments at pH 9. From these experimentally observed values they determined intrinsic KIEs that did not vary significantly with temperature ($\Delta E_a < 0.5 \text{ kJ mol}^{-1}$) and an Arrhenius prefactor ratio that was slightly inflated ($A_H/A_D = 4.0 \pm 1.5$).⁵⁴ A semiclassical treatment of these results would only be valid if the activation energy itself is small, whereas the experimentally determined value of $15.3 \pm 1.2 \text{ kJ mol}^{-1}$ was significant. The results were therefore interpreted as evidence for environmentally coupled tunnelling in which passive fluctuations in the enzyme structure, rather than active dynamics along the reaction coordinate, played the dominant role.

Pu *et al.* provided a possible theoretical explanation of the unusually small temperature dependence of the EcDHFR-catalysed reaction at pH 9.⁶⁰

A combined quantum-mechanical and molecular-modelling approach using ensemble-averaged variational transition-state theory with multidimensional tunnelling (EA-VTST/MT) identified two key features that might contribute to cancelling most of the temperature dependence of the KIE, namely a variation of the transition-state position and temperature dependence of the effective potential for tunnelling. An EA-VTST/MT calculation that included these effects suggested a variation in the KIE of only $\sim 7\%$ between 4 and 45 °C.

A presteady-state analysis at pH 7 revealed an increased temperature dependence of the KIEs ($\Delta E_a = 7.8 \text{ kJ mol}^{-1}$) than had been observed at pH 9.^{54,55} The ratio of the pre-exponential factors ($A_H/A_D = 0.108$) fell just outside the semiclassical range. As above, the significant activation energy ($E_a^H = 29.9 \pm 0.6 \text{ kJ mol}^{-1}$) and relatively small KIEs (between 2.2 and 3) are incompatible with a semiclassical treatment, and instead are indicative of environmentally coupled tunnelling in which active dynamics (gating) play the major role. It is interesting to note that the key point of the computational analysis of the KIEs of EcDHFR catalysis was the smallness of the temperature dependence of the KIEs rather than their temperature independence.⁶⁰ Because the small temperature dependence appears to result not from an intrinsically temperature-independent mechanism but rather from a near-cancellation of two competing temperature-dependent effects, the remaining temperature dependence is difficult to predict and may well be sensitive to changes in the reaction conditions such as pH.

Studies with EcDHFR mutants suggested that the M20, FG and GH loops known to control binding of substrate and cofactor,²² are also involved in controlling the chemical step during EcDHFR catalysis.^{22,61-63} Replacement of Gly 121, a highly mobile residue located in the middle of the FG loop over 19 Å from the active site, with Val, Ala or Leu slowed the hydride-transfer rate dramatically and weakened binding of NADPH.⁶³ While being strictly conserved in all prokaryotic DHFRs, Gly 121 does not appear to form any interactions with other residues. Molecular dynamics (MD) simulations of EcDHFR revealed a strong correlation between the movement of the catalytically important M20 and FG loops.⁶⁴⁻⁶⁷ These correlated motions were only observed in reactive complexes of the enzyme and were absent in the product complex.^{65,66} Mixed quantum-mechanical molecular-mechanical (QM/MM) simulations and genomic sequence analysis have identified a network of hydrogen bonds and van der Waals contacts from Asp 122 on the surface of the protein to the active site.⁴⁰ This network may facilitate hydride transfer, suggesting a direct link between the motion of the FG loop and the catalytic events in the active site.⁶⁸ In good agreement with the kinetic measurements, computation revealed a significant increase in the energy barrier for the hydride transfer of the Gly 121 to Val mutant (EcDHFR-G121V) relative to the wild-type enzyme.³⁹ However, a spectroscopic analysis of the folding properties of EcDHFR and its Gly to Val mutant indicated that the reduced catalytic activity of the mutant protein was the consequence of nonlocal structural effects that originate at the site of mutation and may result in a perturbation of the structure at the active site.⁵⁵

Analysis of the catalytic properties of EcDHFR-G121V at pH 7.0 revealed that, like for EcDHFR, the KIEs were temperature dependent (Figure 8.8) with $\Delta E_a = 7.5 \text{ kJ mol}^{-1}$ and $A_H/A_D = 0.0025$.⁵⁵ The ratio of the pre-exponential factors is more strongly inverse than in the wild type by almost 2 orders of magnitude, indicating that lowered catalytic efficiency of the mutant is due to entropic, rather than enthalpic effects. It appears that as a consequence of a remote structural change in a surface loop the active site of the mutants is less well organised to promote tunnelling, and relies on gating, as evidenced in the stronger temperature dependence of the KIEs in the mutants. Similar conclusions were reached from an analysis at pH 9 of the coordinated effects of the distal residues Gly 121 and Met 42 on hydrogen transfer. Despite a large effect of the single mutations on the reaction rates, their effect on the nature of the transfer seemed small, while the double mutant substantially altered the H-transfer mechanism.^{69,70}

EcDHFR has also been extensively studied using computational methods. Warshel has recently challenged the need to invoke tunnelling to explain unusual temperature dependences in DHFR,⁷¹ but other workers have tried to identify the motions that might promote hydrogen transfer. In addition to the QM/MM studies by Gao and Truhlar mentioned above,^{59,60} Hammes-Schiffer and co-workers have concentrated their attention on the importance of coupled promoting motions for catalysis in EcDHFR using mixed quantum/classical-molecular

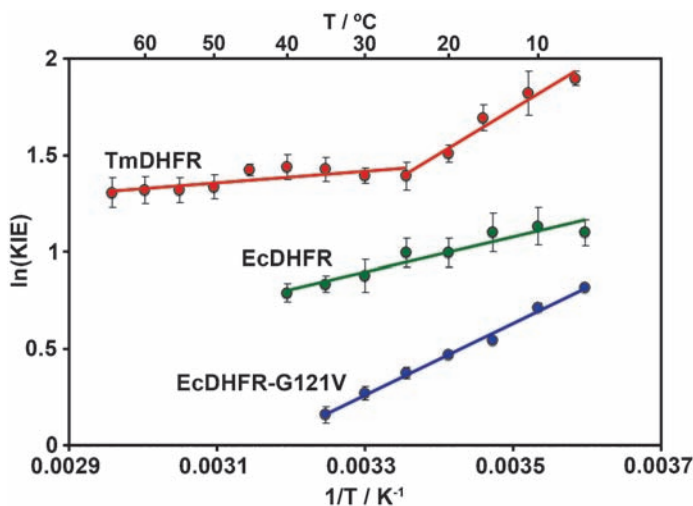


Figure 8.8 Kinetic isotope effects for the hydride transfer from NADPH/NADPD to H_2F on a logarithmic abscissa against the inverse temperature for the reactions catalysed by TmDHFR,¹² EcDHFR⁵⁵ and EcDHFR G121V⁵⁵ at pH 7.0. The temperature dependences of the homologous enzymes are similar at low temperature and indicate significant contributions to the reaction rates from tunnelling. At higher temperature the KIEs for TmDHFR become largely temperature independent.

dynamics with empirical valence bond potentials.^{39–41} These promoting motions are proposed to shorten the hydride donor–acceptor distance, compressing the reaction coordinate, thereby narrowing the barrier to reaction and promoting tunnelling. It was found that quantum effects such as zero-point energy and tunnelling contribute around 10 kJ mol^{-1} towards the lowering of the reaction barrier. The calculated KIE was in good agreement with the previously published experimental value. Their studies also indicated that some promoting motions were absent in the G121V mutant, leading to a 14 kJ mol^{-1} increase in the barrier height – consistent with the decrease in rate observed experimentally.

8.2.2 DHFR from the Thermophile *Bacillus stearothermophilus*

The thermophilic DHFR from *Bacillus stearothermophilus* (BsDHFR) has been studied by Klinman and coworkers.⁵⁸ In this study, kinetic isotope effects were determined using noncompetitive stopped-flow techniques at pH 9, where hydride transfer was rate limiting, allowing direct comparison with data obtained in the steady state. The KIE was found to be temperature dependent over the experimental range, with no breakpoint in the temperature dependence, and gave a slightly inverted $A_{\text{H}}/A_{\text{D}}$ of 0.57. The difference in activation energy ($4.5 \pm 0.6\text{ kJ mol}^{-1}$) was within the semiclassical limits, while the activation energy itself ($E_{\text{a}}^{\text{H}} = 22.7 \pm 0.4\text{ kJ mol}^{-1}$) was similar to that observed for EcDHFR. Based on an environmentally coupled model of tunnelling, this implies contributions from gating. This is different from the situation for EcDHFR. The results for BsDHFR at pH 9 therefore represent a half-way point between the situation for EcDHFR at pH 9, where passive dynamics dominated, the KIE is temperature independent and the $A_{\text{H}}/A_{\text{D}}$ ratio is inflated rather than inverted, and at pH 7, where gating played a significant role, the KIE is temperature dependent and the $A_{\text{H}}/A_{\text{D}}$ ratio is strongly inverted. This implies that the active site of BsDHFR is more flexible than that of EcDHFR, at least at pH 9.

8.2.3 DHFR from the Hyperthermophile *Thermotoga maritima*

The DHFR from the hyperthermophile *Thermotoga maritima* (TmDHFR) is the only known dimeric chromosomal DHFR. The interface of this extremely stable homodimer cannot be disrupted without also denaturing the monomer subunits.⁷² The temperature dependence of the KIE of TmDHFR has been studied by observing the hydride transfer at pH 7 using stopped-flow techniques.^{12,56,57} Hydride transfer is partially rate limiting in the steady state at pH 7, but does not become fully rate limiting even at pH 9. Biphasic behaviour was observed with a breakpoint at around $25\text{ }^\circ\text{C}$ (Figure 8.8). Above $25\text{ }^\circ\text{C}$ the KIE was relatively temperature independent with a small difference in activation energy (2.5 kJ mol^{-1}) and a semiclassical $A_{\text{H}}/A_{\text{D}}$ (1.56). Below this temperature, the KIEs became temperature dependent, increasing as temperature decreased, and gave a large difference in activation energy (19.3 kJ mol^{-1}) and a

strongly inverse A_H/A_D (0.002). The higher-temperature data suggest environmentally coupled tunnelling, but with little contribution from active barrier-modulating dynamics. The lower-temperature data, on the other hand, are indicative of environmentally coupled tunnelling with a significant role for gating. It should be noted that the KIE of TmDHFR at pH 7 displays similar behaviour to that of EcDHFR at pH 9. It would be interesting to see if the temperature dependence of the KIE of TmDHFR is altered at non-physiological pH, either acidic or basic.

In collaboration with the groups of Gao and Truhlar, we have performed QM/MM calculations using EA-VTST/MT to determine the extent of hydride tunnelling in the reaction catalysed by TmDHFR.³⁷ The computationally determined KIEs were consistently below those observed experimentally. Above 25 °C the computational results gave a very similar temperature dependence of the KIE, but the breakpoint and change in temperature dependence below that temperature were not reproduced. This may be due to a conformational change in the enzyme at 25 °C, or loss of a critical motion below 25 °C due to insufficient energy, which were not allowed for in the computational model. The reaction was dominated by quantum-mechanical tunnelling at all temperatures. This study also investigated the experimentally inaccessible TmDHFR wild-type monomer (created simply by deleting the coordinates of one monomer in the dimeric structure). While kinetically compromised relative to the dimer, the hypothetical monomer displayed a similar degree of quantum tunnelling as had been observed for the native dimer.

Comparison of kinetic parameters for EcDHFR, BsDHFR and TmDHFR indicates a decreasing trend in efficiency of hydride transfer with increasing thermophilicity of the protein. Preliminary results from an analysis of the kinetic properties of the psychrophilic DHFR from *Moritella profunda* (MpDHFR)⁷³ confirm this trend (Evans, Loveridge and Allemann, unpublished). It is interesting to note that while often only small changes in the reaction conditions can strongly affect the temperature dependence of the KIE, the ratio of the pre-exponential factors may be a better indicator of the efficiency of the reaction. For instance, the value of A_H/A_D decreases steadily when going from EcDHFR, the most efficient DHFR described here, to TmDHFR at low temperature and to the G121V mutant of EcDHFR. The prediction for the pre-exponential factors for the MpDHFR catalysed reaction would therefore be close to or above unity.

8.3 Temperature Dependence of the KIEs for other Homologous Enzymes

Alcohol dehydrogenases (ADH) are the other family of enzymes where the temperature dependence of the KIEs for several homologues with different temperature optima has been studied in the context of quantum tunnelling. ADH catalyses the interconversion of alcohols and carbonyl compounds, using NAD(P)⁺/NAD(P)H as hydride acceptor/donor. ADH from yeast was the first

enzyme in which tunnelling was demonstrated from a secondary KIE that exceeded the expected value, and from the relationship between the primary and secondary KIEs.⁷⁴ In a classical model of the reaction, these lead to conflicting conclusions regarding the transition state of the reaction and so quantum tunnelling was invoked as a possible alternative pathway.⁷⁵ In order to ensure that the chemical step was rate limiting, these studies used the relatively slow-reacting substrate benzyl alcohol, with semicarbazide present to trap the resulting benzaldehyde and so prevent the reverse reaction. This allowed the use of sensitive competitive experiments that showed an unusually large Swain–Schaad exponent for the secondary, but not primary KIEs. The experimentally determined exponent was 10, far in excess of the expected value.

The effect of active-site structure on tunnelling was probed using the oxidation of benzyl alcohol by ADH from horse liver. The wild-type enzyme showed an almost semiclassical Swain–Schaad exponent, but this was believed to be due to kinetic complexity masking the chemical step. A series of mutants was used to show that as crowding in the active site was increased, and so the rate of product release increased and made less rate limiting, the secondary D/T KIEs but not the secondary H/T KIEs increased.⁷⁶ The Swain–Schaad exponents therefore also increased. This cannot be explained semiclassically or by a tunnelling correction to transition-state theory, and so a method that takes full account of tunnelling is required. A second series of mutants, in which the preorganisation of the reactants in a conformation optimal for tunnelling was disrupted, showed behaviour progressively more similar to that expected semiclassically.⁷⁶ The F93W mutant, in which the greatest evidence of tunnelling was seen, showed an inverted ratio of Arrhenius prefactors, providing further evidence of tunnelling.

The thermophilic ADH from *B. stearothermophilus* showed a breakpoint in the temperature dependence of the primary and secondary KIEs, similar to that observed for the primary H/D KIE for TmDHFR.¹¹ KIEs were within the semiclassical limit and activation energies were large. Above 30 °C, the KIE was temperature independent with a slightly inflated ratio of Arrhenius prefactors ($A_H/A_D = 2.2 \pm 1.1$). Below this temperature the KIEs became temperature dependent, and the ratio of Arrhenius prefactors strongly inverse ($10^{-5} \pm 10^{-5}$). Hydrogen/deuterium exchange experiments demonstrated a change in protein flexibility at 30 °C, mirroring the breakpoint in the temperature dependence of the KIE.⁷⁷ Similarly to TmDHFR, this behaviour may be explained by passive dynamics dominating the reaction above 30 °C where the enzyme has sufficient flexibility. Below 30 °C, these motions become unfavourable and the enzyme must instead rely on low-frequency active gating motions to drive the reaction. The Swain–Schaad exponent for the secondary KIEs was also temperature dependent, demonstrating that the degree of tunnelling is highest at elevated temperatures.¹¹

8.4 Conclusions

A number of different and complementary methods for analysing quantum tunnelling in enzymatic reactions are available to the experimenter. The most

pressing need is to isolate the relevant chemical step of the reaction in order to obtain accurate information about that step alone. Where this is not possible in the steady state under physiological conditions, this can be done either through transient-state kinetics or by employing nonphysiological conditions in the steady state. Examples discussed here include taking measurements at non-physiological pH, use of slow-reacting substrates, or using mutagenesis to alter the mechanism of the enzyme. As has been described, different techniques may give quite different results. The study of a number of different enzyme systems using various experimental techniques has revealed a great deal about tunnelling in enzymatic reactions, and there seems no doubt that hydrogen is transferred in enzymatic reactions by quantum-mechanical tunnelling. However, the question whether the optimisation of enzyme catalysis may entail the evolutionary implementation of chemical strategies that increase the probability of quantum-mechanical tunnelling is still open. The availability of low-frequency motions in enzymes that can change interatomic distances by as much as 1.5 Å may suggest tunnelling has been selected for by evolution. To the best of our knowledge this has only been tested for one enzymatic system because of the difficulty of finding a reaction where the identical H-transfer reaction can be studied experimentally both in the presence and absence of the enzyme. A study by Finke *et al.* of the adenosylcobalamin-dependent diol dehydratase reaction revealed a strong contribution from quantum-mechanical tunnelling to the H abstraction from ethylene glycol.^{13,14} However, the data sets for the enzymatic and the enzyme free reactions were identical indicating that at least this cobalamin dependent enzyme has not evolved to enhance tunnelling. It remains to be seen whether this conclusion holds true for other enzymes or is simply a special case of what is often considered a family of ancient enzymes relying on a cofactor of prebiotic origin.

References

1. E. Fischer, *Ber. Dtsch. Chem. Ges.*, 1894, **27**, 3189.
2. J. B. S. Haldane, *Enzymes*, Longmans, Green, London, 1930.
3. L. Pauling, *Nature*, 1948, **161**, 707.
4. S. Glasstone, K. J. Laidler and H. Eyring, *The Theory of Rate Processes: The Kinetics of Chemical Reactions, Viscosity, Diffusion and Electrochemical Phenomena*, McGraw-Hill, New York, 1941.
5. L. Melander and W. H. Saunders, *Reaction Rates of Isotopic Molecules*, Wiley, New York, 1980.
6. R. P. Bell, *The Tunnel Effect in Chemistry*, Chapman and Hall, London, 1980, 88.
7. K. W. Rickert and J. P. Klinman, *Biochemistry*, 1999, **38**, 12218.
8. J. C. Nesheim and J. D. Lipscomb, *Biochemistry*, 1996, **35**, 10240.
9. S. Knapp and J. P. Klinman, *Eur. J. Biochem.*, 2002, **269**, 3113.
10. Z. D. Nagel and J. P. Klinman, *Chem. Rev.*, 2006, **106**, 3095.
11. A. Kohen, R. Cannio, S. Bartolucci and J. P. Klinman, *Nature*, 1999, **399**, 496.

12. G. Maglia and R. K. Allemann, *J. Am. Chem. Soc.*, 2003, **125**, 13372.
13. K. M. Doll and R. G. Finke, *Inorg. Chem.*, 2003, **42**, 4849.
14. K. M. Doll, B. R. Bender and R. G. Finke, *J. Am. Chem. Soc.*, 2003, **125**, 10877.
15. C. A. Fierke and G. G. Hammes, *Methods Enzymol.*, 1995, Vol. **249**.
16. D. B. Northrop, in: *Isotope Effects on Enzyme-catalysed Reactions* (eds.) W. W. Cleland, M. H. O'Leary, D. B., Northrop University Park Press, Baltimore, MD, 1977, p. 122.
17. D. B. Northrop, in *Enzyme Mechanism from Isotope Effects*, (ed.) P. F. Cook, CRC Press, Boca Raton, FL, 1991.
18. M. J. Sutcliffe and N. S. Scrutton, *Phys. Chem. Chem. Phys.*, 2006, **8**, 4510.
19. J. F. Davies, T. J. Delcamp, N. J. Prendergast, V. A. Ashford, J. H. Freisheim and J. Kraut, *Biochemistry*, 1990, **29**, 9467.
20. M. A. McTigue, J. F. Davies, B. T. Kaufman and J. Kraut, *Biochemistry*, 1993, **32**, 6855.
21. M. A. McTigue, J. F. Davies, B. T. Kaufman and J. Kraut, *Biochemistry*, 1992, **31**, 7264.
22. M. R. Sawaya and J. Kraut, *Biochemistry*, 1997, **36**, 586.
23. M. J. Osborne, J. Schnell, S. J. Benkovic, H. J. Dyson and P. E. Wright, *Biochemistry*, 2001, **40**, 9846.
24. M. J. Osborne, R. P. Venkitakrishnan, H. J. Dyson and P. E. Wright, *Prot. Sci.*, 2003, **12**, 2230.
25. J. Feeney, *Angew. Chem. Int. Ed.*, 2000, **39**, 290.
26. M. G. Casarotto, J. Basran, R. Badii, K. H. Sze and G. C. K. Roberts, *Biochemistry*, 1999, **38**, 8038.
27. D. M. Epstein, S. J. Benkovic and P. E. Wright, *Biochemistry*, 1995, **34**, 11037.
28. D. D. Boehr, H. J. Dyson and P. E. Wright, *Chem. Rev.*, 2006, **106**, 3055.
29. D. D. Boehr, D. McElheny, H. J. Dyson and P. E. Wright, *FASEB J.*, 2005, **19**, A846.
30. D. D. Boehr, D. McElheny, H. J. Dyson and P. E. Wright, *Science*, 2006, **313**, 1638.
31. D. McElheny, J. R. Schnell, J. C. Lansing, H. J. Dyson and P. E. Wright, *Proc. Natl. Acad. Sci. USA*, 2005, **102**, 5032.
32. R. P. Venkitakrishnan, E. Zaborowski, D. McElheny, S. J. Benkovic, H. J. Dyson and P. E. Wright, *Biochemistry*, 2004, **43**, 16046.
33. R. P. Venkitakrishnan, E. Zaborowski, D. McElheny, S. J. Benkovic, H. J. Dyson and P. E. Wright, *Biochemistry*, 2005, **44**, 5948.
34. P. J. Shrimpton, A. Mullaney and R. K. Allemann, *Prot. Struct. Funct. Genetics*, 2003, **51**, 216.
35. P. J. Shrimpton and R. K. Allemann, *Prot. Sci.*, 2002, **11**, 1442.
36. P. J. Shrimpton, PhD Thesis, *A computational investigation of dihydrofolate reductase*, University of Birmingham 2003.
37. J. Y. Pang, J. Z. Pu, J. L. Gao, D. G. Truhlar and R. K. Allemann, *J. Am. Chem. Soc.*, 2006, **128**, 8015.

38. J. Y. Pang, R. K. Allemann, *Phys. Chem. Chem. Phys.* 2007, **9**, 718.
39. J. B. Watney, P. K. Agarwal and S. Hammes-Schiffer, *J. Am. Chem. Soc.*, 2003, **125**, 3745.
40. P. K. Agarwal, S. R. Billeter, P. T. R. Rajagopalan, S. J. Benkovic and S. Hammes-Schiffer, *Proc. Natl. Acad. Sci. USA*, 2002, **99**, 2794.
41. P. K. Agarwal, S. R. Billeter and S. Hammes-Schiffer, *J. Phys. Chem. B*, 2002, **106**, 3283.
42. J. L. Radkiewicz and C. L. Brooks, *J. Am. Chem. Soc.*, 2000, **122**, 225.
43. A. R. Leach and T. E. Klein, *J. Comput. Chem.*, 1995, **16**, 1378.
44. R. Castillo, J. Andres and V. Moliner, *J. Am. Chem. Soc.*, 1999, **121**, 12140.
45. P. L. Cummins, S. P. Greatbanks, A. P. Rendell and J. E. Gready, *J. Phys. Chem. B*, 2002, **106**, 9934.
46. P. L. Cummins and J. E. Gready, *J. Mol. Graph.*, 2000, **18**, 42.
47. P. L. Cummins and J. E. Gready, *J. Comput. Chem.*, 1998, **19**, 977.
48. P. L. Cummins and J. E. Gready, *J. Am. Chem. Soc.*, 2001, **123**, 3418.
49. P. L. Cummins and J. E. Gready, *J. Phys. Chem. B*, 2000, **104**, 4503.
50. S. Hammes-Schiffer, *FASEB J.*, 2007, **21**, A151.
51. S. Hammes-Schiffer and J. B. Watney, *Phil. Trans. R. Soc. B-Biol. Sci.*, 2006, **361**, 1365.
52. S. Hammes-Schiffer and S. J. Benkovic, *Ann. Rev. Biochem.*, 2006, **75**, 519.
53. C. A. Fierke, K. A. Johnson and S. J. Benkovic, *Biochemistry*, 1987, **26**, 4085.
54. R. S. Sikorski, L. Wang, K. A. Markham, P. T. R. Rajagopalan, S. J. Benkovic and A. Kohen, *J. Am. Chem. Soc.*, 2004, **126**, 4778.
55. R. S. Swanwick, G. Maglia, L. H. Tey and R. K. Alleumann, *Biochem. J.*, 2006, **394**, 259.
56. G. Maglia, M. H. Javed and R. K. Alleumann, *Biochem. J.*, 2003, **374**, 529.
57. G. Maglia, PhD Thesis, *The importance of molecular dynamics in dihydrofolate reductase catalysis*, University of Birmingham, 2004.
58. H. S. Kim, S. M. Damo, S. Y. Lee, D. Wemmer and J. P. Klinman, *Biochemistry*, 2005, **44**, 11428.
59. M. Garcia-Viloca, D. G. Truhlar and J. Gao, *Biochemistry*, 2003, **42**, 13558.
60. J. Pu, S. Ma, J. Gao and D. Truhlar, *J. Phys. Chem. B*, 2005, **8551**.
61. C. J. Falzone, P. E. Wright and S. J. Benkovic, *Biochemistry*, 1994, **33**, 439.
62. G. P. Miller and S. J. Benkovic, *Biochemistry*, 1998, **37**, 6336.
63. C. E. Cameron and S. J. Benkovic, *Biochemistry*, 1997, **36**, 15792.
64. T. H. Rod, J. L. Radkiewicz and C. L. Brooks, *Proc. Natl. Acad. Sci. USA*, 2003, **100**, 6980.
65. I. F. Thorpe and C. L. Brooks, *Prot. Struct. Funct. Bioinf.*, 2004, **57**, 444.
66. I. F. Thorpe and C. L. Brooks, *J. Am. Chem. Soc.*, 2005, **127**, 12997.
67. I. F. Thorpe and C. L. Brooks, *J. Phys. Chem. B*, 2003, **107**, 14042.
68. S. J. Benkovic and S. Hammes-Schiffer, *Science*, 2003, **301**, 1196.
69. L. Wang, S. Tharp, T. Selzer, S. J. Benkovic and A. Kohen, *Biochemistry*, 2006, **45**, 1383.
70. L. Wang, N. M. Goodey, S. J. Benkovic and A. Kohen, *Proc. Natl. Acad. Sci. USA*, 2006, **103**, 15753.

71. H. B. Liu and A. Warshel, *J. Phys. Chem. B*, 2007, **111**, 7852.
72. T. Dams, G. Bohm, G. Auerbach, G. Bader, H. Schurig and R. Jaenicke, *Biol. Chem.*, 1998, **379**, 367.
73. Y. Xu, G. Feller, C. Gerday and N. Glansdorff, *J. Bacteriol.*, 2003, **185**, 5519.
74. Y. Cha, C. J. Murray and J. P. Klinman, *Science*, 1989, **243**, 1325.
75. W. P. Huskey and R. L. Schowen, *J. Am. Chem. Soc.*, 1983, **105**, 5704.
76. B. J. Bahnsen, D. H. Park, K. Kim, B. V. Plapp and J. P. Klinman, *Biochemistry*, 1993, **32**, 5503.
77. Z. X. Liang, T. Lee, K. A. Resing, N. G. Ahn and J. P. Klinman, *Proc. Nat. Acad. Sci.*, 2004, **101**, 9556.
78. T. Dams, G. Auerbach, G. Bader, U. Jacob, T. Ploom, R. Huber and R. Jaenicke, *J. Mol. Biol.*, 2000, **297**, 659.

CHAPTER 9

Probing Coupled Motions in Enzymatic Hydrogen Tunnelling Reactions: Beyond Temperature-Dependence Studies of Kinetic Isotope Effects

SAM HAY,^a MICHAEL J. SUTCLIFFE^b AND
NIGEL S. SCRUTTON^a

^a Faculty of Life Sciences, Manchester Interdisciplinary Biocentre, University of Manchester, 131 Princess Street, Manchester, M1 7DN, UK; ^b School of Chemical Engineering and Analytical Science, Manchester Interdisciplinary Biocentre, University of Manchester, 131 Princess Street, Manchester M1 7DN, UK

9.1 Dynamics and Full Tunnelling Models for Enzymatic H-transfer

The potential importance of protein dynamics coupled to tunnelling in enzymatic systems has been highlighted in contributions elsewhere in this volume (Chapters 6 and 8). The role of dynamical processes, and how these could have evolved, remains a key question in enzymology.^{1–4} Of particular interest is whether enzymes have evolved to use quantum tunnelling to the best advantage – by coupling, when necessary, specific protein motions to the reaction coordinate. Whilst it is now widely accepted that hydrogen (proton, hydrogen or

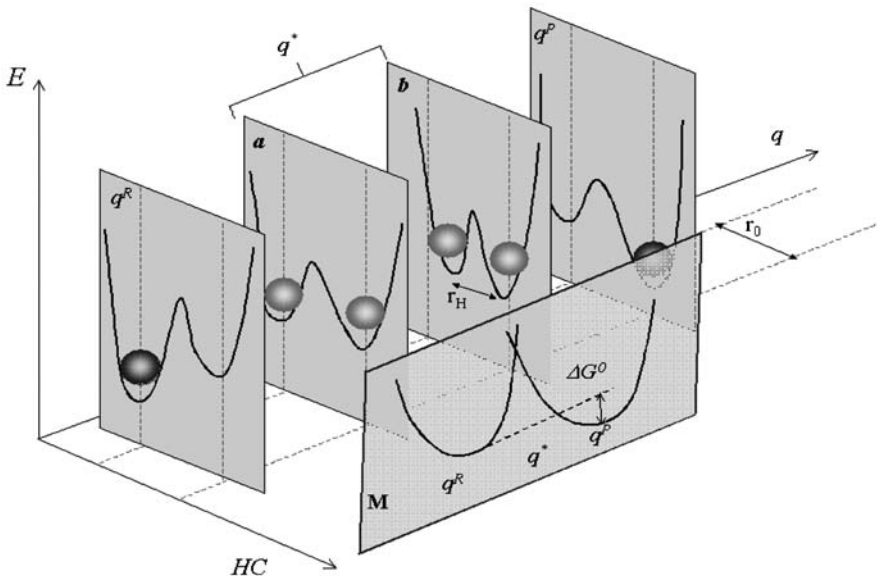


Figure 9.1 A framework for analysing the vibrationally assisted Marcus like full tunnelling models of H transfer. The three axes are: E , energy; q , environmental coordinate (excluding the transferred hydrogen shown as a gray sphere); HC , hydrogen coordinate. The four vertical panels, q^R , a , b , q^P , show the double well potential energy surface during the reaction progress: from the reactant state, q^R ; to a state where the potential energy of the reactant and product states are (nearly) degenerate, but the tunnelling distance, r_0 , is too large for tunnelling to occur, a ; to a ‘tunnelling ready conformation’, b , where the product and acceptor states are (nearly) degenerate and the tunnelling distance, now r_H , is sufficiently small to allow tunnelling to occur with reasonable probability; finally to the product state, q^P . Collectively, a and b can be thought of as a pseudotransition state, q^* . The panel labelled M shows the familiar Marcus like view of the free energy parabolas as functions of this environmental coordinate. Adapted from ref. 24.

hydride)-tunnelling reactions can occur during enzyme-catalysed reactions,^{1,5–10} the role of such compressive or promoting motions remains contentious,³ despite a number of kinetic and computational studies (reviewed in refs. 11–15) demonstrating that experimentally determined kinetic isotope effects (KIEs) are in agreement with environmentally coupled full-tunnelling models^{16–19} (cf. Bell correction type models²⁰). These environmentally coupled models (Figure 9.1) are based on Marcus-like descriptions for electron-transfer reactions,^{21,22} and represent a radical departure from physical frameworks based on semiclassical transition-state theory. The validation of such models requires a multifaceted approach, and in recent years we have begun to provide key experimental and computational evidence that support such models for enzyme-catalysed hydrogen transfer (for recent reviews see refs 12, 23). Our work has relied on a strong interplay between high resolution/time-resolved structural analysis by

X-ray crystallography, detailed computational simulations based on molecular mechanics and QM/MM methodologies, and fast reaction kinetics in solution. This chapter looks at some of the experimental methods that can be used for such purposes.

9.1.1 Towards a More Detailed Understanding of the Temperature Dependence of KIEs

Experimentally, the identification of promoting motions or vibrations is extremely challenging, yet their identification and characterisation underpins much of this field. The first experimental evidence for a role of protein motion during H-tunnelling reactions in enzymes^{25,26} was inferred from observations of KIEs with aberrant temperature dependencies (*i.e.* that do not conform to the predictions of semiclassical transition-state theory or quantum correction models thereof). The conventional wisdom^{27,28} became that if a system had a purely temperature-independent KIE, then promoting motions were not important in the reaction, and the reaction is dominated by tunnelling aided only by thermally equilibrated motion along a collective reaction coordinate (coordinate q in Figure 9.1) – essentially like a Marcus depiction of electron transfer. These are static-barrier models. However, if the KIE is significantly temperature dependent (ΔE_a or $\Delta\Delta H^\ddagger$ greater than $\sim 6 \text{ kJ mol}^{-1}$),²⁰ then the reaction proceeds *via* an environmentally coupled tunnelling reaction in which fast (subpicosecond), nonequilibrated motion along the H-transfer coordinate (coordinate HC in Figure 9.1) modulates the tunnelling barrier (*i.e.* essentially ‘narrowing’ the tunnelling barrier). In between these two extremes, where much of the measured data fall, the KIE data can be modelled using either a reaction proceeding by an environmentally coupled tunnelling mechanism, or by a Bell-type correction model.²⁰ Clearly, either additional experiments, and/or a computational approach are required to distinguish between these two possibilities. In this chapter we describe studies and approaches that have provided further insight into the potential role of promoting motions in enzymatic H-tunnelling. These approaches have provided more in-depth understanding of the mechanism of H-transfer compared with that gained from experimental studies of the temperature dependence of KIEs alone.

9.1.2 Identifying a Promoting Motion in AADH and Rationalising the Apparent Temperature Independence of the KIE For Substrate C H/D Bond Breakage

We have shown that the apparent temperature independence of the observed KIE for the proton-tunnelling reaction during the reductive half-reaction of AADH with tryptamine⁷ can be accommodated within the framework of the environmentally coupled model of Kuznetsov and Ulstrup.^{16,29} Our study combined data from our molecular-dynamics simulations and DFT calculations and kinetic data,^{7,29} revealing that, while the observed KIE for this system is not

measurably temperature dependent – suggesting that a promoting vibration is not important for H-tunnelling – a promoting vibration is nevertheless required to explain the observed magnitude and temperature dependence of the KIE. This motion is localised in the active site of AADH, and is centred on the C₁ and H₁ atoms of the iminoquinone (reactive) intermediate and the carboxylate group of the active site aspartate residue (Figure 9.2(A)). Numerical modelling showed that whilst the reaction rates do not have measurably different enthalpies, they are consistent with a promoting vibration within the environmentally coupled model even when tunnelling proceeds also from vibrationally excited states.²⁹ For a detailed analysis of our numerical modelling, computational simulations and kinetic data, see refs 7,29 – in summary, a localised promoting vibration, with a frequency of $\sim 165\text{ cm}^{-1}$ (Figure 9.2(B)), was identified for the proton-tunnelling step in the oxidation of tryptamine catalysed by AADH and shown to be consistent with there being a weak temperature dependence. This weak dependence of the KIE on temperature might not be measurable experimentally over the limited temperature range available to most enzyme studies (*i.e.* 4–40 °C; Figure 9.2(C)). Interestingly, the identified promoting vibration does not require large-scale dynamics of the protein scaffold but is inherent to the proton donor, the catalytic iminoquinone intermediate, as shown by molecular dynamics simulations of this intermediate and density functional theory calculations. This promoting vibration corresponds to a rotation of the donor C₁/H₁ methylene group, which couples to the acceptor oxygen, O₂, so that these atoms all move toward a configuration from which tunnelling becomes more probable.

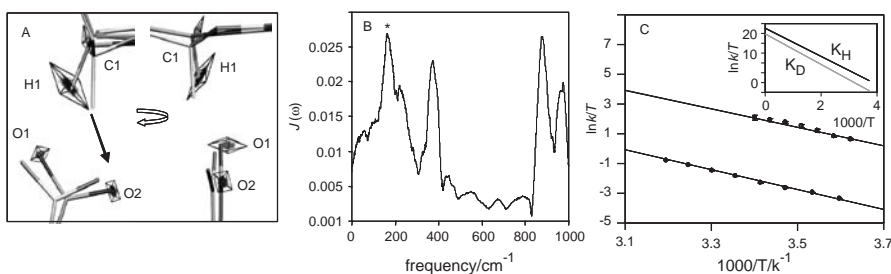


Figure 9.2 Identifying a promoting vibration in AADH. *A*, Orthogonal view of the reactant (dark gray carbon atoms with labels) and the representative structure for tunnelling (RTE, light gray carbon atoms) structures from VTST calculations⁷ with superimposed atomic coordinates for $\sim 165\text{ cm}^{-1}$ vibrations for C₁, H₁, O₁, and O₂ as labelled. The proton is transferred from the C₁ to O₂ atoms as shown by an arrow and the cages represent the principal components for the filtered motion of each atom, which are scaled according to the relative eigenvalues. The $\sim 165\text{ cm}^{-1}$ vibration was determined by spectral density analysis of MD simulations.²⁹ *B*, The velocity spectral densities for the C₁ atom with the $\sim 165\text{ cm}^{-1}$ vibration marked with an asterix. *C*, Eyring plot of the experimentally determined rate constant for proton and deuteron transfer in AADH measured using stopped flow methods.⁷ The data are fit using the model of Kuznetsov and Ulstrup¹⁶ with a promoting vibration of 165 cm^{-1} .²⁹ Adapted from ref. 29, see text for more details.

Additional to this promoting vibration, further motions (*i.e.* preorganisation) are likely to be involved in moving the system toward a tunnelling-ready configuration,⁸ from which the gating motion can take effect. We surmise that the repositioning of O₂ would bring O₂ sufficiently close to H₁ for an electrostatic coupling of their respective vibrations.

The above study suggests that a degree of environmental coupling to the reaction coordinate may be much more widespread than originally thought and perhaps all full-tunnelling models need to include an environmental gating term. The limitation with enzyme systems is the small temperature range available to probe the variation in KIE as a function of temperature. Clearly, additional experimental probes of tunnelling are required to identify promoting motions that do not manifest a measurably temperature-dependent KIE. In addition to temperature there are two other intensive (bulk) properties that can be used to probe an enzyme reaction – viscosity and pressure. Pressure is discussed in Section 9.2, while viscosity is discussed in Section 9.3.3. Also, alternative tunnelling probes (secondary KIEs and driving force) are discussed in Sections 9.3.1 and 9.3.2, respectively.

9.2 Pressure as a Probe of Hydrogen Tunnelling

Hydrostatic pressure offers an alternative to temperature as an independent experimental parameter with which to study enzymatic tunnelling reactions. The use of pressure to study enzymatic H-tunnelling reactions has been pioneered by Northrop.^{30–37} Semiclassical transition-state theory (TST) dictates that pressure effects are associated with differences in vibrational frequencies of isotopic and nonisotopic atoms.^{38–40} These stretching vibrations are insensitive to pressures of a few kbar, and this has been confirmed in pressure-dependence studies of chemical reactions.³⁸ Conversely, chemical systems with inflated isotope effects that cannot be explained by semiclassical TST have shown a significant pressure dependence of both rate and KIE, consistent with a tunnelling mechanism.³⁷ For nontunnelling reactions, substrate isotope effects usually arise from a single transition state and the primary KIEs for these reactions are independent of pressure.^{35,39} Thus, in principle, the pressure dependence of an isotope effect provides an excellent method for distinguishing between over-the-barrier and through-the-barrier (quantum tunnelling) processes.

9.2.1 Steady-State Analysis of the Pressure Dependence of H-transfer: A Case Study with Alcohol Dehydrogenase

The pressure dependence of an observed rate constant arises in absolute rate theory^{31,41} when assuming a quasiequilibrium between the reactant and transition state:

$$\ln k = \ln k_0 - \Delta V^\ddagger p / R_p T \quad (9.1)$$

where $R_p = 83.13 \text{ cm}^3 \text{ mol}^{-1} \text{ bar K}^{-1}$ when the pressure, p , is measured in bar, k_0 is the apparent rate constant extrapolated to 0 bar, and ΔV^\ddagger is the apparent difference between the volume of the reactant state and the transition state, and has units of $\text{cm}^3 \text{ mol}^{-1}$. As mentioned in Section 9.1, a moderately temperature-dependent 1° KIE can be explained by either a Bell-type correction model²⁰ or by an environmentally coupled tunnelling model.^{16–18} Northrop's initial treatment³¹ of pressure effects on the hydride (tunnelling) transfer from chloranil to leucocrystal violet measured by Isaacs *et al.*^{38–40} made use of a Bell-type model:

$$\text{KIE}_{\text{obs}} = \frac{k_{\text{TST}}^{\text{H}}}{k_{\text{TST}}^{\text{D}}} \left(\frac{k_{\text{tun}}^{\text{H}}}{k_{\text{tun}}^{\text{D}}} - 1 \right) \exp(-\Delta \Delta V^\ddagger p / R_p T) + \frac{k_{\text{TST}}^{\text{H}}}{k_{\text{TST}}^{\text{D}}} \quad (9.2)$$

where k_{TST} and k_{tun} are the classical (over-the-barrier) and tunnelling contributions, respectively, to the overall rate of reaction for each isotope. Cho and Northrop then showed a rather complex biphasic pressure dependence of the oxidation of benzyl alcohol by yeast alcohol dehydrogenase (YADH) as manifest by the steady-state V/K 'substrate capture' parameter.⁴² This was interpreted in terms of an increase in the rate of capture of benzyl alcohol at elevated pressure due to an increase in the rate of hydride transfer such that $\Delta V^\ddagger < 0$. These authors posited that at higher pressure, the rate of capture decreases due to a conformational change of the enzyme (that has not otherwise been observed), to a form with weaker binding of NAD^+ (the hydride acceptor). In this study, the authors modified eqn (9.2) to incorporate commitments to catalysis and the equilibrium constant for the proposed conformational change, as well as various volume changes associated with substrate binding and conformational rearrangement. This approach was then extended to a solvent isotope study that uncovered previously unobserved large and inverse kinetic and equilibrium isotope effects for benzyl alcohol oxidation in YADH.³² Finally, the effect of pressure on the KIE for the hydride-transfer reactions catalysed by YADH^{30,33,36} and formate dehydrogenase (YFDH)³⁴ was investigated (reviewed in refs 35,37). Interestingly, the observed 1° KIE significantly increased with pressure in FDH and decreased with pressure in YADH, yet Northrop and coworkers suggested that in both these enzymes the pressure dependence of the KIE arises solely from transition-state phenomena. Furthermore, an investigation of the pressure dependence of the ^{13}C β - 2° KIE in YADH was interpreted to indicate a lack of tunnelling contribution to the observed 1° KIE as the volume change was identical for the 1° KIE and the ^{13}C 2° KIE.^{30,33,36} Northrop instead suggested that the KIE in YADH arises as a result of Lumry's mechanical contribution to the transition state⁴³ and that absolute reaction-rate theory is not adequate to explain H-transfer reactions in enzymes.³⁷ We agree in principle with this latter argument. However, as it is fairly well established that there is a significant tunnelling contribution to benzyl alcohol oxidation in YADH⁶ we

suggest it is perhaps too difficult to deconvolute the effects of pressure variation to mechanism from steady-state measurements alone. With this in mind, we have developed stopped-flow methods with pressure variation (described in the following section) as a means of directly accessing the chemical step, thus bypassing the complexities and limitations that can arise in steady-state studies with enzyme systems.

9.2.2 Pressure Variation and Direct Analysis of the Chemical Step: A Case Study with Morphinone Reductase

The reductive half-reaction of morphinone reductase (MR) involves hydride transfer from the C4 *R*-hydrogen of β -nicotinamide adenine dinucleotide (NADH) to the N5 atom of flavin mononucleotide (FMN) and has been extensively characterised.^{8,9,44,45} Unlike benzyl alcohol oxidation in YADH, this reaction can be directly observed in a rapid-mixing stopped-flow instrument and is kinetically resolved from steps involving coenzyme binding. Additionally, the reaction is essentially irreversible so the observed KIE is the intrinsic KIE.^{8,9,44,45} Crucially, while the 1° KIE of MR is only modest (~ 4 at 298 K), it is highly temperature dependent.^{8,9,44} Additionally, the α - 2° KIE is significantly larger than the equilibrium isotope effect.⁸ We have described the reaction within the context of modern environmentally coupled models of H-tunnelling such that the enzyme requires a promoting motion to move the nicotinamide C4 H sufficiently close to the FMN N5 atom to facilitate tunnelling.

We have measured, using stopped-flow methods, the MR-catalysed hydride-transfer rate as a function of both hydrostatic pressure and temperature (Figure 9.3(A),⁹). Increasing the pressure from 1 bar to 2 kbar accelerates the rate of hydride transfer when both H and D are transferred; the observed 1° KIE also increases with pressure (Figure 9.3(B)). The observed increase in both rate and KIE was unexpected and found to be incompatible with both a Bell-correction model and full tunnelling models that do not incorporate a fast promoting motion along the H-transfer coordinate – where the rate increases and the KIE decreases as the wavefunction overlap increases (Figures 9.4(A) and (B)). A recent study of the pressure and temperature dependence of another putative environmentally coupled H-tunnelling reaction – the proton transfer from the phenylethylamine-derived iminoquinone adduct in the active site of aromatic amine dehydrogenase to the acceptor aspartate residue (S. Hay, P. Hothi and N. S. Scrutton, unpublished work) shows similar trends to those observed with MR. However, with this system a *decrease* in both the observed rate constants and observed KIE was observed. By numerical modelling, we were able to quantitatively show that this trend is consistent with barrier compression in MR using an environmentally coupled tunnelling model.^{9,16} This modelling is described in more detail below.

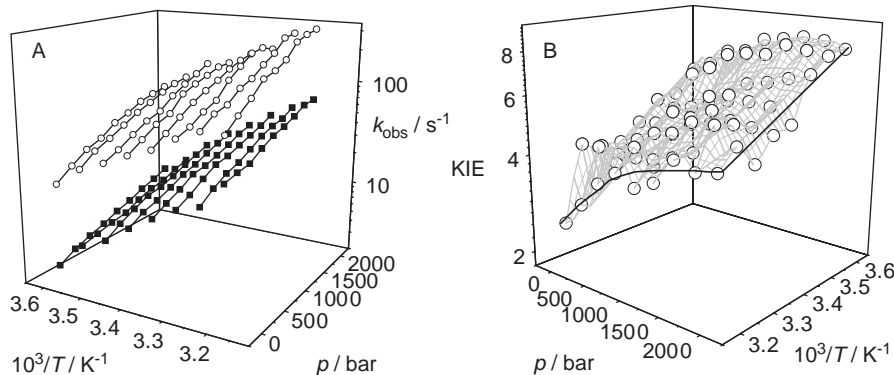


Figure 9.3 High pressure stopped flow. *Top*, The combined effect of temperature and pressure on the rate of hydride transfer during the reductive half reaction of MR measured using a high pressure stopped flow (HPSF). *A*, the observed rate constants for the reaction with NADH (open circles) and (*R*) [4^{2}H] NADH and *B*, the resulting 1° KIE. Adapted in part from ref. 9. See Section 9.2.2 for details. *Bottom*, A schematic of the high pressure component of the High Tech Scientific HPSF (TgK Scientific, Bradford upon Avon) used for these measurements. For a more general description of a stopped flow spectrometer, see previous chapter.

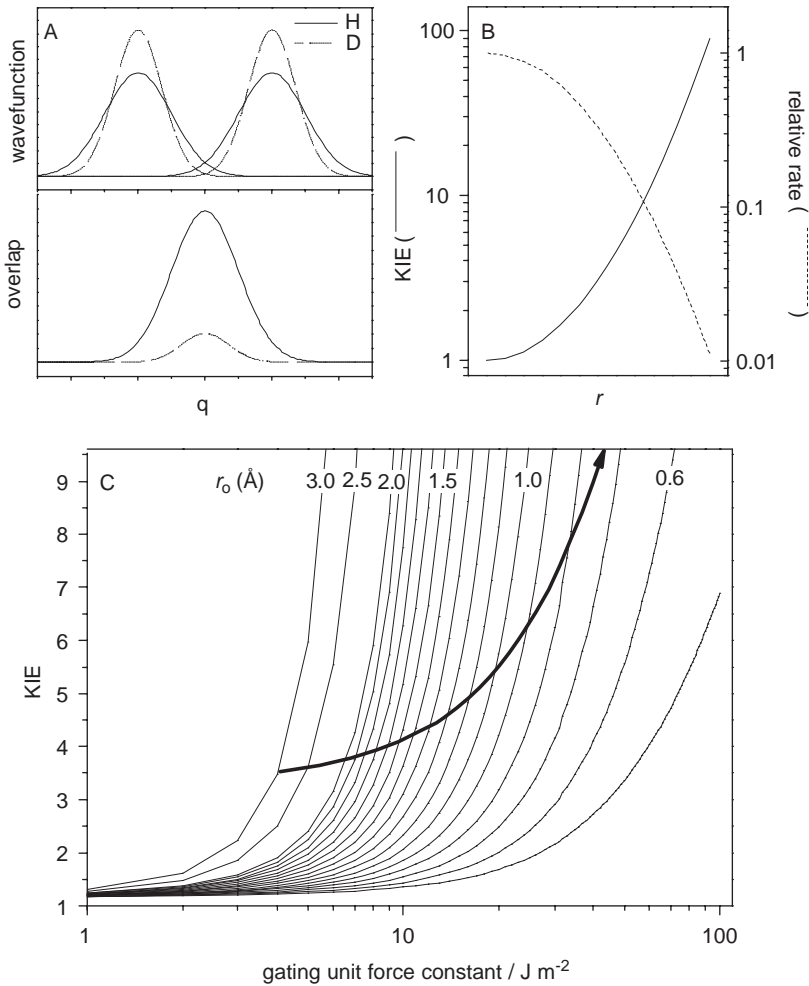


Figure 9.4 Modelling the effect of pressure on an environmentally coupled H tunnelling reaction. *A*, Reactant and product vibrational wavefunctions for H and D showing the reduced wavelength of D relative to H and the resulting wavefunction overlap – essentially the Franck–Condon term. In a static barrier model (tunnelling with absolutely no gating), as the donor–acceptor distance, r , is decreased e.g. due to increasing pressure, the wavefunction overlap increases. The overlap for D increases relatively more rapidly than that of H, causing the rate of the reaction to increase while the KIE decreases (*B*). However, the combined pressure and temperature dependence of the KIE for the hydride transfer during the reductive half-reaction of morphinone reductase showed that both the observed rate constants and KIE increased with pressure (Figure 9.3). This can be explained when an environmentally coupled model, such as that of Kuznetsov and Ulstrup,¹⁶ is used.⁹ In an environmentally coupled model, the donor–acceptor separation oscillates around an equilibrium separation r_0 . If the frequency (related to the oscillator force constant plotted in panel *C*) of this oscillation – the gating motion – is allowed to increase concomitantly while r_0 is decreased, the observed KIE can increase as r_0 is decreased (black arrow). This arises essentially because the overlap of the effective wavefunction (the wavefunction integrated over the gating coordinate) changes shape as r decreases. Adapted from ref. 9.

9.2.3 Modelling the Pressure Dependence of an Environmentally Coupled H-tunnelling Reaction

While a tunnelling reaction does not pass through a transition state, TST provides a tractable method (*i.e.* eqn (9.1)) to interpret the pressure dependence of a tunnelling reaction, yielding apparent ΔV^\ddagger values for tunnelling. This approach has an established record for interpreting pressure effects on electron transfer (pure tunnelling) reactions. Recently, Miyashita and Go described a theoretical treatment of the effect of pressure on electron-transfer (ET) reactions in proteins.⁴⁶ Interestingly, a survey of the literature by these authors showed that typical ΔV^\ddagger values for a protein ET reaction are -10 to -20 $\text{cm}^3 \text{mol}^{-1}$, a range bracketing the values measured for H and D transfer in MR (-15.6 and $-11.8 \text{ kJ mol}^{-1}$, respectively). Protein ET reactions are typically interpreted in terms of Marcus theory,^{21,22} which in turn is based on Fermi's golden rule:²² $k = 2\pi\hbar^{-1}|T_{\text{DA}}|^2 \text{F.C.}$, where T_{DA} is the tunnelling matrix element (electronic factor) and F.C. is the Franck–Condon (nuclear) factor. Miyashita and Go⁴⁶ concluded that, while volume changes associated with both the T_{DA} and F.C. terms contribute to the observed ΔV^\ddagger for protein ET reactions, unless ΔV^\ddagger is very small (*i.e.* $< 1\text{--}2 \text{ cm}^3 \text{ mol}^{-1}$) then the contribution from T_{DA} can be ignored. We took a similar approach in our modelling of the MR reaction.⁹

The pressure dependence of the F.C. factor for an ET reaction is caused by pressure-induced changes to the Marcus reorganisation energy (λ) and driving force (ΔG^0),⁴⁶ but if only the pressure dependence of the KIE is investigated then both $\partial\lambda/\partial p$ and $\partial\Delta G^0/\partial p$ can be largely ignored as they are largely isotope independent.⁹ We concluded that the pressure dependence of the KIE must therefore arise from other elements of the F.C. term – namely an environmental gating term (or promoting motion). The temperature and pressure dependence of the observed KIE was examined using the environmentally coupled tunnelling model of Kuznetsov and Ulstrup.¹⁶ We have described the implementation of this model previously (refs 9,29 and Section 9.1.2) and do so in a similar manner to that used by Knapp and Klinman.^{27,47} In this model, the temperature dependence of the KIE arises primarily from a gating energy term described by an isotope-independent harmonic oscillator, with a smaller contribution arising from thermal population of vibrationally excited reactant and product states. The gating term describes the energy required to change the distance between the donor and accepter wavefunctions prior to tunnelling – to achieve the tunnelling-ready conformation⁴⁸ – and this distance is isotope dependent such that the distance of deuterium transfer is less than the distance of hydrogen transfer. The observed KIE for the reduction of MR with NADH increases when the pressure is increased (Figure 9.3), yet there is no significant change in the temperature dependence of the KIE over the pressure range studied ($\partial\Delta\Delta H^\ddagger/\partial p \sim 0$).⁹ By simulating the KIE, whilst holding the apparent $\Delta\Delta H^\ddagger$ constant and varying the equilibrium donor–acceptor separation, it was possible to reproduce the pressure and temperature dependence of the KIE in MR (Figure 9.4(c),⁹). By directly comparing the measured and calculated KIE values, it was possible to estimate the extent of the barrier compression caused by 2 kbar of hydrostatic

pressure, which appears to be about 0.7 \AA , decreasing from 1.7 \AA to $\sim 1.0\text{ \AA}$.⁹ The magnitude of this apparent compression is not unprecedented. The effect of only 1 kbar of hydrostatic pressure on the X-ray crystal structure of lysozyme has been determined⁴⁹ and these authors found that, while the average RMS shift of atoms was 0.2 \AA , a few atoms moved by $>1\text{ \AA}$.

A consequence of the pressure dependence of the KIE in MR allows the above model to be tested in later work. To maintain a fixed $\Delta\Delta H^\ddagger$ value while the equilibrium donor–acceptor separation was decreased, the frequency of the promoting vibration was allowed to increase with pressure. It may be possible to test this prediction by studying the H-tunnelling reactions of thermophilic alcohol dehydrogenase²⁶ and dihydrofolate reductase⁵⁰ enzymes, which show breakpoints in their Arrhenius and KIE vs. $1/T$ plots. The model predicts that the slopes of the Arrhenius plots will not change with pressure but, if the breakpoint is truly related to promoting vibrations within the enzymes, then the breakpoint will shift with pressure – moving to higher temperatures at increased pressure if the KIE increases with pressure, and conversely, to lower temperatures if the KIE decreases with pressure. Thus, the combined hydrostatic pressure and temperature dependence of KIEs reveals a new experimental probe of promoting motions in H-tunnelling reactions.

9.3. Other Probes of Tunnelling: Future Prospects for Experimental Studies

9.3.1 Secondary KIEs

α -Secondary (2°) KIEs arise when a hydrogen neighbouring the transferred (1°) H is deuterated. The observed 2° KIE is a consequence of a change in the C–H bond force constant of the 1° H caused by 2° deuteration.⁵¹ Several arguments have been invoked to explain this change in force constant. The most widely accepted is that the force constant is altered due to a change in hybridisation state,⁵² that is, the rehybridisation from *e.g.* sp^3 to sp^2 of a carbon atom adjacent to a 2° deuterium. The magnitude of the 2° KIE is considered to indicate the progress of reactants to products at the transition state.⁵¹ In a classical description, 2° KIEs have been used to report on the nature of the transition state,⁵³ with values falling between unity and the equilibrium isotope effect (EIE). Whilst computational studies have warned about such uses,⁵⁴ values observed outside of this range,^{55–57} so-called exalted 2° KIEs, have been used as evidence for a tunnelling contribution to the reaction. Huskey and Schowen⁵⁸ have suggested that exalted 2° KIEs are indicative of coupling of the motion between the 2° hydrogen and that of the 1° hydrogen being transferred, with a concomitant tunnelling contribution to the reaction assuming a truncated Bell tunnel correction to the semiclassical isotope effect. A number of excellent experimental and theoretical treatments on the utility of 2° KIEs have been published in recent years,^{54,59–61} with 2° KIEs often being evaluated in

terms of their Swain–Schaad exponent in the context of a Bell tunnelling correction^{60,61} or variational transition-state theory.⁵⁴

We have recently shown that the 2° KIEs in both MR and a homologue, pentaerythritol tetranitrate reductase (PETNR), are exalted above the EIE,⁸ which for NAD(P)H to NAD(P)⁺ is 1.13.⁶² Surprisingly, we found that the 2° KIEs for MR and PETNR are identical within error, despite significant differences in the temperature dependence of the 1° KIEs of these two enzymes.⁴⁴ We interpreted these data such that the 2° KIEs do not report on the gating component (*i.e.* promoting motion) of the tunnelling mechanism, but rather on what we call the ‘tunnelling-ready configuration’ – the donor–acceptor arrangement immediately preceding the actual tunnelling event (*i.e.* at the intersection of the reactant and product curves along the collective reaction coordinate shown in Figure 9.1). This idea is consistent with the observation that the 2° KIEs measured for MR and PETNR were both temperature independent (within experimental error), as the FMN-NADH arrangement is unlikely to change significantly between about 275–315 K (the accessible temperature range of our study). Kohen *et al.*⁶³ have reported the temperature dependencies of the 1° and 2° D/T and H/T KIEs for the hydride-transfer reaction from benzyl alcohol to NAD⁺ catalysed by a thermophilic alcohol dehydrogenase (ADH-ht). Temperature-independent 1° and 2° KIEs were observed at high temperatures, but both the 1° and 2° KIEs become strongly temperature dependent below about 30°C. These data were initially interpreted in terms of a large tunnelling contribution above 30 °C in ADH-ht with a transition to a minimal tunnelling regime below 30 °C. In light of more contemporary models of H-tunnelling incorporating environmental coupling that allow for temperature-dependent 1° KIEs (Figure 9.1), the htADH data can be reinterpreted [see also Chapter 6]. At temperatures below the breakpoint, the reaction is strongly coupled to a promoting motion, while at temperatures above the breakpoint, the reaction is dominated by what Klinman calls passive dynamics.¹¹ In this regime the enzyme is able to achieve a tunnelling-ready conformation⁸ without the need of a promoting motion. The promoting motion may still be present however, albeit playing only a minor role. This interpretation has also been used to describe the temperature dependence of the 1° KIE in a thermophilic DHFR.⁵⁰ If H-transfer in ADH-ht does occur by tunnelling both below and above the breakpoint, then the temperature dependence of the 2° KIEs at low temperatures is puzzling. Using our interpretation of 2° KIEs (see above and ref. 9), the tunnelling-ready configuration would have to become significantly temperature-dependent below the breakpoint temperature. If tunnelling is not significant below the breakpoint temperature then this study suggests that temperature-dependent 2° KIEs might provide evidence against a significant tunnelling contribution. More studies are required to test these arguments, but in the absence of kinetic complexity, both the magnitude and temperature (in)dependence of 2° KIEs are potentially powerful and independent probes of tunnelling in enzymes.

9.3.2 Driving Force

Protein ET reactions are typically interpreted in terms of Marcus theory.²² In this description, the rate of the reaction is governed by the tunnelling distance (through the electronic coupling term) and to the apparent activation energy (described by the energy of the driving force, ΔG^0 , and reorganisation energy, λ). Gated ET reactions can be demonstrated if the rate of ET violates Marcus theory – *e.g.* if k_{obs} is independent of driving force while being dependent on temperature. Whilst this is often difficult to show, this violation has been demonstrated for the conformationally gated Q_A to Q_B ET reaction in the bacterial reaction-centre complex.⁶⁴

Recently, Brinkley and Roth⁶⁵ have measured the driving force dependence of the rate of hydride transfer during the reductive half-reaction of glucose oxidase with glucose. To alter the driving force, these authors reconstituted the apo-enzyme with chemically modified flavins that have differing midpoint (reduction) potentials. They showed that the rate of hydride transfer is highly dependent on the driving force and that the apparent reorganisation energy is very large ($68 \pm 1 \text{ kcal mol}^{-1}$, $\sim 2.9 \text{ eV}$). Previous studies have shown that the 1° H/D KIE for this reaction is elevated above the semiclassical limit (~ 10) and the Arrhenius prefactor ratio is ~ 1 (ref. 66, and references therein), which is consistent with only a modest amount of environmental gating of this reaction.²⁷ It remains to be seen whether more strongly environmentally coupled hydrogen-tunnelling reactions, where there is a real possibility that the rate of the hydrogen transfer is ‘gated’ by protein motions, also exhibit a driving force dependence.

9.3.3 Viscosity

In addition to temperature and pressure, another intensive (bulk) property that can be used to probe an enzyme reaction is viscosity. Viscosity has been used to probe configurational gating of interprotein ET reactions, such as that between zinc cytochrome *c* and cupriplastocyanin,^{69–72} and for the protein rearrangement following CO dissociation from myoglobin.⁶⁸ We have previously shown that the magnitude and temperature dependencies of the rate and KIE of the reductive half-reaction of methylamine dehydrogenase (MADH) (an environmentally coupled reaction) were unchanged upon the addition of 30% glycerol to the solution²⁵ – an increase in viscosity of 2–3 fold. Conversely, Ohta *et al.* showed a decrease in KIE and increase in apparent enthalpy for the reductive half-reaction of L-phenylalanine oxidase (PAO) upon the addition of 30% glycerol.⁷³ To the best of our knowledge, viscosity has not been used in a more quantitative fashion to directly probe tunnelling reactions in enzymes. It is predicted from von Smoluchowski theory⁷⁴ that the rate of a diffusion-controlled bimolecular reaction will be inversely proportional to the bulk solution viscosity. However, there is some evidence that the viscosity dependence of certain protein–ligand-binding events arise, not through a reduction in the rate of diffusion, but from conformational fluctuations between protein

substrates with differing ligand binding rates.⁷⁵ Kramers⁷⁶ first developed a theoretical treatment of the dynamical influence of solvent viscosity on unimolecular reactions. This model treats the reaction as a Brownian diffusion over an energy barrier (*i.e.* within the context of TST), which is hindered by friction with solvent molecules. In the Kramers model, the rate constant is related to the solvent viscosity through a friction coefficient and the relationship between rate constant and viscosity is more complex than that of a bimolecular reaction. If it is reasonably assumed that the solvent molecules are much smaller than the protein/enzyme under study, the effect of viscosity on the observed rate of a reaction can be described in combination with the Eyring equation according to Ansari *et al.*^{68,69}

$$k_{\text{obs}} = \frac{k_{\text{B}} T}{h} \left(\frac{1 + \sigma}{\eta + \sigma} \right) \exp\left(\frac{\Delta S^{\ddagger}}{R}\right) \exp\left(\frac{-\Delta H^{\ddagger}}{RT}\right) \quad (9.3)$$

where η is viscosity and σ , also in units of viscosity, is the contribution of the protein friction to the total friction of the system. The other terms have their usual meaning. This relationship is shown graphically in Figure 9.5 as a function of viscosity and σ . Of note is that eqn (9.3) predicts that, whilst the rate of a reaction may be strongly dependent on viscosity, the KIE should be independent of viscosity, as σ should be isotope independent. We have recently investigated the viscosity dependence of the rate of hydride transfer during the reductive half-reaction of morphinone reductase with NADH and (*R*)-[4,²H]-NADH (Figure 9.5,⁶⁷). As these measurements were made using a rapid-mixing technique (stopped-flow), we were only able to increase the viscosity by ~10-fold before mixing artefacts made further measurements impossible. Nevertheless, over the viscosity range of about 0.9–9 cP, we observed no significant change in either the observed rate constants or KIE. Typical values of σ measured for gated reactions in proteins are in the order of 0–10 cP.^{68,69,77,78} If a similar magnitude of σ were manifest in MR, then we would expect to see a 2–10-fold decrease in the observed rate of hydride transfer over the viscosity range examined. As this was not observed, either there is no gating of the hydride transfer in MR, or the mechanism of gating of this H-transfer reaction differs from that of the previously characterised gated protein ET reactions. Based on evidence from temperature and pressure studies of the reaction, we think that the latter is probably the case.

Glycosylation of the protein surface is, like solvent viscosogens, thought to decrease dynamic motion throughout the protein. Klinman and coworkers^{79,80} have used this approach to study the rate of hydride transfer in glucose oxidase by utilising various glycoforms of the enzyme varying in their extent of glycosylation⁷⁹ and also by replacing the native polysaccharide coat with various PEG molecules.⁸⁰ No direct correlation between apparent viscosity and chemistry was shown but rather any alteration, both increasing or decreasing the apparent surface viscosity, caused a decrease in fitness of the enzyme – reducing the $A_D:A_T$ ratio away from unity.^{79,80} It is quite likely that protein

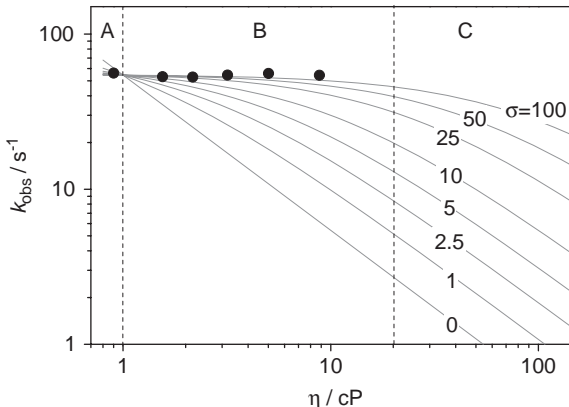


Figure 9.5 The effect of solution viscosity on the observed rate of hydride transfer during the reductive half reaction of morphinone reductase with NADH⁶⁷ (filled circles). The data are modelled (dashed lines) according to eqn (9.3) for increasing values of σ – see text for details. The three regimes A–C describe the conditions when the total friction of the system is dominated by protein friction (A); when both protein and solvent friction dominate (B); and when solvent friction dominates – the Kramers overdamped limit (C).⁶⁸ As the viscosity of water at room temperature is $\sim 1\text{ cP}$, regime A is only relevant at high temperatures.

glycosylation leads to an alteration of the solvation of the protein surface^{81,82} and may, like viscosity, decrease the specific volume and the adiabatic compressibility of the protein interior.⁸³ It is thought that viscosity and hydrostatic pressure may act on proteins similarly by decreasing the internal free volume and perhaps increasing protein rigidity. We are now able to measure both the pressure- and viscosity-dependent environmentally gated H-tunnelling reactions, such as that in MR, and it will be interesting to test this hypothesis further.

9.3.4 Multiple Reactive Configurations and a Place for Single-Molecule Measurements

We have recently identified in a single amino acid mutant of MR what we believe to be multiple reactive configurations of the enzyme–coenzyme complex.⁴⁸ X-ray crystallographic analysis of the complex formed between wild-type MR and the NADH analogue 1,4,5,6-tetrahydro-NADH show the nicotinamide moiety restrained close to the FMN isoalloxazine ring by hydrogen bonds from Asn-189 and His-186. Molecular-dynamics simulations indicated that removal of the Asn hydrogen bond in the N189A mutant allows the nicotinamide moiety to occupy two distinct regions of configurational space not accessible in wild-type enzyme. Stopped-flow spectroscopy of the reaction

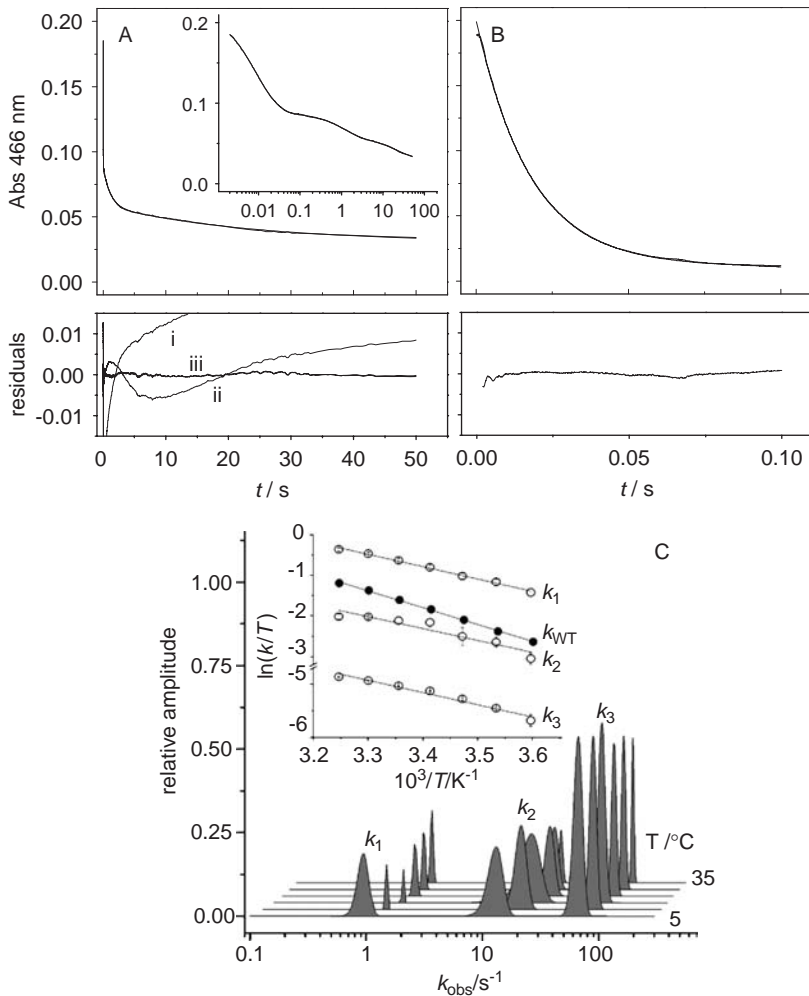


Figure 9.6 Multiple reactive conformations during an H tunnelling reaction. Stopped flow traces of the observed FMN reduction during the reaction of MR (B) and the N189A mutant of MR (A) with NADH. The inset shows the same N189A data on a log scale. Residuals from fits to: 1 exponential (i); 2 exponentials (ii); and, 3 exponentials (iii). The manifestation of the reactive configurations of N189A MR as a function of temperature are shown in panel C. The width of the area under each peak represents the standard error of the observed rate constant. The corresponding Eyring plots of the temperature dependence of each accessible reactive configuration are compared with that of the wild type enzyme in the inset. Adapted from ref. 48.

between the N189A mutant and NADH exhibited multiphasic behaviour, identifying at least four kinetically distinct reactive conformations of the MR-NADH complex, contrasting with the single kinetic phase observed with the wild-type enzyme⁸ (Figure 9.6). Additionally, the magnitudes and temperature

dependencies of the primary and α -secondary KIEs for the fastest three reactive configurations were determined for the N189A mutant enzyme. These KIEs, which differed in both magnitude and temperature dependence, were consistent with hydride transfer by tunnelling, as is seen in the wild-type enzyme.^{8,9,44}

Whilst it is rare to observe different reactive configurations of the same enzyme–coenzyme complex using ensemble (*e.g.* stopped-flow) methods, this study suggests that there could be implications for the interpretation of tunnelling mechanisms, particularly in mutant enzyme systems, when the kinetic data is determined by ensemble measurements, particularly steady-state measurements. Steady-state measurements measure a population-weighted average rate of enzyme turnover. If there are different reactive configurations that exhibit both differing microscopic rate constants and apparent reaction enthalpies, as was seen in the MR N189A mutant,⁴⁸ then the temperature dependence of the apparent KIE (often singly responsible for assigning the mechanism of H-tunnelling) will be quite misleading. It is possible that single-turnover measurements, such as stopped-flow, will not always identify multiple reactive conformations, as they must be sufficiently kinetically distinct to resolve them (typically a >5 -fold difference in rate constant is required). The use of single-molecule fluorescence spectroscopy might provide an attractive alternative to study tunnelling when multiple reactive configurations exist. (*see, e.g.,* refs 84–87). In this method, typically nanomolar concentration of enzyme are immobilised in thin layers upon microscope slides and the fluorescence from single enzyme molecules is imaged using confocal microscopy. Enzyme turnover can be monitored by measuring, for instance, a quenching of cofactor fluorescence upon reduction by a substrate and statistical analysis of the turnover rate of multiple enzyme molecules allows multiple populations and/or multiple reactive conformations to be identified. To our knowledge, this method has not yet been used to measure isotope effects or study H-tunnelling reactions, but we feel that it offers a feasible and important new direction for such studies.

9.4 Conclusions

In recent years, studies of the temperature dependence of 1° KIEs have been used in support of environmentally coupled models of enzymatic H-tunnelling. These models invoke a role for fast protein motions coupled to the H-transfer coordinate, the existence and nature of which has been contentious. Temperature-dependence studies alone will likely not provide in-depth understanding of tunnelling mechanisms, but in combination with new probes (*e.g.* pressure, viscosity, and single-molecule approaches) and computational simulation the prospects are good for detailed atomistic understanding of enzymatic tunnelling reactions. The reader is directed to other contributions in this volume to gain insight into the other theoretical, computational and experimental methods that in combination with approaches described in this chapter will surely advance our understanding of enzyme mechanism at the macroscopic and atomistic levels.

References

1. S. J. Benkovic and S. Hammes-Schiffer, *Science*, 2003, **301**, 1196–1202.
2. S. J. Benkovic and S. Hammes-Schiffer, *Science*, 2006, **312**, 208–209.
3. P. Ball, *Nature*, 2004, **431**, 396–397.
4. D. D. Boehr, D. McElheny, H. J. Dyson and P. E. Wright, *Science*, 2006, **313**, 1638–1642.
5. M. Garcia-Viloca, J. Gao, M. Karplus and D. G. Truhlar, *Science*, 2004, **303**, 186–195.
6. Y. Cha, C. J. Murray and J. P. Klinman, *Science*, 1989, **243**, 1325–1330.
7. L. Masgrau, A. Roujeinikova, L. O. Johannissen, P. Hothi, J. Basran, K. E. Ranaghan, A. J. Mulholland, M. J. Sutcliffe, N. S. Scrutton and D. Leys, *Science*, 2006, **312**, 237–241.
8. C. R. Pudney, S. Hay, M. J. Sutcliffe and N. S. Scrutton, *J. Am. Chem. Soc.*, 2006, **128**, 14053–14058.
9. S. Hay, M. J. Sutcliffe and N. S. Scrutton, *Proc. Natl. Acad. Sci. USA*, 2007, **104**, 507–512.
10. M.H.M. Olsson, J. Mavri and A. Warshel, *Philos. Trans. Roy. Soc. B*, 2006, **361**, 1417–1432.
11. J. P. Klinman, *Biochim. Biophys. Acta*, 2006, **1757**, 981–987.
12. M. J. Sutcliffe, L. Masgrau, A. Roujeinikova, L. O. Johannissen, P. Hothi, J. Basran, K. E. Ranaghan, A. J. Mulholland, D. Leys and N. S. Scrutton, *Philos. Trans. Roy. Soc. B*, 2006, **361**, 1375–1386.
13. L. Wang, N. M. Goodey, S. J. Benkovic and A. Kohen, *Philos. Trans. Roy. Soc. B*, 2006, **361**, 1307–1315.
14. R. K. Allemann, R. M. Evans, L. H. Tey, G. Maglia, J. Y. Pang, R. Rodriguez, P. J. Shrimpton and R. S. Swanwick, *Philos. Trans. Roy. Soc. B*, 2006, **361**, 1317–1321.
15. S. Hammes-Schiffer and J. B. Watney, *Philos. Trans. Roy. Soc. B*, 2006, **361**, 1365–1373.
16. A. M. Kuznetsov and J. Ulstrup, *Can. J. Chem.*, 1999, **77**, 1085–1096.
17. D. Borgis and J. T. Hynes, *J. Phys. Chem.*, 1996, **100**, 1118–1128.
18. W. J. Bruno and W. Bialek, *Biophys. J.*, 1992, **63**, 689–699.
19. R. A. Marcus, *J. Chem. Phys.*, 2006, **125**, 194504–194509.
20. R. Bell, *The Tunnel Effect in Chemistry*, Chapman and Hall, London, 1980.
21. R. A. Marcus, *J. Chem. Phys.*, 1956, **24**, 966–978.
22. R. A. Marcus and N. Sutin, *Biochim. Biophys. Acta*, 1985, **811**, 265–322.
23. M. J. Sutcliffe and N. S. Scrutton, *Phys. Chem. Chem. Phys.*, 2006, **8**, 4510–4516.
24. L. Masgrau, J. Basran, P. Hothi, M. J. Sutcliffe and N. S. Scrutton, *Arch. Biochem. Biophys.*, 2004, **428**, 41–51.
25. J. Basran, M. J. Sutcliffe and N. S. Scrutton, *Biochemistry*, 1999, **38**, 3218–3222.
26. A. Kohen, R. Cannio, S. Bartolucci and J. P. Klinman, *Nature*, 1999, **399**, 496–499.

27. M. J. Knapp and J. P. Klinman, *Eur. J. Biochem.*, 2002, **269**, 3113–3121.
28. M. J. Sutcliffe and N. S. Scrutton, *Eur. J. Biochem.*, 2002, **269**, 3096–3102.
29. L. O. Johannessen, S. Hay, N. S. Scrutton and M. J. Sutcliffe, *J. Phys. Chem. B.*, 2007, **111**, 2631–2638.
30. H. Park, G. Kidman and D. B. Northrop, *Arch. Biochem. Biophys.*, 2005, **433**, 335–340.
31. D. B. Northrop, *J. Am. Chem. Soc.*, 1999, **121**, 3521–3524.
32. D. B. Northrop and Y. K. Cho, *Biophys. J.*, 2000, **79**, 1621–1628.
33. D. B. Northrop and Y. K. Cho, *Biochemistry*, 2000, **39**, 2406–2412.
34. D. J. Quirk and D. B. Northrop, *Biochemistry*, 2001, **40**, 847–851.
35. D. B. Northrop, *Biochim. Biophys. Acta.*, 2002, **1595**, 71–79.
36. H. Park, G. G. Girdaukas and D. B. Northrop, *J. Am. Chem. Soc.*, 2006, **128**, 1868–1872.
37. D. B. Northrop, *Philos. Trans. Roy. Soc. B*, 2006, **361**, 1341–1349.
38. N. S. Isaacs, K. Javaid and E. Rannala, *J. Chem. Soc. Perkin Trans.*, 1978, **2**, 709–711.
39. N. S. Isaacs, in *Isotope Effects in Organic Chemistry*, E. Buncel and C.C. Lee, ed. 1984, Elsevier, London, pp. 67–105.
40. N. S. Isaacs, K. Javaid and E. Rannala, *Nature*, 1977, **268**, 372–372.
41. S. Gladstone, K. J. Laidler and H. Eyring, *The Theory of Rate Processes*, McGraw-Hill, New York, 1951.
42. Y. K. Cho and D. B. Northrop, *Biochemistry*, 1999, **38**, 7470–7475.
43. R. Lumry, *Enzymes*, 1959, **1**, 157–231.
44. J. Basran, R. J. Harris, M. J. Sutcliffe and N. S. Scrutton, *J. Biol. Chem.*, 2003, **278**, 43973–43982.
45. D. H. Craig, P. C. E. Moody, N. C. Bruce and N. S. Scrutton, *Biochemistry*, 1998, **37**, 7598–7607.
46. O. Miyashita and N. Go, *J. Phys. Chem. B.*, 1999, **103**, 562–571.
47. M. J. Knapp, K. Rickert and J. P. Klinman, *J. Am. Chem. Soc.*, 2002, **124**, 3865–3874.
48. C. R. Pudney, S. Hay, Y. Pang, C. Costello, D. Leys, M.J. Sutcliffe and N.S. Scrutton, *J. Am. Chem. Soc.*, 2007, **129**, 13949–13956.
49. C. E. Kundrot and F. M. Richards, *J. Mol. Biol.*, 1987, **193**, 157–170.
50. G. Maglia and R. K. Allemann, *J. Am. Chem. Soc.*, 2003, **125**, 13372–13373.
51. M. Wolfsberg, *Ann. Rev. Phys. Chem.*, 1969, **20**, 449–478.
52. A. Streitwieser, R. H. Jagow, R. C. Fahey and S. Suzuki, *J. Am. Chem. Soc.*, 1958, **80**, 2326–2332.
53. L. Melander and W. H. Saunders, Jr., *Reaction Rates of Isotopic Molecules*, 2nd edn, 1980, Wiley, New York.
54. J. Z. Pu, S. H. Ma, M. Garcia-Viloca, J. L. Gao, D. G. Truhlar and A. Kohen, *J. Am. Chem. Soc.*, 2005, **127**, 14879–14886.
55. P. F. Cook, N. J. Oppenheimer and W. W. Cleland, *Biochemistry*, 1981, **20**, 1817–1825.
56. K. M. Welsh, D. J. Creighton and J. P. Klinman, *Biochemistry*, 1980, **19**, 2005–2016.

57. L. C. Kurz and C. Frieden, *J. Am. Chem. Soc.*, 1980, **102**, 4198–4203.
58. W. P. Huskey and R. L. Schowen, *J. Am. Chem. Soc.*, 1983, **105**, 5704–5706.
59. W. E. Karsten, C. C. Hwang and P. F. Cook, *Biochemistry*, 1999, **38**, 4398–4402.
60. A. Kohen and J. H. Jensen, *J. Am. Chem. Soc.*, 2002, **124**, 3858–3864.
61. J. Hirschi and D. A. Singleton, *J. Am. Chem. Soc.*, 2005, **127**, 3294–3295.
62. P. F. Cook, J. S. Blanchard and W. W. Cleland, *Biochemistry*, 1980, **19**, 4853–4858.
63. A. Kohen and J. P. Klinman, *Chem. Biol.*, 1999, **6**, R191–R198.
64. M. S. Graige, G. Feher and M. Y. Okamura, *Proc. Natl. Acad. Sci. USA*, 1998, **95**, 11679–11684.
65. D. W. Brinkley and J. P. Roth, *J. Am. Chem. Soc.*, 2005, **127**, 15720–15721.
66. Z. D. Nagel and J. P. Klinman, *Chem. Rev.*, 2006, **106**, 3095–3118.
67. S. Hay, C.R. Pudney, M.J. Sutcliffe and N.S. Scrutton, *Angew. Chem. Int. Ed.*, 2008, **47**, 537–540.
68. A. Ansari, C. M. Jones, E. R. Henry, J. Hofrichter and W. A. Eaton, *Science*, 1992, **256**, 1796–1798.
69. M. M. Ivkovic-Jensen and N. M. Kostic, *Biochemistry*, 1997, **36**, 8135–8144.
70. M. M. Ivkovic-Jensen and N. M. Kostic, *Biochemistry*, 1996, **35**, 15095–15106.
71. J. S. Zhou and N. M. Kostic, *J. Am. Chem. Soc.*, 1993, **115**, 10796–10804.
72. J. S. Zhou and N. M. Kostic, *J. Am. Chem. Soc.*, 1992, **114**, 3562–3563.
73. Y. Ohta, E. B. Mukouyama and H. Suzuki, *J. Biochem.*, 2006, **139**, 551–555.
74. M. von Smoluchowski, *Z. Phys. Chem.*, 1917, **92**, 129–168.
75. D. Beece, L. Eisenstein, H. Frauenfelder, D. Good, M. C. Marden, L. Reinisch, A. H. Reynolds, L. B. Sorensen and K. T. Yue, *Biochemistry*, 1980, **19**, 5147–5157.
76. H. A. Kramers, *Physica (Utrecht)*, 1940, **7**, 284–304.
77. L. Qin and N. M. Kostic, *Biochemistry*, 1994, **33**, 12592–12599.
78. L. Liu, J. Hong and M. Y. Ogawa, *J. Am. Chem. Soc.*, 2004, **126**, 50–51.
79. A. Kohen, T. Jonsson and J. P. Klinman, *Biochemistry*, 1997, **36**, 2603–2611.
80. S. L. Seymour and J. P. Klinman, *Biochemistry*, 2002, **41**, 8747–8758.
81. G. Mer, H. Hietter and J. Lefevre, *Nat. Struct. Biol.*, 1996, **3**, 45–53.
82. P. M. Rudd, H. C. Joao, E. Coghill, P. Fiten, M. R. Saunders, G. Opdenakker and R. A. Dwek, *Biochemistry*, 1994, **33**, 17–22.
83. A. Priev, A. Almagor, S. Yedgar and B. Gavish, *Biochemistry*, 1996, **35**, 2061–2066.
84. X. S. Xie and H. P. Lu, *J. Biol. Chem.*, 1999, **274**, 15967–15970.
85. S. Weiss, *Nat. Struct. Biol.*, 2000, **7**, 724–729.
86. H. Neuweiler and M. Sauer, *Anal. Chem.*, 2005, **77**, 178A–185A.
87. S. Myong, B. C. Stevens and T. Ha, *Structure*, 2006, **14**, 633–643.

CHAPTER 10

Computational Simulations of Tunnelling Reactions in Enzymes

JIAYUN PANG,^a NIGEL S. SCRUTTON^b AND MICHAEL J. SUTCLIFFE^a

^a Manchester Interdisciplinary Biocentre, and School of Chemical Engineering and Analytical Science, University of Manchester, 131 Princess Street, Manchester M1 7DN, UK; ^b Manchester Interdisciplinary Biocentre, and Faculty of Life Sciences, University of Manchester, 131 Princess Street, Manchester M1 7DN, UK

10.1 Introduction

The simulation of hydrogen transfer in enzymes provides a uniquely detailed atomistic insight into the reaction. Despite recent advances, such simulations remain challenging due to the importance of both electronic and nuclear quantum effects as well as the effects of protein motion. The incorporation of electronic quantum effects is required for the description of the breakage and formation of chemical bonds. Nuclear quantum effects, such as zero-point energy and hydrogen tunnelling, are also significant. However, over the past decade – with the enhancements in both computer power and theoretical approaches – computational simulations have become increasingly attractive in the study of hydrogen-transfer reactions in enzymes. They can complement experimental studies by providing insight that is difficult to access by experimental approaches, and make predictions that can be tested experimentally. The interplay between experiment and calculations can yield a remarkably complete description of an enzyme-catalysed hydrogen-transfer

process – computational simulations have played a major role in furthering our understanding at the atomic level. Computational simulations vary greatly in the level of accuracy they provide. Broadly speaking, they can be divided into two categories molecular mechanical (MM) and quantum mechanical (QM) methods (see Chapter 2). This chapter discusses these methods, how they can be combined to allow larger systems to be studied quantum mechanically, and how the H-tunnelling event can be simulated and rates and kinetic isotope effects (KIEs) calculated. To illustrate these methods, the proton-tunnelling event catalysed by the enzyme aromatic amine dehydrogenase (AADH) with tryptamine as substrate is presented as a case study.

10.2 Molecular Mechanical Methods

Molecular mechanical methods invoke the greatest level of approximation – they are therefore the least computationally expensive and can be used to model systems containing tens of thousands of atoms. The validity of MM methods is based on several assumptions. First, the Born–Oppenheimer approximation allows the energy of the system to be calculated as a function of the nuclear coordinates alone. Second, the energy of the system can be calculated from simple potential energy functions, such as bond stretching, angle bending and rotation about dihedral angles. Third, parameters that are developed using small molecules can be transferred to larger molecules. Typically, parameters are developed on relatively small model systems, such as individual nucleic acid bases for DNA and short peptides for protein and then applied to larger systems. Based on the above assumptions, a force field is used to describe the properties of the system in MM calculations.¹ Each atom is assigned an atom type, which defines its hybridisation state and local environment. The fundamental computation of a force field-based MM calculation is the calculation of the potential energy for a given conformation of the system. The potential energy of a given conformation is associated through bond parameters of the force field including bond, angles and dihedral angles as well as through space parameters including van der Waals and electrostatic interactions. There are a range of molecular mechanics force fields currently available including AMBER,² CHARMM,³ GROMOS,⁴ CVFF⁵ and OPLS.⁶ AMBER⁷ and CHARMM⁸ are the two most commonly used force fields for the simulations of biomacromolecules. As well as being the names of force fields, AMBER and CHARMM are also the name of two most commonly used software packages, which were designed to run MM calculations using their respective force field. Molecular dynamics (MD) simulation produces a trajectory that defines how the atomic positions and velocities, system energies and temperatures vary with time.

The widely used AMBER force field can be expressed in the following form. The subscript “eq” in the equation represents the equilibrium value for

individual term,⁹

$$E_{\text{total}} = \sum_{\text{bonds}} K_r(r - r_{\text{eq}})^2 + \sum_{\text{angles}} K_\theta(\theta - \theta_{\text{eq}})^2 \\ + \sum_{\text{dihedrals}} \frac{V_n}{2} [1 + \cos(n\phi - \gamma)] + \sum_{i < j} \left[\frac{A_{ij}}{R_{ij}^{12}} - \frac{B_{ij}}{R_{ij}^6} + \frac{q_i q_j}{\epsilon R_{ij}} \right] \quad (10.1)$$

Although natural bond stretching and angle bending are not truly harmonic, the deviations from the equilibrium value are normally small and as a harmonic potential is computationally more efficient, the energies of bond stretching and angle bending are defined by a harmonic approximation using Hooke's law. The energy increases as the bond length (r in eqn (10.1)) or angle (θ in eqn (10.1)) deviates from its equilibrium value. The size of the energetic penalties upon this variation is associated with the force constant (K_r and K_θ in eqn (10.1)).

The third term in eqn (10.1) is to describe bond rotation. The torsion angle of a set of four atoms is defined as a cosine series expansion. V_n refers to the potential energy barrier of bond rotation. The value of n refers to the number of minimum points as the torsion angle is rotated about 360°, while γ is a phase factor that determines where the minima of the torsion angle occur. In the AMBER force field, generally, a torsion potential depends on the atom type of two central atoms and not on the terminal atoms.

The fourth term in eqn (10.1) is the nonbonded interaction, used to describe the van der Waals (VDW) interactions and electrostatic interactions in the system. They are the most computationally expensive parts of force field-based calculations. The van der Waals interactions are calculated using the Lennard-Jones 6-12 potential. The interactions include the combination of the attractive forces (A) and the repulsive forces (B) that are calculated relative to the distance (R) between two atoms (i and j). Electrostatic interactions between two atoms are modulated by the partial charges (q) of each atom, the distance (R) between them and the dielectric constant (ϵ). One common approach representing the charge distribution is an arrangement of partial point charges throughout the molecule. If the charges are restricted to the nuclear centres they are referred to as partial atomic charges or net atomic charges. The electrostatic interactions between two atoms are then calculated as a sum of interactions between pairs of point charges using Coulomb's Law.¹⁰

There are two additional terms in the energy function of the CHARMM force field³

$$E_{\text{UB}} = \sum_{\text{UB}} K_{\text{UB}}(S - S_{\text{eq}})^2 \quad (10.2)$$

$$E_{\text{improper}} = \sum_{\text{impropers}} K_{\text{imp}}(\varphi - \varphi_{\text{eq}})^2 \quad (10.3)$$

where K_{UB} is the Urey–Bradley force constant and S is the distance between the 1,3 atoms in the harmonic potential. K_{imp} is the improper dihedral angle force constant and φ is the improper dihedral angle that refers to the out-of-plane bending. The Urey–Bradley term and the improper dihedral angle term are only used to optimise the fit to vibrational spectra.

10.3 Quantum Mechanical Methods

As an MM system does not explicitly include electrons, chemical bond breakage and formation cannot be studied using MM. To study these processes in enzymatic reactions, quantum mechanical (QM) methods are required. There are a number of quantum mechanical theories for treating molecular systems (see Chapter 2).

10.4 Combined Quantum Mechanical/Molecular Mechanical Methods

Depending on the choice of QM level and computational resource, tens to hundreds of atoms can be included in the system, which is still too small to include the whole enzyme in the calculation. Therefore, combined QM/MM methods have been developed that allow the enzyme active site – typically substrate, cofactor and key residues involved in hydrogen transfer – to be treated at a certain level of QM and the rest of the system modelled by a MM force field. The total energy of the system can then be expressed as the combination of the energy of the MM region, the energy of the QM region and the interaction energy (electrostatic and van der Waals) between the two.

$$E(QM/MM) = E(QM \text{ on QM}) - E(MM \text{ on QM}) + E(MM \text{ on all}) \quad (10.4)$$

The application of QM/MM methods on enzymatic systems is an area of computational chemistry where there is extensive current research and continuous development.¹¹ It was first laid out by Warshel and Levitt in 1976¹² but was only developed for general applications in the past decade and has become the method of choice for studying hydrogen transfer in enzyme systems.

The main problem with the QM/MM approach is how to couple the two parts together. Several methods have been developed to treat the boundary between the QM region and MM region. An early and still widely used scheme is the link atom approach¹³ in which extra atoms – typically hydrogen atoms – are added to the two atoms bonded at the interface of the QM and MM region to maintain the valence (Figure 10.1(A)). Another approach is the local self-consistent field method (LSCF).¹⁴ In this method, the boundary atom is a QM atom whose valence is saturated by a frozen hybrid orbital with predetermined density, pointing towards the MM region. A commonly used approach, which is in the spirit of the LSCF, is the generalised hybrid orbital (GHO) method.¹⁵ A sp^3 carbon is normally chosen as the boundary atom **B** (Figure 10.1(B)).

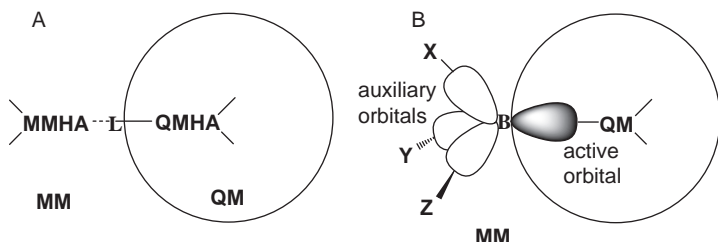


Figure 10.1 Schematic representation of methods for linking the QM and MM regions. **A**, the link atom method, where the link atom is marked with “L” and “MMHA” and “QMHA” stand for MM host atom and QM host atom. **B**, the generalised hybrid orbital (GHO) method, showing the treatment of a covalent bond across the boundary between the QM region and MM region. The boundary atom is denoted with “B”.

B is considered as both a QM and a MM atom. A set of hybrid orbitals are placed on **B** between the QM and MM region. The hybrid orbital pointing towards the QM atoms is called the active orbital that participates in the self-consistent field (SCF) calculation in the QM region and the other three hybrid orbitals are called auxiliary orbitals that generate an MM potential for the boundary atom (Figure 10.1(B)). The GHO method was initially developed for a semiempirical level and has been extended to HF *ab initio* and DFT QM/MM calculations.^{16,17}

10.5 Improving Semiempirical QM Calculations

The combined QM/MM approach would ideally use high level MO or DFT to present the QM part such that accurate results can be obtained. However, these calculations are generally too time consuming to be applied at the present time, particularly when MD simulation needs to be run based on a QM/MM potential requiring simulations over a reasonable timescale (from a few nanoseconds to tens of nanoseconds). On the other hand, semiempirical methods such as AM1 or PM3 are computationally efficient, allowing adequate sampling of the conformational space in the MD simulations. However, in many cases semiempirical methods are not able to provide the desired accuracy in the free energy calculations using the combined QM/MM potential. A successful approach to solve this problem is the augmentation of semiempirical methods in conjunction with reparameterisation for specific enzyme systems (the so-called specific reaction parameter (SRP) approach^{18,19}). It assumes that the general shape and features of the potential energy surfaces are adequately represented by AM1/PM3 and introduces a simple valance bond (SVB) like term (Chapter 4 and Chapter 11) which only corrects the energies at the critical points on the potential energy surface to reproduce the experimental or high level QM results for model reactions.

10.6 Calculation of Potential Energy Surfaces and Free Energy Surfaces

To describe the QM/MM potential energy surface, the location and characterisation of the set of stationary structures (reactant, transition, product states and possible intermediates) have to be identified. In the simplest approach, only the positions of the QM atoms are varied, while the MM part remains frozen at positions obtained from previous calculations. A more accurate way of optimising the relevant structures is to also allow the relaxation of the environment that couples to the QM regions. Due to the large number of possible conformations accessible to the enzyme and its solvation environment, it is desirable to obtain a statistical ensemble of structures to define the reactant, transition and product states. Simulations can be carried out using Monte Carlo or MD methods. Free energies associated with the transformation from the reactant state to transition state (the free energy of activation) and from the reactant state to product state (the free energy of reaction) are of particular interest for enzymatic reactions. The reaction rate constants can be extracted from the free energy of activation.

Free energy profiles can be obtained as the potential of mean force (PMF) along a predefined reaction coordinate that describes how the free energy changes as a particular coordinate is varied. This free energy change includes the averaged effects of the solvent. The PMF can be determined using Monte Carlo simulation or MD simulation. Various methods have been proposed for the calculation of the PMF, such as umbrella sampling and free energy perturbation. The umbrella sampling method samples the free energy at different positions along the reaction coordinate.¹⁰ To achieve enough sampling, an adequate parabolic energy function is added centred in turn at each position along the reaction coordinate. Once the reaction coordinate has been fully explored from the reactant state to transition state and then to product state, the total probability distribution function is obtained and thus the free energy profile is calculated. Further structural properties of the system can be derived from the trajectories obtained from the umbrella sampling.

10.7 Simulation of the H-tunnelling Event

As umbrella sampling is carried out using purely classical mechanics, it is desirable to include the nuclear quantum effects – such as zero-point energy and hydrogen tunnelling – into PMF. This is of particular significance to reactions involving hydrogen transfer. Truhlar, Gao and coworkers (see Chapter 4) have developed an approach for incorporating nuclear quantum effects into simulations of hydrogen-transfer reactions in enzymes known as ensemble-averaged variational transition-state theory with multidimensional tunnelling (EA-VTST/MT).²⁰ The quantised energy correction to the classical PMF is calculated by instantaneous normal mode analysis based on the local harmonic approximation to the vibrational modes orthogonal to the reaction coordinate. However, at this point tunnelling and other quantum effects on the reaction

coordinate are not included. The tunnelling probability is calculated in a separate stage by microcanonically optimised multidimensional tunnelling (μ OMT). It calculates the tunnelling factor κ by optimising the tunnelling path between the paths described by small curvature tunnelling (SCT) and large-curvature tunnelling (LCT) as a function of the energy of the system, where SCT includes mild corner cutting of the minimum energy path (MEP) in the reaction path while in LCT, a straight line tunnelling path, leads to the shortest path with maximised corner cutting. The results from μ OMT are often only (but not always) slightly smaller or the same if one limits the calculation to SCT paths, and so sometimes only SCT is used to simplify the calculations.²¹

Other approaches have also been developed. The path integral method is another way to incorporate nuclear quantum effects in the simulations of enzyme-catalysed hydrogen transfer. In this approach, ensemble averages for the quantum system can be obtained by carrying out a classical simulation in which the quantised particles are represented by ring polymers of classical particles.²² The approach applied by Hammes-Schiffer and coworkers used the mixed quantum/classical molecular dynamics (MQCMD) method, in which selected nuclei are represented as quantum mechanical wavefunctions while the other nuclei are treated classically (Chapter 4).²³ For reviews of methods to include quantum nuclear effects, see refs 24,25.

10.8 Calculation of H-tunnelling Rates and Kinetic Isotope Effects

By studying different isotopes (particularly the protium and deuterium isotopologues) in the calculations of nuclear quantum effects, a rate constant for the respective reactions – and hence the KIE – can be obtained using, for example, the program POLYRATE (see Chapter 4).²⁶ Comparison between the rate constant calculated both with and without a tunnelling contribution gives an indication of the degree of tunnelling in the H-transfer reaction, and analysis of the MEP provides information on the tunnelling process – such as geometry of the substrate and cofactor, the donor–acceptor distance, the representative tunnelling energy (RTE) and the dominant tunnelling mechanism at the RTE (which is associated with the tunnelling path curvature).

10.9 Analysing Molecular Dynamics Trajectories

Postprocessing a trajectory from a MD simulation can be something of a fine art, and the types of analysis used depend to a large extent on the question(s) being asked of the data. A visual inspection of the trajectory using molecular visualisation packages – such as Visual Molecular Dynamics (VMD)²⁷ – is extremely important but only provides a limited understanding of the simulated system. Further analysis using mathematical methods is often necessary.

These include cross correlation analysis²⁸ to investigate how the motions of individual atoms are coupled, spectral density analysis²⁹ to identify key vibrations underlying the H-transfer event, digital filtering³⁰ and principal component analysis (PCA) to investigate further the role of any such vibrations.

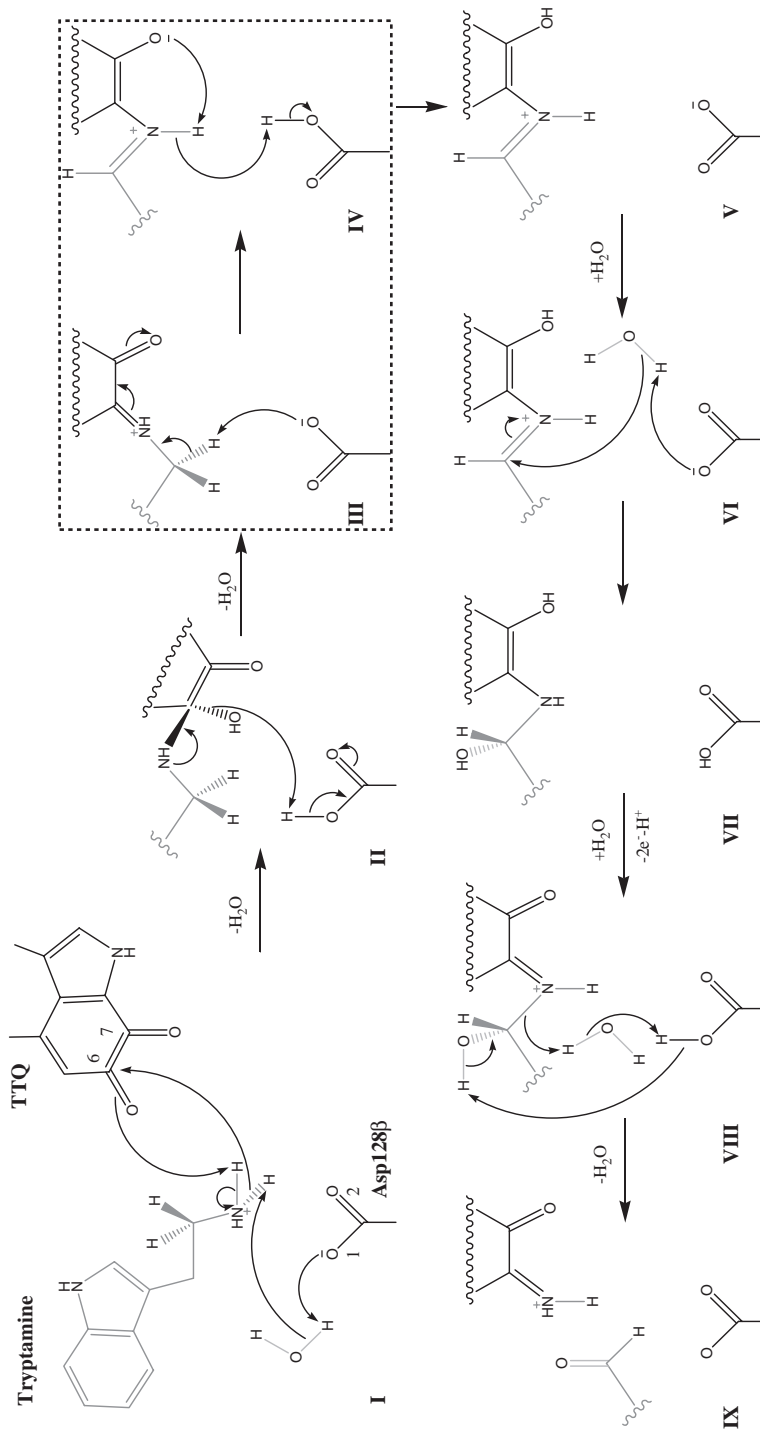
10.10 A Case Study: Aromatic Amine Dehydrogenase (AADH)

Accumulated studies on the enzyme aromatic amine dehydrogenase (AADH) – based on experimental analysis using fast reaction methods,^{31,32} coupled with the availability of high resolution crystal structures of key reaction intermediates³² and combined with computer simulation^{32–34} – have demonstrated the strength of a synergistic interdisciplinary approach in revealing tunnelling mechanisms in atomistic detail.

AADH is a heterotetrameric quinoprotein enzyme that catalyses the oxidative deamination of primary amines – *via* transfer of a proton from a C–H bond of a tryptamine-derived iminoquinone intermediate to the catalytic base, Asp128 β – to form the corresponding aldehyde (Scheme 10.1). The enzyme contains an unusual quinone cofactor, tryptophan tryptophylquinone (TTQ), which is formed through post-translational modification of two tryptophan residues in the small catalytic subunit of the enzyme. The TTQ cofactor is intimately involved in the reaction mechanism through formation of a substrate-derived covalent adduct. The key intermediate for H-tunnelling is the iminoquinone species **III**, from which proton transfer occurs. This rate determining step for reduction of the TTQ cofactor can be observed spectroscopically because proton transfer is concomitant with TTQ reduction. This is the basis for experimental analysis of H-tunnelling using fast reaction methods.

10.10.1 Preparation of the System

Currently, atomic level insight into the tunnelling event can only be obtained from high resolution X-ray structures of catalytically competent intermediates combined with computer simulation.³⁵ The availability of high resolution (ranging from 1.1 Å to 1.6 Å) crystal structures of tryptamine-AADH intermediate complexes in the reductive half-reaction has made computational study feasible.³² The structure of the tryptamine-derived iminoquinone complex (**III**), the starting point of all our simulations, was modelled from the 1.1 Å resolution X-ray crystal structure of the related Schiff base intermediate **V** (protein data bank³⁶ accession code 2AGY).³² Hydrogen atoms were built into the structure using the H-Build subroutine in CHARMM and the structure was solvated.^{32,34} The CHARMM22 all-hydrogen force field³ for the protein residues and TIP3P type³⁷ water molecules were used for the molecular mechanics representation. The QM/MM partition was defined^{32,33} with the QM region consisting of 48 atoms (including 3 HQ type link atoms³⁸ – QM hydrogens without classical van der Waals or bonded force field terms, but that do interact



Scheme 10.1 Schematic overview of the reaction mechanism of the reductive half-reaction of AADH with tryptamine.³² Atoms derived from the substrate are depicted in dark gray, those derived from water in light gray. All other enzyme-derived atoms are depicted in black; the catalytic base, Asp128 β , is labelled in I. The box depicts the proton-tunnelling step, which is also the rate determining step; III and IV refer to the reactant and product of the proton-transfer step, respectively.

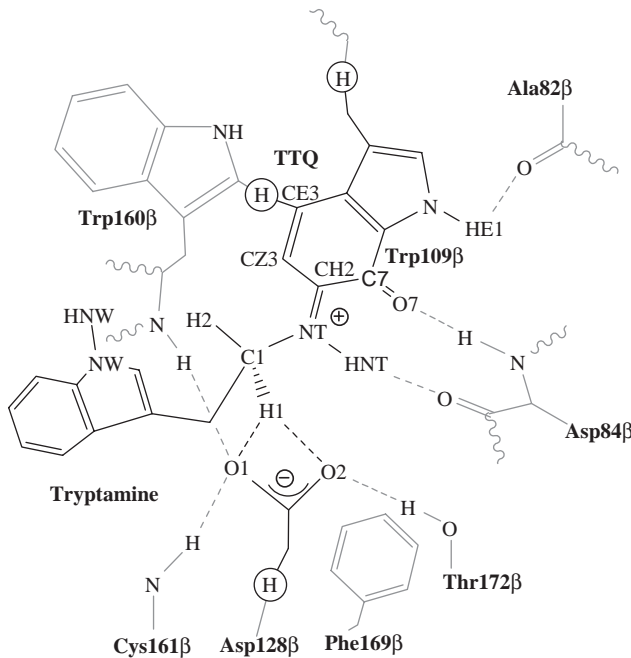


Figure 10.2 The active site of the reactant (see Scheme 10.1), iminoquinone **III**, illustrating the QM/MM partition used in the calculations. The QM region is shown in black and part of the surrounding MM region in gray with link atoms circled; hydrogen bonds between the QM region and active site residues are depicted by dashed lines.

with MM charges; Figure 10.2). Following initial equilibration of the water molecules by MD simulation with fixed protein atoms ($T=300\text{ K}$), the full model was minimised by imposing gradually decreasing harmonic restraints on the protein atom positions. For QM/MM simulations, a stochastic boundary approach was used³⁹ and water was restrained to remain within the simulation system using a spherical deformable potential of radius 25 \AA . The reaction region was defined as a 21 \AA sphere centred on NT (the imine nitrogen; Figure 10.2) – atoms in this region were not subject to positional restraints. The region between spheres radius 21 \AA and 25 \AA was defined as the buffer region – protein heavy atoms in this region were restrained using force constants scaled to increase with distance from the centre of the system. Atoms further than 25 \AA from the centre were fixed. QM/MM minimisation of **III** was carried out using the adopted basis Newton–Raphson minimisation algorithm, to a gradient tolerance of $0.01\text{ kcal mol}^{-1}\text{ \AA}^{-2}$. Both AM1 and PM3 semiempirical methods were used to describe the QM region. The accuracy of the QM level was improved by specific reaction parameters derived^{32,33} from those for a similar system (methylamine dehydrogenase, MADH) that were based on higher level QM calculations for small model systems.⁴⁰

10.10.2 Analysis of the H-tunnelling Step in AADH

To calculate the potential energy barrier corresponding to the H-transfer step, an adiabatic mapping procedure was used to pass from the PM3/CHARMM22 optimised reactant **III** to product **IV**; the reaction coordinate for the proton transfer was defined as $z = [d(\text{C1}-\text{H1}) - d(\text{O}-\text{H1})] \text{ \AA}$. The system was optimised at different values of z , passing from reactant to product in 0.1 Å steps to obtain an indication of the potential energy change associated with the transfer of the proton, and of the suitability of the reaction coordinate chosen. To calculate the classical free energy barrier, umbrella sampling molecular dynamics (PM3/CHARMM22)^{41,42} was used to simulate the proton transfer from **III** to **IV** in 0.1 Å intervals along the reaction coordinate using a force constant of 300 kcal mol⁻¹ Å⁻².³³ The reaction coordinate statistics were combined using the weighted histogram analysis method (WHAM⁴³) to give the PM3/CHARMM22 (classical) free energy profile for proton transfer.

The resulting classical activation free energy ($\Delta G^{\ddagger, C}$) was used to estimate the classical rate constant (the rate constant without inclusion of any tunnelling or quantised vibration contribution). PM3 has been shown to represent poorly the energy of proton transfer in the similar methylamine MADH/methylamine system.^{40,44} It was therefore necessary to correct the energies to provide more realistic values. PM3 can be reparameterised to reproduce experimental data or high-level *ab initio* data for a particular reaction of interest. Alhambra and coworkers⁴⁰ developed specific reaction parameters (SRPs) for the MADH/methylamine system based on higher level quantum mechanical results for small models. They found it was only necessary to modify the parameters for the donor carbon atom involved in the proton transfer to reproduce their higher level results. As the model reactions used in that work also represent the proton transfer in AADH, the SRPs for this carbon atom in MADH were used and single point PM3-SRP/CHARMM22 energy calculations were carried out on the structures along the PM3/CHARMM22 pathways generated by adiabatic mapping. The difference between the PM3/CHARMM22 and PM3-SRP/CHARMM22 energies (relative to the reactant) was then used to adjust the free energy at each z value.³³ This approach was tested by performing a PM3-SRP/CHARMM22 adiabatic mapping procedure, optimising the structures at each point – this procedure gave similar results. The classical reaction path was used to identify contributions of different residues to the reaction (e.g. to QM/MM electrostatic stabilisation) by individually deleting the residues (identified as important from the hydrogen-bond analysis) from each structure in the dynamics trajectory at the reactant (**III**), transition state (TS) and product (**IV**) complexes and recalculating the energy.³³ The difference between the original QM/MM electrostatic energy and the energy with the residue deleted was then the contribution of that particular residue to the electrostatic interaction. It is important to note that the interaction energies calculated in this manner do not include the effects of dielectric shielding. As a result the energies are not directly comparable to experimental results (e.g. $\Delta\Delta G^\ddagger$ for mutated enzymes); however, this type of decomposition analysis is useful for identifying catalytically important interactions.

To calculate the KIE for the proton transfer (the rate for doubly deuterated versus doubly protiated tryptamine as substrate), variational transition state theory calculations with small curvature tunnelling corrections (VTST/SCT)^{24,45,46} were carried out with the CHARMMRATE interface.⁴⁷ For each isotopic reaction, a representative free energy profile was calculated, which included the quantised vibrational energy for the active zone atoms (atoms that were not restrained during the VTST calculation, see below) and the transmission coefficient, which accounts for quantum nuclear effects (including tunnelling) on the reaction coordinate.^{45,48} The VTST/MT rate constant ($k_i^{\text{VTST/MT}}$) was obtained using:

$$k_i^{\text{VTST/MT}}(T) = \kappa_i^{\text{MT}}(T) \frac{k_B T}{h} \exp\left[-\Delta G_i^{\text{TS},\circ}(T)/RT\right] \quad (10.5)$$

where $\Delta G_i^{\text{TS},\circ}(T)$ is the standard state molar free energy of activation for the isotopic reaction i , with the quantised vibrational energy included (thus, it is a quasiclassical activation free energy), and κ_i^{MT} is the transmission coefficient, calculated in this study³³ within the small curvature tunnelling approximation (SCT). T , k_B , h and R are the temperature, and Boltzmann's, Planck's and the gas constants, respectively. The KIE was then obtained by dividing the calculated doubly protiated $k^{\text{VTST/SCT}}$ rate constant by the one calculated for the doubly deuterated substrate reaction.

The starting point for these VTST/SCT calculations was the structure corresponding to the maximum of the PM3/CHARMM22 adiabatic mapping potential energy profile (see above). The QM/MM system was divided into two zones, corresponding to the QM atoms (active zone) and the MM atoms (bath zone). A saddle point, reactant and product were located on the PM3/CHARMM22 potential energy surface by optimising the QM atoms (active zone) embedded in the potential created by the frozen bath zone, and characterised by normal mode analysis. From the saddle point, a minimum energy path (MEP) was then calculated downhill for each isotopic reaction until the energy of the system approached that of the reactant and the product. The Page–McIver algorithm⁴⁹ and a step size, δs , of 0.01 bohr amu^{1/2} were used (where s denotes the mass weighted distance along the MEP; it is defined as zero at the saddle point, <0 at the reactant side and >0 at the product side). First and second derivatives of the energy were calculated at each step and every 10 steps of the MEP, respectively. The vibrational frequencies for the active zone and the PM3/CHARMM22 free energy along the MEP, and thereby $\Delta G_i^{\text{TS},\circ}$, were obtained.

However, as mentioned above, PM3 does not satisfactorily describe the energetics of this type of proton transfer, and tends to underestimate the activation free energy when compared to experiment. Therefore, following the same approach used to correct the classical path, we carried out PM3-SRP/CHARMM22 single point energy calculations along the PM3/CHARMM22 path. The interpolated single point energy corrections (ISPE)⁵⁰ algorithm in POLYRATE²⁶ was used to apply the correction to the potential energy and to

$\Delta G_i^{\text{TS},\circ}$. With the PM3/CHARMM22 vibrational frequencies, $v_i(s)$, and within the harmonic approximation, the zero point energy contribution, $E_{\text{ZPE}}(s)$, was calculated at each point of the MEP with respect to the value at the reactant [$E_{\text{ZPE}}(s) = \sum_{i=1}^{3N} \frac{1}{2} h v_i(s) - \sum_{i=1}^{3N} \frac{1}{2} h v_i(s_R)$] (s_R denotes the reactant of the VTST/SCT calculation). The sum of this zero point energy contribution and the corrected potential energy gives the effective potential used in the calculation of the tunnelling transmission coefficients, κ_i^{MT} .

The classical activation free energy for the proton transfer ($\Delta G^{\ddagger, \text{C}}$) was obtained from umbrella sampling simulations (see above), which sampled over protein configurations. To include the effects of proton tunnelling, we used the transmission coefficient obtained from the VTST/SCT calculations. The contribution of hydrogen tunnelling to the activation free energy ($\Delta G^{\ddagger, \text{Tun}}$)^{45,51} was obtained using:

$$\Delta G^{\ddagger, \text{Tun}}(T) = -RT \ln[\kappa_i^{\text{MT}}(T)] \quad (10.6)$$

The combination of classical molecular dynamics simulations with variational transition state theory calculations including multidimensional tunnelling corrections permits separate analysis of the classical and quantum reactions. Thus, the contribution of tunnelling in lowering the effective free-energy barrier, $\Delta G^{\ddagger, \text{Tun}}$, can be combined with the classical activation free energy to give the phenomenological activation free energy:

$$\Delta G^{\ddagger, \text{Act}}(T) = \Delta G^{\ddagger, \text{C}}(T) + \Delta G^{\ddagger, \text{Tun}}(T) \quad (10.7)$$

Note that the phenomenological activation free energy, $\Delta G^{\ddagger, \text{Act}}$, should also include a term for the quantised vibrational contribution.⁵² Although we have taken the quantised vibrations into account in the calculation of the KIEs (eqn (10.5)), we have not calculated the quantised vibrational contribution to $\Delta G^{\ddagger, \text{Act}}$. This contribution is usually found to lower the classical activation barrier significantly and, in the present case, it may be expected to be similar to that obtained for the related MADH/methylamine system (-3.2 kcal/mol).⁴⁰

The phenomenological activation free energy^{51,53} can be compared with the experimentally derived activation free energy. It predicts a rate constant for this step of:

$$k(T) = \frac{k_B T}{h} \exp[-\Delta G^{\ddagger, \text{Act}}(T)/RT] \quad (10.8)$$

Although the transferring proton (labelled H1 in Figure 10.2) is closer in the reactant complex to the O1 oxygen atom than the O2 oxygen atom of the active site base, Asp 128 β , both of these possibilities were studied in two separate samplings. Data for transfer to O1 and O2, respectively, at 300 K are shown in Table 10.1. Thus, despite the shorter initial O1–H1 distance, a preference for transfer to O2 was seen both kinetically and thermodynamically.

Table 10.1 Kinetic and thermodynamics parameters calculated for the proton transfer to O1 and O2 of Asp128 β .

<i>a</i>	$\Delta G^{\ddagger,C}$	$\Delta_r G$	$\Delta G^{\ddagger,Tun}$	$\Delta G^{\ddagger,Act}$	<i>k</i>	KIE
O1	20.0	4.8	4.6	15.4	38	42
O2	18.1	7.8	4.9	13.2	1500	93
<i>b</i>	$\Delta G^{\ddagger,C}$	$\Delta_r G$	$\Delta G^{\ddagger,Tun}$	$\Delta G^{\ddagger,Act}$	<i>k</i>	KIE
O1	16.4	4.0	2.4	14.0	400	12
O2	12.5	8.1	3.1	9.4	8.83×10^5	30

$\Delta G^{\ddagger,C}$, classical free energy barrier (kcal/mol); $\Delta_r G$, classical free energy of reaction (kcal/mol); $\Delta G^{\ddagger,Tun}$, tunnelling contribution to the free energy barrier (kcal/mol); $\Delta G^{\ddagger,Act}$, phenomenological free energy barrier; *k*, rate constant (s^{-1}). Table 10.1a is from ref. [32] and Table 10.1b is from ref. [33].

The calculated KIEs are significantly elevated over the semiclassical limit of 7, in agreement with the experimental observations of 55 ± 6 ;³² a semiclassical value of $\sim 5\text{--}6$ is obtained when tunnelling is omitted. From the calculated transmission factors, κ , we estimate that in excess of 99% of the reaction proceeds *via* tunnelling (*i.e.* tunnelling increases the rate by >2 orders of magnitude).^{32,33} Breakage of the polarised C–H bond in the AADH:tryptamine adduct is aided by the cationic nature of the iminoquinone and the elevated pK_a (7.1 in free enzyme and 6.0 in the enzyme–substrate complex⁵⁴) of Asp128 β . The product is stabilised partly by delocalisation of the developing negative charge onto the TTQ and partly by hydrogen bonds with the enzyme.³³

10.10.3 Analysis of the Role of Promoting Motions in Driving Tunnelling

This high degree of H-transfer by quantum mechanical tunnelling is consistent with both the highly inflated KIE ($\gg 7$) and the magnitude of the Arrhenius prefactor ratio ($\gg 1$) derived from temperature analysis of reaction rates with protiated and deuterated tryptamine. Further support for tunnelling behaviour is provided by the apparent temperature independence of the primary KIEs,³² coupled with the strong temperature dependence of reaction rates, suggesting that the tunnelling event is driven by motion within the enzyme–substrate complex (*i.e.* motion independent of the isotope being transferred). However, the nature of the motion(s) driving H-tunnelling in enzyme systems is contentious.⁵⁵

The picture of the reaction emerging from our studies of AADH is as follows. The reacting moieties first approach by classical activation to a transferring hydrogen acceptor (H1–O2) separation of $\sim 1.64\text{ \AA}$; prior to this point (Figure 10.3), the reaction coordinate is dominated by heavy atom motions. From this point ($s = -0.77\text{ bohr amu}^{1/2}$; the reaction coordinate,

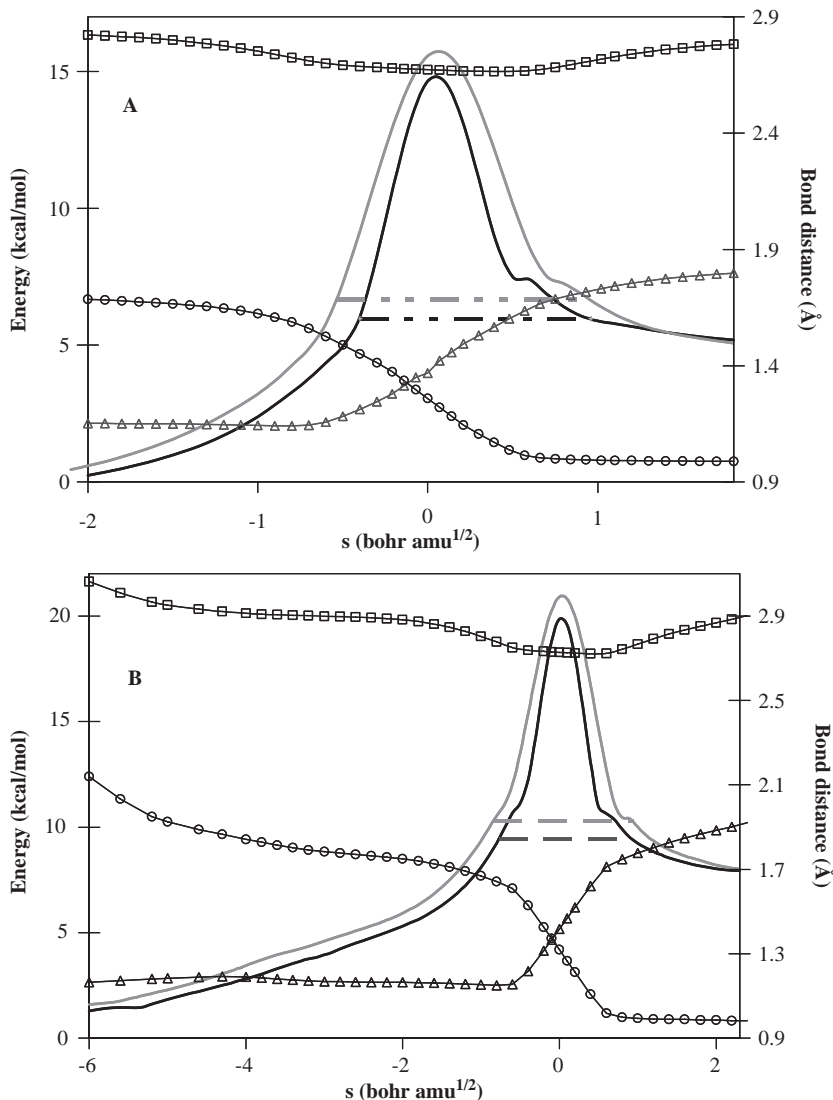


Figure 10.3 Minimum energy paths (including zero point energies) calculated³² to obtain $\Delta G^{\ddagger, \text{Tun}}$ and the KIEs for transfer to (A) O₁ and (B) O₂ (solid lines), and dominant tunnelling energy at 300 K for each isotope (dashed lines). Black and gray lines are for perprotio and perdeutero tryptamine, respectively. The reaction coordinate, *s*, is the mass weighted difference in position from the transition state (1 bohr = 0.529 Å), with *s* = 0 at the top of the barrier and negative at the reactant side. Also shown are the C-H (triangles), H-O (circles) and C-O (squares) distances along these perprotio reaction paths (right hand axis).

s , is the mass-weighted difference in position from the transition state [1 bohr = 0.529 Å], with $s=0$ at the top of the barrier and negative at the reactant side), the proton tunnels a distance of ~0.59 Å through the barrier, at a dominant tunnelling energy ~10.4 kcal/mol below the top of the barrier; proton motion is highly dominant in this region of the reaction coordinate as the proton–donor bond breaks (and the proton tunnels; Figure 10.3). Inspection of the classical free energy profile reveals that, early in the reaction, the H1–O2 average distance shortens to ~2.0 Å at a relatively low energetic cost (< 2 kcal/mol). These calculations revealed that progressing from the reactant to the representative structure for tunnelling to O₂ (*i.e.* the structure corresponding to the dominant tunnelling energy in Figure 10.3; RTE structure) requires significant heavy atom motion (and no significant C–H bond stretching), involving rotation of donor carbon (C1) and the transferring hydrogen (H1) accompanied by a repositioning of O₂ (acceptor) (Figure 10.4).

To investigate further protein motions, and in particular those that could reduce the proton–acceptor distance and thereby promote tunnelling, MD simulations of intermediate III were performed using the CHARMM22 force field and the last 5 ns of the 7 ns trajectory was analysed by cross correlation analysis, principal component analysis and spectral density analysis. Dynamical cross correlation analysis²⁸ was performed on the last 5 ns of the trajectory, after ensuring that the correlation coefficients had converged. Spectral densities²⁹ of the motions were calculated for a 400 ps window (2.0 to 2.4 ns) with coordinates

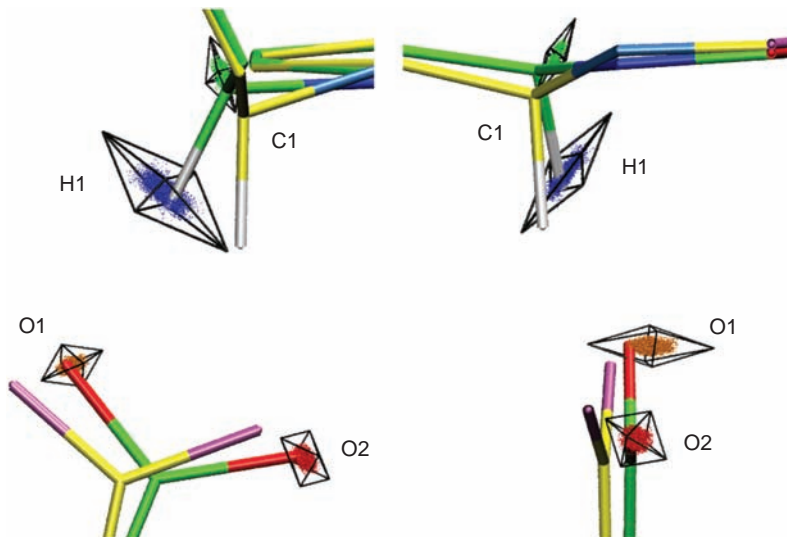


Figure 10.4 Orthogonal views of the reactant (green carbon atoms) and the RTE (yellow carbon atoms) structures from our VTST/MT calculations,³² with superimposed atomic coordinates (coloured dots) for the ~165 cm⁻¹ vibration for C1, H1, O1 and O2. The cages represent the principal components for the filtered motion of each atom, and are scaled according to the relative eigenvalues.

recorded every 4 fs. Digital filtering by frequency deconvolution³⁰ was applied to the same 400 ps window to obtain atomic velocities for a selected frequency range. To gain insight into how the atoms move during the MD simulation, these new velocities were applied to the coordinates in the first frame of the MD trajectory. To compare these movements with those observed in our VTST calculations, the coordinates in this first frame were structurally aligned with the minimised reactant structure from the VTST calculations using atoms in the linker region connecting the quinone and the indole and the sidechain of Asp128 β .

In accord with the above discussion, this analysis also suggested that the O2–H1 distance, critical for tunnelling, can be shortened by rotation of H1 towards O2 and repositioning of the Asp128 β carboxylate – in particular, the motion of H1 is focused on modulating the O2–H1 distance (Figure 10.4). The spectral densities derived from the dynamics simulations suggest³² that this rotation could occur with a frequency of $\sim 165 \text{ cm}^{-1}$, predominantly through motion of H1. However, cross correlation analysis suggests that the motion of H1 is not strongly coupled to O2 or any other neighbouring atom;³² this is further supported by principal component analysis of the covariance.³² The motion of O2 is only coupled to its hydrogen bonding partner, Thr172 β . In turn, the motion of Thr172 β is additionally only coupled to Cys171 β , which is not correlated with O2. Thus, our results show no network of coupled long-range motions that modulate the O2–H1 distance.³² Digital filtering to remove motions outside a $\pm 30 \text{ cm}^{-1}$ window around this frequency of 165 cm^{-1} , followed by mapping the resulting coordinates onto the reactant structure, revealed^{32,34} that this vibration does indeed correspond to the structural changes that occur with C1, H1 and O2 in passing from reactant to the structure corresponding to the RTE (Figure 10.4) and therefore serves as a short-range motion that reduces the proton–acceptor distance – a “promoting motion”. QM frequency calculations – using Gaussian, (Gaussian 03, Gaussian Inc., Wallingford, CT) with initial energy minimisation carried out at the B3LYP/6-31G* level – indicated that this “promoting motion” is inherent to the iminoquinone intermediate. Furthermore, we showed³⁴ by numerical modelling that this short-range vibration – of frequency $\sim 165 \text{ cm}^{-1}$ – is consistent with the ‘gating’ motion in the hydrogen tunnelling model of Kuznetsov and Ulstrup⁵⁶ in an enzymatic reaction with an observed protium/deuterium KIE that is not measurably temperature dependent. Motions other than this promoting motion (*i.e.* pre-organisation) are likely involved in moving the system toward a tunnelling-ready configuration, from which this gating motion can take effect, for example, the repositioning of O2 could bring O2 sufficiently close to H1 for an electrostatic coupling of their respective vibrations to occur.

10.10.4 Comparison of Short-Range Motions in AADH with Long-Range Motions in Dihydrofolate Reductase

As discussed above, our studies of AADH suggest that there is no network of coupled long-range motions that modulate the O2–H1 distance. This is in

contrast to the extensively studied enzyme dihydrofolate reductase from *E. coli* (ecDHFR), where a network of coupled long-range motions was observed by crystallographic study,⁵⁷ NMR relaxation studies,⁵⁸ kinetic studies⁵⁹ and computational simulations.⁶⁰

DHFR catalyses the reduction of 7,8-dihydrofolate (H_2F) to 5,6,7,8-tetrahydrofolate (H_4F) using reduced nicotinamide adenine dinucleotide phosphate (NADPH) as cofactor. The reaction proceeds *via* protonation of the N5 nitrogen of the H_2F pterin ring and hydride transfer from the nicotinamide ring of NADPH to the C6 of the pterin ring. The product tetrahydrofolate is a necessary precursor for the biosynthesis of purines, pyrimidines, and several amino acids. DHFR has therefore been a longstanding pharmacological target and hence has been studied extensively. An early MD simulation of the reactant ternary complex for ecDHFR²⁸ identified correlated and anticorrelated motions – absent in the product complex with 5,6,7,8-tetrahydrofolate – involving many of the same regions of the enzyme implicated by the NMR relaxation studies.⁶¹ Analysis of the amino acid sequences of DHFR from 36 different species suggests that residues both in the active site and distal to the active site are conserved across a wide range of species.⁶⁰ To investigate a possible role for these residues in motions that promote H-tunnelling, combined QM/MM dynamics simulations were used to identify and characterise a network of coupled motions in ecDHFR^{60,62} – in particular, the equilibrium, thermally averaged changes in distances and angles along the collective reaction coordinate were analysed. This facilitated the identification of relatively slow conformational changes – some of which could potentially occur on the experimentally observed millisecond timescale for hydride transfer – that lead to configurations that enable hydride tunnelling.⁶⁰ These conformational changes were identified as arising from a network of equilibrium coupled motions that extend throughout the enzyme (Figure 10.5).⁶⁰ These equilibrium, thermally averaged motions represent conformational changes along the collective reaction coordinate, corresponding to reorganisation of the environment to facilitate hydride transfer by bringing the donor and acceptor closer together, orienting the substrate and cofactor for catalysis, and providing a favourable electrostatic environment. However, these motions are not dynamically coupled to the chemical reaction, but represent equilibrium conformational changes that enable hydride transfer. Comparison of results from a QM/MM dynamics study of *Bacillus subtilis* DHFR⁶³ with those from ecDHFR revealed that a common set of residues play a significant role in the network of coupled motions leading to configurations conducive to hydride transfer for both enzymes.

The observation that the coupled long-range motions are less pronounced and less significant in driving tunnelling in AADH compared to DHFR might be explained as follows. Perhaps the most obvious difference between the tunnelling reaction catalysed by AADH and that catalysed by DHFR is that the former involves transfer of a proton, whereas the latter involves transfer of a hydride. A proton transfer may be facilitated by withdrawal of electron density from the donor–hydrogen bond, which polarises and weakens the C–H

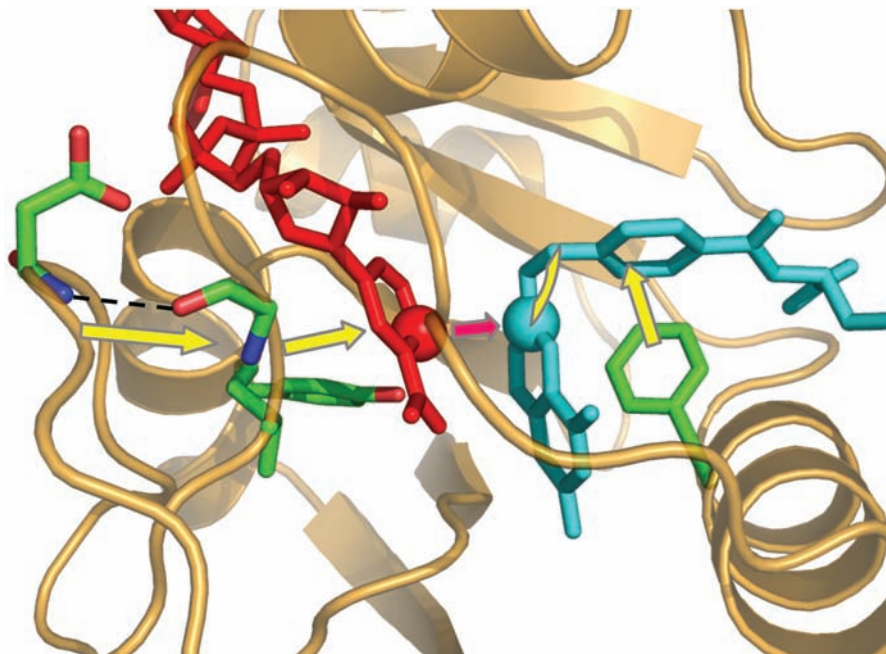


Figure 10.5 Schematic diagram of a portion of a network of long range coupled motions that drive H tunnelling in DHFR, as proposed by Hammes Schiffer and coworkers.⁶⁰ The yellow arrows indicate the coupled promoting motions. C_A and C_D denote the donor and acceptor carbon atoms, respectively, for the hydride tunnelling event, depicted by the pink arrow. DHFR is depicted schematically in bronze and the black dashed line denotes a hydrogen bond.

bond. In AADH, this effect is assisted by the electron poor iminoquinone, facilitating a favourable electrostatic interaction – or even formation of a hydrogen bond – between the strongly polarised C1/H1 and the negatively charged O2. In contrast, in DHFR the vibrations of the donor or acceptor groups will not be so readily coupled because a hydride transfer cannot be facilitated by such an effect – a partial negative charge will not reside on the transferring hydrogen. Therefore, a promoting motion cannot arise from electrostatic interactions developing between the donor and acceptor groups and will instead require mechanical effects to drive the donor and acceptor groups together.

The promoting motion at 165 cm^{-1} identified in AADH arises from the flexibility of the linker region connecting the indole and quinone. In contrast, the substrates of DHFR have less flexible donor and acceptor functional groups; the hydride transfer in DHFR occurs between nicotinamide adenine nucleotide phosphate (NADPH) and dihydrofolate (DHF). This means that a motion that drives the donor and acceptor groups together is more likely to involve large portions of the donor and/or acceptor, driven by forces external

to these regions. Furthermore, substrates and cofactor in DHFR are not covalently bound to the enzyme, as is the case in AADH, so that the donor and acceptor groups are replaced in subsequent catalysis cycles. In AADH, on the other hand, once the iminoquinone has been reduced, the electron gained is transferred to the electron acceptor protein azurin. Because of the evolutionary pressure to interact effectively with azurin, as well as the complexity of the mechanism of the reaction catalysed by AADH, it is less likely that AADH would also have evolved to utilise large-scale motions to drive the proton-transfer step.

10.11 Summary

In summary, the computational simulations of AADH, using both a combined QM/MM method in conjunction with VTST/MT and MM methods – with additional mathematical approaches to analyse the trajectories – gives a valuable and unique insight into how this enzyme works at the atomic level. These studies show that, in the oxidation of tryptamine by AADH, >99.9% of proton transfer proceeds through tunnelling over a distance of $<0.6\text{\AA}$. Importantly, computational studies also show no evidence for a network of coupled long-range motions that modulate the O₂–H₁ distance; the H-tunnelling event is facilitated by fast (subpicosecond) short-range motions. These results have proved particularly powerful when used as part of a multi-disciplinary study alongside fast reaction methods and structural biology. With the “coming of age” of computational enzymology, such an approach is expected to play an increasingly important role in the study of enzyme catalysis.

References

1. A. D. MacKerell, *J. Comput. Chem.*, 2004, **25**, 1584–1604.
2. Y. Duan, C. Wu, S. Chowdhury, M. C. Lee, G. Xiong, W. Zhang, R. Yang, P. Cieplak, R. Luo and T. Lee, *J. Comput. Chem.*, 2003, **24**, 1999–2012.
3. A. D. MacKerell, D. Bashford, M. Bellott, R. L. Dunbrack, J. D. Evanseck, M. J. Field, S. Fischer, J. Gao, H. Guo, S. Ha, D. Joseph-McCarthy, L. Kuchnir, K. Kuczera, F. T. K. Lau, C. Mattos, S. Michnick, T. Ngo, D. T. Nguyen, B. Prodhom, W. E. Reiher, B. Roux, M. Schlenkrich, J. C. Smith, R. Stote, J. Straub, M. Watanabe, J. Wiorkiewicz-Kuczera, D. Yin and M. Karplus, *J. Phys. Chem. B*, 1998, **102**, 3586–3616.
4. W. F. Van Gunsteren and H. J. C. Berendsen, *Angew. Chem. Int. Ed. Engl.*, 1990, **29**, 992–1023.
5. J. R. Maple, U. Dinur and A. T. Hagler, *Proc. Natl. Acad. Sci. USA*, 1988, **85**, 5350–5354.
6. W. L. Jorgensen and J. Tiradorives, *J. Am. Chem. Soc.*, 1988, **110**, 1666–1671.

7. D. A. Case, T. E. Cheatham 3rd, T. Darden, H. Gohlke, R. Luo, J. Merz, K. M. A. Onufriev, C. Simmerling, B. Wang and R. J. Woods, *J. Comput. Chem.*, 2005, **26**, 1668–1688.
8. B. R. Brooks, R. E. Brucoleri, B. D. Olafson, D. J. States, S. Swaminathan and M. Karplus, *J. Comput. Chem.*, 1983, **4**, 187–217.
9. W. D. Cornell, P. Cieplak, C. I. Bayly, I. R. Gould, K. M. Merz, D. M. Ferguson, D. C. Spellmeyer, T. Fox, J. W. Caldwell and P. A. Kollman, *J. Am. Chem. Soc.*, 1995, **117**, 5179–5197.
10. A. R. Leach, *Molecular Modeling: Principles and Applications*, Prentice-Hall, Englewood Cliffs, NJ, 2001.
11. (a) H. M. Senn and W. Thiel, *Curr. Opin. Chem. Biol.*, 2007, **11**, 182–187; (b) H. Lin and D. G. Truhlar, *Theor. Chem. Acc.*, 2007, **117**, 185–199; (c) D. Riccardi, P. Schaefer, Y. Yang, H. B. Yu, N. Ghosh, X. Prat-Resina, P. Konig, G. H. Li, D. G. Xu, H. Guo, M. Elstner and Q. Cui, *J. Phys. Chem. B*, 2006, **110**, 6458–6469.
12. A. Warshel and M. Levitt, *J. Mol. Biol.*, 1976, **103**, 227–249.
13. U. C. Singh and P. A. Kollman, *J. Comput. Chem.*, 1986, **7**, 718–730.
14. V. Thery, D. Rinaldi, J. Rivail, B. Maigret and G. G. Ferenczy, *J. Comput. Chem.*, 1994, **15**, 269–282.
15. J. Gao, P. Amara, C. Alhambra and M. J. Field, *J. Phys. Chem. A*, 1998, **102**, 4714–4721.
16. J. Pu, J. Gao and D. G. Truhlar, *J. Phys. Chem. A*, 2004, **108**, 632–650.
17. J. Pu, J. Gao and D. G. Truhlar, *ChemPhysChem*, 2005, **6**, 1853–1865.
18. C. Alhambra, J. Corchado, M. L. Sanchez, J. Gao and D. G. Truhlar, *J. Am. Chem. Soc.*, 2000, **122**, 8197–8203.
19. L. S. Devi-Kesavan, M. Garcia-Viloca and J. Gao, *Theor. Chem. Acc.*, 2003, **109**, 133–139.
20. D. G. Truhlar, J. Gao, M. Garcia-Viloca, C. Alhambra, J. Corchado, M. L. Sanchez and T. D. Poulsen, *Int. J. Quantum Chem.*, 2004, **100**, 1136–1152.
21. J. Pu, J. Gao and D. G. Truhlar, *Chem. Rev.*, 2006, **106**, 3140–3169.
22. J. K. Hwang and A. Warshel, *J. Am. Chem. Soc.*, 1996, **118**, 11745–11751.
23. S. R. Billeter, S. P. Webb, T. Lordanov and S. Hammes-Schiffer, *J. Chem. Phys.*, 2001, **114**, 6925–6936.
24. J. Gao and D. G. Truhlar, *Annu. Rev. Phys. Chem.*, 2002, **53**, 467–505.
25. S. Hammes-Schiffer, *Curr. Opin. Struct. Biol.*, 2004, **14**, 192–201.
26. J. C. Corchado, Y. Y. Chuang, P. L. Fast, W. P. Hu, Y. P. Liu, G. C. Lynch, K. A. Nguyen, C. F. Jackels, A. Fernandez-Ramos, B. A. Ellingson, B. J. Lynch, J. Zheng, V. S. Melissas, J. Vill, I. Rossi, E. L. Coitio, J. Pu, T. V. Albu, R. Steckler, B. C. Garrett, A. D. Isaacson and D. G. Truhlar, POLYRATE-version 9.7, University of Minnesota, Minneapolis, MN, 2007.
27. W. Humphrey, A. Dalke and K. Schulten, *J. Molec. Graphics*, 1996, **14**, 33–38.
28. J. L. Radkiewicz and C. L. Brooks, *J. Am. Chem. Soc.*, 2000, **122**, 225–231.
29. S. Caratzoulas, J. S. Mincer and S. D. Schwartz, *J. Am. Chem. Soc.*, 2002, **124**, 3270–3276.

30. R. B. Sessions, P. Dauber-Osguthorpe and D. J. Osguthorpe, *J. Mol. Biol.*, 1989, **210**, 617–633.
31. J. Basran, S. Patel, M. J. Sutcliffe and N. S. Scrutton, *J. Biol. Chem.*, 2001, **276**, 6234–6242.
32. L. Masgrau, A. Roujeinikova, L. O. Johannissen, P. Hothi, J. Basran, K. E. Ranaghan, A. J. Mulholland, M. J. Sutcliffe, N. S. Scrutton and D. Leys, *Science*, 2006, **312**, 237–241.
33. L. Masgrau, K. E. Ranaghan, N. S. Scrutton, A. J. Mulholland and M. J. Sutcliffe, *J. Phys. Chem. B*, 2007, **111**, 3032–3047.
34. L. O. Johannissen, S. Hay, N. S. Scrutton and M. J. Sutcliffe, *J. Phys. Chem. B*, 2007, **111**, 2631–2638.
35. M. Garcia-Viloca, J. Gao, M. Karplus and D. G. Truhlar, *Science*, 2004, **303**, 186–195.
36. H. M. Berman, J. Westbrook, Z. Feng, G. Gilliland, T. N. Bhat, H. Weissig, I. N. Shindyalov and P. E. Bourne, *Nucl. Acids Res.*, 2000, **28**, 235–242.
37. W. L. Jorgensen, J. Chandrasekhar, J. D. Madura, R. W. Impey and M. L. Klein, *J. Chem. Phys.*, 1983, **79**, 926–935.
38. N. Reuter, A. Dejaegere, B. Maigret and M. Karplus, *J. Phys. Chem. A*, 2000, **104**, 1720–1735.
39. C. L. Brooks III and M. Karplus, *J. Chem. Phys.*, 1983, **79**, 6312–6325.
40. C. Alhambra, M. L. Sanchez, J. Corchado, J. Gao and D. G. Truhlar, *Chem. Phys. Lett.*, 2001, **347**, 512; erratum: **2002**, **2355**, 2388.
41. G. M. Torrie and J. P. Valleau, *J. Comput. Phys.*, 1977, **23**, 187–199.
42. F. Proust-De Martin, R. Dumas and M. J. Field, *J. Am. Chem. Soc.*, 2000, **122**, 7688–7697.
43. C. Bartels and M. Karplus, *J. Comput. Chem.*, 1997, **18**, 1450–1462.
44. G. Tresadern, S. Nunez, P. F. Faulder, H. Wang, I. H. Hillier and N. A. Burton, *Faraday Discuss.*, 2003, **122**, 223–242.
45. D. G. Truhlar, A. D. Isaacson and B. C. Garret, in *Theory of Chemical Reaction Dynamics*, ed. M. Baer, CRC Press, Boca Raton, FL, 1985, vol. **IV**, pp. 65–136.
46. D. G. Truhlar, in *Isotope Effects in Chemistry and Biology*, ed. H. A. K. Limbach, A., Marcel Dekker, Inc., New York, 2005.
47. M. Garcia-Viloca, 2002, CHARMMRATE 2.0, University of Minnesota, Minneapolis.
48. D. G. Truhlar, J. Gao, C. Alhambra, M. Garcia-Viloca, J. Corchado, M. L. Sanchez and J. Villa, *Acc. Chem. Res.*, 2002, **35**, 341–349.
49. M. Page and J. W. McIver, *J. Chem. Phys.*, 1988, **88**, 922–935.
50. Y. Y. Chuang, J. C. Corchado and D. G. Truhlar, *J. Phys. Chem. A*, 1999, **103**, 1140–1149.
51. M. M. Kreevoy and D. G. Truhlar, in *Investigation of Rates and Mechanisms of Reactions*, ed. D. Bernasconi, John Wiley & Sons, New Yourk, 1986, vol. **1**, p. 13.
52. M. Garcia-Viloca, C. Alhambra, D. G. Truhlar and J. Gao, *J. Chem. Phys.*, 2001, **114**, 9953–9958.

53. L. Masgrau, A. Gonzalez-Lafont and J. M. Lluch, *Chem. Phys. Lett.*, 2002, **353**, 154–162.
54. P. Hothi, K. A. Khadra, J. P. Combe, D. Leys and N. S. Scrutton, *FEBS J.*, 2005, **272**, 5894–5909.
55. P. Ball, *Nature*, 2004, **431**, 396–397.
56. A. M. Kuznetsov and J. Ulstrup, *Can. J. Chem.*, 1999, **77**, 1085–1096.
57. M. R. Sawaya and J. Kraut, *Biochemistry*, 1997, **36**, 586–603.
58. J. R. Schnell, H. J. Dyson and P. E. Wright, *Annu. Rev. Biophys. Biomol. Struct.*, 2004, **33**, 119–140.
59. R. S. Sikorski, L. Wang, K. A. Markham, P. T. R. Rajagopalan, S. J. Benkovic and A. Kohen, *J. Am. Chem. Soc.*, 2004, **126**, 4778–4779.
60. P. K. Agarwal, S. R. Billeter, P. T. R. Rajagopalan, S. J. Benkovic and S. Hammes-Schiffer, *Proc. Natl. Acad. Sci. USA*, 2002, **99**, 2794–2799.
61. (a) C. J. Falzone, P. E. Wright and S. J. Benkovic, *Biochemistry*, 1994, **33**, 439–442; (b) M. J. Osborne, J. Schnell, S. J. Benkovic, H. J. Dyson and P. E. Wright, *Biochemistry*, 2001, **40**, 9846–9859; (c) J. R. Schnell, H. J. Dyson and P. E. Wright, *Biochemistry*, 2004, **43**, 374–383.
62. P. K. Agarwal, S. R. Billeter and S. Hammes-Schiffer, *J. Phys. Chem. B*, 2002, **106**, 3283–3293.
63. J. B. Watney and S. Hammes-Schiffer, *J. Phys. Chem. B*, 2006, **110**, 10130–10138.

CHAPTER 11

Tunnelling does not Contribute Significantly to Enzyme Catalysis, but Studying Temperature Dependence of Isotope Effects is Useful

HANBIN LIU AND ARIEH WARSHEL

Department of Chemistry, University of Southern California, 3620
McClintock Ave., Los Angeles, California 90089-1062, USA

11.1 Introduction

Many proposals have been put forward to rationalise the origin of the large catalytic power of enzymes (see refs [1,2] for a partial list). Unarguably, this is a complex issue where many factors may be assumed to be important. Thus, it is important to find out which proposals account for the major effects in enzyme catalysis. Resolving this issue must, of course, reproduce all key experimental observations, but it cannot be based on accepting the interpretation of the experiments as experimental facts. Here, one needs reliable models that actually simulate all types of experimental observation and allow one to dissect the overall catalytic effect down to its contributions. In other words, once a model reproduces what is actually being observed, it can be used to separate the overall effect to its individual contributions. Since enzymes are very complex systems, probably the most effective models should be based on computational

RSC Biomolecular Sciences

Quantum Tunnelling in Enzyme Catalysed Reactions

Edited by Rudolf K. Allemann and Nigel S. Scrutton

© Royal Society of Chemistry 2009

Published by the Royal Society of Chemistry, www.rsc.org

simulation approaches. Our previous computational studies have indicated that the major effect in enzyme catalysis comes from the preorganisation of the protein environment, where the enzyme plays the role of a super solvent with smaller reorganisation energy than the corresponding reaction in aqueous solutions where the solvent molecules undergo very large changes in their orientation during reaction.² However, in order to verify the observation that electrostatic effects are the key to enzyme catalysis, it is crucial to demonstrate that other proposed effects do not contribute significantly to catalysis. Demonstrating the problems with alternative proposals should not be viewed as a negative campaign, but as an integral part of the scientific philosophy of excluding different proposals by examining their consistency with observed and simulated findings. This work will focus on one of the prominent proposals, namely the idea that nuclear quantum-mechanical (NQM) effects (*e.g.* zero-point energy and tunnelling corrections) play a major role in enzyme catalysis.

In numerous enzymatic reactions, one of the key steps (which is sometimes also the rate-limiting step) is a transfer of a proton, hydride or hydrogen. Since these are comparatively light particles, the transfer is often associated with NQM effects. Thus, it is of significant interest to determine the magnitude of NQM effects in enzymatic reactions and to explore their possible contributions to enzyme catalysis.^{3–10} Furthermore, the temperature dependence of the NQM effects as manifested in the corresponding kinetic isotope effect (KIE) is a topic of significant current interest.^{3,11–14} Part of this interest reflects the hope that this temperature dependence can provide useful information about possible dynamical contributions to enzymatic reactions.^{3,12}

The introduction of methods for simulating NQM effects in enzymatic reactions dates back to the early 1990s, see, *e.g.*, refs [8,10,15,16], and the use of these and alternative simulation methods has recently become quite an active field.^{2,9,11,17–19} Such calculations can, in principle, be used to assess the catalytic contribution of NQMs and to analyse the temperature dependence of KIEs. However, the theoretical challenges are quite different in each of these tasks. That is, while theoretical studies of the catalytic contributions of NQMs have progressed significantly (*e.g.* refs [7,9–11,17–21]), there are major open problems and major challenges of reproducing the observed temperature effects of KIEs by actual microscopic simulations. Apparently, it is possible to account for the observed temperature dependence by using phenomenological vibronic treatments (*e.g.* refs [13–15]) and adjusting key parameters (as was done in refs [3] and [7]). Unfortunately, vibronic treatments, which became very popular recently, involve fundamental problems (see refs [18,19] and this work) and the parameters obtained by a fitting procedure are not expected to provide a quantitative description of the reacting system. On the other hand, it is extremely challenging to evaluate the temperature dependence by computational simulations that do not involve any special parameterisation. In fact, with the exception of the works considered here, we are not aware of any successful attempts to reproduce the temperature dependence of KIE of an enzymatic reaction in a quantitative way by first principle simulations, despite attempts to do so (*e.g.* refs [10,20,22]). On the other hand, studies of the temperature

dependence of NQMs in gas-phase reaction seem to provide more quantitative results.²³

Another important issue is the relationship between the KIE and the distance between the donor and acceptor in hydride-transfer (HT), proton-transfer (PT) and hydrogen-transfer reactions. It is tempting to assume that enzymes catalyse reactions by compressing the distance between the donor and acceptor (*e.g.* ref. [24]) or the related idea of near attack conformation (NAC) (*e.g.* ref. [25]). This would mean that the enzyme leads to a change in the shape of the barrier (and presumably enhances the contribution from tunnelling to catalysis^{25–31}). This idea has also been used to rationalise the temperature dependence of observed KIEs (*e.g.* ref. [29]). On the other hand, our studies seem to indicate that tunnelling effects do not contribute significantly to catalysis (*e.g.* refs [11,19,32]) and that enzymes do not apply strong stress that leads to a significant “compression” relative to the corresponding situation in solution (*e.g.* ref. [18]). Furthermore, our studies (*e.g.* refs [11,19]) and those of others^{21,33} have started to indicate that the KIE and the relative NQM contributions increase rather than decrease when the donor–acceptor distance increases. Obviously it is important to try to resolve these issues by consistent microscopic simulations (where the results are not determined by adjusting arbitrary parameters).

Here, we summarise the results from studies of the temperature dependence of the KIE in different mutants of dihydrofolate reductase (DHFR) and lipoxygenase and discuss the conclusions that emerge from these studies.

11.2 Methods

To quantify the catalytic power of enzymes, it is essential to combine reliability and efficiency. Thus, we performed our studies using the empirical valence bond (EVB) method. The EVB method, which has been described extensively elsewhere (*e.g.* refs [1,34,35]), is particularly useful in cases of NQM calculations, because long simulations are required to obtain convergence of the corresponding free energy in such calculations (where it is helpful if the relevant potential-energy surface is available in an analytical form). In this respect, the EVB approach provides a very powerful tool, in particular when one compares the activation barriers in water and in the enzyme-active site, or in native and mutant enzymes.

The EVB method is a QM/MM method that describes reactions by mixing diabatic states that correspond to classical valence-bond (VB) structures. These states represent the reactant, intermediate (or intermediates) and product states. The potential energies of these diabatic states are represented by classical MM potential functions of the form:

$$H_{ii} = \varepsilon_i = \alpha_{\text{gas}}^i + U_{\text{intra}}^i(\mathbf{R}, \mathbf{Q}) + U_{\text{Ss}}^i(\mathbf{R}, \mathbf{Q}, \mathbf{r}, \mathbf{q}) + U_{\text{ss}}(\mathbf{r}, \mathbf{q}) \quad (11.1)$$

Here, R and Q represent the atomic coordinates and charges of the diabatic states, and r and q are those of the surrounding protein and solvent. α_{gas}^i is the gas-phase energy of the i th diabatic state (where all the fragments are taken to

be at infinity), $U_{\text{intra}}(R, Q)$ is the intramolecular potential of the solute system (relative to its minimum), $U_{\text{ss}}(R, Q, r, q)$ represents the interaction between the solute (S) atoms and the surrounding (s) solvent and protein atoms. $U_{\text{ss}}(r, q)$ represents the potential energy of the protein/solvent system (“ss” designates surrounding-surrounding). The ε_i of eqn (11.1) constitute the diagonal elements of the EVB Hamiltonian (H_{EVB}). The off-diagonal elements of this Hamiltonian, H_{ij} , are assumed to be constant or be represented by a simple function such as an exponential function of the distances between the reacting atoms. These H_{ij} elements are assumed to be the same in the gas phase, in solutions and in the proteins. The adiabatic ground-state energy, E_g , and the corresponding eigenvector, C_g , are obtained by solving the secular equation.

$$H_{\text{EVB}} C_g = E_g C_g \quad (11.2)$$

The EVB classical free-energy surface is evaluated by the free-energy perturbation (FEP) umbrella sampling (US) method described elsewhere (e.g. refs [1,2]). Although the EVB was originally considered to be an oversimplified *ad hoc* approach, it has recently become one of the most widely used methods in modelling chemical processes in condensed phases.^{36–46,9} At any rate, the EVB is particularly effective in studies of catalytic effects since it can be calibrated on the free-energy surface of the solution reaction, and then used (without changing any parameter) for studies of the enzyme and its mutants.

With the analytical EVB surface of the reacting system and its surrounding protein + water system, our task is to obtain the quantum correction to the classical activation free energy. This is done by using the quantum classical path (QCP) centroid path integral approach developed in our studies of NQM effects in chemical reactions in solution and proteins.^{8,10} Note that the QCP has been adopted recently by other research groups (e.g. refs [47–49]).

In the QCP approach, the nuclear quantum-mechanical rate constant is expressed as

$$k_{\text{qm}} = F_{\text{qm}} k_B T / h \exp(-\beta \Delta g_{\text{qm}}^\ddagger) \quad (11.3)$$

where F_{qm} , k_B , T , h , and β are, respectively, the transmission factor, Boltzmann's constant, the temperature, Planck's constant, and $\beta = 1/k_B T$. The quantum-mechanical activation barrier, $\Delta g_{\text{qm}}^\ddagger$, includes almost all the nuclear quantum-mechanical effects, whereas only small effects come from the pre-exponential transmission factor in the case of systems with a significant activation barrier.^{9,50}

The quantum-mechanical free-energy barrier, $\Delta g_{\text{qm}}^\ddagger$, can be evaluated by Feynman's path integral formulation,⁵¹ where each classical coordinate is replaced by a ring of quasiparticles that are subjected to the effective “quantum-mechanical” potential

$$U_{\text{qm}} = \sum_{k=1}^p \frac{1}{2p} M \Omega^2 \Delta x_k^2 + \frac{1}{p} U(x_k) \quad (11.4)$$

Here, $\Delta x_k = x_{k+1} - x_k$ (where $x_{p+1} = x_1$), $\Omega = p/\eta\beta$, M is its mass, and U is the actual potential used in the classical simulation. The total quantum-mechanical partition function can then be obtained by running *classical* trajectories of the quasiparticles with the potential U_{qm} . The probability of being at the transition state is approximated in this way by the probability distribution of the centre of mass of the quasiparticles (the centroid) rather than the classical single point. This approach is formally similar to the strategy of the centroid path integral method.^{52–54} However, the regular centroid approach requires one to consider the trajectory of all the quasiparticles. Thus, the use of this approach in condensed-phase reactions is very challenging and involves major convergence problems. The QCP approach offers an effective and rather simple way for evaluating this probability without significantly changing the simulation program. This is done by propagating classical trajectories on the classical potential-energy surface of the reacting system and using the positions of the atom of the system to generate the centroid position for the quantum-mechanical partition function. More specifically we evaluate the quantum-mechanical partition function by^{8,10,16,19}

$$Z_q(\bar{x}) = Z_{\text{cl}}(\bar{x}) \langle \langle \exp\{-(\beta/p) \sum_k U(x_k) - U(\bar{x})\} \rangle_{\text{fp}} \rangle_U \quad (11.5)$$

where \bar{x} is the centroid position, $\langle \dots \rangle_{\text{fp}}$ designates an average over the free-particle quantum-mechanical distribution obtained with the implicit constraint that \bar{x} coincides with the current position of the corresponding classical particle, and $\langle \dots \rangle_U$ designates an average over the classical potential U . Using eqn (11.5), we can obtain the quantum-mechanical free-energy surface by evaluating the corresponding probability by the same combined FEP/US used in the classical EVB calculations. However, we use the double average of eqn (11.5) rather than an average over a regular classical potential. The main point of the QCP is that the quantum-mechanical free energy function can be evaluated by a centroid approach that is constrained to move on the classical potential (see ref. [10] for details).

Since the EVB provides a fully analytical surface and first derivatives, it offers a very effective way to explore the effect of the fluctuations of the environment on PT and HT reactions. In particular, the electrostatic potential from the fluctuating polar environment interacts with the charge distribution of each resonance structure and thus the fluctuation of the environment is directly included in the time dependence of the EVB Hamiltonian. This point has emerged from our early studies^{2,15,55,56} and is discussed in these works. Here, we will only consider its implication with regards to the NQM effects.

As discussed elsewhere (*e.g.* ref. [15]) we can use the autocorrelation of the fluctuating EVB energy gap and obtain an approximated quasiharmonic rate constant. That is, our starting point is the overall rate constant

$$k_{ab} = \sum_{mm'} k_{am,bm'} \exp\{-E_{am}\beta\} \left/ \sum_m \exp\{-E_{am}\beta\} \right. \quad (11.6)$$

where $\beta = 1/(k_B T)$ (with k_B designating the Boltzmann constant) and E_{am} is the energy of the m th vibronic level of state a . Equation (11.6) is based on the assumption that vibrational states in the reactant well are populated according to Boltzmann distribution. The individual vibronic rate constant, $k_{am,bm'}$, is evaluated by monitoring the energy difference between E_{am} and E_{bm} as a function of the fluctuations of the rest of the molecule. The use of the corresponding fluctuating energy gap and a cumulant expansion (see ref. [57]) gives

$$k_{am,bm'} = |H_{ab}/\hbar|^2 \sum S_{mm'}^2 \int_{-\infty}^{\infty} \exp[(i/\hbar)\langle \Delta\varepsilon_{bm',am} \rangle + \gamma(t)dt] \quad (11.7)$$

$$\gamma(t) = -(i/\hbar)^2 \int (t-t') \langle \Delta\varepsilon(0)\Delta\varepsilon(t') \rangle_a dt'$$

where the $S_{m,m'}$ is the Franck–Condon factor for transition from m to m' and H_{ab} is the off-diagonal electronic matrix element of the EVB Hamiltonian. Here, u is given by

$$u = \varepsilon_b - \varepsilon_a - \langle \Delta\varepsilon_{ba} \rangle_a \quad (11.8)$$

and $\langle \rangle_a$ designates an average obtained over the fluctuations around the minimum of state a .

In the high temperature limit one obtains^{15,57}

$$k_{am,bm'} = |H_{ab}S_{mm'}/\hbar|^2 (\pi\hbar^2/k_B T \lambda)^{1/2} \exp\{-\Delta g_{mm'}^\# \beta\} \quad (11.9)$$

where λ is the “solvent reorganisation energy” defined by

$$\lambda = \langle \Delta\varepsilon_{ba} \rangle_a - \Delta G_0 \quad (11.10)$$

The activation free energy in eqn (11.9) can be approximated by

$$\Delta g_{mm'}^\# \approx \left[\Delta G^0 + \sum_r \hbar\omega_r (m'_r - m_r) + \lambda \right]^2 / 4\lambda \quad (11.11)$$

where ω is the vibrational frequency of the quantised mode.

The above vibronic treatment is only valid in the diabatic limit when $H_{ab}S_{mm}^2$ is sufficiently small. Now, in cases of PT and HT processes, H_{ab} seems to be far too large to justify the diabatic approximation. However, the vibronic treatment may give a very useful insight into the distance dependence of the rate constant in relatively large distances when the diabatic approximation is valid. In this case, we can approximate the KIE by⁵⁸

$$\text{KIE} \cong \bar{k}_{a0,b0}^H / \bar{k}_{a0,b0}^D \cong \int F(\Delta r, T) e^{-58\Delta r^2} dr / \int F(\Delta r, T) e^{-58\Delta r^2/2} dr \quad (11.12)$$

where

$$F(\Delta r, T) = [H_{ab}^2(\Delta r)/(\lambda(\Delta r))^{1/2}] \exp\{-[w(\Delta r) + \Delta g_{00}^\neq(\Delta r)]\beta\} \quad (11.13)$$

where $w(\Delta r)$ is the so-called “work function” that is considered here as the potential of mean force (PMF) for the donor–acceptor distance.

If we assume that λ and H_{ab} are independent of Δr in the region with the largest contribution to k_{00} , we obtain⁵⁸

$$\text{KIE} \cong \frac{\int \exp\{-w^\neq(\Delta r)\beta\} \exp(-58\Delta r^2) dr /}{\int \exp\{-w^\neq(\Delta r)\beta\} \exp\{-58\Delta r^2\sqrt{2}\} dr} \quad (11.14)$$

where $w^\neq = w + \Delta g_{00}^\neq$, eqn (11.14) can be considered as a qualitative guide, but we must keep in mind that we are dealing with a very problematic approximation, whose range of validity has been analysed in our previous work.⁵⁸

11.3 Simulating Temperature Dependence of KIEs in Enzymes

This work will mainly consider our studies of the KIE in DHFR mutants. This will include a study⁵⁹ where we reproduced in a semiquantitative way the effect of different mutations on the classical rate constant, as well as a more recent study⁵⁸ that used the same EVB parameters and performed QCP calculations of the quantised activation free energy for the H and D reactions of the native DHFR⁶⁰ the G121V mutant⁶¹ and the M42W-G121V double mutant.¹²

Our studies of DHFR and its mutants⁵⁹ considered the reaction described schematically in Figure 11.1 in different environments (water, native protein and mutants). The calculations established that the activation barriers are correlated with the corresponding reorganisation energies and work functions (the free energy of bringing the donor and acceptor to an optimal distance). These findings, which are summarised in Figure 11.2, indicate that the catalytic effect in the native enzyme is due to the preorganisation effect and not to dynamical effects (see discussion in ref. [59]). However, the fact that the effects of the mutations include a decrease in the work function, (the w of eqn (11.13)), due to the increase in the distance between the donor and acceptor, left our analysis open to some misunderstandings. Thus, we invested additional effort into exploring the nature of the increase in the donor and acceptor distance and evaluated the quantised activation barriers for donor and acceptor distances of 3.0 Å and 3.5 Å and for different temperatures. The corresponding activation barriers (that include the NQM contributions) were converted to rate constants and the resulting isotope effects were averaged on three independent calculations with different initial conditions and the average results are summarised in Figures 11.3, 11.4 and 11.5. As seen from the figures and as expected from

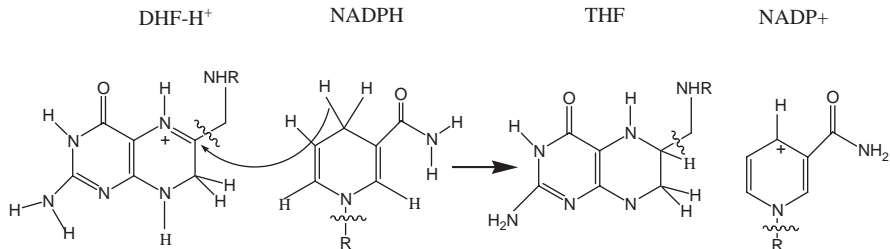


Figure 11.1 The reaction system in DHFR. All the atoms shown (except the NHR and R atoms) are included in region I of the EVB treatment. The figure is taken from ref. [58].

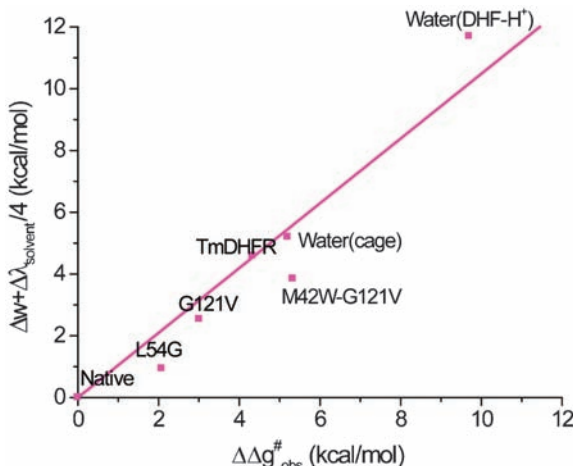


Figure 11.2 The correlation between $\Delta g'$ and $\Delta\lambda + \Delta\bar{w}$. The figure is taken from ref. [59].

eqn (11.14) and from our previous studies,^{18–19,62} the KIE increases significantly upon increase of the donor and acceptor distance. Apparently, the change of the KIE with temperature, at a given distance, is smaller than the changes upon increasing the distance. Thus, it is very likely that the observed temperature dependence reflects the change in donor–acceptor distance from 3.0 Å to 3.5 Å to a large extent.

In order to incorporate the distance dependence of the NQM effects in the calculations of the overall KIE, we followed the spirit of eqn (11.12) and wrote

$$\begin{aligned} \bar{k}_{qm} &\approx \int k(R)_{qm} e^{-w(R)\beta} dR / \int e^{-w(R)\beta} dR \\ &= \int (k_B T/h) e^{-(\Delta g'_{cl}(R)\beta + w(R)\beta)} e^{-\Delta\Delta g'_{qm}(R)\beta} dR / \int e^{-w(R)\beta} dR \end{aligned} \quad (11.15)$$

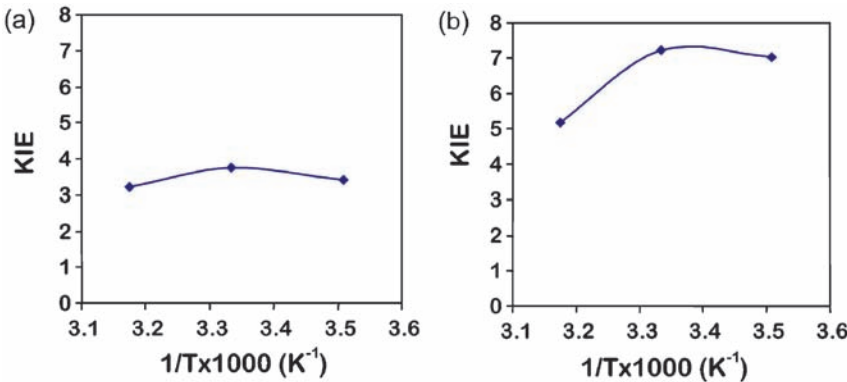


Figure 11.3 The temperature dependence of the KIE in native DHFR for the case when the donor–acceptor distance is kept at 3.0 Å (a) and 3.5 Å (b), respectively. The figure is taken from ref. [58].

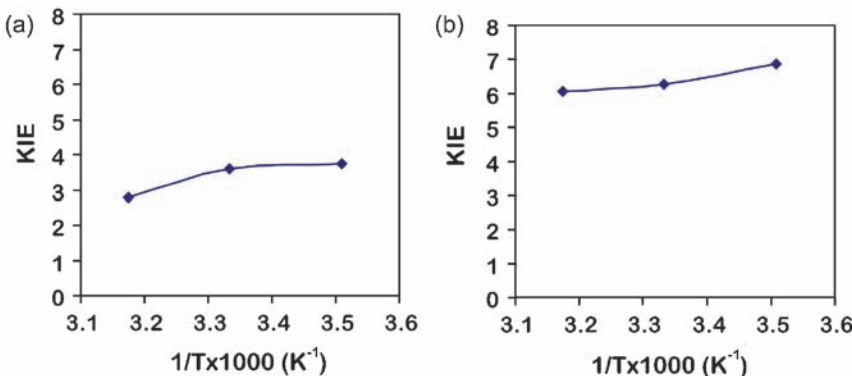


Figure 11.4 The temperature dependence of the KIE in the G121V mutant of DHFR for the case when the donor–acceptor distance is kept at 3.0 Å (a) and 3.5 Å (b), respectively. The figure is taken from ref. [58].

where $\Delta\Delta g_{qm}^{\neq}$ is the quantum correction and R is the donor–acceptor distance. Equation (11.15) was then written as:

$$\bar{k}_{qm} = \int P(R)_{cl}^{\neq} (k_B T / h) e^{-\Delta\Delta g_{qm}^{\neq}(R)\beta} \quad (11.16)$$

where

$$P(R) = e^{-(\Delta g_{cl}^{\neq}(R)\beta + w(R)\beta)} \int e^{-w(R)\beta} dR = e^{-\Delta w^{\neq}(R)\beta} \int e^{-w(R)\beta} dR \quad (11.17)$$

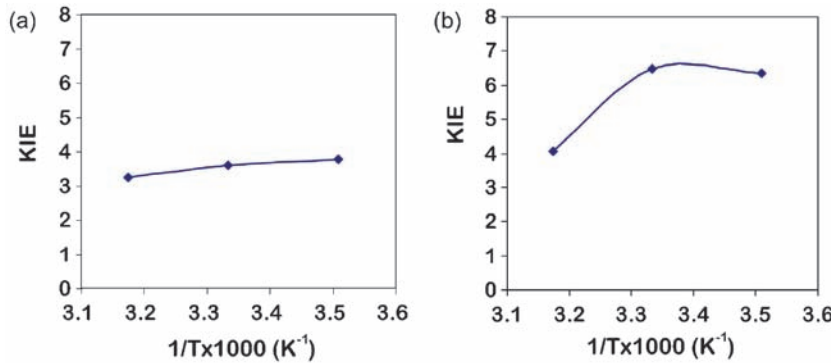


Figure 11.5 The temperature dependence of the KIE in the M42W G121V mutant of DHFR for the case when the donor–acceptor distance is kept at 3.0 \AA (a) and 3.5 \AA (b), respectively. The figure is taken from ref. [58].

is the classical probability of being at the transition state for different values of the donor and acceptor distance and w is, as in eqn (11.12), the PMF for the distance between the donor and acceptor. In other words, we evaluated the overall rate constant by averaging the rates obtained at fixed distances over the distance coordinate. This was done since calculations, where the donor–acceptor distance is free to change, appeared to converge (in terms of the calculated temperature dependence) more slowly than calculations with a fixed distance. Furthermore, performing the calculations at different fixed distances allows us to obtain deeper insight into the origin of the temperature dependence.

In order to evaluate eqn (11.17) we calculated the classical free-energy profiles for the systems studied while constraining the donor and acceptor distance at 3.0 \AA , 3.25 \AA and 3.5 \AA . The calculations were done for a temperature of 300 K and the profiles were shifted in a way that their minima would follow the PMF calculated in ref. [58]. Next, we evaluated the average rate constant of eqn (11.17) while replacing the integral by the average of the contributions from $R = 3.0 \text{ \AA}$, $R = 3.25 \text{ \AA}$ and $R = 3.5 \text{ \AA}$. The calculations were done for both the H and D reactions at 285 K , 300 K and 315 K . The classical activation barrier was fixed at its value at $T = 300 \text{ K}$, assuming that the temperature dependence of the barrier does not significantly affect the temperature dependence of the KIE (this restricted assumption is removed below). The relationship between the classical surfaces at $R = 3.0 \text{ \AA}$, $R = 3.25 \text{ \AA}$ and $R = 3.5 \text{ \AA}$ obtained with the considerations described in ref. [58] are depicted in Figure 11.6. The considerations that led to this figure involved the replacement of the calculated $\Delta w^\neq(R)$ by a parameter $\bar{\Delta w}_\text{eff}^\neq$. This approximation reflects uncertainties about the *ab initio* reference potential for the solution reaction and the difficulties of obtaining exact PMF (see discussion in ref. [58]). However, all the other quantities were obtained from consistent microscopic simulations. The temperature dependence of the KIEs obtained by our analysis are summarised in

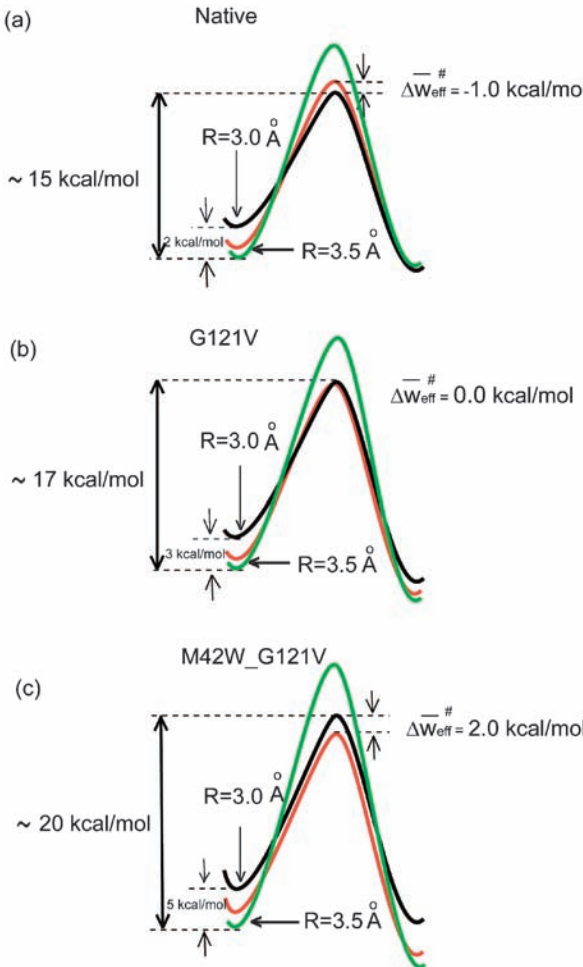


Figure 11.6 The classical free energy profiles for the hydride transfer when the donor acceptor distance is 3.0 Å (in black), 3.25 Å (in red) and 3.5 Å (in green), respectively, for the native DHFR (a), the G121V mutant (b) and the M42W G121V mutant (c). The calculations of the classical surfaces were performed at $T = 300$ K. The figure represents the relative behaviour of the profiles for the optimal values of the $\Delta \bar{W}_{\text{eff}}^{\#}$ of Eq. 11.17. The figure is taken from ref. [58].

Figure 11.7 together with the corresponding experimental results (taken from refs [12,60,61]). Figure 11.7 gives the calculated results, assuming that the classical activation barrier has the same temperature dependence at any R . As seen from the figure, we obtain a reasonable trend, although for the double mutant the calculated KIE occurs at a higher average value than the corresponding experimental results.

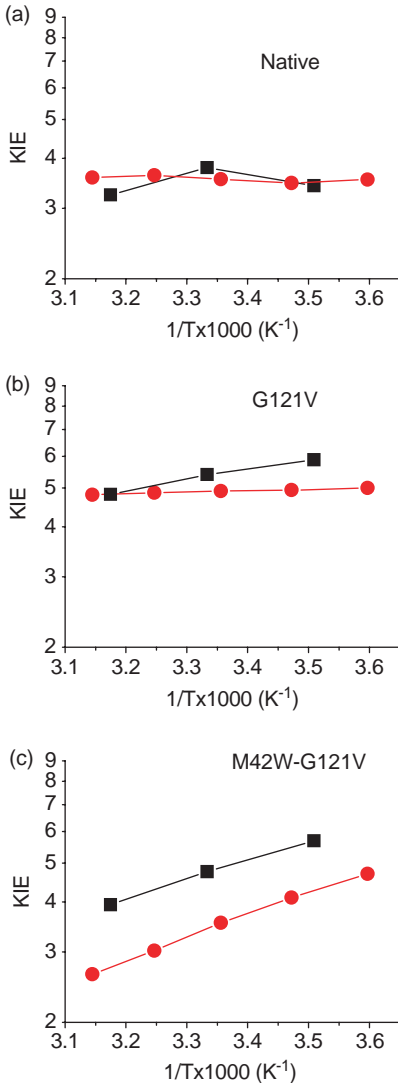


Figure 11.7 The calculated (in black) and observed (in red) temperature dependence of the KIE for the native DHFR (a), the G121V mutant (b) and the M42W G121V mutant (c). The figure is taken from ref. [58].

In order to gain further understanding of the origin of the observed effect we focused on the double mutant, where we have the largest deviation between the calculated and observed results. Here, we first explored the effect of the temperature dependence at a fixed R by taking constant values of 3, 5 and 7 for the KIEs at 3.0; 3.25 and 3.5 Å, respectively, at all temperatures, (this arbitrary assumption allowed us to explore the trend of the vibronic treatment where the

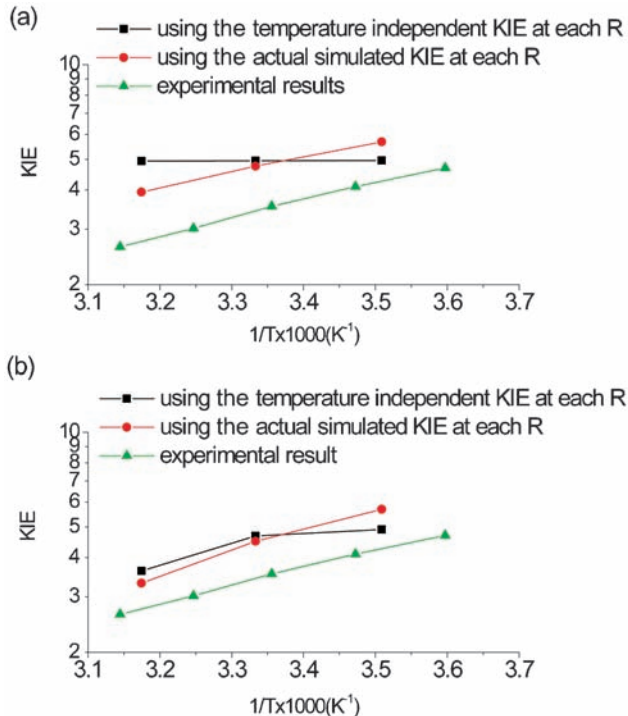


Figure 11.8 The calculated temperature dependence of the KIE of the M42W G121V mutant for the following limits: (a) the case when $\Delta g_{\text{cl}}^{\#}(R)$ is assumed to be temperature independence: while the KIE at each R is temperature independent (■) and while the KIE at each R is temperature dependent (●). The experimental results are designated by (▲). (b) the same as in (a) but with distant dependent $T\Delta S^{\#}$ (see text). The figure is taken from ref. [58].

KIE is independent of the temperature at a fixed R). The corresponding result (Figure 11.8(a)) indicates that the temperature dependence at a fixed R is likely to play a major role in the case of the double mutant. That is, the KIE obtained without this dependence is almost constant at all temperatures, despite the effect of the PMF while for other selections of the PMF and the constant KIE we can get some temperature dependence, it is hard to reproduce the temperature dependence of the KIE by using a reasonable PMF and reasonable constant KIE values that are similar to the average values obtained by the QCP approach at each R .

Finally, we also examined the additional possible effect of the change in activation entropy upon change in distance. As found in ref. [12], there is a large difference between the $-T\Delta S^{\#}$ of the native and double mutant enzymes. This difference is likely to reflect free-energy changes in a much smaller temperature range than 0 to 300 K (which is assumed in deriving $\Delta S^{\#}$) and it can be used to give a rough estimate of the change of $T\Delta S^{\#}$ between $R = 3.0 \text{ \AA}$ and $R = 3.5 \text{ \AA}$. Assuming that $T\Delta S^{\#}$ increases by about 2 kcal/mol between

$R = 3.0 \text{ \AA}$ and $R = 3.5 \text{ \AA}$, we obtained the results depicted in Figure 11.8(b). As seen from this figure we obtained an improved agreement with the experimental results and also obtain a reasonable temperature dependence when the KIE at $R = 3.5 \text{ \AA}$ is temperature independent.

In addition to the above systematic study of DHFR, it is useful to summarise some of the conclusions that emerged from our studies of the KIE in soybean lipoxygenase-1 (SLO-1) here. As stated in the introduction, our initial study (Olsson *et al.* [11]) reproduced, by microscopic simulations the observed KIE and the corresponding activation free energy but did not reproduce the quantitative trend of the observed temperature dependence of the KIE. A subsequent study used longer simulations (unpublished) that yielded better temperature dependence and illustrated clearly that the difficulty of producing exact temperature dependence is associated with the difficulties of sampling the activation barriers for different donor–acceptor distances. However, after reaching this conclusion, we decided to first focus on DHFR rather than on SLO. Nevertheless, it is crucial to clarify a few points about the SLO simulations. First, despite a possible impression that other workers evaluated the

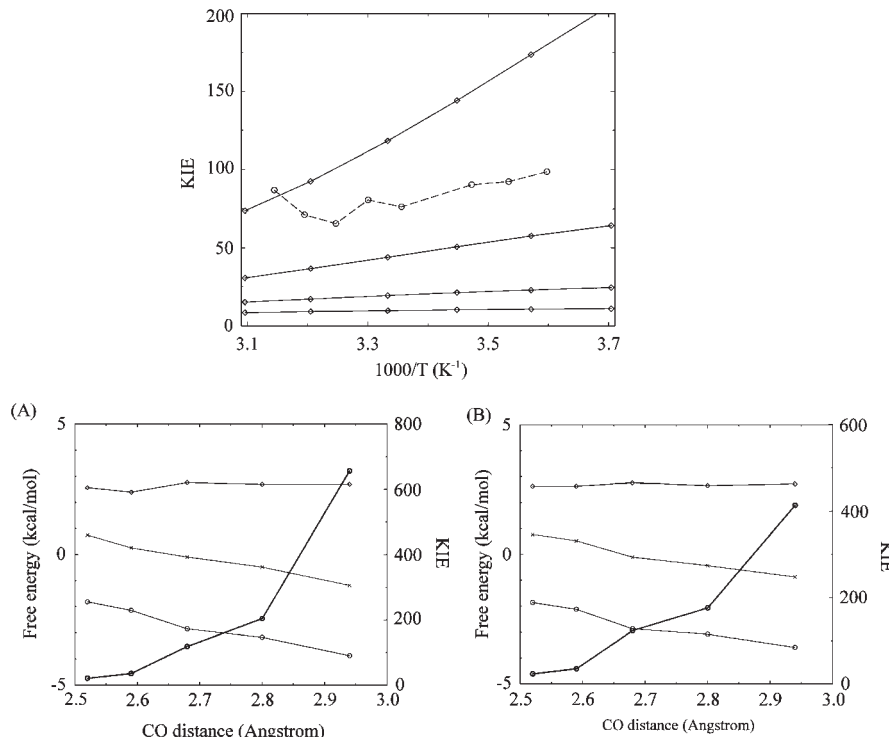


Figure 11.9 The temperature dependence of the KIE of lipoxygenase as a function of assumed $w(R)$ and the kinetic isotope effect as a function of donor and acceptor distance in the reference water solution (A) and in lipoxygenase (B). The figures are taken from ref. [18].

temperature dependence of the KIE of SLO by fully microscopic simulations, this task has not been accomplished to the best of our knowledge. Even the study of Hatcher *et al.*⁶³ was based on the vibronic treatment, rather than on more reliable treatments, like the one used by these authors in their earlier study (ref. [21]), that did not, however, represent the protein by a microscopic description. In this respect it is important to clarify that it is rather trivial to reproduce the temperature dependence of the KIE by adjusting $w(r)$ in eqn (11.13). For example, the observed trend can be reproduced (see Figure 11.9) using $w(r) = 0.6((3.4/r)^{12} - (3.4/r)^6)$. Although the agreement is not perfect, we do not find it useful to improve this agreement by refining $w(r)$. That is, the vibronic treatment can only be considered as a qualitative guide and Figure 11.9 is used only to demonstrate that the temperature dependence can be reproduced easily by phenomenological parameter-fitting approaches.

11.4 Concluding Remarks

This work summarises the conclusions that emerged from our studies of the temperature dependence of the KIE. Before expanding on our findings, it is important to clarify the fundamental difference between parameter fitting to a phenomenological formula (*e.g.* ref. [3]) and the actual microscopic simulations used here and in our previous studies. While it is almost trivial to reproduce the observed effect by arbitrary parameter fitting, it is extremely hard to do so by microscopic simulations. Part of the difficulty is associated with the difficulty of obtaining the exact PMF and a part is associated with the general difficulties of capturing temperature-dependence effects (*e.g.* entropic effects) by current simulation approaches (see discussion in ref. [11]). Here, however, one can use the comparison of the calculated and observed temperature dependence to refine the calculated PMF based on experimental measurements. Doing this while using eqns (11.9) and (11.14) may not be so useful since these equations do not reflect a sufficiently quantitative physical picture. As will be discussed below, even microscopic studies can lead to problematic conclusions if the underlining physical picture is inconsistent. Thus, it is important to explore the information content of KIEs with a clear microscopic physical approach. We believe that this has been done in our simulation studies.

In our view the most basic “qualification” for a reliable interpretation of the meaning of observed KIEs is the ability to reproduce the corresponding observed rate constants and activation barriers by microscopic simulations, without adjusting any special parameters for this purpose. Since our main interest is related to the origin of enzyme catalysis, it is crucial to reproduce the change in activation barriers relative to the corresponding barrier in water. These challenging requirements were satisfied by our studies of DHFR⁵⁹ but have not been yet satisfied (to the best of our knowledge) in other studies. In this respect it is important to note that parameterisation of QM/MM calculations to reproduce isotope effects (*e.g.* ref. [64]) does not necessarily satisfy the above conditions. At any rate, our studies⁵⁹ reproduced the observed catalytic effect in DHFR and

some of its mutants and then explored the temperature dependence of the KIE in the native DHFR and two mutants by microscopic molecular simulations. These studies reproduced the overall observed trend in the temperature dependence in a reasonable way and thus provided a reasonable “first principle” calculation of the temperature dependence of KIE in enzymes. The reason for our relative success has been averaging over different donor–acceptor distances and over different simulations. The use of a full microscopic treatment in modelling the KIE and its temperature dependence has significantly reduced the uncertainties associated with the use of arbitrary parameters and more importantly the problems associated with the use of the vibronic treatment.

The idea that our EVB simulations can actually reproduce reasonable activation barriers, KIEs and dynamical effects has been challenged by some. We do not feel that this issue should be discussed here in detail in light of the wide current use of the EVB, but we would like to clarify that the EVB is so reliable because it focuses on the difference between the solution and enzyme reactions rather than on the absolute barrier in solution. On the other hand, some approaches, that are sometimes used to support the catalytic importance of dynamical effects, involve errors of about 40 kcal/mol and are thus unable to answer any question about catalysis.

In addition to the direct results that emerged from the simulations, we explored several general limits that were not considered in previous studies. First, it was found that the temperature dependence of the KIE of the double mutant cannot be reproduced with a temperature-independent KIE at each distance and with a temperature-independent $\Delta w^\#(R)$. Here we note that the vibronic treatment, that is the basis of many of the studies in the field (*e.g.* refs [3,21,63]) assumes temperature independence at each R . Of course, it is still possible to reproduce the observed KIE with these conditions using an unrealistically fast dependence of the KIE on the distance that would be produced by the vibronic treatment and an arbitrary $\Delta w^\#(R)$. However, the current treatment is aimed at reducing the arbitrariness of the analysis. Thus it is likely that some of the temperature dependence of the KIE reflects the dependence of $\Delta\Delta g_{qm}^\#$ on the temperature at fixed R . We also found that if the activation entropy actually depends on the distance, we can reproduce the temperature dependence of the KIE even with a fixed KIE at each R .

One of the most important findings that emerged from our studies is the establishment of a clear correlation between the increase in the average donor–acceptor distance and the isotope effect. This finding, which is consistent with the qualitative prediction of the vibronic treatment, is apparently opposite to the traditional expectation from NQM corrections. That is, the traditional proposals of NQM contributions to catalysis^{25 31,64} implied that the protein compresses the reaction fragments and leads to a narrow potential and thus to larger tunnelling (Figure 11.10(a)). In this case, one would expect a relationship of the form

$$(KIE)_{tun} \propto \exp\{-K\sqrt{V_0 L}\} \quad (11.18)$$

where V_0 and L are, respectively, the height and width of the barrier.

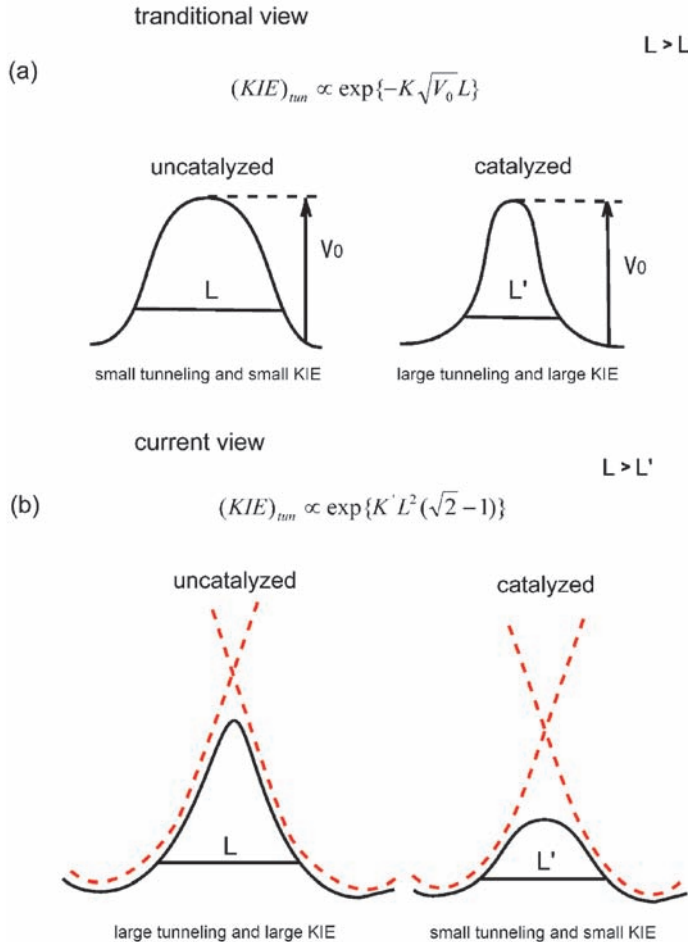


Figure 11.10 The catalytic (anticatalytic effect) of the donor acceptor distance dependence of the NQM in hydride transfer reactions. The traditional idea that the NQM increase upon compression of the donor acceptor distance is described in (a). This view assumes that enzyme catalysis involves an increase in tunnelling due to the compression effects. On the other hand, as shown here, the NQM effects increase when the donor acceptor distance decrease (b) and thus it is hard to rationalise a relationship between NQM and catalysis. The figure is taken from ref. [58].

On the other hand, it has been found here that the isotope effect increases due to the sharp distance dependence of the zero-zero vibrational overlap (Figure 11.10(b)), where the tunnelling contribution follows the relationship (see eqns (11.12)–(11.14))

$$(\text{KIE})_{\text{tun}} \propto \exp\{K'L^2(\sqrt{2} - 1)\} \quad (11.19)$$

Thus, in the more recent view, the NQM effects decrease rather than increase upon compression. This has, of course, a major implication with regards to the idea that NQM effects contribute significantly to enzyme catalysis. In fact, the effects that lead to an increase in the NQM contributions appear to be anti-catalytic. This is mainly due to the fact that the rate constant is smaller for larger donor–acceptor distances.

That the observation of large KIE reflects the increase (rather than decrease) in the distance between the donor and acceptor is seemingly a counterintuitive point and thus still involves significant confusions. Thus, it is useful to consider here a recent misunderstanding of this issue. More specifically, a recent interesting study of SLO-1⁶⁴ explored the effect of changing the width of the gas-phase potential on the calculated KIE in a model of SLO-1. It was concluded that “the decompression of the active site will result in a lower contribution to tunneling . . . thus indicating the importance of the proposed gating promoting modes”. However, this idea is very problematic since, as we found recently, decompression (or increasing the donor–acceptor distance) increases, rather than decreases, the tunnelling contribution.¹⁹ Unfortunately, the analysis of ref. [64] involved arbitrary changes of the width of the intrinsic potential surface (the one of the isolated substrate without the enzyme) instead of using a single potential surface for the substrate and changing the donor–acceptor distance in the presence of the enzyme (as was done in refs [58,59]), or actually reproducing the observed effect of mutations that change the donor–acceptor distance (as was done in ref. [58]). Unfortunately, an arbitrary change of the width of the intrinsic potential does not address or represent the proper physics of hydrogen-transfer processes, since it does not converge to the proper limit at large donor–acceptor separation. More importantly, the treatment of ref. [64] has not explored the effect of the protein since the active-site strain is not likely to cause a significant narrowing of the potential surface of the reacting atoms.

It should be clarified here that the prediction of the vibronic formula about the relationship between the KIE and the donor–acceptor distance has been found before our recent studies (*e.g.* refs [21,65]). However, with the exception of the Hammes-Schiffer work,²¹ we could not find an early realisation that the increase in distance of the KIE leads to a picture that is different from the traditional picture. Furthermore, we are not aware of any study (except our own¹⁸) that actually established the distance dependence of the KIE by proper microscopic simulations, without the use of the problematic diabatic approximation and the vibronic formula. Moreover, we could not find a clear realisation that this finding makes it hard to attribute catalysis to the increase in tunnelling (see below).

Although the qualitative prediction of the vibronic treatment is confirmed by the quantitative path integral simulations, it is important to emphasise that the vibronic treatment provides a very poor approximation in the range of regular donor–acceptor distance that should be described by the adiabatic approximations (see ref. [58]). In fact, the predicted distance dependence of the isotope effect on R is much smaller in the actual path integral simulation than in eqn (11.14). Nevertheless, at long distances when the electronic coupling is small,

the vibronic formula provides a reasonable approximation. Thus, the overall trend of a decrease in KIE upon a decrease in distance follows the trend predicted by the vibronic formula.

The analysis of ref. [58] considered $\Delta\bar{w}_{\text{eff}}^{\#}$ as an adjustable parameter because of uncertainties in the calculated *ab initio* potential surface for the solution reaction and the uncertainties in the PMF. In this respect, one may wonder why such a treatment was not needed in the recent instructive study of the temperature dependence of the KIE of lipoxygenase by Hatcher *et al.*⁶³ This success might reflect the fact that ref. [63] used the phenomenological vibronic expression (although this was done with microscopically derived parameters) and has not explored the performance of such a model on different mutants. Furthermore, ref. [63] used an average donor–acceptor distance (the equivalent of the averaging procedure of eqn (11.17)) and determined this distance by simulations. While this procedure is reasonable, it is unlikely that the average distance can be determined with certainty by simulations in the case of large changes in the PMFs (*i.e.* the double-mutant case) since it will be subjected to the same major convergence problems encountered in our PMF calculations. In fact, evaluation of the average distance should involve PMF-type mapping calculations and no such study was reported in ref. [63].

It is also important to consider here the idea that DHFR increases the reaction rate “through optimisation of the coupling of the environmental dynamics and quantum tunnelling (see ref. [66] or related ideas²⁹) as well as the implication that quantum-mechanical tunnelling is promoted by correlated motions (*e.g.* ref. [20]) and is optimised by the wild-type enzymes.¹² In fact, the tunnelling is smaller in the native enzyme (where the catalysis is maximal) than in the mutant enzyme and this means that the motions that push the reacting system in the mutant enzyme to the native configuration (which can be described as moving to the NAC configuration (*e.g.* ref. [25])) reduce the tunnelling rather than increase it.

A recent interesting study⁶⁷ of mutants of SLO-1 is directly related to the above discussion. This work found that the distant mutation I553G leads to larger KIE and to larger temperature dependence of the KIE than the corresponding effects in the native enzyme. It was argued that this demonstrates that enzymes can make the rate of transfer *via* hydrogen tunnelling significantly more efficient. While this is an interesting point of view, it seems to us that the experiments of ref. [67] simply demonstrate the key role of entropic effects in determining the temperature dependence of NQMs (as pointed out in our early works^{2,11,19}). As shown in ref. [58] and in Figure 11.8, changes in $-\Delta S^{\#}$ with R help to increase the temperature dependence of the KIE. Furthermore, the mutant probably has a larger contribution of tunnelling than the native enzyme (since it has larger r_0 according to ref. [58]). However, this issue must be resolved by microscopic simulations rather than by the use of the vibronic formula with a phenomenological fitting.

It has been suggested that our studies presumably fix the protein and thus are unable to detect promoting motions and of course cannot be used to analyse the effect of such modes. Such an assertion reflects a major misunderstanding.

Not only that we have introduced studies of dynamics and catalytic motions in enzymatic reactions,^{56,68} but also that we usually increase the protein radius to 24 Å when we explore long-range motions (the radius of DHFR is 20 Å). Obviously, when we evaluate the PMF of crucial donor–acceptor distances (*e.g.* ref. [58]) we carefully examine the sensitivity of the results to the increase of the protein radius and also to the position of the centre of the simulation sphere. Of course, those who have not calculated the actual catalytic contribution of dynamical effects (by not comparing the protein and solution motions) may assume that using infinitely large simulations system will give more reliable results. However, such an assumption would reflect a limited experience in the stability of spherical boundary conditions^{69,70} and/or limited experience in evaluation of real observables (*e.g.* activation energies, pK_a and even dynamical effects) as a function of the system size. The main problem with the assertion that somehow our simulations have ignored dynamical effects is probably the fact that those who promote it have not calculated probabilistic effects (like PMF or any actual activation barrier and rate constant). In this way, one may assume that the motions determine the free-energy surfaces (and potential surfaces) rather than the other way around. In other words, at present probably the most careful study of the relationship between the donor–acceptor distance and tunnelling effects is that reported in our work,⁵⁸ where the actual NQM is calculated by the QCP (rather than estimated by the vibronic approximation) and weighted by the probability that corresponds to the calculated PMF. This study includes of course the protein motions and their contributions to the NQM effects. Just showing the well-known fact that the motions exist in the protein is not highly relevant without realising that larger motions exist in the reference reaction in water (see discussion in ref. [19]). Furthermore, overlooking the fact that all reactions involve motions and that the probability of the motions is entirely determined by the free-energy surfaces and PMF (unless we have coherent motions, may lead to serious difficulties in understanding catalysis).

It is useful to discuss here the concept of environmentally coupled quantum-mechanical tunnelling, which is presumably linked to catalysis.^{66,71} Apparently, the concept is also problematic in its implications. That is, if the issue is the role of the modes orthogonal to the donor and acceptor distance (or the protein reorganisation energy) then we are not dealing with anything that is unique to enzymes and in fact the coupling to the environment is significantly smaller in the enzyme than in solution (*e.g.* ref. [19]). If the issue is the donor–acceptor distance, then we have a similar distance in the native enzyme and the reference reaction in water (see ref. [59]).

The idea that coupled modes contribute to catalysis has emerged in different forms in recent years (*e.g.* ref. [72], see also discussion in ref. [19]). The appeal of this idea comes perhaps from the realisation that mutations of distant residues can change the rate of enzymatic reactions. However, this fact is not surprising at all, since the distant residues may change the reorganisation of the key residues in the active site and this geometrical effect is entirely related to the fact that the folding in the active site is determined by the overall folding of the

protein. Further confusion may be due to the assumption that the structural changes observed upon mutations can tell us about the motions that are involved in the reactive event. First, as shown recently⁷³ the reactive trajectories are frequently orthogonal to the conformational changes observed upon mutations. Second, and more importantly, even if the displacements observed upon mutations are along the chemical reaction coordinate, they are not likely to contribute to catalysis. For example, although mutations that increase the distance between the donor and acceptor (*e.g.* the M42W-G121V mutant in DHFR) reduce catalysis, this does not mean that the fluctuations in the opposite direction will contribute to catalysis. That is, although it has been suggested that such motions bring the system to its preorganised position,⁷² this proposal is problematic (see discussion in ref. [59]) since the native enzyme is already in its preorganised position. It is also unlikely that motions that reduce the distance between the donor and acceptor contribute to catalysis by “compressing” the donor and acceptor distance, since the same motions exist in the reference solution reaction. It is also useful to mention that the structural changes observed upon mutation have no dynamical meaning (a mutation process is not a dynamical event but the generation of two different proteins). Furthermore, even a static compression effect would not contribute to catalysis as has been clarified in our systematic analysis of the NAC proposal.⁷⁴ Finally, it is instructive to realise that it is becoming clear now (*e.g.* ref. [75]) that the protein modes are mainly determined by its geometry rather than exact sequence. This observation makes it hard to rationalise specialised coupled modes as a major reason for catalysis (proteins with similar structures catalyse different substrates in very different ways).

It is also useful to comment here on the increasingly popular use of the term “Marcus-like” model (*e.g.* refs [12,65]) for the description provided by the vibronic formula. Such a term may lead to significant confusion as far as enzyme catalysis is concerned. The most serious problem is the possible implication that the reorganisation energy term is closely related to tunnelling effects or dynamical effects. In fact, the reduction of the reorganisation energy by the preorganised enzyme-active site is probably the most important factor in enzyme catalysis^{76,77} and it has enormous effects in completely adiabatic reactions without any significant tunnelling effect. Furthermore, the activation barrier in the vibronic equation is very different from the activation barrier of the given reaction (*e.g.* the activation barrier for the reaction of lipoxygenase is about 14 kcal/mol at 300 K for H transfer,¹⁸ while the activation barrier in the corresponding vibronic equation is about 2 kcal/mol¹⁸). Similarly, $\Delta g^\#$ is much higher than the phenomenological $\Delta E^\#$, which is about 2 kcal/mol.³ Most importantly, while the argument that the *change* in rate constant follows the Marcus relationship is basically correct (as was established in our early works⁷⁸), the attempt to explain catalysis by implying that it is due to the Marcus-like relationship misses the most important issue, which is how the reorganisation is being reduced. The reduction of the reorganisation energy by reorganised polar environment is the reason for enzyme catalysis and not the tunnelling effects.

It might also be useful to comment here on a recent attempt⁶⁷ to consider the reorganisation effects while providing new definitions for the concepts of reorganisation and preorganisation. That is, ref. [67] included the work function in the reorganisation (which is reasonable), but assumed that the reorganisation energy causes mainly enthalpic contributions. It then ascribed the term “preorganisation” to the motions of the reactive region. In our view this new definitions may lead to some confusion and detracts from the attempt to quantify enzyme catalysis. More specifically, the reorganisation energy has been defined in the landmark work of Marcus (*e.g.* refs [79,80]) and evaluated microscopically in many EVB studies (*e.g.* refs [35,59]) as well as in studies of electron-transfer reactions (*e.g.* ref. [50]). The reorganisation energy is the free-energy change when the system is placed on the product surface at the minimum of the reactant state and allowed to relax to the minimum of the product state. This term can include a large entropic contribution, in particular in the reference solution reaction. Now, the term “preorganisation” has been introduced by the inclusion compounds community^{81,82} and extended and quantified for enzyme catalysis by Warshel and coworkers (*e.g.*, refs [1,76,77]). This term defined by the linear response approximation (LRA), where the charging free energy is given by (see ref. [77])

$$\Delta G \cong \frac{1}{2} \left[\langle U_Q - U_0 \rangle_0 + \langle U_Q - U_0 \rangle_Q \right] \quad (11.20)$$

where, U_Q and U_0 are, respectively, the potential energies of the nonpolar and the polar (charged) form of the TS, while $\langle \rangle_a$ designates an average over the indicated charged form. Now, the $\langle \rangle_0$ term reflects the preorganisation effect, which is zero when we deal with the TS in solution, and can be quite significant in enzyme-active sites.

The preorganisation term is directly related to the reorganisation energy, since (see ref. [77]):

$$\lambda = \frac{1}{2} \left[\langle U_Q - U_0 \rangle_0 - \langle U_Q - U_0 \rangle_Q \right] \quad (11.21)$$

Furthermore, the preorganisation determines the catalytic effect, as demonstrated recently.⁸³ The main point for the purpose of the present discussion, however, is that while the motions to the reactive region may be a part of the preorganisation process, they do not contribute to the rate constant and their speed does not determine the *magnitude* of the preorganisation (and thus to catalysis), unless k_{on} is smaller than k_{cat} (see ref. [59]). In other words, the previously defined preorganisation effect is the origin of the reduction of the activation barrier. The new definition does not usually describe a catalytic contribution, and in the cases of mutants, where it reflects an increase in the free energy of the reacting fragments (or a NAC-type effect), we are back to the discussion above. It must be emphasised that the issue here is not polemic or

semantic. That is, in the scientific search for truth it is crucial to have clear definitions in order to be able to accept or reject the corresponding proposals.

Recent works have emphasised the issue of the role of the protein landscape in catalysis (Figure 12 of ref. [77], Figure 3 of ref. [84] and refs [85,86]). Obviously the catalytic landscape exists and we have made major progress in the evaluation of this landscape.⁸⁷ However, this does not change the nature of our catalytic concept. That is, enzymes have complex landscapes with different heights for the chemical barriers in different protein conformations. However, our studies have indicated that the lowest barrier is confined to a rather narrow region and the overall rate constant is simply determined by the lowest barriers. As before, the question is why the low barriers are low (rather than the fact that one should consider several barriers) and again we find that the low barriers are due to the preorganised polar environment [87].

Our studies (*e.g.* refs [19,50]) indicated that the temperature dependence of the KIE does not provide support for the proposal that dynamical effects contribute to catalysis. However, this does not mean that studies of the temperature dependence of the KIE are not very valuable. In particular, by “inverting” the observed isotope effect obtained from the rate constants of eqn (11.17) and by combining theory with experiment, we may use temperature-dependent experiments of the type reported in ref. [12] to construct experimentally determined PMF for the native and mutant enzymes. Such an approach can help in refining simulation approaches and in elucidating the effects of different mutations on the donor–acceptor distance. Furthermore, the theoretical studies may be used to propose more effective mutations that will provide clearer information about the PMF of the donor–acceptor distance and its relationship to the protein-folding landscape.

Acknowledgement

This work was supported by NIH grant GM24492 and by computer time from the University of Southern High Performance Computing and Communication Center (HPCC).

References

1. A. Warshel, *Computer Modeling of Chemical Reactions in Enzymes and Solutions*, John Wiley & Sons, New York, 1991.
2. J. Villa and A. Warshel, *J. Phys. Chem. B*, 2001, **105**, 7887.
3. M. J. Knapp, K. Rickert and J. P. Klinman, *J. Am. Chem. Soc.*, 2002, **124**, 3865.
4. J. Kemsley, *Chem. Eng. News*, 2003, **81**, 29.
5. K. M. Doll, B. R. Bender and R. G. Finke, *J. Am. Chem. Soc.*, 2003, **125**, 10877.
6. S. X. Wang, M. Mure, K. F. Medzihradzky, A. L. Burlingame, D. E. Brown, D. M. Dooley, A. J. Smith, H. M. Kagan and J. P. Klinman, *Science*, 1996, **273**, 1078.

7. N. Lehnert and E. I. Solomon, *J. Biol. Inorg. Chem.*, 2003, **8**, 294.
8. J.-K. Hwang and A. Warshel, *J. Am. Chem. Soc.*, 1996, **118**, 11745.
9. S. R. Billeter, S. P. Webb, P. K. Agarwal, T. Iordanov and S. Hammes-Schiffer, *J. Am. Chem. Soc.*, 2001, **123**, 11262.
10. J.-K. Hwang and A. Warshel, *J. Phys. Chem.*, 1993, **97**, 10053.
11. M. H. M. Olsson, P. E. M. Siegbahn and A. Warshel, *J. Am. Chem. Soc.*, 2004, **126**, 2820.
12. L. Wang, N. M. Goodey, S. J. Benkovic and A. Kohen, *Proc. Natl. Acad. Sci. USA*, 2006, **103**, 15753.
13. A. M. Kuznetsov and J. Ulstrup, *Can. J. Chem.*, 1999, **77**, 1085.
14. E. D. German and A. M. Kuznetsov, *J. Chem. Soc. Farad. T. 1*, 1981, **77**, 397.
15. A. Warshel and Z. T. Chu, *J. Chem. Phys.*, 1990, **93**, 4003.
16. J.-K. Hwang, Z. T. Chu, A. Yadav and A. Warshel, *J. Phys. Chem.*, 1991, **95**, 8445.
17. J. L. Gao and D. G. Truhlar, *Annu. Rev. Phys. Chem.*, 2002, **53**, 467.
18. M. H. M. Olsson, J. Mavri and A. Warshel, *Philos. T. R. Soc. B*, 2006, **361**, 1417.
19. M. H. M. Olsson, W. W. Parson and A. Warshel, *Chem. Rev.*, 2006, **106**, 1737.
20. J. Y. Pang, J. Z. Pu, J. L. Gao, D. G. Truhlar and R. K. Allemann, *J. Am. Chem. Soc.*, 2006, **128**, 8015.
21. E. Hatcher, A. V. Soudackov and S. Hammes-Schiffer, *J. Am. Chem. Soc.*, 2004, **126**, 5763.
22. J. Z. Pu, S. H. Ma, J. L. Gao and D. G. Truhlar, *J. Phys. Chem. B*, 2005, **109**, 8551.
23. J. Villa, A. Gonzalez-Lafont, J. M. Lluch and D. G. Truhlar, *J. Am. Chem. Soc.*, 1998, **120**, 5559.
24. J. Rodgers, D. A. Femic and R. L. Schowen, *J. Am. Chem. Soc.*, 1982, **104**, 3263.
25. J. Luo, K. Kahn and T. C. Bruice, *Bioorganic Chemistry*, 1999, **27**, 289.
26. P. Ball, *Nature*, 2004, **431**, 396.
27. B. J. Bahnsen, T. D. Colby, J. K. Chin, B. M. Goldstein and J. P. Klinman, *Proc. Natl. Acad. Sci. USA*, 1997, **94**, 12797.
28. J. P. Klinman, *Trends Biochem. Sci.*, 1989, **14**, 368.
29. J. S. Mincer and S. D. Schwartz, *J. Phys. Chem. B*, 2003, **107**, 366.
30. M. J. Sutcliffe and M. S. Scrutton, *Philos. T. R. Soc. A*, 2000, **358**, 367.
31. S. D. Schwartz, in *Isotope Effects in Chemistry and Biology*, ed. A. Kohen and H. H. Limbach, CRC, Boca Raton, FL, 2004, p. 475.
32. A. Warshel, *J. Biol. Chem.*, 1998, **273**, 27035.
33. Y. Ohta, A. V. Soudackov and S. Hammes-Schiffer, *J. Chem. Phys.*, 2006, **125**, 144522.
34. J.-K. Hwang, G. King, S. Creighton and A. Warshel, *J. Am. Chem. Soc.*, 1988, **110**, 5297.
35. J. Aqvist and A. Warshel, *Chem. Rev.*, 1993, **93**, 2523.
36. R. Vuilleumier and D. Borgis, *J. Phys. Chem. B*, 1998, **102**, 4261.

37. A. M. Smolyrev and G. A. Voth, *Biophys. J.*, 2002, **82**, 1460.
38. S. R. Billeter, S. P. Webb, T. Iordanov, P. K. Agarwal and S. Hammes-Schiffer, *J. Chem. Phys.*, 2001, **114**, 6925.
39. J. Florian, *J. Phys. Chem. A*, 2002, **106**, 5046.
40. C. Dellago and G. Hummer, *Phys. Rev. Lett.*, 2006, **97**, 245901.
41. K. D. Kreuer, S. J. Paddison, E. Spohr and M. Schuster, *Chem. Rev.*, 2004, **104**, 4637.
42. H. J. Kim and J. T. Hynes, *J. Am. Chem. Soc.*, 1992, **114**, 10508.
43. M. Sierka and J. Sauer, *J. Chem. Phys.*, 2000, **112**, 6983.
44. Y. T. Chang and W. H. Miller, *J. Phys. Chem.*, 1990, **94**, 5884.
45. P. Bala, P. Grochowski, B. Lesyng and J. A. McCammon, *J. Phys. Chem.*, 1996, **100**, 2535.
46. T. V. Albu, J. C. Corchado and D. G. Truhlar, *J. Phys. Chem. A*, 2001, **105**, 8465.
47. M. L. Wang, Z. Y. Lu and W. T. Yang, *J. Chem. Phys.*, 2006, **124**, 124516.
48. Q. Wang and S. Hammes-Schiffer, *J. Chem. Phys.*, 2006, **125**, 184102.
49. D. T. Major and J. L. Gao, *J. Am. Chem. Soc.*, 2006, **128**, 16345.
50. A. Warshel and W. W. Parson, *Q. Rev. Biophys.*, 2001, **34**, 563.
51. R. P. Feynman, *Statistical Mechanics*, Benjamin, New York, 1972.
52. M. J. Gillan, *J. Phys. C. Solid State Phys.*, 1987, **20**, 3621.
53. G. A. Voth, D. Chandler and W. H. Miller, *J. Chem. Phys.*, 1989, **91**, 7749.
54. G. A. Voth, *Adv. Chem. Phys.*, 1996, **93**, 135.
55. A. Warshel, *J. Phys. Chem.*, 1982, **86**, 2218.
56. A. Warshel, *Proc. Natl. Acad. Sci. USA*, 1984, **81**, 444.
57. A. Warshel and J.-K. Hwang, *J. Chem. Phys.*, 1986, **84**, 4938.
58. H. Liu and A. Warshel, *J. Phys. Chem. B*, 2007, **111**, 7852.
59. H. Liu and A. Warshel, *Biochemistry*, 2007, **46**, 6011.
60. R. S. Sikorski, L. Wang, K. A. Markham, P. T. R. Rajagopalan, S. J. Benkovic and A. Kohen, *J. Am. Chem. Soc.*, 2004, **126**, 4778.
61. L. Wang, S. Tharp, T. Selzer, S. J. Benkovic and A. Kohen, *Biochemistry*, 2006, **45**, 1383.
62. A. Warshel, M. H. M. Olsson and J. Villa-Freixa, in *Isotope Effects in Chemistry and Biology*, ed. A. Kohen and H. H. Limbach, CRC, Boca Raton, FL, 2006.
63. E. Hatcher, A. V. Soudackov and S. Hammes-Schiffer, *J. Am. Chem. Soc.*, 2007, **129**, 187.
64. I. Tejero, M. Garcia-Viloca, A. Gonzalez-Lafont, J. M. Lluch and D. M. York, *J. Phys. Chem. B*, 2006, **110**, 24708.
65. M. J. Knapp and J. P. Klinman, *Eur. J. Biochem.*, 2002, **269**, 3113.
66. R. S. Swanwick, G. Maglia, L. Tey and R. K. Allemann, *Biochem. J.*, 2006, **394**, 259.
67. M. P. Meyer, D. R. Tomchick and J. P. Klinman, *Proc. Natl. Acad. Sci. USA*, 2008, **105**, 1146.
68. A. Warshel, *Accounts Of Chemical Research*, 2002, **35**, 385.
69. A. Warshel, P. K. Sharma, M. Kato and W. W. Parson, *Biochim. Biophys. Acta-Proteins And Proteomics*, 2006, **1764**, 1647.

70. R. G. Alden, W. W. Parson, Z. T. Chu and A. Warshel, *J. Am. Chem. Soc.*, 1995, **117**, 12284.
71. G. Maglia and R. K. Allemann, *J. Am. Chem. Soc.*, 2003, **125**, 13372.
72. S. Hammes-Schiffer and S. J. Benkovic, *Annu. Rev. Biochem.*, 2006, **75**, 519.
73. M. Rocca, H. Liu, B. Messer and A. Warshel, *Biochemistry*, 2007, ASAP.
74. M. Strajbl, A. Shurki, M. Kato and A. Warshel, *J. Am. Chem. Soc.*, 2003, **125**, 10228.
75. C. H. Shih, S. W. Huang, S. C. Yen, Y. L. Lai, S. H. Yu and J. K. Hwang, *Prot. Struct. Funct. Bioinf.*, 2007, **68**, 34.
76. A. Warshel, *Proc. Natl. Acad. Sci. USA*, 1978, **75**, 2558.
77. A. Warshel, P. K. Sharma, M. Kato, Y. Xiang, H. Liu and O. M. H. M., *Chem. Rev.*, 2006, **106**, 3210.
78. A. Yadav, R. M. Jackson, J. J. Holbrook and A. Warshel, *J. Am. Chem. Soc.*, 1991, **113**, 4800.
79. R. A. Marcus, *J. Chem. Phys.*, 1956, **24**, 966.
80. R. A. Marcus, *Ann. Rev. Phys. Chem.*, 1964, 155.
81. J. M. Lehn, *Angew. Chem. Int. Ed. Engl.*, 1990, **29**, 1304.
82. D. J. Cram, *Angew. Chem. Int. Ed. Engl.*, 1988, **27**, 1009.
83. A. Warshel, P. K. Sharma, Z. T. Chu and J. Aqvist, *Biochemistry*, 2007, **46**, 1466.
84. Y. Xiang, M. F. Goodman, W. A. Beard, S. H. Wilson and A. Warshel, *Prot. Struct. Funct. Bioinf.*, 2008, **70**, 231.
85. S. J. Benkovic, G. G. Hammes and S. Hammes-Schiffer, *Biochemistry*, 2008, **47**, 3317.
86. M. K. Prakash and R. A. Marcus, *Proc. Natl. Acad. Sci. USA*, 2007, **104**, 15982.
87. M. Rocca, B. Messer, D. Hilvert and A. Warshel, *Proc. Natl. Acad. Sci. USA*, 2008, **105**, 13877.

CHAPTER 12

The Use of X-ray Crystallography to Study Enzymic H-tunnelling

DAVID LEYS

Faculty of Life Sciences, Manchester Interdisciplinary Biocentre, Manchester University, Manchester, M1 7DN, UK

12.1 Introduction

There is growing evidence that the dynamic properties of macromolecules play a central role in their function.^{1–5} In particular enzyme catalysis is now widely accepted to be an inherently dynamic process, with binding and release of substrates, product and other ligands accompanied and/or preceded by protein conformational changes.^{6,7} The exact nature of these changes is often ill understood, and can range from barely perceptible changes in the position or mobility of a few residues to major repositioning of entire protein domains.^{8,9} In addition to the distinct binding events during a catalytic cycle, the catalytic step that involves the chemical transformation itself is inherently dynamic, with bonds being broken and others being formed. It has been postulated that the remarkable catalytic power of enzymes is not merely a consequence of the active-site structure but also of the protein dynamics within the Michaelis complex itself.^{6,7,10–16} Protein vibrations and motions within the active site can couple to the reaction coordinate, supplying a direct link between enzyme catalysis and protein dynamics. Optimisation of an enzyme activity through natural selection could therefore select for the enzymes with both optimal

structure and dynamic properties. The inability of protein-engineering efforts, largely based on the relatively static view of transition-state binding, to mimic the catalytic power of naturally occurring enzymes evidently suggests our understanding of enzyme catalysis remains incomplete.^{17–21} In contrast to protein-structure determination becoming more of a standard technique, the detailed, quantitative study of enzyme dynamics remains at the cutting edge of research and technological developments. In this respect, the study of hydrogen-transfer reactions is particularly informative with regards to the role and nature of catalytically relevant enzyme dynamics.²² As the lightest element, hydrogen behaviour is more significantly governed by quantum-mechanical physics than other elements, with a de Broglie wavelength similar to predicted transfer distances. The overlap between donor and acceptor wavefunctions is a very sensitive function of the donor–acceptor distance on the sub-Angstrom scale. As a direct consequence, the rate of H-transfer will strongly depend on the donor–acceptor distance. Thus, the study of hydrogen-transfer kinetics can be used as an exquisite probe for enzyme motions connected to the active site as illustrated elsewhere in this volume. Ideally, from the viewpoint of a structural biologist, the ultimate goal is to experimentally observe and follow the entire hydrogen-transfer event to atomic detail, complementing the wealth of kinetic data that has become available on these enzymes. However, no single experimental technique allows such a detailed observation to be made at present. Instead, structural biology techniques traditionally provide “snapshots” of protein structures based on ensemble measurements, with the inherent loss of temporal and/or dynamic information. Hence, the only techniques presently available to us that can study atomic structure at the single-molecule level over time are computational modelling studies.^{5,11,23–25} Thus, our present understanding of protein dynamics is often at best qualitative, with quantitative studies requiring an interdisciplinary and iterative approach that combines (several) experimental structural biology techniques with computational studies. This chapter focuses on the use of X-ray crystallography to inform upon the understanding of hydrogen-transfer reactions, providing a background to the technique as well as introducing recent examples of work in our group illustrating its use, limitations and interface with other techniques.

12.2 X-ray Crystallography: A Brief Overview

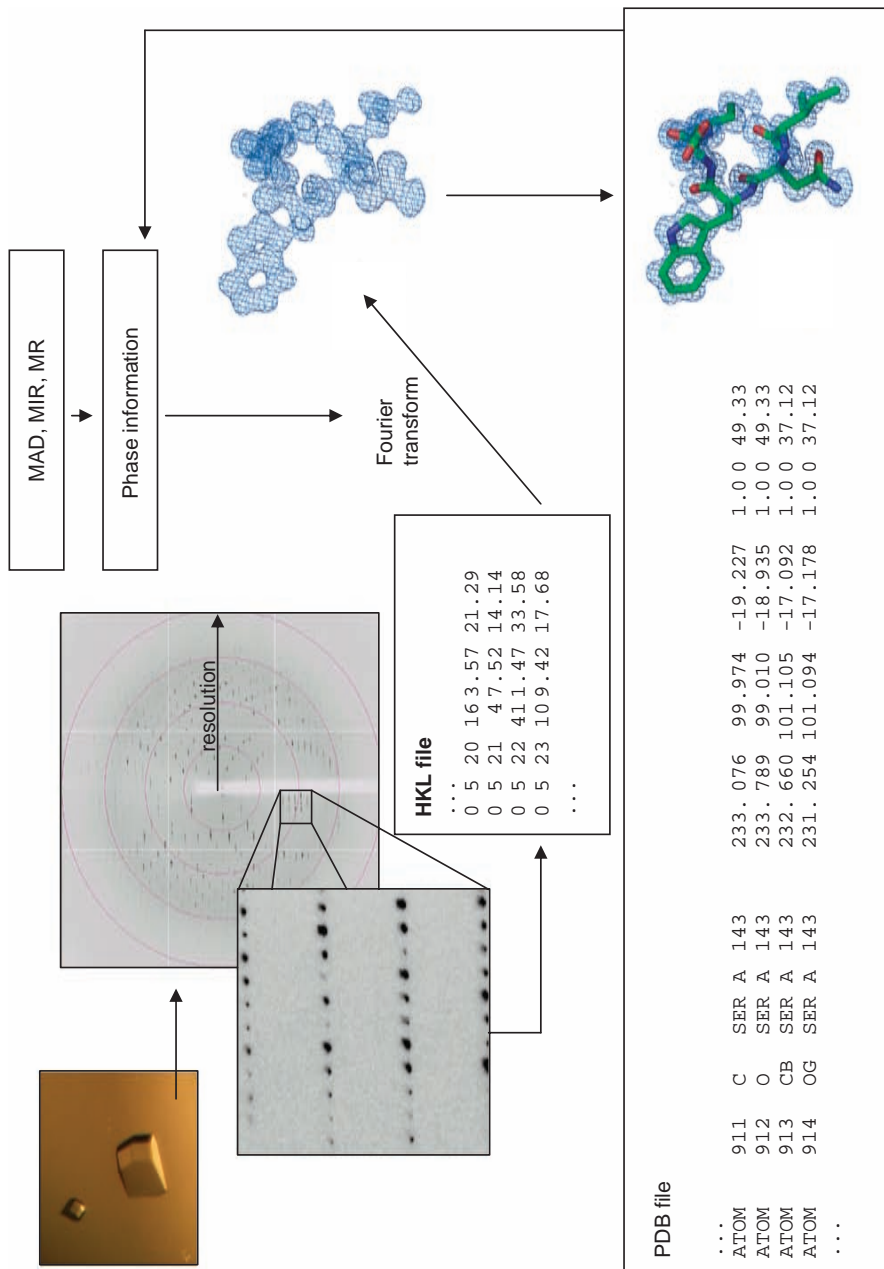
In theory, the scattering of X-rays by macromolecules has the potential to allow real-time observation of single molecules at the atomic level. If we were able to detect the scattering of X-rays by a single macromolecule over time, we could reconstitute an image of the macromolecule’s electron density using either a lens (*i.e.* traditional microscope) or through a Fourier transform of the scattering patterns. In practice, the difficulties with handling a sample the size of a single macromolecule, the extreme low signal intensity, the lack of a suitable X-ray lens, as well as X-ray-related radiation damage mean that crystals of macromolecules are the only samples that routinely yield useful information.

Recent advances using the extreme brightness of free-electron lasers hint at the future possibility of observing single molecules by X-ray scattering.^{26–29} In contrast to the scattering by a single macromolecule, the ordered array of molecules in a crystal lattice (which can contain in the order of 10^{14} molecules) leads to readily observable diffraction patterns that consist of a series of discrete reflections as predicted by Bragg's Law. The distinct intensity and phase of each reflection is a function of the electron density present within the unit cell of the sample and a Fourier transform of all measured reflections yields the three-dimensional electron-density maps most biochemists will be familiar with (Figure 12.1; for excellent books providing more in depth introductions to the field of crystallography see refs [30–32]). Thus, the exact position of each atom determines the observed intensities of all the reflections or, in other words, the intensity and phase of each reflection depends on the entire structure present within the unit cell. Therefore, X-ray crystal structures cannot be determined for a small part of the molecule of interest, in contrast to other techniques such as NMR where a signal can be related to a discrete element within the molecule. As a consequence, it is essential to collect data for all reflections that can be observed to allow for construction of interpretable electron-density maps and reliable model building and refinement.

12.2.1 Accuracy of X-ray Diffraction Structures

The quality of the model and the level of functional interpretation are largely governed by the resolution obtained. The larger the angle to which reflections are measured, the higher the resolution of the electron-density map obtained (*i.e.* the smaller the value in Å the better the resolution), with the majority of crystal structures reported at $\sim 1.5\text{--}2.0\text{\AA}$ resolution (Figure 12.2). The recent capacity increase in 3rd-generation synchrotron sources and dedicated macromolecular crystallography beam lines has all but removed the incident X-ray intensity as the limiting factor in obtaining high-resolution data. Instead, the resolution is limited for the majority of cases by the quality and inherent order of the macromolecular crystal itself.

Figure 12.1 Schematic overview of X-ray crystallographic methodology. Following successful crystallisation, all reflections (to a given resolution) arising from an X-ray diffraction experiments are recorded. The intensities of the individual reflections (as recorded in a HKL file, with each reflection denoted by a unique set of 3 indices H, K and L), together with associated phases are used to calculate a 3-dimensional electron density map. Initial, approximate phases are derived from the experimental methods MIR/MAD or through molecular replacement;^{30–32} model derived phases are used for further calculations. The electron density map can be interpreted in terms of an atomic model, of which the atomic coordinates and associated B factor (as recorded in the PDB file) can be refined against the recorded intensities (using appropriate stereochemical restraints).



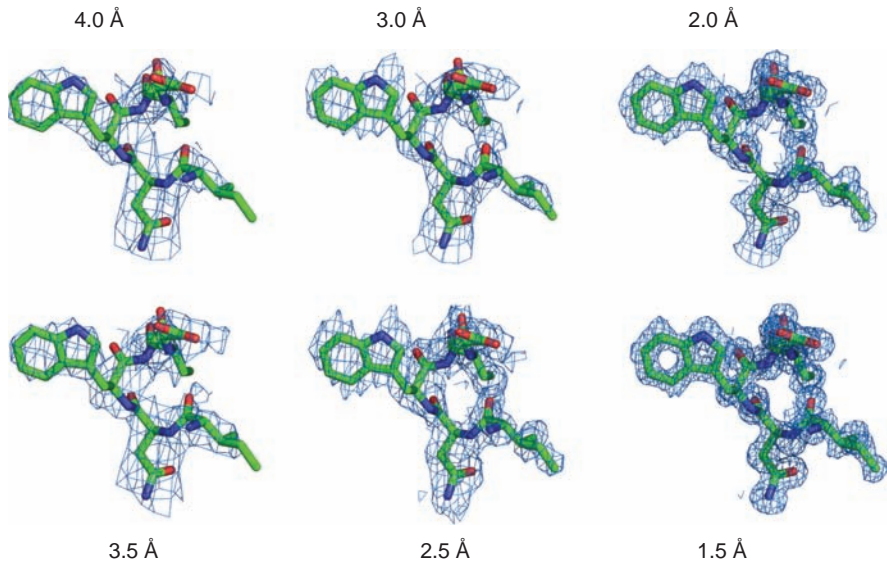


Figure 12.2 The effect of resolution on level of detail observed. Electron density maps calculated with data extending up to 4.0 Å and, in steps of 0.5 Å, ultimately to 1.5 Å. The corresponding structure to 1.0 Å can be seen in Figure 12.1. Note how the individual backbone carbonyl groups can be discerned from 2.5 Å onwards, while the characteristic “hole” in the aromatic rings can be seen from 2.0 Å onwards. The exact orientation of the Asn residue can only be obtained reliably with data extending beyond 1.5 Å.

Unfortunately, the phase information is lost in the diffraction experiment, making construction of an interpretable electron-density map from the collected data alone impossible. The solution to the phase problem is to derive (approximate) phases either through additional experiments (*e.g.* multiple isomorphous replacement (MIR) or multiwavelength anomalous dispersion (MAD)) or by using a homologous protein structure in molecular replacement (MR). The exact methodologies in each case are outside the scope of this chapter and have been reviewed in refs [30–32]. It is sufficient to know that once an interpretable electron-density map is obtained (*e.g.* a map that reveals structural features that allow unambiguous building of model) phase information needed for further calculations is usually derived from the model itself (Figure 12.1). Once an initial model is obtained, it is refined in terms of atomic coordinates and an associated term called the B-factor that describes the average displacement for a given atom from its coordinates. Hence, for an average 200 amino acid structure an approximate 6000 parameters need to be refined. With the exception of higher-resolution structures, the experimental observations to parameters ratio is usually low and approaches ~1. During refinement, this ratio is improved to a certain extent by the incorporation of

stereochemical restraints on the individual atomic positions based upon the high-resolution structures of individual amino acids and small peptides.^{33,34} In brief, refinement programs aim to reduce the difference between the observed diffraction intensities and those calculated from the model as well as minimising deviation from the stereochemical restraints. The traditional indicator for the agreement of a structure with the data is the R-factor that describes the residual difference between intensities calculated from the model and those observed. In addition, a small subset of data ($\sim 5\%$) is excluded from the refinement process to allow calculation of R_{free} .³⁵ The latter procedure has been devised to avoid over-refinement of the model. Given the low observations to parameters ratio and the fact that diffraction data contains inherent measurement errors, refinement could lead to erroneously modelling the inherent inaccuracy of the data. It is, furthermore, relatively easy to construct an overparameterised model (e.g. by adding solvent molecules, explicit H-atoms, or refining anisotropic B-factors as opposed to isotropic in each case without experimental justification) where the superfluous parameters tend to model the measurements errors or mask inherent model errors. Random errors during data collection will, however, not be correlated between individual reflections, so that over-refinement against the working data set will lead to an increase in the $R - R_{\text{free}}$ difference. Hence, refinement is guided by both monitoring a decrease in R and R_{free} as well as ensuring the difference between R and R_{free} remains minimal during refinement.

As mentioned before, the number of parameters included in the model can vary significantly and depends on the resolution and data quality obtained (Figure 12.3). As resolution increases multiple occupancies will become apparent for a subset of residues (usually solvent exposed) in which case multiple, alternative coordinates per atom as well as the relative occupancy of each conformation are added to the model (Figure 12.3(b)). In addition to protein atoms, a macromolecular model will most likely contain ordered solvent atoms that can be reliably observed from resolutions from $\sim 2.7 \text{ \AA}$. With increasing resolution, more and more water molecules can be observed, often up to the second hydration shell when approaching $\sim 1.5 \text{ \AA}$ (Figure 12.3(a)).^{36,37} Hydrogen atoms are rarely directly observed in crystal structures as their X-ray scattering is very weak, so that only those structures exceeding $\sim 1.2 \text{ \AA}$ contain any experimental information regarding hydrogen-atom position (Figure 12.3(c); although $<0.9 \text{ \AA}$ is needed to observe the majority of H-atoms in a structure).³⁸ Adding hydrogen atoms to a structure and refining their position independently is rarely done, and often the position of the hydrogen atoms is fixed with respect to the heavy atoms. Finally, the atomic B-factors of the model can be refined anisotropically as opposed to the standard isotropic refinement (Figure 12.3(d)), adding 5 additional parameters per atom to the model (6 parameters to define the orientation and shape of ellipsoid rather than 1 to define a sphere).³⁹

It can be difficult to independently assess the accuracy of a given X-ray structure and what can reliably be deduced, especially when studying aspects of the model that did not feature in papers reporting the structure. Several excellent reviews are available that elaborate on this issue.⁴⁰⁻⁴² In short, X-ray

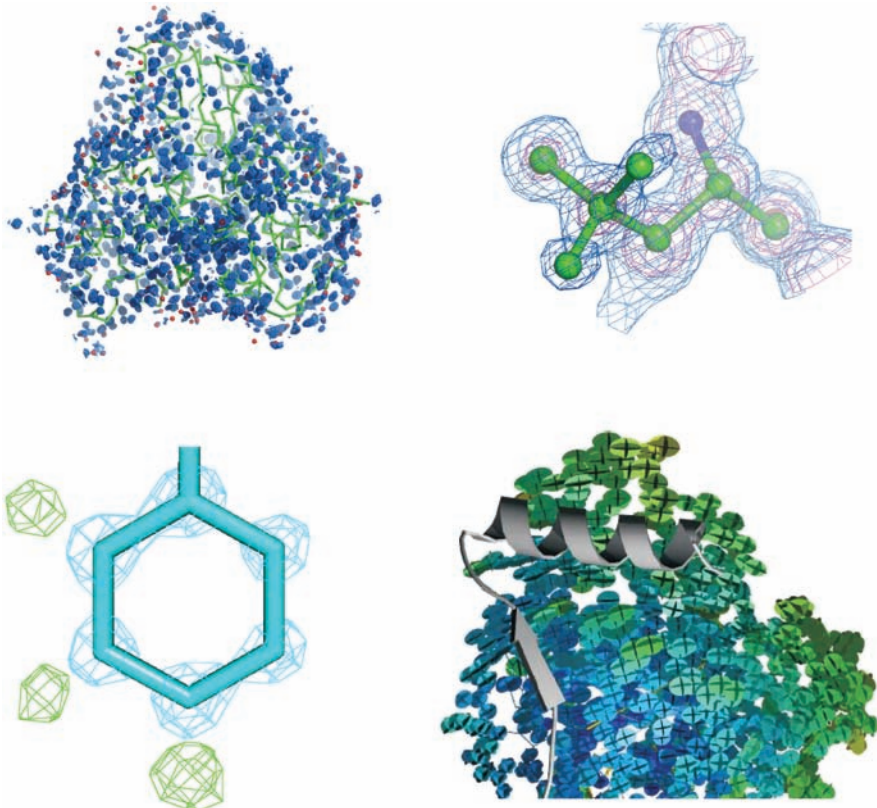


Figure 12.3 Additional levels of model complexity for higher resolution structures. (a) Solvent structure: Individual water molecules observed for a 45 kDa protein at near atomic resolution. (b) Multiple conformations: a dual conformation for a Leu residue can be readily observed in this 1.1 Å electron density map, with higher contour levels (in pink) revealing only density for the carbon position common to both conformations. (c) Hydrogen atoms: an electron density map calculated to display features unaccounted for by the model clearly depicts the positions of certain Phe aromatic hydrogen atoms, supporting the needs to incorporate explicit hydrogen atoms into the model to accurately reflect the data. (d) Anisotropic B factors: ellipsoid representation of the anisotropic B factors for a single protein domain, the common orientation and elongation of these ellipsoids clearly illustrates this domain can undergo a hinge motion in the crystal.

structures tend to be more accurate with increasing resolution obtained. For low to medium-resolution structures ($\sim 3.5\text{--}2.5\text{ \AA}$) certain amino acids can be modelled in the incorrect rotamer, while some irregular loop regions can be misconstrued. The exact orientation of residues such as His, Gln and Asn is often derived from the surrounding hydrogen-bonding patterns observed (the

relatively small difference between the individual C, N and O electron density becomes apparent from $\sim 1.6\text{ \AA}$ onwards). Guidelines as to what the appropriate range of values should be for individual indicators of data quality (R_{merge} , $I/\sigma I$, multiplicity, completeness), of refinement (R/R_{free}) and of the stereochemistry of the model (Ramachandran plots, r.m.s.d. from standard values for bond lengths and angles) are available by different authors that provide a consensus view by the crystallographic community.^{40–42} It is important to realise that most of these quality indicators are overall values that, with the exception of Ramachandran plots, reveal little about the relative accuracy of the position of individual elements within the structure. While certain indicators are available that provide a more detailed indication of accuracy, these are rarely reported. A useful general rule is to assume that the error on the average position ranges from approximately 1/20th to 1/10th of the resolution, with a 2.0 \AA structure having an approximate $\sim 0.1\text{--}0.2\text{ \AA}$ deviation on the individual atomic positions. Obviously, the position of those elements that display an element of disorder (indicated by significantly higher than average B-factors) will be less accurately determined.

When studying the H-transfer reactions, where the transfer rate is likely to be a very sensitive function of the donor–acceptor distance on the sub-Angstrom scale, it becomes clear that it is paramount to obtain the highest resolution possible when studying the structure of enzymes that catalyse H-transfer reactions. Ideally, a resolution better than 1.0 \AA should be obtained that allows highly accurate definition of both donor and acceptor groups and, when possible, the H-atom position itself. In practice, only a minority of protein structures has been determined to this level of accuracy due to the fact that most protein crystals have a diffraction limit in the region of $\sim 1.5\text{--}2.5\text{ \AA}$. Hence, one must bear in mind that the data supporting the vast majority of crystal structures will not rigorously justify interpretations at the sub- \AA scale. Most importantly, when studying enzyme reactions in detail, it becomes of crucial importance to determine a structure that corresponds to the Michaelis complex or is known to mimic the latter (*e.g.* substrate analogue complexes or substrate-inactive enzyme). As mentioned above, enzyme catalysis is a highly dynamic process where ligand-binding events likely induce or alter both the dynamical behaviour of protein as well as the ligand, and thus the active-site properties.

12.2.2 Dynamic Information from X-ray Crystallography

Although X-ray crystallography is generally associated with providing a “snapshot”, static picture of a protein structure, dynamic information can be obtained. For a single-crystal structure, this is mostly limited to the B-factor (also called the Debye–Waller temperature factor) information that describes the extent to which the electron density corresponding to a particular atoms (or group) is smeared out due to thermal motion.⁴³ At higher resolutions, the B-factor can be anisotropically refined, leading to an ellipsoid describing the electron density rather than the isotropically sphere.³⁹ This allows the user to

gauge both the extent and main directions of a particular atom motion within the crystal structure (Figure 12.3(d)).⁴⁴ It is important to realise that crystal packing can alter the mobility of those structure elements involved in lattice contacts, and these should therefore be interpreted with care. Unfortunately, a crystal structure presents an ensemble and time-averaged picture of a protein structure so that is not possible to detect the timescale of, or indeed any coupling between, individual motions. However, logical assumptions regarding the possible coupling of motions can often be made on the basis of connectivity or proximity of the individual elements. Last but not least, B-factor distributions need to be analysed with care, as errors in the model (in either occupancy or position) are often masked by erroneously high B-factors.^{40–42}

A recent addition to crystallographic refinement procedure is the use of TLS (translation-libration-screw) refinement that models the anisotropic motion of rigid bodies corresponding to (usually) individual protein domains or sub-units.^{45,46} As it requires only a few parameters to describe the coherent motion of an entire domain, TLS refinement can be carried out at medium resolution and often provides a useful indication as to the inherent protein dynamical behaviour. Similar to B-factor analysis, caution is needed for physical interpretation of TLS parameters as, like any other form of displacement parameter, they will mask errors as well as a variety of different displacement types.

Crystallography becomes much more informative with regards to studying protein dynamics when several individual crystal structures can be compared, ideally providing a set of “snapshots” of structures along a reaction coordinate.⁴⁷ While structure determination of a protein structure or protein–ligand complex has become more standard, obtaining insight into transient, intermediate structures is significantly more challenging. A first and important prerequisite is that the protein crystals are catalytically active without significant crystal-quality deterioration, which fortunately holds true for a significant proportion of enzymes. In those cases where the crystal can catalyse the reaction under steady-state conditions, it can be possible to determine the structure of the intermediate preceding the rate-limiting step, either by determining the structure during steady-state turnover, or by flash cooling the crystal under steady-state conditions and determining the corresponding structure at cryogenic temperatures.⁴⁸ It is important to keep in mind that the kinetics of catalysis (and possibly the rate-limiting step) are likely altered in the crystal when compared to the solution state. Furthermore, the relatively slow diffusion of substrates in, and products out, of a crystal is likely to complicate such steady-state experiments for fast enzymes. In contrast, presteady-state experiments offer the possibility of determining the structure of any intermediates that accumulate to a significant extent within the crystal during turnover. The level of occupancy for an individual intermediate to be reliably detected and refined depends on the resolution obtained and the presence of spatially overlapping, alternative species. However, it is highly unlikely that any species populated at <15–25% can be studied even at resolutions approaching 1.0 Å. This is an important limitation of X-ray crystallography when studying transient intermediate species as it is unlikely that high-energy conformations

can be populated at these levels. To perform presteady-state experiments, it is important to realise the reaction initiation needs to be synchronised throughout the crystal as X-ray structures will represent an ensemble average of those molecules illuminated by the X-ray beam. Enzyme reactions in crystals can be initiated through a range of techniques, similar to those used when studying presteady-state kinetics in solution.^{47,49,50} The obvious differences due to the nature of the sample (crystal as opposed to solution) and data collection (relatively slow X-ray diffraction experiment as opposed to a range of real-time spectroscopic methods) make transfer of established solution techniques for reaction initiation nontrivial. In contrast to the rapid mixing that is possible for solutions, crystal reactions initiated by diffusion will need to rely on the bulk transfer of substrate throughout the crystal. Although present-day synchrotron sources have made it possible to routinely collect data from 10–100 µm size crystals, complete mixing of interstitial mother liquor in such (small) crystals with the bulk solution is likely to still take one to several seconds (note that a pH shift is significantly more rapid due to the rapid transfer of protons in solution). Similarly, the flash-cooling procedure used to routinely cool crystals to 100 K for data collection consists of simply looping the crystal and plunging into liquid N₂, a process that again will take time of the order of seconds.⁵¹ While the time spans of the order of a second are obviously a significant problem for those enzymes that can complete turnover in a fraction of a second, these approaches have been successfully used to determine structures of intermediate species for reactions that are considerably slower.^{52,53} More rapid and synchronous reaction initiation can occur through appropriate illumination (including with X-rays) of crystals. In rare cases, the natural function of the enzyme or protein requires light to perform catalysis or undergo a conformational change.^{54–57} For the majority of enzyme systems that are not inherently dependent on light, caged substrate compounds can be soaked into enzyme crystals and uncaged using short, high-intensity illumination prior to rapid flash cooling.⁵⁸ Alternatively, uncaging can be performed at low temperatures (allowing for long exposures needed in the case of low efficiency) and the reaction initiated by a (transient) temperature jump.⁵⁹ Illumination with a high X-ray dose will lead to a degree of damage of protein crystals by ionisation processes, especially when powerful X-ray sources are used.⁶⁰ The photoelectrons generated can get localised in protein or associated cofactor moieties. Recently, these effects have been used to initiate enzyme reactions by careful crystallographic “redox titration” through (white beam) X-ray exposure.^{61,62}

It is unlikely a single crystal will yield the structure of a series of distinct intermediates as this would require reinitiation of the reaction following high-intensity X-ray exposure as well as (rapid) heating to room temperature. The combination of the latter effects is rarely tolerated by a macromolecular crystal. Hence, the experimentalist will have to use distinct crystals and systematically vary the time span between reaction initiation and freeze trapping and/or data collection in order to obtain a series of distinct crystal structures. The fact that individual crystals (through variations in size, quality and crystal handling) can display distinct kinetics necessitates probing multiple candidate crystals. Except

for those cases where very high resolution is routinely obtained for the distinct candidate intermediate structures, the interpretation of the corresponding electron density often will require additional information as to the nature of the trapped species to allow unambiguous modelling. For those systems that contain a cofactor (or substrate) that absorbs in the UV-VIS region and reports on the catalytic cycle, this can be obtained through microspectrophotometric methods.^{63–66} In this case the UV-VIS spectrum of the crystal can be collected prior to (and after) data collection to ensure sufficient population and positive identification of a particular intermediate (and exclude X-ray radiation effects during data collection).

In contrast to the standard monochromatic X-ray diffraction experiments, the use of polychromatic or Laue crystallography offers the scope of near-instantaneous data collection and hence the possibility of collecting multiple data sets on a single crystal.^{67–70} While multiple images are recorded for different orientations of a protein crystal during standard X-ray diffraction experiments, the use of Laue crystallography allows collection of near-complete data sets using a single, short exposure as most reflections will satisfy Bragg's law for a given crystal orientation. Using Laue crystallography in combination with laser-induced reaction initiation has been remarkably successful in producing a time-resolved atomic insight into the reaction mechanism and protein dynamics of certain model systems, although there are few light-inducible systems and fewer that will be compatible with the constraints of Laue-crystallography (*e.g.* near perfect crystals, strong diffraction, small lattice).

12.3 Examples of H-tunnelling Systems Studied by Crystallography

When studying the H-transfer step in an enzymatic catalytic cycle at the atomic level, the ultimate goal is to determine the structure of the intermediates immediate prior to and after the H-transfer event. In view of the many caveats associated with X-ray crystallography as described above it is clear this is a highly ambitious goal that can only be attained to a certain level for the distinct enzyme systems. In the following sections we will describe a few model systems that have been studied by X-ray crystallography as well as associated structural biology techniques and illustrate in each case the recent advances in understanding.

12.3.1 Crystallographic Studies of AADH Catalytic Mechanism

The enzyme aromatic amine dehydrogenase (AADH) and the related methylamine dehydrogenase (MADH) are inducible periplasmic quinoproteins produced by Gram-negative bacteria to allow growth on primary (aromatic) amines as a source of carbon and nitrogen.^{71,72} In *Alcaligenes faecalis*, AADH is specific for phenylethylamines and other aromatic amines, but also reacts to a lesser extent with primary aliphatic amines.^{71,74} MADH, on the other hand, is

highly specific for smaller amines such as methylamine or ethylamine.⁷³ Both enzymes exhibit an $\alpha_2\beta_2$ heterotetrameric structure with each β -subunit possessing a covalently bound redox-active tryptophan tryptophylquinone (TTQ) cofactor (Figure 12.4).⁷⁴ The oxidative deamination reaction proceeds in two steps. In the reductive half-reaction, the substrate-derived amino group is incorporated into the TTQ cofactor through acid–base catalysis by a conserved Asp residue, resulting in conversion from quinone into N-quinol.^{74,75} The TTQ cofactor is subsequently reoxidised by electron transfer to a periplasmic type-I blue copper protein, azurin and amicyanin in case of AADH and MADH, respectively.^{76,77}

In both AADH and MADH, significantly elevated KIEs are associated with the TTQ reduction step which is concomitant with the H-transfer from a substrate C α proton to the catalytic Asp residue. AADH crystals diffract routinely to ~ 1.2 Å and are catalytically active with a wide range of amine substrates providing an attractive model system to study the AADH catalytic mechanism and the H-transfer step in particular. Within the wide substrate range accepted by AADH, tryptamine displays an unusually high KIE of ~ 55

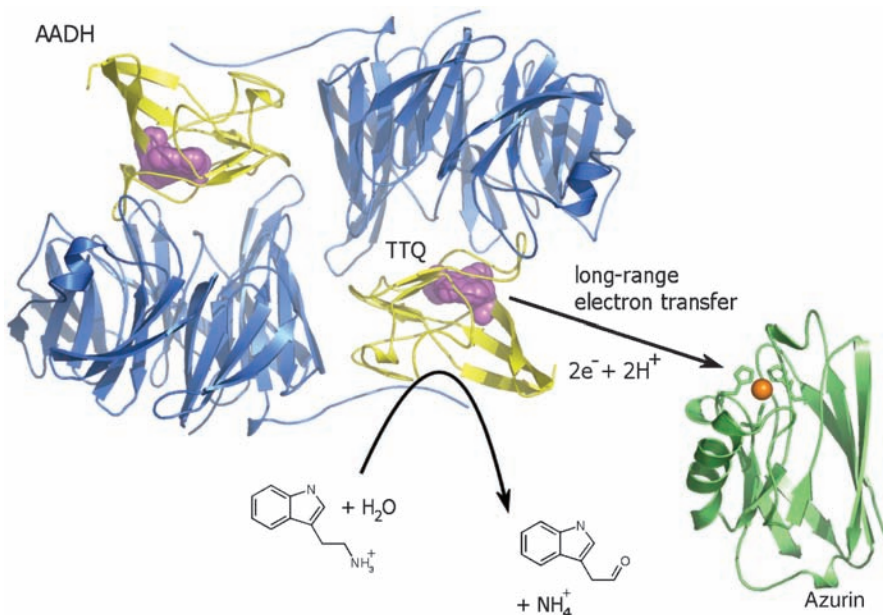
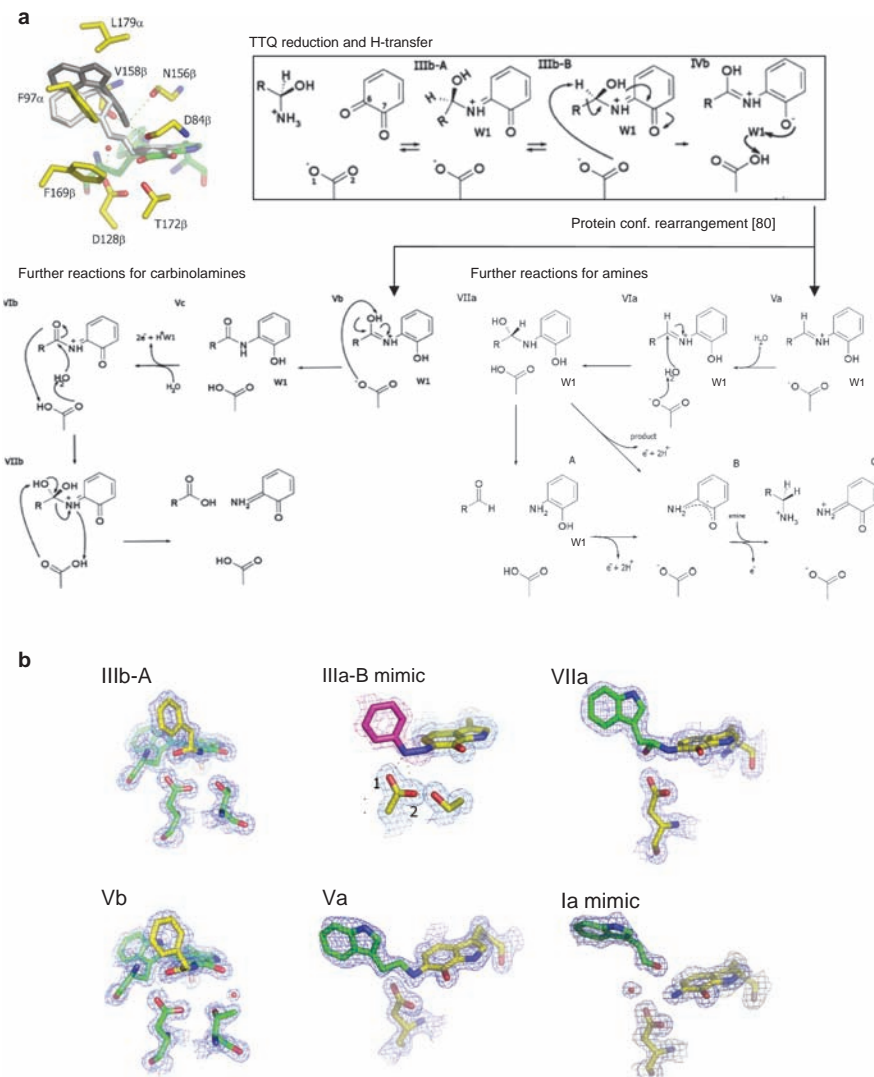


Figure 12.4 Overview of the AADH crystal structure and function. The AADH model is represented in cartoon form with the α subunit in blue, the β subunit in yellow, and the TTQ cofactor in magenta spheres. The reductive half reaction with tryptamine is depicted in detail in Figure 12.5(a). The oxidative half reaction consists of two consecutive long range electron transfer events to the single electron carrier azurin that is depicted in the green cartoon with the copper atom as an orange sphere (from *Pseudomonas putida*; PDB code 1NWO).

with a k_{lim} of $503 \pm 5 \text{ s}^{-1}$ at 277 K, while substrates like benzylamine only display a relatively modest KIE of ~ 4.8 with a k_{lim} of $1.81 \pm 0.02 \text{ s}^{-1}$ (at 298 K).^{78 79} The structure of distinct intermediates in the AADH reaction with distinct substrates is needed to provide a molecular explanation of the observed kinetic properties. Initially, the reaction was initiated through decaging of caged tryptamine and benzylamine that have proved unsuccessful in both cases due to either binding of the caged compound in the active site (for tryptamine) or the inability to isolate a crystal structure corresponding to an intermediate species (for benzylamine). However, rapid soaking with tryptamine and immediate flash cooling following TTQ reduction (as visually observed by



crystal decolouration from green to colourless) resulted in crystal structures of a covalent tryptamine:AADH TTQ adduct, one structure that was determined to 1.1 Å (assigned as species Va in Figure 12.5).⁷⁸ Despite prolonged efforts using various variations on the rapid soaking and flash cooling no structures representing intermediates prior to TTQ reduction could be obtained with tryptamine. On the other hand, extending the time span between TTQ reduction and flash cooling led to either a distinct species corresponding to an S-carbinolamine-TTQ-adduct or the reduced enzyme in complex with a tryptamine substrate molecule (species VIIa, Figure 12.5). Near identical structures could be obtained using similar protocols with distinct AADH crystal forms that shows the reaction path is largely independent of crystal packing. In order to obtain information about the AADH active-site structure prior to H-transfer the 1.4 Å structure with the inhibitor phenylhydrazine was determined (a model for species IIIa-B in Figure 12.5). Compared with the native enzyme structure, the only notable changes are a slight rotation of the TTQ away from the carboxylate group of catalytic Asp¹²⁸β and minor repositioning of the side chain of Thr¹⁷²β, which now forms a hydrogen bond with Asp¹²⁸β O2 (3.0 Å). The

Figure 12.5 AADH mechanism as derived from the structure of key intermediates. (a) To the left side, the AADH active site is represented by atom coloured sticks: green carbons, TTQ cofactor; other carbons, yellow. The position occupied by the substrate in complex with the reduced AADH is depicted in dark gray, and the positions in intermediate V of substrate and TTQ are in light gray; putative hydrogen bonds are shown as green dashed lines. In addition, on the right side a schematic overview of the mechanism of amine/carbinolamine oxidation by AADH is presented. For clarity, only part of the TTQ cofactor is represented, whereas the aromatic moiety of the different substrates is indicated by an *R*. Intermediates during the reductive half reaction are numbered by *roman numerals* in accordance with refs [78–80]. To differentiate between both types of substrate, amine derived intermediates are labelled with *a*, while the corresponding carbinolamine derived intermediates are labelled *b*. Intermediates during the oxidative half reaction are labelled by *letters*, with *A* representing the *N* quinol state, *B* the *N* semiquinone state, and *C* the *N* quinone state (only presented for reaction with amines). The active site water molecule (or ammonia in case of a steady state mechanism, see ref. [81]) is denoted *W1*. Whether a conformational equilibrium between IIIb A and IIIb B occurs depends on the nature of the *R* side chain. (b) Active site structures and associated electron density of intermediates in the AADH reductive half reaction with distinct substrates/inhibitors. Atoms are coloured according to atom type, with substrate derived carbon atoms respectively in magenta (phenylhydrazine), yellow (*R* phenylethanolamine) and green (tryptamine). For clarity, only substrate or inhibitor derived atoms are shown, in addition to the side chain atoms for residues Asp¹²⁸β (and Thr¹⁷²β) and part of the TTQ cofactor. Intermediates are labelled by roman numerals corresponding to panel a. The covalent phenylhydrazine AADH complex is used as a model for intermediate IIIa B while the reduced AADH structure in complex with tryptamine is used to model the Michaelis complex (I).

phenylhydrazine nitrogen, which mimics the iminoquinone-reactive C1 donor atom, is within the hydrogen-bonding distance of Asp¹²⁸β O1 (2.8 Å) and in van der Waals contact with Asp¹²⁸β O2 (3.2 Å). In principle, either Asp¹²⁸β oxygen could act as proton acceptor, leading to two distinct possible intermediates following H-transfer.

Due to the atomic resolution obtained for most intermediates the interpretation of the electron density was straightforward and the first covalent TTQ adduct immediately after reduction was refined as an tryptamine imino-quinol adduct. Surprisingly, the iminium double bond was not in plane with the TTQ-quinol moiety. Instead, the electron density obtained is consistent with movement of the C1 = N bond out of plane by ~60° increasing the distance between C1 and Asp¹²⁸β O1 and O2 to 3.7 Å and 4.1 Å, respectively (Figure 12.5). No evidence for protonation of Asp¹²⁸β was observed from the 1.1 Å electron-density map (*e.g.* no asymmetric electron density could be observed that would correspond to a protonated carboxylate). Hence, it was concluded that the structure corresponds to an intermediate formed following proton transfer from Asp¹²⁸β to the TTQ O7 *via* the nitrogen Schiff base in a two-step process, and this was found to be consistent with QM/MM simulations. This additional proton-transfer step substantially increases the C1–acceptor distances, ensures irreversibility of the H-tunnelling step while it poised the enzyme for the next step in the catalytic cycle that involves Asp¹²⁸β assisted hydrolysis of the C1 = N double bond. Indeed, analysis of crystals that were flash cooled 5–10 min after TTQ reduction reveals an electron density that corresponds to an S-carbinolamine adduct, consistent with activation of a water molecule positioned in between C1 and Asp¹²⁸β by the latter, leading to attack of the *si* face of the C1 = N bond (Figure 12.5). Although carbinolamines are inherently unstable in water, the latter intermediate is stable under anaerobic conditions for several days, as revealed by anaerobically obtained crystal structures and mass spectrometric analysis. After oxidation of the enzyme, hydrolysis of the carbinolamine is facilitated by creation of a good leaving group (*i.e.* the aminoquinone) and the possible introduction of a water molecule between Asp¹²⁸β O2 and the aminoquinone.

During experiments aimed at obtaining intermediates with aromatic substrates it became apparent that AADH reacts, albeit slowly, with the corresponding carbinolamines present in solution when significant buildup of aromatic aldehyde products occurs in the presence of ammonia.⁷⁹ It was established that in contrast to the fast oxidation of primary amines, carbinolamine oxidation catalysed by AADH is approximately ~10⁵–10⁷ times slower. These inherently slow rates greatly facilitate the study the AADH mechanism (carbinolamines have a high similarity with the natural substrates (both in terms of structure and reaction mechanism)) by the above-described methods as the reaction initiation by simple bulk diffusion becomes sufficiently fast compared to the turnover rates.

Using both phenylaminoethanol and indol-3-aminoethanol as alternative substrates in similar soaking protocols yields crystal structures for distinct intermediates that correspond to those observed with tryptamine, but most

importantly also yields the high-resolution structure of a catalytically competent phenylaminoethanol-derived iminium-TTQ adduct, corresponding to a pre-H-transfer intermediate (species IIIb-A in Figure 12.5). In this case the substrate-derived aromatic moiety adopts a conformation that is distinct from that modelled for the corresponding tryptamine derived TTQ iminoquinone adduct (see below), with a proton-Asp¹²⁸β O2 distance estimated to be 3.7 Å, approximately 1.0 Å further away than the corresponding tryptamine iminoquinone model. This increase in distance is reflected in the approximately 10⁷-fold slower TTQ reduction rate with phenylaminoethanol as compared with primary amines. Furthermore, a water molecule (labelled W1 in Figure 12.5(a)) is observed near TTQ C6 and is likely derived from the collapse of the preceding carbinolamine TTQ-adduct. Given the position, this water molecule can be involved in the consecutive proton transfers that follow TTQ reduction. Furthermore, research into the AADH oxidative half-reaction revealed a water molecule to be positioned near the TTQ O7 concomitant on protein rearrangement following reduction.⁸⁰ It is postulated this rearrangement drives the water molecule close to C6 to a position near O7 where it can act as a proton acceptor during oxidation. Furthermore, steady-state turnover studies have indicated that in the presence of high substrate levels the oxidised aminoquinone species is not hydrolysed prior to substrate attack, so that the water molecule discussed above could in fact be an ammonia molecule during the steady state.⁸¹

In conclusion, crystallographic results suggest that AADH active site requires little motion to catalyse the reaction as protein-derived atoms are in near-identical positions for the distinct intermediate structures obtained. It, furthermore, reveals a complex set of further H-transfers and protein rearrangement that likely follows the initial C1–H bond breakage. On the basis of the distinct positions obtained for substrate-derived aromatic moieties for different substrates (*e.g.* phenyl- versus indole-containing (carbinol)amines) it suggests that conformational differences could account in part for the variation in KIE and reaction rates with distinct amine substrates, with the smaller nonindol compounds such as β-phenylethylamine undergoing conformational reorganisation prior to H-transfer.

The high-resolution AADH structures obtained were used for analysis of H-tunnelling in AADH by QM/MM computational methods.^{78,82} These methods modelled the tryptamine-derived iminoquinone-AADH species and calculated the reaction path involving C1–H bond breakage. These calculations were in accord with solution data and suggest reacting moieties first approach by classical activation to a H1–O2 separation of ~1.64 Å, the reaction coordinate dominated by heavy-atom motions. From this point the proton tunnels a distance of ~0.59 Å through the barrier. The possibility of protein motions promoting tunnelling was investigated using molecular-dynamics simulations. These suggest that the O2–H1 distance, critical for tunnelling, can be shortened by rotation of H1 toward O2 and repositioning of the Asp¹²⁸β carboxylate. Molecular-dynamics simulations and density functional theory calculations showed a subpicosecond short-range promoting vibration is inherent to the

iminoquinone intermediate.⁸³ However, no network of coupled long-range promoting motions that modulate the O2–H1 distance is detected.

12.3.2 Crystallographic Studies of MR

Morphinone reductase (MR) is a FMN-dependent enzyme that catalyses the NADH-dependent saturation of the carbon–carbon bond of both morphinone and codeinone (Figure 12.6).⁸⁴ The enzyme belongs to the old yellow enzyme (OYE) family of flavoproteins, including other well-studied proteins such as estrogen-binding protein (EBP) from *Candida albicans*, pentaerythritol tetranitrate (PETN) reductase from *Enterobacter cloacae* and glycerol trinitrate reductase from *Agrobacterium radiobacter*.^{85–87} It has been shown that MR catalysis proceeds in two half-reactions, reductive and oxidative, that involve three H-transfers by an environmentally coupled quantum tunnelling mechanism.⁸⁸ The reductive half-reaction involves hydride transfer of the NADH C4 R-hydrogen to the FMN N5 atom. In contrast to AADH and the related enzyme PETN, MR requires a promoting motion to facilitate tunnelling, a notion that is consistent with combined pressure and temperature effects on the 1° KIE and modelling of the reaction parameters.^{88–90} The crystal structures of the NADH-oxidised MR or NAD⁺-reduced MR are difficult to obtain due to the low affinity for the NAD⁺ product ($\gg 1\text{ mM}$) and the rapid reaction rates that prohibit determining the structure of the Michaelis complex through simple soaking methods. Instead, the nonreactive NADH analogue, 1,4,5,6-TetrahydroNADH (NADH₄), an excellent mimic of the natural coenzyme, was used to determine the structure of wild-type MR in complex with NADH₄.⁹¹ The MR–NADH₄ complex was determined at 1.3 Å resolution to inform on the geometry of coenzyme binding and hydride transfer (Figure 12.6). No significant differences between the structure of MR in complex with NADH₄ compared with that of MR (determined at 2.0 Å) in the absence of ligand could be detected. The bound NADH₄ molecule was easily located in the active-site electron density, with temperature factors suggesting incomplete occupancy despite using NADH₄ concentrations exceeding 100 mM. The structure suggests only few hydrogen bonds are formed between MR and NADH₄; two are made to the carbonyl oxygen of the nicotinamide moiety from residues Asn-189 and His-186, a third is established between Tyr-356 and the pyrophosphate moiety of the bound nucleotide. Using the NADH₄ coordinates to model NADH reveals the C4–N5 distance to be 3.4 Å with angle 95°, which is in accord with other crystal structures of flavoenzyme–ligand complexes.⁹²

In contrast to the WT enzyme, which has only one detectable reactive configuration, the mutation of N189A induces multiple reactive configurations (MRCs) that were observed using ensemble fast reaction methods. For the majority of these species it is shown that hydride transfer occurs *via* an environmentally coupled H-tunnelling mechanism. Molecular-dynamics simulations were performed using the MR–NADH₄ structure to investigate the dynamic properties of the enzyme–NADH complex. While the nicotinamide moiety

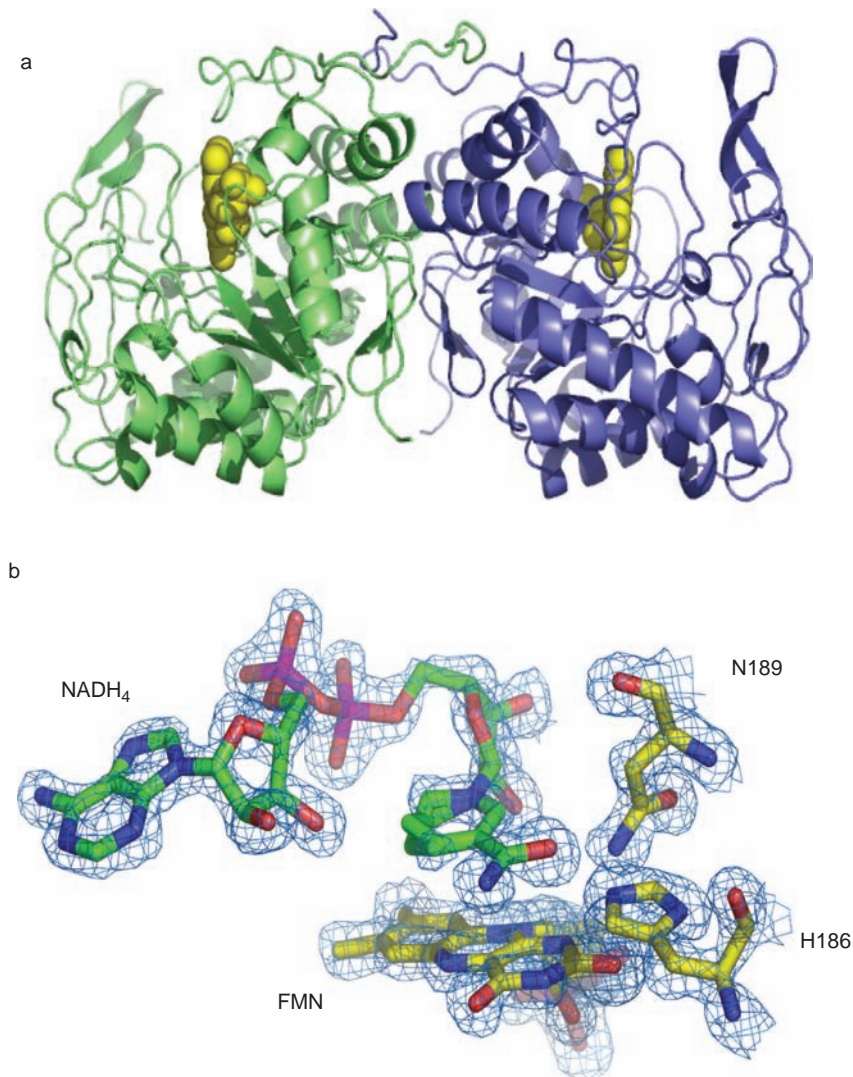


Figure 12.6 Overview of the MR NADH₄ crystal structure. (a) The MR model is represented in cartoon form with the one monomer coloured blue and the other green. The associated FMN cofactors are depicted as yellow spheres. (b) The active site of MR in complex with NADH₄. Key residues and both FMN and NADH₄ are shown in atom coloured sticks, with carbons coloured green for amino acids, yellow for the FMN and cyan for the NADH₄. The corresponding region of the electron density map is contoured at 1.5 sigma and shown as a blue mesh. Notice how multiple conformations are observed for the NADH₄ nicotinamide ring.

occupies a similar position relative to the FMN in wild-type and N189A MR during a significant part of dynamics simulations, a region of configurational space not accessed in wild-type was observed for the N189A mutant. In the latter configuration, the C4-H atom is more readily poised for hydride transfer to N5 ($3.2 \pm 0.4 \text{ \AA}$) than in configuration 1 ($3.5 \pm 0.4 \text{ \AA}$), which is supported by the observation that hydride transfer is faster for one of the MRCs in the N189A enzyme when compared with wild-type MR. The implications of MRCs on analysing tunnelling reactions are discussed more fully in the Chapter 9 by Hay *et al.*

12.4 Conclusions

At present, X-ray crystallography remains the most commonly used technique to study protein structure, due to the relatively rapid and accurate results obtained. It provides an ensemble- and time-averaged picture of the lowest-energy conformation in the crystalline form with quality and level of model complexity largely governed by the resolution obtained. Therefore, information about protein dynamics and possible impact on enzyme catalysis, in particular for H-tunnelling processes, is difficult to extract from X-ray crystallographic experiments. Not only is data of the highest resolution required to model structures with sub-Angstrom accuracy, it is furthermore necessary to provide insight for the relevant transient structures, *e.g.* intermediate species preceding and following the H-tunnelling event. The latter requirement is difficult to fulfil, and the different methods that have successfully allowed one to trap such transient species are often highly system specific. The AADH studies discussed herein illustrate it is possible to obtain structural information for intermediate structures immediately preceding and following a H-transfer step, but in each case the structure represents a low-energy species that will require significant conformational rearrangement (of the substrate derived atoms) in order to attain a “tunnelling-ready” conformation. When these rearrangements represent brief excursions to higher-energy conformations of enzyme and/or substrate, it is unlikely they can be detected by X-ray crystallographic methods due to their low population. Instead, more often than not, the X-ray crystallographer resorts to determining the structure of a stable complex that mimics the intermediate structures, *e.g.* inhibitor–enzyme complexes as illustrated by the phenylhydrazine–AADH and NADH₄–MR complex structures. Information about enzyme dynamics derived from X-ray crystallography alone is therefore at best qualitative. It is, however, at the interface with other structural biology techniques such as NMR and most importantly with computational studies that X-ray crystallography proves most useful. As illustrated in the examples above, X-ray crystallography can provide the necessary starting models for detailed computational simulation studies that can provide quantitative insights into the enzyme mechanism.

References

1. J. F. Swain and L. M. Gierash, *Curr. Opin. Struct. Biol.*, 2006, **16**, 102.
2. N. Popovych, S. Sun, R. H. Ebright and C. G. Kalodimos, *Nat. Struct. Mol. Biol.*, 2006, **13**, 831.
3. H. Frauenfelder, P. W. Fenimore and R. D. Young, *IUBMB Life*, 2007, **59**, 506.
4. M. Vendruscolo, *Curr. Opin. Struct. Biol.*, 2007, **17**, 15.
5. G. Dodson and C. S. Verma, *Cell. Mol. Life Sci.*, 2006, **63**, 207.
6. G. G. Hammes, *Biochemistry*, 2003, **41**, 8221.
7. R. M. Daniel, R. V. Dunn, J. L. Finney and J. C. Smith, *Annu. Rev. Biophys. Biomol. Struct.*, 2003, **23**, 69.
8. A. Gutteridge and J. Thornton, *FEBS Lett.*, 2004, **567**, 67.
9. A. Gutteridge and J. Thornton, *J. Mol. Biol.*, 2005, **346**, 21.
10. A. Tousignant and J. N. Pelletier, *Chem. Biol.*, 2004, **11**, 1037.
11. D. Antoniou, J. Basner, S. Núñez and S. D. Schwartz, *Chem. Rev.*, 2006, **106**, 3170.
12. S. Hammes-Schiffer and S. J. Benkovic, *Annu. Rev. Biochem.*, 2006, **75**, 519.
13. K. F. Wong, T. Selzer, S. J. Benkovic and S. Hammes-Schiffer, *Proc. Natl. Acad. Sci. USA*, 2005, **102**, 6807.
14. M. H. Olsson, W. W. Parson and A. Warshel, *Chem. Rev.*, 2006, **106**, 1737.
15. P. K. Agarwal, *J. Am. Chem. Soc.*, 2005, **127**, 15248.
16. E. Z. Eisenmesser, O. Millet, W. Labiekovsky, D. M. Korzhnev, M. Wolf-Watz, D. A. Bosco, J. J. Skalicky, L. E. Kay and D. Kern, *Nature*, 2005, **438**, 117.
17. D. Hilvert, *Annu. Rev. Biochem.*, 2000, **69**, 751.
18. D. N. Bolon, C. A. Voigt and S. L. Mayo, *Curr. Opin. Chem. Biol.*, 2002, **6**, 125.
19. J. Kaplan and W. F. DeGrado, *Proc. Natl. Acad. Sci. USA*, 2004, **101**, 11566.
20. J. R. Pineda and S. D. Schwartz, *Philos. Trans. R. Soc. Lond. B. Biol. Sci.*, 2006, **361**, 1433.
21. V. L. Schramm, *J. Biol. Chem.*, 2007, **282**, 28297.
22. Z. D. Nagel and J. P. Klinman, *Chem. Rev.*, 2006, **106**, 3095.
23. H. M. Senn and W. Thiel, *Curr. Opin. Chem. Biol.*, 2007, **11**, 182.
24. R. A. Friesner and V. Guallar, *Annu. Rev. Phys. Chem.*, 2005, **56**, 389.
25. S. E. Feller, *Methods Mol. Biol.*, 2007, **400**, 89.
26. J. Hajdu, *Curr. Opin. Struct. Biol.*, 2000, **10**, 569.
27. R. Neutze, G. Huldt, J. Hajdu and D. van der Spoel, *Rad. Phys. Chem.*, 2004, **71**, 905.
28. N. H. Chapman, S. P. Hau-Riege, M. J. Bogan, S. Bajt, A. Barty, S. Boutet, S. Marchesini, M. Frank, B. W. Woods, W. H. Benner, R. A. London, U. Rohner, A. Szöke, E. Spiller, T. Möller, C. Bostedt, D. A. Shapiro, M. Kuhlmann, R. Treusch, E. Plönjes, F. Burmeister, M. Bergh, C. Caleman, G. Huldt, M. M. Seibert and J. Hajdu, *Nature*, 2007, **448**, 676.

29. M. J. Bogan, W. H. Benner, S. Boutet, U. Rohner, M. Frank, A. Barty, M. M. Seibert, F. Maia, S. Marchesini, S. Bajt, B. Woods, V. Riot, S. P. Hau-Riege, M. Svenda, E. Marklund, E. Spiller, J. Hajdu and H. N. Chapman, *Nano. Lett.*, 2008, **8**, 310.
30. J. Drenth, *Principles of Protein X-ray Crystallography*, Springer, New York, NY, 1999.
31. D. Blow, *Outline of Crystallography for Biologists*, Oxford University Press, New York, NY, 2002.
32. G. Rhodes, *Crystallography Made Crystal Clear*, Academic Press, Burlington, VT, 2006.
33. P. R. Evans, *Acta Crystallogr. D. Biol. Crystallogr.*, 2007, **63**, 58.
34. M. Jaskolski, M. Gilski, Z. Dauter and A. Wlodawer, *Acta Crystallogr. D. Bio. Crystallogr.*, 2007, **63**, 611.
35. A. T. Brunger, *Nature*, 1992, **355**, 472.
36. O. Carugo, *Acta Crystallogr. D. Biol. Crystallogr.*, 1999, **55**, 479.
37. P. A. Karplus, *Curr. Opin. Struct. Biol.*, 1994, **4**, 770.
38. R. Berisio, V. S. Lamzin, F. Sica, K. S. Wilson, A. Zagari and L. Mazzarella, *J. Mol. Biol.*, 1999, **292**, 845.
39. E. A. Merritt, *Acta Crystallogr. D. Bio. Crystallogr.*, 1999, **55**, 1109.
40. A. Wlodawer, W. Minor, Z. Dauter and M. Jaskolski, *FEBS J.*, 2008, **275**, 1.
41. E. N. Brown and S. Ramaswamy, *Acta Crystallogr. D. Bio. Crystallogr.*, 2007, **63**, 941.
42. S. Borman, *Chem. Eng. News*, 2007, **85**, 11.
43. Z. Yuan, J. Zhao and Z. X. Wang, *Protein Eng.*, 2003, **16**, 109.
44. E. D. Getzoff, K. N. Gutwin and U. K. Genick, *Nat. Struct. Biol.*, 2003, **10**, 663.
45. J. Painter and E. A. Merritt, *Acta Crystallogr. D. Bio. Crystallogr.*, 2006, **62**, 439.
46. A. Korostelev and H. F. Noller, *J. Mol. Biol.*, 2007, **373**, 1058.
47. D. Bourgeois and A. Royant, *Curr. Opin. Struct. Biol.*, 2005, **15**, 538.
48. X. Ding, B. F. Rasmussen and G. A. Petsko, *D. Ringe Bioorg. Chem.*, 2006, **34**, 410.
49. R. Callender and R. B. Dyer, *Chem. Rev.*, 2006, **106**, 3031.
50. I. Schlichting and R. S. Goody, *Method. Enzymol.*, 1997, **277**, 467–490.
51. E. Garman, *Curr. Opin. Struct. Biol.*, 2003, **13**, 545.
52. I. Zegers, R. Loris, G. Dehollander, A. Fattah Haikal, F. Poortmans, J. Steyaert and L. Wyns, *Nat. Struct. Biol.*, 1998, **5**, 280.
53. I. Leiros, S. McSweeney and E. Hough, *J. Mol. Biol.*, 2004, **339**, 805.
54. D. J. Heyes and C. N. Hunter, *Trends Biochem. Sci.*, 2005, **30**, 642.
55. L. O. Essen and T. Klar, *Cell. Mol. Life Sci.*, 2006, **63**, 1266.
56. D. Zhong, *Curr. Opin. Chem. Biol.*, 2007, **11**, 174.
57. K. J. Hellingwerf, *Antonie Van Leeuwenhoek*, 2002, **81**, 51.
58. D. Bourgeois and M. Weik, *New perspectives in kinetic protein crystallography using caged compounds*, R. Givens, (ed.), in *Dynamic Studies in Biology*, Wiley-VCH, 2005, pp. 410–434.

59. T. Ursby, M. Weik, E. Fioravanti, M. Delarue, M. Goeldner and D. Bourgeois, *Acta Crystallogr. D. Biol. Crystallogr.*, 2002, **58**, 607.
60. R. B. Ravelli and E. F. Garman, *Curr. Opin. Struct. Biol.*, 2006, **16**, 624.
61. G. I. Berglund, G. H. Carlsson, A. T. Smith, H. Szoke, A. Henriksen and J. Hajdu, *Nature*, 2002, **417**, 463.
62. V. Adam, A. Royant, V. Niviere, F. P. Molina-Heredia and D. Bourgeois, *Structure*, 2004, **12**, 1729.
63. A. R. Pearson, A. Mozzarelli and G. L. Rossi, *Curr. Opin. Struct. Biol.*, 2004, **14**, 656.
64. A. R. Pearson, R. Pahl, E. G. Kovaleva, V. L. Davidson and C. M. Wilmot, *J. Synchrotron Radiat.*, 2007, **14**, 92.
65. T. Beitlich, K. Kühnel, C. Schulze-Briese, R. L. Shoeman and I. Schlichting, *J. Synchrotron Radiat.*, 2007, **14**, 11.
66. G. Katona, P. Carpentier, V. Nivière, P. Amara, V. Adam, J. Ohana, N. Tsanov and N. D. Bourgeois, *Science*, 2007, **316**, 449.
67. M. Schmidt, R. Pahl, V. Srajer, S. Anderson, Z. Ren, H. Ihee, S. Rajagopal and K. Moffat, *Proc. Natl. Acad. Sci. USA*, 2004, **101**, 4799.
68. S. Rajagopal, S. Anderson, V. Srajer, M. Schmidt, R. Pahl, K. Moffat, *Structure*, **2005**, *13*, 55.
69. D. Bourgeois, B. Vallone, F. Schotte, A. Arcovito, A. E. Miele, G. Sciara, M. Wulff, P. Anfinrud and M. Brunori, *Proc. Natl. Acad. Sci. USA*, 2003, **100**, 8704.
70. F. Schotte, M. Lim, T. A. Jackson, A. V. Smirnov, J. Soman, J. S. Olson, G. N. Phillips Jr, M. Wulff and P. A. Anfinrud, *Science*, 2003, **300**, 1944.
71. M. Nozaki, *Methods Enzymol.*, 1987, **142**, 650.
72. A. Y. Chistoserdov, *Microbiology*, 2001, **147**, 2195.
73. V. L. Davidson, in *Principles and Applications of Quinoproteins*, ed. V. L. Davidson, Marcel Dekker Inc, New York, 1993, pp. 73–95.
74. Y. L. Hyun and V. L. Davidson, *Biochemistry*, 1995, **34**, 816.
75. S. Govindaraj, E. Eisenstein, L. H. Jones, J. Sanders-Loehr, A. Y. Chistoserdov, V. L. Davidson and S. L. Edwards, *J. Bacteriol.*, 1994, **176**, 2922.
76. N. Sukumar, Z.-W. Chen, D. Ferrari, A. Merli, G. L. Rossi, H. D. Bellamy, A. Y. Chistoserdov, V. L. Davidson and F. S. Mathews, *Biochemistry*, 2006, **45**, 13500.
77. M. Husain and V. L. Davidson, *J. Biol. Chem.*, 1985, **260**, 14626.
78. L. Masgrau, A. Roujeinikova, L. O. Johannissen, P. Hothi, J. Basran, K. E. Ranaghan, A. J. Mulholland, M. J. Sutcliffe, N.S. Scrutton and D. Leys, *Science*, 2006, **312**, 237.
79. A. Roujeinikova, P. Hothi, L. Masgrau, M. J. Sutcliffe, N. S. Scrutton and D. Leys, *J. Biol. Chem.*, 2007, **282**, 23766.
80. A. Roujeinikova, N. S. Scrutton and D. Leys, *J. Biol. Chem.*, 2006, **281**, 40264.
81. G. R. Bishop, Z. Zhu, T. L. Whitehead, R. P. Hicks and V. L. Davidson, *Biochem. J.*, 1998, **330**, 1159.
82. L. Masgrau, K. E. Ranaghan, N. S. Scrutton, A. J. Mulholland and M. J. Sutcliffe, *J. Phys. Chem. B*, 2007, **111**, 3032.

83. L. O. Johannissen, S. Hay, N. S. Scrutton and M. J. Sutcliffe, *J. Phys. Chem. B*, 2007, **111**, 2631.
84. H. L. Messihah, N. C. Bruce, B. M. Sattelle, M. J. Sutcliffe, A. W. Munro and N. S. Scrutton, *J. Biol. Chem.*, 2005, **280**, 27103.
85. N. D. Madani, P. J. Malloy, P. Rodriguez-Pombo, A. V. Krishnan and D. Feldman, *Proc. Natl. Acad. Sci. USA*, 1994, **91**, 922.
86. C. E. French, S. Nicklin and N. C. Bruce, *J. Bacteriol.*, 1997, **178**, 6623.
87. J. R. Snape, N. A. Walkley, A. P. Morby, S. Nicklin and G. F. White, *J. Bacteriol.*, 1997, **179**, 7796.
88. J. Basran, R. J. Harris, M. J. Sutcliffe and N. S. Scrutton, *J. Biol. Chem.*, 2003, **278**, 43973.
89. C. R. Pudney, S. Hay, M. J. Sutcliffe and N. S. Scrutton, *J. Am. Chem. Soc.*, 2006, **128**, 14053.
90. S. Hay, M. J. Sutcliffe and N. S. Scrutton, *Proc. Natl. Acad. Sci. USA*, 2007, **104**, 507.
91. C. R. Pudney, S. Hay, J. Pang, C. Costello, D. Leys, M. J. Sutcliffe and N. S. Scrutton, *J. Am. Chem. Soc.*, 2007, **129**, 13949.
92. M. W. Fraaije and A. Mattevi, *Trends Biochem. Sci.*, 2000, **25**, 126.

CHAPTER 13

The Strengths and Weaknesses of Model Reactions for the Assessment of Tunnelling in Enzymic Reactions

RICHARD L. SCHOWEN

Departments of Chemistry, Molecular Biosciences, and Pharmaceutical Chemistry, University of Kansas, Lawrence, KS, USA

Chemical reactions occurring *in vivo* take place in a complex environment, and reactions of interest to readers of this book commonly occur in the active site of an enzyme. The biological environment, including active sites, modifies some or all of the properties of the reaction so that its thermodynamics, kinetics, stoichiometry, stereochemistry, *etc.*, may be quite different from the corresponding properties of apparently similar reactions in the absence of the enzyme.

The essence of enzyme-catalysed reactions is that they proceed far more rapidly than in the absence of the enzyme. The catalytic power of enzymes is large, producing accelerations of as much as 20 to 25 orders of magnitude,^{1–4} and is thought to have increased by natural selection during the period of 3–4 billion years since the origin of life on the Earth.^{5–8} One result of large catalytic accelerations by enzymes is a high chemical signal-to-noise ratio in the organismic physiology: only very little of the physiological reaction (possibly as little as 1 part in 20 to 25 orders of magnitude) occurs nonenzymically. Thus, the organismic chemistry is that, and only that, produced by natural selection.

Because of this fact, the organismic chemistry is reliable and stable, readily altered by enzyme mutations and thus subject to evolution, and can also be made subject to delicate regulation by the coevolution of enzyme-regulatory systems.^{9,10}

In the last two decades, the issue of quantum tunnelling as a catalytic feature of enzymic reactions has arisen and a corpus of experimental, theoretical, and conceptual studies has appeared. Nearly all of this work is summarised in the other chapters of the book now before the reader. In addition, the reader will find it useful to consult the publications¹¹ issuing from a Discussion meeting of the Royal Society, held in November 2005, as well as a thematic issue¹² of *Chemical Reviews*. Valuable reviews of quantum tunnelling in enzymic and model reactions were presented in a recently published work¹³ on “Hydrogen-Transfer Reactions” especially in the chapters of Part III, Quantum Tunnelling and Protein Dynamics,¹⁴ and in chapters by Benkovic and Hammes-Schiffer,¹⁵ and by Banerjee, Truhlar, Dybala-Defratyka, and Paneth.¹⁶ The present chapter addresses some of the issues dealt with in the same work by Amyes and Richard,¹⁷ Kirby,¹⁸ Schöneich,¹⁹ and Schowen.²⁰ The present chapter is meant to present a self-contained treatment, but it will duplicate the cited articles as little as possible.

13.1 Model Reactions for Biochemical Processes^{21–23}

When one gives a value for the acceleration produced by an enzyme (*e.g.*, “20 to 25 orders of magnitude”), one is reporting the ratio of a rate constant for the enzymic reactionⁱ to the rate constant of a suitable nonenzymic (“uncatalysed”) reaction. This ratio is a simple, quantitative measure of the power of the enzyme as a catalyst under specific circumstances. Enzymic catalytic power and the means by which (a) it has developed under evolutionary pressure, and (b) it is generated by the various structural and dynamical properties of the enzyme molecule, are matters of intense interest in chemistry and biology.

To specify the catalytic power of an enzyme therefore presupposes a knowledge of the kinetics of the enzymic reaction and the kinetics of “a suitable nonenzymic (‘uncatalysed’) reaction.” A quick calculation illustrates that obtaining the latter knowledge may be far from simple. If a very good enzyme indeed were to cause its target reaction to occur as fast as possible, thus at the same rate as a typical molecular vibration (about 10^{13} s^{-1}) then a catalytic acceleration of 10^{20} means the nonenzymic reaction will occur with a rate constant of 10^{-7} s^{-1} or a half-life time of 80 days. To follow such a reaction for five half-life times would – dauntingly – require data collection for more than a year. Enzymes with more common rate constants, like 10^3 s^{-1} , and a similar

ⁱAll enzymic reactions have at least two rate constants, in the simplest case denoted k_{cat} (a first order rate constant) and k_{cat}/K_M (a second order rate constant). Radzicka and Wolfenden⁴ have suggested that the ratio of k_{cat} to the “uncatalysed” rate constant be called the *rate enhancement* and that the ratio of k_{cat}/K_M to the “uncatalysed” rate constant be called the *catalytic proficiency*. The distinction and its significance have been dealt with quite tediously by R.L. Schowen in ref. 30, pp 767–768.

catalytic acceleration would require data-collection periods of 10^{10} years. In such cases, measurements of the nonenzymic reaction clearly must be made under drastic, forcing conditions, *e.g.* high temperatures or unusual solvents, with the findings then being carefully extrapolated to enzymic reaction conditions. Few scientists have been willing or able to make the requisite investments of time, energy, and other resources to obtain such data. An exception is fortunately provided by Richard Wolfenden and his coworkers (for recent examples, see refs 24–26), to whom enzymology owes a good deal of what is known about the kinetics of useful nonenzymic reactions.

Nonenzymic reactions that are related in various ways to enzyme-catalysed reactions are often known as *models* or *model reactions* for the enzymic reaction.^{21–23} The kinetics of such reactions can provide the “uncatalysed rate constant” for the calculation of enzymic catalytic power, and studies of their mechanisms can provide extraordinarily useful baselines for thinking about the ways in which enzymes achieve their catalytic power.

For many of us, the ideally suitable model reaction is one that passes through a transition state that is as nearly as possible structurally identical to the transition state for enzyme action, in its substrate-derived parts. Such a model reaction would seem nearly equivalent to the enzymic reaction except that the enzyme and its apparatus of catalytic acceleration are missing. One might then begin to imagine how each element of the enzyme structure interacts in the catalytic transition state with the substrate-derived fragments and thereby undertake the construction of an account, interaction by interaction, of the enzyme-induced reduction in the free energy of the transition state or, equivalently, the reduction in the height of the free-energy barrier to reaction.

The ideal can rarely (perhaps never) be fully achieved, but some reasonable approximations can sometimes be reached, and in fact the cases of most interest for many readers of this book – that is, reactions that may involve hydrogen tunnelling – are among them. The examples include enzymic reactions that correspond to mechanistically very well-characterised processes where the potential for various kinds of catalysis and the nature of structure-reactivity relationships are well established. Here, it may not generally be possible to simulate the active-site situation very persuasively but even if the nonenzymic system used is a remote and intrinsically unsatisfying simulacrum of the enzymic system, the characteristics of these reactions have been so thoroughly studied that extrapolations from poor model reactions to active-site structures and conditions can be a rational expectation.

The examples to be exploited in this chapter are among those enzymic reactions in which cofactors such as nicotinamide species, flavins/dihydroflavins, cobalamin species, thiamin diphosphate, pyridoxal species, and redox cofactors formed in post-translational reactions are deeply involved in the major chemical transformations. In a reasonable number of these cases, cofactor reactions can be examined in the absence of the enzyme. While the needed extrapolation to active-site reactions may be more complex than it would superficially seem, the relevance and thus the utility of the model-reaction results remains considerable.

Hereafter in this chapter, two such cases will be explored for the purpose of considering what can be deduced, and what cannot be deduced, from comparisons of model reactions with enzymic reactions.

13.2 Model Reactions Relevant to Enzymic Tunnelling

Brief further general considerations are in order for the specific model reactions related to systems addressed in this volume. Quantum tunnelling in enzyme catalysis has been demonstrated or reasonably hypothesised chiefly for hydrogen-transfer (H-transfer) reactions. The entity being transferred is commonly categorised as a proton H^+ ; a hydrogen atom, H^\bullet ; or a hydride ion, H^\ominus . This is a useful or at least pictorially convenient formal distinction although the concept of proton-coupled electron transfer renders it problematic (see the chapter by Nocera in this volume). Tunnelling has been considered as a mechanism of enzymic H-transfer in all three categories.

13.3 Isotope Effect Temperature Dependences²⁷ and the Configurational-Search Framework (CSF) for their Interpretation

Both in nonenzymic and enzymic systems, isotope effects and the temperature dependence of isotope effects in H-transfer reactions have served in studies near room temperature as the main diagnostic criteria for tunnelling. In order to simplify the discussions of the comparison of model reactions with enzymic reactions, I shall adopt a simplistic pictorial and qualitative version of an account that has been used in a far more scrupulous and quantitative way, mainly by Allemann, Klinman, Kohen, Scrutton, Sutcliffe, and their co-worker (see for further enlightenment the chapters in this volume by Hammes-Schiffer, Kohen, Klinman, Sutcliffe, Truhlar, and Warshel). I shall refer to this account in its simplified version as the *configurational-search framework* or CSF.

There are three general categories of experimental observations on isotope effects and their temperature dependences. Table 13.1 shows the main points involved. The three categories of observations^{28 30} are:

- (1) the traditionally expected temperature dependence, with the entire isotope effect reflected in a difference in the enthalpies or energies of activation and thus possessing a negligible entropic component;
- (2) an underdependence of the isotope effect on temperature in which the isotopic difference in the enthalpies of activation is smaller than for the traditional model;
- (3) an overdependence of the isotope effect on temperature, in which the isotopic difference in the enthalpies of activation is larger than for the traditional model.

Table 13.1 Three categories of isotope effect data and their significance within the configurational search framework (CSF).

<i>Reaction property</i>	<i>Observation</i>	<i>Significance</i>
$k_{\text{H}}/k_{\text{D}}$ near 25 °C	values up to around 7–10 for C–H(D) fission consistent with reactant state <i>vs.</i> transition state isotopic zero point energy (ZPE) differences.	Values in this range (called below “small isotope effects”) do not indicate but also do not preclude tunnelling.
$(\Delta H^{\ddagger}_{\text{D}} - \Delta H^{\ddagger}_{\text{H}})$ $= (E_{\text{aD}} - E_{\text{aH}})$	values considerably larger (25, 50, 100) become difficult to explain on a simple nontunnelling model. $= RT \ln [(k_{\text{H}}/k_{\text{D}})_T]$ traditionally dependent on temperature	Values so large tend to suggest tunnelling as a possible explanation (called below “large isotope effects”). Consistent with absence or presence of tunnelling for small isotope effects but consistent only with substantial tunnelling for large isotope effects.
	$< RT \ln [(k_{\text{H}}/k_{\text{D}})_T]$ under-dependent on temperature	Consistent with dynamically assisted, largely isotope independent search for a preorganised tunnelling configuration, followed by isotope dependent tunnelling.
	$> RT \ln [(k_{\text{H}}/k_{\text{D}})_T]$ over-dependent on temperature	Consistent with a dual search for a tunnelling configuration with resonant energy levels and short tunnelling distance, followed by tunnelling.
$(\Delta S^{\ddagger}_{\text{D}} - \Delta S^{\ddagger}_{\text{H}}) = R \ln (A_{\text{D}}/A_{\text{H}})$	$= \text{ca. } 0$ ($A_{\text{D}}/A_{\text{H}} = 1$) traditionally dependent on temperature	Consistent with absence or presence of tunnelling for small isotope effects but consistent with substantial tunnelling for large isotope effects.
	$< \text{ca. } 0$ ($A_{\text{D}}/A_{\text{H}} < 1$) under-dependent on temperature	Consistent with dynamically assisted, largely isotope independent search for a preorganised tunnelling configuration, followed by isotope dependent tunnelling.
	$> \text{ca. } 0$ ($A_{\text{D}}/A_{\text{H}} > 1$) over-dependent on temperature	Consistent with a dual search for a tunnelling configuration with resonant energy levels and short tunnelling distance, followed by tunnelling.

Each of these categories of isotopic enthalpy relationships necessarily entails entropic relationships, as shown in Table 13.1. Within the configuration-search framework, each category corresponds to specific circumstances with respect to the physical mechanism of reaction.

13.3.1 The Traditionally Dependent Category

Before evidence of widespread quantum tunnelling in hydrogen-transfer reactions became available, the most common model for isotope effects in such reactions was a simple zero-point energy model (see the review of this model by Melander and Saunders in ref. 31, Section 2.2.2). All or nearly all of the isotope effect was taken to reflect the total isotopic zero-point energy difference for vibrational modes of the reactant state, diminished by the total isotopic zero-point energy difference for the *stable* vibrational modes of the transition state. Such a model generates maximal H/D isotope effects of 7–10 near room temperature. The entire isotope effect will arise from the isotopic difference in enthalpies of activation with the entropies of activation being equal or nearly equal for the isotopic reactions, thus:

$$\begin{aligned} (\Delta H_{\text{D}}^{\ddagger} - \Delta H_{\text{H}}^{\ddagger}) &= (E_{\text{aD}} - E_{\text{aH}}) = RT \ln[(k_{\text{H}}/k_{\text{D}})_T], \\ (\Delta S_{\text{D}}^{\ddagger} - \Delta S_{\text{H}}^{\ddagger}) &= R \ln(A_{\text{D}}/A_{\text{H}}) = 0. \end{aligned}$$

These conditions yield the customary result that the isotope effect decreases as temperature rises, becoming roughly unity at infinite temperature.³¹

Experimental observations in this class therefore are consistent with a reaction in which no tunnelling is occurring if the isotope effect near room temperature is in the range of 7–10 or less. However, much larger isotope effects have been observed with the traditional temperature dependence (see the chapter by Klinman in this volume), almost certainly indicative of tunnelling, so that even the cases consistent with nontunnelling reaction must also be considered consistent with tunnelling as well.

13.3.2 The Underdependent Tunnelling Category

Underdependence on temperature of an isotope effect refers to a difference in isotopic enthalpies of activation smaller than the traditional expectation, $(\Delta H_{\text{D}}^{\ddagger} - \Delta H_{\text{H}}^{\ddagger}) < RT \ln[(k_{\text{H}}/k_{\text{D}})_T]$.

Because this condition will generate isotope effects too small at higher temperatures, there must be a compensating condition on the entropy difference such that $(\Delta S_{\text{D}}^{\ddagger} - \Delta S_{\text{H}}^{\ddagger}) < 0$.

In the limit at which $(\Delta H_{\text{D}}^{\ddagger} - \Delta H_{\text{H}}^{\ddagger}) = 0$, the isotopic enthalpies of activation will be equal and the isotope effect will become independent of temperature, although the isotopic rate constants themselves may ($\Delta H_{\text{D}}^{\ddagger} = \Delta H_{\text{H}}^{\ddagger} > 0$) or may not ($\Delta H_{\text{D}}^{\ddagger} = \Delta H_{\text{H}}^{\ddagger} = 0$) be dependent on temperature. In either case, $(\Delta S_{\text{H}}^{\ddagger} - \Delta S_{\text{D}}^{\ddagger}) = R \ln[(k_{\text{H}}/k_{\text{D}})]$, where $(k_{\text{H}}/k_{\text{D}})$ is the temperature-independent isotope effect. In Arrhenius terms, $A_{\text{H}}/A_{\text{D}} = (k_{\text{H}}/k_{\text{D}})$.

Underdependence results from cases in which the reaction readily and reversibly enters a state, by means of a vibrational exploration, in which the reactant and product energy levels match and in which the hydrogen-transfer distance is short enough that the H and D nuclear wavefunctions in reactant and product states overlap sufficiently to allow tunnelling. Then, the reaction proceeds by tunnelling between these matched levels. The vibrational search makes a contribution to the enthalpies of activation for both isotopic species, perhaps amounting to their entirety, but it is the same or nearly the same for both. The isotopic probability ratio for tunnelling of H and D then gives the apparently entropic contribution, amounting to much of or the whole of the isotope effect. The result is an isotope effect derived from the relative tunnelling probabilities, which are temperature independent, combined with an enthalpy of activation that is isotope independent and derived from the energetic cost of the vibrational search. When the reactant state itself fulfils the requirements for efficient tunnelling, no initial search is required and the reaction proceeds by tunnelling with no activation energy. The location of an appropriate tunnelling configuration as just described is most likely to occur when the configuration is preorganised in the reaction environment, as could easily be the case in evolved enzymes. In model reactions or nonenzymic reactions, evidence corresponding to preorganised tunnelling configurations is rare (for an exception see Kwart *et al.*³²) and the customary observations involve an overdependence of the isotope effect on temperature,^{33–35} as described below.

Because the isotope effect arises within the configurational-search framework from the isotopic tunnelling-probability ratio for the configuration in which the search culminates, it does not derive from the reactant zero-point energy difference. Instead it results from the different reactant–product wavefunction overlaps for the two isotopic atoms. Thus there is no zero-point energy limitation on the value of the isotope effect, which can be quite large, *e.g.*, of the order of hundreds. Indeed, any isotope effect, large or small, is consistent with tunnelling on this model.

13.3.3 The Overdependent Tunnelling Category

Overdependence on temperature of an isotope effect refers to a difference in isotopic enthalpies of activation larger than the traditional expectation, $(\Delta H_{\text{D}}^{\ddagger} - \Delta H_{\text{H}}^{\ddagger}) > RT \ln[(k_{\text{H}}/k_{\text{D}})_T]$.

Because this condition would tend to generate isotope effects too large at higher temperatures, there must be a compensating condition on the entropy difference such that $(\Delta S_{\text{D}}^{\ddagger} - \Delta S_{\text{H}}^{\ddagger}) > 0$.

Inevitably the Eyring plots for the two species must cross at $T_c = (\Delta H_{\text{D}}^{\ddagger} - \Delta H_{\text{H}}^{\ddagger}) / (\Delta S_{\text{D}}^{\ddagger} - \Delta S_{\text{H}}^{\ddagger})$. The entropy condition is often expressed in terms of an Arrhenius treatment, $A_{\text{D}} > A_{\text{H}}$, in place of the simple expectation that $A_{\text{D}} = A_{\text{H}}$.

Overdependence results when an initial vibrational search locates a tunnelling state where the energy-matching (resonance) criterion is met but the

distance over which tunnelling must occur is still too large for effective tunnelling. A further search is needed for a state that combines a sufficiently short tunnelling distance with an energy-level match. The first search may well be essentially isotope independent, but the energetic cost of the further search may be quite different for the two isotopic cases. This is because the narrower nuclear wavefunction for deuterium may place greater energetic demands on attaining a state with an adequately short tunnelling distance. The result may then be that the enthalpy of activation for the heavier isotopic case is considerable larger than for the lighter isotopic case. The apparent isotopic entropy difference then combines the relative tunnelling probabilities with the result of extrapolating to infinite temperature the linear segment of the Arrhenius or Eyring plots near the experimental temperature, often producing $A_D > A_H$ or $\Delta S^\ddagger_D > \Delta S^\ddagger_H$.

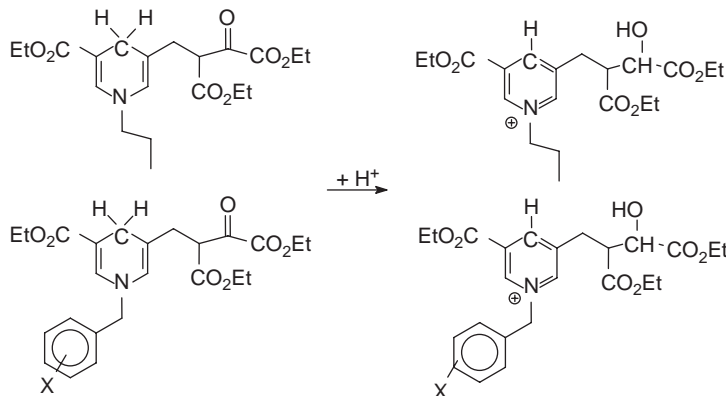
13.4 Example 1. Hydride Transfer in a Thermophilic Alcohol Dehydrogenase

The first enzymic reaction for which hydrogen tunnelling was suggested and then demonstrated, by Klinman and her coworkers, was the action of alcohol dehydrogenase.³⁶ There are a number of different alcohol dehydrogenases and a larger number of other dehydrogenases in which a hydride ion is transferred between a nicotinamide cofactor and the carbonyl/alcohol group of a substrate, cofactor and substrate being bound in proximity in a ternary complex with the enzyme.³⁷

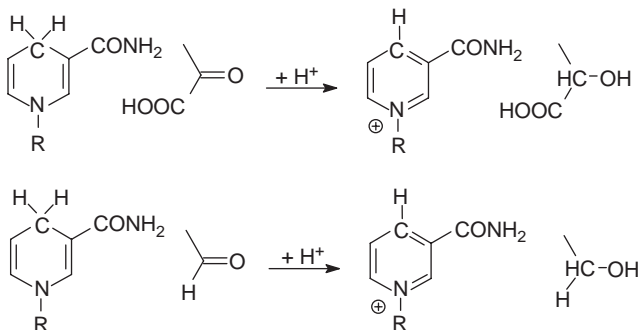
13.4.1 The Kirby Walwyn Intramolecular Model Reaction

A model reaction for the hydride-transfer event was designed by Kirby and Walwyn for the specific case of lactate dehydrogenase.^{38,39} They constructed an intramolecular reaction between a nicotinamide-like moiety and a lactate-like moiety, held in proximity by a covalent tether (Figure 13.1; see also Table 13.2). By a thoughtful choice of reaction conditions, Kirby and Walwyn succeeded in achieving an efficient intramolecular H-transfer reaction (ketone reduction) in readily measured periods of time. The measured rate constants for the various cases fall within the limits $1\text{--}100 \times 10^{-3}\text{ s}^{-1}$. This range then provides a baseline “uncatalysed” rate constant for comparison with k_{cat} values (or values of other kinetic parameters) for any active-site reaction of nicotinamide cofactors to reduce carbonyl species of adequate electronic and steric similarity.

Studies of the nicotinamide-dependent enzyme S-adenosylhomocysteine hydrolase,⁴⁰ in which rate constants were measured for both productive and abortive^{41–43} hydride-transfer reactions, provide values of 11 s^{-1} for productive (catalysed) and $1.5 \times 10^{-3}\text{ s}^{-1}$ (abortive, uncatalysed) processes. Because the rate constant for abortive reduction is essentially the same as that for the intramolecular model reaction (see above), it is apparent that the enzyme is exerting no catalytic influence other than that deriving from the simple



Kirby-Walwyn model reaction for lactate dehydrogenase



Enzyme active site reactions for lactate dehydrogenase (upper) and alcohol dehydrogenase (lower)

Figure 13.1 At the top, the intramolecular hydride transfer reactions of two series of compounds designed by Kirby and Walwyn as models for lactate dehydrogenase, for which the active site transformation is shown at the bottom, along with the similar transformation of alcohol dehydrogenase.

intramolecular character of the reaction in the enzyme-active site. The productive reduction on the other hand experiences an acceleration beyond the proximity effect of $(11 \text{ s}^{-1})/(1.5 \times 10^{-3} \text{ s}^{-1})$ or about 7×10^3 . It can then be concluded that this enzyme accelerates the hydride-transfer steps by 3–4 orders of magnitude over the proximity effect. The significance of this work for the alcohol-dehydrogenase case is that it provides a rate constant of about 10^{-3} s^{-1} (at the lower end of the Kirby–Walwyn range) as a rate constant for hydride transfer from NADH to a ketone, very likely catalysed only by the approximation of the two reactants.

Table 13.2 Comparison of the properties of nonenzymic (model) and enzymic reactions related to alcohol-dehydrogenase catalysis.

<i>Reaction property</i>	<i>Nonenzymic reaction</i>		<i>Enzymic reaction</i>	
k_H near 25 °C (s ⁻¹)	ca. 10 ⁻³ s ⁻¹ (Kirby Walwyn model) ^a		k_{cat}	10 s ⁻¹ rate enhancement ca. 10 ⁴
k_H/k_D near 25 °C	5.8 (reduction by 4,4 d ₂ NADH of N benzylacridinium ion)		4.5 (oxidation of 1,1 d ₂ benzyl alcohol by NAD ⁺)	
	protio	deutero	protio	deutero
ΔH^\ddagger , kcal/mol	6.6 ± 0.1	8.2 ± 0.1	23.6 ± 0.6	31.4 ± .7
A , s ⁻¹	9.8 ± 2.0 × 10 ⁷	4.1 ± 0.8 × 10 ⁸	ill determined ^b	ill determined ^b
A_H/A_D , E_{aD} , E_{aH} , kcal/mol	1/4.3, 1.8 ± 0.2		small but ill determined,	7.8 ± 1.8

^aSee text for discussion.

^bIn both competitive and noncompetitive experiments, results in this temperature range extrapolated to generate large errors in A .

13.4.2 The Powell Bruice Tunnelling Model Reaction^{44,45}

Very effective model reactions for nicotinamide-dependent enzymic reactions, with particular relevance to catalysis of tunnelling by enzymes, were provided by Powell and Bruice in 1983.⁴⁵ The Powell-Bruice studies made use of reasonable analogues of NADH (e.g., N-benzylnicotinamide species) as reductants but the most relevant studies employed acridinium ions rather than ketones or aldehydes as hydride acceptors. Since the reactions were bimolecular, the rate constants can be used only in a complex manner to estimate a catalytic acceleration (see ref. 20, Chart 4.1, and the appendix to ref. 20, Section 4.8), so attention will instead be centred on the role of these studies to illuminate the catalysis of tunnelling in enzymic reactions such as the action of alcohol dehydrogenases.

The most important evidence is the temperature dependence of the combined primary and secondary isotope effects for the reduction of the N-methylacridinium cation by 4,4-d₂-N-p-tolyl dihydronicotinamide and the corresponding diprotio compound. Near 25 °C, the isotope effect k_{HH}/k_{DD} is a little less than 6, so that the traditional expectation for $(\Delta H^\ddagger_D - \Delta H^\ddagger_H)$ would be about 4–5 kJ/mol. In fact the value is $(\Delta H^\ddagger_D - \Delta H^\ddagger_H) = 39.5 - 31.9 = 7.6$ kJ/mol, a quite clear case of overdependence. Indeed, if the isotopic entropies were equal, the enthalpy difference would generate an isotope effect of around 22 at 25 °C, rather than around 6 as observed. Extrapolation of the data, however, shows that the linear Arrhenius plots cross between 500 K and 600 K. This leads to the condition $(\Delta S^\ddagger_D - \Delta S^\ddagger_H) > 0$ or $A_D > A_H$. Indeed the calculated value of A_D/A_H is 4.3.

Powell and Bruice treated their data by the then-state-of-the-art technique of the Bell tunnelling correction, which suggested that the extent of tunnelling in the diprotio reaction was such that the reaction was accelerated by around 3-fold. This would mean that a tunnelling event is responsible for about 3/4 of the product formed. Modern quantitative treatments have not yet been applied to these data. But if we take the entire reaction to proceed by tunnelling and

apply the pictorial version of the CSF, the isotopic enthalpies of activation of 39.5 (D) and 31.9 (H) kJ/mol result from the energetic cost of achieving, first, a potential tunnelling state with energy levels matched between reactant and product states (an isotope-independent search) and then an isotope-dependent search for a state in which the tunnelling distance is short enough for efficient reaction, with the cost being greater for the less delocalised D nucleus. The sum of these costs generates the observed enthalpies. The tunnelling probability for the more delocalised H should be greater than that for D so that the Arrhenius intercept at infinite temperature should have $A_H > A_D$. Instead, the greater slope of the Arrhenius line for D, because of the greater cost of locating a shorter tunnelling distance for D, reverses the expected intercepts and accounts for the observation that $A_D = 4.3A_H$.

It seems a very reasonable feature of the CSF that this category of isotope-effect signature (overdependence on temperature, resulting from a complicated and partially isotope-dependent search for a workable tunnel configuration in a system where little or no preorganisation exists) is exactly that historically noted in nonenzymic systems,^{33,34} where preorganisation would arise only by coincidence, unless deliberately designed by the experimenter.

13.4.3 Enzymic Tunnelling in Alcohol Dehydrogenases

Nagel and Klinman²⁷ have reviewed, among many other examples, the history of tunnelling studies on alcohol dehydrogenases. Under appropriate circumstances, alcohol dehydrogenases exhibit both of the forms of isotope-effect temperature dependence that function as signatures of tunnelling, overdependence of the isotope effect on temperature, signalling tunnelling in a relatively unorganised environment, and underdependence of the isotope effect on temperature, signalling tunnelling in a preorganised environment.

We may take as a single example here, for comparison with the studies of Powell and Bruice, the examination⁴⁶ by Kohen *et al.* in 1999 of the temperature dependence of the isotope effect for oxidation of benzyl alcohol (HH or DD) by NAD⁺ with catalysis by the alcohol dehydrogenase of *Bacillus stearothermophilus*, a thermophilic microbe adapted to an ambient temperature around 60 °C. The results are shown in Figure 13.2. Let us focus first on the data between 6 and 30 °C. Table 13.1 compares the enzymic and nonenzymic data. Because the Powell–Bruice model reaction, the reduction of an acridinium cation, is rather structurally distant from a carbonyl reduction, we made use of the Kirby–Walwyn reaction to deduce a catalytic acceleration of about 4 orders of magnitude (note that the data refer to the reaction of the thermophilic enzyme well below its optimum temperature). However, it is notable that both the enzymic and nonenzymic reactions produce the signal of tunnelling associated with tunnelling from a state that must be located by a search for configurations with vibrational levels energetically matched for the reactant and product states, followed by a search to bring the tunnelling distances into sufficiently small values that efficient tunnelling can occur: *i.e.* the signal of an

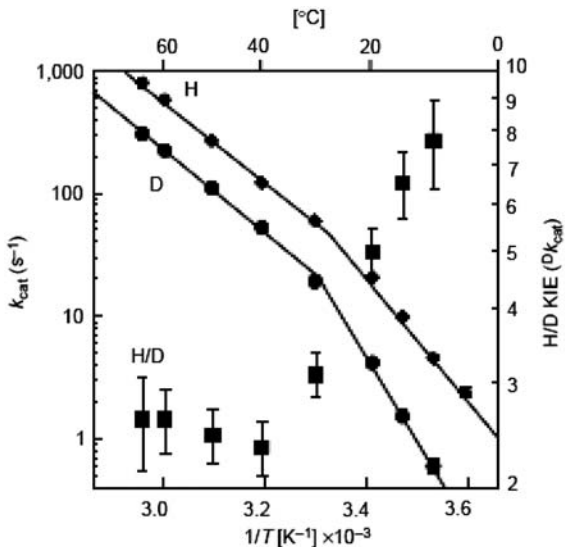


Figure 13.2 Reproduction with permission of Figure 4 from Kohen *et al.* (1999), illustrating the temperature dependence of k_{cat} values (black filled circles) for catalysis by the alcohol dehydrogenase from the thermophilic *Bacillus stearothermophilus* of the oxidation of phenylCH₂OH and phenylCD₂OH by NAD⁺. The black filled squares show the isotope effect. The data below 30 °C do not define A_H/A_D well but the data are clearly overdependent on temperature: the isotope effect around 25 °C is 4.5, implying an enthalpy difference of around 1 kcal/mole, while the lines shown correspond to a difference of 7.8 kcal/mol, which would generate an isotope effect of 400 000. The data above 30 °C give a roughly temperature independent isotope effect of 2.5, corresponding to an enthalpy difference of about 0.6 kcal/mol. The lines drawn indicate a difference of 0.5 kcal/mol. This fails to test the underdependence on temperature but the isotope effects give no discernable trend with temperature and the enthalpy difference is unquestionably far smaller than below 30 °C. The two regimes correspond to two different tunnelling models implied by the configuration search framework (CSF).

overdependence of the isotope effect on temperature. The isotope effects themselves are similar in magnitude (around 6 for the nonenzymic reaction and around 4–5 for the enzymic reaction) and within the allowed range for a simple zero-point energy isotope effect in both cases. Thus the isotope-effect magnitudes alone contain no evidence of tunnelling in either enzymic or nonenzymic reaction. The differences in isotopic enthalpies of activation, however, correspond to larger isotope effects than observed (1.6 kcal/mol for the nonenzymic reaction, which would produce an isotope effect of 14 instead of 6; 7.8 kcal/mol for the enzymic reaction, which would produce an isotope effect of over 10⁵ instead of 4–5). The greater degree of overdependence in the enzymic reaction may reflect the larger energy demands of the requisite searches for tunnelling configurations in the “stiff” environment of a thermophilic enzyme at low

temperatures than is true for the less restrictive solution environment of the nonenzymic reaction.

13.4.4 Model Reactions and the Catalytic Power of Alcohol Dehydrogenase

If the estimate of a catalytic acceleration of *ca.* 4 orders of magnitude is even approximately correct for the low-temperature regime of the *B. stearothermophilis* alcohol dehydrogenase, then it is clear that the enzyme is accelerating by some orders of magnitude a reaction that in nonenzymic systems proceeds mainly or completely by a tunnelling mechanism. Thus, the enzyme is enhancing the rate of tunnelling, *i.e.* the number of molecules that reach the product state by the tunnelling path in a unit of time. The details are best understood by considering the low-temperature regime of the temperature dependence for the enzyme in combination with the high-temperature case, which appears to fit the underdependence category of the CSF, thus an essentially isotope-independent rapid-equilibrium search for a preorganised tunnelling configuration, followed by a rate-limiting tunnel event at this configuration, the isotope effect equal to the temperature-independent probability ratio for isotopic tunnelling.

This mechanism implies the availability of a tunnelling configuration, pre-organised by enzyme evolution, in which energy levels are adjusted to a resonant condition and tunnelling distances are appropriate for efficient tunnelling. Such a preorganised configuration, or the capacity of the enzyme to generate it, should presumably have been evolved for stability or accessibility near the 60 °C optimum for organismic function. Its stability – and thus availability – in other temperature ranges would be uncertain, and would depend on the enthalpy and entropy contributions to the free energy of formation of the preorganised state. The data of Kohen *et al.*, as they proposed, seem consistent with the loss of such a site in the protein structure as the temperature falls below 30 °C. Then, the search for a site meeting both the energy-resonant and tunnelling-distance criteria becomes more energy demanding and isotope dependent.

Extrapolation of the lines in Figure 13.2 from the high-temperature regime to a temperature well within the low-temperature regime, *viz.*, 10 °C, indicates that preservation of the preorganised site at low temperatures would have further accelerated the reaction of the H-substrate by about 2.2-fold, and reaction of the D-substrate by about 5.7-fold. The larger factor for the D-substrate, within the CSF, reflects the greater energetic difficulty in the face of a nonpreorganised active site, of achieving an adequate tunnelling configuration for the D-substrate, with its narrower wavefunction.

The fact that the more general isotope-independent preorganisation seems to account for most of the total catalytic acceleration of around 4 orders of magnitude and the final tunnelling-distance adjustment only about 1 order of magnitude is revealing and would have been difficult, at least for this writer, to

have predicted. It may also be worth noting that the fact that both the model reaction and the enzymic reaction proceed by a tunnelling mechanism, and in the low-temperature regime by somewhat similar tunnelling mechanisms, does *NOT* indicate that the enzyme is failing to enhance the efficiency of the tunnelling event. Furthermore, there is no good basis in isotope-effect theory or practice to assume that more “dramatic” expressions of the temperature-dependence anomalies that signal tunnelling (larger or smaller values of A_H/A_D ; larger or smaller values of the isotopic difference in enthalpies of activation) in any way correlate with the *degree of rate acceleration* effected by enzyme intervention. On the contrary, the magnitudes of these measures may derive from structural or dynamic qualities of the tunnelling process as opposed to its effects on rate, as is suggested by the CSF. In the present case, the biphasic nature of the enzymic temperature dependence strongly suggests that the enzyme indeed intervenes with some success in tuning the tunnelling event throughout the temperature range for greater catalytic power.

The observation of tunnelling in the model reaction *DOES*, however, indicate that the sequence of a two-stage search for energy resonance and for a short tunnelling distance, followed by tunnelling in an appropriate configuration, can be a feature of systems not explicitly targeted by evolutionary design for this mechanism. Alcohol dehydrogenases therefore have not invented the mechanism of hydride transfer by tunnelling but have instead accelerated the existing tunnelling mechanism by several orders of magnitude and then, in the present case, changed the enzymic mechanism near the temperature optimum for the host organism by introduction of a thermally attainable, fully preorganised tunnelling configuration. This mechanistic change does not appear to have been introduced in order to achieve higher rates of hydride transfer. At 60 °C, reaction of the H-substrate occurs with a rate constant of about 600 s^{-1} , that of the D-substrate with a rate constant of about 220 s^{-1} , whereas extrapolation from the low-temperature regime indicates that reaction by the low-temperature mechanism would have occurred for both substrates at around 2000 s^{-1} (the low-temperature isotopic dependences cross near this temperature). Thus, the change in mechanism occurs with a sacrifice of around 3.3-fold in rate for the H-substrate and around 9-fold for the D-substrate. This sacrifice may have been necessitated by the fragility of protein structure at the higher temperature, such that a wide-ranging search of the sort hypothesised at lower temperatures would have pressed the enzyme too close to the unfolding precipice at 60 °C.

13.5 Example 2. Hydrogen-Atom Transfer in Methylmalonyl Coenzyme A Mutase (MCM)

MCM is one of a class of enzymes that rely on the cofactor adenosylcobalamin, in which a cobalt ion is bound at its four equatorial coordination sites into the tetrapyrrole ring of a corrin nucleus, the two axial coordination sites being occupied in one case by either a tethered ligand or an enzyme ligand, in the

other by an adenosyl ligand secured by a C–Co bond to the 5'-carbon of adenosyl (the structures and chemistry of the cofactors and enzyme reactions are lucidly presented by Frey and Hegeman,⁴⁷ the role of the enzymes in metabolism is discussed by McMurry and Begley⁴⁸). The homolytic fission of the Co-adenosyl bond enables the catalysis of radical reactions,⁴⁹ including H-atom transfers as observed with MCM.⁵⁰

The role of model reactions in this class of enzymes and indeed for understanding of tunnelling in enzymes more generally is illuminated by a study of tunnelling in MCM by Chowdhury and Banerjee.^{52,53} The subject of cobalamin-dependent enzymes and tunnelling was reviewed¹⁶ more broadly by Banerjee *et al* in 2006.

MCM catalyses an overall reaction (Figure 13.3) in which the thiol ester of Coenzyme A with methylmalonate, $\text{^{\ominus}OOCCH(CH}_3\text{)COSCoA}$, binds in proximity to an adenosylcobalamin cofactor. The adenosyl-cobalt bond is believed⁵³ to undergo homolysis with coupling to the abstraction by the 5'-adenosyl radical of a hydrogen atom from the substrate methyl group: *i.e.* these two events are either simultaneous or near-simultaneous. This overall process was kinetically isolated, or largely so, by Chowdhury and Banerjee^{51,52} in stopped-flow studies of the transient kinetics. In rapid subsequent reactions, the COSCoA group migrates to the radical centre, the new radical recovers the H-atom from the waiting 5'-deoxyadenosine, the Co–C bond is reformed to restore the cofactor, and the product succinyl Coenzyme A ($\text{^{\ominus}OOCCH}_2\text{CH}_2\text{ COSCoA}$) is liberated. The evidence for tunnelling in the enzymic reaction will be considered below; it consists chiefly of a large isotope effect combined with an overdependence of the isotope effect on temperature. Both nonenzymic and enzymic studies are summarised in Table 13.3 and in Figure 13.3.

Valuable further insight into the nature of the catalytic power of MCM has been provided from model-reaction studies by Finke and his coworkers.^{54–56} These studies are described in the following section.

13.5.1 Nonenzymic Tunnelling in the Finke Model^{54–56} Reactions for MCM

Finke and his coworkers have constructed several models for the action of cobalamin-dependent enzymes. For the modelling of MCM, they employed adenosylcobalamin itself in ethylene glycol solution (Figure 13.3). At temperatures of 80 °C and higher, the homolytic fission of the C–Co bond proceeds with thermal activation. The solvent ethylene glycol serves as the H-atom source, but in addition to H-atom transfer, the adenosyl radical undergoes a cyclisation reaction, forming a 5'-to-8 C–C bond, and can also be trapped by radical reagents such as the stable nitroxyl radical TEMPO. These observations have led to the idea that the C–Co homolysis and H-transfer reactions are not coupled in the model system, as it appears they are in the enzymic reaction (see above). The reaction is kinetically first order in the substituted cobalamin with a rate constant of approximately $4 \times 10^{-10}\text{ s}^{-1}$ as extrapolated to the

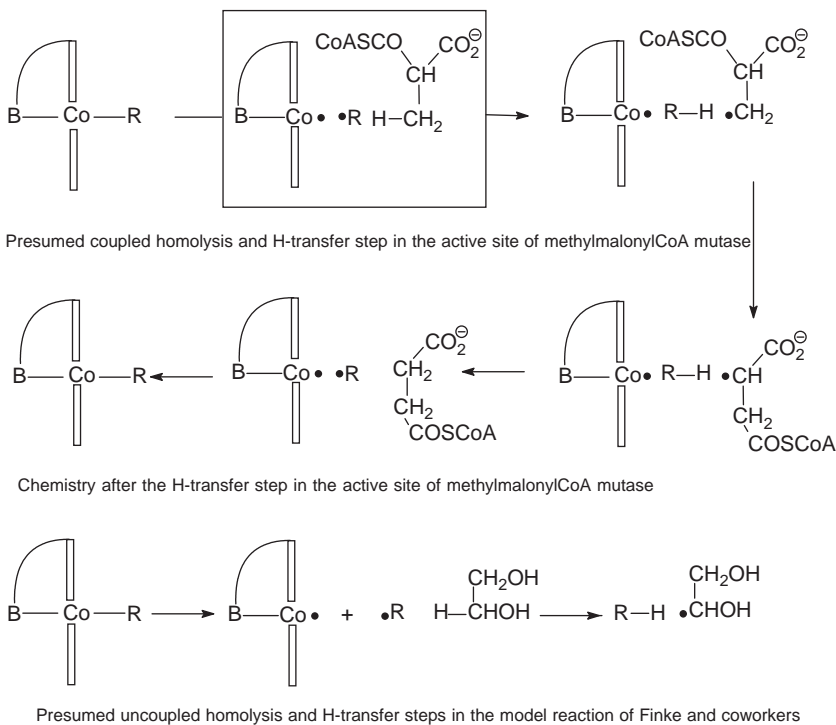


Figure 13.3 Schematic depictions of enzymic and nonenzymic reactions related to the action of methylmalonyl coenzyme A mutase (MCM). In the upper equation, the step during the action of MCM in which homolysis of the cobalt carbon bond linking the metal to 5' adenosyl and H atom abstraction by the 5' adenosyl radical from the substrate are thought to occur in a coupled reaction. Events following generation of the substrate radical are also shown. In the lower equation, the chemical events in the model system devised by Finke and his coworkers (uncoupled homolysis, followed by H atom transfer in competition with other fates of the adenosyl radical). The narrow boxes about the cobalt represent the tet rapyrrole corrin ligand that encircles cobalt in the cofactor, B is an axially coordinated base (a histidine imidazole in the enzyme and an adenine or alkoxide in the model), and R is adenosyl in the enzyme and methyl, adenosyl, or neopentyl in the model reaction. In the enzymic reaction, the rearrangement shown, leading to succinyl Coenzyme A follows the substrate radical generation process. In the model reaction, both the radical formed from the solvent ethylene glycol and the adenosyl radical go on to various fates.

neighbourhood of room temperature, where the values of k_{cat} for MCM are of the order of 100 s^{-1} . This shows the catalytic rate enhancement for the enzyme to be around 10^{12} -fold. This is a very respectable acceleration, amounting to a reduction in the free-energy barrier by the enzyme of 16.8 kcal/mol. Waddington and Finke⁵⁶ showed that the enthalpic barrier to the nonenzymic reaction is around 35 kcal/mol, opposed by a positive entropy of activation of

Table 13.3 Comparison of the properties of nonenzymic (model) and enzymic reactions related to methylmalonylCoA mutase catalysis.

<i>Reaction property</i>	<i>Nonenzymic reaction^a</i>	<i>Enzymic reaction</i>
k_H near 25 °C (s ⁻¹)	4×10^{-10} (adenosyl [Ado]) 3×10^{-4} (neopentyl [Np])	$k_{cat} = 125$ (Ado) rate enhancement ca. 10^{12} for adenosyl, 10^6 for neopentyl
k_H/k_D near 25 °C	ca. 26 (Ado) ca. 23 (Np)	35.6 at 20 °C (Ado)
ΔH^\ddagger , kcal/mol	protio 34.5 ± 0.8 (Ado) 32.2 ± 0.6 (Np)	protio 18.8 ± 0.8 (Ado) deutero 22.2 ± 0.8 (Ado)
ΔS^\ddagger , cal/Kmol	14 ± 1 (Ado) 33 ± 2 (Np)	18.2 ± 0.8 (Ado) 23.3 ± 0.8 (Ado)
A_H/A_D , E_{aH} , E_{aD} , kcal/mol	0.16 ± 0.07, 3.0 ± 0.3 (Ado) 0.14 ± 0.07 , 3.1 ± 0.3 (Np)	0.078 ± 0.009 , 3.41 ± 0.07 (Ado)

^aDirectly measured rate constants are thought to refer to the C–Co homolysis step and not to the subsequent isotope dependent step. Isotope effects, isotopic A ratios and isotopic differences in activation energies were obtained from competition experiments.

around 14 cal/K mol. Both the rate constants and the activation parameters presumably describe the C–Co homolysis step, not the H-transfer step.

Isotope effects and their temperature dependences were obtained by two techniques. In one, use was made of the amount of cyclised adenosine as an internal standard, taking its rate of formation to be the same in $(\text{CH}_2)_2(\text{OH})_2$ and in $(\text{CD}_2)_2(\text{OH})_2$ as solvents. From the mass-spectrometric ratio of the signal for the standard to the signal for adenosine in samples from $(\text{CH}_2)_2(\text{OH})_2$ and the ratio of the signal for standard to the signal for adenosine-5'-*d* in samples from $(\text{CD}_2)_2(\text{OH})_2$, the isotope effect k_H/k_D for the H-transfer reaction was calculated. In a second approach with the 8-MeO-derivative of adenosylcobalamin, a mixture of the two isotopic solvents was employed for thermolysis with the ratio of protio-adenosine and deutero-adenosine being determined by mass spectrometry directly. Both methods gave the same results. A plot of $\ln(k_H/k_D)$ vs. $1/T$ yielded A_H/A_D and $(E_{aH} - E_{aD})$ from which the enthalpy and entropy data in Table 13.3 were calculated. The data for the neopentyl derivative were obtained near room temperature, justifying extrapolations of the temperature dependences.

The isotope effects for the nonenzymic reactions shown in Table 13.3 are between 20 and 30 near room temperature, thus well above the 7–10 expected for nontunnelling reactions. It is clear that tunnelling or another phenomenon producing exaggerated isotope effects is at work. Tunnelling is confirmed by the overdependence of the isotope effect on temperature. An isotope effect of 25 would, on the simple ZPE model, correspond to an isotopic difference in

enthalpies of activation of about 2 kcal/mol, while a value of around 3 kcal/mol is observed. Within the CSF, this kind of value indicates an initial, isotope-independent search for an energy-resonant tunnelling state, followed by a search for a state with a sufficiently short tunnelling distance, the latter being more energetically demanding for the less delocalised D-reactant and accounting for the relatively enhanced enthalpy or energy of activation for the D-reactant. Within the state located in the dual search, tunnelling occurs. The value of A_H/A_D then is fixed both by the isotopic probability ratio for tunnelling, which would be expected to favour H over D, and by the fact that the larger energy demand for location of the D-tunnelling configuration automatically tends to generate small values of A_H/A_D . The observed values of around 0.1–0.2 are consistent with the common observation that the larger energy requirement for D-tunnelling outweighs the lower probability of D-tunnelling in the determination of the ratio of intercepts of isotopic Arrhenius plots at infinite temperature.^{33,34}

The searches for resonant states with short tunnelling distances presumably take place in this nonenzymic reaction by vibrational, rotational, and possibly translational reorganisations of the solvent H(D)-donors that form the immediate environment of the radical centre to which H(D)-atom transfer will occur. Although the isotope-effect data contain no information at the qualitative level that would indicate whether tunnelling constitutes the only pathway of H-transfer in the nonenzymic reaction, the apparent linearity of the Arrhenius dependences of the isotope effects are consistent with the entirety of the reaction proceeding by a single (presumably tunnelling) mechanism.

Unlike the situation with the Bell tunnelling approach used in earlier times, in which the tunnelling signatures could be used to generate a “tunnelling correction,” and thus an estimate of the degree to which tunnelling is occurring, the configurational-search framework at the qualitative level provides no such guidelines. Furthermore, since the tunnelling event in the model reaction is believed to take place in a reaction subsequent to the rate-limiting homolysis of the C–Co bond, we have no rate constant for the tunnelling event even for the H-compounds.

13.5.2 Enzymic Tunnelling in MCM

The Chowdhury-Banerjee study^{51,52} of 2000 provided excellent evidence for tunnelling in the apparently coupled homolysis/H-transfer reaction step of MCM action with methylmalonyl CoA and methyl-*d*₃-malonyl CoA as substrates (Table 13.3). Presteady-state stopped-flow kinetic studies permitted determination of the intrinsic rate constant for this step, and isotope effects were measured from 5–20 °C (H) and 5–37 °C (D). The isotope effect, here as in the model reactions a combination of primary and secondary effects, was about 36 at 20 °C, exceeding the value of 7–10 expected on a simple nontunnelling model. The isotope effect suggests an isotopic difference in ΔH^\ddagger or E_a on the nontunnelling model of 2.2 kcal/mol, while the observed value is 3.4 kcal/mol,

thus indicating an overdependence on temperature, as in the model reaction. The free-energy barrier to the coupled homolysis/H-transfer enzymic reaction is about 13.4 kcal/mol, compared to 30.3 kcal/mol for the nonenzymic reaction, a reduction in the barrier height induced by enzymic catalysis therefore being about 17 kcal/mol. This quantity is in correspondence with the value of the rate acceleration generally cited as a factor of 10^{12} . If it emerges that indeed the enzymic reaction is coupled and the nonenzymic reaction uncoupled, it seems possible that the conversion of the uncoupled reaction, requiring the expenditure of the full Co–C homolytic bond dissociation energy, to a coupled reaction without such a kinetic requirement may constitute part of the catalytic strategy of MCM. The catalysis appears almost wholly in the enthalpy of activation (16 of 17 kcal/mol), consistent both with a lowering of the barrier through coupling homolytic fission to H-transfer and with involvement of enzyme dynamics or structure in providing tunnelling states at lower energies.

In the enzymic reaction, the value of A_H/A_D is around 0.08, consistent with the overdependence model, on which this value reflects probably opposing contributions of the isotopic ratio of tunnelling probabilities ($H > D$) and the influence of a larger configurational-search energy for the D substrate, relative to that for the H substrate (which automatically favours $A_D > A_H$) with the latter effect as usual prevailing.

13.5.3 Model Reactions and MCM Catalytic Power

Three features of the tunnelling reactions in nonenzymic and enzymic reactions are similar: isotope effects around 20–40; A_H/A_D values near 0.1; and isotopic differences in energies of activation of 3–4 kcal/mol. This resemblance led Doll and Finke⁵⁵ to conclude that in the MCM case and possibly more generally, there is “no enzymic enhancement of tunnelling.” It seems clear, however, that in the enzymic system tunnelling events generate product at 10^{12} times the rate that product is generated by a similar tunnelling mechanism in the nonenzymic system.

The logical flaw in the argument for a lack of enzymic enhancement of tunnelling would seem to lie in the belief that an enzymic enhancement in the rate of the tunnelling reaction will produce changes in the characteristic signatures of tunnelling, in this case the isotope effect, the isotopic A-ratios, or the isotopic differences in activation energy. None of these values is greatly different in the nonenzymic and enzymic reactions, but the belief that an acceleration by the enzyme in the rate of the tunnelling reaction would, with complete generality, produce observable changes in the three values named above is not supported by what we know today.

Instead, the answer to the question of whether such changes would or would not occur depends, within the CSF, on the means by which the enzymic acceleration occurred. For example, an enzyme – say, MCM – might have provided such transition-state stabilisation for a nontunnelling transition state

that a nontunnelling mechanism would prevail for the enzyme, while tunnelling would proceed as observed in the model reaction. It would then be expected that quite ordinary isotope effects, a roughly unit value of the A-ratio, and a difference in energies of activation corresponding to the isotope effect would all be measured for the enzymic reaction. Alternatively, as was seen at high temperatures with the thermophilic alcohol dehydrogenase, the low-temperature mechanism of tunnelling (and the signature of its double-search mechanism, an overdependence on temperature) was lost at around 30 °C. At higher temperatures, it was replaced by a different mechanism of tunnelling, and its own signature of an underdependence on tunnelling, reflecting the availability of a preorganised tunnelling state at higher temperatures.

However, the enzymic and nonenzymic data for MCM are quite consistent with the entirety of *each* mechanism proceeding by a dual search process, consisting of an isotope-independent search for an energy-resonant state and an isotope-dependent search for a short tunnel distance. The enzymic rate is faster and there is an “enzymic enhancement of tunnelling,” presumably with little or no alteration in the *mechanism* of tunnelling, the enhancement conceivably as large as a factor of 10¹². A more detailed discussion of the factors involved in this comparison was given last year by Banerjee, Truhlar, Dybala-Defratyka, and Paneth.¹⁶

13.6 The Roles of Theory in the Comparison of Model and Enzymic Reactions

Modern quantum theory has reached such a stage of development that, particularly in combination with simulation methods, it serves a number of vital roles in chemical biology, in the interpretation of experimental data, in the exploration of fundamental concepts, and in predictions to be tested by experiment.^{57–61} The simplified and qualitative use made in the present chapter of the configurational search formulation is, in actual practice, replaced by quantitative and more exact theoretical treatments capable of much deeper insight (see Chapter 6). Furthermore, as already emphasised, other theoretical approaches are providing their own insights. The situation is partly in a period of clarification at present, but it can certainly be expected that in the not too distant future the theoretical approaches will converge on a picture of tunnelling in enzyme action and in related model reactions that will be general and satisfying. It is this writer’s belief that the main lines of that picture will not be greatly distinct from the qualitative view offered in this article.

13.7 Model Reactions, Enzymic Accelerations, and Quantum Tunnelling

The two cases presented here are ones in which enzymes have accelerated a tunnelling reaction while remaining with the same mode of tunnelling

(thermophilic alcohol dehydrogenase at lower temperatures, by some 3 or 4 orders of magnitude, or methylmalonylCoA mutase by up to 12 orders of magnitude) or accelerated a tunnelling reaction while changing the mode of tunnelling (thermophilic alcohol dehydrogenase at higher temperatures). There will be other examples in which the interplay of enzyme catalysis with the scope and limitations of organic and inorganic chemistry will have produced other combinations of model-reaction chemistry and enzymic chemistry. Many such examples are already known or could readily have been put together, but I have not done that. And, of course, it will be in the context of quantitative and general theoretical approaches that the final story will be written.

References

1. M. G. Snider, B. S. Temple, R. Wolfenden, *J. Phys. Org. Chem.*, 2004, **17**, 586–591.
2. B. G. Miller, R. Wolfenden, *Annu. Rev. Biochem.* 2002, **71**, 847–885.
3. R. Wolfenden, M. J. Snider, *Acc. Chem. Res.*, 2001, **34**, 938–945.
4. A. Radzicka, R. Wolfenden, *Science* (Washington, DC), 1995, **267**, 90–93.
5. S. A. Benner, S. O. Sassi, E. A. Gaucher, *Adv. Enzymol. Rel. Areas Molec. Biol.*, 2007, **75** (Protein Evolution), 1–132.
6. J. M. Thomson, E. A. Gaucher, M. F. Burgan, D. W. De Kee, T. Li, J. P. Aris, S. A. Benner, *Nature Genetics*, 2005, **37**, 630–635.
7. E. A. Gaucher, J. M. Thomson, M. F. Burgan, S. A. Benner, *Nature*, 2003, **425**, 285–288.
8. S. A. Benner, M. D. Caraco, J. M. Thomson, E. A. Gaucher, *Science* (Washington, DC), 2002, **296**, 864–868.
9. M. Nars, M. Vihinen, *Molec. Biol. Evol.*, 2001, **18**, 312–321.
10. S. Krappmann, W. N. Lipscomb, G. H. Braus, *Proc. Natl. Acad. Sci. USA*, 2000, **97**, 13585–13590.
11. P. L. Dutton, A. W. Monroe, N. S. Scrutton, and M. J. Sutcliffe (ed.) *Philos. Trans. Royal Soc. B*, 2006, **361**, 1293–1455.
12. V. Schramm (ed.) *Chem. Rev.*, 2006, **106**, issue 8, 3029–3496.
13. J. T. Hynes, J. P. Klinman, H.-H. Limbach and R. L. Schowen, (ed.), *Hydrogen-Transfer Reactions*, VCH-Wiley, Weinheim, FRG, 2006.
14. Ref. 13, 1207–1415.
15. S. J. Benkovic, S. Hammes-Schiffer, Ref. 13, 1439–1454.
16. R. Banerjee, D. G. Truhlar, A. Dybala-Defrattyka, P. Paneth, Ref. 13, 1473–1496.
17. T. L. Amyes and J. P. Richard, Ref. 13, 949–974.
18. A. J. Kirby, Ref. 13, 975–1012.
19. C. Schöneich, Ref. 13, 1013–1036.
20. R. L. Schowen, Ref. 13, 1037–1078.
21. E. M. Kosower, *Molecular Biochemistry*, McGraw-Hill Book Co., New York, 1962.

22. T. C. Bruice and S. J. Benkovic, *Bioorganic Mechanisms*, W. A. Benjamin, Inc., New York, 1966.
23. W. P. Jencks, *Catalysis in Chemistry and Enzymology*, McGraw-Hill Inc., New York, 1969.
24. R. Wolfenden, *Chem. Rev.*, 2006, **106**, 3379–3396.
25. G. K. Schroeder, C. Lad, P. Wyman, N. H. Williams, R. Wolfenden, *Proc. Natl. Acad. Sci.*, 2006, **103**, 4052–4055.
26. B. P. Callahan, Y. Yuan, R. Wolfenden, *J. Am. Chem. Soc.*, 2005, **127**, 10828–10829.
27. Z. D. Nagel, J. P. Klinman, *Chem. Rev.*, 2006, **106**, 3095–3118.
28. F. E. Romesberg, R. L. Schowen, *Adv. Phys. Org. Chem.*, 2004, **39**, 27–77.
29. Y. Kim; M. M. Kreevoy, *J. Am. Chem. Soc.*, 1992, **114**, 7116–7123.
30. A. Kohen and H.-H. Limbach, (ed.), *Isotope Effects in Chemistry and Biology*, Taylor & Francis, Boca Raton, 2006.
31. L. Melander, W. H. Saunders, *Reaction Rates of Isotopic Molecules*, John Wiley & Sons, New York, 1980, pp. 147 ff.
32. H. Kwart, M. W. Brechbiel, R. M. Acheson, D. C. Ward, *J. Am. Chem. Soc.*, 1982, **104**, 4671–4672.
33. R. P. Bell, *The Tunnel Effect in Chemistry*, Chapman and Hall, London, 1980.
34. E. F. Caldin, *Chem. Rev.*, 1969, **69**, 135–156.
35. J. Braun, R. Schwesinger, P. G. Williams, H. Morimoto, D. E. Wemmer, H.-H. Limbach, *J. Am. Chem. Soc.*, 1996, **118**, 11101–11110.
36. Y. Cha, C. J. Murray, J. P. Klinman, *Science* (Washington, DC), 1989, **243**, 1325–1330.
37. A. R. Clarke and T. R. Dafforn in M. L. Sinnott (ed.), *Comprehensive Biological Catalysis*, Academic Press, London 1998, vol III, 1–75.
38. A. J. Kirby, D. R. Walwyn, *Gazz. Chim. Ital.*, 1987, **117**, 667–680.
39. A. J. Kirby, D. R. Walwyn, *Tet. Lett.*, 1987, **28**, 2421–4.
40. X. Yang, Y. Hu, D. Yin, M. A. Turner, M. Wang, R. T. Borchardt, P. L. Howell, K. Kuczera, R. L. Schowen, *Biochemistry*, 2003, **42**, 1900–1909.
41. D. J. Porter, *J. Biol. Chem.*, 1993, **268**, 66–73.
42. D. J. Porter, F. L. Boyd, *J. Biol. Chem.*, 1992, **267**, 3205–3213.
43. D. J. Porter, F. L. Boyd, *J. Biol. Chem.*, 1991, **266**, 21616–21625.
44. M. F. Powell, T. C. Bruice, *J. Am. Chem. Soc.*, 1982, **104**, 5834–5836.
45. M. F. Powell, T. C. Bruice, *J. Am. Chem. Soc.*, 1983, **105**, 7139–7149.
46. A. Kohen, R. Cannio, S. Bartolucci, J. P. Klinman, *Nature*, 1999, **399**, 496–499.
47. P. A. Frey and A. Hegeman, *Enzymatic Reaction Mechanisms*, Oxford University Press, Oxford and New York, 2007, pp. 190–200.
48. J. McMurry, T. Begley, *The Organic Chemistry of Biological Pathways*, Roberts and Company, Englewood, Colorado, 2005, pp 238–241; 379–400.
49. R. Banerjee, S. W. Ragsdale, *Annu. Rev. Biochem.*, 2003, **72**, 209–247.
50. R. Banerjee, *Chem. Rev.*, 2003, **103**, 2083–2094.
51. S. Chowdhury, R. Banerjee, *Biochemistry*, 2000, **39**, 7998–8006.
52. S. Chowdhury, R. Banerjee, *J. Am. Chem. Soc.*, 2000, **122**, 5417–5418.

53. R. Padmakumar, R. Padmaka, R. Banerjee, *Biochemistry*, 1997, **36**, 3713–3718.
54. K. M. Doll, B. R. Bender, R. G. Finke, *J. Am. Chem. Soc.*, 2003, **125**, 10877–10884.
55. K. M. Doll, R. G. Finke, *Inorg. Chem.*, 2003, **42**, 4849–4856.
56. M. D. Waddington, R. G. Finke, *J. Am. Chem. Soc.*, 1993, **115**, 4629–4640.
57. H. Lin, D. G. Truhlar, *Theor. Chem. Acc.*, 2007, **117**, 185–199.
58. M. H. M. Olsson, W. W. Parson, A. Warshel, *Chem. Rev.*, 2006, **106**, 1737–1756.
59. M. Karplus, J. Kuriyan, *Proc. Natl. Acad. Sci., USA*, 2005, **102**, 6679–6685.
60. M. Garcia-Viloca, J. Gao, M. Karplus, D. G. Truhlar, *Science* (Washington, DC), 2004, **303**, 186–195.
61. M. Karplus, *Acc. Chem. Res.*, 2002, **35**, 321–323.

CHAPTER 14

Long-Distance Electron Tunnelling in Proteins

ALEXEI A. STUCHEBRUKHOV

Department of Chemistry, University of California, Davis, CA 95616, USA

14.1 Introduction

The most remarkable aspect of electron transfer (ET) in proteins is that it occurs *via* quantum-mechanical tunnelling.^{1–6} Typically, redox centres that exchange an electron are separated by distances of the order of 15–30 Å. In vacuum, tunnelling over such long distances would be impossible. In proteins, the intervening organic medium facilitates tunnelling by providing low-lying virtual quantum states that result in the effective lowering of the tunnelling barrier, and the exchange at physiological rates becomes possible.⁶ It is remarkable that the whole biological energy-transduction machinery, of which electron transport is a major part,^{7,8} is based on such a subtle quantum-mechanical phenomenon, given that most of biology does not require quantum mechanics at all.

For a number of years, a major question has been whether specific electron-tunnelling pathways exist.^{3–6} This question is still debated in the literature, because the pathways are not observed directly, and the interpretation of experimental results involves ambiguities. The extremely small tunnelling interactions (of the order of 10^{-1} to 10^{-4} cm⁻¹) are difficult to calculate accurately. Despite the remarkable recent progress in the area,^{9–15} some important problems remain unresolved. The accurate prediction of the absolute rates of long-distance electron-transfer reactions and other biological charge-transfer reactions, including proton-coupled reactions, is a particularly challenging problem.

On the one hand, the current theoretical calculations are consistent with the idea of specific tunnelling paths;^{10,15–17} on the other, some experimental studies show that the mutations of the amino acids along the path do not significantly change the rates of ET. Dutton and coworkers have proposed⁶ empirical relations for the rates of biological ET's, which are based on the averaged characteristics of the protein medium, such as local density, rather than the detailed structural data, which appear to agree well with the experimental data. In recent years, there has been significant progress in understanding of how these two pictures can be reconciled, see, *e.g.*, ref. [18], however a number of issues require further study. In particular, the possible role of protein dynamics in averaging the paths has not been completely understood yet.^{19,20} Since the tunnelling amplitudes are not directly observed in experiments, many issues can only be resolved by performing accurate quantum calculations on realistic systems that involve dynamics of the system. This is a challenging computational problem. The difficulties, however, are not only purely technical or computational; in general, tunnelling in many-electron systems is a nontrivial physical problem.

This chapter reviews some of the theoretical issues of electron transfer in proteins. We focus on what is happening with an electron at the transition state of an ET reaction, when it tunnels through the protein medium. Our special interest is the many-electron aspect of the phenomenon. The key approach to be discussed is the method of tunnelling currents¹⁷ developed by the author. Reviews of other approaches and topics not covered here can be found in refs [9–13]. In this review we do not cover issues related to activation of ET reaction, *i.e.* how the protein medium reorganises to achieve a configuration at which electron tunnelling takes place. Among important aspects here are the nature of the protein medium reorganisation and the entropy of activation, the role of quantum modes of the medium, control of the reaction by protein dynamics, and the distance dependence of the reorganisation energy and the driving force. We do not consider also in great detail all the medium dynamic effects, including both non-Condon and non-Born–Oppenheimer effects.²¹ The classic reviews of Marcus and Sutin and that of Newton^{11,12} discuss in detail earlier theoretical and experimental work in the field.

It should be mentioned that electron tunnelling is not the only possible mechanism of electron transfer. In some cases, the hopping mechanism or a combination of tunnelling and hopping are responsible for charge transfer over long distances. This occurs when sufficient energy is available for direct excitation of an electron/hole to the band of the excited states. One example of such a mechanism is electron transfer in DNA, discussed extensively in recent years.^{14,22–25}

14.2 Electronic Coupling and Tunnelling Pathways

The majority of ET reactions in proteins are nonadiabatic owing to the weakness of interaction between the redox sites. In this limit, the rate of ET is

proportional to the square of the electronic coupling matrix element T_{DA} that connects distant redox sites.^{11,12} This matrix element and the associated tunnelling process are the main focus of the present chapter.

The matrix element T_{DA} is a pure electronic quantity. Usually, in order to express the rate of ET in terms of the electronic coupling, both Condon and Born–Oppenheimer (BO) approximations are made (or tacitly assumed). The first approximation assumes independence of the transfer matrix element of the medium nuclear configuration – practically it means that if we calculated T_{DA} at a nuclear configuration that is not exactly the transition state, we assume that the transfer matrix element at the transition state is approximately the same. The deviations from the Condon approximation are briefly discussed in Section 14.5.

The BO approximation (for donor and acceptor states D and A) practically means independence of the transfer matrix element T_{DA} of the vibrational state of the medium in which the tunnelling transition is taking place. In other words, in this approximation the electronic coupling is calculated at a specific fixed nuclear configuration of the system, disregarding the actual nuclear motion. The dependence of the rate (but not the matrix element) on the vibrational state enters into theory in this case only in the form of the Franck–Condon vibrational factors.

In the BO approximation, the wavefunction of the system (in the initial state D , or the final state A) is the product of the electronic and vibrational wavefunctions, and the distribution of total energy between electronic and vibrational degrees of freedom is fixed. Thus, one can define the energy of the tunnelling electron and the corresponding height of the tunnelling barrier. As the distance between donor and acceptor increases beyond some characteristic distance L_{BO} (L_{BO} is 10–15 Å according to the estimate in ref. [21]) the BO approximation breaks down. When this happens, the energy of the tunnelling electron is no longer a well-defined quantity. The total energy, electronic plus vibrational, of the quantum state from which the transition occurs is fixed, of course, but the distribution of energy between the vibrational and electronic degrees of freedom is no longer fixed and will depend on the tunnelling distance. In this case, the theory of the rate takes a more complicated form, in which the electronic coupling depends on the vibrational state of the system. In this review, we assume the BO approximation holds and treat the tunnelling coupling T_{DA} as a pure electronic quantity that is calculated at some fixed nuclear configuration of the system.

Technically, the tunnelling coupling in donor–bridge–acceptor (D – B – A) systems is often described in terms of the superexchange model, following the steps of McConnell and Larsson's early treatment of the problem.^{26–29} The equivalence of superexchange and tunnelling is discussed, *e.g.* in refs [12,30–32]. Based on the superexchange model, several methods for the calculation of the electronic tunnelling matrix element (ME) have been developed.^{12,13,33–52}

We begin with a brief review of these methods and then move on to discuss the method of tunnelling currents, the main subject of the chapter. For a more detailed discussion of the superexchange methods, and a more complete

reference list of the early work, the reader is referred to a comprehensive review of the subject by Newton.¹²

14.2.1 Direct Method

In this method the matrix element is calculated directly.¹² Suppose we know two diabatic states $|D\rangle$ and $|A\rangle$ that correspond to two redox states of the system – electron on the donor and on the acceptor, respectively – and the configuration of the system is that of the transition state, *i.e.* the states have the same energy E_0 . Then the transfer matrix element is

$$T_{DA} = \frac{H_{DA} - E_0 S_{DA}}{1 - S_{DA}^2} \quad (14.1)$$

where H is the Hamiltonian of the system (at the transition-state configuration), $H_{DA} = \langle D|H|A \rangle$, $E_0 = \langle A|H|A \rangle = \langle D|H|D \rangle$ is the tunnelling energy, and $S_{DA} = \langle A|D \rangle$ is the overlap integral. Typically, for long-distance ET, the overlap S_{DA} is very small and therefore can be neglected in the denominator. The above expression can be used in both one- and many-electron formulations of the problem. This method has been used in the past for relatively strongly coupled $D-B-A$ systems, *e.g.* refs [12,37].

For long-distance tunnelling, the potential problems with the above approach are as follows. First, the diabatic states, in practice, are well defined only in the region of their localisation and perhaps in the barrier region adjacent to it, and are poorly defined in the region of the other redox site, where the other function is admixed. In other words, the “tails” of the diabatic states are not well defined. Therefore, in the region where $|D\rangle$ is well defined, $|A\rangle$ is poorly defined, and *vice versa*. Both H_{DA} and S_{DA} , which are integrals over the whole space, are not well defined then, because of the contribution of the regions around donor and acceptor complexes where either one or the other function is not well defined. Second, the tunnelling energy E_0 can be determined only approximately. If so, in the above formulation, the very small matrix element is evaluated as a difference of two large numbers (notice that E_0 is the total energy of the system), each of which can be evaluated only approximately.

14.2.2 Avoided Crossing

In some cases, it is possible to calculate directly the energy difference between the two adiabatic (*i.e.* exact) states. Usually, these are the ground and the first excited state in the system, which are some mixtures of diabatic $|D\rangle$ and $|A\rangle$ states owing to their (unknown) coupling T_{DA} . To extract T_{DA} in this method, the parameters of the system, such as external charges, are varied in such a way as to make the two adiabatic states experience an avoided crossing, at which the minimum-energy distance between the states is determined. This energy distance then is twice the magnitude of the matrix element T_{DA} .

For long-distance tunnelling, the couplings are typically of the order 10^{-1} – 10^{-2} cm⁻¹ or less. To find the avoided crossing point with such accuracy is not easy, at best. (This “needle in a haystack” problem is discussed in ref. [50].) Moreover, the excited-state energy of a large many-electron system needs to be evaluated here with impractical accuracy. The method, however, can be used for calculations of some not very large systems⁵⁰. In particular, for relatively small symmetric D – B – A systems, the calculation of the energy splitting can be carried out at various levels of *ab initio* theory.^{33 36} For symmetric D – B – A systems, the transition state is well defined by symmetry, which makes these kinds of calculations particularly suitable.

14.2.3 Application of Koopmans’ Theorem

At the self-consistent-field (SCF) level, to determine the splitting of two adiabatic states one can rely on Koopmans’ theorem.^{12,33 36} In this case, one assumes that there is no electronic relaxation of the core orbitals, and the only difference in the initial and final electronic state is the orbital of a single transferring electron. Thus, for example, for a system with an odd number of electrons, N , the initial and final (many-electron) states represented by one-Slater determinant will be $|D\rangle = |(\text{core})\phi_d\rangle$ and $|A\rangle = |(\text{core})\phi_a\rangle$, and the two adiabatic states are $|\psi_+\rangle = |(\text{core})\phi_+\rangle$ and $|\psi_-\rangle = |(\text{core})\phi_-\rangle$, where

$$\phi_{\pm} = (\phi_d \pm \phi_a)/\sqrt{2} \quad (14.2)$$

The $N-1$ core orbitals are assumed to be the same. Then, one can show that the splitting of two adiabatic states $|\psi_{\pm}\rangle$, *i.e.* the total electronic energy difference between the two states,

$$\Delta = (E_- - E_+) \quad (14.3)$$

is the same as the distance between the energies of one-electron HOMO and HOMO-1 orbitals for a triplet state of $N+1$ electron system, $|(\text{core})\phi_+\phi_-\rangle$. A nontrivial fact is that to find the energy splitting of an N -electron system, one performs a calculation on an $N+1$ electron system! This clever method is limited unfortunately to symmetric systems, and is as accurate as Koopmans’ theory. The method has been reported to produce reliable results for not very small electronic couplings, typically greater than 10 – 100 cm⁻¹. The importance of electronic relaxation effects has been examined by comparing the results based on Koopmans’ theorem and those from direct SCF evaluation of the energy splitting between adiabatic states.^{33 36}

In the following sections, we will describe an approach to treat tunnelling with the method of tunnelling currents, in which an approximation based on the “frozen core” and one tunnelling electron picture, similar to that assumed in Koopmans’ theory, is utilised.

14.2.4 Generalised Mulliken Hush Method

Cave and Newton proposed the following method.^{38,39} For some configuration of the system that is not necessarily that of the transition state, two adiabatic states – the ground state and the first excited state – are calculated. Any of the available many-electron methods, including correlated ones, can be used. In addition, the dipole moment matrix μ_{ij} is calculated using these adiabatic states. They assume then that the diagonalisation of the matrix μ_i is associated with the same transformation as that which mixes diabatic states into adiabatic ones. The former is easily found, and the coupling T_{DA} then can be determined. The method can be justified using a perturbation theory argument. Assuming that the system is far from the crossing point, the adiabatic states are:

$$|\Psi_1\rangle = |a\rangle + \frac{T_{DA}}{\Delta E_{ab}} |b\rangle \quad (14.4)$$

$$|\Psi_2\rangle = |b\rangle - \frac{T_{DA}}{\Delta E_{ab}} |a\rangle \quad (14.5)$$

where $|A\rangle$ and $|b\rangle$ are the corresponding diabatic states, and ΔE_{ab} is their energies' difference. In the above expressions, the assumption has been made that the overlap between $|a\rangle$ and $|b\rangle$ is zero (we will return to this point later). With these states the transition dipole moment μ_{12} is evaluated. If now an additional assumption is made that the matrix element between diabatic states μ_{ab} is zero, the following relation between T_{DA} and μ_{12} is derived:

$$T_{DA} = \frac{\mu_{12}}{\Delta\mu_{ab}} \Delta E_{ab} \quad (14.6)$$

where $\Delta\mu_{ab} = \mu_{bb} - \mu_{aa}$ is the difference of dipole moments in two diabatic states. This difference is roughly eR_{ab} , where R_{ab} is the distance between the donor and acceptor sites, or can be evaluated more accurately using $\Delta\mu_{ab} = \Delta\mu_{12}$. This method has the nice feature that the system does not need to be brought into resonance to evaluate the coupling. A number of interesting applications of this Generalised Mulliken–Hush (GMH) method have been reported by the authors.^{13,40,41}

For long-distance tunnelling, both assumptions, $S_{ab} = \langle a|b\rangle = 0$ and $\mu_{ab} = 0$, are not necessarily valid. However, a generalisation of the Cave–Newton GMH method can be used that avoids these assumptions. In this scheme, three calculations at slightly different configurations are made, and three pairs of functions are found: $|\Psi_i^{(n)}\rangle$, $n = 1, 2, 3$, $i = 1, 2$. Each of the functions is approximately:

$$|\Psi_1^{(n)}\rangle = |a\rangle + \frac{H_{ab} - E_a^{(n)} S_{ab}}{\Delta E_{ab}^{(n)}} |b\rangle \quad (14.7)$$

$$|\Psi_2^{(n)}\rangle = |b\rangle - \frac{H_{ab} - E_b^{(n)} S_{ab}}{\Delta E_{ab}^{(n)}} |a\rangle \quad (14.8)$$

With these functions, three transition dipole moments are calculated:

$$\mu_{12}^{(n)} = \mu_{ab} + \mu_{aa} \frac{H_{ab} - E_b^{(n)} S_{ab}}{\Delta E_{ab}^{(n)}} - \mu_{bb} \frac{H_{ab} - E_a^{(n)} S_{ab}}{\Delta E_{ab}^{(n)}} \quad (14.9)$$

for $n=1,2,3$. From these three equations, three unknowns H_{ab} , S_{ab} , and μ_{ab} are determined and then the transfer matrix element T_{DA} is evaluated using eqn (14.1). For reliability, more than three points can be examined. The tunnelling energy E_0 entering eqn (14.1) is found approximately by extrapolating the external parameter, at which three pairs of energies ($E_a^{(n)}, E_b^{(n)}$) were determined, to a point where the energies E_a and E_b cross, as described in ref. [50].

As seen, in this method one avoids the direct evaluation of the matrix elements entering into eqn (14.1) by finding them from the calculated transition matrix elements of the dipole operator. The remarks made earlier about the potential problems with the evaluation of eqn (14.1) apply here. In addition, here we rely upon the accuracy of the evaluation of the adiabatic states, and assume that the extremely small admixture of the second diabatic state, which is proportional to T_{DA} , is accurately represented in our states. These admixed components, however, appear only in the far tail of the adiabatic states. It is not clear, *a priori*, how accurately this extremely small admixture will be captured by the usual variation procedures employed in the evaluation of the adiabatic states, in particular of the excited state.

14.2.5 The Propagator Method

In a one-electron description, a method that is based on perturbation theory treatment can be used. This technique grew out of the early work of Larsson,^{27,28} and Marcus with coworkers⁴² and was first applied in refs [43–46]. In principle, the method can be generalised to many-electron systems as well,⁹ but for large biological systems such treatment becomes impractical. In the one-electron approximation, however, the method can be applied for treatment of very large systems, such as entire proteins.

The problem is cast in terms of weakly coupled donor–bridge–acceptor complexes. The donor and acceptor are redox groups in the protein, and the bridge is the protein itself. The key property to be evaluated is the electronic propagator or Green’s function (GF) of the protein. The matrix element has been shown to have the form:

$$T_{DA}^{(0)} = \sum_{ij} V_{di} G_{ij}(E) V_{ja} \quad (14.10)$$

where V_{di} and V_{ja} are the coupling matrix elements of the donor and acceptor orbitals to the nearest atomic orbitals of the protein, and $G_{ij}(E)$ is the electronic propagator between the $|i\rangle$ th and $|j\rangle$ th atomic orbitals of the protein,

$$G_{ij}(E) = \langle i | (H_B - E)^{-1} | j \rangle \quad (14.11)$$

where H_B is the protein/bridge Hamiltonian, *i.e.* part of the protein that excludes the donor and acceptor complexes, and E is the tunnelling energy. The problem of nonorthogonality of the atomic orbitals has been addressed in ref. [47], where modifications of the above expression have been obtained.

To evaluate the expression (14.10) for T_{DA} , and to avoid diagonalisation or inversion of big matrices, the expressions can be rewritten as a system of linear equations with a sparse matrix $(H_B - E)_{ij}$ and solved iteratively.⁴⁶ This procedure can be applied to very large systems, which can include as many as 10^6 atomic orbitals.

The smallness of the coupling V is related to a sensible partitioning of the problem into donor, bridge, and acceptor complexes, and a correct choice of donor and acceptor states.⁴⁸ The partitioning, however, is not unique, and the smallness of the coupling is not obvious, in particular when the coupling between the donor, bridge, and acceptor complexes is covalent. What makes the perturbation theory applicable is that the donor and acceptor orbitals are always delocalised over several atoms of their respective redox complexes. If both the partitioning and the zero-th order donor and acceptor orbitals $|D\rangle$ and $|A\rangle$ are chosen correctly, the terms V_{di} and V_{aj} then represent the coupling of the atomic orbitals of the Bridge to delocalised molecular orbitals. That is, V s are not just nearest-neighbour interatomic interactions, but these interactions multiplied (or scaled) by the small coefficients of expansion of $|D\rangle$ and $|A\rangle$ in the atomic basis set of the complex. Thus, for the perturbation theory to be applicable it is essential that the donor and acceptor complexes contain several atoms.⁴⁸

The tunnelling problem is equivalent to that of scattering between two localised states $|D\rangle$ and $|A\rangle$, and the above eqn (14.10) is the lowest (“Born”) perturbation theory expression for the scattering amplitude.⁴⁹ Naturally, the expression can be generalised and higher-order terms in V can be included. In practice, however, the inclusion of such higher terms becomes sensible only if an infinite number of them can be summed up. (As is usually the case with perturbation theory, either a single low-order term is sufficient, or an infinite number of perturbation terms need to be taken into account.)

As in the scattering theory, the complete series for the transfer amplitude has the form

$$T = V + VGV + VGVGV + VGVGVGV + \dots \quad (14.12)$$

In application to tunnelling problems, one can think that the “scattering” occurs between the initial and final localised states of the tunnelling electron by the atoms of the protein. The operator V represents the coupling of the initial and final states and their coupling to the bridge, whereas G is the propagator in the bridge, eqn (14.11). Since typically there is no direct coupling between the initial and final states, the odd terms in eqn (14.12) disappear, and V then is equivalent to similar term in eqn (14.10).

The summation of *all* important terms of eqn (14.12) results in the following expression for the transfer matrix element:⁵⁰

$$T_{DA} = \frac{T_{DA}^{(0)}}{\sqrt{(1 - \Sigma'_{aa})(1 - \Sigma'_{dd})}} \quad (14.13)$$

where $T_{DA}^{(0)} = \Sigma_{da}$ is the lowest-order expression given previously, eqn (14.10), and Σ_{aa} and Σ_{dd} are the so-called self-energies of the Green functions for the tunnelling electron in the donor and acceptor states, respectively, and the prime denotes a derivative in energy. The corrections captured in the above expression account for the delocalisation of the diabatic donor and acceptor states in the protein medium. The expressions for self-energies Σ_{aa} and Σ_{dd} have the same structure as $T_{DA}^{(0)} = \Sigma_{da}$ and can be computed using the same technique of sparse matrices as for $T_{DA}^{(0)}$. Calculations on Ru-modified proteins⁴ showed that the new expression gives results that are nearly identical to those obtained with exact diagonalisation of the Hamiltonian matrix, even when intermediate resonances are present in the medium (in contrast to $T_{DA}^{(0)}$, which diverges for such cases). The advantage of the former method, of course, is that it can be applied to systems that may be too large for a direct diagonalisation.

In proteins, charge transfer can occur *via* electron or hole transfer or a combination of both.¹² The relative contribution of different channels is an important characteristic of the tunnelling coupling. The separate contributions of hole and electron transfer to the total amplitude T_{DA} , without explicit calculation of molecular orbitals of the protein, and without diagonalisation of the Hamiltonian matrix, can be obtained with a method described in ref. [46]. The method treats the above expressions for *complex* tunnelling energies, and uses analytical properties of the tunnelling amplitudes.

The success of the described methods is determined by the quality of the effective one-electron Hamiltonians used in the calculation. In practice, semi-empirical extended Hückel or tight-binding Hamiltonians are often used, which are simple and efficient, but not very accurate. Kurnikov and Beratan⁵¹ have explored construction of more accurate effective Hamiltonians for proteins based on *ab initio* calculations.

14.2.6 Protein Pruning

For the biological ET problem, it is not necessary to do sophisticated first principles calculations on the whole proteins. The tunnelling nature of electronic communication between redox sites makes the size of the protein region involved in propagating the transferring electron relatively small, *i.e.* the problem is local. A natural approach, therefore, is to perform calculations in two stages: first to examine the whole protein with approximate one-electron methods, to identify the most important parts of the protein in order to simplify the system – the procedure that we call protein pruning⁵³ – and then to proceed with more accurate many-electron *ab initio* treatments.

Protein pruning is the method to identify those amino acids of the protein that are involved in propagation of the tunnelling electron. Several similar strategies have been proposed to achieve this goal.^{9,54–57} The idea is to probe the sensitivity of the electronic coupling to computer-induced changes in the protein and to eliminate groups that are not important. A similar idea of computerised search (artificial intelligence, AI, search) was developed by Marcus and Siddarth.⁴² The method relies on the efficiency of a one-electron evaluation of the tunnelling matrix element. Such calculations have been performed on several systems.^{58–62} The pruning procedure naturally leaves intact donor and acceptor complexes and identifies a number of amino acids that make up the tunnelling bridge between them. Typically, the pruned molecule contains 10–20 amino acids and redox complexes.

14.2.7 Tunnelling Pathways

From the biological perspective, it is important to know exactly how and where in the protein electron tunnelling occurs.¹⁶ There are two possibilities. If the tunnelling electron is delocalised on a scale larger than a typical dimension of the protein's amino acids, then, as far as electronic coupling between redox centres is concerned, the detailed structure of the protein is not important for its biological function. The protein matrix can be viewed in this case as an effective medium, perhaps not totally homogeneous, but lacking detailed structure, whose only purpose is to lower the tunnelling barrier, and to make long-distance electronic communication between redox sites possible.^{5,6}

However, if the wavelength of the tunnelling electron is small, then the detailed structure of the protein medium intervening between redox centres becomes important, the pathways do exist^{3,16} and a number of fundamental questions about the role of tunnelling pathways in biological function and their molecular evolution arise.^{58,59}

The question of whether or not tunnelling paths exist in proteins is still debated in the literature. This question is beyond the scope of the present review, and an interested reader is referred to recent discussions of the topic.^{3,6,9–10} Qualitatively, the wavelength of the tunnelling electron turns out to be of an atomic size, and the tunnelling paths are certainly localised in the “frozen” protein structures. However, protein dynamics can significantly reduce the structural effects (see below). This may explain the reported success of empirical relations for electron transfer rates in proteins, which ignore detailed chemical structure of the protein, yet account for its density inhomogeneity.⁶ Also, the existence of these paths may not necessarily indicate their importance for biological function, provided electron transfer is not the rate-limiting step.⁶

The first model of the tunnelling pathways, which viewed them as specific sequences of atoms along which electron tunnelling occurs, was developed by Beratan and Onuchic.¹⁶ Each path in this model is associated with a weight, which is calculated as a product of three different empirical factors – for each

transfer through a covalent bond, hydrogen bond, and van der Waals contact between atoms along the path. The tunnelling path (or paths) is the sequence of atoms with the largest weight. The motivation of this approach stems from the exponential decay of tunnelling wavefunctions. Each pathway can be regarded as a Feynman path, and the weight factors can be understood as absolute values of their quantum amplitudes. The neglect of the sign of the amplitude is equivalent to neglect of interference effects. The development of this simple and practically useful model, which now includes both interferences and multiple paths, has been reviewed by the authors.^{9,10}

14.3 The Method of Tunnelling Currents

14.3.1 General Relations

Detailed information about the tunnelling process can be obtained with the method of tunnelling currents.¹⁷ The general idea of the approach is to examine the dynamics of charge redistribution in a system that is artificially “clamped” at the transition state, when donor and acceptor states are degenerate. To find the transition state, one can simulate a fluctuating electric field within the protein, as described in refs [12,63]. The fluctuating field shifts redox potentials of donor and acceptor complexes and bring them to resonance, at which point electron tunnelling occurs. The transition state of ET, *i.e.* the resonance condition, is obviously not unique.

The tunnelling dynamics is described by the following time-dependent wavefunction:

$$|\Psi(t)\rangle = \cos\left(\frac{T_{DA}t}{\hbar}\right)|D\rangle - i \sin\left(\frac{T_{DA}t}{\hbar}\right)|A\rangle \quad (14.14)$$

where $|D\rangle$ and $|A\rangle$ are diabatic donor and acceptor states, and T_{DA} is the transfer matrix element. The diabatic states are localised on their respective complexes, but their exponentially small tunnelling tails extend over the whole protein. In both one- and many-electron formulations of the problem the time dependence of the wavefunction is the same. The periodic change of the wavefunction from donor to acceptor state (the wavefunction “perestroika”) results in periodic variations of charge distribution in the system. The redistribution of charge is associated with current. It is this tunnelling current that we are focusing on in this method.

The redistribution of charge in the system during the tunnelling transition can be described in terms of current density $\vec{j}(\vec{r}, t)$ and its spatial distribution $\vec{J}(\vec{r})$. The appropriate expressions for these quantities are obtained from the continuity equation,

$$\frac{\partial \hat{\rho}}{\partial t} = -\nabla \hat{\vec{j}} \quad (14.15)$$

which for the tunnelling state eqn (14.14) yields

$$\vec{j}(\vec{r}, t) = -\vec{J}(\vec{r}) \sin \frac{2T_{DA}t}{\hbar}, \quad \vec{J}(\vec{r}) = -i\langle A | \hat{\vec{j}}(r) | D \rangle \quad (14.16)$$

As expected, the periodic variation of charge distribution is associated with a periodic time-dependent current $\vec{j}(\vec{r}, t)$. The spatial distribution of current $\vec{J}(\vec{r})$, however, remains the same during the dynamic process. Given also the form of $\vec{J}(\vec{r})$, one concludes that $\vec{J}(\vec{r})$ is not related to the specific periodic time dependence of the wavefunction eqn (14.14), but rather is a more general characteristic of the quantum transition between states $|D\rangle$ and $|A\rangle$. The streamlines of the current $\vec{J}(\vec{r})$ represent the so-called quantum Bohmian trajectories.⁶⁴ The tunnelling transition therefore can be characterised by the current $\vec{J}(\vec{r})$.

Alternatively, one can introduce atomic populations P_a , and corresponding *interatomic* currents J_{ab} as:

$$\frac{dP_a}{dt} = \sum_b j_{ab}, \quad j_{ab} = -J_{ab} \sin \frac{2T_{DA}t}{\hbar} \quad (14.17)$$

The spatial distribution of the tunnelling current is described here in terms of the matrix J_{ab} . In this approach, the total current through an atom is proportional to the probability that the tunnelling electron will pass through this atom during the tunnelling jump.

Both interatomic currents J_{ab} and current density $\vec{J}(\vec{r})$ provide full information about the tunnelling process and, in particular, about the distribution of the tunnelling current in space, *i.e.* about the tunnelling pathways.

In the one-electron approximation, the expressions for tunnelling currents have the following form:

$$\vec{J}(\vec{r}) = \frac{\hbar}{2m} (\psi_D \nabla \psi_A - \psi_A \nabla \psi_D) \quad (14.18)$$

where ψ_D and ψ_A are donor and acceptor diabatic states, and

$$J_{ai,bj} = \frac{1}{\hbar} (H_{ai,bj} - E_0 S_{ai,bj}) (C_{ai}^D C_{bj}^A - C_{ai}^A C_{bj}^D) \quad (14.19)$$

where ai and bj are indices of the atomic orbitals on atoms a and b , H and S are the Hamiltonian and overlap matrices, and C^D and C^A are the coefficients of expansion for states $|D\rangle$ and $|A\rangle$ in the atomic basis set of the system. The total interatomic current between two atoms, J_{ab} , is a sum of $J_{ai,bj}$ over all orbitals of these atoms.

The sign of the current is associated with its direction – a positive J_{ab} , for example, corresponds to current from atom b to atom a . But most importantly, the sign reflects the quantum nature of currents. Since basis functions of the

stationary states $|D\rangle$ and $|A\rangle$ can be chosen to be real, all information about quantum-mechanical phases, and interferences, is contained in the sign of quantum amplitudes. Addition of positive and negative amplitudes, for example, results in destructive interference. Tunnelling currents, by their meaning, are quantum amplitudes, and therefore their signs contain information about interferences in the tunnelling process.

The total current through a given atom is proportional to the probability that a tunnelling electron will pass through this atom during the tunnelling jump. The total atomic current is given by the sum:

$$J_a^+ = \sum_{b'} J_{ab} \quad (14.20)$$

where the summation is restricted to positive contributions J_{ab} , which describe the tunnelling current from various atoms b to atom a . Both the interatomic currents J_{ab} and the total atomic currents J_a^+ can be utilised for visualisation of the tunnelling process and tunnelling pathways. For example, the magnitude of J_a^+ can be taken as an indicator that the atom is involved in the tunnelling process, see, *e.g.*, ref. [59], and Figure 14.2.

The information about all tunnelling paths and their interferences is contained in matrix J_{ab} , which describes the total tunnelling flow in an atomic representation. The analysis of the tunnelling flow gives a rigorous description of where electronic paths are localised in space. For example, if a specific atomic path exists, one can find it using the method of steepest descent, that is: begin from a donor atom d and find an atom b_1 to which the current $J_{b_1,d}$ is maximum, then go to atom b_1 , repeat the procedure and find atom b_2 , *etc.*, until the acceptor atom a is reached. The sequence of atoms: $d, b_1, b_2, \dots, b_n, a$ is the tunnelling path. Of course, this procedure will work only if a single atomic path exists. Usually, the structure of the tunnelling flow is more complicated and many interfering paths exist simultaneously. A more careful analysis of J_{ab} is required in this case.

Remarkably, both $\vec{J}(\vec{r})$ and J_{ab} turn out to be related to the tunnelling matrix element:

$$T_{DA} = -h \sum_{a \in \Omega_D, b \notin \Omega_D} J_{ab} = -h \int_{\partial\Omega_D} (\vec{ds} \cdot \vec{J}) \quad (14.21)$$

In the above formula Ω_D is the volume of space that comprises the donor complex, and $\partial\Omega_D$ is its surface. These relations for electron-transfer reactions were first derived in refs [65–67] using the conservation of charge argument. Similar relations of the coupling matrix element to tunnelling current were derived in the solid-state physics context by Bardeen.⁶⁸

In the methods for computing tunnelling matrix elements reviewed above, the most significant problem is that the diabatic states, by their nature, are well

defined only in the regions of the localisation of the charge, and perhaps in the tunnelling barrier, but not in the far region of the other site. As a result, in a volume integral, representing the matrix elements such as $\langle A|H|D \rangle$ over states D and A , there are major regions (around the donor and acceptor) where one function is well defined, but the other is not. This can potentially lead to numerical errors. To avoid this problem, in the calculation one would somehow need to use the region of the barrier only, where both functions D and A are well defined. This is exactly what the tunnelling current method accomplishes. The above expressions for the matrix element involve only the surface in the region of the barrier, where both $|D\rangle$ and $|A\rangle$ are well defined. This is similar to the transition-state theory, where the rate is evaluated on the surface dividing reactants and products.⁶⁹ Using this technique, extremely small tunnelling matrix elements can be evaluated, Figure 14.1.

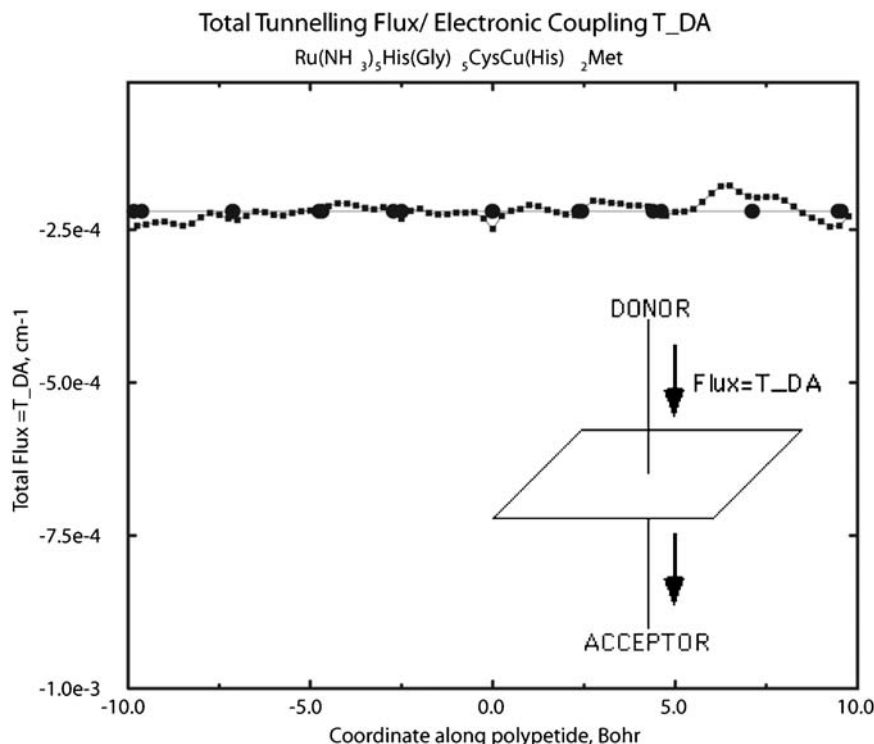


Figure 14.1 Transfer tunnelling matrix element calculated by eqn (14.21) for the $\text{Ru}^{2+/\text{3}+}(\text{Gly})_5\text{Cu}^{2+/\text{1}+}$ system two metal complexes connected by a peptide chain.⁶³ The distance between donor and acceptor is about 30 Å. The total flux is shown as a function of the position of the dividing surface oriented perpendicular to the Ru-Cu axis.

14.3.2 Many-Electron Picture

In a many-electron formulation of the problem, the main results cited earlier remain unchanged, except that now the diabatic states $|D\rangle$ and $|A\rangle$ should be understood as many-electron states, and the operators that act on them should be written in many-electron form. The detailed derivations can be found in the original papers,^{67,70} and in a detailed review of the method.¹⁷ Below, we summarise the key ideas.

14.3.2.1 Calculation of Current Density. Hartree Fock Approximation

To calculate the spatial distribution of the tunnelling current $J(\vec{r})$ one needs first to determine diabatic donor and acceptor states $|D\rangle$ and $|A\rangle$ and then to evaluate the many-electron matrix element given by eqn (14.16) for an appropriate many-electron current density operator.

Suppose states $|D\rangle$ and $|A\rangle$ are single-determinant many-electron functions, which are written in terms of (real) canonical molecular orbitals $\varphi_{i\sigma}^D$ and $\varphi_{i\sigma}^A$, where σ is the spin index, $\sigma = \alpha, \beta$. These are the optimised orbitals obtained from Hartree–Fock calculations of states $|D\rangle$ and $|A\rangle$. Using standard rules for matrix elements of one-electron operators,⁷¹ one can evaluate the expression for the current \vec{J} , eqn (14.16). The final expressions, however, are much simplified, and some important physical insights are gained if the molecular orbitals $\varphi_{i\sigma}^D$ and $\varphi_{i\sigma}^A$ are made biorthogonal,^{72–74} by a rotation of these orbitals, one with respect to the other, in the Hilbert space. In this case, the overlap matrix of states $|A\rangle$ and $|D\rangle$ becomes diagonal,

$$\langle \varphi_{i\sigma}^A | \varphi_{j\sigma}^D \rangle = \delta_{ij} s_i^\sigma \quad (14.22)$$

Such orbitals are also known as corresponding orbitals, and have been utilised in the ET problem by Newton,^{75,76} Friesner,³⁷ and Goddard⁷⁷ and their co-workers in the past.

If now $|D\rangle$ and $|A\rangle$ are two such biorthogonalised states, with p orbitals in α -spin and q orbitals in β -spin, the expression for currents takes the form:

$$\vec{J}(\vec{r}) = -\frac{\hbar}{2m} \langle A | D \rangle \sum_{i,\sigma} \frac{1}{s_i^\sigma} [\varphi_{i\sigma}^A(\vec{r}) \nabla \varphi_{i\sigma}^D(\vec{r}) - \varphi_{i\sigma}^D(\vec{r}) \nabla \varphi_{i\sigma}^A(\vec{r})] \quad (14.23)$$

where

$$\langle A | D \rangle = \prod_i^p s_i^\alpha \prod_j^q s_j^\beta \quad (14.24)$$

The total current in the system is given by the sum of contributions from the corresponding orbitals of donor and acceptor states.

This expression is an obvious generalisation of the one-electron picture. Now, different pairs of corresponding (overlapping) orbitals of donor and acceptor states contribute to the current density. The smaller the overlap between the corresponding orbitals in the donor and acceptor wavefunctions, *i.e.* the greater the change of an orbital between the $|D\rangle$ and $|A\rangle$ states, the greater is the contribution of a given pair of orbitals to the current.

Typically, the major contribution to the current is due to one particular pair of external orbitals, which describes the tunnelling electron. The orbitals of other (“core”) electrons just shift slightly, due to polarisation effects. Their contribution enters as an electronic Franck–Condon factor in the expression for the tunnelling electron current. This factor (product of overlaps of individual core orbitals) is the overlap of the wavefunctions of the core electrons in the donor and acceptor states. The idea that the description of the tunnelling process can be reduced to a “Franck–Condon dressed” one-electron picture was introduced first by Newton who arrived at this picture in his corresponding orbitals analysis of the tunnelling splitting.^{12,75,76}

The shift of the core orbitals in donor and acceptor states does not appear to be significant, *i.e.* their Franck–Condon factor is of the order of unity. This is a surprising result since the canonical orbitals of the core electrons change significantly in donor and acceptor states,^{12,76} which is in line with a significant redistribution of charge in donor and acceptor complexes upon ET.

In practice, the currents are calculated in terms of the atomic basis functions. The molecular orbitals are found as linear combinations of these functions, and tunnelling currents are calculated according to formulas given in ref. [17]. The tunnelling matrix element is evaluated as a surface integral of the current, eqn (3.8), Figure 14.1.

14.3.2.2 Interatomic Tunnelling Currents

The many-electron atomic formalism is developed in a similar way to that of current density. The idea is to derive kinetic equations for atomic populations that describe the charge redistribution in the system during the tunnelling transition, eqn (14.17). The major steps in the formalism leading to these equations are as follows.

First, one needs an operator of the total atomic population that would correspond to P_a . For this purpose, the Mulliken population operators are used. Let a set of real functions, $\phi_\nu(x)$, $\nu = 1, \dots, K$, be any particular atomic set that is chosen for electronic-structure calculation, and $|\nu\sigma\rangle$, $|\mu\sigma'\rangle$, *etc.* are corresponding atomic spin orbitals. The states describing different electrons will be distinguished by an additional index a , $|\nu\sigma(a)\rangle$. In terms of these states, for the a th electron the population operator is written as:

$$\hat{p}_{\nu\sigma}(a) = \frac{1}{2} \sum_{\mu=1}^K (|\nu\sigma(a)\rangle S_{\nu\mu}^{-1} \langle \mu\sigma(a)| + |\mu\sigma(a)\rangle S_{\mu\nu}^{-1} \langle \nu\sigma(a)|) \quad (14.25)$$

The operator of the total population of the state $|\nu\sigma\rangle$, $\hat{P}_{\nu\sigma}$, is the sum of the above operators over all electrons in the system:

$$\hat{P}_{\nu\sigma} = \sum_{a=1}^N \hat{p}_{\nu\sigma}(a) \quad (14.26)$$

The atomic populations are found by summing the contributions of all orbitals of a given atom.

Using the above population operators, one can now describe dynamics of the atomic populations. The time evolution of the system is described by eqn (14.14). The average value of the population of any atomic state $|\nu\sigma\rangle$ at time t during the tunnelling transition is given by

$$P_{\nu\sigma}(t) = \langle \Psi(t) | \hat{P}_{\nu\sigma} | \Psi(t) \rangle \quad (14.27)$$

and the rate of change of the population is

$$\frac{dP_{\nu\sigma}(t)}{dt} = -\frac{T_{DA}}{\hbar} (\langle D | \hat{P}_{\nu\sigma} | D \rangle - \langle A | \hat{P}_{\nu\sigma} | A \rangle) \sin(2T_{DA}t/\hbar) \quad (14.28)$$

The above kinetic equation can be cast in the following form,

$$\frac{dP_{\nu\sigma}}{dt} = \sum_{\mu} j_{\nu\sigma,\mu\sigma} \quad (14.29)$$

where the kinetic coefficients $j_{\nu\sigma,\mu\sigma}$ have the meaning of interatomic exchange currents. Summation over all orbitals of a given atom results in a kinetic equation of the form of eqn (14.17).

The calculations of all matrix elements entering into the above equations is described in ref. [70], where the explicit expressions for interatomic currents J_{ab} in terms of the molecular orbitals of the diabatic states $|D\rangle$ and $|A\rangle$ are given. Thus, the interatomic current J_{ab} , can be obtained from the first principles calculations. When the matrix J_{ab} is known, the analysis of the tunnelling pathways, and the calculation of the transfer matrix element T_{DA} can be carried out as described in the previous section.

In the Hartree–Fock approximation, the expressions for interatomic tunnelling currents J_{ab} in terms of the MOs of donor and acceptor states were obtained in ref. [70]. These expressions, in the case of a nonorthogonal atomic basis, although straightforward for numerical implementation, are quite complicated, and therefore are difficult to deal with practically. The main problem is that in the formally exact HF expressions for interatomic currents, the proper tunnelling-current contributions are mixed with the local polarisation currents of the core orbitals.

While the significance of the latter has not been clarified, this mixing rendered the interatomic currents formulation complicated, and was a major obstacle in practical implementation of *ab initio* interatomic currents. A significant

simplification can be achieved, however, if the one tunnelling orbital approximation (OTO, see below) is used. In the OTO approximation, we neglect the polarisation currents, assuming the core orbitals do not change at all, thereby simplifying the formalism.⁷⁸ One interesting example of interatomic tunnelling currents is shown in Figure 14.2. The shown system is a model for electron tunnelling in a Ru-modified protein, azurin, the system in which an electron needs to tunnel between two strands of the protein *via* hydrogen bonds.⁷⁹

Practically, the concept of interatomic currents is the most useful one in describing tunnelling in such complex systems as proteins. One should keep in mind, however, that this concept is as unambiguous as the concept of individual atoms in the protein itself. As is well known, because of the overlaps of atomic orbitals, the separation of individual atoms in a molecule is not uniquely defined. Within this ambiguity, the interatomic currents are not uniquely defined as well. Here, we present a description that is based on the Mulliken separation technique, which allows a complete theory to be rigorously developed. Obviously, other separation procedures would result in slightly different interatomic currents. (The degree of variation due to this ambiguity has not been carefully examined yet. To a large extent, this is a purely theoretical issue, since the individual current, as well as individual tunnelling paths, are not directly observed or quantified.) What remains unique, however, is the total current through the system, which according to eqn (14.21) is equal to the tunnelling matrix element, a unique quantity for a given quantum system, and a given transition. Thus, the tunnelling matrix element calculated by the technique of interatomic currents does not depend on the separation scheme used to define interatomic currents; however, the currents themselves can vary (we expect slightly) with the separation technique.

14.4 Many-Electron Aspects

A number of interesting issues are related to the many-electron nature of the tunnelling problem in electron-transfer reactions.¹² Can one specific orbital represent a tunnelling charge, and if so, how is such an orbital found? A naive guess, based on Koopmans' approximation, is that it is the canonical HOMO of the system. However, the electronic relaxation effects are not taken into account in this picture. We showed that in fact if such a pair of orbitals exists, it should be found in a special (biorthogonalisation) procedure, and the resulting orbitals are the corresponding orbitals rather than the usual canonical ones. This picture is valid, however, only in the Hartree–Fock approximation. Can the tunnelling event (*i.e.* tunnelling dynamics of the many-electron system) be correctly described by HF wavefunctions? The tunnelling charge can polarise the background electrons as it moves through the background of other electrons of the protein. Thus, the tunnelling should be more properly described in terms of the motion of a “polaron-like” structure. To account for these (correlation) effects, one needs to go beyond Hartree–Fock methods.

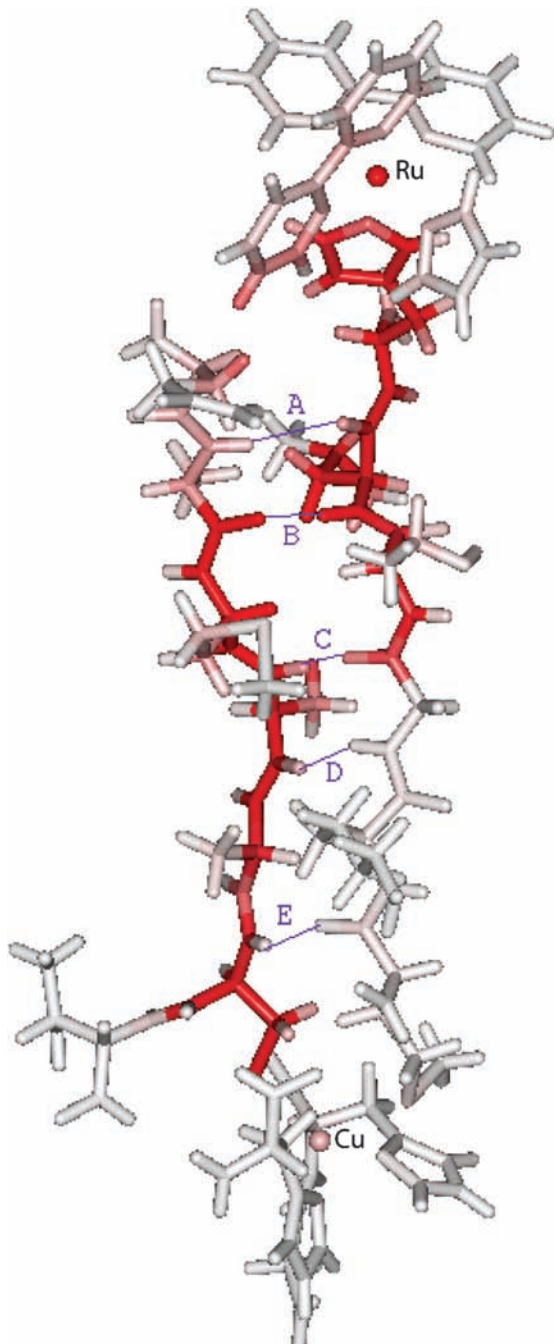


Figure 14.2 Distribution of interatomic tunnelling currents in a (His126) Ru modified azurin⁴ system. The donor (Cu^{1+}) and acceptor (Ru^{3+}) are coupled by two protein strands, and an electron has to jump from one strand to the other in the reaction using hydrogen bonds between the strands. The identified pathway shows how this happens.⁷⁹

14.4.1 One Tunnelling Orbital (OTO) Approximation and Polarisation Effects

The total current in eqn (14.24), is a sum of the current due to tunnelling charge *per se*, and current due to polarisation effects. In the Hartree–Fock approach, all electrons in the systems are treated on an equal footing and, therefore, the expressions for both tunnelling and polarisation currents are similar in structure. The major contribution to the current, however, is due to one particular pair of orbitals, which describes the tunnelling electron. The orbitals of other (“core”) electrons just shift slightly, due to the polarisation interaction with the tunnelling charge, and their contribution to the total current can be neglected. The net core orbitals’ contribution therefore enters only as the electronic Franck–Condon factor^{75,76} in the expression for the tunnelling electron current, as explained in more detail below.

The relative stability of the core orbitals suggests a simple approximation in which only one pair of tunnelling orbitals is considered, while the rest is assumed to be frozen. This is the one tunnelling orbital (OTO) approximation. In this approximation, the two redox states have the form:

$$|D\rangle = |\varphi_0^D, \text{core}^D\rangle, \quad |A\rangle = |\varphi_0^A, \text{core}^A\rangle \quad (14.30)$$

where $|\varphi_0^D\rangle$ and $|\varphi_0^A\rangle$ is a pair of tunnelling orbitals, and the $|\text{core}\rangle$ represent the rest of the biorthogonal orbitals, which remain practically unchanged in the transition.

If such an approximation is adopted, the tunnelling current density takes the form:

$$\vec{J}(\vec{r}) = -\frac{\hbar}{2m} \langle D|A \rangle^{(0)} [\varphi_0^A(\vec{r}) \nabla \varphi_0^D(\vec{r}) - \varphi_0^D(\vec{r}) \nabla \varphi_0^A(\vec{r})] \quad (14.31)$$

where

$$\langle D|A \rangle^{(0)} = \langle \text{core}^D | \text{core}^A \rangle = \prod_{i \neq 0} s_i \quad (14.32)$$

Rigorously speaking, in OTO the core part of the wavefunctions should be considered unchanged, or frozen, and therefore the above overlap should be exactly equal to unity. We, however, will use both the rigorous form, and a “semirigorous” form of OTO approximation, where the overlap $\langle D|A \rangle^{(0)}$ is allowed to be less than one. The reason for this is discussed later.

The individual pairs of the core orbitals do not contribute to tunnelling current density *per se*, because $|\varphi_i^D\rangle$ and $|\varphi_i^A\rangle$ ($i \neq 0$) are practically the same. Moreover, the core orbitals are localised, therefore the contribution to the current is due to a small number of such orbitals. Yet, their overall indirect contribution to total current, in the form of the electronic Franck–Condon factor, $\langle \text{core}^D | \text{core}^A \rangle$ may be substantial. Indeed, the total overlap of the two

cores is a product of a large number of terms corresponding to overlaps of individual core orbitals eqn (14.32). Each overlap s_i in eqn (14.32) for $i \neq 0$ is close to unity; however, the product involves a large number of such terms, and therefore may differ substantially from unity. For example, in the examples that we considered, this term typically ranges from 0.6 to 0.8. We do not exclude, however, that in some cases the core overlap could be significantly smaller.

The considerations presented above suggest that the one tunnelling orbital approximation can be used in long-distance tunnelling calculations. There is also a more fundamental argument⁸⁰ in favour of such an approximation, as described below.

14.4.2 The Limitation of the SCF Description of Many-Electron Tunnelling

The expression for currents, and therefore for the matrix element T_{DA} , eqn (14.21), is given by the sum over pairs of corresponding orbitals, $i=0, \dots, N$. Each of the terms has the following structure:

$$J_i = \langle D | A \rangle^{(i)} \langle \varphi_i^D | \hat{J} | \varphi_i^A \rangle \quad (14.33)$$

where the first factor is the product of pairwise overlaps of all orbitals except for the i th one, and the second factor is the matrix element taken over the i th pair of orbitals. As is seen, the first factor is an electronic analogue of the Franck–Condon overlap, which is given here by

$$\langle D | A \rangle^{(i)} = \prod_{j \neq i} \langle \varphi_j^D | \varphi_j^A \rangle \quad (14.34)$$

For this form of the matrix element to be correct, a specific separation of dynamic timescales should exist in the system. Namely, as expression (14.33) suggests, the interaction associated with the mixing of the i th pair of orbitals should be much weaker (and therefore slower) than that of other orbitals. Such is the case, for example, in nonadiabatic proton transfer, where the transfer matrix element has exactly the same form:⁸¹

$$T_{DA} = \langle \chi_f | \chi_i \rangle \langle f | V | i \rangle \quad (14.35)$$

Here, the first term is the overlap of vibrational functions, and the second term is the matrix element of electronic interaction V between two electronic states. Equation (14.35) is obtained only for a weak (nonadiabatic) electronic interaction, *i.e.* for small V .⁸¹ The mixing of two vibrational states χ_i and χ_f in the same electronic state would occur on a much faster scale, compared to that of the weak interaction V .

Taking this analogy literally, one has to assume that in the above expression for current, eqn (14.35), the mixing of the i th pair of orbitals $-|\varphi_i^D\rangle$ and $|\varphi_i^A\rangle$ should be much slower than that of the other orbitals. In the Hartree–Fock

SCF picture, however, all orbitals are equivalent, and in the expression for current (14.24) all orbitals enter on an equal footing, *i.e.* symmetrically. This symmetric form of the expression (14.24) makes it impossible that the requirement of timescale separation be satisfied for all orbitals. This is obviously a general limitation of the SCF procedure. The only case when the SCF expression eqn (14.24) is correct is when only one specific term dominates the others. In this case the smaller terms would formally violate the requirement of timescale separation, and hence would be in error, but since they are small it practically will not matter.

In our case, there is one special pair of tunnelling orbitals that indeed has a timescale of mixing very different from the rest of the system. Only one pair of orbitals, namely $-|\varphi_0^D\rangle$ and $|\varphi_0^A\rangle$, corresponds to significant redistribution of charge in the system and therefore has a small overlap, and therefore has weak interaction (an equivalent to term $\langle f|V|i\rangle$ in eqn (14.35)). The rest of the orbitals, which we call core orbitals, experience only weak polarisation shifts upon the change of the electronic state, they have close to unity overlaps (terms equivalent to $\langle\chi_f|\chi_i\rangle$ in eqn (14.35)), and therefore have a very short timescale of mixing. For the tunnelling pair of orbitals the requirement of timescale separation is satisfied, and the contribution has the expected form of eqn (14.35):

$$J_0 = \langle D|A\rangle^{(0)} \langle\varphi_0^D|\hat{J}|\varphi_0^A\rangle \quad (14.36)$$

For all other pairs of orbitals, the separation of timescales is not satisfied, however, these terms are small and hence can simply be neglected. In cases when such terms are not small and cannot be neglected, the HF description is not applicable.

In all the numerical examples that we considered so far, we saw that indeed there is always only one pair of orbitals that mostly contributes to the currents; however, not always is the contribution of other orbitals completely negligible. On purely theoretical grounds, it is not clear if the dominance of one pair of orbitals should always be the case. Practically, however, it appears that the one tunnelling orbital approximation is working rather well, and one can adopt it as a tool to probe the tunnelling dynamics in many-electron systems.

14.4.3 Correlation Effects. Polarisation Cloud Dynamics. Beyond Hartree Fock Methods

When an electron tunnels through the protein medium, it moves in the sea of other electrons. The tunnelling potential is, to a large extent, due to interaction of the tunnelling electron with other electrons in the medium. There is also an opposite effect, of course, namely the polarisation of the background electrons by the tunnelling electron. The energy of the tunnelling electron, its tunnelling velocity, and tunnelling timescale⁸¹ are not much different from those of the

valence electrons of the medium. This means that the reaction of these background electrons to a moving tunnelling charge will be quick enough to dynamically follow it. Therefore, as the tunnelling electron moves through the protein, it drags with itself an electron polarisation cloud of background electrons. The compound nature of this tunnelling quasiparticle object is rather complex. An additional complication is due to a virtual inseparability of the tunnelling electron from those in the polarisation cloud because of the electron-exchange effect. (A tunnelling electron, as it passes an atom of the medium, can exchange with the electrons of that atom.) How can one quantitatively describe such a complex tunnelling object?

At the SCF level of description of $|D\rangle$ and $|A\rangle$ states, the effect of the polarisation cloud moving together with the tunnelling charge is not captured. The latter is obviously due to dynamic correlation between the electrons in the systems, an effect that is not present at the SCF level.

To explore the significance of these correlation effects and to estimate the accuracy of Hartree–Fock calculations, one needs to modify the description of $|D\rangle$ and $|A\rangle$ states and to include some relevant excited states that correspond to the tunnelling electron/hole localised on the intermediate atoms of the medium, with other electrons adjusted to it. These effects have not been explored to any extent yet.

14.4.4 Quantum Interference Effects. Quantised Vertices

The wave nature of the transferring electron manifests itself not only in the electron's ability to penetrate classically forbidden barriers, but also in the interference effects. If the electronic coupling is due to several tunnelling paths, each of them associated with an amplitude – a positive or negative number, then the total tunnelling amplitude, which is a sum of the partial amplitudes, can be enhanced (constructive interference) or diminished (destructive interference) depending on the relative signs of the individual paths' amplitudes. Thus, for example, two coupling paths are not necessarily better than one, in the case of destructive interference.⁶⁶ This counterintuitive effect is of a purely quantum nature. Typically, the quantum phases, *i.e.* the signs of the partial amplitudes, are sensitive to the nuclear configuration of the system, and therefore thermal motion of the system would result in averaging of these effects, on the one hand, and cause fluctuations of the coupling matrix element, on the other.¹⁹

Another interesting manifestation of the interference effects is the presence of quantised vortices in the tunnelling currents.⁸² This feature of electron tunnelling can be seen in Figure 14.3, in which the distribution of tunnelling current in the $\text{Ru}^{2+/3+}\text{-(Gly)}_n\text{-Cu}^{2+/1+}$ system is shown. The prominent feature in the tunnelling current is the presence of vortices. It turns out these vortices are of the same nature as those observed in superfluid helium,^{83,84} and in many other quantum systems – superconductors, plasma, spin systems, wave fronts, and others.^{85 87}

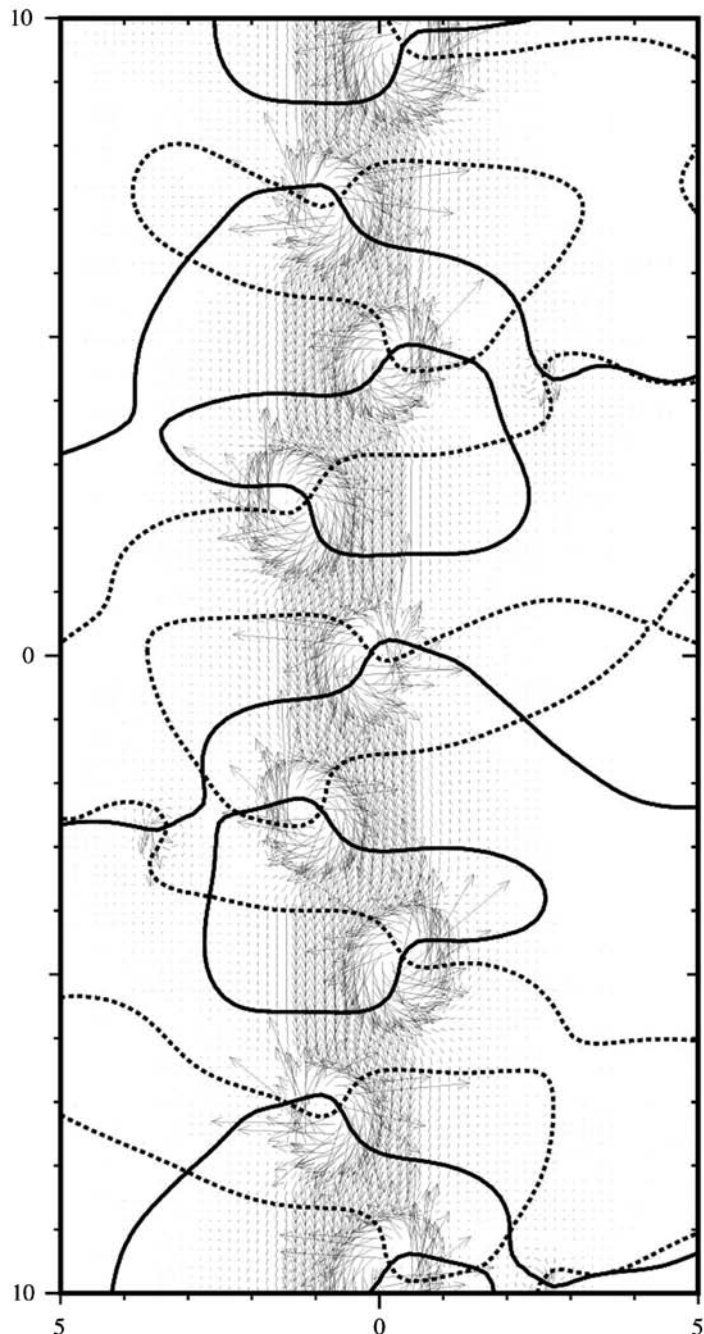


Figure 14.3 Vortex structure of the tunnelling flow along the polypeptide molecular wire, such as that shown in Figure 14.2. The vortices originate at points where nodal lines of donor and acceptor orbitals intersect.

The mathematical nature of these vortices is related to the nodes of complex wavefunctions. The phenomenon was first described by Dirac.⁸⁸ If we have a complex wavefunction, which can be written as

$$\psi = \rho^{1/2} e^{i\phi} \quad (14.37)$$

the current density is related to the gradient of the phase ϕ ,

$$\vec{J}(\vec{r}) = \rho(\vec{r}) \left(\frac{\hbar}{m} \right) \nabla \phi(\vec{r}) \quad (14.38)$$

If complex ψ happens to be zero at some point, the phase ϕ is not defined, and the quantum flux has a vortex structure around such a point. The vortices are “quantised”, as explained in ref. [82].

In the tunnelling problem, the wavefunction of the tunnelling particle can be written in the form (cf. eqn (14.1)) $\psi(\vec{r}) = [\varphi_0^D(\vec{r}) + i\varphi_0^A(\vec{r})]/\sqrt{2}$, where $-\varphi_0^D(\vec{r})$ and $\varphi_0^A(\vec{r})$ are donor and acceptor orbitals. Both $-\varphi_0^D(\vec{r})$ and $\varphi_0^A(\vec{r})$ have nodes, because they are excited states of the Hamiltonian. The nodes of donor and acceptor orbitals are some surfaces in 3D space. The intersections of these surfaces with the xy plane form lines, which are shown in Figure 14.3. The crossing points of the nodal lines of donor and acceptor orbitals then point to the centres of vortices. In Figure 14.3 they are shown as crossing points of solid and dotted lines, which indicate nodes of real and imaginary parts of the wavefunction of the tunnelling electron, respectively.

The intricate structure of the tunnelling flow provides information on how electron tunnelling through molecular wires such as polypeptide chains actually occurs. This picture of the tunnelling flow is a remarkable illustration to Bohmian hydrodynamic interpretation of quantum mechanics.⁶⁴

The analogy with quantum liquids suggests a qualitative picture of biological electron tunnelling in which chains of atoms of the protein matrix form a network of molecular tubes connecting the donor and acceptor, over which the “quantum electron liquid” can flow. Electrons can tunnel in such tubes only when there is a fluctuational quantum-mechanical resonance between the initial and final states,¹¹ thus, although always connected, these tubes can be thought to open up only infrequently, allowing gradual (and incoherent) leakage of electrons from donor to acceptor. The overall process also resembles quantum percolation.

14.4.5 Electron Transfer or Hole Transfer? Exchange Effects

Electron transfer is associated with a superexchange coupling *via* virtual states in which both donor and acceptor complexes are oxidised; the hole transfer is due to virtual excited states in which both donor and acceptor are reduced. In the latter case a (virtual) hole is present in the protein medium while in the former case an additional (virtual) electron is present. Of course a combination of electron and hole transfer is also possible – a process in which virtual states of both types are involved.¹²

Experimentally these two cases are impossible to distinguish, because in both cases the initial and final states of the system are the same. Yet, it is interesting to know which case of coupling actually occurs in real systems.

An interesting example that provides some insights into the above issue and shows the effects of the many-electron nature of tunnelling transitions, is a simple model system, H-(He-He- . . . -He-He)-H⁺, in which electron tunnelling occurs between two protons, across a chain of three He atoms.⁸⁹

Figure 14.4 displays the spatial distribution of the tunnelling current along the molecular axis. As can be seen in Figure 14.4, the electron tunnelling occurs right through the centres of He atoms. At first sight, this is counterintuitive, because the 1s orbital of He is doubly occupied and the next available orbital for an additional (tunnelling) electron lies above the vacuum level (electron affinity of He is negative). That would mean that direct tunnelling through He atoms should be more difficult than through the vacuum, and therefore the tunnelling electron should try to avoid He atoms. The streamlines of the current should then look like the lines of the magnetic field expelled from a superconducting sphere. Yet the calculation shows that electrons move right through the centres of He atoms. What is actually happening is explained by the exchange of the tunnelling electron and electrons with the same spin in 1s orbitals of He atoms. Such a process can be also interpreted as a hole transfer.

This calculation also indicates that any kind of substance is likely to be better than vacuum for electrons to tunnel through! Water in proteins, for example, can definitely facilitate the electronic coupling if cavities or gaps filled with water are present along the tunnelling path.^{40 41,59}

14.5 Dynamical Aspects

We finally briefly mention an interesting issue related to the effects of the dynamics of the protein structure on electron tunnelling.^{20,90,91} Protein dynamics is an integral part of the transfer mechanism, and thermal motions are needed to bring the donor and acceptor states into resonance. There are however, other important implications of protein dynamics.

First, the ET transition state is not unique, and the resonance at which tunnelling occurs may be achieved at slightly different configurations of the protein matrix. The tunnelling jump itself occurs on a timescale (order of fs or less) much shorter than that of protein dynamics. Therefore, tunnelling in different molecules will occur through slightly different instantaneous configurations of the protein. To take this effect into account in the rate, one needs to average $|T_{DA}|^2$ over thermal configurations of the protein and examine the sensitivity of the pathways. This averaging, at least in some cases, can perhaps explain the success of phenomenological/empirical relations for rates of ET in proteins that take into account only local density of the protein medium but not their detailed structure.⁶ These are static or inhomogeneous effects.

The second effect is of a dynamical nature. Since the tunnelling jump occurs on such a short timescale, the protein structure can certainly be considered as fixed during the jump. Yet, protein dynamics can modify the tunnelling event.

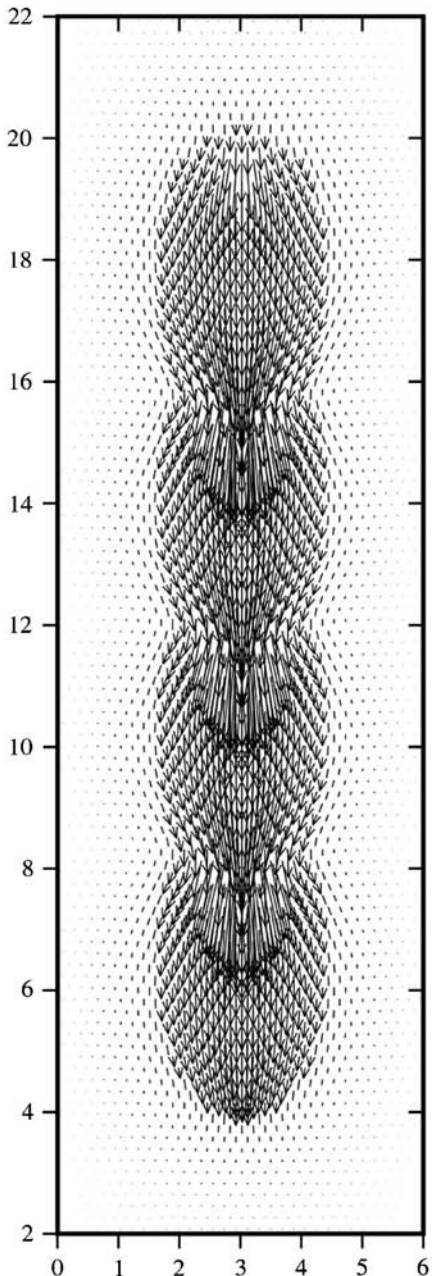


Figure 14.4 The distribution of tunnelling current in the $\text{H He He He H}^+ \rightarrow \text{H}^+ \text{He He He H}$ transition. Electron tunnelling occurs through centres of He atoms, and involves exchange with He 1s electrons. The process can also be interpreted as hole transfer. This many electron effect is incorporated in the one tunnelling orbital description.⁸⁹

This occurs *via* inelastic tunnelling.^{19,91} Although the protein structure is fixed on the timescale of tunnelling, due to the elastic properties of the medium through which the electron propagates, it can exchange energy with the medium by exciting a vibration or receiving energy from the medium. In other words, the tunnelling occurs simultaneously with a vibrational transition of the protein medium.

One can think that the tunnelling electron, as it jumps from atom to atom in the protein, will slightly change the momenta of these atoms by sharp “kicks”, without shifting them in space. Thus, a tunnelling electron can leave a trace of excitations along the path, and in principle this can allow for direct observation of the tunnelling paths.

Quantitatively, inelastic tunnelling is described by the probability $P(\varepsilon)$ that the tunnelling electron will exchange energy ε with the protein when it makes the tunnelling jump from donor to acceptor. The longer the distance between donor and acceptor, the larger the probability that such an energy exchange will occur. The function $P(\varepsilon)$ can be obtained from molecular simulations of the protein dynamics.⁹¹

There is no doubt that the above dynamic effects are present in proteins; however, it is not clear how strongly they modify the rate of electron transfer in real systems. At present there is no consensus on how important the described effects are, and work is in progress to do both the accurate electronic-structure calculations of electronic coupling and the dynamical simulations of realistic models required to understand these effects. Both static and inelastic tunnelling effects are reflected in the dependence of the tunnelling matrix element T_{DA} on the configuration of the system.⁹¹

Another interesting question is the sensitivity of the pathways to slow and large-amplitude configurational changes of the protein. The question is: does the (dynamic) inhomogeneity of the protein structure randomise the pathways to an extent that individual paths determined for a fixed configuration of the protein become meaningless?

The positive answer to the last question shifts the tunnelling description toward Dutton's limit of the unstructured, effective dielectric protein medium.⁶ The negative answer pushes the picture closer to Gray's limit of individual pathways.³ It is understood, however, that the actual picture is somewhere in between these two extremes. Of particular interest also are the cases when the tunnelling electron is coupled to proton transfer discussed elsewhere in this book, see also ref. [92]; in some of these reactions the proton transfer mediates the coupling and thereby localises the tunnelling electron to a specific pathway. The issue of the sensitivity of the tunnelling paths is related to a fundamental biological question, namely whether or not there are specific, evolutionary optimised tunnelling routes between redox centres in proteins.

Acknowledgments

This work has been supported by the National Institutes of Health and by the National Science Foundation.

References

1. D. DeVault and B. Chance, *Biophys. J.*, 1966, **6**, 825.
2. D. DeVault, *Quantum Mechanical Tunnelling in Biological Systems*, Cambridge University Press, Cambridge, 1984.
3. H. B. Gray and J. R. Winkler, *Ann. Rev. Biochem.*, 1996, **65**, 537–561.
4. R. Langen, I. Chang, J. P. Germanas, J. H. Richards, J. R. Winkler and H. B. Gray, *Science*, 1995, **268**, 1733.
5. C. C. Moser, J. M. Keske, K. Warncke, R. S. Farid and L. P. Dutton, *Nature*, 1992, **355**, 796.
6. C. C. Page, C. C. Moser, X. Chen and P. L. Dutton, *Nature*, 1999, **402**, 47–52.
7. V. P. Skulachev, *Membrane Bioenergetics*, Springer, Berlin, 1988.
8. W. A. Cramer and D. B. Knaff, *Energy Transduction in Biological Membranes*, Springer, 1990.
9. S. S. Skourtis and D. Beratan. Vol. 106, pp. 377, *Adv. Chem. Phys.* 1999.
10. J. J. Regan and J. N. Onuchic. Vol. 107, pp. 497, *Adv. Chem. Phys.* 1999.
11. R. A. Marcus and N. Sutin, *Biochim. Biophys. Acta*, 1985, **811**, 265.
12. M. D. Newton. Vol. 767, pp. 91, *Chem. Rev.* 1991.
13. M. D. Newton. Vol. 77, pp. 255, *Int. J. Quant. Chem.* 2000.
14. M. Bixon and J. Jortner, *Adv. Chem. Phys.*, 1999, **106**, 35.
15. A. A. Stuchebrukhov, *Theor. Chem. Acc.*, 2003, **110**, 291–306.
16. J. N. Onuchic, D. N. Beratan, J. R. Winkler and H. B. Gray. Vol. 258, pp. 1740, *Science*, 1992.
17. A. A. Stuchebrukhov, *Adv. Chem. Phys.*, 2001, **118**, 1–44.
18. M. L. Jones, I. V. Kurnikov and D. N. Beratan, *J. Phys. Chem. A*, 2002, **106**, 2002.
19. I. Daizadeh, E. S. Medvedev and A. A. Stuchebrukhov, Effect of protein dynamics on biological electron transfer, *Proc. Nat. Acad. Sci. U.S.A.*, 1997, **94**, 3703–3708.
20. I. A. Balabin and J. N. Onuchic, *Science*, 2000, **114**, 114.
21. E. S. Medvedev and A. A. Stuchebrukhov, *Pure Appl. Chem.*, 1998, **70**, 2201–2210.
22. E. Eggers, M. E. Michel-Beyerle and B. Giese, *J. Am. Chem. Soc.*, 1998, **120**, 12950.
23. B. Giese, *Acc. Chem. Res.*, 2000, **33**, 631.
24. M. Ratner, *Nature*, 1999, **397**.
25. Y. A. Berlin, A. L. Burin and M. A. Ratner, *J. Am. Chem. Soc.*, 2001, **123**, 260.
26. H. M. McConnel, *J. Chem. Phys.*, 1961, **35**, 508.
27. S. Larsson, *J. Am. Chem. Soc.*, 1981, **103**, 4034.
28. S. Larsson, *J. Chem. Soc. Faraday Trans.*, 1983, **2**, 1375.
29. S. Larsson, *Biochim. Biophys. Acta*, 1998, **1365**, 294.
30. A. A. Stuchebrukhov and R. A. Marcus, *J. Chem. Phys.*, 1993, **98**, 8443–8450.
31. J. M. Lopez-Castillo, A. Filali-Mouhim, I. L. Plante and J. P. Jay-Gerin, *J. Phys. Chem.*, 1995, **99**, 6864.

32. A. Nitzan, J. Jortner, J. Wilkie, A. L. Burin and M. A. Ratner, *J. Phys. Chem.*, 2000, **104**, 5661.
33. C. Liang and M. D. Newton, *J. Phys. Chem.*, 1992, **96**, 2855.
34. L. Curtis, C. A. Naleway and J. R. Miller, *J. Phys. Chem.* 1995, **99**, 1182; **97**, 4050.
35. K. D. Jordan and M. N. Paddon-Row, *J. Phys. Chem.*, 1992, **96**, 1188.
36. K. Kim, K. D. Jordan and M. N. Paddon-Row, *J. Phys. Chem.*, 1994, **98**, 11053.
37. L. Y. Zhang, R. Murphy and R. A. Friesner, *J. Chem. Phys.*, 1997, **107**, 450.
38. R. Cave and M. D. Newton, *Chem. Phys. Lett.*, 1996, **249**, 15.
39. R. Cave and M. D. Newton, *J. Chem. Phys.*, 1997, **106**, 9213.
40. N. E. Miller, M. C. Wander and R. J. Cave, *J. Phys. Chem. A*, 1999, **103**, 1084.
41. E. W. Castner, D. Kennedy and R. J. Cave, *J. Phys. Chem. A*, 2000, **104**, 2869.
42. P. Siddarth and R. A. Marcus, *J. Phys. Chem.* 1993, **94**, 2985; **97**, 2400.
43. J. W. Evenson and M. Karplus, *Science*, 1993, **262**, 1247.
44. M. Gruschus and A. Kuki, *J. Phys. Chem.*, 1993, **97**, 5581.
45. J. J. Regan, S. M. Risser, D. N. Beratan and J. N. Onuchic, *J. Phys. Chem.*, 1993, **97**, 13083.
46. A. A. Stuchebrukhov, *Chem. Phys. Lett.*, 1994, **225**, 55–61.
47. A. A. Stuchebrukhov, *Chem. Phys. Lett.*, 1997, **265**, 643–648.
48. I. Daizadeh, J. N. Gehlen and A. A. Stuchebrukhov, *J. Chem. Phys.*, 1997, **106**, 5658–5666.
49. M. Ratner, *J. Phys. Chem.*, 1990, **94**, 4877.
50. D. J. Katz and A. A. Stuchebrukhov, *J. Chem. Phys.*, 1998, **109**, 4960–4970.
51. I. Kurnikov and D. N. Beratan. Vol. 105, pp. 9561, *J. Chem. Phys.* 1996.
52. L. Y. Zhang and R. A. Friesner, *Proc. Natl. Acad. Sci. USA*, 1998, **95**, 13603.
53. J. N. Gehlen, I. Daizadeh, A. A. Stuchebrukhov and R. A. Marcus, *Inorg. Chim. Acta*, 1996, **243**, 271–282.
54. S. S. Skourtis, J. J. Regan and J. N. Onuchic, *J. Phys. Chem.*, 1994, **98**, 3379.
55. C. H. Nakagawa, Y. Koyama and T. Okada, *J. Biochem.*, 1994, **115**, 891.
56. A. Okada, T. Kakitani and J. Inoue, *J. Phys. Chem.*, 1995, **99**, 2946.
57. J. J. Regan, A. J. Dibilio, R. Langen, L. K. Skov, J. R. Winkler and H. B. Gray, *Chem. Biol.*, 1995, **2**, 489.
58. I. Daizadeh, D. M. Medvedev and A. A. Stuchebrukhov, *Molec. Biol. Evol.*, 2002, **19**, 406–415.
59. D. M. Medvedev, I. Daizadeh and A. A. Stuchebrukhov, *J. Am. Chem. Soc.*, 2000, **122**, 6571–6582.
60. D. Medvedev and A. A. Stuchebrukhov, *J. Theor. Biol.*, 2001, **210**, 237–248.
61. M. S. Cheung, I. Daizadeh, A. A. Stuchebrukhov and P. F. Heelis, *Bioophys. J.*, 1999, **76**, 1241–1249.

62. J. Antony, D. M. Medvedev and A. A. Stuchebrukhov, *J. Am. Chem. Soc.*, 2000, **122**, 1057–1065.
63. J. Kim and A. Stuchebrukhov, *J. Phys. Chem. B*, 2000, **104**, 8606–8613.
64. J. F. Cushing and A. S. Goldstein, *Bohmian Mechanics and Quantum Theory: An appraisal*, Kluwer Academic, Dordrecht, Holland, 1996.
65. A. A. Stuchebrukhov, *J. Chem. Phys.*, 1996, **104**, 8424–8432.
66. A. A. Stuchebrukhov, *J. Chem. Phys.*, 1997, **107**, 6495–6498.
67. A. A. Stuchebrukhov, *J. Chem. Phys.*, 1998, **108**, 8499–8509.
68. J. Bardeen, *Phys. Rev. Lett.*, 1961, **6**, 57–59.
69. W. H. Miller, S. D. Schatz and J. W. Tromp, *J. Chem. Phys.*, 1983, **79**, 4889.
70. A. A. Stuchebrukhov, *J. Chem. Phys.*, 1998, **108**, 8510–8520.
71. A. Szabo and N. S. Ostlund, *Modern Quantum Chemistry*, Macmillan, New York 1982.
72. A. T. Amos and G. G. Hall, *Proc. Roy. Soc. (London) A*, 1961, **263**, 483.
73. H. King, R. E. Stanton, H. Kim, R. E. Wyatt and R. G. Parr, *J. Chem. Phys.*, 1967, **47**, 1936.
74. A. F. Voter and W. A. Goddard, *Chem. Phys.*, 1981, **57**, 253.
75. M. D. Newton, *J. Phys. Chem.*, 1988, **92**, 3049.
76. M. D. Newton, K. Ohta and E. Zhong, *J. Phys. Chem.*, 1991, **95**, 2317.
77. E. P. Bierwagen, T. R. Coley and W. A. Goddard, *Parallel computing in computational chemistry* (ACS symposium series, **592**), 1995, pp. 84–96.
78. A. A. Stuchebrukhov, *J. Chem. Phys.*, 2003, **118**, 7898–7906.
79. X. H. Zheng and A. A. Stuchebrukhov, *J. Phys. Chem. B*, 2003, **107**, 9579–9584.
80. X. H. Zheng, Y. Georgievskii and A. A. Stuchebrukhov, *J. Chem. Phys.*, 2004, **121**, 8680–8686.
81. Y. Georgievskii and A. A. Stuchebrukhov, *J. Chem. Phys.*, 2000, **113**, 10438–10450.
82. I. Daizadeh, J. X. Guo and A. Stuchebrukhov, *J. Chem. Phys.*, 1999, **110**, 8865–8868.
83. L. Onsager, *Nuovo Cimento 6 Supp.*, 1949, **2**, 249.
84. R. P. Feynman, *Phys. Rev.*, 1954, **94**, 262.
85. E. A. McCullough and R. E. Wyatt, *J. Chem. Phys.*, 1971, **54**, 3578.
86. J. O. Hirschfelder, A. C. Cristoph and W. E. Palke, *J. Chem. Phys.*, 1974, **61**, 5435.
87. J. O. Hirschfelder, C. J. Goeble and L. W. Bruch, *J. Chem. Phys.*, 1974, **61**, 5456.
88. P. A. M. Dirac, *Proc. Roy. Soc. Lond. A*, 1931, **133**, 60.
89. J. Wang and A. A. Stuchebrukhov, *Int. J. Quantum Chem.*, 2000, **80**, 591–597.
90. I. Daizadeh and A. A. Stuchebrukhov, *Abstr. Pap. Am. Chem. Soc.*, 1997, **214**, 227-PHYS.
91. E. S. Medvedev and A. A. Stuchebrukhov, *J. Chem. Phys.*, 1997, **107**, 3821–3831.
92. A. A. Stuchebrukhov, *J. Theor. Comput. Chem.*, 2003, **2**, 91–118.

CHAPTER 15

Proton-Coupled Electron Transfer: The Engine that Drives Radical Transport and Catalysis in Biology

STEVEN Y. REECE AND DANIEL G. NOCERA

Department of Chemistry, 6-335, Massachusetts Institute of Technology, 77 Massachusetts Avenue, Cambridge, Massachusetts 02139-4307, USA

15.1 Introduction

Enzymes often rely on the coupling of electrons and protons to control primary metabolic steps involving energy transduction, charge transport and catalysis. Mitchell first recognised the importance of electron/proton coupling in biological energy storage with his proposal of proton translocation driven by electron transfer.¹ Since this seminal work, proton-coupled electron transfer (PCET) mechanisms^{2,3} have been shown to underlie amino-acid radical generation and transport⁴ along with the activation of most substrate bonds at enzyme-active sites.⁵ Table 15.1 lists some of the many enzymes that operate by mechanisms involving radicals.⁶ Most, if not all, couple the electron and proton strongly in the management of the radical and/or substrate.

In the PCET event, electron and proton movement need not be synchronous; the proton can affect the electron transport even when the electron and proton do not move together.⁷ Furthermore, the *same* electron and proton do not have to couple throughout an entire biological transformation. As the electron

Table 15.1 Enzymes that operate by radical mechanisms. Adapted from ref. [6].

heme proteins	mononuclear copper	Photosystem II
cytochrome P450s	galactose oxidase	radical SAM
peroxidases	multicopper	lysine 2,3 aminomutase
catalase	laccase	pyruvate formate lyase and activase
prostaglandin synthase	ascorbate oxidase	anaerobic ribonucleotide reductase (class III)
nitric oxide synthase	Cu, Zn, Mn, Ni, Fe superoxide dimutases	biotin synthase
di-iron complexes	flavoproteins	lipoyl ACP synthase
methane mono oxygenase	DNA photolyase	benzylsuccinate synthase and activase
fatty acyl ACP desaturase	flavoprotein oxidases	spore photoproduct lyase
ribonucleotide reductase (class I)	nitric oxide synthase	coproporphyrinogen III oxidase (HemN)
toluene mono oxygenase	adenosylcobalamin	molybdopterin synthesis and MoaB
mononuclear iron	glutamate mutase	glycerol dehydratase and activase
lipoxygenase	methyl malonyl CoA mutase	pyrophosphate
isopenicillin N synthase	dioldehydrase	pyruvate:ferredoxin oxidoreductase
catechol dioxygenases	ribonucleotide reductase (class II)	pyruvate oxidase (FAD)
taurine dioxygenase	lysine 5,6 aminomutase	quinoproteins
hydroxypropyl phosphonate epoxidase	methyleneglutarate mutase	methanol dehydrogenase
prolyl 4 hydroxylase	ethanolamine ammonia lyase	glucose dehydrogenase
lysyl 5 hydroxylase	isobutyryl CoA mutase	copper amine oxidases
clavaminate synthase	methylamine dehydrogenase	tetrahydropterins
γ butyrobetaine hydroxylase	lysyl oxidase	aromatic amino acid hydroxylases
thymine hydroxylase		nitric oxide synthase
deacetoxycephalosporin C synthase		

moves, it may encounter different protons along a transport chain. All that is required for a PCET event is that the kinetics and thermodynamics of electron transport depend on the position of a specific proton or set of protons at any given time.

PCET is a unique charge transport process in biology that steps beyond conventional treatments of biological charge transport^{8,9} such as those based on Marcus' theory for electron transfer.¹⁰⁻¹² As the electron moves, the pK_{as} of redox cofactors change, but to predict the kinetics, knowledge of the driving force of the reaction alone is insufficient. The charge redistribution resulting

from electron and proton motion will affect the energy associated with the reorganisation of the surrounding environment. In addition, the electronic coupling depends on overlap of both the electronic and proton vibrational wavefunctions of the donor and acceptor states, each of which will change parametrically with the proton coordinate. At a more extreme level, PCET involves a process that falls outside the confines of conventional theory because the process includes the breaking and making of chemical bonds.

PCET charge transport and activation events in enzymes embody quantum catalysis inasmuch as PCET is intrinsically a quantum-mechanical effect due to tunnelling of both the electron and proton. The caveat to PCET is that the transfer of the proton, as the heavier particle, is fundamentally limited to short distances,⁷ whereas the electron, as the lighter particle, may transfer over very long distances.^{13–15} When transport distances are short, the electron and proton may transfer together. When they are long, however, the predicament of the disparate transfer distances is resolved by the evolution of enzymes to control proton-transfer (PT) and electron-transfer (ET) coordinates on very different length scales.⁵ Adding to the challenge of effecting PCET over long distances with appreciable rates are the requirements that charge transport occur under mild physiological conditions, with minimal thermodynamic driving force, with low overpotentials, and with specificity. To do so, enzymes impart exquisite thermodynamic and kinetic control over the electron and proton during radical transport and catalysis events.

At an experimental level, an initial indication that proton motion may be coupled to electron transfer in redox-active enzymes comes from the thermodynamic cycling of the cofactors involved. Electrochemical experiments may reveal pH-dependent reduction potentials and rates of ET and/or catalysis.¹⁶ Kinetic isotope studies on the rate of the redox reaction in D₂O vs. H₂O may additionally reveal the quantum-mechanical effects of proton tunnelling to the overall reaction rate.¹⁷ Direct detection of protonation state changes associated with a redox event can be achieved when the electronic structure of the redox-active cofactor is sensitive to the proton. This situation occurs when the relevant acid/base group is in strong electronic communication with the electronic orbitals associated with oxidation/reduction, as is the case for amino-acid radicals, flavin and quinone cofactors, heme cofactors (for protonation events at the axial ligands), and nonheme and FeS clusters. Direct measurements of proton movement within specific hydrogen-bonded residues is expected as 2-D IR techniques,^{18,19} coupled to unnatural amino acid substitution,^{20,21} are developed and applied to the study of natural systems.

Figure 15.1 presents two basic scenarios for PCET in biology. The electron and proton may transfer along the unidirectional path with or without X–H bond breaking. The former describes long-range ET in biology. Here, electron transport along pathways containing X–H ··· Y bonds is modulated by the hydrogen bond, typically *via* the electronic-coupling matrix element.^{22,23} The coupling between the proton and electron is more pronounced when X–H bond breaking is involved. This subclass of PCET includes hydrogen-atom transfer (HAT), which is the specific case of an electron and a proton originating from

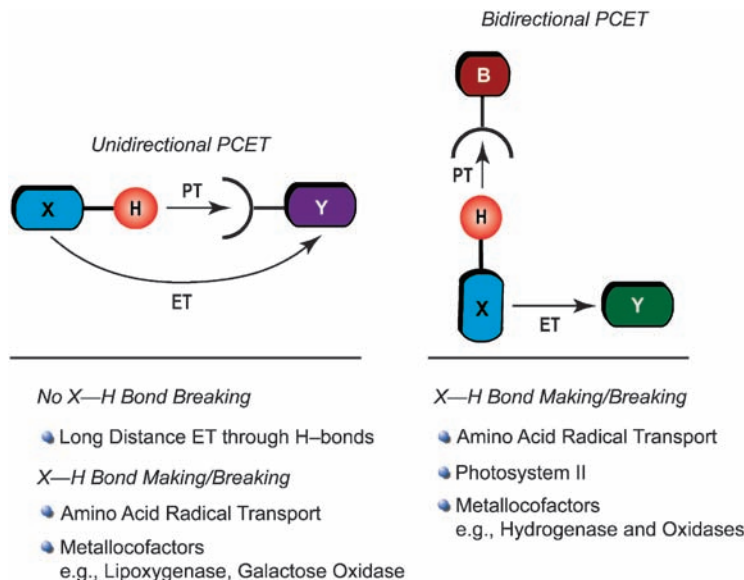


Figure 15.1 Two basic scenarios for PCET in biology: unidirectional PCET, which may involve bond making/breaking; and, bidirectional PCET, where PT to a base occurs along a separate coordinate than ET. This pathway is usually accompanied by bond breaking/making.

the same atom.^{24,25} Amino-acid radical generation often occurs by HAT²⁶ as does the activation of the C—H bonds of substrates by oxidised cofactors such as those in lipoxygenase,^{27,28} galactose oxidase^{29–31} and ribonucleotide reductase.³² In these cases, the thermodynamics for transport of the electron and proton compel that they couple as illustrated by the square scheme shown in Figure 15.2. The thermodynamic driving force for the diagonal PCET pathway is the sum of the driving forces of the constituent ET and PT stepwise pathways, which are indicated along the edges of the square scheme.^{7,33} For the case of amino-acid radicals and for substrate activation at physiological pHs, the intermediate states of the stepwise paths are energetically uphill. If the HAT pathway is energetically favoured with regard to these uphill steps for initial ET or PT, then the reaction will be directed along the diagonal.

Bidirectional electron and proton transfer characterises the other major category of PCET in biology (Figure 15.1). Theoretical treatments of PCET confirm that proton motion can affect electron transport even when the electron and proton do not move along unidirectional coordinates.^{34–41} The case of bidirectional PCET is more frequent than might be expected because the evolution of this pathway permits enzymes to manage the disparate electron and proton length scales. Electrons can transfer into and out of active sites over long distances in concert with protons that hop to or from the active site along amino-acid side chains or among structured water channels.²³

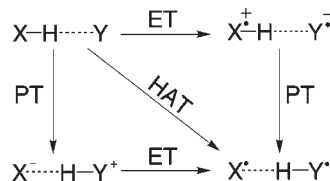


Figure 15.2 Square scheme describing the thermochemistry of a HAT reaction. The overall reaction free energy is obtained by combining the relevant reduction potentials and pK_a s corresponding to stepwise ET/PT (or PT/ET) reactions around the edges. Yet, in many cases, direct HAT along the diagonal is favoured in order to avoid energetic intermediates.

Mono-oxygenases such as cytochrome P450^{42–45} and peroxidases^{46–48} are exemplars of enzymes that operate by this type of PCET in biology. Redox activation of these enzymes to produce heme-oxo intermediates of Compounds I and II putatively occurs with the movement of protons along water channels or amino-acid side chains connecting the redox cofactor to the external aqueous environment.⁴⁹

Other oxidases also derive function from bidirectional PCET pathways at the enzyme-active site. As the first step in photosynthesis, Photosystem II (PSII) uses sunlight to extract electrons from water for the production of NADPH and to generate a proton gradient across the cell membrane for ATP production, with molecular oxygen produced as a byproduct. As the oxygen evolving complex (OEC) in PSII steps through its various S-states,^{50–52} substrate-derived protons are shuttled to the lumen *via* a proton exit channel. The classical functional schemes of PSII suggested that Y_Z was linked to the exit channel *via* H190^{53,54} and hence was the nexus for the requisite electron and proton transport of OEC. However, the more recently obtained X-ray crystal structures^{55–57} show the Y_Z -H190 pair to be relatively isolated by α -helices (see Figure 15.3). Rather, the structures suggest that the D61 residue may be the headwater of this proton exit channel, since it is putatively hydrogen bonded to a Mn-bound water.⁵⁸ D61 is diametrically opposite to Y_Z , which has long been known^{59–61} to be the electron relay between the reaction centre and OEC. The structures of PSII, coupled with biochemical data, also suggest that bidirectional PCET may be used to generate amino-acid radicals. For the reasons described in Figure 15.2, oxidation of Y_Z should be facilitated by proton dissociation from the phenolic oxygen. H190 is appropriately positioned in hydrogen bonding contact to Y_Z to accept a proton upon phenol oxidation. Site-directed mutagenesis studies reveal that H190 facilitates oxidation of Y_Z by P680⁺ by a factor of at least 200 in rate.^{62–64} Thus, redox activity from Y_Z may be supported by PT to *and* from H190 as electrons are transferred through the phenol ring of tyrosine.

Bidirectional PCET is also operable in the concerted function of the bacterial photosynthetic reaction centre in *Rhodobacter sphaeroides*. Excitation of the reaction centre initiates charge separation *via* ET, which results in the

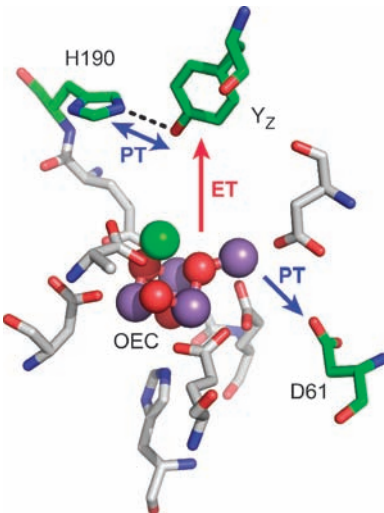


Figure 15.3 The 3.4\AA resolution structure of the oxygen evolving complex (OEC) from Photosystem II (PSII) and the immediate peptide environment adapted from ref. [55] (PDB code 1S5L; Mn in purple, O in red, and Ca in green). Y_Z , $\text{H}190$, and $\text{D}61$ residues are highlighted with green. The direction of proposed PT and ET pathways are indicated with arrows.

sequential two-electron reduction of quinone Q_B . The quinone reduction is coupled to two sequential proton uptakes to form the hydroquinone (ubiquinol), the second of which is a strongly coupled PCET event.⁶⁵ Mutagenesis, isotope, proton uptake and chemical rescue studies have revealed that the reduction of Q_B by the second electron is inextricably coupled to PT from E212,^{66,67} and that it is this ET step that triggers proton translocation. Cytochrome bc_1 couples the oxidation of hydroquinone at the Q_0 binding site to translocation of the protons across the membrane *via* either concerted two-electron chemistry or conformationally gated one-electron chemistry involving the semiquinone intermediate.⁶⁸ Crofts has shown that the subsequent oxidation of ubiquinol by the bc_1 complex⁶⁹ is extremely slow owing to high activation and reorganisation energies that are unexpected based on Marcus theory. These anomalous kinetic features have been attributed^{70–72} to the electron/proton coupling mechanism of the type that has been unveiled by PCET studies.

Bidirectional PCET is also prevalent in reductases such as hydrogenase and nitrogenase. With regard to the former, crystal structures of hydrogenases^{73–75} indicate that the mechanism for hydrogen production occurs by transporting protons into the active site along pathways distinct from those traversed by the electron equivalents. Electrons are putatively injected into the active site *via* a chain of $[\text{FeS}]$ clusters, while proton channels and acidic/basic residues at the active site manage the substrate inventory.⁷⁶ The 2 electrons and 2 protons of

hydrogenase pale in comparison to that of the nitrogenase active site,^{77 80} which manages 8 electrons and 8 protons in the reduction of N₂ to NH₃ (and one equivalent of H₂). The overall mechanism remains undefined,⁸¹ though studies with model systems show that coupling of electrons to protons appears to be imperative to N₂ reduction.^{82,83}

This chapter presents our approach to developing new chemical and biological tools to unravel the mechanistic details of PCET. The discussion will begin by presenting model systems designed to disentangle the proton- and electron-tunnelling events for unidirectional and bidirectional PCET. With lessons learned from these model systems, we show that PCET may be exploited in biomimetic redox-active heme platforms, which display unprecedented multi-functional, catalytic activity. The chapter concludes with the case study of radical-based quantum catalysis in a natural biological enzyme, class I *E. coli* ribonucleotide reductase (RNR). This enzyme utilises both unidirectional and bidirectional PCET to transport redox equivalents from an assembled diiron-tyrosyl radical cofactor to the active site over 35 Å away *via* an amino-acid radical hopping pathway spanning two protein subunits.

15.2 PCET Model Systems

The need to account for the effect of proton motion on ET in the PCET problem requires the development of new methods in chemistry and biology. In devising these new approaches, lessons learned from the study of ET should not be ignored. Paramount among these is the benefits garnered from mechanistic studies of unimolecular ET over a fixed distance. This is best seen from the large body of work in the 1970s on the *bimolecular* ET reactions between redox proteins (primarily cytochrome *c*) and untethered small molecule reactants.¹⁰ Diffusion of reactants and large Coulombic contributions obscured the factors governing ET events. Only with the advent of new methods that enabled ET to be examined over fixed distances were theories able to be tested and redox reactions developed with predictability.^{84,85} The same benefits are expected to be garnered from studying PCET at fixed distance – but the challenge is compounded by the requirement to control two distances – that of ET and that of PT. The task is a challenge to synthesis because it must deliver control over the primary coordination sphere for tuning the ET event and control over the secondary coordination sphere for tuning the PT event. In biology, the secondary and tertiary structure about redox cofactors provides a fixed-distance pathway for PT. Such principles need to be incorporated in models designed to probe the mechanistic details of PCET. Some of these strategies under development in our group are described below.

15.2.1 Unidirectional PCET Networks

Electron transfer donor–acceptor supramolecules assembled by hydrogen bonds and/or salt bridges (Figure 15.4) afford model systems for interrogating

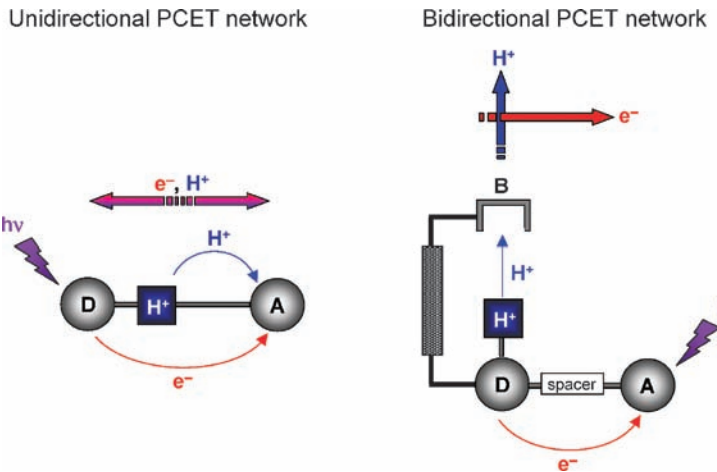
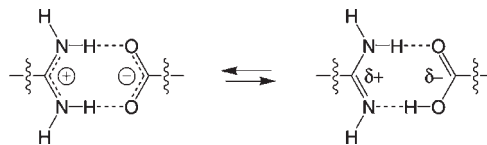


Figure 15.4 Model unidirectional and bidirectional PCET networks. D is a photoexcitable donor, A is an electron acceptor and $[H^+]$ is a hydrogen bonded interface.

the PCET mechanisms of ET through hydrogen bonds. In these constructs, both the ET and PT distances are defined, with the caveat that the proton can be located anywhere within the interface. An electron donor (D) and acceptor (A) are assembled with a PT interface ($\cdots[H^+]\cdots$), thus aligning ET and PT coordinates in a unidirectional D $\cdots[H^+]\cdots$ A fashion. PCET is triggered by laser excitation of the donor or acceptor and kinetically resolved by performing time-resolved spectroscopy. These systems have provided tangible kinetic benchmarks for PCET reactions^{86–93} and stimulated the development of theories to describe PCET.^{8,40}

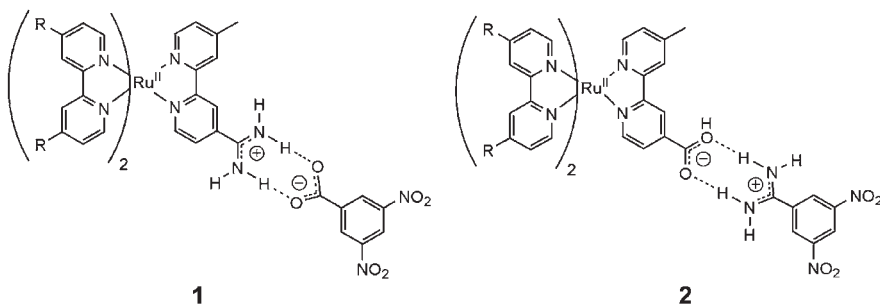
The initial D $\cdots[H^+]\cdots$ A construct ($[H^+] = [(COOH)_2]$, D = zinc(II) porphyrin, A = dinitrobenzene) exploited the propensity of carboxylic acids to form cyclic dimers in low-polarity, nonhydrogen-bonding solvents.⁸⁶ Observation of a deuterium isotope effect for charge separation and recombination revealed the coupling between electron and proton. Within the $\cdots[(COOH)_2]\cdots$ interface, proton displacement on one side of the dicarboxylic acid interface is compensated by the concomitant displacement of a proton from the other side. Because charge redistribution within this interface is negligible, the only available mechanism for PCET arises from the dependence of the electronic coupling matrix element on the position of the protons within the interface.^{37,94,95} Similar results have been obtained for donors and acceptors separated by guanine–cytosine base pairs^{96–98} and related interfaces^{99,100} where net proton motion within the interface is minimal.

To induce proton motion along an ET pathway, unidirectional systems with asymmetric interfaces, such as amidinium-carboxylate salt bridges (Scheme 15.1), between donor–acceptor pairs have been constructed.^{89–93} The pronounced effect



Scheme 15.1

of the proton on the ET rate is immediately evident from a comparative kinetics study of a D---[amidinium-carboxylate]---A complex **1** and its inverted interfacial D---[carboxylate-amidinium]---A counterpart **2** ($D = \text{Ru}(\text{bpy})_3^{2+}$, $A = \text{dinitrobenzene}$).^{89,92} The rate of charge transfer between donor and acceptor along a linear D---(carboxylate-amidinium)---A pathway ($k_{\text{PCET}} = 3.1 \times 10^8 \text{ s}^{-1}$) is attenuated ~ 40 -fold when the interface is switched, D---(amidinium-carboxylate)---A. From these experiments, we find that the driving force and reorganisation energy depend on the charge distribution of the electron and the proton because the initial and final charge values are dependent on whether the process corresponds to ET, PT or PCET. Therefore, the two parameters that determine the rate of a charge-transfer reaction, the activation energy and the electronic coupling, depend on the reaction pathway. The coupling of the charge shift resulting from electron *and* proton motion to the polarisation of the surrounding environment thus embodies the essential distinguishing characteristic of a PCET reaction.



The direct detection of PCET intermediates by transient spectroscopy has been uncovered by assembling **3** with **4** or **5**. This reaction may be followed by monitoring the growth and decay of the porphyrin cation radical transient absorption. Figure 15.5 shows the TA spectrum of a PCET event, which is obscured by the dynamics of the porphyrin S_1 and T_1 excited states (solid circles in Figure 15.5(b)). Probing the PCET reaction at the isosbestic point for the S_1 and T_1 spectra (Figure 15.5(a)) nulls the $S_1 \rightarrow T_1$ dynamics (solid circles in the Figure 15.5(c)) and the optical changes associated with PCET are revealed (open circles in Figure 15.5(c)).

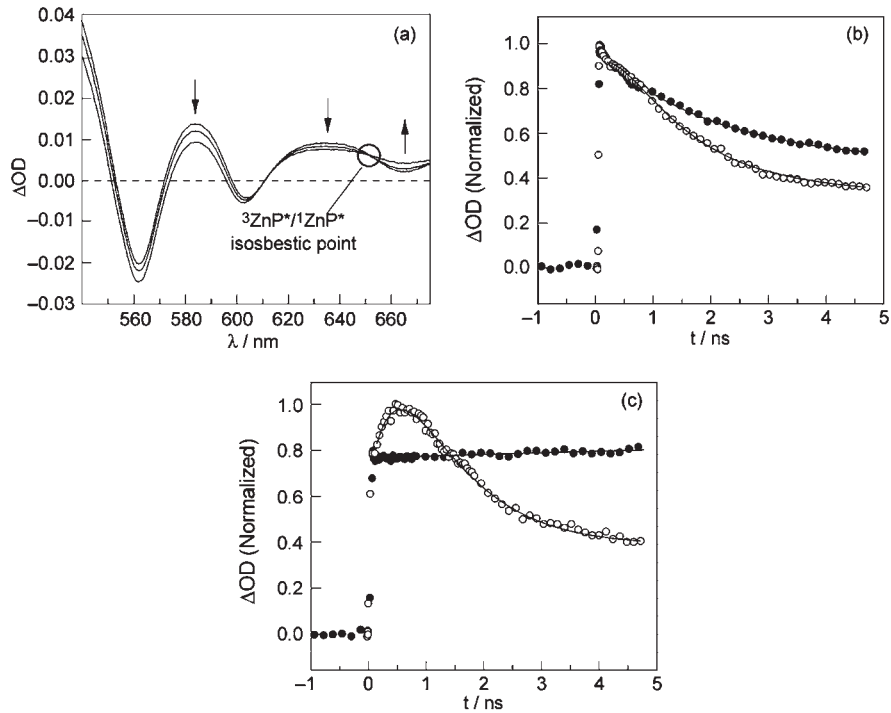
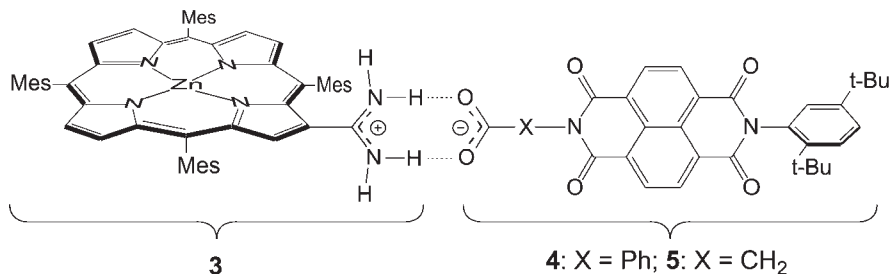


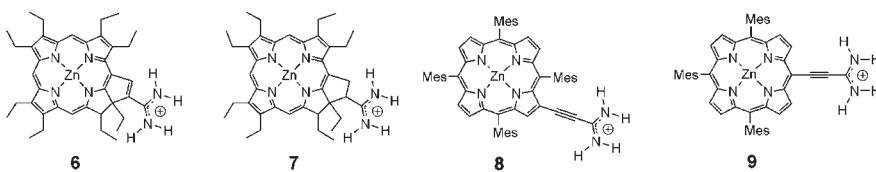
Figure 15.5 (a) Pump probe transient spectra of **3** showing isosbestic point for S_1 and T_1 excited states. Pump probe kinetics for **1** (solid circles) and **1:5** (open circles) probed at: (b) 615 nm (nonisosbestic point) and (c) 650 nm (isosbestic point).



The forward and reverse rate constants ($k_{\text{PCET(fwd)}} = 9 \times 10^8 \text{ s}^{-1}$ and $k_{\text{PCET(rev)}} = 14 \times 10^8 \text{ s}^{-1}$) of **3:4/5** are attenuated by nearly two orders of magnitude when compared with that measured for a dyad consisting of nearly identical donor and acceptor moieties positioned in a comparable geometry, but *via* covalent bonds rather than hydrogen bonds.¹⁰¹ Since the thermodynamic driving

force and solvent reorganisation energies for ET in these two systems are comparable, this comparison implies that the hydrogen bonds attenuate the electronic coupling between the electron donor and acceptor. The nuclear and electronic contributions to the PCET reaction may be unravelled from temperature-dependent kinetics measurements.¹⁰² A small electronic coupling term ($V=2.4\text{ cm}^{-1}$) supports the contention that the hydrogen-bonding interface is the bottleneck for electronic coupling in this system. Extension of the temperature-dependent measurements to a deuterated salt bridge yields a surprising result. The kinetic isotope effect switches from normal at high temperature ($k_{\text{H}}/k_{\text{D}} \sim 1.2$, 300 K) to inverted at low temperature ($k_{\text{H}}/k_{\text{D}} \sim 0.9$, 120 K). Theoretical interpretations of the result describe a model wherein proton fluctuations within the hydrogen-bonding bridge dynamically modulate electronic coupling for ET, and consequently the rate of charge-separation becomes sensitive to the nature of proton vibrational modes within the bridge.¹⁰³ Thermal population of vibrational excited states may be a cause of the reverse isotope effect in this system, where the low-frequency mode of interest is a localised 3-atom N–H–O vibration in the hydrogen bond. This microscopic insight into the role of mediating protons is very pertinent to collinear PCET in biology, where asymmetrical hydrogen-bonding networks are frequently the bottlenecks for electron transport. This level of understanding was only reached when the relevant dynamics are isolated in well-defined and spectroscopically accessible model systems such as **3:4:5**.

Despite the new advances that **3** affords to the investigation of PCET, the proton could not be observed in the electronic absorption spectrum because of steric clashing between the protons of the amidinium and the protons at the β and meso position of the porphyrin ring. The amidinium twists from the plane (by 54°), disrupting the electronic communication between the porphyrin ring and the $[\text{H}^+]$ interface. Thus only minor shifts of the Soret and Q bands are observed with the protonation state of the amidine/amidinium interface. To surmount this drawback, the amidinium was spatially extended away from the porphyrin in **6** and **7**.¹⁰⁴ Electronic communication out to the $[\text{H}^+]$ interface is maintained in **6** with the double bond of the isocyclic five-membered ring of purpurin as evidenced by the large spectral changes of the porphyrin absorption spectrum upon alteration of the amidinium/amidine protonation state (no such change is observed for the chlorin homolog **7**, see Figure 15.6). The spectral changes of **6** have been exploited to determine the ground and excited state pK_{as} and to determine whether the interface is ionised or neutral for a given acceptor.¹⁰⁴



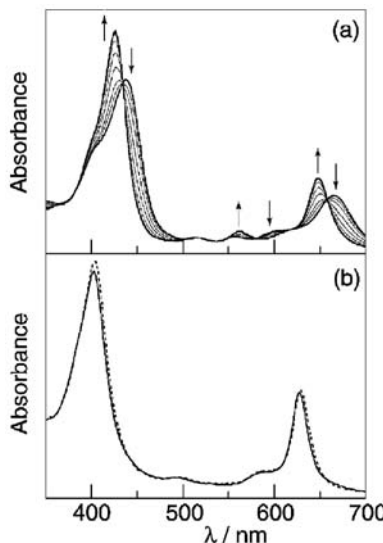


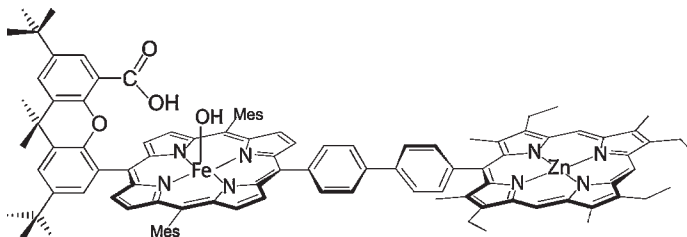
Figure 15.6 Absorption spectra of (a) amidinium purpurin **5** and (b) amidinium chlorin **6** in the presence of varying additions of base (arrows indicate spectral changes upon addition of the base). Taken from ref. [7].

Given that the overall kinetics of the PCET reaction is dictated by the protonation state of the interface, the system has proven powerful in studying PCET. The tautomeric form of the $[H^+]$ interfaces shown in Scheme 1 may be “ dialled in” with the appropriate choice of pK_{as} .¹⁰⁵ The PCET kinetics differ significantly for an electron that traverses the neutral interface versus the charged interface owing to: (i) disparate coupling to the polarisation of surrounding medium (ii) changes in driving force by virtue of the pK_a dependence of the redox potentials of the donor and acceptor and (iii) differentiated electronic coupling for both tautomers. Given that all the essential factors that control a PCET reaction are perturbed by the charge distribution within the proton-transfer network, this knowledge of the electronic structure of the interface has been essential to advancing our understanding of the PCET mechanism. More recently, the design of the $[H^+]$ interface has been improved by preparing alkynyl amidinium porphyrins **8** and **9**.¹⁰⁶ The alkyne group preserves strong coupling between the amidinium moiety and porphyrin macrocycle such that the acid–base properties of the $[H^+]$ interface are reflected in absorption changes of the Soret and Q-bands as in **6**. However, the system adds one new dimension to our PCET studies by removing the angular dependence of the conjugation between the amidinium and porphyrin moieties. Because the intervening alkyne spacer has cylindrical orbital symmetry, differences in electronic coupling as a function of rotation of the amidinium are alleviated. Together, **6**, **8** and **9** will prove to be powerful probes of unidirectional PCET.

15.2.2 Bidirectional PCET Networks

The unidirectional PCET networks of the foregoing section impose an inherent limitation on negotiating the length-scale disparity between PT and ET. The network is assembled by the hydrogen bonds of the PT interface; hence, PT distances are confined to the hydrogen-bond length scale imposed by the assembled salt bridge. To overcome this limitation, we have constructed PCET model systems shown in Figure 15.4 in which ET and PT coordinates are orthogonalised. The PT distance is established by a rigid scaffold that poises an acid–base group above an ET conduit. In the “Hangman” porphyrin architecture, a carboxylic acid or amidine is positioned over a $\text{PFe}^{\text{III}}(\text{OH})$ (P = porphyrin) redox platform *via* a xanthene or dibenzofuran spacer.^{107 109} By appending an electron acceptor or donor to the porphyrin platform, a PCET reaction may be established with PT to or from the hanging group. The Hangman constructs allow us to investigate the role of proton tunnelling in PCET incisively because the PT distance is easily tuned with the length of the Hangman pillar.

Initial studies have centred on appending a Zn(II) porphyrin photochemical electron donor to the Hangman platform, **10**. Despite rapid quenching of the photoreductant, no spectroscopic confirmation of PCET intermediates has been observed.¹¹⁰ The high-spin nature of the five-coordinate $\text{Fe}^{\text{III}}\text{-OH}$ metal centre requires large nuclear rearrangement from an out-of-plane $\text{Fe}^{\text{III}}\text{-OH}$ to an in-plane $\text{Fe}^{\text{II}}\text{-OH}_2$ centre upon reduction; this rearrangement results in a prohibitively large reorganisation energy for electron transfer. Thus, PCET is unable to compete with a rapid energy-transfer mechanism, despite a strongly favourable driving force for the former. These results highlight the difficulty of orchestrating photoinduced PCET reactions at metallo-cofactors; stereo-electronic factors of the heme manifest in such a way as to impede the bond making/breaking PCET reactions. This challenge may be overcome by appending a photoexcitable donor in which energy transfer is extremely slow, or, alternatively, by using an acceptor with a low-spin electron configuration in both the oxidised and reduced form.

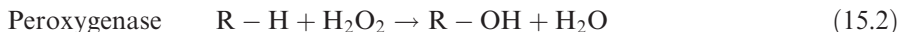


10

15.2.3 PCET Biocatalysis

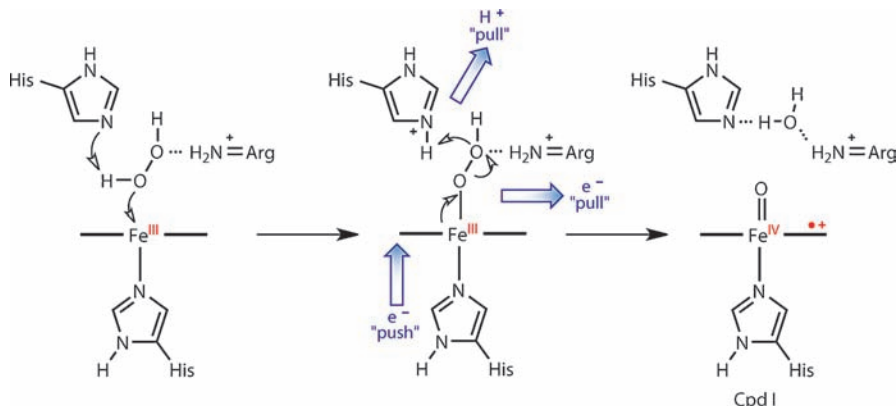
The disposition of an orthogonal PT network distal to a heme redox cofactor is a prevalent motif in enzymes that derive their function from oxygen activation.

Accordingly, the “Hangman” synthetic active site is a faithful structural and functional model of heme-containing enzymes that activate oxygen.¹¹¹ These enzymes may be divided into subclasses as defined by their chemical reactivity:¹¹²



These enzymes are responsible for a wide array of biological redox processes¹¹³ including plant cell-wall biosynthesis, lignin formation,¹¹⁴ removal of xenobiotics and signalling during oxidative stress¹¹⁵ (the peroxidases); the removal of cytotoxic hydrogen peroxide *in vivo* while avoiding the formation of harmful hydroxyl radical species¹¹⁶ (catalases); effecting a variety of metabolic oxidation reactions (cytochrome P450).^{113,117,118} Many of these diverse biological redox processes are performed *via* the highly oxidised intermediate, Compound I (Cpd I).^{113,117,121} Cpd I is two redox levels above Fe^{III} consisting of an Fe^{IV}=O, ferryl-oxo, and an associated organic radical (*e.g.*, a porphyrin π-radical cation or a protein-derived aromatic amino-acid radical). Cpd I formation results from heterolysis of the O–O bond of hydrogen peroxide (or oxygen twice reduced) ligated to ferric heme. Heterolytic cleavage may be coupled to PT to affect release of neutral H₂O. Such a mechanism requires a precisely positioned acid/base residue in the distal pocket of the heme active site.^{113,117,119,122,125} For example, in horseradish peroxidase (HRP), two residues in the distal cavity (His42 and Arg38) assist Cpd I formation by shuttling protons to facilitate H₂O release (see Scheme 15.2).^{126,129} In this way, the histidine does the “pull” part of the “push-pull mechanism” for peroxide activation.^{113,120,130,131} The “push” part of the mechanism is performed by an electron-rich proximal histidine ligand.^{117,120,132} Also, a “pull” effect, the distal Arg38 residue likely aligns H₂O₂ in the active site and contributes to polarisation of the O–O bond.¹¹⁵ Similar mechanisms have been proposed for Cpd I formation in cytochrome *c* peroxidase (CcP),¹¹² catalases,¹³³ and P450 cytochromes.^{111,118,119} For the latter, the lack of acid-base “pull” residues in the distal cavity may be compensated by a “strong push” from an electron-rich proximal cysteinate ligand.^{117,131,135,136}

Investigations of “push-pull effects” on Cpd I formation have been performed using heme model systems^{120,126,137,140} and re-engineered myoglobin.^{126,128,141} O–O heterolysis in acylperoxy porphyrin complexes is enhanced when electron-rich axial ligands are introduced or electron-releasing groups are attached to the *meso*-positions of the metalloporphyrin ring, simulating the



Scheme 15.2

“push”.^{120,137} “Pull effects” have been *indirectly* simulated in model complexes by using substituted peroxybenzoic acids.^{120,138,139} Selective mutations in the distal cavity of myoglobin mutants have demonstrated the importance of a precisely positioned histidine as a proton shuttle – an H⁺ “pull” residue – to the redox selectivity of peroxide O–O bond activation.^{126–128,141} The advantage of re-engineered proteins, as opposed to typical model systems, is that the H⁺ pull residue is structurally established by the secondary and tertiary structure of the protein environment; the secondary coordination environment of model compounds is difficult to control. Because H⁺ residues are not oriented, “pull” effects cannot be systematically investigated. It is on this count that “Hangman” metallo-active sites are distinguished from typical model compounds.

The hanging acid group mimics the amino-acid residues that position water in the distal cavities of heme peroxidases¹⁴² by precisely positioning an acid–base functional group over the face of heme.¹⁰⁷ We have exploited the well-defined architecture of the Hangman cleft to examine the pull effect *directly* using cryogenic stopped-flow methods.¹⁴³ Homolysis of the O–O bond, resulting in Fe^{IV}=O, Cpd II formation, could not be observed, even under conditions that are known to favour Cpd II formation in typical model heme cofactors. The appended H⁺ donor in the Hangman system exerts kinetic control over O–O bond activation by exclusively favouring a proton-coupled O–O heterolysis over the competing homolysis pathway. Formation of Cpd I is thus accomplished by coupling PT to an internal 2e⁻ redox event of the heme cofactor.

This proton-controlled, 2e⁻ (heterolysis) vs. 1e⁻ (homolysis) specificity in heme oxidation sheds light on the exceptional catalytic performance of the Hangman cofactor. The system performs facile P-450 like epoxidation of olefins at high turnover (>10³).^{108,118} In the absence of substrate, the Cpd I type intermediate reacts with peroxide to generate oxygen and water in a catalase-like reactivity, also at exceptionally high turnover (>10³).¹⁴⁴ Mono-oxygenase oxidation and catalase activities are lost when the scaffold is extended, as the

proton must now transfer over long distance, or when the pK_a of the hanging acid–base group is increased.¹⁰⁹ Catalase activity¹⁴⁵ and $1H^+ \cdot 2e^-$ PCET¹⁴⁶ and are retained when the heme cofactor is substituted with other similar redox-active platforms (*i.e.* salens and salophens).^{147–149}

The studies on these Hangman porphyrins and other macrocyclic redox platforms clearly demonstrate that exceptional catalysis may be achieved when redox and PT properties of a cofactor are controlled independently. A key requirement is that the PT distance is kept short, which is accomplished by orthogonalising ET and PT coordinates in the Hangman construct, faithfully capturing the functional and structural properties of mono-oxygenases. In doing so, the Hangman platforms exhibit a multifunctional activity of a single metalloporphyrin-based scaffold and in this way reproduce that of natural heme-dependent proteins, which employ a conserved protoporphyrin IX cofactor to affect a myriad of PCET-promoted chemical reactivities.

15.3 PCET in Enzymes: A Study of Ribonucleotide Reductase

The study of PCET in natural systems provides the convenience that both the ET and PT groups are held at fixed distance by the secondary and tertiary structure of the protein. The laborious synthesis attendant to constructing fixed-distance ET and PT pathways is therefore averted. However, PCET investigations of the natural systems bring the new challenge that the PCET reaction is typically part of a more complicated cascade of events including, but not limited to, protein–protein interactions, binding/release of substrate, protons or redox equivalents, and intraprotein conformational dynamics, all of which may be necessary for enzymatic function. Thus, the PCET event must be isolated in the biological system, prompting us to develop new biochemical and biophysical methods for the study of PCET in biology. Paramount among these new methods are:

- Photoactive non-natural amino acids/redox platforms that enable PCET to be phototriggered.
- Non-natural amino acids that permit the examination of ET and PT by control of pK_a and redox potentials.
- The implementation of new biochemical methods that permit the non-natural amino acids to be selectively introduced along putative PCET pathways of the enzyme.

With these advances, we have created “photoRNRs”, and isolated and observed PCET in ribonucleotide reductase (RNR). This enzyme was chosen as the venue of our studies of PCET in biology because it contains the consummate PCET pathway in biology, transferring the equivalent of an electron and proton over 35 Å across two subunits.

15.3.1 The PCET Pathway in RNR

Class I *E. coli* ribonucleotide reductase (RNR) is composed of two homodimeric subunits designated $\alpha 2$ and $\beta 2$, and a complex between the two catalyses the reduction of nucleoside diphosphates (NDPs) to deoxynucleoside diphosphates (dNDPs).^{4,26,150} $\beta 2$ harbours the diferric tyrosyl radical (${}^{\bullet}\text{Y}122$) cofactor that initiates nucleotide reduction by generating a transient thiyl radical (${}^{\bullet}\text{C}439$) in the enzyme-active site located in $\alpha 2$.¹⁵¹ The crystal structures of both $\alpha 2$ and $\beta 2$ have been solved independently^{152–154} and a docking model has been proposed¹⁵² that places the Y^{\bullet} on $\beta 2$ at a distance $>35\text{ \AA}$ away from the C439 residue on $\alpha 2$. Although extensive discussion has accompanied the construction of the PCET pathway, ${}^{\bullet}\text{Y}122 \rightarrow \text{W}48 \rightarrow \text{Y}356$ in $\beta 2$ to $\text{Y}731 \rightarrow \text{Y}730 \rightarrow \text{C}439$ in $\alpha 2$, shown in Figure 15.7,^{4,155–159} radical transport has escaped direct investigation.

15.3.2 PCET in the $\beta 2$ Subunit of RNR

As the proposed gatekeeper for radical transport between $\alpha 2$ and $\beta 2$, Y356 is pre-eminent to the PCET pathway of RNR. The limited repertoire of natural amino acids does not allow an informative perturbation to be made, and thus we have recently turned to site-specific insertions of unnatural amino acids into $\beta 2$ at Y356 using protein ligation methods.¹⁶⁰ We have replaced Y356 with a

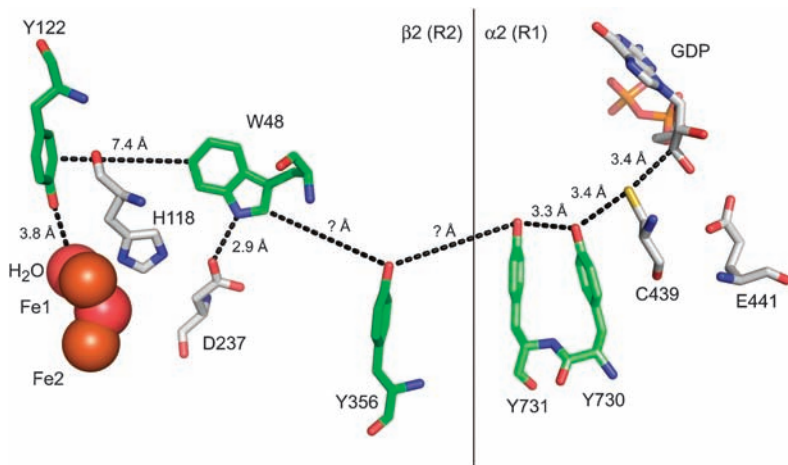
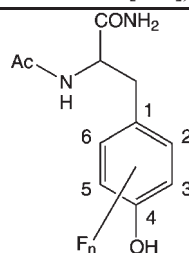


Figure 15.7 Conserved residues of class I RNR that compose the putative PCET pathway for radical transport from ${}^{\bullet}\text{Y}122$ in $\beta 2$ to C439 in the $\alpha 2$ active site. Distances are from the separate crystal structures of the $\alpha 2$ ¹⁵² and $\beta 2$ ¹⁵⁴ subunit from the *E. coli* enzyme. Residues where the radical has been directly observed or trapped via site specific replacement with non natural amino acid analogues are highlighted in green.^{4,164,176} Y356 is not located in either the $\beta 2$ or $\alpha 2$ crystal structures, hence its distance from W48 and Y731 is unknown.

series of fluorotyrosine,^{162,162} 3-nitrotyrosine,¹⁶³ DOPA,¹⁶⁴ and aniline¹⁶⁵ unnatural amino acids, thus allowing us to systematically vary both the pK_a and reduction potential (E_p) of the radical at this position. The fluorotyrosines (F_nY) listed in Table 15.2 have permitted the most detailed investigation owing to a systematic variation in $E_p(F_nY^\bullet/F_nY^-)$ s (from -50 mV to $+270\text{ mV}$ relative to $E_p(Y^\bullet/Y^-)$ between $6 < \text{pH} < 9$) and pK_{as} (from 5.6 to 9.9).¹⁶⁶ pH rate profiles of deoxynucleotide production by the $F_nY356-\beta 2/\alpha 2$ complexes suggest that the rate-determining step in RNR turnover can be changed from conformational gating to radical transport, by altering the reduction potential at position 356 with F_nYs .¹⁶² Figure 15.8 plots the activity of each $F_nY356-\beta 2$ relative to wild type vs. E_p of F_nY^\bullet relative to Y^\bullet . For $E_p > 80\text{ mV}$ vs. Y^\bullet , the activity of RNR is inhibited and by $E_p > 200\text{ mV}$, nucleotide reduction is no longer detectable. These studies support the contention that Y356 is a redox active amino acid on the radical propagation pathway. Open and filled circles in Figure 15.8 represent deprotonated and protonated F_nY residues in the modified $\beta 2$ constructs, respectively, based on the pK_{as} in Table 15.1. Both deprotonated and protonated forms have similar activities for $E_p < 80\text{ mV}$ vs. Y^\bullet , establishing that the protonation state of Y356 does not affect the activity of the enzyme and hence that a proton at Y356 is not obligated to the pathway. These results lead us to propose that upon oxidation of Y356, the proton is transferred “off-pathway” in an orthogonal manner to bulk solution, either directly or via amino-acid residues of the enzyme. This result becomes more profound when taken together with the suggestion that the oxygen of a water/hydroxo bound to Fe1 in the resting-state crystal structure of $\beta 2^{154}$ is the likely PT partner of Y122.⁴ With oxidation and reduction of the Y122 and Y356 termini coupled to an orthogonal PT over a short distance, radical transport

Table 15.2 Physical properties of fluorotyrosine derivatives substituted for Y356 in $\beta 2$ (Data from ref. [166]).

Fluorotyrosine	pK_a	$E_p(F_nY^\bullet/F_nY^-)/mV$ vs. NHE
Ac Y NH ₂	9.9	642
Ac 3,5 F ₂ Y NH ₂	7.2	755
Ac 2,3 F ₂ Y NH ₂	7.8	810
Ac 2,3,5 F ₃ Y NH ₂	6.4	853
Ac 2,3,6 F ₃ Y NH ₂	7.0	911
Ac F ₄ Y NH ₂	5.6	968



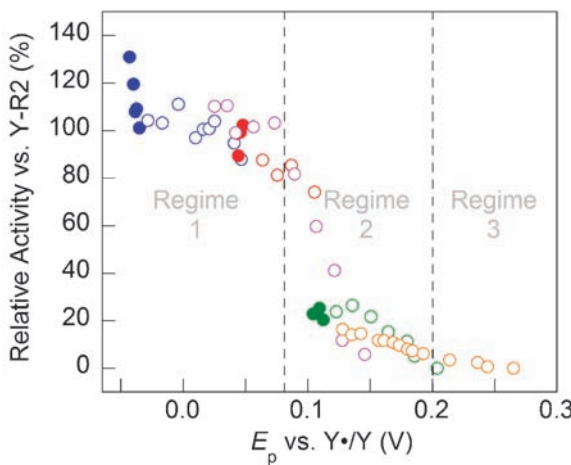


Figure 15.8 Redox potential regimes of RNR activity.¹⁶² Relative activities of $\text{F}_n\text{Y}_{356}\beta 2\text{s}$ vs. $\text{Y}\beta 2$, plotted as a function of peak reduction potential difference between the corresponding $\text{Ac F}_n\text{Y}^*\text{NH}_2$ and $\text{Ac Y}^*\text{NH}_2$: (●, ○) 3,5 $\text{F}_2\text{Y}_{356}\beta 2$, (●, ○) 2,3 $\text{F}_2\text{Y}_{356}\beta 2$, (○) 2,3,5 $\text{F}_3\text{Y}_{356}\beta 2$, (●, ○) 2,3,6 $\text{F}_3\text{Y}_{356}\beta 2$, and (○) $\text{F}_4\text{Y}_{356}\beta 2$. Filled circles represent data points where $\text{pH} < \text{p}K_a$ of the corresponding $\text{Ac F}_n\text{Y}^*\text{NH}_2$; open circles represent data points where $\text{pH} > \text{p}K_a$ of the corresponding $\text{Ac F}_n\text{Y}^*\text{NH}_2$. The three different regimes of RNR activity are highlighted as either gated by a physical/conformational change (regime 1), rate limited by radical transport (regime 2), or reduced to background levels (regime 3) depending on the peak reduction potential difference between the corresponding $\text{Ac F}_n\text{Y}^*\text{NH}_2$ and $\text{Ac Y}^*\text{NH}_2$. Reproduced with permission from *J. Am. Chem. Soc.*, **128**, 1562. Copyright 2006 Am. Chem. Soc.

through $\beta 2$ may occur *via* long-range ET. However, we reiterate that Y_{356} is thermally labile in the crystal structure of $\beta 2$ ¹⁵⁴ and hence its location between W48 of $\beta 2$ and Y731 of $\alpha 2$ is unknown and may vary during turnover.

Against this backdrop of a long-distance ET in $\beta 2$, a further insight into the role of PCET has come from transient kinetic studies of W–Y dipeptides. We have shown that the rate and, moreover, the directionality of radical transfer between W and Y in dipeptides can be controlled by changing the pH of the bulk solution, thereby affecting the reduction potentials of the corresponding radicals.¹⁶⁷ At physiological pHs, Y^* has a lower reduction potential and the direction of ET is $\text{W}^*-\text{Y} \rightarrow \text{W}-\text{Y}^*$; the direction changes at high pH, $\text{W}-\text{Y}^* \rightarrow \text{W}^*-\text{Y}$. These results dovetail with biochemical studies of RNR. Nordlund and Eklund^{153,168} were the first to recognise the potential mechanistic importance of W48 and $[\text{W48H}]^+$ by proposing the $\text{Fe1} \rightarrow \text{H118} \rightarrow \text{D237} \rightarrow \text{W48}$ pathway in cofactor assembly and nucleotide reduction, based on the structurally analogous and spectroscopically well-characterised $\text{Fe}(\text{heme}) \rightarrow \text{H} \rightarrow \text{D} \rightarrow \text{W}$ ET pathway in cytochrome *c* peroxidase. Subsequent studies have shown that under certain conditions $[\text{W48H}]^+$ plays a key role in cofactor assembly.^{169,172}

These results, taken with site-directed mutagenesis studies,¹⁷³ have led us to support a model in which W48 is central to a PCET pathway in β 2 that directs both the cofactor assembly and the initiation of nucleotide reduction.⁴ As for the latter, previous studies have shown that one β 2 subunit can turnover multiple α 2s, thus PCET likely occurs in the forward and reverse direction along the 35 Å pathway every time nucleotide reduction occurs.^{4,174} The crystal structure β 2¹⁵⁴ shows that the indole nitrogen of W48 is hydrogen bonded to the carboxylate oxygen of D237 located 2.9 Å away (Figure 15.7). Based on the W–Y dipeptide results, D237 most likely provides a site to incorporate bidirectional PCET by coupling ET along the radical transport pathway to an orthogonal PT to or from W48, thus providing a mechanism in β 2 to control the direction of radical transport between Y122 and Y356.

15.3.3 PCET in α 2 Subunit of RNR: PhotoRNRs

The Y731 \leftrightarrow Y730 \leftrightarrow C439 triad in α 2 connects Y356 of β 2 to the active site. As shown by the distances in Figure 15.7, the triad is in hydrogen-bonding contact. The *in-vivo* suppressor tRNA/aminoacyl-tRNA synthetase method¹⁷⁵ has recently been employed to site specifically incorporate 3-aminotyrosine (NH_2Y) at positions 731 and 730.¹⁷⁶ The reduction potential of $\text{NH}_2\text{Y}^\bullet$ is 0.19 V lower than that of Y^\bullet , therefore $\text{NH}_2\text{Y}730/731$ serves as an effective thermodynamic trap in radical transport. Upon mixing $\text{NH}_2\text{Y}730/731\alpha$ 2 with β 2 in the presence of RNR substrate and effector followed by freeze-quenching of the reaction, a new organic radical was observed in the X-band EPR spectrum that was attributed to $\text{NH}_2\text{Y}730/731^\bullet$.¹⁷⁶ Surprisingly, the mutants retained activity, albeit at levels attenuated from that of the wild type. These experiments provide direct evidence that Y730/731 are redox-active residues in the radical transport pathway of RNR, however, they do not report on the PCET mechanism for radical formation.

We have developed the methods summarised in Figure 15.9 to investigate PCET along the pathway in α 2. The general strategy has been to retain the 20-mer C-terminal peptide tail (β C20, $\text{NH}_2\text{--YLVGQIDSEVDTDDLSNFQL--COOH}$) of the β 2 subunit because this peptide contains the critical Y356 and the binding determinant of β 2 to α 2.^{155,177} Solid-phase peptide synthesis affords the 20-mer peptide, which we then extend manually to append a variety of photo-oxidants proximal to Y356 on the peptide (Figure 15.9, red circle). Laser excitation of the photo-oxidant generates $^\bullet\text{Y}356$, therein bypassing hole generation at the metallocofactor in β 2 and allowing us to instantaneously “turn on” the PCET pathway in RNR.

The key to implementing the photoRNR strategy is the photogeneration of $^\bullet\text{Y}356$. Suitable phototriggers of Y^\bullet are shown in Table 15.3. All the compounds shown may, upon excitation, accept an electron from tyrosine, however, those highlighted in red may also accept the phenolic proton. Radical generation has been characterised by time-resolved absorption and emission spectroscopies. All have virtues and drawbacks for radical generation in a proteinacious

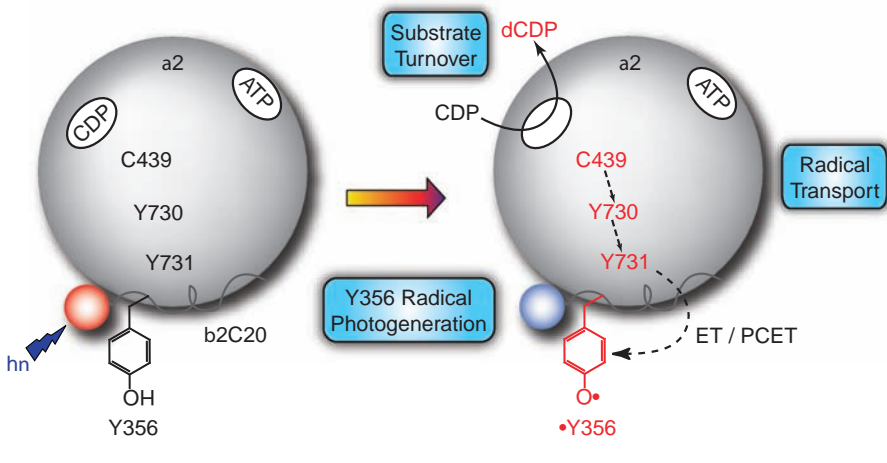
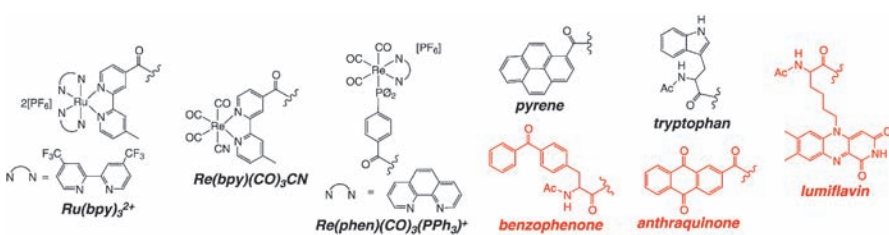


Figure 15.9 Experimental design of photoRNPs for the study of radical transport along $\cdot\text{Y}356 \rightarrow \text{Y}731 \rightarrow \text{Y}730 \rightarrow \text{C}439$ pathway. $\cdot\text{Y}356$ is generated photochemically by a proximal photo oxidant (red circle) on the $\beta 2\text{C}19$ peptide. NDP, nucleoside diphosphate substrate; dNDP, deoxyribonucleoside diphosphate product; $\beta 2\text{C}19$, 19 mer C terminal peptide tail of $\beta 2$.

Table 15.3 Phototriggers of tyrosyl radicals for use in photoRNPs (red circle in Figure 15.9).



environment. Photoionisation of W with UV light ($\lambda < 290 \text{ nm}$) irreversibly generates W^\bullet , which in turn oxidises Y within the pH range relevant to RNR.¹⁶⁷ However, a drawback with tryptophan-based peptide constructs is the UV-light needed to excite the tryptophan. Deep-UV excitation falls within the absorption envelope of RNR, thus presenting a significant problem for the direct kinetic analysis of $\alpha 2$ -bound peptides owing to “inner-filter” optical effects and protein instability. The viability of benzophenone-containing (BPA) amino acids and anthraquinone (Anq) as excited-state oxidants of tyrosine were explored next.¹⁷⁸ Excitation of the BPA- and Anq-modified peptides with light of $\lambda > 320\text{--}365 \text{ nm}$

yields the $(\text{BPA}^{\cdot}/\text{Anq}^{\cdot})-\text{Y}^{\cdot}$ diradical at pH 7.5 on the sub-ns timescale. Figure 15.10(a) illustrates that the radical photogeneration is retained within the full-length BPA-Y- β C19 peptide. Moreover, BPA is sufficiently oxidising that it can produce the radicals of non-natural fluorotyrosines, $\text{F}_n\text{Y}^{\cdot}$, at high yield.¹⁶⁶ The exciting wavelength can be pushed deeper into the visible by using the metal-to-ligand charge transfer (MLCT) excited state of Re(I) polypyridyl complexes.¹⁷⁹ The MLCT excited state is highly energetic and presents a significant overpotential for tyrosine oxidation. $\text{Re}(\text{bpy})(\text{CO})_3\text{CN}$ and $\text{Re}(\text{phen})(\text{CO})_3(\text{PPh}_3)^+$ can oxidise deprotonated Y and protonated Y, respectively (Figure 15.10(b)). For the former, Y oxidation was investigated with $\text{Re}(\text{I})-\text{F}_n\text{Y}$ pairs; charge separation occurs *via* ET with a large reorganisation energy, while charge recombination occurs in the Marcus inverted region.¹⁸⁰ The additional energy and exceptionally long lifetime of the MLCT excited state of the $\text{Re}(\text{phen})(\text{CO})_3(\text{PPh}_3)^+$ complex is crucial for the PCET of Y (with protonated phenol) oxidation, as coupled proton transfer involves smaller couplings¹⁸¹ between the reactant and product surfaces that slow down the reaction rate.¹⁸¹ In this case, by appending the tyrosine to an ancillary ligand, remote from the electron-accepting polypyridyl ligand in MLCT excitation, Y oxidation occurs *via* a unidirectional electron cascade with proton transfer to the environment.¹⁸² The MLCT excited state of [Re] in combination with the F_nY unnatural amino acids provides a selective method for generation of $\text{F}_n\text{Y}^{\cdot}$ at physiological pHs.¹⁸⁰

All of the photopeptides trigger RNR turnover. Figure 15.11 plots the turnover measured upon excitation of the Ac-W-Y- β C19, Ac-BPA-Y- β C19, Anq-Y- β C19, and [Re]-3,5-F₂Y- β C19 peptides bound to α 2. The experiments

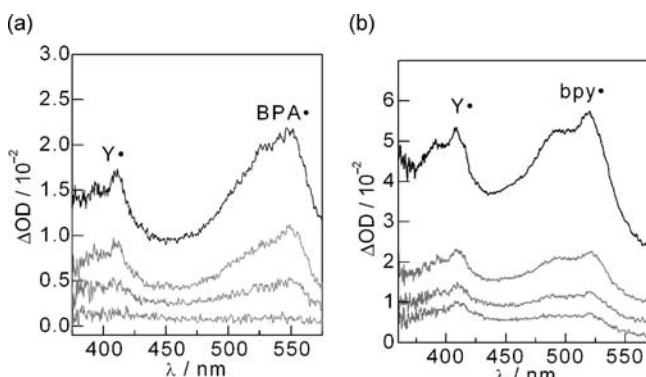


Figure 15.10 (a) Transient absorption spectra of BPA Y- β C19 obtained 65 (—), 415 ns, 1, and 10 μ s (—) following 320 nm excitation. (b) Transient absorption spectra of a solution of [Re] Y at pH 12 obtained 15, 65, 115, and 215 ns after a 355 nm, 5 ns laser pulse. Reproduced with permission from *J. Am. Chem. Soc.*, **127**, 9448 and *J. Am. Chem. Soc.*, **129**, 8500. Copyright 2005 and 2007 Am. Chem. Soc.

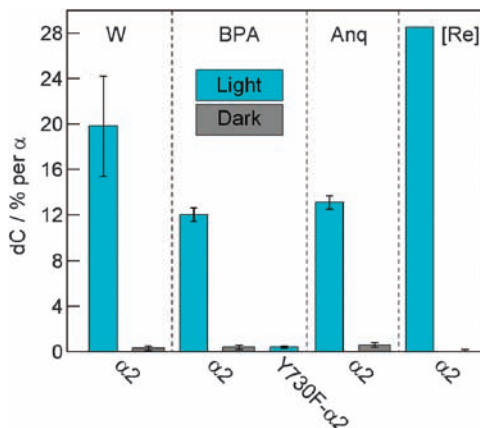


Figure 15.11 Light initiated, single turnover assays for each of the peptide: α 2 systems studied to date. The headings refer to the photooxidant used on the β C19 peptide: Ac W Y β C19,¹⁶⁵ Ac BPA Y β C19,¹⁷⁸ Anq Y β C19,¹⁷⁸ and [Re] 3,5 F₂Y β C19.¹⁸⁷ The bars refer to light (■) reactions and dark (▨) controls. For 100% turnover, each dimer of α 2 would produce 2 molecules of dCDP.

were performed under single-turnover conditions, in the presence of CDP substrate and ATP effector, and with an excess of peptide in solution such that all α 2 was bound. The enzyme is active when excited by light and inactive in the dark. The ability of a small peptide to replace the entire β 2 subunit mimics the radical initiation process of class II RNRs,^{183,184} in which the small molecule adenosylcobalamin initiates thiyl radical formation directly on α 2. Thus, by controlling the radical initiation pathway, we have succeeded in converting a class I RNR to its simpler class II counterpart.

Mutation of Y730 to F turns the photoRNR off (see Figure 15.11, Y730F data). The X-ray crystal structure of the Y730F- α 2 variant has been solved¹⁸⁵ and shows that the mutation breaks the hydrogen-bond network between Y731 and C439 while maintaining the protein fold and the distance among the π -systems of the aromatic rings. The disruption of the proton-transfer network does little to perturb the direct electron-transfer super-exchange pathway since ET proceeds through the aromatic residues¹⁸⁶ whose distance is unchanged in the mutant. The mutation does, however, increase the tunnelling distance for the proton, assuming that noncrystallographically identified water molecules are not present in the structure. The O---S distance from Y731 to C439 is 5.9 Å in Y730F- α 2, whereas in wt- α 2 the longest distance between phenol-O and thiol-S atoms is 3.4 Å. As illustrated in Figure 15.12, the attenuation of turnover is consistent with the interruption of the proton transfer pathway, providing strong evidence that radical transport is indeed pathway specific in α 2 and proceeds along a collinear PCET pathway involving the tyrosines.

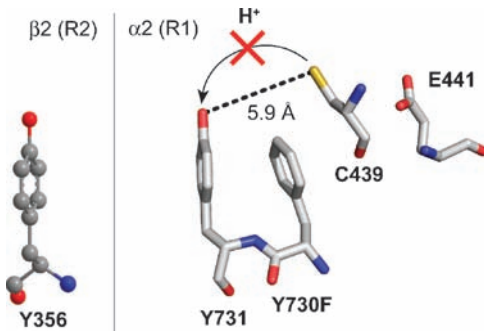


Figure 15.12 The PCET pathway of Y730F_{α2} mutant imposes an O–S distance from C439 to Y731 ($d = 5.9 \text{ \AA}$) that is too long for the proton to transfer. The inactivity of the mutant protein is consistent with the interruption of proton transfer along the PCET pathway. Reproduced with permission from *J. Am. Chem. Soc.*, **129**, 8500. Copyright 2007 Am. Chem. Soc.

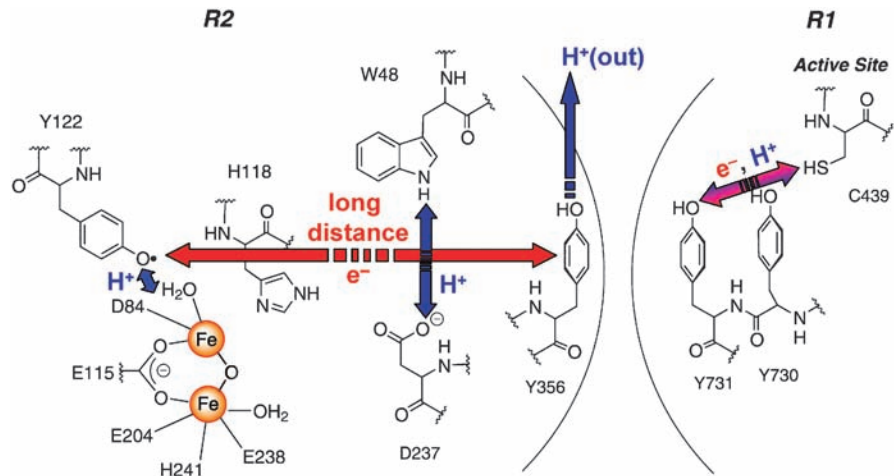


Figure 15.13 Proposed model for radical transport in RNR. The mode of transport at the interface (between Y356 and 731) is undefined.

15.3.4 A Model for PCET in RNR

Figure 15.13 presents the current model for PCET in RNR. Beginning at the cofactor, an orthogonal PT between Y122 and the di-iron cofactor establishes the need only for the transfer of an electron through the span of β2. Oxidation of Y356, the redox terminus of the β2 pathway, demands a PCET reaction, but this too appears to involve a PT that is orthogonal to the ET pathway. By moving the protons at Y122 and Y356 off pathway, the radical transport in β2

involves a long-distance ET coupled to short PT hops at the tyrosine endpoints. In setting up the radical transport pathway in this fashion, the very different PT and ET length scales are aptly managed in RNR. The D236-W48 hydrogen bond may control the directionality of ET in β 2. Dipeptide W-Y studies are consistent with this contention. Within α 2, the activity studies of the Ac-(W/BPA)- β C20 peptide and α 2, together with those of the Y730/731F α 2 mutant suggests a unidirectional PCET pathway through α 2 into the active site. RNR appears to incorporate all the variances of PCET mechanisms in its transport of a radical across two subunits and over 35 Å.

The [Re]-3,5-F₂Y- β C19 peptide generated the highest RNR turnover observed to date (Figure 15.11). We have begun a transient spectroscopic investigation of this peptide bound to α 2 in an attempt to resolve the ${}^{\bullet}\text{Y}356 \rightarrow \text{Y}731$ radical hop from the peptide into the protein. Figure 15.14 shows the transient absorption spectra obtained upon excitation of the [Re]-3,5-F₂Y- β C19:Y731F- α 2 complex.¹⁸⁷ The Y731F mutation prevents radical transport into α 2 and isolates the observed photochemistry to that of the *bound* peptide. The UV-vis absorbance features for the reduced [Re]⁰ ($\lambda_{\text{max}} \sim 525$ nm) and oxidised 3,5-F₂Y[•] ($\lambda_{\text{max}} = 395$ nm) are spectrally well separated. The 3,5-F₂Y[•] absorbance feature is significantly shifted from that of Y[•] ($\lambda_{\text{max}} = 410$ nm) to allow for visualisation of the ${}^{\bullet}\text{3,5-F}_2\text{Y}356 \rightarrow \text{Y}731$ radical hop upon removal of the Y731F mutation. The experiment is powerful because it permits PCET contribution to the kinetics to be deconvolved by exploiting the E_p and pK_a differences of the F_nY as we have done in the studies described in Section 15.3.2.

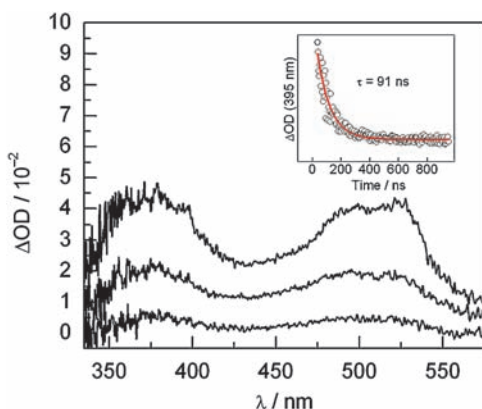


Figure 15.14 TA spectra of a 100 μM solution of [Re] 3,5 F₂Y βC19 in the presence of 140 μM Y731F α2, 1 mM CDP, and 3 mM ATP in 20% glycerol at pH 8.2. Spectra were recorded at 65, 115, and 215 ns. Inset: Single wavelength absorbance kinetics recorded at 395 nm. Reproduced with permission from *J. Am. Chem. Soc.*, **129**, 13828. Copyright 2007 Am. Chem. Soc.

15.4 Concluding Remarks

PCET functions at the heart of redox-based catalysis in biology. Charge transport, amino-acid radical initiation and reactivity, and substrate activation all rely on various PCET mechanisms. New functional schemes and mechanistic distinctions for PCET in biology have been uncovered owing to advances in synthetic, biochemical and physical methods. In our labs: (1) hydrogen-bond assembled supramolecules permit unidirectional PCET to be explored; (2) transient spectroscopies allow for direct detection and kinetic characterisation of PCET intermediates; and (3) the Hangman active site effectively models the secondary coordination sphere of heme cofactors that undergo PCET-based catalysis. Additionally, the examination of PCET in RNR relies on an array of innovations including: (4) the synthesis and physical characterisation of unnatural amino acids to study the PCET of tyrosyl radicals, (5) the use of protein-ligation methods to incorporate these unnatural amino acids into β_2 , (6) the development and characterisation of photoactive peptides that are competent in ${}^{\bullet}\text{Y356}$ photogeneration, and (7) the design and characterisation of photoRNRs for the study of PCET in RNR subunits. These techniques now place the discipline on the threshold to study biological PCET at the same rigorous mechanistic level that is common to model systems.

Acknowledgements

We acknowledge the stimulating collaboration with Joanne Stubbe on the PCET mechanism of RNR catalysis, as well as all the members of the group, past and present, who have contributed to these fundamental PCET studies over the years. The National Institutes of Health supported this work with grant GM47274.

References

1. P. Mitchell, *Nature*, 1961, **191**, 144.
2. S. Y. Reece, J. M. Hodgkiss, J. Stubbe and D. G. Nocera, *Philos. Trans. Roy. Soc. B*, 2006, **361**, 1351.
3. M. H. V. Huynh and T. J. Meyer, *Chem. Rev.*, 2007, **107**, 5004.
4. J. Stubbe, D. G. Nocera, C. S. Yee and M. C. Y. Chang, *Chem. Rev.*, 2003, **103**, 2167.
5. C. J. Chang, M. C. Y. Chang, N. H. Damrauer and D. G. Nocera, *Biochim. Biophys. Acta*, 2004, **1655**, 13.
6. P. A. Frey, A. D. Hegeman and G. H. Reed, *Chem. Rev.*, 2006, **106**, 3302.
7. J. M. Hodgkiss, J. Rosenthal and D. G. Nocera, in *Handbook of Hydrogen Transfer. Physical and Chemical Aspects of Hydrogen Transfer*, ed. J. T. Hynes, J. P. Klinman, H.-H. Limbach and R. L. Schowen, Wiley-VCH, Weinheim, Germany, 2006, **vol. 2.4.17**, pp. 503–562.
8. R. I. Cukier and D. G. Nocera, *Annu. Rev. Phys. Chem.*, 1998, **49**, 337.
9. R. I. Cukier, *ACS Symp. Ser.*, 2004, **883**, 145.

10. R. A. Marcus and N. Sutin, *Biochim. Biophys. Acta*, 1985, **811**, 265.
11. H. B. Gray and J. R. Winkler, *Quart. Rev. Biophys.*, 2003, **36**, 341.
12. C. C. Moser, C. C. Page and P. L. Dutton, *Philos. Trans. Roy. Soc. B*, 2006, **361**, 1295.
13. C. C. Moser, J. M. Keske, K. Warncke, R. S. Farid and P. L. Dutton, *Nature*, 1992, **355**, 796.
14. J. R. Winkler and H. B. Gray, *Chem. Rev.*, 1992, **92**, 369.
15. H. B. Gray and J. R. Winkler, *Annu. Rev. Biochem.*, 1996, **65**, 537.
16. K. A. Vincent, A. Parkin and F. A. Armstrong, *Chem. Rev.*, 2007, **107**, 4366.
17. B. A. Diner, D. A. Force, D. W. Randall and R. D. Britt, *Biochemistry*, 1998, **37**, 17931.
18. I. J. Finkelstein, H. Ishikawa, S. Kim, A. M. Massari and M. D. Fayer, *Proc. Nat. Acad. Sci.*, 2007, **104**, 2637.
19. L. P. DeFlores and A. Tokmakoff, *J. Am. Chem. Soc.*, 2006, **128**, 16520.
20. W. Liu, A. Brock, S. Chen, S. Chen and P. G. Schultz, *Nat. Methods*, 2007, **4**, 239.
21. M. R. Pratt and T. W. Muir, *Chem. Biol.*, 2007, **2**, 537.
22. D. N. Beratan, J. N. Betts and J. N. Onuchic, *Science*, 1991, **252**, 1285.
23. J. Lin, I. A. Balabin and D. N. Beratan, *Science*, 2005, **310**, 1311.
24. R. I. Cukier, *Biochim. Biophys. Acta Bioenerg.*, 2004, **1655**, 37.
25. R. I. Cukier, *J. Phys. Chem. B*, 2002, **106**, 1746.
26. J. Stubbe and W. A. van der Donk, *Chem. Rev.*, 1998, **98**, 705.
27. A. Kohen and J. P. Klinman, *Acc. Chem. Res.*, 1998, **31**, 397.
28. Z.-X. Liang and J. P. Klinman, *Curr. Opin. Struct. Biol.*, 2004, **14**, 648.
29. A. Maradufu, G. M. Cree and A. S. Perlin, *Can. J. Chem.*, 1971, **49**, 3429.
30. J. W. Whittaker, *Arch. Biochem. Biophys.*, 2005, **433**, 227.
31. N. Ito, S. E. V. Phillips, K. D. S. Yadav and P. F. Knowles, *J. Mol. Biol.*, 1994, **238**, 794.
32. J. Stubbe, M. Ator and T. Krenitsky, *J. Biol. Chem.*, 1983, **258**, 1625.
33. J. M. Mayer, *Annu. Rev. Phys. Chem.*, 2004, **55**, 363.
34. R. I. Cukier, *J. Phys. Chem.*, 1995, **99**, 16101.
35. R. I. Cukier, *J. Phys. Chem.*, 1996, **100**, 15428.
36. R. I. Cukier, *J. Phys. Chem. A*, 1999, **103**, 5989.
37. R. I. Cukier, S. Daniels, E. Vinson and R. J. Cave, *J. Phys. Chem. A*, 2002, **106**, 11240.
38. A. Soudackov and S. Hammes-Schiffer, *J. Chem. Phys.*, 1999, **111**, 4672.
39. A. Soudackov and S. Hammes-Schiffer, *J. Chem. Phys.*, 2000, **113**, 2385.
40. S. Hammes-Schiffer, *Acc. Chem. Res.*, 2001, **34**, 273.
41. S. Hammes-Schiffer, *Acc. Chem. Res.*, 2006, **39**, 93.
42. T. L. Poulos, B. C. Finzel, I. C. Gunsalus, G. C. Wagner and J. Kraut, *J. Biol. Chem.*, 1985, **260**, 16122.
43. T. L. Poulos, B. C. Finzel and A. J. Howard, *J. Mol. Biol.*, 1987, **195**, 687.
44. M. Vidakovic, S. G. Sligar, H. Li and T. L. Poulos, *Biochemistry*, 1998, **37**, 9211.
45. B. Meunier, S. P. de Visser and S. Shaik, *Chem. Rev.*, 2004, **104**, 3947.

46. M. A. Miller, M. Coletta, J. M. Mauro, L. D. Putnam, M. F. Farnum, J. Kraut and T. G. Traylor, *Biochemistry*, 1990, **29**, 1777.
47. S. L. Newmyer and P. R. Ortiz de Montellano, *J. Biol. Chem.*, 1995, **270**, 19430.
48. M. Tanaka, K. Ishimori, M. Mukai, T. Kitagawa and I. Morishima, *Biochemistry*, 1997, **36**, 9889.
49. A. E. Pond, A. P. Ledbetter, M. Sono, D. B. Goodin and J. H. Dawson, in *Electron Transfer in Chemistry*, ed. V. Balzani, Wiley-VCH, Weinheim, Germany, 2001, **vol. 3.1.4**, pp. 56–104.
50. C. W. Hoganson and C. Tommos, *Biochim. Biophys. Acta*, 2004, **1655**, 116.
51. J. S. Vrettos and G. W. Brudvig, *Philos. Trans. R. Soc. Lond. B.*, 2002, **357**, 1395.
52. M. Haumann, P. Liebisch, C. Muller, M. Barra, M. Grabolle and H. Dau, *Science*, 2005, **310**, 1019.
53. C. Tommos and G. T. Babcock, *Acc. Chem. Res.*, 1998, **31**, 18.
54. C. Tommos and G. T. Babcock, *Biochim. Biophys. Acta*, 2000, **1458**, 199.
55. K. N. Ferreira, T. M. Iverson, K. Maghlaoui, J. Barber and S. Iwata, *Science*, 2004, **303**, 1831.
56. S. Iwata and J. Barber, *Curr. Opin. Struct. Biol.*, 2004, **14**, 447.
57. B. Loll, J. Kern, W. Saenger, A. Zouni and J. Biesiadka, *Nature*, 2005, **438**, 1040.
58. T. J. Meyer, M. H. V. Huynh and H. H. Thorp, *Angew. Chem. Int. Ed.*, 2007, **46**, 5284.
59. B. Barry and G. T. Babcock, *Proc. Natl. Acad. Sci. USA*, 1987, **84**, 7099.
60. R. J. Debus, B. A. Barry, G. T. Babcock and L. McIntosh, *Proc. Natl. Acad. Sci. USA*, 1988, **85**, 427.
61. R. J. Debus, B. A. Barry, I. Sithole, G. T. Babcock and L. McIntosh, *Biochemistry*, 1988, **27**, 9071.
62. B. A. Diner, P. J. Nixon and J. W. Farchaus, *Curr. Opin. Struct. Biol.*, 1991, **1**, 546.
63. H.-A. Chu, A. P. Nguyen and R. J. Debus, *Biochemistry*, 1995, **34**, 5839.
64. R. J. Debus, *Biochim. Biophys. Acta*, 2001, **1503**, 164.
65. M. Y. Okamura, M. L. Paddock, M. S. Graige and G. Feher, *Biochim. Biophys. Acta*, 2000, **1458**, 148.
66. M. L. Paddock, G. Feher and M. Y. Okamura, *Biochemistry*, 1997, **36**, 14238.
67. E. Nabedryk, M. L. Paddock, M. Y. Okamura and J. Breton, *Biochemistry*, 2007, **46**, 1176.
68. A. Osyczka, C. C. Moser, F. Daldal and P. L. Dutton, *Nature*, 2004, **427**, 607.
69. E. A. Berry, M. Guergova-Kuras, L.-S. Huang and A. R. Crofts, *Annu. Rev. Biochem.*, 2000, **69**, 1005.
70. A. R. Crofts, M. Guergova-Kuras, R. Kuras, N. Ugulava, J. Y. Li and S. J. Hong, *Biochim. Biophys. Acta*, 2000, **1459**, 456.

71. A. R. Crofts, *Annu. Rev. Physiol.*, 2004, **66**, 689.
72. A. R. Crofts, *Biochim. Biophys. Acta*, 2004, **1655**, 77.
73. J. W. Peters, *Curr. Opin. Struct. Biol.*, 1999, **9**, 670.
74. Y. Nicolet, C. Piras, P. Legrand, C. E. Hatchikian and J. C. Fontecilla-Camps, *Structure*, 1999, **7**, 13.
75. A. Berkessel, *Curr. Opin. Chem. Biol.*, 2001, **5**, 486.
76. J. C. Fontecilla-Camps, A. Volbeda, C. Cavazza and Y. Nicolet, *Chem. Rev.*, 2007, **107**, 4273.
77. D. C. Rees and J. B. Howard, *Curr. Opin. Chem. Biol.*, 2000, **4**, 559.
78. B. K. Burgess and D. J. Lowe, *Chem. Rev.*, 1996, **96**, 2983.
79. T. C. Yang, N. K. Maeser, M. Laryukhin, H. I. Lee, D. R. Dean, L. C. Seefeldt and B. M. Hoffman, *J. Am. Chem. Soc.*, 2005, **127**, 12804.
80. O. Einsle, F. A. Tezcan, S. L. A. Andrade, B. Schmid, M. Yoshida, J. B. Howard and D. C. Rees, *Science*, 2002, **297**, 1696.
81. L. C. Seefeldt, I. Dance and D. R. Dean, *Biochemistry*, 2004, **43**, 1401.
82. C. J. Pickett and J. Talarmin, *Nature*, 1985, **317**, 652.
83. D. V. Yandulov and R. R. Schrock, *Science*, 2003, **301**, 76.
84. J. R. Winkler, D. G. Nocera, K. M. Yocom, E. Bordignon and H. B. Gray, *J. Am. Chem. Soc.*, 1982, **104**, 5798.
85. D. G. Nocera, J. R. Winkler, K. M. Yocom, E. Bordignon and H. B. Gray, *J. Am. Chem. Soc.*, 1984, **106**, 5145.
86. C. Turró, C. K. Chang, G. E. Leroi, R. I. Cukier and D. G. Nocera, *J. Am. Chem. Soc.*, 1992, **114**, 4013.
87. C. Y. Yeh, S. E. Miller, S. D. Carpenter and D. G. Nocera, *Inorg. Chem.*, 2001, **40**, 3643.
88. N. H. Damrauer, J. M. Hodgkiss, J. Rosenthal and D. G. Nocera, *J. Phys. Chem. B*, 2004, **108**, 6315.
89. J. A. Roberts, J. P. Kirby and D. G. Nocera, *J. Am. Chem. Soc.*, 1995, **117**, 8051.
90. J. A. Roberts, J. P. Kirby, S. T. Wall and D. G. Nocera, *Inorg. Chim. Acta*, 1997, **263**, 395.
91. Y. Deng, J. A. Roberts, S. M. Peng, C. K. Chang and D. G. Nocera, *Angew. Chem. Int. Ed. Engl.*, 1997, **36**, 2124.
92. J. P. Kirby, J. A. Roberts and D. G. Nocera, *J. Am. Chem. Soc.*, 1997, **119**, 9230.
93. J. P. Kirby, N. A. van Dantzig, C. K. Chang and D. G. Nocera, *Tetrahedron Lett.*, 1995, **36**, 3477.
94. R. I. Cukier, *J. Phys. Chem.*, 1994, **98**, 2377.
95. X. G. Zhao and R. I. Cukier, *J. Phys. Chem.*, 1995, **99**, 945.
96. J. L. Sessler, B. Wang, S. L. Springs and C. T. Brown, in *Comprehensive Supramolecular Chemistry*, vol. **4**, ed. Y. Murakami, Pergamon Press, Oxford, 1996, pp. 311–336.
97. M. D. Ward, *Chem. Soc. Rev.*, 1997, **26**, 365.
98. V. Y. Shafirovich, S. H. Courtney, N. Ya and N. E. Geacintov, *J. Am. Chem. Soc.*, 1995, **117**, 4920.

99. T. H. Ghaddar, E. W. Castner and S. S. Isied, *J. Am. Chem. Soc.*, 2000, **122**, 1233.
100. C. J. Chang, J. D. K. Brown, M. C. Y. Chang, E. A. Baker and D. G. Nocera, in *Electron Transfer in Chemistry*, ed. V. Balzani, Wiley-VCH, Weinheim, Germany, 2001, **vol. 3.2.4**, pp. 409–461.
101. A. Osuka, R. Yoneshimaj, H. Shiratori, S. Okada, S. Taniguchi and N. Mataga, *Chem. Comm.*, 1998, 1567.
102. J. M. Hodgkiss, N. H. Damrauer, S. Pressé, J. Rosenthal and D. G. Nocera, *J. Phys. Chem. B*, 2006, **110**, 18853.
103. S. Presse and R. Silbey, *J. Chem. Phys.*, 2006, **124**, 164504/1.
104. J. Rosenthal, J. M. Hodgkiss, E. R. Young and D. G. Nocera, *J. Am. Chem. Soc.*, 2006, **128**, 10474.
105. E. R. Young, J. Rosenthal and D. G. Nocera, *Chem. Commun.* 2007, submitted for publication.
106. J. Rosenthal, E. R. Young and D. G. Nocera, *Inorg. Chem.*, 2007, **46**, 8668.
107. C. Y. Yeh, C. J. Chang and D. G. Nocera, *J. Am. Chem. Soc.*, 2001, **123**, 1513.
108. C. J. Chang, L. L. Chang and D. G. Nocera, *J. Am. Chem. Soc.*, 2003, **125**, 1866.
109. L. L. Chng, C. J. Chang and D. G. Nocera, *Org. Lett.*, 2003, **5**, 2421.
110. J. M. Hodgkiss, A. Krivokapic and D. G. Nocera, *J. Phys. Chem. B.*, 2007, **111**, 8258.
111. K. S. Suslick, in *The Porphyrin Handbook*, ed. K. M. Kadish, K. M. Smith and R. Guilard, Academic Press, San Diego, 2000, **Vol. 4**, pp. 41–63.
112. A. E. Pond, A. P. Ledbetter, M. Sono, D. B. Goodin and J. H. Dawson, in *Electron Transfer in Chemistry*, ed. V. Balzani, Wiley-VCH, Weinheim, Germany, 2001, **vol. 3.1.4**, pp. 56–104.
113. *Cytochrome P-450 Structure, Mechanism and Biochemistry*, 2nd edn, ed. P. R. Ortiz de Montellano, Plenum Press, New York, 1995.
114. T. L. Poulos and R. E. Fenna, In *Metal Ions in Biological Systems*, ed. H. Sigel and A. Sigel, Dekker, New York, 1994, **Vol. 30**, pp. 25–75.
115. J. N. Rodriguez-Lopez, D. J. Lowe, J. Hernandez-Ruiz, A. N. P. Hiner, F. Garcia-Canovas and R. N. F. Thorneley, *J. Am. Chem. Soc.*, 2001, **123**, 11838.
116. B. Meunier, in *Biomimetic Oxidations Catalyzed by Transition Metal Complexes*, ed. B. Meunier, Imperial College, London, 2000, pp. 171–214.
117. M. Sono, M. P. Roach, E. D. Coulter and J. H. Dawson, *Chem. Rev.*, 1996, **96**, 2841.
118. I. G. Denisov, T. M. Makris, S. G. Sligar and I. Schlichting, *Chem. Rev.*, 2005, **105**, 2253.
119. H. B. Dunford, *Heme Peroxidases*, Wiley, New York, 1999.
120. Y. Watanabe, In *The Porphyrin Handbook*, ed. K. M. Kadish, K. M. Smith and R. Guilard, Academic Press, San Diego, 2000, **Vol. 4**, pp. 97–117.

121. M. Newcomb, R. Zhang, R. E. P. Chandrasena, J. A. Halgrimson, J. H. Horner, T. M. Makris and S. G. Sligar, *J. Am. Chem. Soc.*, 2006, **128**, 4580.
122. N. C. Veitch and A. T. Smith, *In Advances in Inorganic Chemistry*, Academic Press, New York, 2001, **Vol. 51**, pp. 107–162.
123. M. Newcomb and R. E. P. Chandrasena, *Biochem. Biophys. Res. Commun.*, 2005, **338**, 394.
124. R. Davydov, S. Chemerisov, D. E. Werst, T. Rajh, T. Matsui, M. Ikeda-Saito and B. M. Hoffman, *J. Am. Chem. Soc.*, 2004, **126**, 15960.
125. A. N. P. Hiner, E. L. Raven, R. N. F. Thorneley, F. Garcia-Canovas and J. N. Rodriguez-Lopez, *J. Inorg. Biochem.*, 2002, **91**, 27.
126. S.-I. Ozaki, M. P. Roach, T. Matsui and Y. Watanabe, *Acc. Chem. Res.*, 2001, **34**, 818.
127. T. L. Poulos and J. Kraut, *J. Biol. Chem.*, 1980, **255**, 8199.
128. T. Matsui, S.-I. Ozaki, E. Lioung, G. N. Phillips and Y. Watanabe, *J. Biol. Chem.*, 1999, **274**, 2838.
129. E. Derat and S. Shaik, *J. Phys. Chem. B*, 2006, **110**, 10526.
130. T. L. Poulos, In *Advances in Inorganic Biochemistry*; ed. G. L. Eichhorn and L.G. Marzilli, Elsevier, New York, 1988, **Vol. 7**, pp. 1–36.
131. J. H. Dawson, *Science*, 1988, **240**, 433.
132. H. A. Heering, C. Indiani, G. Regelsberger, C. Jakopitsch, C. Obinger and G. Smulevich, *Biochemistry*, 2002, **41**, 9237.
133. I. Fita and M. G. Rossmann, *J. Mol. Biol.*, 1985, **185**, 21.
134. M. T. Green, J. H. Dawson and H. B. Gray, *Science*, 2004, **304**, 1653.
135. M. T. Green, *J. Am. Chem. Soc.*, 2006, **128**, 1902.
136. R. K. Behan and M. T. Green, *J. Am. Chem. Soc.*, 2006, **128**, 11471.
137. J. T. Groves and Y. Watanabe, *J. Am. Chem. Soc.*, 1988, **110**, 8443.
138. K. Yamaguchi, Y. Watanabe and I. Morishima, *J. Am. Chem. Soc.*, 1993, **115**, 4058.
139. T. G. Traylor and J. P. Ciccone, *J. Am. Chem. Soc.*, 1989, **111**, 8413.
140. W. Nam, M. H. Lim and S.-Y. Oh, *Inorg. Chem.*, 2000, **39**, 5572.
141. Y. Watanabe and T. Ueno, *Bull. Chem. Soc. Jpn.*, 2003, **76**, 1309.
142. T. M. Makris, K. von Koenig, I. Schlichting and S. G. Sligar, *Biochemistry*, 2007, **46**, 14129.
143. J. D. Soper, S. V. Kryatov, E. V. Rybak-Akimova and D. G. Nocera, *J. Am. Chem. Soc.*, 2007, **129**, 5069.
144. J. Rosenthal, L. L. Chng, S. D. Fried and D. G. Nocera, *Chem. Commun.*, 2007, 2642.
145. J. Y. Yang, J. Bachmann and D. G. Nocera, *J. Org. Chem.*, 2006, **71**, 8706.
146. S.-Y. Liu and D. G. Nocera, *Tetrahedron Lett.*, 2006, **47**, 1923.
147. S.-Y. Liu and D. G. Nocera, *J. Am. Chem. Soc.*, 2005, **127**, 5278.
148. S.-Y. Liu, J. D. Soper, J. Y. Yang, E. V. Rybak-Akimova and D. G. Nocera, *Inorg. Chem.*, 2006, **45**, 7572.
149. J. Y. Yang and D. G. Nocera, *J. Am. Chem. Soc.*, 2007, **129**, 8192.

150. A. Jordan and P. Reichard, *Annu. Rev. Biochem.*, 1998, **67**, 71.
151. J. Stubbe and P. Riggs-Gelasco, *Trends Biochem. Sci.*, 1998, **23**, 438.
152. U. Uhlin and H. Eklund, *Nature*, 1994, **370**, 533.
153. P. Nordlund, B.-M. Sjöberg and H. Eklund, *Nature*, 1990, **345**, 593.
154. M. Högbom, M. Galander, M. Andersson, M. Kolberg, W. Hofbauer, G. Lassmann, P. Nordlund and F. Lendzian, *Proc. Natl. Acad. Sci.*, 2003, **100**, 3209.
155. I. Climent, B.-M. Sjöberg and C. Y. Huang, *Biochemistry*, 1992, **31**, 4801.
156. M. Sahlin, G. Lassmann, S. Pötsch, B.-M. Sjöberg and A. Gråslund, *J. Biol. Chem.*, 1995, **270**, 12361.
157. B. Katterle, M. Sahlin, P. P. Schmidt, S. Pötsch, D. T. Logan, A. Gråslund and B.-M. Sjöberg, *J. Biol. Chem.*, 1997, **272**, 10414.
158. M. Ekberg, S. Pötsch, E. Sandin, M. Thunnissen, P. Nordlund, M. Sahlin and B.-M. Sjöberg, *J. Biol. Chem.*, 1998, **273**, 21003.
159. S. E. Parkin, S. Chen, B. A. Ley, L. Mangravite, D. E. Edmondson, B. H. Huynh and J. M. Bolliger Jr., *Biochemistry*, 1998, **37**, 1124.
160. T. W. Muir, *Annu. Rev. Biochem.*, 2003, **72**, 249.
161. C. S. Yee, M. C. Y. Chang, J. Ge, D. G. Nocera and J. Stubbe, *J. Am. Chem. Soc.*, 2003, **125**, 10506.
162. M. R. Seyedsayamdst, C. S. Yee, S. Y. Reece, D. G. Nocera and J. Stubbe, *J. Am. Chem. Soc.*, 2006, **128**, 1562.
163. C. S. Yee, M. R. Seyedsayamdst, M. C. Y. Chang, D. G. Nocera and J. Stubbe, *Biochemistry*, 2003, **42**, 14541.
164. M. R. Seyedsayamdst and J. Stubbe, *J. Am. Chem. Soc.*, 2006, **128**, 2522.
165. M. C. Y. Chang, C. S. Yee, D. G. Nocera and J. Stubbe, *J. Am. Chem. Soc.*, 2004, **126**, 16702.
166. M. R. Seyedsayamdst, S. Y. Reece, D. G. Nocera and J. Stubbe, *J. Am. Chem. Soc.*, 2006, **128**, 1569.
167. S. Y. Reece, J. Stubbe and D. G. Nocera, *Biochim. Biophys. Acta*, 2005, **1706**, 232.
168. P. Nordlund and H. Eklund, *J. Mol. Biol.*, 1993, **232**, 123.
169. J. M. Bollinger Jr., D. E. Edmonson, B. H. Huynh, J. Filley, J. R. Norton and J. Stubbe, *Science*, 1991, **253**, 292.
170. J. M. Bollinger Jr., W. H. Tong, N. Ravi, B. H. Huynh, D. E. Edmondson and J. Stubbe, *J. Am. Chem. Soc.*, 1994, **116**, 8024.
171. J. Baldwin, C. Krebs, B. A. Ley, D. E. Edmondson, B. H. Huynh and J. M. Bollinger Jr., *J. Am. Chem. Soc.*, 2000, **122**, 12195.
172. C. Krebs, S. Chen, J. Baldwin, B. A. Ley, U. Patel, D. E. Edmondson, B. H. Huynh and J. M. Bollinger Jr., *J. Am. Chem. Soc.*, 2000, **122**, 12207.
173. U. Rova, K. Goodtzova, R. Ingemarsson, G. Behravan, A. Gråslund and L. Thelander, *Biochemistry*, 1995, **34**, 4267.
174. J. Ge, G. Yu, M. A. Ator and J. Stubbe, *Biochemistry*, 2003, **42**, 10071.
175. J. Xie and P. G. Schultz, *Nat. Rev. Mol. Cell Biol.*, 2006, **7**, 775.
176. M. R. Seyedsayamdst, J. Xie, C. T. Y. Chan, P. G. Schultz and J. Stubbe, *J. Am. Chem. Soc.*, 2007, **129**, 15060.
177. I. Climent, B.-M. Sjöberg and C. Y. Huang, *Biochemistry*, 1990, **30**, 5164.

178. S. Y. Reece, M. R. Seyedsayamdst, J. Stubbe and D. G. Nocera, *J. Am. Chem. Soc.*, 2007, **129**, 8500.
179. S. Y. Reece and D. G. Nocera, *J. Am. Chem. Soc.*, 2005, **127**, 9448.
180. S. Y. Reece, M. R. Seyedsayamdst, J. Stubbe and D. G. Nocera, *J. Am. Chem. Soc.*, 2006, **128**, 13654.
181. C. Constantine, M. Robert and J.-M. Savéant, *J. Am. Chem. Soc.*, 2007, **129**, 9953.
182. T. Irebo, S. Y. Reece, M. Sjödin, D. G. Nocera and L. Hammarström, *J. Am. Chem. Soc.*, 2007, **129**, 15462.
183. P. Reichard, *Trends Biochem. Sci.*, 1997, **22**, 81.
184. S. S. Licht, G. J. Gerfen and J. Stubbe, *Science*, 1996, **271**, 477.
185. M. Eriksson, U. Uhlin, S. Ramaswamy, M. Ekberg, K. Regnström, B.-M. Sjöberg and H. Eklund, *Structure*, 1997, **5**, 1077.
186. M. Lee, M. J. Shephard, S. M. Risser, S. Priyadarshy, M. N. Paddon-Row and D. N. Beratan, *J. Phys. Chem. A.*, 2000, **104**, 7593.
187. S. Y. Reece, M. R. Seyedsayamdst, J. Stubbe and D. G. Nocera, *J. Am. Chem. Soc.*, 2007, **129**, 13828.

Subject Index

Note: page numbers in *italic* refer to figures or tables.

- AADH *see* aromatic amine hydrogenase
acetate ion 121–3
activation energy 2
 DFT calculations 30–1
 differences between isotopologues 163, *164*
 free-energy analysis of enzyme system 4–7, 98–9
 and nuclear-motion quantum effects 64
activation entropy 13
active dynamics 183–4
 see also gating
active site geometries/crowding 149, 152–3, 157
adenosylcobalimin 305–6
adenosylhomocysteine hydrolase 298–9
ADH *see* alcohol dehydrogenases
adiabatic hydrogen transfer vii, 89–94
 dihydrofolate reductase study 94–7
Alcaligenes faecalis 278
alcohol dehydrogenases (ADH) 55–6, 64, *133*
 Arrhenius-behaviour deviations 143–5
 crowding and active site geometry 149
 model reactions 298–304
 reviews of studies 174–5, 193–4
 Swain–Schaad relationships 142–3
AMBER force field 220–2
amidinium derivatives 352, 353, 355, 356
amino-acid radical 345, 348
anthracene hydroxylation 31–2
aromatic amine dehydrogenase (AADH) 201–3
QM/MM simulation 226–8
 dihydrofolate reductase compared 235–8
 H-tunnelling step 229–32
 role of promoting motions 232–3
 reaction mechanism 227
X-ray crystallographic studies 278–84
Arrhenius behaviour 139–42, 143–4, 154, 172–4, 182
association constants 13
atomic orbitals 21
B-factor 270–1, 272–3, 274, 275–6
B3LYP method 29–33, 119
Bacillus stearothermophilus ADH 194, 302, 303
 DHFR 188, 192
Bacillus subtilis 97
Bell correction/model 136–7, 161, 180–1, 201, 204
Bell, R. P. vii
benzene hydroxylation 31–2
benzyl alcohol oxidation 204
Bigeleisen equation 163
Born–Oppenheimer Approximation 22, 220, 316
bovine serum amine oxidase 141
BQCP sampling technique 112, 120
breakpoint temperature x–xiii, 183, 210
Bruno–Bialek model 141

- canonical variational theory 40–2, 51
carbon–hydrogen bond activation *see* hydrogen transfer reactions
catalytic power 292–3, 303–4, 309–10
catalytic proficiency 4
centroid path integral simulations *see* hybrid classical and quantum path; quantum classical path
CHARMM force field 220, 221–2
application to AADH 226–35
chloroacetic acid 126
chorismate mutase enzymes 8–10
compound I/II 358–9
compression effect 262
computational methods, overviews of 18–19, 22–34, 36–9, 106–7, 243–6
configuration interaction (CI) theory 25
configurational-search framework 294, 310
conformation/configuration 10, 15, 67, 133–4, 268
active/passive dynamics defined 183–4
conformational sampling 79–80, 148–9, 155–6
long-distance electron tunnelling 339–41
single molecule fluorescence measurements 213–15
see also gating; preorganisation
coupling and coupled motion 168
see also proton-coupled electron transfer; vibronic coupling
covalent catalysis 13–14
cytochrome P450 349, 358, 359
DFT calculations 30–1
- Debye–Waller temperature factor 275
density functional theory (DFT) 18–19, 28–30
free energy of activation 30–1
kinetic isotope calculations 31–2
DHFR *see* dihydrofolate reductase
dielectric continuum vi, 82
dihydrofolate reductase (DHFR) x, 94–7, 186–8
conformations 56
coupling compared to AADH 235–8
experimental studies 186–7
- hybrid quantum/classical molecular-dynamics approach 94–7
mutants temperature dependence of KIE 248–56
studies reviewed 175
Bacillus stearothermophilus 192
Escherichia coli 187, 188–92
Thermotoga maitima 192–3
direct methods *see* experimental methods
donor–acceptor distance 88, 244, 257–9, 261
dynamical bottleneck 38
- EA-VTST *see* ensemble-averaged EA-VTST/MT 224–5
Eigen, M. vi
electron transfer historical overview v–vi
see also electron tunnelling; proton-coupled electron transfer
electron tunnelling in proteins 145, 208, 211, 314–15
electronic coupling and tunnelling pathways 315–17
many electron formulation 328, 331
correlation effects 335–6
electron *vs* hole transfer 338–9
limitation of self-consistent-field description 334–5
one tunnelling orbital approximation 333–4
polarisation effects 333–4, 335–6
protein dynamics 211, 339–41
quantum interference/vortices 336–8
superexchange methods avoided crossing 317–18
direct method 317
generalised Mulliken–Hush method 319–20
Koopman’s theorem 318
propagator method 320
protein pruning 322–3
tunnelling currents method 324–7
current density/Hartree–Fock approximation 328–9
interatomic tunnelling currents 329–31

- electron-density maps 270–5
 electronic tunnelling matrix element 316
 electronic-structure calculations 22–7
 electronically adiabatic proton-transfer
 90–7
 electrostatic stabilisation 11, 13
 empirical valence bond method (EVB)
 90, 92, 223, 244–8
 ensemble-averaged variational transition-state theory (EA/VTST) 39, 51–5, 106
 with multidimensional tunnelling
 (EA-VTST/MT) 224–5
 entropy, activation 13
 environmental coordinates 38–9
 environmentally coupled tunnelling,
 definition of 168
 see also vibronic coupling
 enzyme activity
 catalytic power 292–3, 303–4, 309–10
 overviews 97–100, 242–4, 268–9
 equilibrium isotope effects 163, 171
 equilibrium secondary zone 54
Escherichia coli 361
 DHFR 97, 187, 188–92
 EVB *see* empirical valence bond method
 experimental methods 184–6, 194–5
 case studies
 alcohol dehydrogenases 193–4
 dihydrofolate reductases 186–93
 competitive *vs* noncompetitive
 measurements 168–9, 186
 mixed-labelling experiments 169–70
- Feynman path integral 106–7, 107–9, 245
 Finke model reaction 305–8
 fluorescence spectroscopy 95, 215
 fluorotyrosine derivatives 362
 Fock matrix 23–4
 force fields 220–2
 Franck–Condon expression vi, vii,
 145, 146, 147, 247
 and pressure dependence 208
 free-energy of activation *see*
 activation energy
 free-energy perturbation theory 112–13
 frequency calculations 27
- full tunnelling models 132–6, 199–203
 aspects of tunnelling correction
 Arrhenius plots 139–42
 Bell correction 136–7
 Swain-Schaad relationship 137–9
 focus on kinetic isotope effect 134–5
 simple physical model 145–9
 soybean lipoxygenase study 149–57
- galactose oxidase 348
 gating 141, 153, 175, 203, 206, 211
 defined 183–4
 viscosity as probe 211–12
 generalised orbital method 222–3
 glucose oxidase 211, 212
 Grote-Hynes transition coefficient 109
 ground-state, destabilisation of 8–11
- Hamilton operator 20, 37
 hangman porphyrin architecture 357–60
 Hartree–Fock theory 22–3
 and electron tunnelling 328–9, 335–6
 Heisenberg Uncertainty Principle
 19–20
- hybrid classical and quantum path
 integral computations 105–7, 246
 centroid path integral simulations
 110–12, 126
 computational details 119–20
 estimating kinetic isotope effects
 111–16
 path integral quantum transition-state theory 107–9
- potential-energy surface 116
 combined QM/MM potentials
 116–18
 MOVB potential 118–19
- study examples
 decarboxylation of *N*-methyl
 Picolate 123–6
 proton tranfer/chloroacetic acid
 and methoxystyrenes 126
 proton tranfer/nitroethane and
 acetate ion 121–3
- hydration 8, 11
 hydride transfer *see* hydrogen transfer

- hydrogen bonds 11–13
hydrogen transfervii–xiii
adiabatic nature 89–90
common pathways 131, 132
coupling and coupled motion 168, 183
hydrogen atom 62, 347–8
importance of quantum effects 67,
105, 161–2
methods of study 132–5
as rate-limiting step 165–7
- inelastic tunnelling 341
isoinertial coordinates 48–9
isotope effect *see* kinetic isotope
effect
isotopologues 163
- kinetic complexity 165–8
kinetic isotope effects (KIE) vii, ix–xii
basic concepts/definitions 162–3, 180
intrinsic *vs* observed KIE 134, 166–7
primary *vs* secondary KIE 163–5
coupling and coupled motion 168,
183, 201
DFT calculations 31–2
experimental methods 184–6
competitive *vs* noncompetitive
measurements 168–9
mixed-labelling experiments 169–70
kinetic complexity 165–8
pressure dependence 203–9
as probe for tunnelling 170–4, 180–2
effects categorised 294–8
secondary KIE 171–2, 209–10
test cases reviewed 174–6, 186–94
reliable/not reliable interpretation of
256–64, 309
semiclassical origin of 135–6
temperature dependence *see*
temperature dependence
Kirby–Walwyn model reaction 298–300
Kleinert’s variational perturbation
theory 111, 113–15, 127
Koopman’s theorem 318, 331
Kramers model 212
Kuznetsov–Ulstrup model 201
- lactate dehydrogenase 298, 299
Laplacian 20–2
large-curvature tunnelling 43–5, 50–1,
225
Laue crystallography 278
LCAO 25–6
Lee, Yang and Parr (LYP) correlation
functional 29
Lewis resonance structures 118
linear combination of atomic orbitals
(LCAO) 25–6
linear response theory 85
lipoxygenase *see* soybean lipoxygenase
liver alcohol dehydrogenase 55–6, 64
local self-consistent field 222–3
long-distance electron tunnelling *see*
electron tunnelling
LSCF method 222
LYP correlation functional 29
- many-electron formulation 328, 331–9
mapping potentials 93
Marcus-like models 161–2, 176, 200–1,
211
critically discussed 262
and full tunnelling behaviour 145–9
MCM *see* methylmalonyl coenzyme
methoxystyrenes 126
methylamine dehydrogenase 65, 229,
278–9
methylmalonyl-CoA mutase (MCM)
304–5
catalytic power 309–10
enzymic tunnelling 308–9
model reactions 304–5
nonenzymic tunnelling (Fink model)
305–8
Michaelis complex 275
Michaelis–Menten formulation 3
minimum energy path 40–1, 43, 49,
52, 225
aromatic amine dehydrogenase 233
mixed-labelling experiments 169–70
MM/QM computations *see* quantum-
mechanical/molecular-
mechanical

- model reactions
 background and definitions 291–4
 classified/categorised isotope effects 294–8
 configurational-search framework 294, 310
 hydride transfer in alcohol dehydrogenase 298, 310, 311
 catalytic power 303–4
 enzymic tunnelling 301–2
 intramolecular model reaction (Kirby–Walwyn) 298–300
 tunnelling model (Powell–Bruice) 300–1
 hydrogen-atom transfer in methyl-malonyl-CoA mutase 304–5, 311
 enzymatic tunnelling 308–9
 nonenzymic tunnelling (Finke model) 305–8
 model systems in PCET
 bidirectional networks 357–60
 unidirectional networks 351–6
 molecular dynamics
 analysing trajectories 225–6
 with quantum transitions (MDQT) 93
 molecular orbital/valence-bond theory 106, 118–19
 molecular orbitals 25–6
 molecular-mechanics 18, 32–4, 55, 90, 106, 220–2
see also quantum-mechanical/molecular-mechanical simulations
 Møller–Plesset theory 25
 morphinone reductase 205–7, 210, 212, 213
 multiple reactive configurations 213–15
 X-ray crystallographic studies 284–6
 motion-coupled tunnelling *see* coupling
 MOVB theory 106, 118–19
 MQCMD method 225
 Mulliken–Hush method 319–20
 multidimensional tunnelling 36, 38, 47–51
 multistate continuum theory 82, 86, 87
 mutagenesis, site-directed/specific 14, 151
 near-attack conformations 10, 244
 nitroethane 121–3
 nitrogenase 351
 nonadiabatic reactions vii
 proton-coupled electron transfer 80–5
 application to lipoxygenase 85–9
 nonenzymic reactions *see* model reactions
 nonenzymic tunnelling 305–8, 310
 Northrop method 167–8, 186, 204
 nuclear quantum effects 64, 105–6, 111, 243–4, 246–7
 one tunnelling orbital approximation 333–4
 one-dimensional tunnelling 45–6
 oxidases 133, 141, 211, 348, 349, 358
 oxygen-evolving complex 349, 350
 oxygenases 32–3, 348, 349, 358
see also soybean lipoxygenase
 passive dynamics 183–4, 210
see also preorganisation
 path integral computations *see* hybrid classical and quantum path; quantum classical path
 PCET *see* proton-coupled electron transfer
 pentaerythritol tetranitrate reductase 210
 Perdew and Wang (PW9) correlation functional 29
 phenylalanine oxidase 211
 photoRNR methods 364–8
 photosystem (II) 349, 350
 PI-FEP/UM method *see* hybrid classical and quantum path
 integral computations
 Planck's constant 19
 PMF *see* potential of mean force
 polarisation effects 333–4
 POLYRATE program 225
 porphyrins 352, 353, 355, 357–60
 potential energy surface calculation 224
 potential of mean force (PMF) 44, 53, 119, 224, 248, 260
 Powell–Bruice model reaction 300–1

- preorganisation 148–9, 243, 263, 303
defined 183–4
work term viii–ix
- prephenate 8–10
- pressure dependence 203
alcohol dehydrogenase 203–5
morphine reductase 205–8
- primary–secondary coupling 168
- propagator method 320–2
- protein pruning 322–3
- proton transfer *see* hydrogen transfer
- proton-coupled electron transfer (PCET) vii
- background and summaries 80–1, 97–100, 345–7, 370
bidirectional processes 348–51
unidirectional processes 347–8
- model systems 351
bidirectional networks 357–60
hangman porphyrin architecture 357–60
unidirectional networks 351–6
- ribonucleotide reductase study 360–1
 α_2 subunit 364–8
 β_2 subunit 361–4
radical transfer model 368–9
- vibronically noadiabatic reactions
general theoretical formulation 81–5
lipoxygenase study 85–9
- purine nucleoside phosphorylase 105
- PW9 correlation functional 29
- QCP method *see* quantum classical path centroid integral
- QM/MM simulations *see* quantum-mechanical/molecular-mechanical
- QTST approach 107–9
- quantised vortices 336–8
- quantum classical path centroid integral simulations (QCP) 107, 111, 245–8
- conclusions about tunnelling 256–64
- KIE temperature effects 248–56
- see also* hybrid classical and quantum path integral
- quantum effects overview 161–76
- quantum path integral computations
see hybrid classical and quantum path; quantum classical path
- quantum-mechanical/molecular-mechanical (QM/MM) simulations 90, 219–20
- analysing molecular dynamics trajectories 225–6
- empirical valence bond method 90, 92, 244–8
- improving semi-empirical QM calculations 223
- molecular-mechanics/force fields 220–2
- potential energy/free energy surfaces 224
- simulation of hydrogen tunnelling event 224–5
- tunnelling rates and kinetic isotope effects 225
- quantum-mechanics
basic principles of 18–34
incorporating into transition-state theory 37–9
quench-flow techniques 186
- R-factor 273
- radical mechanisms/transport 345, 346
- Ramachandran plots 275
- rate limiting steps 165–8, 184–5, 195
- rate, reaction vii–viii
free energies and thermodynamic cycle 5–6
quantifying enzymic acceleration 292–3
for unimolecular conversion of substrate 2–3
- reagent coordinates 38–9
- reorganisation 263
- Rhodobacter sphaeroides* 349
- ribonucleotide reductase 348, 351
PCET study 360–1
 α_2 subunit 364–8
 β_2 subunit 361–4
radical transport model 368–9
- ring-of-beads technique 112

- saddle points 38–9, 51
 Schrödinger Equation 20–1
 secondary KIE 143, 163–4, 171–2, 209–10
 self-consistent field 222–3
 and electron tunnelling 318, 334–5
 serine proteases 11–13
 simulations *see* computational methods
 single-molecule measurements 213–15
 site-directed/specific mutagenesis 14, 151
 Slater exchange function 28–9
 Slater-type orbitals 25
 small-curvature tunnelling 43–5, 50–1, 225
 solvation 6, 8, 11
 soybean lipoxygenase x
 isotopic properties of catalysis 149–50
 mechanism 133
 proton-coupled electron transfer 85–9, 98–9
 simulations discussed/contrasted 255–6
 temperature dependence of KIE 60–1, 150–7, 260
 specific reaction parameter 223
 static secondary zone 52–4
 steady-state measurements 186, 195
 stopped-flow technique 185–6
 with pressure variation 205–7
 styrene epoxidation 30–1
 superexchange methods 316–24
 Swain–Schaad relationship 134–5, 164–5
 and Northrop method 167–8
 probing for tunnelling 137–9, 142–3, 171–2
 taurine dioxygenase (TauD) 32–3
 temperature dependence of KIE x–xiii, 172–4, 181–2, 201–2
 categorised as
 overdependent tunnelling 294, 295, 297–8
 traditionally dependent 294, 295, 296
 underdependent 294, 295, 296–7
 reliability of interpretations discussed 256–64
 and simple model for tunnelling 143–4, 146–8, 155, 157
 thermodynamic circle 4, 5
- Thermotoga maritima* DHFR 58–9, 188, 192–3
 thymidylate synthase 176
 TIP3P model 119
 transient-state measurements 186, 195
 transition-state theory (classical) v–viii, 1–2, 179
 enzyme flexibility and dynamics 14–15
 free-energy analysis 4–7
 incorporating quantum-mechanical effects 37–8
 rate and rate constants 2–4
 transition structures
 conformations 9–10
 selective stabilisation 11–14
 stabilisation of vs ground-state destabilisation 8–11
 translation-libration-screw (TLS) 276
 transmission coefficient 38, 42–3, 62–3
 Bigeleisen equation 163
 multidimensional tunnelling 47–51
 one-dimensional tunnelling 45–6
 triosephosphate isomerase 65
 tryptamine oxidation 201–3
 tunnelling 45
 multi-dimensional 47–51
 nonenzymic 305–8, 310
 one-dimensional 45–6
 significance in enzymatic reactions 182–4
 tunnelling currents method 324–7
- umbrella sampling 107, 111–13, 224
- valence bond terms *see* empirical valence bond
 variational transition-state theory (VTST) 18, 38–9, 106, 224–5
 applications
 aromatic amine dehydrogenase 226–38
 dihydrofolate reductase 56–60
 liver alcohol dehydrogenase 55–6, 64
 methylmalonyl-CoA mutase 60–2, 63, 64

- soybean-lipoxygenase-1 60–1
summary of literature/perspectives 62–6
ensemble averaging 51–5
gas-phase theory 39–42
quantum-mechanical rate theory 67
transmission coefficient 42–5
 multi-dimensional tunnelling 47–51
 one-dimensional tunnelling 45–6
vibronic coupling 15, 36, 168
 active and passive dynamics compared 183–4
computational approaches discussed 243, 259–62
long- and short-range motions 235–8
modelling 200–3
 pressure effect 205–9
role of promoting motions analysed 232–5
and temperature independence 201–3, 257
vibronically noadiabatic reactions 97–100
viscosity effects 211–13
Visual Molecular Dynamics 225
- vortex structure, quantised 336–8
Vosko–Wilk–Nusair correlation 28–9
VTST *see* variational transition-state theory
- Wentzel–Kramers–Brillouin (WBK) approximation 45–6
Westheimer model 135–6
- X-ray crystallography 268–9, 286
 and AADH 226
accuracy of structures/electron-density maps 270–5
dynamic information 275–8
study examples 278
 aromatic amine dehydrogenase 278–84, 286
 morphinone reductase 284–6
- yeast alcohol dehydrogenase 203–5
- zero-curvature tunnelling 42–3, 49
zero-point energy 26–7, 36, 161, 180, 163, 164
Zn(II) porphyrin 357